

# **Developing SABRE as an analytical tool in NMR**

Lyrelle Stacey Lloyd

A thesis submitted for the degree of doctor of philosophy

Department of Chemistry

University of York

March 2013

## Abstract

Work presented in this thesis centres around the application of the new hyperpolarisation technique, SABRE, within nuclear magnetic resonance spectroscopy, focusing on optimisation of the technique to characterise small organic molecules. While pyridine was employed as a model substrate, studies on a range of molecules are investigated including substituted pyridines, quinolines, thiazoles and indoles are detailed.

Initial investigations explored how the properties of the SABRE catalyst effect the extent of polarisation transfer exhibited. The most important of these properties proved to be the rate constants for loss of pyridine and hydrides as these define the contact time of pyridine with the *parahydrogen* derived hydride ligands in the metal template. The effect of changing the temperature, solvent or concentration of substrate or catalyst are rationalised. For instance, the catalyst **ICy(a)** exhibits relatively slow ligand exchange rates and increasing the temperature during hyperpolarisation increases the observed signal enhancements.

These studies have revealed a second polarisation transfer template can be used with SABRE in which two substrate molecules are bound. This allows the possibility of investigation of larger substrates which might otherwise be too sterically encumbered to bind.

Another significant advance relates to the first demonstration that SABRE can be used in conjunction with an automated system designed with Bruker allowing the acquisition of scan averaged, phase cycled and traditional 2D spectra. The system also allowed investigations into the effect of the polarisation transfer field and application of that knowledge to collect single-scan  $^{13}\text{C}$  data for characterisation. The successful acquisition of  $^1\text{H}$  NOESY,  $^1\text{H}$ - $^1\text{H}$  COSY,  $^1\text{H}$ - $^{13}\text{C}$  2D and ultrafast  $^1\text{H}$ - $^1\text{H}$  COSY NMR sequences is detailed for a 10 mM concentration sample, with  $^1\text{H}$  data collected for a 1 mM sample.

A range of studies which aim to demonstrate the applicability of SABRE to the characterisation of small molecules and pharmaceuticals have been conducted.

## Table of Contents

Developing SABRE as an analytical tool in NMR .....	1
Abstract .....	2
Table of Contents .....	3
List of Figures .....	20
List of Tables.....	44
List of Equations .....	53
Acknowledgements .....	54
Declaration .....	55
1 Chapter 1 – Introduction .....	56
1.1 NMR spectroscopy .....	56
1.1.1 NMR spectroscopy.....	57
1.1.2 Increasing sensitivity of NMR through instrumental developments .....	58
1.2 Hyperpolarisation in NMR.....	60
1.2.1 Hyperpolarisation.....	60
1.2.2 Brute force.....	60
1.2.3 Optical pumping.....	62
1.2.3.1 Optical pumping in NMR .....	63
1.2.3.2 Optical pumping in MRI.....	66
1.2.4 Dynamic nuclear polarisation .....	68
1.2.5 <i>Parahydrogen</i> induced polarisation .....	71

	4
1.2.5.1	<i>Parahydrogen</i> applied to NMR spectroscopy ..... 71
1.2.5.2	Inorganic applications of PHIP ..... 74
1.2.5.3	Biological applications of PHIP ..... 75
1.2.5.4	Comparison of PASADENA and ALTADENA..... 78
1.2.6	Signal amplification by reversible exchange ..... 79
1.2.6.1	Introduction to SABRE..... 79
1.2.6.2	Theory behind transfer..... 80
1.2.6.3	The phosphine ligand vs. the carbene ligand..... 81
1.2.6.4	Phosphine-based catalysts..... 81
1.2.6.5	Crabtree's catalyst applied to SABRE..... 84
1.2.6.6	Carbene-based catalysts..... 87
1.2.6.7	Carbene-analogues of Crabtree's catalyst applied to SABRE..... 89
1.2.7	Only <i>Parahydrogen</i> SpectroscopY (OPSY) ..... 90
1.2.7.1	Introduction to OPSY ..... 90
1.3	Experimental considerations ..... 90
1.3.1	Production of <i>parahydrogen</i> ..... 90
1.3.2	Description of observed signals ..... 91
1.3.3	NMR described in terms of product operators..... 93
1.3.3.1	Introduction to product operator terms <sup>85</sup> ..... 93
1.3.3.2	Using product operators to understand <i>parahydrogen</i> induced polarisation (PHIP) ..... 96



1.3.3.3	Using product operators to understand the $^1\text{H}$ OPDY NMR sequences <sup>86</sup> .....	97
1.4	Thesis aims .....	97
2	Chapter 2 - Catalyst synthesis .....	101
2.1	Introduction .....	101
2.1.1	Required properties of a SABRE catalyst .....	101
2.1.2	Literature based SABRE results in which phosphine-based catalysts are used .....	102
2.1.3	Progression from phosphine-based SABRE catalysts to carbene-based SABRE catalysts .....	104
2.1.4	Literature-based SABRE results in which carbene-based catalysts are used .....	107
2.2	Experimental considerations .....	107
2.2.1	Terminology .....	107
2.2.1.1	SABRE using an NMR tube – the shake method (method 1) .....	107
2.2.1.2	SABRE using a flow probe – the flow method (method 2) .....	108
2.2.1.3	Comparison of method 1 to method 2 .....	111
2.2.1.4	Considerations when discussing the effect of the magnetic field of polarisation .....	112
2.2.1.5	Effect of changing the sign of magnetic field of polarisation on resultant $^1\text{H}$ NMR spectra .....	113
2.2.1.6	Calculation of enhancements .....	114
2.2.1.7	Catalyst forms .....	115

2.2.2	Effect of method 1 on the resultant $^1\text{H}$ NMR spectra obtained without incorporation of enriched <i>parahydrogen</i> .....	116
2.2.3	Reproducibility of NMR spectra when SABRE is implemented.....	118
2.2.3.1	Reproducibility of method 1 .....	118
2.2.3.2	Reproducibility of method 2.....	119
2.2.4	Mechanism of activation of SABRE catalysts.....	120
2.2.5	Mechanism of reversible exchange of active species .....	122
2.3	Effect of changing the carbene ligand on polarisation transfer efficiency .....	123
2.3.1	Synthesis .....	124
2.3.2	Comparison of structural properties.....	124
2.3.2.1	Comparison of TEP, cone angle and buried volume of PCy <sub>3</sub> , IMes, SIMes and ICy .....	124
2.3.2.2	Comparison of <b>IMes(a)</b> , <b>SIMes(a)</b> and <b>ICy(a)</b> .....	126
2.3.2.3	Comparison of the active hydrogenation products of <b>IMes(a)</b> , <b>SIMes(a)</b> and <b>ICy(a)</b> .....	130
2.3.3	Comparison of ligand exchange rate constants and activation parameters of <b>IMes(a)</b> , <b>SIMes(a)</b> and <b>ICy(a)</b> .....	132
2.3.3.1	Thermodynamic activation parameters observed for the loss of pyridine <i>trans</i> to the hydride ligands from hydrogenated <b>IMes(a)</b> , <b>SIMes(a)</b> and <b>ICy(a)</b> .....	133
2.3.3.2	Thermodynamic activation parameters observed for the loss of hydride ligands from hydrogenated <b>IMes(a)</b> , <b>SIMes(a)</b> and <b>ICy(a)</b> in the presence of pyridine .....	134
2.3.4	Comparison of polarisation transfer efficiency into pyridine of <b>IMes(a)</b> , <b>SIMes(a)</b> and <b>ICy(a)</b> .....	135

2.4	Summary .....	137
3	Chapter 3 - Investigation of SABRE effect.....	139
3.1	Introduction .....	139
3.2	Effect of magnetic field during the polarisation transfer step on polarisation transfer efficiency.....	139
3.2.1	Effect of magnetic field during the polarisation transfer step on polarisation transfer efficiency into pyridine .....	142
3.2.2	Effect of magnetic field during the polarisation transfer step on polarisation transfer efficiency into deuterated pyridines.....	143
3.3	Effect of temperature during the polarisation transfer step on polarisation transfer efficiency.....	145
3.3.1	Effect of changing the temperature of polarisation transfer efficiency into pyridine using <b>IMes(a)</b> .....	147
3.3.2	Effect of changing the temperature of polarisation transfer efficiency into pyridine using <b>SIMes(a)</b> .....	148
3.3.3	Effect of changing the temperature of polarisation transfer efficiency into pyridine using <b>ICy(a)</b> .....	150
3.3.4	Comparison of the effect of temperature on the polarisation transfer efficiency into pyridine using <b>IMes(a)</b> , <b>SIMes(a)</b> and <b>ICy(a)</b> .....	151
3.4	Effect of concentration during the polarisation transfer step on polarisation transfer efficiency.....	152
3.4.1	Effect of concentration when ratio of pyridine to catalyst remains constant on polarisation transfer efficiency.....	154
3.4.2	Effect of concentration when concentration of catalyst remains constant on polarisation transfer efficiency.....	160
3.5	Effect of solvent on polarisation transfer efficiency .....	165

3.6	Summary .....	167
4	Chapter 4 - Optimisation of quinoline .....	170
4.1	Introduction .....	170
4.1.1	Quinoline analogues as drugs.....	170
4.1.1.1	Quinine and quinidine.....	170
4.1.1.2	Chloroquine and hydroxychloroquine .....	172
4.1.1.3	8-hydroxyquinoline analogues.....	175
4.1.2	Characterisation of quinoline in methanol .....	176
4.2	Initial studies into polarisation transfer efficiency into quinoline.....	177
4.2.1	Effect of changing catalyst on polarisation transfer efficiency into quinoline.....	177
4.2.2	Characterisation of <b>IMes(c)</b> hydrogenated in the presence of quinoline	179
4.2.3	Rate constants and thermodynamic activation parameters of <b>IMes(c)</b> hydrogenated in the presence of quinoline.....	181
4.2.3.1	Thermodynamic activation parameters observed for the loss of hydride ligands from <b>IMes(c)</b> hydrogenated in the presence of quinoline.....	181
4.2.3.2	Thermodynamic activation parameters observed for the loss of quinoline ligands from hydrogenated <b>IMes(c)</b> .....	182
4.3	Further optimisation of polarisation transfer efficiency into quinoline .....	183
4.3.1	Effect of changing temperature during the polarisation transfer step on polarisation transfer efficiency into quinoline .....	183
4.3.1.1	Effect of temperature during the polarisation transfer step on polarisation transfer efficiency into quinoline using <b>IMes(c)</b> .....	183

4.3.1.2	Effect of temperature during the polarisation transfer step on polarisation transfer efficiency into quinoline using <b>SIMes(c)</b> .....	185
4.3.1.3	Effect of temperature during the polarisation transfer step on polarisation transfer efficiency into quinoline using <b>ICy(c)</b> .....	186
4.3.1.4	Comparison of the effect of temperature during the polarisation transfer step on polarisation transfer efficiency into quinoline using <b>IMes(c)</b> , <b>SIMes(c)</b> and <b>ICy(c)</b> .....	187
4.3.2	Effect of changing magnetic field during the polarisation transfer step on polarisation transfer efficiency into quinoline .....	189
4.3.3	Effect of changing concentration on polarisation transfer efficiency into quinoline.....	191
4.3.4	Effect of changing solvent on polarisation transfer efficiency into quinoline.....	192
4.4	Mechanism of polarisation transfer into quinoline using SABRE .....	193
4.4.1	Polarisation of quinoline derivatives.....	195
4.4.1.1	Naphthalene .....	195
4.4.1.2	Investigation into the effect of changing the position of the nitrogen on polarisation transfer efficiency.....	195
4.4.1.3	Investigation into the effect of moving a methyl group of methylquinolines on polarisation transfer efficiency.....	197
4.4.1.4	Phenazine .....	199
4.4.2	Investigations in polarisation transfer route into quinoline using the selective OPSYdq sequence.....	200
4.5	Summary .....	204
5	Chapter 5 – Implementing SABRE with advanced NMR methods.....	206

	10
5.1	Introduction .....206
5.2	Development of method 2 applied to 1D NMR sequences .....207
5.2.1	Method 2 applied to 1D $^1\text{H}$ NMR sequences .....207
5.2.1.1	Investigations into the effect of changing exposure time to <i>parahydrogen</i> on resultant $^1\text{H}$ NMR spectra .....207
5.2.1.2	Method 2 applied to $^1\text{H}$ OPSY NMR sequence .....208
5.2.1.3	Method 2 applied to $^1\text{H}$ NOESY NMR sequence .....209
5.2.2	Method 2 applied to 1D $^{13}\text{C}$ and $^{13}\text{C}\{^1\text{H}\}$ NMR sequences .....212
5.2.2.1	Method 2 applied to utilising $^{13}\text{C}$ magnetisation without $^1\text{H}$ decoupling .....213
5.2.2.2	Method 2 applied to utilising $^{13}\text{C}$ magnetisation with $^1\text{H}$ decoupling ... .....217
5.2.2.3	Method 2 applied to $^{13}\text{C}$ INEPT NMR sequences .....225
5.2.2.4	Method 2 applied to $^1\text{H}$ decoupling of the INEPT sequence .....237
5.2.2.5	Utilisation of polarisation transfer to two different nuclei to increase information gain .....239
5.2.2.6	Hyperpolarised $^{13}\text{C}$ NMR spectra using standard reagent concentrations .....243
5.3	Development of method 2 applied to 2D NMR sequences .....244
5.3.1	Method 2 applied to $^1\text{H}$ - $^1\text{H}$ 2D homonuclear NMR sequences .....244
5.3.1.1	Method 2 applied to $^1\text{H}$ - $^1\text{H}$ COSY NMR sequence .....245
5.3.1.2	Method 2 applied to $^1\text{H}$ - $^1\text{H}$ OPSYdq-COSY NMR sequence .....245
5.3.2	Method 2 applied to $^1\text{H}$ - $^{13}\text{C}$ 2D heteronuclear NMR sequences .....248

5.3.2.1	Method 2 applied to the $^1\text{H}$ - $^{13}\text{C}$ HSQC NMR sequence.....	248
5.3.2.2	Method 2 applied to the $^1\text{H}$ - $^{13}\text{C}$ HMBC NMR sequence.....	250
5.3.2.3	Method 2 applied to the $^1\text{H}$ - $^{13}\text{C}$ HMQC NMR sequence.....	253
5.3.2.4	Investigations into removal of artefacts observed in hyperpolarised 2D NMR spectra .....	256
5.4	Development of method 1 applied to 2D NMR sequences.....	259
5.4.1	Method 1 applied to $^1\text{H}$ - $^1\text{H}$ 2D homonuclear NMR sequences.....	260
5.5	Summary .....	263
6	Chapter 6 – Applying SABRE.....	269
6.1	Introduction .....	269
6.2	Investigations into polarisation transfer efficiency to pyridine analogues.....	275
6.2.1	The effect of basicity on the level of observed polarisation transfer in a series of <i>para</i> -substituted pyridines .....	275
6.2.2	Effect of substitution on the level of polarisation transfer to the binding pyridine ring and substituents .....	280
6.2.2.1	Polarisation transfer efficiency trends observed within the methylpyridines.....	281
6.2.2.2	Polarisation transfer efficiency trends observed within the phenylpyridines .....	282
6.2.2.3	Polarisation of 3-benzoylpyridine and 4-(4-chlorobenzoyl)pyridine .... .....	284
6.3	Polarisation of substrates without a pyridine subunit.....	286
6.3.1	Investigation into the polarisation of indole .....	286
6.3.2	Investigation into the polarisation of thiazole.....	287

6.3.2.1	Investigation into the polarisation of 2-aminothiazole .....	287
6.3.2.2	Investigation into the polarisation of 2-amino-4-methyl thiazole, 2-amino-4-phenyl thiazole and 2-amino-4-(4-chlorophenyl) thiazole .....	290
6.3.2.3	Investigation into the polarisation of benzothiazole .....	292
6.3.3	Polarisation of commercial drugs.....	294
6.4	Effect of polarisation transfer efficiency in complex mixtures .....	295
6.4.1	Effect of polarisation transfer efficiency to competing substrates.....	295
6.4.1.1	Competition between pyridine and 2-aminothiazole .....	296
6.4.1.2	Competition between 2-aminothiazole and quinoline .....	298
6.4.1.3	Competition between 4-methylpyridine and 4-phenylpyridine .....	300
6.4.2	Utilisation of the $^1\text{H}$ OPSYdq NMR sequence .....	302
6.5	Reaction of 4-carboxaldehydepiperidine with methanol .....	304
6.5.1	The spontaneous reaction of 4-carboxaldehydepiperidine with methanol.	305
6.5.2	Monitoring the spontaneous reaction of 4-carboxaldehydepiperidine with methanol using SABRE .....	310
6.5.3	The acid catalysed reaction of 4-carboxaldehydepiperidine with methanol.... .....	312
6.5.4	Monitoring the acid catalysed reaction of 4-carboxaldehydepiperidine with methanol using SABRE .....	315
6.6	Summary .....	317
7	Chapter 7 – Conclusions and future work.....	319
7.1	Conclusions .....	319
7.2	Future work .....	324



8	Chapter 8 – Experimental .....	327
8.1	Instrumentation and chemical sources.....	327
8.1.1	NMR spectrometers .....	327
8.1.2	Preparation of <i>parahydrogen</i> .....	327
8.1.3	Source of solvents and chemicals .....	328
8.2	Standard methods .....	328
8.2.1	Hyperpolarisation method 1 – shake method.....	328
8.2.2	Hyperpolarisation method 2 – flow method.....	328
8.2.3	Calculation of <sup>1</sup> H NMR enhancement factors.....	329
8.2.4	Considerations when discussing the effect of the magnetic field of polarisation on polarisation transfer efficiency.....	330
8.2.5	Effect of changing PTF on the polarisation transfer efficiency into various substrates.....	332
8.2.5.1	Effect of changing PTF on polarisation transfer efficiency into pyridine with <b>SIMes(a)</b> .....	332
8.2.5.2	Effect of changing PTF on polarisation transfer efficiency into pyridine using <b>ICy(a)</b> .....	333
8.2.5.3	Effect of changing PTF on polarisation transfer efficiency into pyridine using <b>ICy<sub>2</sub>(a)</b> .....	334
8.2.5.4	Effect of changing PTF on polarisation transfer efficiency into 3,4,5- <i>d</i> <sub>3</sub> -pyridine using <b>SIMes(a)</b> .....	335
8.2.5.5	Effect of changing PTF on polarisation transfer efficiency into quinoline using <b>IMes(b)</b> .....	336
8.2.5.6	Effect of changing PTF on polarisation transfer efficiency into 4-methylpyridine using <b>SIMes(a)</b> .....	337

8.2.5.7	Effect of changing PTF on polarisation transfer efficiency into 3-methylpyridine using <b>SIMes(a)</b> .....	338
8.2.5.8	Effect of changing PTF on polarisation transfer efficiency into 2-aminothiazole using <b>IMes(a)</b> .....	339
8.2.5.9	Effect of changing PTF on polarisation transfer efficiency into 3-phenylpyridine using <b>IMes(a)</b> .....	340
8.2.5.10	Effect of changing PTF on polarisation transfer efficiency into 4-phenylpyridine using <b>IMes(a)</b> .....	341
8.2.6	Calculation of rate constants for ligand loss and thermodynamic activation parameters .....	342
8.2.7	Procedure for investigating the effect of changing temperature of polarisation on polarisation transfer efficiency.....	342
8.3	Additional experiments .....	343
8.3.1	Relative excess of hydrogen gas present in an NMR sample interrogated using method 1 .....	343
8.3.2	Calculations relating to the solubility of hydrogen gas in methanol.....	344
8.3.2.1	Calculations based on equations reported in Solubility of Gases in Liquids <sup>212</sup> .....	344
8.3.2.2	Calculations based on equations reported by Liu <i>et al.</i> <sup>214</sup> .....	345
8.3.3	Calculation of estimated integrals of thermally polarised spectra for low concentration samples .....	346
8.3.4	Thermally polarised spectra of quinoline using standard concentrations for comparison .....	348
8.4	Reactions .....	349
8.4.1	[Ir(COD)Cl] <sub>2</sub> <sup>215</sup> .....	349

8.4.2	$[\text{Ir}(\mu\text{-MeO})(\text{COD})]_2^{216}$ .....	350
8.4.3	$[\text{Ir}(\text{IMes})(\text{COD})\text{Cl}]^{104}$ ( <b>IMes(a)</b> ).....	350
8.4.4	$[\text{Ir}(\text{IMes})(\text{COD})\text{NCMe}]\text{PF}_6^{80}$ ( <b>IMes(b)</b> ).....	351
8.4.5	$[\text{Ir}(\text{SIMes})(\text{COD})\text{Cl}]^{104}$ ( <b>SIMes(a)</b> ) .....	351
8.4.6	$[\text{Ir}(\text{SIMes})(\text{COD})\text{NCMe}]\text{PF}_6^{80}$ ( <b>SIMes(b)</b> ) .....	351
8.4.7	<i>Bis</i> -1,3-cyclohexyl imidazole hydrochloride ( <b>ICy.HCl</b> ) <sup>217</sup> .....	351
8.4.8	$[\text{Ir}(\text{ICy})(\text{COD})\text{Cl}]^{104}$ ( <b>ICy(a)</b> ) .....	352
8.4.9	$[\text{Ir}(\text{ICy})_2(\text{COD})]\text{Cl}^{104}$ ( <b>ICy<sub>2</sub>(a)</b> ) .....	352
8.5	Characterisation of catalyst precursors and active polarisation transfer catalysts .....	353
8.5.1	$[\text{Ir}(\text{COD})\text{Cl}]_2$ .....	353
8.5.2	$[\text{Ir}(\mu\text{-MeO})(\text{COD})]_2$ .....	353
8.5.3	$[\text{Ir}(\text{IMes})(\text{COD})\text{Cl}]$ ( <b>IMes(a)</b> ).....	353
8.5.4	$[\text{Ir}(\text{IMes})(\text{py})_3(\text{H})_2]\text{Cl}$ .....	353
8.5.5	$[\text{Ir}(\text{IMes})(\text{quinoline})_2(\text{H})_2(\text{NCMe})]\text{Cl}$ .....	354
8.5.6	$[\text{Ir}(\text{IMes})(\text{COD})(\text{NCMe})]\text{PF}_6$ ( <b>IMes(b)</b> ).....	358
8.5.7	$[\text{Ir}(\text{SIMes})(\text{COD})\text{Cl}]$ ( <b>SIMes(a)</b> ) .....	358
8.5.8	$[\text{Ir}(\text{SIMes})(\text{py})_3(\text{H})_2]\text{Cl}$ .....	358
8.5.9	<i>Bis</i> -1,3-cyclohexyl imidazole hydrochloride ( <b>ICy.HCl</b> ).....	359
8.5.10	$[\text{Ir}(\text{ICy})(\text{COD})\text{Cl}]$ ( <b>ICy(a)</b> ) .....	359
8.5.11	$[\text{Ir}(\text{ICy})(\text{py})_3(\text{H})_2]\text{Cl}$ .....	359
8.5.12	$[\text{Ir}(\text{ICy})_2(\text{COD})]\text{Cl}$ ( <b>ICy<sub>2</sub>(a)</b> , 800.58 g mol <sup>-1</sup> ).....	360

8.6	Acetal and hemiacetal products of 4-carboxaldehydepiperidine and methanol	360
8.6.1	$^1\text{H}$ and $^{13}\text{C}$ NMR data for 4-carboxaldehydepiperidine	361
8.6.2	$^1\text{H}$ and $^{13}\text{C}$ NMR data for the hemiacetal product, $\text{NC}_5\text{H}_4\text{-}p\text{-CH(OMe)(OH)}$	361
8.6.3	$^1\text{H}$ and $^{13}\text{C}$ NMR data for the acetal product, $\text{NC}_5\text{H}_4\text{-}p\text{-CH(OMe)}_2$	362
8.7	$^1\text{H}$ and $^{13}\text{C}$ NMR data for substrates in methanol	362
8.7.1	Substituted piperidines	362
8.7.1.1	3-phenylpiperidine	362
8.7.1.2	4-phenylpiperidine	363
8.7.1.3	3-benzoylpiperidine	363
8.7.1.4	4-(4-chlorobenzoyl)piperidine	363
8.7.2	Quinoline and substituted quinolines	364
8.7.2.1	Quinoline	364
8.7.2.2	Isoquinoline	364
8.7.2.3	4-methylquinoline	365
8.7.2.4	7-methylquinoline	365
8.7.2.5	8-methylquinoline	366
8.7.3	Other substrates	366
8.7.3.1	Indole	366
8.7.3.2	2-amino-4-(4-chlorophenyl)thiazole	367
8.7.3.3	Benzothiazole	367
9	Chapter 9 - Appendices	368

9.1	Complete data collected for the calculation of thermodynamic activation parameters .....	368
9.1.1	Collection of NMR data for the calculation of exchange rates .....	368
9.1.2	Information pertaining to Dynafit <sup>108</sup> .....	369
9.1.2.1	Data file used for the model of the determination for the rate of loss of hydride ligands from <b>Carbene(a)</b> .....	369
9.1.2.2	Data file used for the model of the determination for the rate of loss of substrate from <b>Carbene(a)</b> .....	370
9.1.2.3	Data file used for the model of the determination for the rate of loss of hydride ligands from <b>IMes(c)</b> and <b>SIMes(c)</b> .....	372
9.1.3	Calculation of thermodynamic activation parameters .....	374
9.1.4	Treatment of errors.....	374
9.1.5	Collected rate constants and thermodynamic activation parameters for a sample of <b>SIMes(a)</b> hydrogenated in the presence of pyridine .....	375
9.1.6	Collected rate constants and thermodynamic activation parameters for a sample of <b>ICy(a)</b> hydrogenated in the presence of pyridine.....	377
9.1.7	Collected rate constants and thermodynamic activation parameters for a sample of <b>IMes(c)</b> hydrogenated in the presence of quinoline.....	378
9.1.8	Collected rate constant data for a sample of <b>SIMes(c)</b> hydrogenated in the presence of quinoline .....	380
9.2	Product operators of INEPT NMR experiments prior to FID acquisition.....	380
9.2.1	Product operators of the INEPTnd NMR sequence .....	380
9.2.1.1	Starting with $I_z$ .....	380
9.2.1.2	Starting with $I_z S_z$ .....	381
9.2.1.3	Starting with $I_z R_z$ .....	381

9.2.1.4	Starting with $I_x S_x$ .....	381
9.2.2	Product operators of the INEPT_phase NMR sequence with a 45° initial pulse .....	381
9.2.2.1	Starting with $I_z$ .....	381
9.2.2.2	Starting with $I_z S_z$ .....	381
9.2.2.3	Starting with $I_z R_z$ .....	382
9.2.3	Product operators of the INEPT_phase NMR sequence with a 90° initial pulse .....	382
9.2.3.1	Starting with $I_z$ .....	382
9.2.3.2	Starting with $I_z S_z$ .....	382
9.2.3.3	Starting with $I_z R_z$ .....	382
9.3	Adapted pulse sequences used within this thesis .....	383
9.3.1	Standard 90° pulse acquire sequence – ph_zg .....	383
9.3.2	$^1\text{H}$ OPSYdq NMR pulse sequence – ph_OPsYdq .....	384
9.3.3	Selective OPSYdq sequence – OPSYdq_2shaped90_mkIII .....	386
9.3.4	1D $^1\text{H}$ NOESY NMR pulse sequence – ph_selnogp .....	388
9.3.5	1D $^1\text{H}$ NOESY NMR pulse sequence – ph_selnogp_noloopdummy .....	391
9.3.6	1D refocused $^{13}\text{C}\{^1\text{H}\}$ NMR pulse sequence ( $^{13}\text{C}\{^1\text{H}\}_\text{JR}$ ) – ph_zg_refocus .....	395
9.3.7	1D $^{13}\text{C}\{^1\text{H}\}$ NMR pulse sequence refocused for both J coupling and chemical shift evolution ( $^{13}\text{C}\{^1\text{H}\}_\text{JCSR}$ ) – ph_zg_refocused_J+CS .....	396
9.3.8	1D $^{13}\text{C}$ INEPT NMR pulse sequence – ph_ineptnd .....	397

9.3.9	1D $^{13}\text{C}$ INEPT NMR pulse sequence with phase change – ph_inept_phase .....	399
9.3.10	1D $^{13}\text{C}\{^1\text{H}\}$ INEPT NMR pulse sequence – ph_ineptrd.....	401
9.3.11	2D $^1\text{H}$ - $^1\text{H}$ OPSYdq-COSY NMR pulse sequence – ph_OPSTYdq_2D ...	403
9.3.12	2D NMR pulse sequences .....	405
9.4	X-ray crystallography data for $[\text{Ir}(\text{SIMes})(\text{COD})(2\text{-methylpyridine})]\text{PF}_6$ .....	407
9.5	Publications <sup>67</sup> .....	415
10	Abbreviations .....	419
11	References .....	424

## List of Figures

Figure 1.1 First $^1\text{H}$ NMR spectrum of ethanol published by Arnold <i>et al.</i> <sup>9</sup> .....	58
Figure 1.2 Photo demonstrating the relative size of some available NMR sample tubes demonstrating different diameters. The required sample volumes for each sample tube is written in parenthesis, from left to right, 5 mm (600 $\mu\text{L}$ ), 1.7 mm (35 $\mu\text{L}$ ) and 1 mm (7 $\mu\text{L}$ ). Image taken from the publication by Molinski (2009). <sup>13</sup> .....	59
Figure 1.3 $^{31}\text{P}$ signals obtained in a single scan at 4.2 K from a sample containing 2 M [ $1\text{-}^{13}\text{C}$ ] sodium acetate and 1 M sodium phosphate. The bottom scan was completed without low field thermal mixing, and the top completed with low field thermal mixing. Picture taken from the publication by Gadian <i>et al.</i> <sup>16</sup> .....	62
Figure 1.4 $^{129}\text{Xe}$ NMR spectra of human blood with thermally polarised (top) and hyperpolarised (bottom) $^{129}\text{Xe}$ . Picture reproduced from publication in 1996 by Bifone <i>et al.</i> <sup>23</sup> .....	63
Figure 1.5 $^{13}\text{C}$ NMR spectra of $1\text{-}^{13}\text{C}$ -acetic acid with thermal distribution (bottom) and hyperpolarised by thermal mixing with optically pumped $^{129}\text{Xe}$ . Picture reproduced from the 2009 publication by Lisitza <i>et al.</i> <sup>27</sup> .....	65
Figure 1.6 $^{129}\text{Xe}$ and $^1\text{H}$ MRI images of the rat brain. a) Grey-scale $^{129}\text{Xe}$ image, b) False colour suposition of $^{129}\text{Xe}$ image on a $^1\text{H}$ spin-echo image and c) $^1\text{H}$ spin-echo. Figure reproduced from a paper published in 1997 by Swanson <i>et al.</i> <sup>24</sup> .....	66
Figure 1.7 Structure and schematic representation of the biosensor molecule designed to bind xenon to a protein with high affinity and specificity, proposed in a publication by Spence <i>et al.</i> <sup>29</sup> The cage binding xenon, cryptophane-A, is shown in black with a purple tether and red biotin ligand. ....	67
Figure 1.8 The $^{129}\text{Xe}$ NMR spectra depicting the detection of biotin – avidin binding using xenon NMR. The left spectra show binding in the absence of native biotin, and the right spectra show binding in the presence of native biotin. Images taken from the publication by Spence <i>et al.</i> <sup>30</sup> .....	67



Figure 1.9  $^{13}\text{C}$  coronal projection images of a rat. The images were acquired (a) 1 s and (b) 3 s after injection of  $^{13}\text{C}$ -urea. Image taken from a publication by Wolber *et al.*<sup>34</sup> .. 69

Figure 1.10 Left, sixteen spectra of the carbonyl resonance in  $[\text{U-}^{13}\text{C}]$ -L-proline resulting from a series of TJ-DNP experiments. These spectra can be averaged (right) to improve the observed signal to noise ratio. Image taken from a publication by Joo *et al.*<sup>36</sup> ..... 70

Figure 1.11 Schematic showing the relative populations the wavefunctions available to a) normal hydrogen and b) *parahydrogen*. ..... 72

Figure 1.12 Schematic showing the magnetic distribution and NMR signals that result for an  $\text{H}_2$  addition product of a) normal hydrogen and b) *parahydrogen*. Figure reproduced from a paper published by Duckett *et al.*<sup>40</sup> ..... 73

Figure 1.13 Schematic of the mechanism of the hydrogenation of olefins by Wilkinson's catalyst as of 1994. Adapted from a paper published in 1994 by Duckett *et al.*<sup>51</sup> ..... 74

Figure 1.14 Structures of new complexes detected and postulated by Duckett *et al.*<sup>51</sup> in the 1994 publication concerning new intermediates in the mechanism of hydrogenation by Wilkinson's catalyst where a) is the Rh(III)/Rh(I) dimer  $\text{H}_2\text{Rh}(\text{PPh}_3)_2(\mu\text{-Cl})_2\text{Rh}(\text{PPh}_3)(\text{olefin})$  and b) shows the structures of the possible isomers of the  $\text{RhH}_2\text{Cl}(\text{PPh}_3)_2(\text{olefin})$  intermediate. .... 75

Figure 1.15 Reaction of  $[\text{IrCl}(\text{CO})(\text{PPh}_3)_2]$  with *parahydrogen* in the presence of pyridine. Image reproduced from the 2007 publication by Wood *et al.*<sup>56</sup> ..... 75

Figure 1.16 Hydrogenation reactions of **1**, 2-(2-methoxyethoxy)ethylphenylpropiolate and **2**, *bis*[2-(2-methoxyethoxy)ethyl]acetylenedicarboxylate with products termed **1a** and **2a** respectively. Adapted from the 2008 paper published by Reineri *et al.*<sup>54</sup> ..... 77

Figure 1.17 Single scan  $^{13}\text{C}$  spectrum of  $^{13}\text{C}$  labelled substrate **2a** (see Figure 1.16) extracted in  $\text{D}_2\text{O}$  after hydrogenation with *parahydrogen*. a) was recorded as soon as was practical after the hydrogenation step, and b) was collected after relaxation (5 min). Image taken from the 2008 publication by Reineri *et al.*<sup>54</sup> ..... 77

- Figure 1.18 Hydrogenation reaction of a) styrene to b) ethylbenzene with [1,4-bis(diphenylphosphino)butane](1,5-cyclooctadiene)rhodium BF<sub>4</sub> including relevant labels. Adapted from a publication in 2009 by Korchak *et al.*<sup>57</sup> ..... 78
- Figure 1.19 <sup>1</sup>H NMR at 7 T and PHIP spectra collected after *parahydrogenation* at stated polarisation field and acquisition at 7 T. \* denotes signals corresponding to bound ethylbenzene. Reproduced from a publication in 2009 by Korchak *et al.*<sup>57</sup> ..... 79
- Figure 1.20 Schematic of the SABRE process showing non-hydrogenative transfer of hyperpolarised states from *parahydrogen* to a substrate via a metal catalyst. Adapted from the publication by Adams *et al.* (2009).<sup>58</sup> ..... 79
- Figure 1.21 The general structure of a SABRE catalyst (a) and the simplified schematic utilised by the theory reported in Adams *et al.* (2009)<sup>59</sup> (b), where M = metal and Sub = substrate. The hydride pairs (H) are derived from *parahydrogen* in each case. .... 80
- Figure 1.22 Structure of Crabtree's catalyst. .... 81
- Figure 1.23 Generic structure and reaction of the 1-methylcyclohexene rings investigated in a publication by Crabtree and Davis,<sup>70</sup> using terpinen-4-ol as an example. The side view of the conformation of interest is also shown, where a) refers to the product formed by directed hydrogenation and b) refers to the product formed by counterdirected hydrogenation..... 82
- Figure 1.24 Structures of selected substrates investigated in a publication by Crabtree and Davis<sup>70</sup> This group are characterised by the alcohol group being bound directly to the ring. .... 82
- Figure 1.25 Deuteration reaction investigated in the 2001 paper published by Ellames *et al.*<sup>71</sup> ..... 83
- Figure 1.26 A simplified mechanism for HD exchange in the presence of deuterium oxide by Crabtree's catalyst, reproduced from a paper published by Ellames *et al.*<sup>71</sup> in 2001..... 84
- Figure 1.27 Comparison of low field NMR spectra with SABRE enhancement (left) and thermal polarisation (right). Single-scan <sup>1</sup>H FIDs and corresponding spectra (inset) of

the indicated volumes of pyridine in 0.4 ml methanol solutions. Image taken from the publication by Gong <i>et al.</i> <sup>62</sup> .....	86
Figure 1.28 A time profile of the hydrogenation of 1-octene with [Ir(COD)(IMes)Cl] presented in the 2006 publication by Vazquez-Serrano <i>et al.</i> <sup>73</sup> .....	88
Figure 1.29 Labelling of niclosamide (Bayer AG) adapted from the 2010 publication by Nilsson and Kerr. <sup>78</sup> .....	88
Figure 1.30 Chemical structure and X-ray structure of [Ir(IMes')(NCMe) <sub>3</sub> (R)]PF <sub>6</sub> taken from a publication by Torres <i>et al.</i> <sup>80</sup> .....	89
Figure 1.31 Typical <sup>1</sup> H NMR spectra of hyperpolarised quinoline indicating various signal forms. ....	92
Figure 1.32 The <sup>1</sup> H OPSYdq NMR sequence, adapted from a publication by Aguilar <i>et al.</i> <sup>84</sup> .....	97
Figure 2.1 Plot of the relative absolute signal strengths for the three pyridine proton sites (relative to signals for free pyridine at equilibrium). Results represent the average of 5 measurements, each recorded immediately after shaking the NMR tube in a 0.5 x10 <sup>-4</sup> T field. Taken from a publication by Atkinson <i>et al.</i> (2009). <sup>61</sup> .....	103
Figure 2.2 Definition of the cone angle for phosphines, taken from a publication by Clavier and Nolan (2010). <sup>98</sup> .....	105
Figure 2.3 Definition of the cone angle for carbenes, taken from a publication by Clavier and Nolan (2010). <sup>98</sup> .....	106
Figure 2.4 Definition of per cent buried volume, taken from a publication by Clavier and Nolan (2010). <sup>98</sup> .....	106
Figure 2.5 Schematic of the polarisor used in method 2. Adapted from a publication by Cowley <i>et al.</i> (2011). <sup>66</sup> .....	108
Figure 2.6 Photo of MKI polarisor.....	110
Figure 2.7 Photos of MKII polarisor.....	110

Figure 2.8 Photo of MKIII polarisor. ....	111
Figure 2.9 Observed $^1\text{H}$ NMR signal of selected quinoline resonances, where quinoline is polarised with <b>IMes(c)</b> . This data is presented with the field of addition of parahydrogen taking place at -60 G to +60 G in increments of +20 G. ....	113
Figure 2.10 Structures of the generic catalyst precursor systems used throughout this thesis namely <b>Carbene(a)</b> , <b>Carbene(b)</b> and <b>Carbene(c)</b> . ....	115
Figure 2.11 Structures of each catalyst in its active form after the addition of hydrogen and substrate in a 20 fold excess. ....	115
Figure 2.12 Structures of carbenes used within this thesis, namely a) IMes, b) SIMes and c) ICy. ....	116
Figure 2.13 Relative energy difference of magnetic states in an NMR sample at Earth's magnetic field and the high field of an NMR spectrometer. ....	116
Figure 2.14 Graphical representation of the observed $^1\text{H}$ signal enhancement in thirty NMR spectra of quinoline hyperpolarised with <b>IMes(c)</b> using method 2. ....	119
Figure 2.15 Mechanism of the activation of $[\text{Ir}(\text{IMes})(\text{COD})\text{Cl}]$ proposed by Cowley <i>et al.</i> <sup>66</sup> ....	120
Figure 2.16 Bottom: $^1\text{H}$ NMR spectrum of $[\text{Ir}(\text{SIMes})(\text{COD})(\text{py})]\text{Cl}$ in $\text{CDCl}_3$ and top: the same sample with added pyridine. ....	121
Figure 2.17 Potential intermediates in the route of hydride ligand loss from <b>IMes(a)</b> investigated by DFT published in a paper published by Cowley <i>et al.</i> <sup>66</sup> ....	122
Figure 2.18 Structures of carbene ligands used within this thesis, namely a) IMes, b) SIMes and c) ICy ....	123
Figure 2.19 Structures of a) <b>IMes(a)</b> , b) <b>SIMes(a)</b> and c) <b>ICy(a)</b> . ....	126
Figure 2.20 The crystal structures of <b>IMes(a)</b> , <b>SIMes(a)</b> and <b>ICy(a)</b> copied from a publication by Kelly <i>et al.</i> <sup>94</sup> ....	127

- Figure 2.21 Crystal structures of **SIMes(a)** ( $[\text{Ir}(\text{SIMes})(\text{COD})\text{Cl}]$ ) taken from a publication by Kelly *et al.*<sup>94</sup> and  $[\text{Ir}(\text{SIMes})(\text{COD})(2\text{-methylpyridine})]\text{PF}_6$  collected as part of this thesis. The  $\text{PF}_6$  counter ion for the latter has been omitted for clarity. Presented with C in black, N in blue, Ir in yellow, H in peach and Cl in green. .... 129
- Figure 2.22 Structures of the active hydrogenation products of **IMes(a)**, **SIMes(a)** and **ICy(a)**..... 130
- Figure 2.23 X-ray crystal structure of  $[\text{Ir}(\text{H})_2(\text{IMes})(\text{py})_3]^+$ . Structure taken from a publication by Cowley *et al.* 2011.<sup>66</sup> ..... 131
- Figure 2.24 The reaction co-ordinate for the dissociative reaction for loss of ligand. . 132
- Figure 1.1 Intensity of the  $^1\text{H}$  NMR signal enhancement of the *para* proton resonance of pyridine when polarised using **IMes(a)** at the indicated fields from 0 G to 150 G, in increments of 5 G. Image taken from the supplementary information of the publication by Cowley *et al.* (2011).<sup>66</sup> ..... 140
- Figure 1.2 Structures of pyridine and the pyrazole-based substrates investigated in the publication by Dücker *et al.* (2012)<sup>65</sup> labelled as a) pyridine, b) pyrazole, c) 1-methylpyriazole, d) 3-methylpyrazole, e) 3-phenylpyrazole, f) 3-(3-bromophenyl)pyrazole, g) indazole, h) 3,5-dimethylpyrazole and i) 3,5-diphenylpyrazole. .... 141
- Figure 1.3 Structures of a) 3,4,5- $d_3$ -pyridine and b) 2,6- $d_2$ -pyridine. .... 143
- Figure 1.4 Relative  $^1\text{H}$  NMR signal strength of the *ortho* proton resonance of 3,4,5- $d_3$ -pyridine polarised by **SIMes(a)**. These data are presented as a function of the magnetic field of polarisation which varies from -150 G to +10 G in increments of +10 G. .... 144
- Figure 1.5 Relative  $^1\text{H}$  NMR signal strength of the a) *ortho*, b) *meta* and c) *para* proton resonance of 2,6- $d_2$ -pyridine polarised with **SIMes(a)**. These data are presented as a function of the magnetic field of polarisation which varies from -150 G to +10 G in increments of +10 G..... 144
- Figure 1.6 Observed  $^1\text{H}$  NMR signal of a) *ortho*, b) *meta* and c) *para* proton resonance of 2,6- $d_2$ -pyridine polarised with **SIMes(a)**. This data is presented with the field of

addition of <i>parahydrogen</i> taking place at -150 G to +10 G in increments of +10 G, but collected from +10 G to -150 G.....	145
Figure 1.7 Thermal $^1\text{H}$ NMR spectra of 2,6- $d_2$ -pyridine recorded before (top) and after (bottom) the investigation using <b>SIMes(a)</b> with method 2.....	145
Figure 1.8 Relative $^1\text{H}$ NMR signal enhancement to pyridine resonances obtained with <b>IMes(a)</b> as a function of temperature. ....	148
Figure 1.9 Relative $^1\text{H}$ NMR signal enhancement to pyridine resonances obtained with <b>SIMes(a)</b> as a function of temperature. ....	149
Figure 1.10 Relative $^1\text{H}$ NMR signal enhancement to pyridine resonances obtained with <b>ICy(a)</b> as a function of temperature.....	150
Figure 1.11 Relative $^1\text{H}$ NMR polarisation transfer to the <i>ortho</i> , <i>meta</i> and <i>para</i> resonances of pyridine when <b>IMes(a)</b> , <b>SIMes(a)</b> , and <b>ICy(a)</b> are used as the polarisation transfer catalyst in methanol as a function of temperature of <i>parahydrogen</i> addition.....	151
Figure 1.12 Reproduced pictorial description of the results of the catalyst loading study completed in a publication by Atkinson <i>et al.</i> (2009). <sup>61</sup> .....	153
Figure 1.13 Reproduced pictorial description of the results of the catalyst loading study in a publication by Cowley <i>et al.</i> (2011). <sup>66</sup> .....	153
Figure 1.14 Thermal $^1\text{H}$ NMR spectrum of pyridine (top) and a typical hyperpolarised spectrum (bottom) polarised with <b>IMes(a)</b> using method 1 at 2 G. The catalyst and substrate are at 1% of the standard concentration (0.02 mg <b>IMes(a)</b> and 0.05 $\mu\text{l}$ pyridine).....	157
Figure 1.15 Graphical representation of the enhancement observed over three days of a concentration study where the ratio of <b>IMes(a)</b> to pyridine is kept constant (Table 1.8). .....	158
Figure 1.16 Deuteration level of the <i>ortho</i> position of pyridine when reacted with <b>IMes(a)</b> in $d_4$ -methanol over a period of 48 hours. For sample numbers, refer to Table 1.7.....	159

- Figure 1.17 Graphical representation of the effect of pyridine concentration on the resultant signal enhancement (left) and signal to noise ratios (right) of free pyridine signals when pyridine is hyperpolarised with a standard concentration of **IMes(b)** in the presence of a stoichiometric amount of acetonitrile. .... 161
- Figure 1.18 The graphical representation of Table 1.11 investigating the effect of pyridine concentration on the resultant signal enhancement of free pyridine signals when hyperpolarised with a standard concentration of **IMes(a)** in the presence of a stoichiometric amount of acetonitrile..... 163
- Figure 1.19 The graphical representation of Table 1.10 and Table 1.11 investigating the effect of pyridine concentration on the resultant signal enhancement of free pyridine signals when hyperpolarised with a standard concentration of **IMes(a)** in the presence of a stoichiometric amount of acetonitrile..... 164
- Figure 1.20 A 3D graphical interpretation in magnitude (*ortho* only) of Table 1.13, indicating the polarisation transfer to pyridine with **IMes(a)** under the indicated conditions. .... 166
- Figure 4.1 Structures of a) quinine and b) quinidine. Copied from Raheem *et al.* (2003).<sup>110</sup> ..... 170
- Figure 4.2 Structure of a) chloroquine and b) hydroxychloroquine. .... 172
- Figure 4.3 Structure of Clioquinol. .... 175
- Figure 4.4 Structure of quinoline with positions labelled. .... 176
- Figure 4.5 Structures of two potential products formed when **IMes(c)** reacts with hydrogen in the presence of quinoline and acetonitrile. .... 179
- Figure 4.6 The <sup>1</sup>H NMR signals corresponding to the hydride ligands observed when **IMes(c)** is activated in the presence of quinoline and hydrogen. .... 180
- Figure 4.7 The aromatic region of a <sup>1</sup>H NMR spectrum observed at 243 K when **IMes(c)** is activated in the presence of quinoline and hydrogen, with a ratio of 1:4 catalyst to substrate. ‘F’ denotes the signals corresponding to free quinoline and ‘B’ denotes the signals corresponding to proton 2 of quinoline bound to the catalyst. .... 180

Figure 4.8 Graphical representation of the effect of changing the temperature of the polarisation step on the $^1\text{H}$ NMR signal enhancement of quinoline when polarised with <b>IMes(c)</b> at a PTF of 2 G.....	184
Figure 4.9 Graphical representation of the effect of changing the temperature of the polarisation step on the $^1\text{H}$ NMR signal enhancement of quinoline when polarised with <b>SIMes(c)</b> at a PTF of 2 G.....	186
Figure 4.10 Graphical representation of the effect of changing the temperature of the polarisation step on the $^1\text{H}$ NMR signal enhancement of quinoline when polarised with <b>ICy(c)</b> at a PTF of 2 G.....	187
Figure 4.11 Graphical representation of observed $^1\text{H}$ NMR signal enhancement in the signal for position 2 of quinoline when polarised using <b>IMes(c)</b> , <b>SIMes(c)</b> and <b>ICy(c)</b> using method 1 at a PTF of 2 G and various temperatures.....	188
Figure 4.12 Graphical representation of observed $^1\text{H}$ NMR signal enhancement in the signal for the <i>para</i> position of pyridine when polarised using <b>IMes(a)</b> , <b>SIMes(a)</b> and <b>ICy(a)</b> (left) and of observed $^1\text{H}$ NMR signal enhancement in the signal for the 2 position of quinoline when polarised using <b>IMes(c)</b> , <b>SIMes(c)</b> and <b>ICy(c)</b> (right), both using method 1 at a PTF of 2 G and various temperatures.....	189
Figure 4.13 Effect of changing the PTF during polarisation of quinoline polarised using method 2 with <b>IMes(b)</b> .....	190
Figure 4.14 Graphical representation of the $^1\text{H}$ NMR signal enhancement levels of quinoline when polarised with <b>IMes(b)</b> at various PTF using method 2.....	191
Figure 4.15 A 3D representation of Table 4.13 showing the $^1\text{H}$ NMR signal enhancement when quinoline is polarised with <b>IMes(c)</b> at room temperature and a PTF of 2 G in various solvents.....	192
Figure 4.16 Thermally polarised $^1\text{H}$ NMR COSY of quinoline, with the signal intensity increased such that any weak couplings can be observed.....	194
Figure 4.17 Structure of naphthalene.....	195
Figure 4.18 Structures of a) quinoline and b) isoquinoline.....	195



Figure 4.19 Structures of a) 4-methylquinoline, b) 7-methylquinoline and c) 8-methylquinoline. ....	197
Figure 4.20 Structure of phenazine. ....	199
Figure 4.21 $^1\text{H}$ NMR spectrum of phenazine where bottom is thermally polarised and top is hyperpolarised using method 1 with <b>IMes(b)</b> in methanol. ....	199
Figure 4.22 Labelled structure of quinoline together with the 21 potential $I_z S_z$ pairs. .	200
Figure 4.23 A series of selective $^1\text{H}$ OPSYdq spectra of quinoline polarised with <b>IMes(c)</b> using method 2. The bottom spectrum in each set is a thermal $^1\text{H}$ NMR spectrum to act as a reference. The spectra are grouped by resonance (the rectangle) and the second selected resonance is indicated by a square. ....	202
Figure 5.1 Labelled structure of quinoline. ....	206
Figure 5.2 Thermally polarised $^1\text{H}$ NMR spectrum of quinoline. ....	207
Figure 5.3 Effect of changing the time of addition of <i>parahydrogen</i> on the $^1\text{H}$ enhancement observed to the indicated positions of quinoline (10 mM) when polarised with <b>IMes(c)</b> (0.5 mM) using method 2. ....	208
Figure 5.4 Plot of the effect of PTF on the signal intensity in the resultant $^1\text{H}$ OPSYdq NMR spectrum of quinoline hyperpolarised with <b>IMes(b)</b> using method 2 where the PTF is set to -150 G (bottom) to 0 G (top). For clarity, the plot has been split into three sets of equal relative intensity, where the left set shows protons 2, 4 and 8, middle set shows protons 5 7 and 6, and right set shows proton 3. ....	209
Figure 5.5 Thermally polarised 1D $^1\text{H}$ NOESY spectrum of quinoline (100 mM), top, and hyperpolarised using method 2 with <b>IMes(c)</b> (5 mM), bottom, presented on the same scale. Position 4 of quinoline was selected, and the inset traces show the observed nOe correlations to positions 5 and 3. ....	210
Figure 5.6 Thermally polarised 1D $^1\text{H}$ NOESY spectrum of quinoline (10 mM), top, and hyperpolarised spectrum achieved using method 2 with <b>IMes(c)</b> (0.5 mM), bottom, presented on the same scale. Position 4 of quinoline was selected, and the inset traces show the observed nOe correlations to positions 5 and 3. ....	211

Figure 5.7 Thermally polarised coupled (top, 9216 scans) and decoupled (bottom, 101 scans) $^{13}\text{C}$ NMR spectra of quinoline.....	213
Figure 5.8 Single scan $^{13}\text{C}$ NMR spectrum of quinoline hyperpolarised with <b>IMes(b)</b> at PTF of 10 G using method 2.....	214
Figure 5.9 A series of single scan $^{13}\text{C}$ NMR spectra of quinoline hyperpolarised with <b>IMes(c)</b> using method 2, where the PTF is increased from -150 G (bottom) to 0 G (top) in increments of 30 G.....	215
Figure 5.10 Schematic of the effect of multiple quantum states on the resultant signal. .....	216
Figure 5.11 Schematic of the effect of selected combinations of multiple quantum states on the resultant signal.....	216
Figure 5.12 $^{13}\text{C}$ signals which present with the $I_z T_z$ state. Left is a quaternary carbon signal and right is a CH carbon signal. ....	217
Figure 5.13 Schematic depicting the effect of decoupling on antiphase signals. ....	218
Figure 5.14 Schematic of the refocused $^{13}\text{C}\{^1\text{H}\}$ NMR sequence termed the $^{13}\text{C}\{^1\text{H}\}$ _JR NMR sequence. $\tau$ denotes a delay corresponding to a $^1\text{H}$ - $^{13}\text{C}$ coupling constant.....	218
Figure 5.15 A series of single scan $^{13}\text{C}\{^1\text{H}\}$ _JR NMR spectra optimised for a one bond coupling of quinoline hyperpolarised with <b>IMes(c)</b> using method 2 where the PTF is increased from -150 G (bottom) to 0 G (top) in increments of 30 G. ....	219
Figure 5.16 A series of single scan $^{13}\text{C}\{^1\text{H}\}$ _JR NMR spectra optimised for a two bond coupling of quinoline hyperpolarised with <b>IMes(c)</b> using method 2 where the PTF is increased from -150 G (bottom) to 0 G (top) in increments of 30 G. ....	220
Figure 5.17 Single scan $^{13}\text{C}\{^1\text{H}\}$ _JR NMR spectra optimised for a two bond coupling with a PTF of -90 G (bottom) and one bond coupling with a PTF of 0 G (top) of quinoline hyperpolarised using method 2 with <b>IMes(c)</b> . ....	221
Figure 5.18 Schematic of the refocused $^{13}\text{C}\{^1\text{H}\}$ NMR sequence termed the $^{13}\text{C}\{^1\text{H}\}$ _JCSR $^{13}\text{C}$ NMR sequence. $\tau$ denotes a delay corresponding to a $^1\text{H}$ - $^{13}\text{C}$ coupling constant. ....	222

- Figure 5.19 A series of single scan  $^{13}\text{C}\{^1\text{H}\}$ \_JCSR NMR spectra optimised for a one bond coupling of quinoline hyperpolarised with **IMes(c)** using method 2 where the PTF is increased from -150 G (bottom) to 0 G (top) in increments of 30 G. .... 222
- Figure 5.20 A series of single scan  $^{13}\text{C}\{^1\text{H}\}$ \_JCSR NMR spectra optimised for a two bond coupling of quinoline hyperpolarised with **IMes(c)** using method 2 where the PTF is increased from -150 G (bottom) to 0 G (top) in increments of 30 G. .... 223
- Figure 5.21 Single scan  $^{13}\text{C}\{^1\text{H}\}$ \_JCSR spectra optimised for one bond couplings (top) and two bond couplings (bottom), of quinoline hyperpolarised with **IMes(c)** using method 2 where the PTF is set to 0 G. .... 224
- Figure 5.22 Optimised  $^{13}\text{C}\{^1\text{H}\}$ \_JR NMR spectrum (top) and optimised  $^{13}\text{C}\{^1\text{H}\}$ \_JCSR NMR spectrum. .... 225
- Figure 5.23 Schematic of the standard  $^{13}\text{C}$  INEPTnd sequence.  $\tau$  denotes a delay corresponding to a  $^1\text{H}$ - $^{13}\text{C}$  coupling constant. .... 226
- Figure 5.24 Thermally polarised  $^{13}\text{C}$  INEPTnd NMR spectra of quinoline optimised for one bond (top) and two bond (bottom) coupling. .... 226
- Figure 5.25 Thermally polarised  $^{13}\text{C}$  INEPTnd NMR spectra of quinoline optimised for two bond couplings (8 Hz, top and 19 Hz bottom). .... 227
- Figure 5.26 Single scan  $^{13}\text{C}$  INEPTnd NMR spectra of quinoline optimised for a two bond coupling, hyperpolarised using method 2 with **IMes(c)** at a PTF of -50 G (bottom) and 0 G (top). .... 228
- Figure 5.27 Single scan  $^{13}\text{C}$  INEPTnd NMR spectra of quinoline optimised for a one bond coupling, hyperpolarised using method 2 with **IMes(c)** at a PTF of -50 G (bottom) and 0 G (top). .... 229
- Figure 5.28 Single scan  $^{13}\text{C}$  INEPTnd NMR spectra of quinoline hyperpolarised with **IMes(c)** at a PTF of -50 G where the first pulse is  $90^\circ$  and the sequence is optimised for two bond couplings (bottom) and one bond couplings (top). .... 230
- Figure 5.29 Various hyperpolarised coupled and decoupled  $^{13}\text{C}$  NMR spectra of quinoline. a)  $^{13}\text{C}$  NMR spectrum collected at a PTF of 0 G, b) a refocused  $^{13}\text{C}\{^1\text{H}\}$

NMR spectrum collected at a PTF of 0 G and c) a  $^{13}\text{C}$  INEPTnd NMR spectrum optimised for two bond couplings collected at a PTF of -50 G. ....231

Figure 5.30 Schematic of the  $^{13}\text{C}$  PH\_INEPT NMR sequence, adapted from Haake *et al.*<sup>150</sup> which differs from the INEPTnd sequence in that the first pulse has a  $90^\circ$  phase change and is a  $45^\circ$  pulse. This is adapted for use in this research such that the first pulse can be  $90^\circ$  or  $45^\circ$ , to be termed INEPT\_phase.  $\tau$  denotes a delay corresponding to a  $^1\text{H}$ - $^{13}\text{C}$  coupling constant. ....232

Figure 5.31 Single scan  $^{13}\text{C}$  INEPT\_phase NMR spectra of quinoline hyperpolarised with **IMes(c)** at a PTF -65 G where the first pulse is  $90^\circ$  and the sequence is optimised for two bond couplings (bottom) and one bond couplings (top). ....233

Figure 5.32 Single scan  $^{13}\text{C}$  INEPT\_phase NMR spectra of quinoline optimised for one bond couplings hyperpolarised using method 2 with **IMes(c)**, the first pulse on  $^1\text{H}$  is  $90^\circ$ , and PTF occurs at -65 G (bottom) and 0 G (top). ....234

Figure 5.33 Single scan  $^{13}\text{C}$  INEPT\_phase NMR spectra of quinoline optimised for a one bond coupling, hyperpolarised using method 2 with **IMes(c)** at a PTF of -65 G and the first pulse on  $^1\text{H}$  is  $90^\circ$  (bottom) and  $45^\circ$  (top). ....235

Figure 5.34 Single scan transfer  $^{13}\text{C}$  INEPT NMR spectra of quinoline hyperpolarised with **IMes(c)** showing the optimised INEPTnd (bottom) and optimised INEPT\_phase (top) spectra. ....236

Figure 5.35 Schematic of the  $^{13}\text{C}$  INEPTrd NMR sequence.  $\tau$  and  $\Delta$  denote delays corresponding to a  $^1\text{H}$ - $^{13}\text{C}$  coupling constant. ....237

Figure 5.36 Single scan  $^{13}\text{C}\{^1\text{H}\}$  INEPTrd NMR spectra of quinoline hyperpolarised with **IMes(c)** at a PTF of 0 G, optimised for two bond couplings (bottom) and one bond couplings (top). These spectra have been presented in magnitude mode. ....238

Figure 5.37 Single scan  $^{13}\text{C}\{^1\text{H}\}$  INEPTrd NMR spectra optimised for one bond couplings of quinoline hyperpolarised using method 2 with **IMes(c)** at a PTF of -50 G (bottom) and 0 G (top). These spectra have been presented in magnitude mode. ....239

- Figure 5.38 Showing a  $^{13}\text{C}$  NMR spectrum of quinoline hyperpolarised at a PTF of -65 G (bottom) and a  $^{13}\text{C}$  INEPTnd NMR spectrum (top) completed immediately after the first sequence. These spectra have been presented in magnitude mode. .... 240
- Figure 5.39 Showing a  $^{13}\text{C}\{^1\text{H}\}$  NMR spectrum of quinoline hyperpolarised at a PTF of 0 G (bottom) and a  $^{13}\text{C}$  INEPTnd NMR spectrum (top) completed immediately after the first sequence. These spectra have been presented in magnitude mode. .... 241
- Figure 5.40 Showing: bottom, a  $^{13}\text{C}$  NMR spectrum of quinoline hyperpolarised at a PTF of -50 G and top, a  $^{13}\text{C}\{^1\text{H}\}$  INEPTrd spectrum completed immediately after the first sequence. These spectra have been presented in magnitude mode. .... 242
- Figure 5.41  $^{13}\text{C}\{^1\text{H}\}$  INEPTrd NMR spectra of quinoline (100 mM) hyperpolarised using method 2 with **IMes(c)** (5 mM) at a PTF of -50 G with 1 scan (bottom), and 8 scans (middle), and  $^{13}\text{C}\{^1\text{H}\}$  INEPTrd NMR spectra of quinoline (300 mM) hyperpolarised using method 2 with **IMes(c)** (15 mM) at a PTF of -50 G with 1 scan (top). These spectra have been presented in magnitude mode, and are scaled relative to each other according to the y-axis. .... 243
- Figure 5.42 Thermally polarised  $^1\text{H}$ - $^1\text{H}$  COSY NMR spectrum of quinoline. .... 244
- Figure 5.43  $^1\text{H}$ - $^1\text{H}$  COSY NMR spectrum of quinoline hyperpolarised using method 2 with **IMes(c)** at a PTF of 0 G. .... 245
- Figure 5.44  $^1\text{H}$ - $^1\text{H}$  OPSY-COSY sequence adapted from that proposed in a publication by Aguilar *et al.*<sup>84</sup> in 2007. .... 246
- Figure 5.45  $^1\text{H}$ - $^1\text{H}$  OPSYdq-COSY NMR spectra of quinoline (100 mM) hyperpolarised with **IMes(c)** (5 mM) at a PTF of 0 G (left) and -50 G (right). .... 246
- Figure 5.46  $^1\text{H}$ - $^1\text{H}$  OPSYdq-COSY NMR spectra of quinoline (10 mM) hyperpolarised with **IMes(c)** (0.5 mM) at a PTF of 0 G (left) and -50 G (right), with long range correlations labelled between positions 2 and 4 (triangles), positions 5 and 7 (hexagons) and positions 6 and 8 (squares). .... 247
- Figure 5.47 Thermally polarised  $^1\text{H}$ - $^{13}\text{C}$  HSQC NMR spectrum of quinoline. .... 248

Figure 5.48 $^1\text{H}$ - $^{13}\text{C}$ HSQC NMR spectra of quinoline (100 mM) hyperpolarised using method 2 with <b>IMes(c)</b> (5 mM) at a PTF of 0 G (left) and -60 G (right). .....	249
Figure 5.49 $^1\text{H}$ - $^{13}\text{C}$ HSQC NMR spectra of quinoline (100 mM) hyperpolarised with <b>IMes(c)</b> (5 mM) at a PTF of -30 G. ....	249
Figure 5.50 $^1\text{H}$ - $^{13}\text{C}$ HSQC NMR spectra of quinoline (100 mM) hyperpolarised using method 2 with <b>IMes(c)</b> (5 mM) at a PTF of -30 G, expanded to include the observed noise at the top and bottom of the spectrum (left). The 3D representation is also included on the right.....	250
Figure 5.51 Thermally polarised $^1\text{H}$ - $^{13}\text{C}$ HMBC NMR spectrum of quinoline. ....	251
Figure 5.52 $^1\text{H}$ - $^{13}\text{C}$ HMBC NMR spectra of quinoline (100 mM) hyperpolarised with <b>IMes(c)</b> (5 mM) utilising the MKII polarisor at a PTF of 0 G (left) and -60 G (right). .....	251
Figure 5.53 $^1\text{H}$ - $^{13}\text{C}$ HMBC NMR spectra of quinoline (10 mM) hyperpolarised with <b>IMes(c)</b> (0.5 mM) utilising the MKIII polarisor at a PTF of -50 G. ....	252
Figure 5.54 Thermally polarised $^1\text{H}$ - $^{13}\text{C}$ HMQC NMR spectrum of quinoline optimised for two bond couplings. ....	253
Figure 5.55 $^1\text{H}$ - $^{13}\text{C}$ HMQC NMR spectra of quinoline (100 mM) hyperpolarised using method 2 with <b>IMes(c)</b> (5 mM) at a PTF of 0 G (left) and -60 G (right), and optimised for one bond couplings.....	254
Figure 5.56 $^1\text{H}$ - $^{13}\text{C}$ HMQC NMR spectra of quinoline (100 mM) hyperpolarised using method 2 with <b>IMes(c)</b> (5 mM) at a PTF of 0 G (left) and -60 G (right), and optimised for two bond couplings. ....	254
Figure 5.57 $^1\text{H}$ - $^{13}\text{C}$ HMQC NMR spectra of quinoline (10 mM) hyperpolarised with <b>IMes(c)</b> (0.5 mM) at a PTF of -50 G and optimised for two bond couplings. ....	255
Figure 5.58 $^1\text{H}$ - $^{13}\text{C}$ HMBC NMR spectra of quinoline (100 mM) hyperpolarised using method 2 with <b>IMes(c)</b> (5 mM). The spectrum on the left was collected with an f1 spectral width of 50 ppm centred around 140 ppm, and the spectrum on the right was collected with an f1 spectral width of 80 ppm centred around 155 ppm. ....	257

Figure 5.59  $^1\text{H}$ - $^{13}\text{C}$  HMBC NMR spectra of quinoline (100 mM) hyperpolarised using method 2 with **IMes(c)** (5 mM). The spectra were collected with an f1 spectral width of 80 ppm centred around 155 ppm with 64 increments (left) and 128 increments (right).

.....257

Figure 5.60  $^1\text{H}$ - $^{13}\text{C}$  HMBC NMR spectrum (left) and  $^1\text{H}$ - $^{13}\text{C}$  HMQC NMR spectrum (right) of quinoline hyperpolarised using method 2 with **IMes(c)** at a PTF of -50 G. In each spectrum, 2 scans were used for each of the 32 increments. ....258

Figure 5.61 Acid-catalysed hydrolysis of 2-(4-nitrophenyl)-1,3-dioxolane acetal (reactant). ....259

Figure 5.62  $^1\text{H}$ - $^1\text{H}$  ufCOSY NMR spectra of quinoline (100 mM) (L-R) thermally polarised spectra, hyperpolarised using method 1 with **IMes(c)** (5 mM) at a PTF of 0 G and hyperpolarised with **IMes(c)** (5 mM) at a PTF of 65 G, presented with internal projections. ....260

Figure 5.63 A thermally polarised  $^1\text{H}$ - $^1\text{H}$  COSY NMR spectrum including labels corresponding to the peaks integrated. ....261

Figure 5.64  $^1\text{H}$ - $^1\text{H}$  ufCOSY NMR spectra of quinoline (10 mM) (L-R) thermally polarised, hyperpolarised using method 1 with **IMes(c)** (0.5 mM) at a PTF of 0 G and hyperpolarised using method 1 with **IMes(c)** (0.5 mM) at a PTF of 65 G, with internal projections. ....262

Figure 5.65  $^1\text{H}$ - $^1\text{H}$  ufCOSY NMR spectra of quinoline (1 mM) hyperpolarised with **IMes(c)** (0.05 mM) at 0 G (left) and hyperpolarised with **IMes(c)** (0.05 mM) at a PTF of 65 G (right), presented with internal projections. ....262

Figure 5.66  $^{13}\text{C}$  INEPTnd NMR spectra of quinoline optimised for two bond couplings (8 Hz, top and 19 Hz bottom) hyperpolarised using **IMes(c)**. Using a TXI probe, each spectrum was collected using an average of 8 scans. ....265

Figure 5.67  $^1\text{H}$ - $^{13}\text{C}$  HMQC NMR spectra of quinoline (100 mM) hyperpolarised with **IMes(c)** (5 mM) at a PTF of -50 G and optimised for two bond couplings with decoupler turned on. Selected signals have been expanded for comparison. ....266

Figure 5.68 $^1\text{H}$ - $^{13}\text{C}$ HMQC NMR spectra of quinoline (100 mM) hyperpolarised with <b>IMes(c)</b> (5 mM) at a PTF of -50 G and optimised for two bond couplings with decoupler turned off. Selected signals have been expanded for comparison.....	267
Figure 6.1 Structures of a) tryptophan, b) melatonin and c) serotonin. ....	269
Figure 6.2 Structure of Thiamine, Vitamin B <sub>1</sub> .....	270
Figure 6.3 Structures of a) trimethoprim b) sulphamethoxazole and c) 1-[ <i>N,N</i> -dimethylaminomethyl]-5-bromoisatin-3-{1'-[4''-( <i>p</i> -chlorophenyl) thiazole-2''-yl] thio semicarbazone. <sup>167</sup> .....	270
Figure 6.4 Structure of Pittsburgh B. ....	271
Figure 6.5 Structures of a) albendazole, b) anastrozole, c) bicalutamide, d) esomeprazole, e) gefitinib and f) mebendazole.....	271
Figure 6.6 List of the 4-substituted pyridines investigated, namely: (a) 4-carbonitrilepyridine, (b) 4-hydroxypyridine, (c) 4-carboxamidepyridine, (d) 4-carboxaldehydepyridine, (e) isonicotinic acid, (f) 4-phenylpyridine, (g) 4-methylpyridine and (h) 4-aminopyridine. Each substrate is presented with the $pK_a$ of the nitrogen position. <sup>106,145,195-202</sup> .....	276
Figure 6.7 Showing the observed polarisation to the <i>ortho</i> position of a series of four substituted pyridines compared to the $pK_a$ of the N-position of those substrates. ....	277
Figure 6.8 Showing the sum of the modulus of polarisation transfer to both <i>ortho</i> and <i>meta</i> positions of a series of four substituted pyridines compared to the $pK_a$ of the N-position of those substrates. ....	278
Figure 6.9 Hydride region of thermal $^1\text{H}$ NMR spectra of the named substrates polarised using method 1 and <b>IMes(a)</b> .....	279
Figure 6.10 Structures of phenol and benzonitrile.....	279
Figure 6.11 Labelled structures of a) 2-methylpyridine, b) 3-methylpyridine and c) 4-methylpyridine. ....	281



Figure 6.12 Labelled structures of a) 2-phenylpyridine, b) 3-phenylpyridine and c) 4-phenylpyridine.....	282
Figure 6.13 Graphical representation of the effect of changing bubbling time on the polarisation transfer to 3-phenylpyridine.....	284
Figure 6.14 Structure of 3-benzoylpyridine and 4-(4-chlorobenzoyl)pyridine.....	284
Figure 6.15. Structures of a) indole and b) 1-methylindole.....	286
Figure 6.16 Structure of thiazole.....	287
Figure 6.17 Structure of 2-aminothiazole.....	287
Figure 6.18 Thermal $^1\text{H}$ NMR spectrum of 2-aminothiazole (top) with a typical hyperpolarised spectrum of 2-aminothiazole (bottom) polarised with method 1 and <b>IMes(a)</b> .....	288
Figure 6.19 Observed $^1\text{H}$ NMR signal enhancement of 2-aminothiazole hyperpolarised at a PTF of -150 G to +10 G in increments of 10 G using method 2 and <b>IMes(a)</b> .....	289
Figure 6.20 Structure of 2-amino-4-methyl thiazole.....	290
Figure 6.21 Structures of (a) 2-amino-4-phenyl thiazole and (b) 2-amino-4-(4-chlorophenyl) thiazole.....	290
Figure 6.22 Observed NMR signal enhancement of 2-amino-4-(4-chlorophenyl)thiazole polarised with <b>IMes(c)</b> . This data is presented with a PTF of -140 G (bottom) to 0 G in increments of 20 G. The left shows the effect on $^1\text{H}$ NMR spectra and the right shows the effect on the $^1\text{H}$ OPSYdq NMR spectra.....	291
Figure 6.23 Structure of benzothiazole.....	292
Figure 6.24 Effect of changing field of hydrogen addition on polarisation transfer to benzothiazole using method 2 and <b>IMes(c)</b> . a) shows all $^1\text{H}$ resonances, b) shows signals corresponding to the proton 2, c) to protons 4 and 7 and d) to protons 5 and 6.....	293

Figure 6.25 $^{13}\text{C}$ spectra of benzothiazole after 8 scans hyperpolarised with a PTF of -60 G.....	294
Figure 6.26 Structures of a) pyridine and b) 2-aminothiazole. ....	296
Figure 6.27 Structures of a) pyridine, b) 2-aminothiazole and c) quinoline.....	298
Figure 6.28 The hydride region of the reaction of hydrogen with 2-aminothiazole with <b>IMes(a)</b> (bottom) or <b>IMes(c)</b> (top). ....	299
Figure 6.29 The $^1\text{H}$ NMR spectrum of 2-aminothiazole hyperpolarised with <b>IMes(c)</b> using method 1, with 2-aminothiazole and hydride regions depicted.....	299
Figure 6.30 The hydride region observed for the following, bottom to top; sample 1 (2-aminothiazole and <b>IMes(c)</b> ), sample 2 (quinoline and <b>IMes(c)</b> ) and sample 3 (quinoline, 2-aminothiazole and <b>IMes(c)</b> ) from Table 6.14.....	300
Figure 6.31 Structures of a) 4-methylpyridine and b) 4-phenylpyridine. ....	300
Figure 6.32 The $^1\text{H}$ NMR spectra of a mixture of compounds with (bottom) the thermal $^1\text{H}$ NMR spectrum and (top) the $^1\text{H}$ OPSYdq NMR spectrum hyperpolarised with <b>IMes(a)</b> by method 1. ....	303
Figure 6.33 $^1\text{H}$ NMR spectra of pyridine completed in 90 % protonated methanol. Top, thermal $^1\text{H}$ NMR spectrum and, bottom, $^1\text{H}$ OPSYdq NMR spectrum. ....	303
Figure 6.34 Spontaneous reaction reported in a publication by Plater <i>et al.</i> <sup>204</sup> .....	304
Figure 6.35 Reaction reported in a publication by de la Fuente and Dominguez. <sup>205</sup> ....	305
Figure 6.36 Spontaneous reaction of 4-carboxaldehydepiperidine in the presence of methanol.....	305
Figure 6.37 Thermal $^1\text{H}$ NMR spectra of 4-carboxaldehydepiperidine in $d_4$ -methanol and $\text{CDCl}_3$ , where black circles correspond to 4-carboxaldehydepiperidine, and blue circles correspond to the hemiacetal product. ....	306
Figure 6.38 $^1\text{H}$ NMR spectra in chloroform of bottom, 4-carboxaldehydepiperidine and top, 4-carboxaldehydepiperidine and protonated methanol.....	307

- Figure 6.39 Thermal  $^1\text{H}$  NMR spectrum (bottom) of 4-carboxaldehyde pyridine dissolved in chloroform- $d_1$  with an addition of methanol and  $^1\text{H}$  EXSY spectra of the same sample with various mixing times (d8) where the 4-( $\text{CH}(\text{OMe})(\text{OH})$ )py of the hemiacetal is excited (top three). The \* symbol denotes the excited resonance..... 308
- Figure 6.40 Thermal  $^1\text{H}$  NMR spectrum (bottom) of 4-carboxaldehyde pyridine dissolved in chloroform- $d_1$  with an addition of methanol and  $^1\text{H}$  NOESY spectrum of the same sample where the 4-( $\text{CH}(\text{O})$ )py of 4-carboxaldehyde pyridine is excited (top). The \* symbol denotes the excited resonance. .... 309
- Figure 6.41  $^1\text{H}$  NMR spectra in chloroform of bottom, 4-carboxaldehyde pyridine and top, 4-carboxaldehyde pyridine and protonated ethanol. .... 310
- Figure 6.42 ESI mass spectrum of 4-carboxaldehyde pyridine in methanol stored at room temperature without the presence of acid..... 312
- Figure 6.43 ESI mass spectrum of 4-carboxaldehyde pyridine in methanol stored at room temperature in the presence of acid..... 313
- Figure 6.44 ESI mass spectrum of 4-carboxaldehyde pyridine in methanol stored at 50  $^\circ\text{C}$ , without the presence of acid..... 313
- Figure 6.45 ESI mass spectrum of 4-carboxaldehyde pyridine in methanol stored at 50  $^\circ\text{C}$  in the presence of acid..... 313
- Figure 6.46 Reaction products of 4-carboxaldehyde pyridine observed in mass spectroscopy..... 314
- Figure 7.1 Structures of **ICy(a)** and **ICy<sub>2</sub>(a)**. .... 325
- Figure 8.1 Effect of changing PTF on polarisation transfer efficiency into pyridine using **SIMes(a)**. .... 332
- Figure 8.2 Graphical representation of the effect of changing PTF on polarisation transfer efficiency into poyridine using **SIMes(a)**..... 332
- Figure 8.3 Effect of changing PTF on polarisation transfer efficiency into pyridine using **ICy(a)**..... 333

Figure 8.4 Graphical representation of the effect of changing PTF on polarisation transfer efficiency into pyridine using <b>ICy(a)</b> . .....	333
Figure 8.5 Effect of changing PTF on polarisation transfer efficiency into pyridine using <b>ICy<sub>2</sub>(a)</b> . .....	334
Figure 8.6 Graphical representation of the effect of changing PTF on polarisation transfer efficiency into pyridine using <b>ICy<sub>2</sub>(a)</b> . .....	334
Figure 8.7 Effect of changing PTF on polarisation transfer efficiency into 3,4,5-d <sub>3</sub> -pyridine using <b>SIMes(a)</b> . .....	335
Figure 8.8 Graphical representation of the effect of changing PTF on polarisation transfer efficiency into 3,4,5-d <sub>3</sub> -pyridine using <b>SIMes(a)</b> . .....	335
Figure 8.9 Effect of changing PTF on polarisation transfer efficiency into quinoline using <b>IMes(b)</b> . .....	336
Figure 8.10 Graphical representation of the effect of changing PTF on polarisation transfer efficiency into quinoline using <b>IMes(b)</b> . .....	336
Figure 8.11 Effect of changing PTF on polarisation transfer efficiency into 4-methylpyridine using <b>SIMes(a)</b> . .....	337
Figure 8.12 Graphical representation of the field profile of <b>SIMes(a)</b> with 4-methylpyridine. ....	337
Figure 8.13 Effect of changing PTF on polarisation transfer efficiency into 3-methylpyridine using <b>SIMes(a)</b> . .....	338
Figure 8.14 Graphical representation of the effect of changing PTF on polarisation transfer efficiency into 3-methylpyridine using <b>SIMes(a)</b> . .....	338
Figure 8.15 Effect of changing PTF on polarisation transfer efficiency into 2-aminothiazole using <b>IMes(a)</b> . .....	339
Figure 8.16 Graphical representation of the effect of changing PTF on polarisation transfer efficiency into 2-aminothiazole using <b>IMes(a)</b> . .....	339

Figure 8.17 Effect of changing PTF on polarisation transfer efficiency into 3-phenylpyridine using <b>IMes(a)</b> .....	340
Figure 8.18 Graphical representation of the effect of changing PTF on polarisation transfer efficiency into 3-phenylpyridine using <b>IMes(a)</b> .....	340
Figure 8.19 Effect of changing PTF on polarisation transfer efficiency into 4-phenylpyridine using <b>IMes(a)</b> .....	341
Figure 8.20 Graphical representation of the effect of changing PTF on polarisation transfer efficiency into 4-phenylpyridine using <b>IMes(a)</b> .....	341
Figure 8.21 The reaction co-ordinate for the dissociative reaction for loss of ligand. .	342
Figure 8.22 Graphical representation of the absolute integrals of the three positions of pyridine observed in a single scan $^1\text{H}$ NMR spectrum at the indicated volumes. The equations of the trend lines are included.....	347
Figure 8.23 $^1\text{H}$ NMR spectrum of $[\text{Ir}(\text{IMes})(\text{H})_2(\text{quinoline})_2(\text{NCMe})]\text{Cl}$ . .....	355
Figure 8.24 $^1\text{H}$ NMR spectrum of $[\text{Ir}(\text{IMes})(\text{H})_2(\text{quinoline})_2(\text{NCMe})]\text{Cl}$ expanded to show the complicated aromatic region, including the relative integrals of the signals.	355
Figure 8.25 $^{13}\text{C}\{^1\text{H}\}$ NMR spectrum of $[\text{Ir}(\text{IMes})(\text{H})_2(\text{quinoline})_2(\text{NCMe})]\text{Cl}$ . .....	356
Figure 8.26 $^1\text{H}$ - $^1\text{H}$ COSY NMR spectrum of $[\text{Ir}(\text{IMes})(\text{H})_2(\text{quinoline})_2(\text{NCMe})]\text{Cl}$ . ..	356
Figure 8.27 $^1\text{H}$ - $^1\text{H}$ COSY NMR spectrum of $[\text{Ir}(\text{IMes})(\text{H})_2(\text{quinoline})_2(\text{NCMe})]\text{Cl}$ expanded to investigate the correlations corresponding to the hydride ligands. Left shows the correlations of the hydride ligands to each other, and right shows the correlations of the hydride ligands to the others protons in the complex. ....	357
Figure 8.28 $^1\text{H}$ - $^{13}\text{C}$ HMQC NMR spectrum $[\text{Ir}(\text{IMes})(\text{H})_2(\text{quinoline})_2(\text{NCMe})]\text{Cl}$ optimised for 2 bond couplings.....	357
Figure 8.29 The spontaneous and acid catalysed reactions of 4-carboxaldehydepipridine (a) with methanol producing a hemiacetal (b) and an acetal (c). .....	360
Figure 8.30 Labelled structure of 4-carboxaldehydepipridine. ....	361

Figure 8.31 Labelled structure of the hemiacetal product resulting from the spontaneous reaction of 4-carboxaldehydepipridine with methanol.....	361
Figure 8.32 Labelled structure of the acetal product resulting from the acid catalysed reaction of 4-carboxaldehydepipridine with methanol.....	362
Figure 8.33 Labelled structure of 3-phenylpipridine. ....	362
Figure 8.34 Labelled structure of 4-phenylpipridine. ....	363
Figure 8.35 Labelled structure of 3-benzoylpipridine.....	363
Figure 8.36 Labelled structure of 4-(4-chlorobenzoyl)pipridine. ....	363
Figure 8.37 Labelled structure of quinoline.....	364
Figure 8.38 Labelled structure of isoquinoline. ....	364
Figure 8.39 Labelled structure of 4-methylquinoline. ....	365
Figure 8.40 Labelled structure of 7-methylquinoline. ....	365
Figure 8.41 Labelled structure of 8-methylquinoline. ....	366
Figure 8.42 Labelled structure of indole.....	366
Figure 8.43 Labelled structure of 2-amino-4-(4-chlorophenyl)thiazole.....	367
Figure 8.44 Labelled structure of benzothiazole.....	367
Figure 9.1 A plot of the percentage of bound ligands and free substrate derived from $^1\text{H}$ EXSY NMR spectra against the mixing time implemented. This data was collected at 300 K and monitored the loss of hydride ligands from <b>ICy(a)</b> to free hydrogen.....	368
Figure 9.2 The Eyring plots derived for the loss of hydride ligands and pipridine ligands from <b>SIMes(a)</b> in the presence of pipridine with associated equations, produced from the data presented in Table 9.1.....	375
Figure 9.3 The Eyring plots derived for the loss of hydride ligands and pipridine ligands from <b>ICy(a)</b> in the presence of pipridine with associated equations, produced from the data presented in Table 9.4.....	377

Figure 9.4 The Eyring plots derived for the loss of hydride ligands and quinoline ligands from **IMes(c)** in the presence of quinoline with associated equations, produced from the data presented in Table 9.7.....379

Figure 9.5 X-ray crystallography structure of  $[\text{Ir}(\text{SIMes})(\text{COD})(2\text{-methylpyridine})]\text{PF}_6$ .  
.....407

## List of Tables

Table 1.1 Comparison of probe performance of a 1-mm TXI Microliter probe, a 5-mm TXI probe and a 5-mm cryoprobe, where $V_{\text{tot}}$ is the total sample volume required, $V_{\text{obs}}$ is the volume pulsed by the probe, and S/N refers to the signal to noise ratio. These experiments were carried out on 172 $\mu\text{g}$ (0.5 $\mu\text{mol}$ ) sample of sucrose in the $V_{\text{tot}}$ , collected with one scan, processed with a line broadening of 1. Enhancements are calculated based on results gained from the 5-mm conventional TXI probe. Table adapted from a 2002 publication by Schlotterbeck <i>et al.</i> <sup>14</sup> .....	60
Table 1.2 Characteristic shifts of signals corresponding to the hydride ligands of $[\text{IrCl}(\text{H})_2(\text{PPh}_3)_2(\text{L})]$ where L corresponds to the stated biologically relevant substrates. For purine and adenine, a, b and c refer to different isomers of the resultant iridium complex. Data collated from the 2007 publication by Wood <i>et al.</i> <sup>56</sup> .....	76
Table 1.3 Required product operators required to describe a system containing two coupled spins, <b>I</b> and <b>S</b> . .....	94
Table 2.1 Carbonyl stretching frequencies for compounds $[(\text{L})\text{Ni}(\text{CO})_3]$ (TEP, $\text{cm}^{-1}$ ). Copied from a publication by Kelly III <i>et al.</i> (2008). <sup>94</sup> .....	105
Table 2.2 Comparison of the two methods, method 1 and method 2, which can be used in the application of SABRE in NMR.....	111
Table 2.3 Effect of method 1 on a sample shaken with normal hydrogen or air. ....	117
Table 2.4 Results from reproducibility experiment for method 1 with <b>IMes(a)</b> and pyridine, presented as absolute values. ....	118
Table 2.5 Thermodynamic data collected and published by Cowley <i>et al.</i> <sup>66</sup> for the loss of pyridine and hydride ligands from <b>IMes(a)</b> . ....	122
Table 2.6 Comparison of the structural properties of the carbene ligands investigated in this thesis, IMes, SIMes and ICy. Values for PCy <sub>3</sub> have also been included. ....	125
Table 2.7 Selected angles for $[(\text{NHC})\text{Ir}(\text{COD})\text{Cl}]$ from a publication by Kelly <i>et al.</i> <sup>94</sup> where <i>cis</i> and <i>trans</i> are relative to the carbene. ....	127



Table 2.8 Selected bond lengths for [(NHC)Ir(COD)Cl] in Å, from a publication by Kelly <i>et al.</i> <sup>94</sup> where <i>cis</i> and <i>trans</i> are relative to the carbene.....	127
Table 2.9 Selected NMR data for the catalytic precursors <b>IMes(a)</b> , <b>SIMes(a)</b> and <b>ICy(a)</b> in methanol.....	128
Table 2.10 Selected angles for [Ir(SIMes)(COD)Cl] ( <b>SIMes(a)</b> ) from a publication by Kelly <i>et al.</i> <sup>94</sup> and [Ir(SIMes)(COD)(2-methylpyridine)]PF <sub>6</sub> collected as part of this thesis, where <i>cis</i> and <i>trans</i> are relative to the carbene. ....	129
Table 2.11 Selected bond lengths for [Ir(SIMes)(COD)Cl] ( <b>SIMes(a)</b> ) from a publication by Kelly <i>et al.</i> <sup>94</sup> and [Ir(SIMes)(COD)(2-methylpyridine)]PF <sub>6</sub> collected as part of this thesis, where <i>cis</i> and <i>trans</i> are relative to the carbene.....	130
Table 2.12 Selected NMR data for the active catalysts in methanol, where ‘eq’ indicates the number of equivalents observed. The carbene value * for <b>IMes(a)</b> is quoted for [Ir(IMes)(py) <sub>2</sub> (H) <sub>2</sub> Cl] in DCM.....	131
Table 2.13 Activation parameters for the loss of pyridine when <b>IMes(a)</b> , <b>SIMes(a)</b> and <b>ICy(a)</b> precursors are used. Data for <b>IMes(a)</b> was quoted in a publication by Cowley <i>et al.</i> (2011). <sup>66</sup> * denotes value was calculated either by extrapolation in the case of <b>SIMes(a)</b> or using published data in the case of <b>PCy<sub>3</sub></b> . ....	133
Table 2.14 Activation parameters for the loss of hydride ligands when <b>IMes(a)</b> , <b>SIMes(a)</b> and <b>ICy(a)</b> precursors are used. Data for <b>IMes(a)</b> was quoted in a publication by Cowley <i>et al.</i> (2011). <sup>66</sup> * denotes the value was calculated by extrapolation.....	134
Table 2.15 Typical observed <sup>1</sup> H NMR signal enhancement to pyridine when <b>IMes(a)</b> , <b>SIMes(a)</b> and <b>ICy(a)</b> are used as precursors in method 1 hyperpolarised at 2 G. ....	136
Table 1.1 Results reported in a publication by Atkinson <i>et al.</i> (2009) <sup>61</sup> upon changing the field of polarisation on a sample of pyridine polarised by SABRE using [Ir(PCy <sub>3</sub> )(H) <sub>2</sub> (py) <sub>3</sub> ]BF <sub>4</sub> . ....	140
Table 1.2 <sup>1</sup> H NMR signal enhancement of pyridine observed for <b>IMes(a)</b> , <b>SIMes(a)</b> and <b>ICy(a)</b> using method 2, quoted at the magnetic field which resulted in the maximum observed <sup>1</sup> H NMR signal enhancement. ....	143

Table 1.3 Predicted rate constants of hydride and pyridine ligand loss calculated from thermodynamic data in Chapter 2 for <b>IMes(a)</b> , <b>SIMes(a)</b> and <b>ICy(a)</b> at the indicated temperatures. ....	146
Table 1.4 <sup>1</sup> H NMR signal enhancement to the <i>ortho</i> , <i>meta</i> and <i>para</i> proton resonances of pyridine in the presence of <b>IMes(a)</b> in methanol when the polarisation transfer step occurs at the indicated temperatures with the predicted rate constants of hydride and pyridine ligand exchange calculated from thermodynamic data in Chapter 2. ....	147
Table 1.5 Observed <sup>1</sup> H NMR signal enhancement to the <i>ortho</i> , <i>meta</i> and <i>para</i> proton resonances of pyridine in the presence of <b>SIMes(a)</b> in methanol when the polarisation transfer step occurs at various temperatures with the predicted rate constants of hydride and pyridine ligand exchange calculated from thermodynamic data in Chapter 2. ....	149
Table 1.6 Observed <sup>1</sup> H NMR signal enhancement to the <i>ortho</i> , <i>meta</i> and <i>para</i> proton resonances of pyridine in the presence of <b>ICy(a)</b> in methanol when the polarisation transfer step occurs at various temperatures with the predicted rate constants of hydride and pyridine ligand exchange calculated from thermodynamic data in Chapter 2. ....	150
Table 1.7 The amounts of <b>IMes(a)</b> and pyridine used in the concentration experiments. Each sample contained 0.6 ml <i>d</i> <sub>4</sub> -methanol. ....	155
Table 1.8 Showing the <sup>1</sup> H NMR signal enhancement levels, and signal to noise ratios, of free pyridine proton resonances observed with indicated concentrations of <b>IMes(a)</b> and pyridine (Table 1.7) across three days. Columns labelled ‘Enhan’ contain the observed <sup>1</sup> H NMR signal enhancement, and columns labelled ‘S/N’ contain the signal to noise ratio. *Enhancements for the 1 % sample are calculated based on a predicted thermally polarised signal integral (see Experimental). ....	156
Table 1.9 Table showing the extent polarisation transfer achieved in a single scan at the indicated concentrations of <b>IMes(a)</b> and pyridine using method 2, polarised in a magnetic field of 75 G. ....	160
Table 1.10 Table detailing the signal enhancement levels and signal to noise ratios of free pyridine resonances observed with indicated concentrations of pyridine, a standard concentration of <b>IMes(b)</b> and a stoichiometric volume of acetonitrile. Columns labelled ‘Enhan’ contain the observed <sup>1</sup> H NMR signal enhancement, and columns labelled ‘S/N’	

contain the signal to noise ratio. \*denotes the bound pyridine signal was not base-line resolved from the free pyridine signal and therefore the value is a combination of both signals. + denotes the value refers to the bound pyridine signal alone, not the free signal.

.....	161
Table 1.11 Table detailing the signal enhancement levels and signal to noise ratios of free pyridine resonances observed with indicated concentrations of pyridine, a standard concentration of <b>IMes(a)</b> and a stoichiometric volume of acetonitrile.....	162
Table 1.12 Time required to fully activate <b>IMes(a)</b> in the indicated solvents where pyridine is the substrate.....	165
Table 1.13 Polarisation transfer to pyridine using <b>IMes(a)</b> under the indicated conditions. The notation ‘n/a’ denotes the experiments could not be completed due to the temperature being significantly below melting point of DMSO.....	166
Table 1.14 The key chemical shifts and chemical shift differences observed for three SABRE catalysts, relevant to the mechanism of polarisation transfer. ‘Py trans to hydride’ refers to the <i>ortho</i> proton only.....	168
Table 4.1 The observed $^1\text{H}$ and $^{13}\text{C}$ NMR shifts of quinoline in $d_4$ -methanol.....	177
Table 4.2 $^1\text{H}$ NMR signal enhancement for quinoline when polarised using method 1 with <b>ICy(a)</b> at room temperature and a PTF of 2 G. ....	177
Table 4.3 $^1\text{H}$ NMR signal enhancement for quinoline when polarised using method 1 with <b>IMes(c)</b> , <b>SIMes(c)</b> and <b>ICy(c)</b> at room temperature and a PTF of 2 G. ....	178
Table 4.4 $^1\text{H}$ NMR signal enhancement for quinoline when polarised using method 1 with <b>IMes(c)</b> with protonated and deuterated acetonitrile, at room temperature and a PTF of 2 G.....	179
Table 4.5 Activation parameters for the loss of hydrides for the <b>IMes(c)</b> and quinoline system compared to the same data for the <b>IMes(a)</b> and pyridine system.....	181
Table 4.6 Activation parameters for the loss of substrate for the <b>IMes(c)</b> and quinoline system compared to the same data for the <b>IMes(a)</b> and pyridine system. * denotes the value was calculated by extrapolation.....	182

Table 4.7 <sup>1</sup> H NMR signal enhancement for quinoline when polarised using <b>IMes(c)</b> using method 1 at a PTF of 2 G when the polarisation transfer step occurs at the indicated temperatures with the predicted rate constants of hydride and pyridine ligand exchange calculated from thermodynamic data in Appendix.....	184
Table 4.8 Experimentally measured rate constants of ligand loss from <b>IMes(c)</b> and <b>SIMes(c)</b> in the presence of quinoline.....	185
Table 4.9 <sup>1</sup> H NMR signal enhancement for quinoline when polarised using <b>SIMes(c)</b> using method 1 at a PTF of 2 G when the polarisation transfer step occurs at the indicated temperatures.....	185
Table 4.10 <sup>1</sup> H NMR signal enhancement for quinoline when polarised using <b>ICy(c)</b> using method 1 at a PTF of 2 G when the polarisation transfer step occurs at the indicated temperatures.....	187
Table 4.11 <sup>1</sup> H NMR signal enhancement for quinoline when polarised using <b>IMes(c)</b> , <b>SIMes(c)</b> and <b>ICy(c)</b> using method 1 at 2 G when the polarisation transfer step occurs at the indicated temperatures.....	188
Table 4.12 <sup>1</sup> H NMR signal enhancement of quinoline when polarised using method 1 with <b>IMes(c)</b> at a PTF of 2 G at the indicated concentrations.....	191
Table 4.13 <sup>1</sup> H NMR signal enhancement when quinoline is polarised with <b>IMes(c)</b> at room temperature and a PTF of 2 G in various solvents.....	192
Table 4.14 <sup>1</sup> H NMR signal enhancement when the indicated quinoline analogues are polarised with <b>IMes(b)</b> at room temperature and 2 G. * denotes the signals are not base line resolved in the thermally polarised or hyperpolarised spectrum. Therefore, the quoted signal enhancement correlates to both signals together.....	196
Table 4.15 <sup>1</sup> H NMR signal enhancement when the indicated methylquinolines are polarised with <b>IMes(b)</b> at room temperature and 2 G. * denotes the signals are not base line resolved in the hyperpolarised spectrum. Therefore, the quoted signal enhancement correlates to both signals together.....	197
Table 4.16 Correlations observed in free quinoline when interrogated using the selective OPSYdq sequence, where a '√' denotes a correlation was observed, 'w' denotes a weak	

correlation is observed, 'X' denotes a correlation was not observed, 'O' refers to the selective $^1\text{H}$ OPSYdq NMR experiments and 'C' refers to the $^1\text{H}$ COSY NMR spectrum. ....	203
Table 5.1 Signal to noise ratios relating to the thermally polarised 1D $^1\text{H}$ NOESY spectrum of quinoline (100 mM) and hyperpolarised spectrum achieved using method 2 with <b>IMes(c)</b> (5 mM). Position 4 of quinoline was selected, and nOe correlations to positions 5 and 3 were observed. ....	210
Table 5.2 Signal to noise ratios relating to the thermally polarised 1D $^1\text{H}$ NOESY spectrum of quinoline (10 mM) and hyperpolarised with <b>IMes(c)</b> (0.5 mM). Position 4 of quinoline was selected, and nOe correlations to positions 5 and 3 were observed. .	211
Table 5.3 Showing the increased signal intensity of the $^1\text{H}$ - $^1\text{H}$ ufcOSY NMR spectra of quinoline (100 mM) hyperpolarised with <b>IMes(c)</b> (5 mM) at 0 G and hyperpolarised with <b>IMes(c)</b> (5 mM) at 65 G, compared to the thermally polarised spectrum. ....	261
Table 6.1 $^1\text{H}$ polarisation observed with a PTF of 2 G and 65 G, and $^1\text{H}$ OPSYdq polarisation observed with a PTF of 2G for the <i>ortho</i> and <i>meta</i> position of a series of 4-substituted pyridines. ....	277
Table 6.2 The sum of the observed $^1\text{H}$ polarisation with a PTF of 2 G and 65 G, and $^1\text{H}$ OPSYdq polarisation with a PTF of 2G for the <i>ortho</i> and <i>meta</i> position of a series of 4-substituted pyridines. ....	278
Table 6.3 Observed $^1\text{H}$ enhancements of 2-, 3- and 4-methylpyridine when polarised with <b>IMes(a)</b> . ....	281
Table 6.4 Observed $^1\text{H}$ enhancements of 3- and 4-methylpyridine when polarised with <b>SIMes(a)</b> and 2-methylpyridine when polarised with <b>SIMes(b)</b> . ....	282
Table 6.5 Comparison of the enhancement observed for 3-phenylpyridine and 4-phenylpyridine.....	283
Table 6.6 Observed $^1\text{H}$ NMR polarisation transfer to 3-benzoylpyridine polarised with <b>IMes(a)</b> at a PTF of 2 G and 65 G.....	285

Table 6.7 Observed $^1\text{H}$ NMR polarisation transfer to 4-(4-chlorobenzoyl)pyridine polarised with <b>IMes(a)</b> with a PTF of 2 G and 65 G.....	285
Table 6.8. Observed $^1\text{H}$ polarisation transfer to indole in the presence of <b>IMes(c)</b> . ....	286
Table 6.9 Observed $^1\text{H}$ NMR signal enhancement for 2-amino-4-methyl thiazole.....	290
Table 6.10 Observed $^1\text{H}$ NMR signal enhancement for benzothiazole using method 1 and <b>IMes(a)</b> and <b>IMes(c)</b> .....	292
Table 6.11 Observed polarisation transfer to benzothiazole using <b>IMes(c)</b> and method 2 with a PTF of 0 G and -60 G.....	293
Table 6.12 Outlining the concentrations of catalyst and substrate for each sample in 0.6 ml $d_4$ -methanol for a standard competition study between two substrates. ....	296
Table 6.13 Observed $^1\text{H}$ NMR signal enhancement for the competition study between pyridine ( <i>ortho</i> , <i>meta</i> and <i>para</i> ) and 2-aminothiazole (T4 and T5) using <b>IMes(a)</b> . ....	297
Table 6.14 Results from the competition study between 2-aminothiazole (Thia, T4 and T5) and quinoline (Quin, Q2, Q3, Q4, Q5, Q6 and Q7). ....	298
Table 6.15 Results from the competition study between 4-methylpyridine ( <i>ortho</i> , <i>meta</i> and methyl) and 4-phenylpyridine ( <i>o</i> -py and <i>m</i> -py of the pyridyl ring, and <i>o</i> -ph and <i>m+p</i> -ph of the phenyl ring). ....	301
Table 6.16 Percentage of each compound involved in the reversible reaction of 4-carboxyaldehydepipridine with methanol as a function of temperature. The calculations are based on the integrals of the <b>CH(O)</b> of 4-carboxyaldehydepipridine and <b>CH(OMe)(OH)</b> of the corresponding hemiacetal. ....	309
Table 6.17 Observed $^1\text{H}$ polarisation transfer to 4-carboxyaldehydepipridine (aldehyde) and the hemiacetal product (hemiacetal) found in a sample of 4-carboxyaldehydepipridine dissolved in $d_4$ -methanol in the presence of <b>IMes(a)</b> . ....	310
Table 6.18 Observed $^1\text{H}$ polarisation transfer to 4-carboxyaldehydepipridine (aldehyde) and the hemiacetal product (hemiacetal) found in a sample of 4-carboxyaldehydepipridine dissolved in $d_1$ -chloroform in the presence of <b>IMes(a)</b> , with and without the presence of protonated methanol.....	311

Table 6.19 Collated data from mass spectroscopy study of the reaction products of 4-carboxaldehydepiperidine with methanol. The stated ratios are based on the response factors from the mass spectroscopy. ....	314
Table 8.1 The excess of hydrogen present in sample interrogated by method 1 at various levels of catalyst loading. ....	344
Table 8.2 Amount of dissolved hydrogen (mmol) in a standard method 1 sample at various temperatures, predicted as by Equation 8.2. ....	345
Table 8.3 The amount of dissolved hydrogen (mmol) in method 1 samples at various temperatures as predicted by Equation 8.3a+b. ....	346
Table 8.4 The absolute integrals of the three positions of pyridine observed in a single scan $^1\text{H}$ NMR spectrum at the indicated volumes. ....	347
Table 8.5 The absolute integrals of the three positions of pyridine observed in a single scan $^1\text{H}$ NMR spectrum at the indicated volumes. The integrals for the 1 mM (0.05 $\mu\text{L}$ ) sample have been calculated according to Figure 8.22. ....	348
Table 8.6 Parameters used for selected 2D sequences with the flow system, where 'sw' is the spectral width, 'centre' is the centre of the spectral width, 'rg' is the receiver gain, 'ns' is the number of scans, 'td' is the number of increments and 'aq' is the acquisition time of each scan. ....	348
Table 9.1 Rate constants (quoted to 3 d.p.) for the loss of pyridine and hydride ligands from <b>SIMes(a)</b> in the presence of pyridine at the indicated temperatures, with corresponding lower and upper limits to a 95 % confidence level. ....	375
Table 9.2 The thermodynamic parameters of activation for the loss of hydride ligands and pyridine ligands from <b>SIMes(a)</b> in the presence of pyridine. ....	376
Table 9.3 Predicted rates loss of pyridine and hydride ligands from <b>SIMes(a)</b> at the specified temperatures. ....	376
Table 9.4 Rate constants (quoted to 3 d.p.) for the loss of pyridine and hydride ligands from <b>ICy(a)</b> in the presence of pyridine at the indicated temperatures, with corresponding lower and upper limits to a 95 % confidence level. ....	377

Table 9.5 The thermodynamic parameters of activation for the loss of hydride ligands and pyridine ligands from <b>ICy(a)</b> in the presence of pyridine.....	378
Table 9.6 Predicted rates loss of pyridine and hydride ligands from <b>ICy(a)</b> at the specified temperatures.....	378
Table 9.7 Rate constants (quoted to 3 d.p.) for the loss of quinoline and hydride ligands from <b>IMes(c)</b> in the presence of quinoline at the indicated temperatures, with corresponding lower and upper limits to a 95 % confidence level. ....	378
Table 9.8 The thermodynamic parameters of activation for the loss of hydride ligands and quinoline ligands from <b>IMes(c)</b> in the presence of quinoline. ....	379
Table 9.9 Predicted rates loss of quinoline and hydride ligands from <b>IMes(c)</b> at the specified temperatures.....	379
Table 9.10 Rate constants (quoted to 3 d.p.) for the loss of quinoline and hydride ligands from <b>SIMes(c)</b> in the presence of quinoline at the indicated temperatures, with corresponding lower and upper limits to a 95 % confidence level. ....	380
Table 9.11 Fractional Atomic Coordinates ( $\times 10^4$ ) and Equivalent Isotropic Displacement Parameters ( $\text{\AA}^2 \times 10^3$ ) for sbd1108. $U_{eq}$ is defined as 1/3 of of the trace of the orthogonalised $U_{ij}$ tensor. ....	409
Table 9.12 Anisotropic Displacement Parameters ( $\text{\AA}^2 \times 10^3$ ) for sbd1108. The Anisotropic displacement factor exponent takes the form: - $2\pi^2[h^2a^*^2U_{11}+...+2hka \times b \times U_{12}]$ . ....	410
Table 9.13 Bond Lengths for sbd1108.....	411
Table 9.14 Bond angles for sbd1108.....	413
Table 9.15 Hydrogen Atom Coordinates ( $\text{\AA} \times 10^4$ ) and Isotropic Displacement Parameters ( $\text{\AA}^2 \times 10^3$ ) for sbd1108. ....	414



## List of Equations

Equation 1.1 The overall wavefunction of a system can be split into five components, the electronic, nuclear, translational, rotational and vibrational wavefunctions.....	90
Equation 2.1 Equation used to calculate the $^1\text{H}$ NMR signal enhancement. ....	114
Equation 8.1 Equation used to calculate the $^1\text{H}$ NMR signal enhancement. ....	329
Equation 8.2 Mole fraction of hydrogen, $x_g$ , dissolved in methanol at 1.013 bar pressure of gas, where $T$ = temperature in K, taken from Solubility of Gases in Liquids. <sup>212</sup> .....	344
Equation 8.3 a) To calculate Henry's Law constant for hydrogen dissolved in methanol, where $H$ = Henry's Law constant (MPa), $T$ = temperature in K and $P$ = pressure in Pa, taken from Liu <i>et al.</i> <sup>214</sup> b) Henry's Law correct at a specified temperature, where $x_{\text{H}_2}$ is the mole fraction of hydrogen dissolved in methanol. ....	346
Equation 9.1 Reaction mechanism and differential equations used by Dynafit together with user data to calculate the rate of loss of hydride ligands from a catalyst.....	370
Equation 9.2 Reaction mechanism and differential equations used by Dynafit together with user data to calculate the rate of loss of substrate ligands from a catalyst, with pyridine used as an example. ....	372
Equation 9.3 Reaction mechanism and differential equations used by Dynafit together with user data to calculate the rate of loss of hydride ligands from <b>IMes(c)</b> activated in the presence of quinoline. ....	374
Equation 9.4 Eyring equation.....	374

## Acknowledgements

Firstly, I would like to thank my supervisors, Prof. Simon Duckett and Prof. Gary Green for giving me the opportunity to learn invaluable research skills in a research environment, and for their help and patience during my time as a PhD student. I would like to thank Dr David Williamson for acting as my IPM for a year and a half and for widening my knowledge into the spin physics relating to NMR. I would like to thank Dr Ryan Mewis for acting as my mentor, and as my IPM for the second half of my studies. His insights into the inner workings of the polarisors have also proved very useful. I would like to extend my thanks to AstraZeneca for financially supporting me through my studies, and more specifically to Drs Christopher Sleight, Mike Bernstein, Richard Lewis, and Steve Coombes for their support during my studies. I am also very grateful to Bruker for allowing me to use the three polarisers developed during the progression of this thesis, and allowing me to contribute data to help in their development.

I would like to thank the various post docs and research assistants of the Duckett group who have helped my understanding of the research environment including Ralph Adams, Mike Cowley, Beatriz Eguillor, Marianna Fekete, Jose Hernandez, Iman Khazal and Fran Suarez. I would also like to thank the other people I've worked with in the lab such as fellow students Kate Appleby, Chris Armstrong, Kevin Atkinson, Guan Dexin, Richard Green, Sarah-Louise Henshaw, Richard John and Majid Khan, but in particular, Louise Highton, Jon Holmes, Alex Hooper, Freek Reskin and Tom Robinson for making my time at York not only educational but enjoyable also.

On a more personal note, I would like to thank my mum, Carolyn, for all her support not just through my PhD but throughout my life, and my dad, Mik, for giving me the excuse to escape every so often. I would also like to thank the pool team I captained during my time here and Jess Mather for her friendship and patience.

## Declaration

I hereby declare that all the work presented within this thesis is original to the best of my knowledge, except where stated, and has not been submitted or published for other degrees.

The work undertaken in this thesis was completed with part funding from AstraZeneca. The work also involved collaboration with Bruker BioSpin.

Work within this thesis also resulted in a publication in the Journal of American Chemical Society (Lloyd *et al.* *Journal of the American Chemical Society* **2012**, *134*, 12904), presented in the Appendices of this thesis.

## 1 Chapter 1 – Introduction

A wide range of analytical techniques are used in the field of biomedical and pharmaceutical research, including mass spectrometry (MS), and infrared (IR) and ultra-violet (UV) spectroscopy. While techniques such as IR and UV spectroscopy can prove very useful, these are dependent on a response factor. This means that in a sample containing two substrates in the same concentration, the signal derived from those substrates will not necessarily have the same integral. Nuclear magnetic resonance (NMR) responds the same to all signals of the same type and therefore is independent of a response factor.<sup>1</sup> This means it is a quantitative technique even in complex mixtures. NMR also has the ability to distinguish between nuclei of different chemical environments based on the effects of electron cloud density of nearby nuclei, and advanced pulsed NMR methods have allowed the user to investigate the connectivity of NMR active nuclei.

Within the pharmaceutical industry, NMR has found many applications both in the liquid and solid state.<sup>1-4</sup> Solid state chemistry is very important in formulation chemistry as 80-90 % of commercial drugs are solid.<sup>4</sup> It can be used to investigate solid forms of a drug in a tablet in the presence of excipients,<sup>5</sup> interactions between the drug and excipients, stability of active complexes in solid solutions,<sup>6</sup> and identification of potential impurities or degradation products from long storage.<sup>4</sup> While solid state NMR is a very important application of NMR within the pharmaceutical industry, only liquid state NMR will be discussed from here on as only this type of measurements are completed experimentally.

In the liquid state, NMR is most commonly used in drug discovery. It can be used in the identification of metabolites<sup>3</sup> but it has a widespread use in the characterisation of substrates and impurities in the initial development of potential new drugs.<sup>7</sup> It is the potential application of SABRE to these pharmaceutical uses of NMR that will be considered within this thesis.

### 1.1 NMR spectroscopy

One of the main drawbacks of NMR spectroscopy is the inherent insensitivity. The limit of detection for NMR is in the range  $10^{-9}$  to  $10^{-11}$  mol however for more sensitive

techniques this reaches  $10^{-13}$  mol for laser-induced fluorescence and MS and  $10^{-12}$  to  $10^{-15}$  mol for Fourier transform infrared and Raman spectroscopy.<sup>1</sup> The reasons for this, and current methods being used to overcome the insensitivity, are discussed below.

### 1.1.1 NMR spectroscopy

Analysis by NMR requires the presence of nuclei which has a nuclear spin quantum number which does not equal 0, such as  $^1\text{H}$  which has a nuclear spin quantum number of a  $\frac{1}{2}$ .<sup>8</sup> In the presence of an external magnetic field, the derived energy states split according to this nuclear spin quantum number such that spin  $\frac{1}{2}$  nuclei give two energy levels,  $+\frac{1}{2}$  and  $-\frac{1}{2}$ , spin 1 nuclei give three energy levels ( $+1$ ,  $0$  and  $-1$ ) and spin  $\frac{3}{2}$  nuclei give four energy levels ( $+\frac{3}{2}$ ,  $+\frac{1}{2}$ ,  $-\frac{1}{2}$  and  $-\frac{3}{2}$ ). The extent to which these energy levels are populated is defined by the Boltzmann distribution which is dependent on the external field. In this thesis, only  $^1\text{H}$  and  $^{13}\text{C}$  nuclei are considered, both of which have a nuclear spin quantum number of  $\frac{1}{2}$ .

Collectively, the spins in a certain chemical environment combine to produce a bulk magnetisation and as such are considered to be responsive to radiofrequency pulses and therefore can be manipulated. A  $90^\circ$  pulse can be used to 'push' bulk magnetisation away from its relaxed state after which the spins begin to immediately precess in a precise manner towards the relaxed state. The frequency of this precession is unique to the chemical environment and therefore a number of chemical environments can be recorded to produce a Free Induction Decay (FID). This is then processed with a Fourier transform function to produce a spectrum, indicating a signal for each chemical environment.

NMR is reliant on the Boltzmann distribution. The spins present in the two observed energy levels of a spin  $\frac{1}{2}$  nuclei act against each other, and consequently without a population difference between the two levels, no signal would be observed.

Unfortunately, the energy difference between the energy levels of interest in NMR is small and therefore the population difference created by the Boltzmann distribution is also small. Methods of increasing the energy difference between these states are therefore discussed.

### 1.1.2 Increasing sensitivity of NMR through instrumental developments

One method to increase the sensitivity of NMR is to increase the energy difference between the states of interest, such that the Boltzmann distribution of spins allows a greater population difference. There are two ways to achieve this, first increasing the applied magnetic field and secondly, decreasing the temperature.

The first NMR spectrum was published in 1951 in a paper by Arnold *et al.*<sup>9</sup> and showed the three distinct chemical shifts present in ethanol, shown in Figure 1.1. The paper also includes the procedure for methanol, propanol, butanol and pentanol with accurate integrations of the associated peaks.

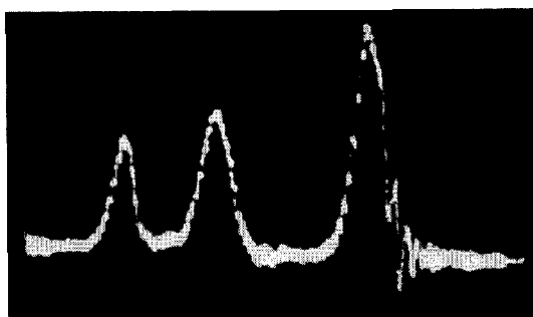


Figure 1.1 First  $^1\text{H}$  NMR spectrum of ethanol published by Arnold *et al.*<sup>9</sup>

Over the coming years,<sup>8,10</sup> significant advances in the field of NMR were published, the most significant of which is perhaps the development of superconducting magnetic fields,<sup>11</sup> before which only iron-cored magnets were used. This allowed spectroscopists to work at much higher fields, giving not only greater sensitivity but also better resolution.

The second greatest advance in increasing the sensitivity of NMR spectroscopy after the increase in magnetic field strength was the invention of the CryoProbe.<sup>12</sup> In a normal probe, random thermal motion of electrons in the required conductors can result in a noise contribution to any spectrum recorded. In a CryoProbe, these conductors, required for the transmit/receive coils and tuning and matching circuits, are cooled with liquid nitrogen or liquid helium, along with some other electronic components in some probes, to reduce the noise created by these components. This has been shown to increase the sensitivity of NMR by three fold.<sup>1</sup>

Other advances in NMR include the invention of high resolution capillary tube NMR. While this does not affect the sensitivity of the method, the amount of sample required for detection is greatly reduced. A standard NMR tube is 5 mm in diameter however probes are now commercially available which accept capillary NMR tubes with diameters of 1.7 mm and 1 mm (see Figure 1.2).

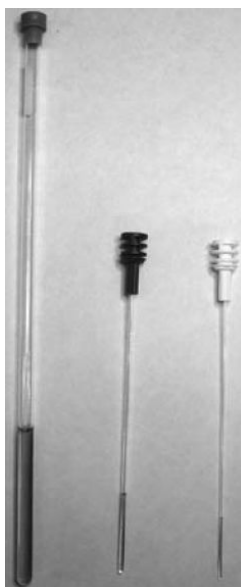


Figure 1.2 Photo demonstrating the relative size of some available NMR sample tubes demonstrating different diameters. The required sample volumes for each sample tube is written in parenthesis, from left to right, 5 mm (600  $\mu\text{L}$ ), 1.7 mm (35  $\mu\text{L}$ ) and 1 mm (7  $\mu\text{L}$ ). Image taken from the publication by Molinski (2009).<sup>13</sup>

In 2002, Schlotterbeck *et al.*<sup>14</sup> published a paper in which the volume of sample, and therefore mass of substrate, was correlated to the signal to noise of signals collected via a small range of probes. The results of this investigation are presented in Table 1.1.

Probe	$V_{\text{tot}}$	$V_{\text{obs}}$	Reported S/N	S/N / $\mu\text{mol}$ in $V_{\text{obs}}$	Enhancement
1-mm TXI microliter	5	2.5	276	1104	5.0
5-mm conventional TXI	550	278	55	220	1.0
5-mm TXI cryoprobe	550	278	181	651	3.0
5-mm TXI cryoprobe with 1-mm sample	22	10	195	858	3.9

Table 1.1 Comparison of probe performance of a 1-mm TXI Microliter probe, a 5-mm TXI probe and a 5-mm cryoprobe, where  $V_{\text{tot}}$  is the total sample volume required,  $V_{\text{obs}}$  is the volume pulsed by the probe, and S/N refers to the signal to noise ratio. These experiments were carried out on 172  $\mu\text{g}$  (0.5  $\mu\text{mol}$ ) sample of sucrose in the  $V_{\text{tot}}$ , collected with one scan, processed with a line broadening of 1. Enhancements are calculated based on results gained from the 5-mm conventional TXI probe. Table adapted from a 2002 publication by Schlotterbeck *et al.*<sup>14</sup>

The results presented in Table 1.1 show significantly increased mass sensitivity can be achieved by using either a cryoprobe or microliter probe when compared to the conventional 5-mm probe.

## 1.2 Hyperpolarisation in NMR

Advances in the practical aspects of NMR spectroscopy such as larger magnets and CryoProbes can only increase sensitivity, and compared to other techniques, NMR is still relatively insensitive. Methods to create non-Boltzmann distributions are therefore being investigated and are discussed below.

### 1.2.1 Hyperpolarisation

Hyperpolarisation is a method by which the sensitivity of NMR is increased not through increasing the difference observed in the Boltzmann distribution through increasing the magnetic field or decreasing the temperature of the sample, but by forcing the population into a non-Boltzmann distribution. The methods by which this condition is met are discussed below.

### 1.2.2 Brute force

The idea of hyperpolarisation by brute force was first published in 1958 by Abragam and Proctor.<sup>15</sup> In brute force NMR, hyperpolarisation is not produced by creating a non-Boltzmann distribution but rather, the equilibrium Boltzmann distribution of the sample



is altered.<sup>16</sup> This can take a long time because nuclear relaxation becomes slow at low temperatures due to loss of molecular motion.<sup>17</sup> This problem can be alleviated by either the addition of a relaxant<sup>17</sup> or through low field thermal mixing,<sup>16</sup> a form of cross-polarisation transfer.

The idea of adding a relaxant to hyperpolarise  $^{129}\text{Xe}$  was considered in a paper published by Krjukov *et al.*<sup>17</sup> in 2005. For xenon nuclei in bulk solid at 77 K and a magnetic field of 0.1 T, a typical spin relaxation time is 2.5 hours. If the temperature is reduced to 4.2 K, the relaxation time increases to 60 hours for natural xenon and 180 hours for isotopically enriched xenon. It is therefore clear to see that to hyperpolarise xenon through brute force effectively, it would be advantageous to reduce the time required to achieve this. Here, the addition of both oxygen and helium as relaxants were considered. However, the observation that the  $T_1$  of  $^{129}\text{Xe}$  was reduced significantly meant that if xenon gas is to be used as a contrast agent in imaging, the relaxant must be removed. This unfortunately proved to be impractical in application. The removal of oxygen requires the sample to be heated to 100 K which resulted in relaxation of the hyperpolarised xenon due to a strong temperature and field  $T_1$  dependence, before the oxygen could be removed.

The group then investigated the addition of  $^3\text{He}$  as a relaxant. At 1.5 K, this had the effect to reduce the  $T_1$  of xenon from around 2 days to 200 mins at 10 T or 2 min at 1 T. The loss of polarisation in xenon was investigated during removal of the  $^3\text{He}$  relaxant. The sample was heated to 30 K to remove the helium resulting in only 37 % of the original polarisation present in xenon remaining in the sample. This was partly overcome by the addition of  $^4\text{He}$  prior to removal of  $^3\text{He}$ . This then had the effect to retain 68 % of xenon polarisation after helium removal.

In a paper published by Gadian *et al.*<sup>16</sup> in 2012, the idea of combining brute force with low field thermal mixing was revisited. This is where nuclei that are dipolar-coupled to each other exchange polarisation. A major drawback of this method is that exposure to the low field must be very quick as the short  $T_1$  values typical at low fields would allow loss of polarisation. The significant improvement posed in the published Gadian paper was to derive the polarisation from a large solvent  $^1\text{H}$  pool to a small amount of nuclei of interest without the use of radiofrequencies. Before each experiment the sample is saturated at resonance field, exposed to a higher polarisation field, then transiently

reduced to a very low mixing field and restored to resonance field to allow acquisition of the required NMR data. The extent of polarisation  $^1\text{H}$ ,  $^{13}\text{C}$ ,  $^{15}\text{N}$ ,  $^{23}\text{Na}$  and  $^{31}\text{P}$  can be explored by varying the strength or duration of either the high polarisation field or low mixing field.

Initially, the respective rates of polarisation ( $T_p$ ) of the various nuclei were investigated. In a solution of  $[1-^{13}\text{C}]$  sodium acetate powder, it was shown that  $T_p$  was closer to the  $T_1$  of  $^1\text{H}$  rather than  $^{13}\text{C}$ . This idea was repeated on a sample of 2 M  $[1-^{13}\text{C}]$  sodium acetate and 1 M sodium phosphate in which the  $T_p$  to  $^{31}\text{P}$  also approaches the  $T_1$  of  $^1\text{H}$  rather than  $^{31}\text{P}$ . The effect of this on the signal to noise ratios of the resultant  $^{31}\text{P}$  spectra are shown in Figure 1.3.

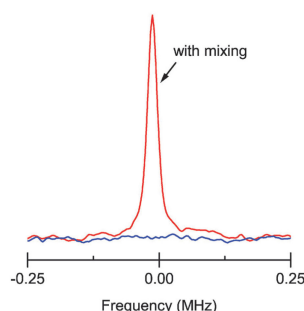


Figure 1.3  $^{31}\text{P}$  signals obtained in a single scan at 4.2 K from a sample containing 2 M  $[1-^{13}\text{C}]$  sodium acetate and 1 M sodium phosphate. The bottom scan was completed without low field thermal mixing, and the top completed with low field thermal mixing. Picture taken from the publication by Gadian *et al.*<sup>16</sup>

It was also observed that the addition of 0.1 mM dysprosium-diethylene triamine pentaacetic acid (DTPA) to act as a low-temperature relaxation agent had little effect on the  $T_1$  values of  $^{13}\text{C}$  or  $^{31}\text{P}$  but shortened the  $T_1$  of  $^1\text{H}$  from 170 s to 90 s and consequently shortened the observed  $T_p$  values. The addition therefore has a great advantage.

### 1.2.3 Optical pumping

Optical pumping is a hyperpolarisation technique by which a non-Boltzmann distribution of spins is created. This is created by transferring the angular momentum from laser photons to electronic spins and then to nuclear spins, temporarily enhancing the nuclear spin polarisation. Circularly polarised light can be used to pump electronic spins of gaseous alkali metal vapours into non-equilibrium population distributions.<sup>18</sup> It

was also observed that the nuclear spin polarisation of noble gases could consequently be greatly enhanced through collision and spin exchange with electronically spin polarised alkali atoms.<sup>19</sup> This is possible because in the gas phase, the electronic spin of the alkali metal and nuclear spin of any other material are coupled by dipolar cross-relaxation.<sup>20</sup>

Typical gases to be hyperpolarised using optical pumping are  $^3\text{He}$  and  $^{129}\text{Xe}$ .  $^3\text{He}$  is quicker to hyperpolarise than  $^{129}\text{Xe}$ , and due to a higher gyromagnetic ratio, also yield greater signal to noise ratios in resultant NMR or MRI. It is consequently useful for void space imaging of the lungs.<sup>21</sup> On the other hand,  $^{129}\text{Xe}$  take a longer time to hyperpolarise and has a lower resultant signal to noise but is much more soluble in blood.<sup>22</sup> It is therefore useful when investigating blood and tissues.<sup>23-25</sup>

### 1.2.3.1 Optical pumping in NMR

Xenon has a highly polarisable electron cloud and therefore its chemical shift is sensitive to its surroundings, resulting in a chemical shift range of over 7000 ppm depending on the chemical environment.<sup>18</sup> Commonly, NMR studies concerning xenon will involve an exchange of some sort, for instance, between red blood cells and plasma.<sup>23</sup>

In 1996, a paper was published by Bifone *et al.*<sup>23</sup> to discuss the idea of using hyperpolarised xenon to investigate human blood solutions. The group reported enhancements of 3 orders of magnitude larger than thermal signals. This is shown in Figure 1.4, where spectra of thermally polarised and hyperpolarised xenon in human blood are compared.

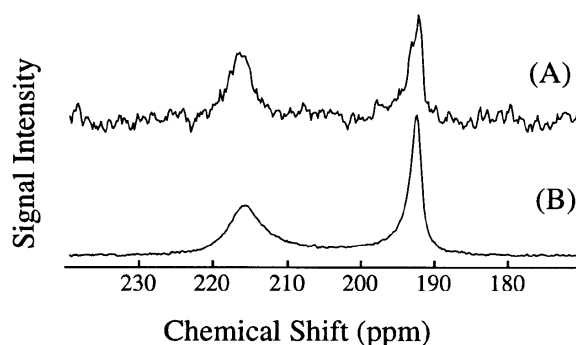


Figure 1.4  $^{129}\text{Xe}$  NMR spectra of human blood with thermally polarised (top) and hyperpolarised (bottom)  $^{129}\text{Xe}$ . Picture reproduced from publication in 1996 by Bifone *et al.*<sup>23</sup>

The two signals observed in the  $^{129}\text{Xe}$  NMR spectra in Figure 1.4 correspond to xenon bound to red blood cells (at 216 ppm) and xenon dissolved in saline/plasma mixture (192 ppm). This increase in sensitivity of  $^{129}\text{Xe}$  NMR and the significant difference in chemical shifts between dissolved xenon and bound xenon have therefore allowed the real time observation of transfer of xenon to red blood cells.

Xenon polarised through optical pumping could also undergo low field thermal mixing to transfer polarisation into other, less sensitive nuclei, in the same way as was observed for the brute force method.<sup>26,27</sup> This was considered by Bowers *et al.*<sup>26</sup> in a paper they published in 1993 in which polarisation was transferred to  $^{13}\text{CO}_2$ . The group reported an enhancement of 200 fold in the  $^{13}\text{C}$  NMR spectrum of isotopically enriched  $^{13}\text{CO}_2$ , and that the direction of the circularly polarised light used to polarise the xenon had a direct effect on the resultant NMR spectrum. If the light was right circularly polarised, the  $^{13}\text{C}$  signal was observed in phase, where if left circularly polarised light is used, the  $^{13}\text{C}$  signal was observed  $180^\circ$  out of phase.

This idea was extended in a paper published in 2009 by Lisitza *et al.*<sup>27</sup> Here, polarisation was transferred to 1- $^{13}\text{C}$ -acetic acid by mixing both substrate and hyperpolarised xenon in the gas phase and freezing the mixture by emersion in liquid nitrogen. To prevent  $T_1$  relaxation the mixture is standardly stored at 0.5 T, and moved to a field of 0.1 – 0.5 mT for a short time (0.1-0.3 s). The sample is then transferred back to a field of 0.5 T to preserve the polarisation. The sample is then thawed during which time the xenon evaporates and acetic acid becomes liquid. The  $^{13}\text{C}$  spectrum of the 1- $^{13}\text{C}$ -acetic acid is collected approximately 5-8 seconds after thawing, and compared to a thermal spectrum of the same sample. A maximum signal enhancement of 5 fold was observed, with corresponding spectra shown in Figure 1.5.

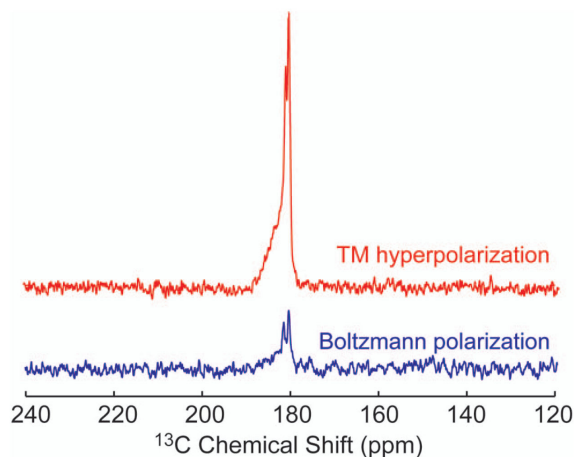


Figure 1.5  $^{13}\text{C}$  NMR spectra of 1- $^{13}\text{C}$ -acetic acid with thermal distribution (bottom) and hyperpolarised by thermal mixing with optically pumped  $^{129}\text{Xe}$ . Picture reproduced from the 2009 publication by Lisitza *et al.*<sup>27</sup>

Extrapolating to allow for the effect of the  $^{13}\text{C}$   $T_1$  during the time between thermal mixing and interrogation by NMR, it was calculated that an enhancement of  $\sim 10$  fold was achieved at time of thermal mixing.

Polarisation is also able to transfer from the hyperpolarised xenon gas through the spin polarisation-induced nuclear Overhauser effect (SPINOE). When laser polarised gas is dissolved in a solution, cross-relaxation and polarisation transfer is possible through a novel manifestation of the nOe effect.<sup>18,28</sup>

In a paper published in 2003 by Cherubini *et al.*,<sup>28</sup> the efficiency of thermal mixing and the SPINOE effect are compared with reference to polarisation transfer from hyperpolarised Xe to  $^{13}\text{CS}_2$ . To achieve the SPINOE effect, a mixture of hyperpolarised xenon and  $^{13}\text{CS}_2$  is set to a temperature of 196 K where the mixture is liquid. Maximum signal enhancement of the  $^{13}\text{C}$  signal was observed 2 min after the liquid had formed. To achieve the thermal mixing effect, the mixture of hyperpolarised xenon and  $^{13}\text{CS}_2$  was frozen in liquid nitrogen and moved to a low field appropriate for thermal mixing for a short time, then thawed to 196 K and interrogated by NMR. During the course of these experiments, it was found that polarisation of  $^{13}\text{C}$  by thermal mixing (maximum 390 fold enhancement) was much more efficient the SPINOE effect (maximum  $\sim 70$  fold enhancement).

### 1.2.3.2 Optical pumping in MRI

Hyperpolarised noble gases also have applications within magnetic resonance imaging (MRI). This has been considered in  $^{129}\text{Xe}$  imaging of the brain,<sup>24</sup> and  $^3\text{He}$  void space imaging of lungs.<sup>21</sup>

In 1997, a paper was published by Swanson *et al.*<sup>24</sup> as a discussion into the applicability of hyperpolarised  $^{129}\text{Xe}$  to brain imaging, primarily to investigate regional cerebral blood flow (rCBF), by model of a rat brain. In order for this to be possible, the hyperpolarised states of  $^{129}\text{Xe}$  must survive transport through the lungs, into the blood and then to the brain, and remain long enough after this point to yield useful information. The group were successful in obtaining NMR spectra of the rat brain proving the xenon had travelled that far, and then in obtaining  $^{129}\text{Xe}$  images of the rat brain, shown in Figure 1.6.

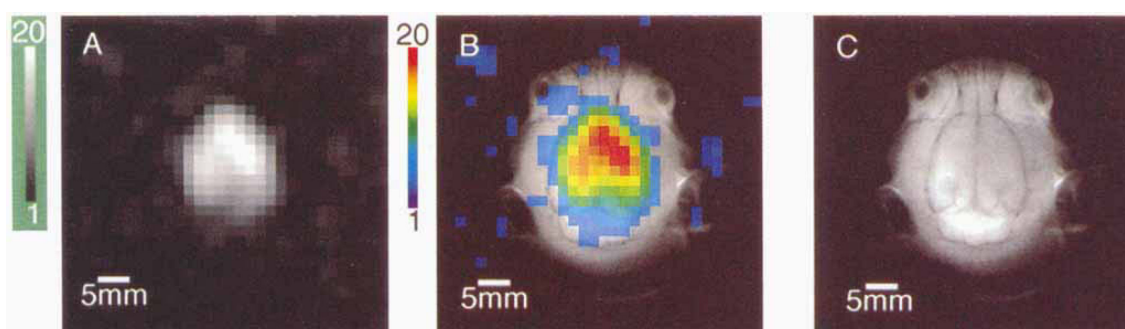


Figure 1.6  $^{129}\text{Xe}$  and  $^1\text{H}$  MRI images of the rat brain. a) Grey-scale  $^{129}\text{Xe}$  image, b) False colour suposition of  $^{129}\text{Xe}$  image on a  $^1\text{H}$  spin-echo image and c)  $^1\text{H}$  spin-echo. Figure reproduced from a paper published in 1997 by Swanson *et al.*<sup>24</sup>

The combination of the false colour  $^{129}\text{Xe}$  image and  $^1\text{H}$  spin-echo image shown in Figure 1.6b indicates the  $^{129}\text{Xe}$  is distributed through the brain tissue, as xenon has a greater affinity for brain tissue over blood, and is not observed in the surrounding fat or muscle. It is also observed that less signal is observed in the cerebellum compared to the cerebrum, possibly due to reduced blood flow in the cerebellum. Complications to bring this sort of imaging to the commercial environment still exist due to the large volume of xenon required for human measurements, and additions of oxygen to prevent anoxia and lower xenon concentrations to reduce anaesthetic effects, will also be required.

Two papers published by Spence *et al.* in 2001<sup>29</sup> and 2004<sup>30</sup> report a biotin-derivatized caged-xenon biosensor for avidin, a protein found in birds, reptiles and amphibians. An example of the sensor developed is shown below in Figure 1.7.

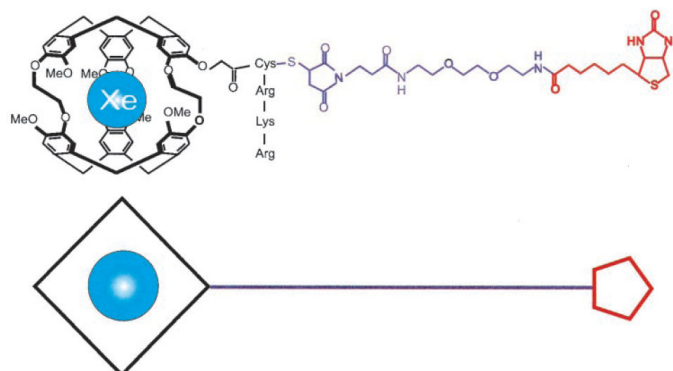


Figure 1.7 Structure and schematic representation of the biosensor molecule designed to bind xenon to a protein with high affinity and specificity, proposed in a publication by Spence *et al.*<sup>29</sup> The cage binding xenon, cryptophane-A, is shown in black with a purple tether and red biotin ligand.

The signal corresponding to xenon in the free biosensor is shown to shift upon addition of avidin. To ensure the change in chemical shift observed was a result of binding to avidin, and not proximity to avidin, the experiment was repeated in the presence of avidin bound to native biotin. In this case, no change in the chemical shift was observed confirming the change was due to binding. These spectra are presented below in Figure 1.8.

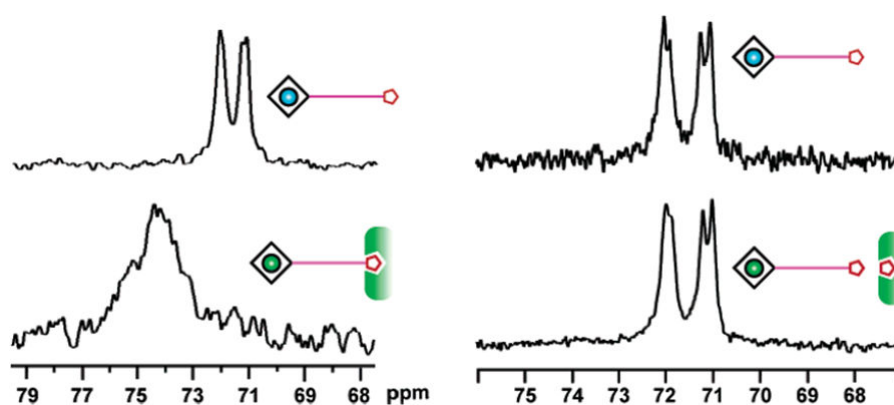


Figure 1.8 The  $^{129}\text{Xe}$  NMR spectra depicting the detection of biotin – avidin binding using xenon NMR. The left spectra show binding in the absence of native biotin, and the right spectra show binding in the presence of native biotin. Images taken from the publication by Spence *et al.*<sup>30</sup>

This work demonstrates the possibility of using hyperpolarised xenon to act as a biosensor, which could be used within imaging.

Hyperpolarised  $^3\text{He}$  has also been used in medical imaging when considering regional pulmonary functional and microstructural imaging, as reported by Costella *et al.*<sup>21</sup> in 2012. The current method for the diagnosis and long term monitoring of asthma is relatively insensitive to small changes in airway function and therefore the new method of hyperpolarised  $^3\text{He}$  MRI imaging is considered. This method was successful and therefore the group were able to use  $^3\text{He}$  images to investigate the effect of methacholine (a bronchoconstrictor) and salbutamol (an asthma drug) on lung function to better understand underlying conditions.

#### 1.2.4 Dynamic nuclear polarisation

Dynamic Nuclear Polarisation (DNP) is a hyperpolarisation technique by which the nuclei of interest are polarised by the transfer of spin polarisation from electrons. The electron is polarised through exposure to microwaves, and transfer to the nuclei of interest can occur through one of four mechanisms: the solid effect (SE), the cross effect (CE), thermal mixing (TM) or the Overhauser effect (OE).<sup>31,32</sup> As the sample is made colder, weaker microwave sources are required to polarise the sample. The addition of a radical is always required. In the case of chemically-induced DNP (CIDNP), a different mechanism is present, called the radical pair mechanism.

The solid effect, cross effect and thermal mixing are only possible when the sample is solid, and therefore does not apply to liquid samples. The Overhauser effect is present in liquid samples however it is only efficient at low fields and therefore cannot occur in a strong magnet. It is therefore difficult to complete high resolution NMR spectroscopy that requires signal averaging using DNP. Two groups have developed methods to overcome this barrier, and this work will be discussed below.

In a paper published in 2003 by Ardenkjaer-Larsen *et al.*,<sup>33</sup> a method for generating highly polarised nuclear spins in solution using DNP is proposed and extended upon in a second paper in 2004.<sup>34</sup> The method involves the sample being cooled using liquid helium ( $\sim 4$  K) in a 3.35 T magnet and irradiated with  $\sim 94$  GHz microwaves to produce a solid hyperpolarised by DNP. This is then rapidly dissolved in a suitable solvent inside the DNP polarisor such that a solution of molecules with hyperpolarised nuclear spins is produced and can consequently be transferred into a high resolution NMR spectrometer for interrogation. With a sample of [ $^{13}\text{C}$ ]-urea and a trityl radical dissolved



in glycerol, hyperpolarisations of 37 % for  $^{13}\text{C}$  and 7.8 % for  $^{15}\text{N}$  were obtained using this method corresponding to enhancements of 44, 400 and 23, 500 fold respectively.<sup>33</sup> The method was then demonstrated for use within MRI.<sup>34</sup> A rat was injected with [ $^{13}\text{C}$ ]-urea and subsequently imaged. 1 s after injection, the first image revealed heart muscles, and 2 seconds later, the collected image included the vascular system of the kidneys. These images are presented in Figure 1.9.

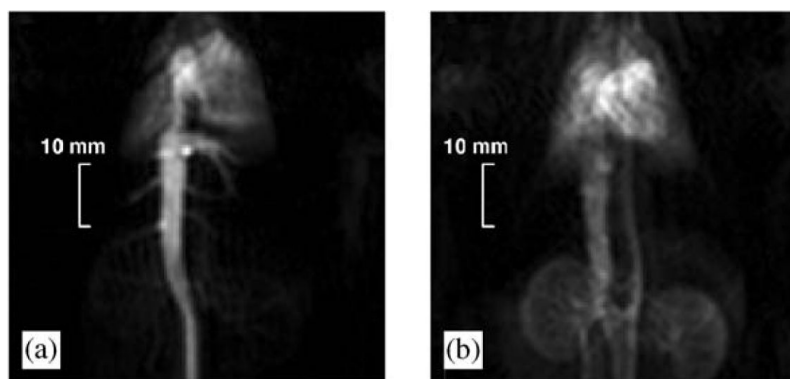


Figure 1.9  $^{13}\text{C}$  coronal projection images of a rat. The images were acquired (a) 1 s and (b) 3 s after injection of  $^{13}\text{C}$ -urea. Image taken from a publication by Wolber *et al.*<sup>34</sup>

The dissolution method described above has also been applied to the characterisation of small molecules using DNP in a publication by Day *et al.*<sup>35</sup> They reported enhancements of  $\sim 10^3$ - $10^4$  fold for the six molecules investigated, namely indomethacin, quinine, progesterone, alprenalol, acetaminophen and nicotinamide. A complication was observed with this method in that the protonated glassing agents, methanol and DMSO, also received significant levels of hyperpolarisation and produced large side bands. These have the potential to mask potential substrate signals.

In 2006, Joo *et al.*<sup>36</sup> also published a method to produce a liquid sample hyperpolarised by DNP, termed as ‘Temperature Jump High-Frequency Dynamic Nuclear Polarisation’ (TJ-DNP) in the paper. In this case, the sample is cooled to 90 K and hyperpolarised by DNP using a 140 GHz microwave source. The sample is then melted rapidly using a 10.6  $\mu\text{m}$  infrared pulse and interrogated by NMR at 300 K. This method holds the major advantage that it can be repeated and therefore, standard high-resolution NMR sequences can be acquired using hyperpolarised samples. The paper reports enhancement levels similar to those reported by Ardenkjaer-Larsen *et al.*<sup>33</sup> An example of the reproducibility of the method and consequent signal averaging achieved using

this method is presented in Figure 1.10 for a 1D  $^{13}\text{C}$  NMR spectrum of  $[\text{U-}^{13}\text{C}]$ -L-proline.

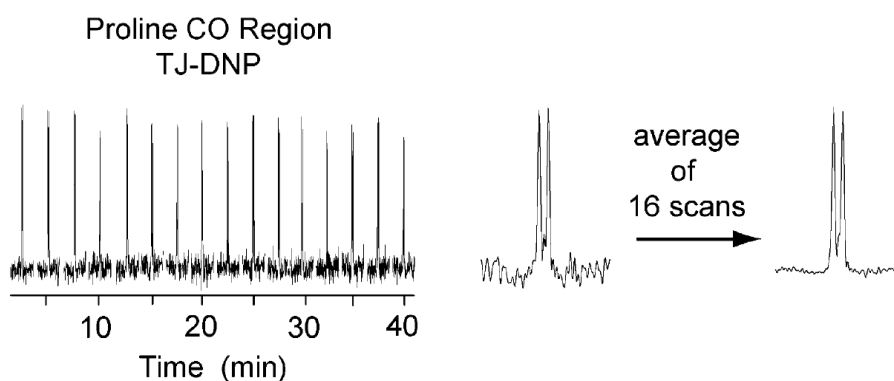


Figure 1.10 Left, sixteen spectra of the carbonyl resonance in  $[\text{U-}^{13}\text{C}]$ -L-proline resulting from a series of TJ-DNP experiments. These spectra can be averaged (right) to improve the observed signal to noise ratio. Image taken from a publication by Joo *et al.*<sup>36</sup>

DNP can be used in biological applications such as the detection and investigation of tumours. In a paper published in 2010,<sup>37</sup> Wilson *et al.* reported the use of DNP to probe a series of enzymatic pathways. They first investigated if a co-polarised solution of  $^{13}\text{C}$  bicarbonate and  $[\text{1-}^{13}\text{C}]$  pyruvate were able to divulge information about pH and pyruvate metabolism, and importantly, if the presence of one hyperpolarised complex did not interfere with the other. During the course of the experiment, it was observed that the two complexes did not interfere with each other through studies of images with both complexes and images with just pyruvate, however, results of the tumour studies were less positive. The pH was calculated based on the integral of the  $^{13}\text{C}$  bicarbonate and  $^{13}\text{C}$   $\text{CO}_2$  using the Henderson-Hasselbalch equation, with a normal value expected to be between 7.28 and 7.40. The ratio of hyperpolarised lactate to pyruvate was also investigated, and was expected to be between 0.20 and 0.52. In a normal mouse, the highest levels of lactate were found in the kidneys where lactate is excreted, and most abdominal regions having the ratio in the range 0.2-0.3. Studies on mice with tumours found that the malignant cells showed higher levels of lactate (ratios in the range 0.43 – 0.58) and were more acidic with a pH in the range 6.6 to 7.0, in comparison to surrounding normal abdominal tissues, however the average of 5 values of each were found to not be statistically different from each other. This was explained by the difficulty in finding positions which were fully benign or fully malignant. In a second experiment, it was also observed that images of four different complexes could be obtained through observation of  $[\text{1-}^{13}\text{C}]$  pyruvate,  $[\text{1-}^{13}\text{C}]$  pyruvate hydrate,  $^{13}\text{C}$

bicarbonate and  $^{13}\text{C}$  carbon dioxide. The ability to investigate more than one hyperpolarised species in one image reduces the time required to individually hyperpolarise each complex of interest, for instance,  $^{13}\text{C}$  bicarbonate can take up to 3.5 hours to hyperpolarise greater than 95 % of the sample.

In a paper published in 2011,<sup>38</sup> Park *et al.* reported the use of DNP to understand the early response to the chemotherapeutic drug, Temozolomide, often used to treat remaining tumour cells after surgery. This was completed by looking at the metabolism of pyruvate to lactate in the human tumour cells implanted into rats. This new method could detect changes in the metabolism of the tumours cells within 2 days and in some cases within 1 day, but the standard method of investigation did not show reduction until between 5-7 days. This difference could prove to be significant as it provides a method to investigate the effect of the drug treatment such that treatment of the tumour can be adjusted accordingly as soon as possible.

These techniques are reasonably well developed and illustrate the potential of hyperpolarisation techniques applied to biological systems.

### 1.2.5 Parahydrogen induced polarisation

Parahydrogen induced polarisation (PHIP) is a method of hyperpolarisation that derives the hyperpolarised state from one of the spin isomers of hydrogen, *parahydrogen*.

#### 1.2.5.1 Parahydrogen applied to NMR spectroscopy

$^1\text{H}$  has a nuclear spin quantum number of a  $\frac{1}{2}$  and can therefore take the value  $+\frac{1}{2}$  or  $-\frac{1}{2}$ , commonly written as  $\alpha$  or  $\beta$  respectively. Therefore, in  $\text{H}_2$  these values can combine to produce four molecular nuclear spin wavefunctions of  $\alpha\alpha$ ,  $(\alpha\beta - \beta\alpha)$ ,  $(\alpha\beta + \beta\alpha)$  and  $\beta\beta$ , where the normalisation factors have been omitted for simplicity. These four spin configurations can be further grouped according to the symmetry of their nuclear spin wavefunction with respect to exchange of the nuclei. Exchange of nuclei for  $\alpha\alpha$ ,  $(\alpha\beta + \beta\alpha)$  and  $\beta\beta$  leads to no change in the sign of the nuclear wavefunction and so can be considered symmetric. When dihydrogen is found in these three states it is termed *orthohydrogen* and corresponds to the nuclear triplet. Exchange of the nuclei in the  $(\alpha\beta - \beta\alpha)$  term leads to a change of sign and therefore is considered to have an antisymmetric nuclear wavefunction. This is the singlet state of dihydrogen and is

termed *parahydrogen*. Normal hydrogen contains 75 % *orthohydrogen* and 25 % *parahydrogen*.

The strength of the signal that is detected in an NMR experiment is dependent on the relative difference between the populations of magnetic energy levels that are probed. In the case of normal hydrogen, the four energy states are nearly equally populated at room temperature (see Figure 1.11a) according to the Boltzmann distribution resulting in only 1 in 32,000 protons being observable in a 9.4 T (400 MHz) magnetic field. In the case of pure *parahydrogen*, only one of the four potential spin configurations ( $\alpha\beta$ - $\beta\alpha$ ) is populated leading to a large population difference between the four magnetic states (see Figure 1.11b). The selection of this state is discussed in section 1.3.1. This is a non-Boltzmann spin distribution and so consequently can be termed as a hyperpolarised state.

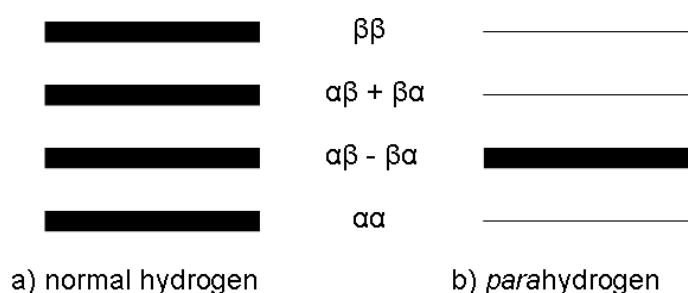


Figure 1.11 Schematic showing the relative populations the wavefunctions available to a) normal hydrogen and b) *parahydrogen*.

As the magnetic spins of *parahydrogen* are effectively antiparallel to each other meaning it has no net nuclear spin, it is not observable by NMR spectroscopy until its symmetry is broken. Traditionally, this means the hydrogen molecule must be incorporated into another molecule via for the enhancement to be observed. This can be achieved through direct hydrogenation and the result has been called *parahydrogen induced polarisation (PHIP)*.<sup>39</sup> This hydrogenation is commonly of a metal complex to form two chemically distinct hydrides. These two protons can be represented by the labels  $\alpha\alpha$ ,  $\alpha\beta$ ,  $\beta\alpha$  and  $\beta\beta$  which exist in four different energy levels when placed in a magnetic field.

When the metal complex has been hydrogenated with normal hydrogen, shown in Figure 1.12a, the populations of the four available magnetic states follow the Boltzmann distribution, leading to the observation of a small signal in NMR spectroscopy. When

the same hydrogenation is completed with *parahydrogen*, the initial ( $\alpha\beta$ - $\beta\alpha$ ) state of *parahydrogen* can only populate either the  $\alpha\beta$  and  $\beta\alpha$  states in the hydrogenation product. This leads to a large population difference between magnetic states in the product; a hyperpolarised state. This is shown in Figure 1.12b. When this state is interrogated by NMR, enhanced signals are observed.

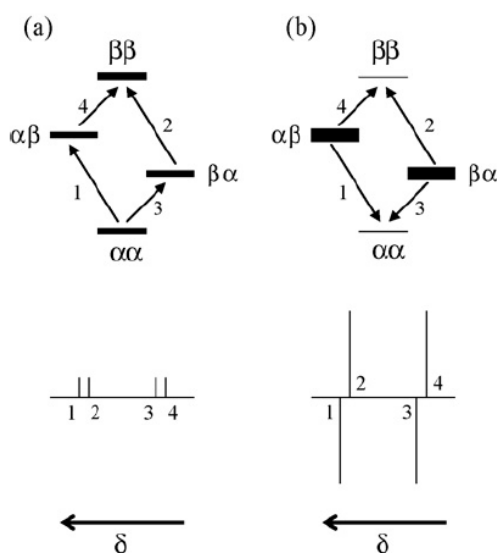


Figure 1.12 Schematic showing the magnetic distribution and NMR signals that result for an  $H_2$  addition product of a) normal hydrogen and b) *parahydrogen*. Figure reproduced from a paper published by Duckett *et al.*<sup>40</sup>

An important consideration of applying *parahydrogen* to NMR through PHIP is the requirement to use a  $45^\circ$  pulse rather than a  $90^\circ$  pulse.<sup>41</sup> This is because the signals derived from *parahydrogen* are maximised using a  $45^\circ$  pulse (see section 1.3.3.2).

The idea of creating an enhanced nuclear state through hydrogenation with of *parahydrogen* was first postulated in a paper published in 1986 by Bowers and Weitekamp<sup>42</sup> and was experimentally observed in a publication by the same group in 1987.<sup>43</sup> The effect was termed PASADENA to stand for ‘*parahydrogen* and synthesis allow dramatically enhanced nuclear alignment’. PASADENA occurs when the *parahydrogen* is added to the sample at high fields. The Eisenberg group experimentally observed<sup>44</sup> the PHIP phenomenon almost concurrently but was misinterpreted as an observation of chemically induced dynamic nuclear polarisation (CIDNP). In 1987, the group published a second paper<sup>45</sup> explaining the observation using the prediction of PHIP published by Bowers and Weitekamp<sup>42</sup> with new systems.

A year later in 1988, Pravica and Weitekamp<sup>46</sup> also published a new method of PHIP. In this case the *parahydrogen* was added to the solution outside the NMR spectrometer and therefore the magnetic states are created at low field. This was termed ALTADENA to stand for ‘adiabatic longitudinal transport after dissolution engenders nuclear alignment’. Both methods are followed by interrogation by NMR at high field.

These are complex phenomena and have been reviewed by Natterer and Bargon,<sup>41</sup> Duckett and Sleight,<sup>47</sup> and more recently by Duckett and Mewis<sup>48</sup> and Duckett and Blazina.<sup>49</sup>

### 1.2.5.2 Inorganic applications of PHIP

The enhancement gained through the application of PHIP has allowed the detection of very low concentration and short lived complexes and intermediates in inorganic chemistry.<sup>40,41,47,50</sup> A paper published in 1994 by Duckett *et al.*<sup>51</sup> (with corrections published in 1997<sup>52</sup>) discussed the observation of new intermediates in hydrogenation catalysed by Wilkinson’s catalyst, achieved through the application of PHIP. Up to the point of publication of the paper, the mechanism of Wilkinson’s catalyst, a well-studied catalyst for the hydrogenation of olefins, was postulated as shown in Figure 1.13.

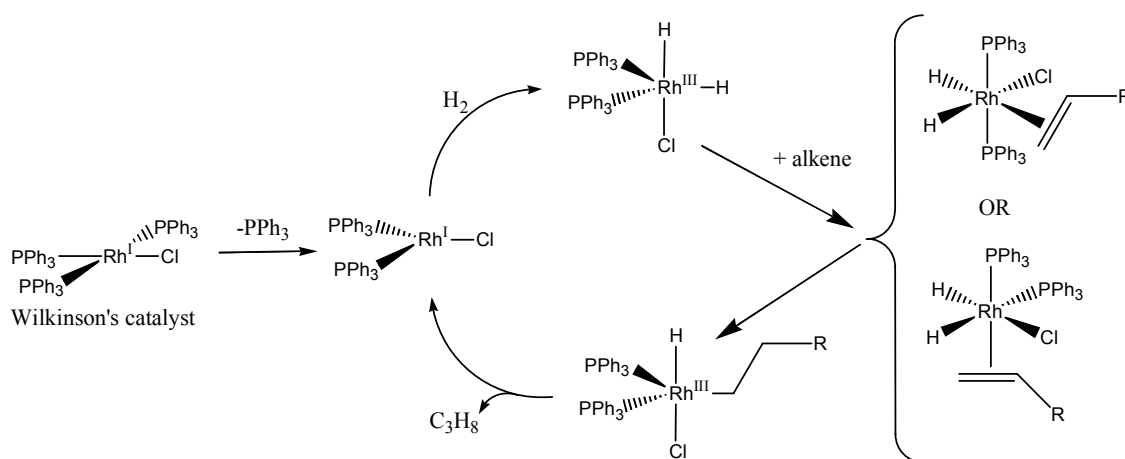


Figure 1.13 Schematic of the mechanism of the hydrogenation of olefins by Wilkinson’s catalyst as of 1994. Adapted from a paper published in 1994 by Duckett *et al.*<sup>51</sup>

Although this mechanism was generally accepted, the geometry of the 6-coordinate complex is unknown due to limitations of the methods used, with two isomers postulated in literature, shown far right in Figure 1.13. The key finding of the

investigation was observed accessibility of the Rh(III)/Rh(I) dimers (shown in Figure 1.14a) whose stability increased upon decreasing the electron richness of the olefin to be hydrogenated. These dimers can form 6-coordinate complexes in which the phosphine ligands are cis to each other. The nature of the ligand trans to the second phosphine is not concluded in the publication, both isomers are shown in Figure 1.14b.

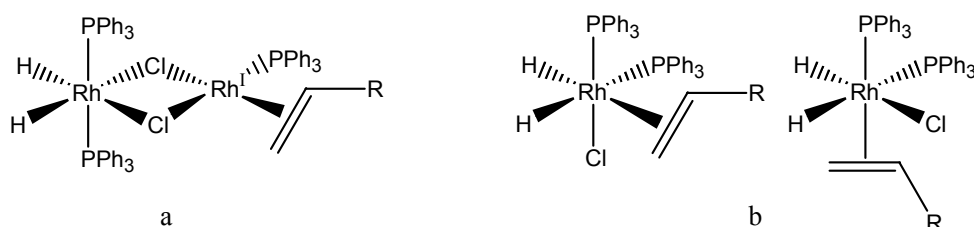


Figure 1.14 Structures of new complexes detected and postulated by Duckett *et al.*<sup>51</sup> in the 1994 publication concerning new intermediates in the mechanism of hydrogenation by Wilkinson's catalyst where a) is the Rh(III)/Rh(I) dimer  $\text{H}_2\text{Rh}(\text{PPh}_3)_2(\mu\text{-Cl})_2\text{Rh}(\text{PPh}_3)(\text{olefin})$  and b) shows the structures of the possible isomers of the  $\text{RhH}_2\text{Cl}(\text{PPh}_3)_2(\text{olefin})$  intermediate.

### 1.2.5.3 Biological applications of PHIP

*Parahydrogen* induced polarisation has also been used in biologically-relevant applications, most significantly in the production of contrast agents for MRI,<sup>48,53-55</sup> but also in detection of biological substrates.<sup>56</sup>

A paper published in 2007 by Wood *et al.*<sup>56</sup> discussed the application of PHIP to the detection of picomole amounts of biological substrates. This was achieved by the addition of *parahydrogen* to  $[\text{IrCl}(\text{CO})(\text{PPh}_3)_2]$  to act as a receptor in the presence of the substrate of interest in toluene. The reaction followed the scheme in Figure 1.15.

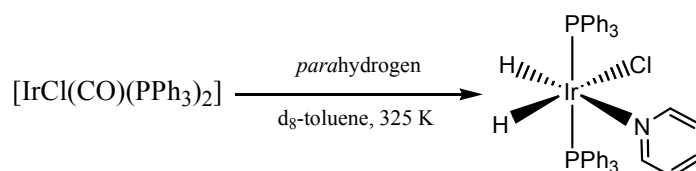


Figure 1.15 Reaction of  $[\text{IrCl}(\text{CO})(\text{PPh}_3)_2]$  with *parahydrogen* in the presence of pyridine. Image reproduced from the 2007 publication by Wood *et al.*<sup>56</sup>

The detection was then considered through the enhanced hydride regions, which will change depending on which substrate is bound to the complex, created by shaking the sample in the presence of *parahydrogen* and quickly inserting the sample into the

magnet. Using this method, it was found possible to detect 50 pmol of pyridine yielding hydrides at -21.03 ppm and -21.82 ppm. The characteristic hydride shifts of other biologically relevant molecules were also investigated, shown in Table 1.2.

Substrate (L)	Chemical shift of resultant hydrides ligands (ppm) / (ratio of products)
pyridine	-21.03, -21.82
benzimidazole	-19.22, -22.19
purine	a) -21.28, -22.7 b) -20.86, -21.82 c) -19.57, -21.86 / (100:18.6:0.8)
adenine	a) -21.37, -22.74 b) -20.90 c) -20.69, -22.22

Table 1.2 Characteristic shifts of signals corresponding to the hydride ligands of  $[\text{IrCl}(\text{H})_2(\text{PPh}_3)_2(\text{L})]$  where L corresponds to the stated biologically relevant substrates. For purine and adenine, a, b and c refer to different isomers of the resultant iridium complex. Data collated from the 2007 publication by Wood *et al.*<sup>56</sup>

In 2008, a paper was published by Reineri *et al.*<sup>54</sup> discussing the production of hyperpolarised  $^{13}\text{C}$  MRI contrast agents using PHIP. To produce a suitable  $^{13}\text{C}$  MRI contrast agent via PHIP, the molecule must obey a number of rules. The first is that it must contain an unsaturated bond that can be efficiently hydrogenated via a metal catalyst, commonly a triple bond. This unsaturated bond must also be adjacent to a carbonyl group such that a carbon with a long  $T_1$  is polarised, limiting the loss of polarisation due to relaxation. The polarisation is transferred to this carbon centre through scalar coupling with the protons derived from *parahydrogen*.

These ideas were taken a further step by the group when extending the applicability to MRI. For clinical use in imaging, it is preferable for the contrast agent to be water soluble and non-toxic. In many cases, the catalysts required for hydrogenation are not water soluble and the metals required in those catalysts are toxic to humans. The substrates to be investigated were therefore designed to contain (oligo)oxyethylenic chains such that the hydrogenated product was water soluble, but could be hyperpolarised in chloroform where the catalyst is more efficient. The group investigated the applicability of two potential new  $^{13}\text{C}$  MRI contrast agents: 2-(2-methoxyethoxy)ethyl phenylpropionate (asymmetric, Figure 1.16a) and *bis*[2-(2-methoxyethoxy)ethyl]acetylenedicarboxylate (symmetric, Figure 1.16b).



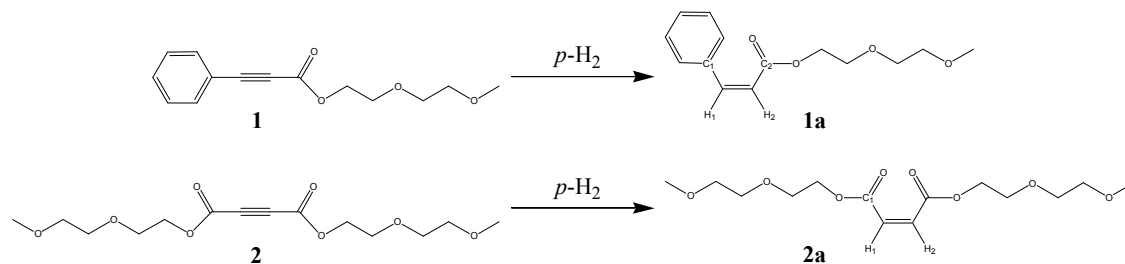


Figure 1.16 Hydrogenation reactions of **1**, 2-(2-methoxyethoxy)ethylphenylpropiolate and **2**, bis[2-(2-methoxyethoxy)ethyl]acetylenedicarboxylate with products termed **1a** and **2a** respectively. Adapted from the 2008 paper published by Reineri *et al.*<sup>54</sup>

Upon PHIP hydrogenation with the catalyst [bis(diphenylphosphino)butane](1,5-cyclooctadiene)rhodium(I) tetrafluoroborate, the asymmetric substrate, **1**, only exhibited enhanced  $^{13}\text{C}$  NMR signals under ALTADENA conditions and not under PASADENA conditions. The symmetric substrate, **2**, also exhibited enhanced  $^{13}\text{C}$  NMR signals but under both PASADENA and ALTADENA conditions. This, together with the information that **2a** showed a degree of water solubility meant substrate **2a** was taken further. It was then possible to complete the hydrogenation reaction in chloroform and transfer the hyperpolarised substrate into water for *in vivo* administration, thus saving time compared to standard methods of elimination of solvent and catalyst and dissolution in water.

To complete a measurement, the catalyst and substrate **2** were dissolved in a 6:1 chloroform to acetone mixture and the hydrogenation with *parahydrogen* completed.  $\text{D}_2\text{O}$  is then quickly added, and the sample shaken to dissolve the hyperpolarised hydrogenated substrate in the water. This is then allowed to settle for a short time before the water is moved to a second NMR tube for interrogation by  $^{13}\text{C}$  NMR spectroscopy. The resultant spectrum is shown in Figure 1.17.

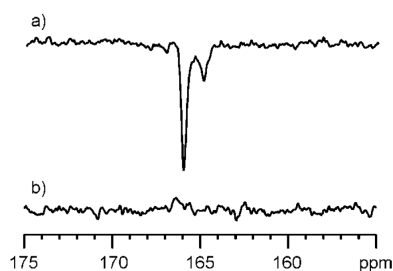


Figure 1.17 Single scan  $^{13}\text{C}$  spectrum of  $^{13}\text{C}$  labelled substrate **2a** (see Figure 1.16) extracted in  $\text{D}_2\text{O}$  after hydrogenation with *parahydrogen*. a) was recorded as soon as was practical after the hydrogenation step, and b) was collected after relaxation (5 min). Image taken from the 2008 publication by Reineri *et al.*<sup>54</sup>

Two  $^{13}\text{C}$  signals are observed in Figure 1.17; one corresponding to **2a** dissolved in  $\text{D}_2\text{O}$ , at 165.99 ppm, and one corresponding to **2a** dissolved in residual chloroform, 164.82 ppm. The enhancement of this signal was calculated to be around 100 fold. While a significant enhancement, this value might be much higher if the phase separation step is optimised to be quicker. The group consequently provided a new potential method by which to produce hyperpolarised  $^{13}\text{C}$  MRI contrast agents, which may be further optimised through selection of substrates with more optimal separation before and after hydrogenation.

#### 1.2.5.4 Comparison of PASADENA and ALTADENA

A paper published in 2009 by Korchak *et al.*,<sup>57</sup> investigated the effect on resultant NMR spectra of completing *parahydrogenation* of styrene to ethylbenzene with the catalyst [1,4-bis(diphenylphosphino)butane](1,5-cyclooctadiene)rhodium  $\text{BF}_4$ , shown in Figure 1.18, at a set number of magnetic fields.

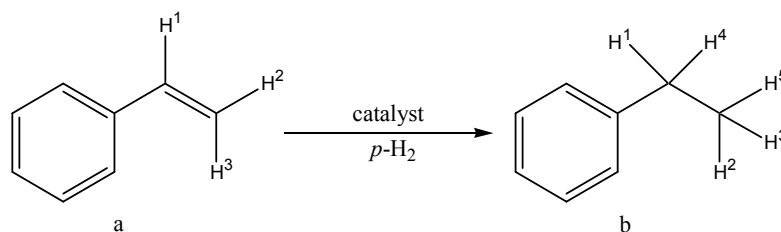


Figure 1.18 Hydrogenation reaction of a) styrene to b) ethylbenzene with [1,4-bis(diphenylphosphino)butane](1,5-cyclooctadiene)rhodium  $\text{BF}_4$  including relevant labels. Adapted from a publication in 2009 by Korchak *et al.*<sup>57</sup>

Strong PHIP signals can be observed at all fields of *parahydrogenation* investigated, shown in Figure 1.19. It shows the ALTADENA-type spectrum obtained at 0.1 mT is characterised by the net polarisation of the two groups having opposite sign gradually changes to a PASADENA-type spectrum, characterised by antiphase multiplets, as the field of *parahydrogenation* is increased. Below 0.2 mT, hyperpolarisation is also observed in the aromatic protons, attributed to transfer from the  $\text{CH}_2$  group through scalar coupling.

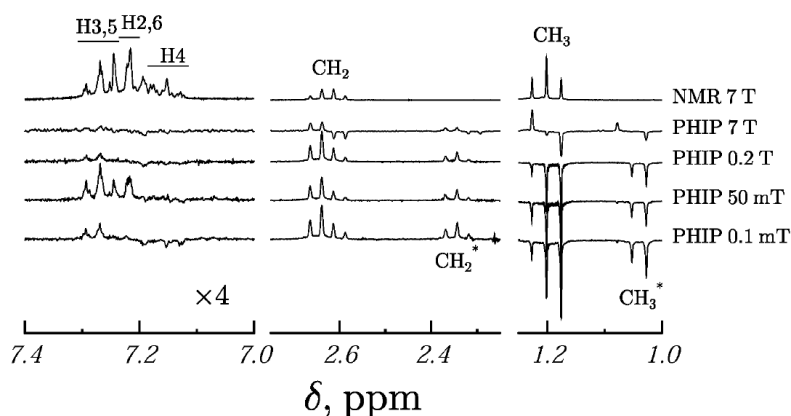


Figure 1.19  $^1\text{H}$  NMR at 7 T and PHIP spectra collected after *parahydrogenation* at stated polarisation field and acquisition at 7 T. \* denotes signals corresponding to bound ethylbenzene. Reproduced from a publication in 2009 by Korchak *et al.*<sup>57</sup>

## 1.2.6 Signal amplification by reversible exchange

### 1.2.6.1 Introduction to SABRE

Signal Amplification By Reversible Exchange (SABRE) is a form of non-hydrogenative PHIP. The *parahydrogen* molecule is not incorporated into the substrate of interest unlike conventional PHIP experiments. Instead, the *parahydrogen* molecule undergoes a reversible oxidative addition reaction with a metal centre. This metal centre is also able to facilitate the reversible exchange of the substrate of interest, creating a metal template through which the *parahydrogen* and substrate are able to come into temporary contact with each other (Figure 1.20). It is through this template that the hyperpolarised state is able to transfer from *parahydrogen* to the substrate.

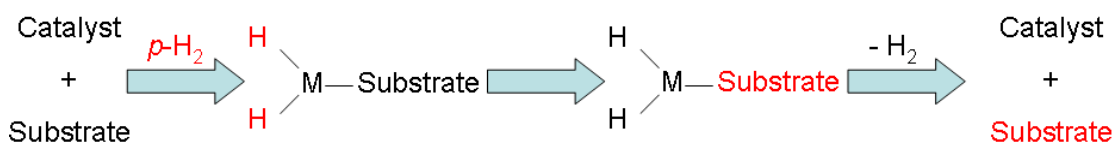


Figure 1.20 Schematic of the SABRE process showing non-hydrogenative transfer of hyperpolarised states from *parahydrogen* to a substrate via a metal catalyst. Adapted from the publication by Adams *et al.* (2009).<sup>58</sup>

A major benefit of SABRE is that the substrate is not hydrogenated during interrogation. It has therefore negated the need for unsaturated precursors, as would be required for PHIP, and provides a catalytic system as the substrate is not consumed.

### 1.2.6.2 Theory behind transfer

In a paper published by Adams *et al* (2009),<sup>59</sup> the theory behind the spontaneous polarisation transfer observed in SABRE was discussed. The paper presented a theory based on a simplified model in which polarisation transfer is only considered via scalar coupling and chemical shift evolution between *parahydrogen*-derived hydrides and a single substrate molecule containing only one proton pair. A schematic of this is shown in Figure 1.21.

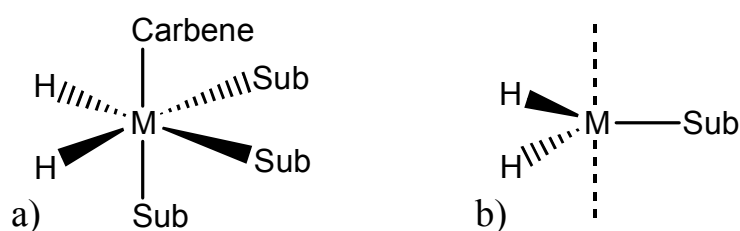


Figure 1.21 The general structure of a SABRE catalyst (a) and the simplified schematic utilised by the theory reported in Adams *et al.* (2009)<sup>59</sup> (b), where M = metal and Sub = substrate. The hydride pairs (H) are derived from *parahydrogen* in each case.

There are two significant differences between the real life situation and the model. In reality, polarisation is transferred into both equatorial sites however this is modelled as only one equatorial site. The substrate has also been modelled as a single pair of protons. This is because a typical substrate, such as pyridine, can contain five or more nuclei thereby creating a large scalar coupling network, which is time consuming to model. Within the model, the term spin referred to nuclear spins only and the term scalar coupling referred to isotropic spin-spin couplings, often known as J-coupling. The model complex is therefore a four-spin system comprising of two spins originating from *parahydrogen* and two spins from bound substrate.

The results from this theoretical study completed in MATHEMATICA<sup>TM,60</sup> showed that the scalar coupling network between the *parahydrogen* derived hydrides and pair of protons on the substrate across the magnetically active metal centre allows the transfer of polarisation within the complex. This transfer is greatly affected by the fine balance between the scalar coupling and chemical shift effects of the system. As a result of this, the process is therefore both magnetic field and time dependent (based on the lifetime of the complex). This model is said to be consistent with results obtained in a later paper published by Adams *et al.*<sup>58</sup>

### 1.2.6.3 The phosphine ligand vs. the carbene ligand

In the literature, two main types of catalyst have been investigated in the field of SABRE. These have the structure  $[\text{Ir}(\text{L})(\text{COD})(\text{Cl}/\text{py})]$ , where L is either a phosphine ligand<sup>58,61-65</sup> or a carbene ligand.<sup>66,67</sup> It is therefore important to consider the differences between these two ligands.

### 1.2.6.4 Phosphine-based catalysts

The most common phosphine based SABRE catalyst is Crabtree's catalyst, shown in Figure 1.22.

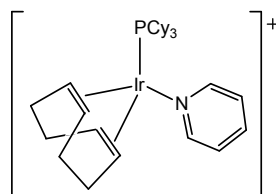


Figure 1.22 Structure of Crabtree's catalyst.

Crabtree's catalyst is a well-known hydrogenation catalyst.<sup>68-70</sup> When it was introduced, it was found to exhibit a much faster hydrogenation rate than the previously used Wilkinson's catalyst for substrates such as cyclohexene and 1-methylcyclohexene.<sup>68</sup> It was later observed that Crabtree's catalyst also showed significantly increased activity against sterically hindered alkenes such as 2,3-dimethylbut-2-ene<sup>69</sup> for which Wilkinson's catalyst showed no activity.

The ability to direct the hydrogenation completed using Crabtree's catalyst in homogeneous reactions is discussed in a paper published in 1986 by Crabtree and Davis<sup>70</sup> It was observed that by the addition of an alcohol group to a 1-methylcyclohexene ring (see Figure 1.23), the ring is able to take on a configuration where the alcohol group can take a pseudoaxial position.

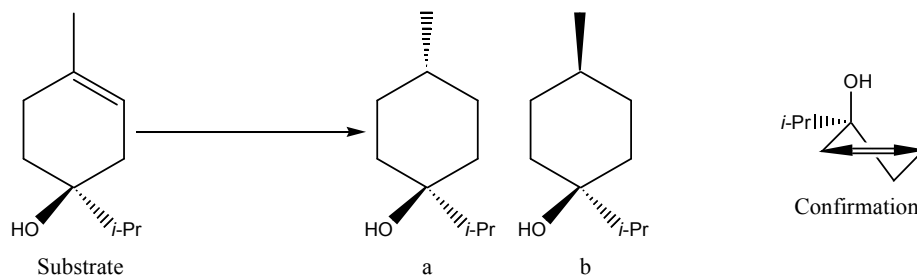


Figure 1.23 Generic structure and reaction of the 1-methylcyclohexene rings investigated in a publication by Crabtree and Davis,<sup>70</sup> using terpinen-4-ol as an example. The side view of the conformation of interest is also shown, where a) refers to the product formed by directed hydrogenation and b) refers to the product formed by counterdirected hydrogenation.

The confirmation means one face (with the OH group) is more polar than the other (the face without an OH group), leading to an opportunity to direct the hydrogenation using solvent. The behaviour of the substrate in the presence of Crabtree's catalyst in a polar solvent will be hard to predict however, in a non-polar solvent such as dichloromethane (DCM), it can be predicted that the polar face of the substrate will turn towards the catalyst. This leads to a directing effect when considering hydrogenation of such a substrate, resulting in hydrogenation on the polar face of the substrate and consequently leading to the production of the desired product. Initially, the substrates in Figure 1.24 were investigated, all of which possess a hydroxyl functional group.

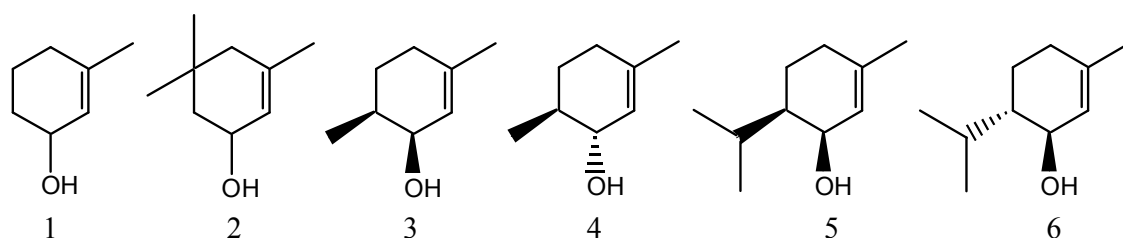


Figure 1.24 Structures of selected substrates investigated in a publication by Crabtree and Davis<sup>70</sup> This group are characterised by the alcohol group being bound directly to the ring.

The hydrogenation of these substrates using Crabtree's catalyst was proven to be successful. A total yield of a minimum of 97.3 % was found in each case, and of that yield, a minimum of 96.2 % was the directed product. A series of substrates with an exo-cyclic alcohol group or oxygen based functional group, such as an ether or ketone group, were also investigated with varying degrees of success.

Crabtree's catalyst is also a known H-D exchange catalyst.<sup>71</sup> In a paper published in 2001 by Ellames *et al.*,<sup>71</sup> The effect of changing the substituents on various ketone and

acid derivatives on deuteration by Crabtree's catalyst was investigated. The basic reaction investigated is shown in Figure 1.25.

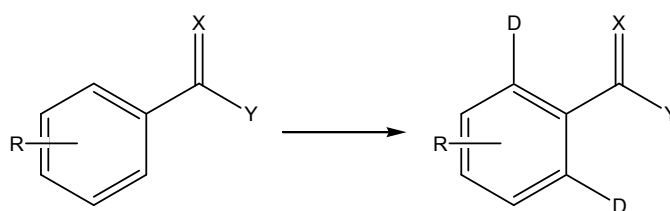


Figure 1.25 Deuteration reaction investigated in the 2001 paper published by Ellames *et al.*<sup>71</sup>

The group found that the exchange of protons mediated by Crabtree's catalyst is maximised through the addition of an  $sp^2$  hybridised nitrogen or oxygen atom via a five membered metallacycle. In general, if the electron donation to the directing heteroatom is increased, the degree of deuterium incorporation increases. It was also observed that mono-*ortho* substitution did not affect the level of deuteration observed to the second *ortho* site and that bulky *meta* substituents hindered deuterium incorporation.

The group also presented a simplified mechanism for the exchange process in the presence of deuterium oxide ( $D_2O$ ), reproduced in Figure 1.26.

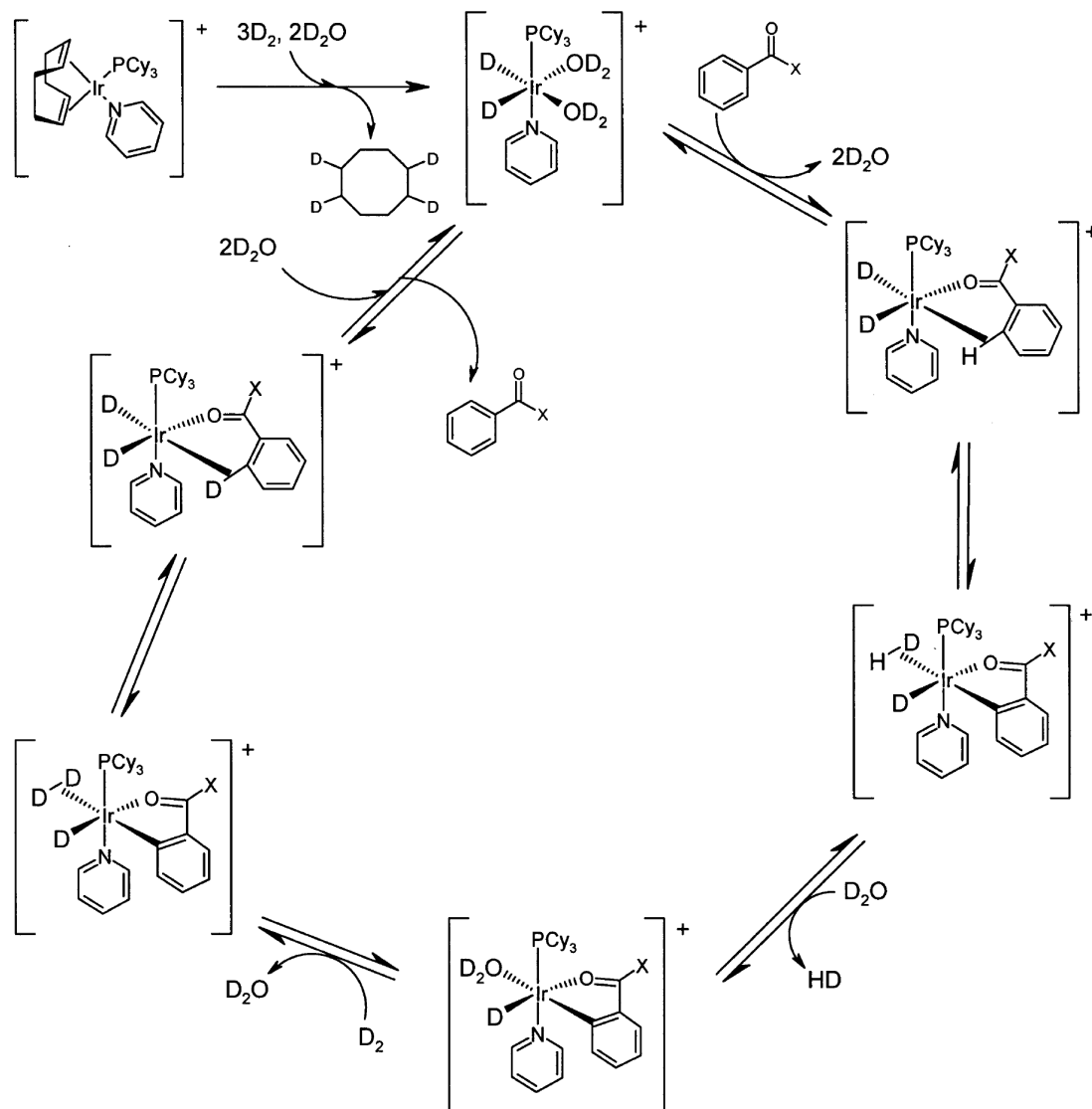


Figure 1.26 A simplified mechanism for HD exchange in the presence of deuterium oxide by Crabtree's catalyst, reproduced from a paper published by Ellames *et al.*<sup>71</sup> in 2001.

It is possible to observe that first the catalyst is activated in the presence of three equivalents of deuterium gas, 2 equivalents to hydrogenate the COD to octane, and the third to add to the metal centre through an oxidative addition. The deuterium oxide then binds to the two vacant sites producing the active catalyst,  $[\text{Ir}(\text{PCy}_3)(\text{D})_2(\text{D}_2\text{O})_2(\text{py})]\text{PF}_6$ . The mechanism then shows deuteration of the *ortho* position to a directing group, where the deuterium atoms are sourced from  $\text{D}_2\text{O}$ .

#### 1.2.6.5 Crabtree's catalyst applied to SABRE

The SABRE phenomenon was first published by Adams *et al.* in 2009 in Science.<sup>58</sup> The paper concerned polarisation transfer into pyridine and nicotinamide, indicating



enhancements in not only  $^{13}\text{C}$ ,  $^{15}\text{N}$ , but also  $^1\text{H}$ ,  $^{19}\text{F}$  and  $^{31}\text{P}$  signals, a significant advantage over DNP in which  $^1\text{H}$  enhancement is not routinely available. It also alluded to applications within MRI.

These ideas were investigated in greater detail in a paper of the same year by Atkinson *et al.*<sup>61</sup> Here, Crabtree's catalyst was altered such that the phosphine ligand is changed. A series of 8 phosphines were investigated to show the catalyst containing a  $\text{PCy}_2\text{Ph}$  ligand exhibited the greatest polarisation transfer into pyridine, where Crabtree's catalyst exhibited the second greatest polarisation transfer into pyridine. The paper also indicated that varying temperature or magnetic field of the polarisation step can have a great effect on the extent of polarisation transfer by the SABRE effect.

SABRE has also been applied to the detection of low concentrations of amino acids and peptides,<sup>64</sup> and the effect of changing the magnetic field of polarisation on the extent of polarisation transfer exhibited by Crabtree's catalyst also investigated.<sup>65</sup> The SABRE effect has even been applied to low field NMR in papers published by Gong *et al.*<sup>62</sup> and Theis *et al.*<sup>63</sup> In the paper published by Gong *et al.*<sup>62</sup> thermally polarised spectra collected on a low field NMR spectrometer have been compared to those collected under hyperpolarised conditions using SABRE with Crabtree's catalyst. The resultant spectra are presented in Figure 1.27.

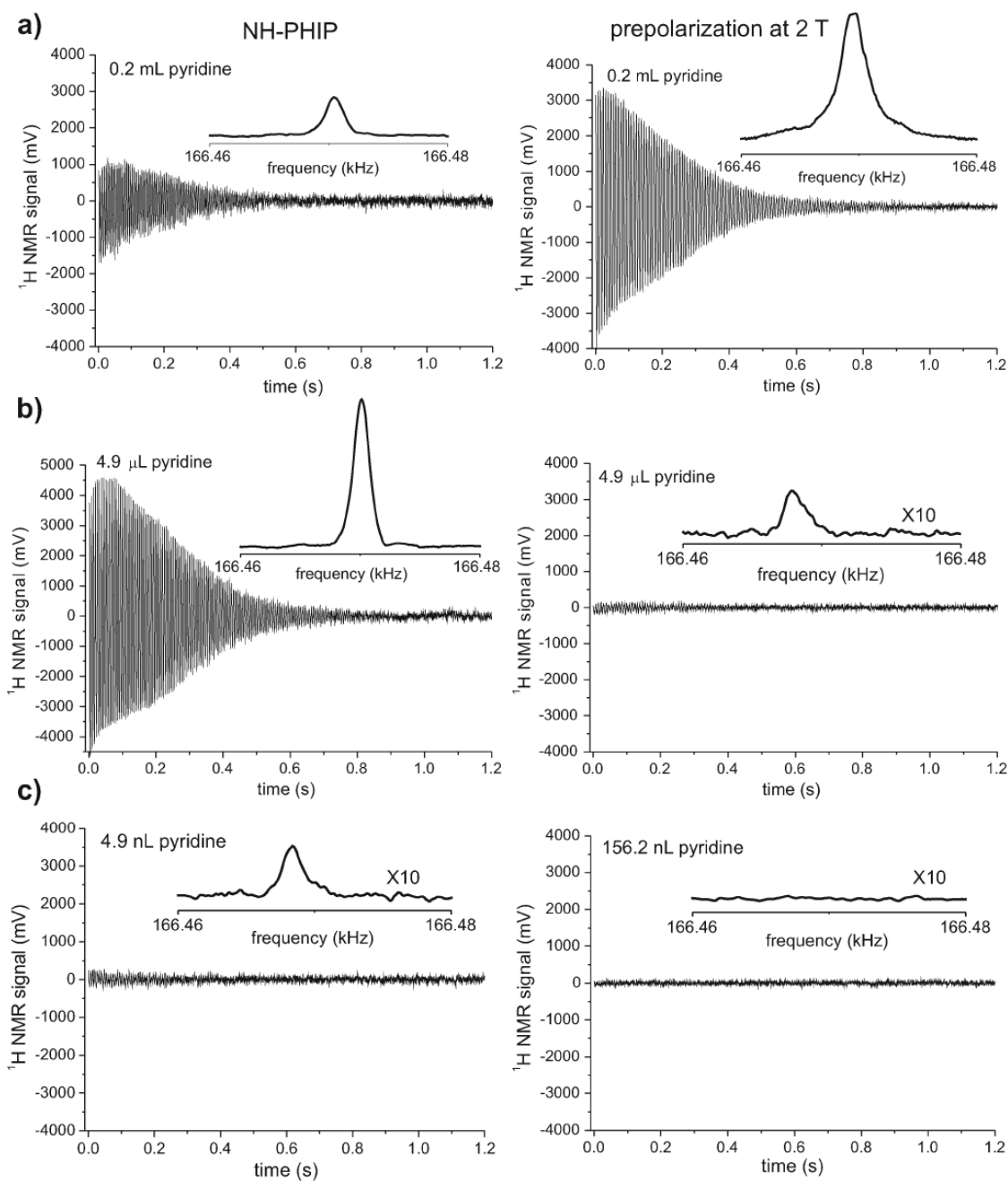


Figure 1.27 Comparison of low field NMR spectra with SABRE enhancement (left) and thermal polarisation (right). Single-scan  $^1\text{H}$  FIDs and corresponding spectra (inset) of the indicated volumes of pyridine in 0.4 ml methanol solutions. Image taken from the publication by Gong *et al.*<sup>62</sup>

Figure 1.27 shows volumes of pyridine as low as 4.9 nL can be observed using the SABRE technique, where it is not observed using thermally polarised conditions. The signal intensity observed for the 4.9  $\mu\text{L}$  pyridine sample is also significantly greater in the SABRE polarised spectrum.

The paper published by Theis *et al.*<sup>63</sup> extended this to include polarisation of <sup>15</sup>N pyridine. The application of SABRE has allowed the collection of a low field <sup>15</sup>N NMR spectrum of <sup>15</sup>N labelled pyridine in a single scan, but also pyridine with naturally abundant nitrogen in 128 averaged scans.

#### 1.2.6.6 Carbene-based catalysts

There are also two SABRE papers which consider the carbene-based catalyst, [Ir(IMes)(COD)Cl] (**IMes(a)**)<sup>66,67</sup> which is a carbene analogue of Crabtree's catalyst. Complexes composed of a carbene ligand tethered to a metal centre are published for their activities in alkylation of amines with alcohols,<sup>72</sup> hydrogenation,<sup>73,74</sup> regioselective hydrothiolation of alkynes,<sup>75</sup> as potential organic light emitting diodes<sup>76</sup> and biological activities as antimicrobial and anti-tumour agents.<sup>76</sup>

In a 2001 publication by Lee *et al.*,<sup>74</sup> the carbene analogue of Crabtree's catalyst [Ir(COD)(py)(SIMes)]PF<sub>6</sub> was synthesised and tested for its hydrogenation activity. Of the four simple systems investigated, it was only in the case of 1-methyl-1-cyclohexene at elevated temperatures that the new complex offered an improvement over the previously employed Crabtree's catalyst. This was a significant result as Crabtree's catalyst is not thermally stable and therefore the carbene analogues may offer a method to investigate hydrogenations at higher temperatures.

The activity for hydrogenation of carbene analogues of Crabtree's catalyst was also discussed in a 2006 publication by Vazquez-Serrano *et al.*,<sup>73</sup> in which a large number of alternative catalysts were considered. The activity of [Ir(COD)(IMes)Cl] in the hydrogenation of 1-octene is discussed here due to the catalysts application to SABRE. When hydrogenating 1-octene with [Ir(COD)(IMes)Cl], a number of products were observed by the group; octane, *trans*-2-octene, *cis*-2-octene and a range of unidentified internal isomers of octene. A time profile of the reaction is presented in Figure 1.28.

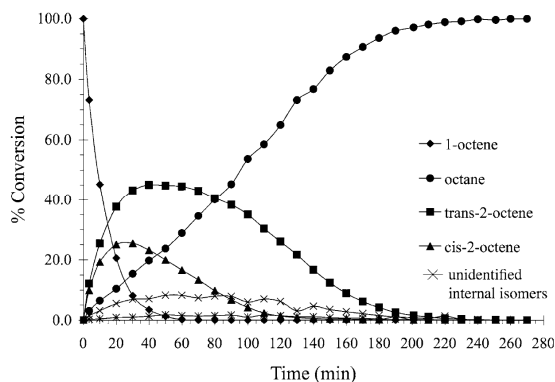


Figure 1.28 A time profile of the hydrogenation of 1-octene with  $[\text{Ir}(\text{COD})(\text{IMes})\text{Cl}]$  presented in the 2006 publication by Vazquez-Serrano *et al.*<sup>73</sup>

The Crabtree's analogues,  $[\text{Ir}(\text{L})(\text{COD})\text{Cl}]$  and  $[\text{Ir}(\text{L})_2(\text{COD})]\text{Cl}$  have also been shown to exhibit HD exchange much like Crabtree's catalyst.<sup>77,78</sup> A specific example of this type of catalyst exhibiting better efficiency than Crabtree's catalyst can be found in the 2010 publication by Nilsson and Kerr.<sup>78</sup> Here, the group deuterate the Bayer AG anthelmintic drug, niclosamide as shown in Figure 1.29.

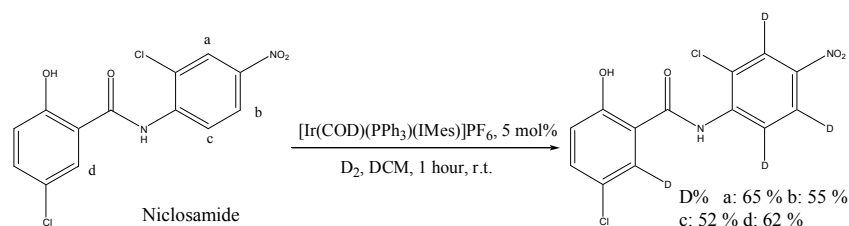


Figure 1.29 Labelling of niclosamide (Bayer AG) adapted from the 2010 publication by Nilsson and Kerr.<sup>78</sup>

The application of the catalyst  $[\text{Ir}(\text{COD})(\text{IMes})(\text{PPh}_3)]\text{PF}_6$  over Crabtree's catalyst resulted in a significant improvement in the extent of deuteration of the substrate. With a catalyst concentration of 5 mol% for 1 hour at room temperature under  $\text{D}_2$  gas, the catalyst  $[\text{Ir}(\text{COD})(\text{IMes})(\text{PPh}_3)]\text{PF}_6$  achieved a minimum of 52 % incorporation of deuterium to sites *a*, *b*, *c* and *d*. Under the same conditions with Crabtree's catalyst, less than 15 % incorporation of deuterium on positions *a* and *b* only was observed (labels in reference to Figure 1.29).

An important structural observation has also been made concerning carbene-analogues of Crabtree's catalyst. There are examples in the literature<sup>79</sup> of complexes possessing a carbene ligand which CH activates to a metal in an intramolecular manor. Of particular

interest are those where one of the methyl groups in the mesitylene rings of IMes<sup>80,81</sup> binds to a metal. This is illustrated in Figure 1.30.

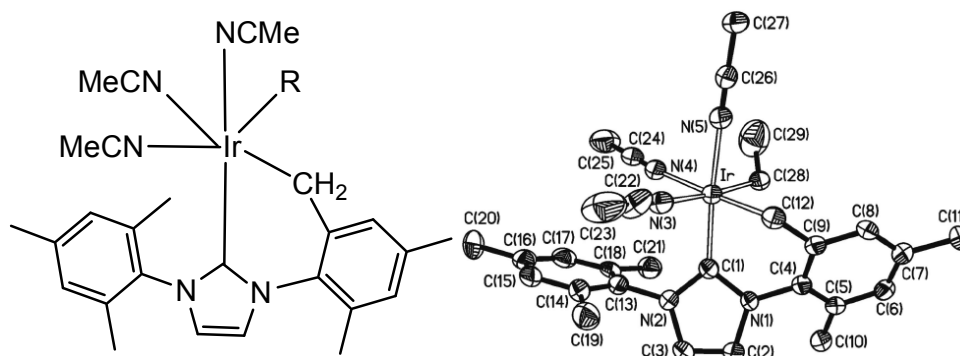


Figure 1.30 Chemical structure and X-ray structure of  $[\text{Ir}(\text{IMes}')(\text{NCMe})_3(\text{R})]\text{PF}_6$  taken from a publication by Torres *et al.*<sup>80</sup>

#### 1.2.6.7 Carbene-analogues of Crabtree's catalyst applied to SABRE

The increase in polarisation transfer to pyridine via SABRE using a carbene-based catalyst rather than a phosphine base catalyst was first published by Cowley *et al.*<sup>66</sup> in 2011. 243 fold enhancements were reported to the *ortho* position of pyridine in a single scan <sup>1</sup>H NMR spectrum under 3 bar *para*hydrogen, and 6, 000 fold <sup>1</sup>H signal enhancement was observed for pyridine at 3 T in an MRI system. This paper also introduced an automatised polarisation flow system for use with SABRE. This flow system increased accuracy in the application of a magnetic field during the polarisation transfer step. The polarisation transfer field which produces the greatest signal enhancement in pyridine could therefore be investigated to  $\pm 5$  G, observed for pyridine polarised with  $[\text{Ir}(\text{IMes})(\text{COD})\text{Cl}]$  to be 70 G.

This catalyst was also used in a paper published by Lloyd *et al.*<sup>67</sup> to investigate the application of SABRE to 2D sequences, achieved through the use of the previously mentioned polarisor or ultrafast methods by Lucio Frydman.<sup>82,83</sup> These results are discussed further in Chapter 5.

## 1.2.7 Only *Parahydrogen* Spectroscopy (OPSY)

### 1.2.7.1 Introduction to OPSY

The OPSY sequence was first described in a publication by Aguilar *et al.*<sup>84</sup> in 2007. The OPSY sequence is designed to select specific magnetic states within an interrogated substrate, for instance, double quantum terms ( $I_z S_z$ ) can be selected using a double quantum filter in the OPSYdq sequence. This is particularly useful when looking at SABRE experiments as *parahydrogen* starts in a singlet state. When a molecule of *parahydrogen* adds to a metal centre in an oxidative manner to create two hydrides, the zero quantum (ZQ), single quantum (SQ) and double quantum (DQ) terms evolve. When these are combined with other molecular spins, a large number of terms are generated across the spin system. Within this spin system, the multiple quantum terms (MQ) are able to transfer into the substrate. In a thermal sample (without *parahydrogen*), double quantum terms are not observable by a single  $90^\circ$  pulse due to symmetry rules and are not observable by use of a OPSYdq sequence because they are present in a very low proportion. Addition of polarisation derived from *parahydrogen* through the SABRE technique means double quantum states are much more prominent. This phenomenon allows for the observation of only nuclei which have double quantum states derived from *parahydrogen*, filtering out signals that have not been affected by *parahydrogen* and so has the potential to ‘light up’ specific compounds polarised by SABRE within the NMR spectrum. This has been considered further in section 1.3.3.

## 1.3 Experimental considerations

### 1.3.1 Production of *parahydrogen*

The overall wavefunction ( $\Psi_{\text{overall}}$ ) for a homonuclear system can be separated into the following five components, the electronic, nuclear, translational, rotational and vibrational wavefunctions ( $\Psi_e, \Psi_n, \Psi_t, \Psi_r$  and  $\Psi_v$ , Equation 1.1).

$$\Psi_{\text{overall}} = \Psi_e \times \Psi_n \times \Psi_t \times \Psi_r \times \Psi_v$$

Equation 1.1 The overall wavefunction of a system can be split into five components, the electronic, nuclear, translational, rotational and vibrational wavefunctions.

According to the symmetry postulate of quantum mechanics, dihydrogen must have an antisymmetric overall wavefunction, therefore one of the five wavefunction components must also be antisymmetric. In the case of homonuclear diatomics, the vibrational, translational and electronic wavefunctions are symmetric however the rotational and nuclear wavefunctions can be either symmetric or antisymmetric in nature. As described in section 1.2.5.1 (pg 71), *parahydrogen* has an antisymmetric nuclear wavefunction and therefore the rotational wavefunction must be symmetric to ensure the overall wavefunction is antisymmetric. This means that *parahydrogen* can only take even values of  $J$  (rotational quantum number), and so is able to form the most stable spin isomer of hydrogen where  $J = 0$ . If normal hydrogen gas is cooled to 20 K in the presence of a suitable spin exchange catalyst, the majority of spins fall into the most stable spin isomer where  $J = 0$ , and so hold a symmetric rotational wavefunction, becoming *parahydrogen*. Further details of the experimental production of *parahydrogen* are included in the Experimental section.

### 1.3.2 Description of observed signals

In a thermally polarised  $^1\text{H}$  NMR spectrum, it would be expected that the spectrum could be phased such that all signals are in absorption. Due to the application of *parahydrogen* through SABRE, this is not the case for many of the spectra presented in this thesis. An example of typical hyperpolarised spectrum is shown in Figure 1.31.

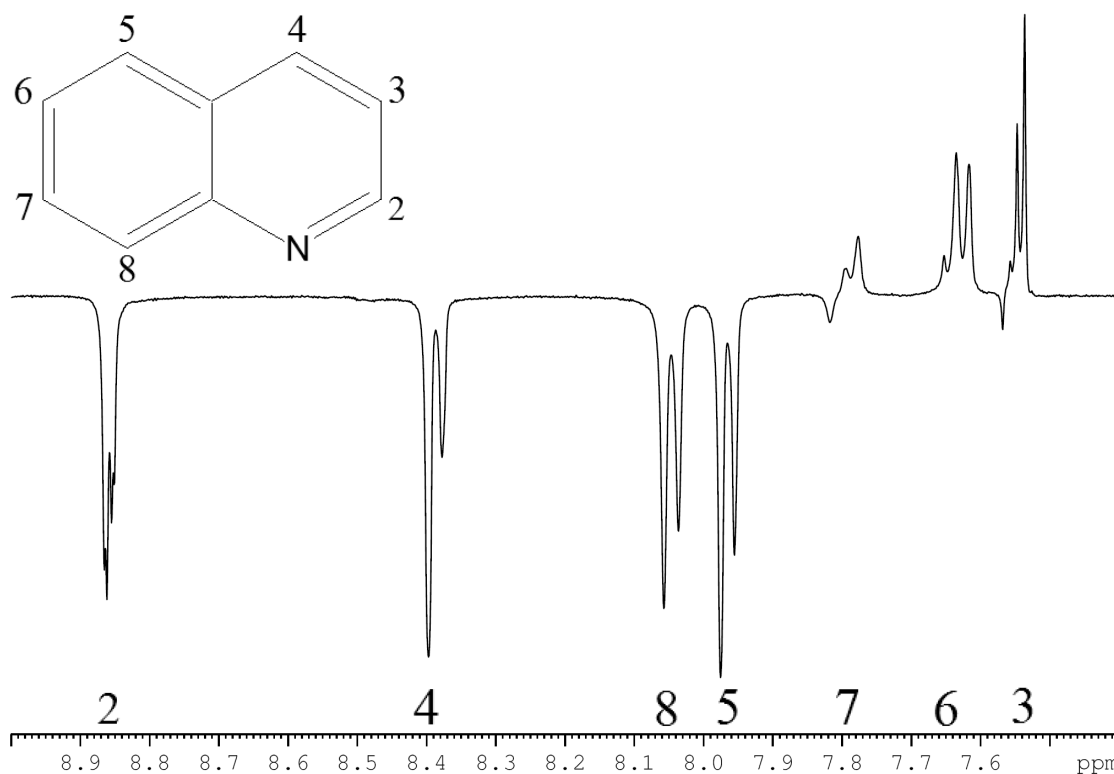


Figure 1.31 Typical  $^1\text{H}$  NMR spectra of hyperpolarised quinoline indicating various signal forms.

Figure 1.31 indicates three different types of signal that could potentially be observed when applying *parahydrogen* to NMR investigations. The first type of signal presents as an enhanced version of the thermally polarised signal, in absorption but with a larger integral, observed in Figure 1.31 for proton 6. The second type of signal presents as  $180^\circ$  out of phase relative to thermally polarised signals i.e. in emission, observed in Figure 1.31 for protons 2, 4, 5 and 8. There is also a third presentation in which the signals appear antiphase. This is shown in Figure 1.31 for proton 7 and to a lesser extent, for proton 3. The enhancements quoted throughout this thesis also represent the sign of the signals observed. A positive enhancement value indicates the signal was of positive phase, and a negative enhancement values indicates the signal was of negative phase. In the case of an antiphase signal, the integral of whole peak is taken and therefore contains a mixture of both absorption and emission character. The quoted enhancement is therefore lower as a result of cancellation of the antiphase signal.



### 1.3.3 NMR described in terms of product operators

#### 1.3.3.1 Introduction to product operator terms<sup>85</sup>

Considering NMR in terms of product operators provides a set of quantum mechanical operators which can be used to describe spin states which broadly fit into the traditional vector model and extend to where the vector model falls down. In the case of an uncoupled, spin- $\frac{1}{2}$  nuclei,  $\mathbf{I}$ , the four product operators,  $\frac{1}{2}\hat{E}$ ,  $\hat{I}_x$ ,  $\hat{I}_y$  and  $\hat{I}_z$  are required. The first is retained for purely formal reasons and will not be discussed again. The final three correspond to the bulk x, y and z magnetisation of a single spin in the rotating frame and are termed single spin operators or in-phase operators.

The application of an RF pulse is considered to be aligned to either the x axis or y axis, with such a frequency that it causes a rotation in the magnetisation. When an RF pulse is applied to create a rotation of  $\beta$  degrees, it is referred to as  $\beta_x$  or  $\beta_y$  depending on which axis that pulse is applied to. This has the following effects on the above mentioned product operators.

$$\begin{array}{ll} \hat{I}_x - (\beta_x) \rightarrow \hat{I}_x & \hat{I}_x - (\beta_y) \rightarrow \hat{I}_x \cos\beta - \hat{I}_z \sin\beta \\ \hat{I}_y - (\beta_x) \rightarrow \hat{I}_y \cos\beta + \hat{I}_z \sin\beta & \hat{I}_y - (\beta_y) \rightarrow \hat{I}_y \\ \hat{I}_z - (\beta_x) \rightarrow \hat{I}_z \cos\beta - \hat{I}_y \sin\beta & \hat{I}_z - (\beta_y) \rightarrow \hat{I}_z \cos\beta + \hat{I}_x \sin\beta \end{array}$$

These states must also be considered with respect to the free precession experienced after the application of an RF pulse. This is considered for the frequency of the precession,  $\Omega$ , for a period of time,  $t$ .

$$\begin{array}{l} \hat{I}_x - (\Omega t) \rightarrow \hat{I}_x \cos(\Omega t) + \hat{I}_y \sin(\Omega t) \\ \hat{I}_y - (\Omega t) \rightarrow \hat{I}_y \cos(\Omega t) - \hat{I}_x \sin(\Omega t) \\ \hat{I}_z - (\Omega t) \rightarrow \hat{I}_z \end{array}$$

This idea can then be extended to include a second spin, labelled  $\mathbf{S}$ , which is coupled to the first. The spin  $\mathbf{S}$  can be described in the same way as the spin  $\mathbf{I}$  in that four product operators,  $\frac{1}{2}\hat{E}$ ,  $\hat{S}_x$ ,  $\hat{S}_y$  and  $\hat{S}_z$ , are required, and evolve in the same manor under  $\beta_x$ ,  $\beta_y$ ,

and  $\Omega t$ . As the two spins are coupled, 16 product operators are required to describe the system, as outlined in Table 1.3.

		$\frac{1}{2}\hat{E}$	$\hat{S}_x$	$\hat{S}_y$	$\hat{S}_z$
2x	$\frac{1}{2}\hat{E}$	$\frac{1}{2}\hat{E}$	$\hat{S}_x$	$\hat{S}_y$	$\hat{S}_z$
	$\hat{I}_x$	$\hat{I}_x$	$2\hat{I}_x\hat{S}_x$	$2\hat{I}_x\hat{S}_y$	$2\hat{I}_x\hat{S}_z$
	$\hat{I}_y$	$\hat{I}_y$	$2\hat{I}_y\hat{S}_x$	$2\hat{I}_y\hat{S}_y$	$2\hat{I}_y\hat{S}_z$
	$\hat{I}_z$	$\hat{I}_z$	$2\hat{I}_z\hat{S}_x$	$2\hat{I}_z\hat{S}_y$	$2\hat{I}_z\hat{S}_z$

Table 1.3 Required product operators required to describe a system containing two coupled spins, **I** and **S**.

This has created nine new terms together with the single spin operators. The  $2\hat{I}_z\hat{S}_z$  term is a form of  $z$  polarisation. The remaining terms can then be split into terms of transverse polarisation, discussed below, and multiple quantum terms which are discussed later.

$2\hat{I}_x\hat{S}_z$ ,  $2\hat{I}_y\hat{S}_z$ ,  $2\hat{I}_z\hat{S}_x$  and  $2\hat{I}_z\hat{S}_y$  are forms of transverse polarisation, sometimes referred to as antiphase operators. These can be detected indirectly as they evolve into observable in-phase terms. Manipulation of these terms with respect to  $\beta$  must be considered carefully, and as such,  $\beta$  must be separated for each spin to  $(\beta)_I$  and  $(\beta)_S$ . For instance, application of  $(\beta)_I$  to **S** will have no effect if **I** represents  $^1\text{H}$  and **S** represents  $^{13}\text{C}$ . After an RF pulse, evolution due to chemical shift must be considered as before, however, because the spins are coupled, evolution due to J-coupling ( $J_{IS}$ ) must also be considered. First, this is considered for the single spin operators.

$$\hat{I}_x - (\pi J_{IS}t) \rightarrow \hat{I}_x \cos(\pi J_{IS}t) + 2\hat{I}_y\hat{S}_z \sin(\pi J_{IS}t) \quad \hat{S}_x - (\pi J_{IS}t) \rightarrow \hat{S}_x \cos(\pi J_{IS}t) + 2\hat{I}_z\hat{S}_y \sin(\pi J_{IS}t)$$

$$\hat{I}_y - (\pi J_{IS}t) \rightarrow \hat{I}_y \cos(\pi J_{IS}t) - 2\hat{I}_x\hat{S}_z \sin(\pi J_{IS}t) \quad \hat{S}_y - (\pi J_{IS}t) \rightarrow \hat{S}_y \cos(\pi J_{IS}t) - 2\hat{I}_z\hat{S}_x \sin(\pi J_{IS}t)$$

$$\hat{I}_z - (\pi J_{IS}t) \rightarrow \hat{I}_z \quad \hat{S}_z - (\pi J_{IS}t) \rightarrow \hat{S}_z$$

Second, this is considered for the terms referring to transverse magnetisation, the antiphase terms.

$$2\hat{I}_x\hat{S}_z - (\pi J_{IS}t) \rightarrow 2\hat{I}_x\hat{S}_z \cos(\pi J_{IS}t) + \hat{I}_y \sin(\pi J_{IS}t)$$

$$2\hat{I}_y\hat{S}_z - (\pi J_{IS}t) \rightarrow 2\hat{I}_y\hat{S}_z \cos(\pi J_{IS}t) - \hat{I}_x \sin(\pi J_{IS}t)$$

$$2\hat{I}_z\hat{S}_z - (\pi J_{IS}t) \rightarrow 2\hat{I}_z\hat{S}_z$$

$$2\hat{I}_z\hat{S}_x - (\pi J_{IS}t) \rightarrow 2\hat{I}_z\hat{S}_x\cos(\pi J_{IS}t) + \hat{S}_y\sin(\pi J_{IS}t)$$

$$2\hat{I}_z\hat{S}_y - (\pi J_{IS}t) \rightarrow 2\hat{I}_z\hat{S}_y\cos(\pi J_{IS}t) - \hat{S}_x\sin(\pi J_{IS}t)$$

The terms  $2\hat{I}_x\hat{S}_x$ ,  $2\hat{I}_x\hat{S}_y$ ,  $2\hat{I}_y\hat{S}_y$  and  $2\hat{I}_y\hat{S}_x$  are multiple quantum coherences between the spins. These terms are not directly observable. For a two spin system, there are two types of multiple quantum coherence, the double quantum coherence and zero quantum coherence, each with an x and y component. The four coherences outlined below can be combined to produce the four multiple coherences stated above.

$$DQ_x = \frac{1}{2} (2\hat{I}_x\hat{S}_x - 2\hat{I}_y\hat{S}_y) \qquad DQ_y = \frac{1}{2} (2\hat{I}_y\hat{S}_x + 2\hat{I}_x\hat{S}_y)$$

$$ZQ_x = \frac{1}{2} (2\hat{I}_x\hat{S}_x + 2\hat{I}_y\hat{S}_y) \qquad ZQ_y = \frac{1}{2} (2\hat{I}_y\hat{S}_x - 2\hat{I}_x\hat{S}_y)$$

In these cases, evolution under chemical shift must be considered differently. Double quantum states evolve under the sum of the two spin frequencies ( $\Omega_I + \Omega_S$ ) and zero quantum states evolve under the difference of the two spin frequencies ( $\Omega_I - \Omega_S$ ). Multiple quantum states do not evolve under J-coupling between themselves ( $J_{IS}$ ) in a weak coupling regime, but can evolve with respect to a coupling to a third spin.

$$DQ_x - ((\Omega_I + \Omega_S)t) \rightarrow DQ_x\cos((\Omega_I + \Omega_S)t) + DQ_y\sin((\Omega_I + \Omega_S)t)$$

$$ZQ_x - ((\Omega_I - \Omega_S)t) \rightarrow ZQ_x\cos((\Omega_I - \Omega_S)t) + ZQ_y\sin((\Omega_I - \Omega_S)t)$$

In thermally equilibrated NMR, nuclei start with longitudinal z-magnetisation,  $I_z$  or  $S_z$ . They evolve as described below upon interrogation with a  $90^\circ$  pulse.

$$\begin{aligned} \hat{I}_z - (90^\circ_y) &\rightarrow \hat{I}_z\cos(90) + \hat{I}_x\sin(90) \rightarrow \hat{I}_x - (\Omega_I t) \rightarrow \hat{I}_x\cos(\Omega_I t) + \hat{I}_y\sin(\Omega_I t) - (\pi J_{IS}t) \rightarrow \\ &\hat{I}_x\cos(\Omega_I t)\cos(\pi J_{IS}t) + 2\hat{I}_y\hat{S}_z\cos(\Omega_I t)\sin(\pi J_{IS}t) + \hat{I}_y\sin(\Omega_I t)\cos(\pi J_{IS}t) - \\ &2\hat{I}_x\hat{S}_z\sin(\Omega_I t)\sin(\pi J_{IS}t) \end{aligned}$$

These four terms can be further separated. The  $\hat{I}_y$  term produces the imaginary FID. The amplitude of the  $\hat{I}_x$  term can be rewritten using the following trigonometric identity,

$$\cos A \cos B = \frac{1}{2}(\cos(A+B) + \cos(A-B))$$

as below such that an in-phase doublet is observed.

$$\hat{I}_x\cos(\Omega_I t)\cos(\pi J_{IS}t) = \hat{I}_x[\frac{1}{2}\cos((\Omega_I + \pi J_{IS})t) + \frac{1}{2}\cos((\Omega_I - \pi J_{IS})t)]$$

The single quantum coherences ( $2\hat{I}_y\hat{S}_z$  and  $2\hat{I}_x\hat{S}_z$ ) are not directly observable but evolve into observable magnetisation during the acquisition time. This is an important observation for consideration of more complicated sequences, for instance the COSY and INEPT NMR sequences.

### 1.3.3.2 Using product operators to understand *parahydrogen* induced polarisation (PHIP)

Two coupled magnetically and chemically inequivalent protons derived from one *parahydrogen* molecule, such as those observed in an asymmetric hydrogenation product, are present in an  $\hat{I}_z\hat{S}_z$  state, not an  $\hat{I}_z$  and  $\hat{S}_z$  state. This has a significant result on the NMR spectra produced. In this case, both **I** and **S** represent *parahydrogen* derived protons. In the case of PASADENA, the hyperpolarised states are prepared at high field inside the spectrometer and the  $2\hat{I}_z\hat{S}_z$  state is dominant. In the case of ALTADENA where the states are prepared outside the magnet in low field, the states,  $\frac{1}{2}(2\hat{I}_z\hat{S}_z) \pm \frac{1}{2}(\hat{I}_z - \hat{S}_z)$ , are present.<sup>86</sup> Both these cases share the  $2\hat{I}_z\hat{S}_z$  starting state which will be considered further. As both **I** and **S** are protons,  $\beta_y^I$  and  $\beta_y^S$  are equal but have initially been separated for ease of understanding of the transformations.

$$2\hat{I}_z\hat{S}_z - (\beta_y^I) \rightarrow 2\hat{I}_z\hat{S}_z \cos(\beta_y^I) + 2\hat{I}_x\hat{S}_z \sin(\beta_y^I) - (\beta_y^S) \rightarrow 2\hat{I}_z\hat{S}_z \cos(\beta_y^I) \cos(\beta_y^S) + 2\hat{I}_z\hat{S}_x \cos(\beta_y^I) \sin(\beta_y^S) + 2\hat{I}_x\hat{S}_z \sin(\beta_y^I) \cos(\beta_y^S) + 2\hat{I}_x\hat{S}_x \sin(\beta_y^I) \sin(\beta_y^S)$$

$$\Rightarrow 2\hat{I}_z\hat{S}_z \cos^2(\beta) + 2\hat{I}_z\hat{S}_x \cos(\beta) \sin(\beta) + 2\hat{I}_x\hat{S}_z \sin(\beta) \cos(\beta) + 2\hat{I}_x\hat{S}_x \sin^2(\beta)$$

Upon application of a  $90^\circ$  pulse, all terms with a  $\cos(\beta)$  component become unobservable as  $\cos(90) = 0$ . This leaves the  $2\hat{I}_x\hat{S}_x \sin^2(\beta)$  term which is a multiple quantum term and therefore not directly observable. It is therefore necessary to apply a pulse which does not equal  $90^\circ$ , however  $\sin(\beta)\cos(\beta)$  is maximised when  $\beta$  equals  $45^\circ$ . In a  $^1\text{H}$  NMR spectrum, this leads to the observation of antiphase doublets at both  $\Omega_I$  and  $\Omega_S$ . In PASADENA, these are of equal intensity, however in ALTADENA, the addition of the  $\hat{I}_z$  and  $\hat{S}_z$  states produces complications.<sup>87</sup>

### 1.3.3.3 Using product operators to understand the $^1\text{H}$ OPSY NMR sequences<sup>86</sup>

The  $^1\text{H}$  OPSY NMR sequence is an important sequence in the application of SABRE as it allows the observation of states derived from *parahydrogen* while filtering out thermal signals. The  $^1\text{H}$  OPSYdq NMR sequence is presented in Figure 1.32.

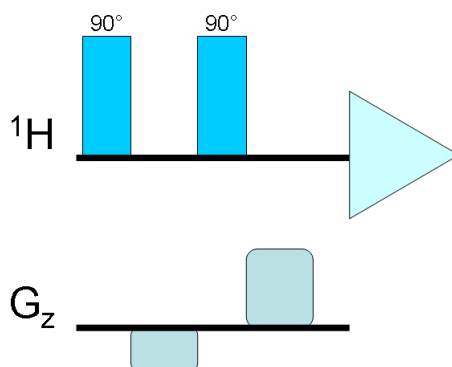


Figure 1.32 The  $^1\text{H}$  OPSYdq NMR sequence, adapted from a publication by Aguilar *et al.*<sup>84</sup>

As discussed before, the addition of *parahydrogen* to a complex results in the two protons being in the state  $2\hat{I}_z\hat{S}_z$ . After a  $90^\circ_x$  pulse, the state  $2\hat{I}_y\hat{S}_y$  is produced. This evolves as a mixture of zero and double quantum states, as presented below, under  $(\Omega_I + \Omega_S)$  and  $(\Omega_I - \Omega_S)$ , as discussed in section 1.3.3.1.

$$2\hat{I}_y\hat{S}_y - (\Omega_I t), (\Omega_S t) \rightarrow 2\hat{I}_y\hat{S}_y \cos(\Omega_I t) \cos(\Omega_S t) + 2\hat{I}_y\hat{S}_x \cos(\Omega_I t) \sin(\Omega_S t) \\ + 2\hat{I}_x\hat{S}_x \sin(\Omega_I t) \cos(\Omega_S t) + 2\hat{I}_x\hat{S}_y \cos(\Omega_I t) \sin(\Omega_S t)$$

A second  $90^\circ$  pulse is proceeded and followed by gradient pulses which act to filter out thermal polarisation and select the chosen coherence. For instance, in the case of the  $^1\text{H}$  OPSYdq NMR sequence, the second set of gradients are 2 times the size of the first to select the double quantum coherences. In the case of the  $^1\text{H}$  OPSYzq NMR sequence, the second set of gradients are not present to select zero quantum coherences.

## 1.4 Thesis aims

The main aim of this research project is to further develop the recently illustrated hyperpolarisation technique, SABRE, for use within the pharmaceutical industry. At the start of this project, knowledge of the SABRE technique was established and published,<sup>58,61</sup> and knowledge of the carbene catalyst **IMes(a)** was established but not

yet published. Knowledge of temperature and magnetic field dependence was also hinted at within the literature<sup>61,65,66</sup> however in depth, experimental investigations into these effects had not yet been completed. This project began with a more extensive investigation into methods of optimisation for the SABRE technique including different carbene catalysts (a task divided across the whole research group), different temperatures, different magnetic fields of polarisation and different solvents then had previously been completed. For these optimisation investigations, pyridine was used as a reference substrate, as this had been shown to exhibit significant polarisation transfer in the literature, and therefore allowed the ability to compare my results with those in the literature.

The application of the SABRE technique to high resolution NMR in the pharmaceutical industry was also required. Development of commonly used characterisation sequences such as the COSY and HMBC have also been investigated. Of particular importance, when this approach is to be applied to the pharmaceutical industry, is to understand the functional group tolerance of SABRE and limits of detection, ideally to the level of 0.5 – 50 µg of material. This thesis outlines the progress made toward these goals in three years of study.

Chapter 2 provides a brief description of the methods and terminology included throughout this thesis, particularly in reference to a new flow system able to facilitate the use of SABRE. It then goes on to discuss the mechanisms involved in activation of SABRE catalysts and of the exchange of ligands from the active complex. The chapter then goes on to discuss the structural and electronic differences between three carbene catalysts investigated including not just the active catalysts, but also the catalytic precursors. Preliminary studies into the effect of these structural and electronic differences on the extent of polarisation transfer are also reported.

These concepts are extended in Chapter 3. Here the effect of other variables which alter the extent of polarisation transfer into pyridine such as the magnetic field of polarisation transfer, temperature of polarisation transfer, concentration of substrate and catalyst, and solvent are investigated. The magnetic field and temperature of polarisation transfer is also investigated as a function of catalyst. It is reported that each variable has a significant effect on the extent of polarisation transfer into pyridine, and these changes are found to be different according to which catalyst is investigated. The potential

reasons for the different changes on extent of polarisation transfer are discussed including the rate constants of ligand exchange, the excess of hydrogen gas available to the sample and varying combinations of active complexes.

In Chapter 4, these concepts are extended to include the new, larger substrate, quinoline. This consists of a pyridine ring fused to a benzene ring creating an aromatic substrate with seven magnetically inequivalent protons. Initial investigations into quinoline revealed the catalysts used as standard did not facilitate polarisation transfer into quinoline however, addition of acetonitrile to the system allowing significant polarisation transfer into quinoline. The result of this addition on the structure of the active species is discussed. The effects of temperature and magnetic field of polarisation transfer, concentration and solvent on the extent of polarisation transfer are then investigated. The mechanism of polarisation transfer into quinoline is also investigated through the interrogation of quinoline analogues and application of selective  $^1\text{H}$  OPSYdq NMR sequences to quinoline.

Quinoline is again used in order to investigate the application of SABRE to a number of NMR sequences as discussed in Chapter 5. It was chosen for this task because in contrast to pyridine, it contains two quaternary carbons, which will help in understanding the application of SABRE to 2D heteronuclear sequences. Investigations range from  $^1\text{H}$  and  $^{13}\text{C}$  1D sequences to  $^1\text{H}$ - $^1\text{H}$  and  $^1\text{H}$ - $^{13}\text{C}$  2D sequences using a flow method which allows automated repolarisation of a sample during acquisition of a data set. Those involving  $^{13}\text{C}$  are of particular interest due to the lower natural abundance and gyromagnetic ratio compared to  $^1\text{H}$ . The effects of SABRE polarisation on these sequences is discussed and covers routes to apply decoupling to  $^{13}\text{C}$  sequences and sequentially receives data. The application of SABRE to the ultrafast COSY is also discussed.

Chapter 6 then looks at the wider applicability of SABRE. This includes investigating how different substrates might react to polarisation transfer via SABRE from the basicity of the substrate to the effect of increasing the size of the substrate and therefore how far into a given substrate polarisation transfer via the SABRE technique can progress. The potential for substrates without a pyridyl group, such as thiazole and indole analogues are also discussed and extended in order to look at current commercially available drugs. A second potential complication of pharmaceutical NMR

is considered in the form of competitive substrates in solution. The reaction of 4-carboxaldehydepiperidine with methanol is also discussed in reference to NMR spectroscopy, SABRE hyperpolarisation methods and mass spectroscopy studies.



## 2 Chapter 2 - Catalyst synthesis

### 2.1 Introduction

In October 2009, information about the SABRE technique was limited. Within the literature SABRE had only been reported where phosphine-based catalysts had been utilised<sup>58,61</sup> and work within the research group had just begun into the carbene-based catalyst, [Ir(IMes)(COD)Cl] (later published in 2011).<sup>66</sup> Crude empirical observations that a magnetic field dependence and temperature dependence on polarisation transfer through SABRE had been made, but not rationalised. The work presented in this thesis illustrates a series of investigations into SABRE that seek to improve the understanding of which properties lead to significant polarisation transfer (covered in this chapter) and how these properties can be altered to optimise polarisation transfer.

One of the most important factors when considering an investigation into the SABRE technique must be the catalyst itself. This forms a template through which the hyperpolarised magnetic states associated with the *parahydrogen* derived hydride ligands are able to transfer their hyperpolarisation into the substrate.

#### 2.1.1 Required properties of a SABRE catalyst

The SABRE technique is based on the polarisation transfer of hyperpolarised magnetic states from *parahydrogen*-derived hydride ligands to nuclei associated with a substrate ligand, where both are bound to a catalytic metal centre. This substrate then dissociates from the metal catalyst such that the hyperpolarised magnetic states are observable in the signals associated with the free substrate. Consequently, the chosen catalyst must provide a platform to which the substrate of interest is able to weakly bind, such that binding occurs to allow polarisation transfer. This binding must be reversible such that the hyperpolarised states become present in the free substrate. It is also important for the hydride ligands to undergo a reversible exchange with hydrogen, such that the hyperpolarised states in the system can be replenished.

There are a number of factors that must be considered when investigating SABRE catalysts. Firstly, as the SABRE catalyst will be used in NMR spectroscopy, it is important the catalyst used is present in relatively low concentration such that the

signals associated with the catalyst do not interfere with the signals associated with the substrate of interest. Secondly, it is also important that the catalyst is not paramagnetic in nature as this will provide a method of relaxation for the hyperpolarised magnetic states which will be interrogated.<sup>88</sup> Thirdly, if the metal nucleus is NMR active, it also has the potential to induce large splitting patterns or changes in chemical shifts, which may complicate the resulting spectra.<sup>89,90</sup> The active versions of current SABRE catalysts are unstable when exposed to air, and consequently, a stable precursor that can be isolated is used. This brings an additional requirement for the metal to be able to undergo an activation reaction, which in all catalysts published to date, has been the oxidative addition of dihydrogen gas. To this end, a COD ligand is utilised. The two double bonds on the COD ligand undergo hydrogenation, producing octane which does not interact with the active catalyst. There are many reports of stable complexes of the type  $[\text{Ir}(\text{carbene})(\text{COD})\text{Cl}]$  which can be isolated.<sup>80,91-96</sup>

The presence of oxygen gas must also be eliminated owing to its paramagnetic properties meaning it may have the ability to enhance the rate of relaxation of hyperpolarised states within the reaction mixture.<sup>88</sup>

For the initial investigations into the effect of changing the catalyst, a model substrate was also required. This substrate required a heteroatom with a lone pair to bind to the metal, with nitrogen or oxygen being the first choice. It is also important for the chemical shift associated with that substrate to be distinct from those associated with the catalyst, tending towards an aromatic system. Additionally, it must also be small to reduce any potential problems with binding as a result of steric bulk. This led to the selection of pyridine, a 6-membered aromatic ring which contains a nitrogen atom with an available lone pair for bonding, and a chemical shift range from 7.2 ppm to 8.6 ppm which is base-line-resolved from any signals associated with likely catalysts.

### 2.1.2 Literature based SABRE results in which phosphine-based catalysts are used

When the SABRE phenomenon was first reported by Adams *et al.* (2009),<sup>58</sup> the catalyst  $[\text{Ir}(\text{COD})(\text{NCMe})(\text{PCy}_3)]\text{BF}_4$  was utilised. This underwent a reaction with excess substrate and hydrogen in methanol to produce  $[\text{Ir}(\text{H})_2(\text{PCy}_3)(\text{substrate})_3]\text{BF}_4$  as the active catalytic species. A method was described in which a Young's tap NMR tube was charged with the catalyst, excess substrate and *parahydrogen*, then shaken to dissolve

the gas in the headspace into the solution and then interrogated by  $^1\text{H}$  NMR spectroscopy. This resulted in observation of enhanced free pyridine signals, in which the observed  $^1\text{H}$  NMR signals appeared in emission (in a downward direction). In this hyperpolarised NMR spectrum, emission peaks corresponding to the bound ligands of  $[\text{Ir}(\text{PCy}_3)(\text{substrate})_3(\text{H})_2]\text{BF}_4$  are also observed. This suggests that at low field, spontaneous polarisation transfer occurs from *parahydrogen* to the substrate via temporary association with the metal template. Polarisation transfer to  $^{13}\text{C}$ ,  $^{15}\text{N}$ ,  $^{19}\text{F}$  and  $^{31}\text{P}$  nuclei has also been reported.<sup>58</sup>

Polarisation transfer to pyridine through the SABRE technique using such phosphine catalysts has been extended further, reported in a paper published by Atkinson *et al.* (2009).<sup>61</sup> Here, a number of different phosphine catalysts were investigated. These complexes were prepared *in situ* by the addition of the appropriate phosphine to a solution of  $[\text{Ir}(\text{COD})(\text{py})_2]\text{BF}_4$ . This enabled a series of samples to be prepared, containing  $[\text{Ir}(\text{COD})(\text{py})_2]\text{BF}_4$ , 1 equivalent of the required phosphine ( $\text{PCy}_3$ ,  $\text{PPhCy}_2$ ,  $\text{PEt}_3$ ,  $\text{P}^i\text{Pr}_3$ ,  $\text{P}^n\text{Bu}_3$ ,  $\text{P}^t\text{Bu}_3$  and  $\text{P}(1\text{-naphthyl})_3$ ) and an excess of pyridine in  $\text{d}_4$ -methanol. These samples were investigated using states prepared in a magnetic field of  $0.5 \times 10^{-4}$  T, but interrogated at high field. The extent of polarisation transfer into pyridine (presented as an enhancement) they achieved when the states were prepared at  $0.5 \times 10^{-4}$  T is presented in Figure 2.1.

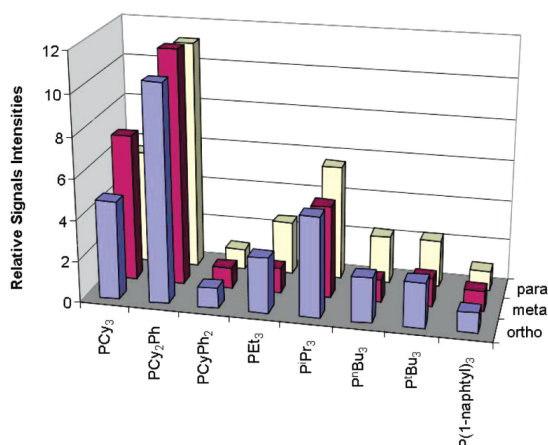


Figure 2.1 Plot of the relative absolute signal strengths for the three pyridine proton sites (relative to signals for free pyridine at equilibrium). Results represent the average of 5 measurements, each recorded immediately after shaking the NMR tube in a  $0.5 \times 10^{-4}$  T field. Taken from a publication by Atkinson *et al.* (2009).<sup>61</sup>

It can be deduced from Figure 2.1 that changing the phosphine has a great effect on the amount of polarisation transferred to the pyridine via the metal template. The most significant polarisation transfer is observed when the strong electron donor and most sterically demanding phosphine, PPhCy<sub>2</sub> is used, with a maximum observed <sup>1</sup>H NMR signal enhancement of around 11 fold was found.

### 2.1.3 Progression from phosphine-based SABRE catalysts to carbene-based SABRE catalysts

As described in section 2.1.2, pg 102, phosphine-based iridium catalysts can be effective polarisation transfer catalysts for the SABRE technique. Carbenes show similar binding motifs to phosphines but are stronger electron donors<sup>94</sup> (Chapter 1). The carbene analogues were therefore investigated for the ability to transfer polarisation through SABRE.

Phosphines and carbenes are neutral species which both contain a lone pair of electrons. This lone pair is able to bind to a metal centre to create a metal-ligand bond. The properties of phosphines and carbenes are determined by the electron donating properties and steric bulk. The most common scale used to consider the electron donating properties of such ligands (L) is the Tolman's Electronic Parameter (TEP).<sup>97</sup> This method detects the  $\nu_{\text{CO}}$  by infra-red spectroscopy of the [Ni(CO)<sub>3</sub>(L)] complex, chosen because it is easily formed by a simple reaction and the carbonyl stretching frequency is resolved and sharp.<sup>97</sup> It also allows a measure of electronic donation which is unaffected by the size of the ligand. Interpretation of the TEP works on the principle that as the electron donation experienced by the metal increases, the more back bonding is experienced by the carbonyl ligands, in turn creating a longer CO bond length. This change is detected by infra-red spectroscopy as a change in frequency and as such, the lower the observed  $\nu_{\text{CO}}$ , the greater the electron donation that is experienced by the metal from the ligand. Considering the TEP of many different phosphines and carbenes, it is possible to observe that in general carbenes show stronger electron donation properties than the phosphines<sup>94</sup> (see Table 2.1).

Ligand (L)	solvent	TEP (cm <sup>-1</sup> )
PPh <sub>3</sub>	CHCl <sub>3</sub>	2068.9
PEt <sub>3</sub>	CHCl <sub>3</sub>	2061.7
P( <i>p</i> -MeC <sub>6</sub> H <sub>4</sub> ) <sub>3</sub>	CHCl <sub>3</sub>	2066.7
P( <i>i</i> Pr) <sub>3</sub>	CH <sub>2</sub> Cl <sub>2</sub>	2059.2
PCy <sub>3</sub>	CH <sub>2</sub> Cl <sub>2</sub>	2056.4
SIPr	CH <sub>2</sub> Cl <sub>2</sub>	2052.2
SIMes	CH <sub>2</sub> Cl <sub>2</sub>	2051.5
IPr	CH <sub>2</sub> Cl <sub>2</sub>	2051.5
IMes	CH <sub>2</sub> Cl <sub>2</sub>	2050.7
ICy	CH <sub>2</sub> Cl <sub>2</sub>	2049.6

Table 2.1 Carbonyl stretching frequencies for compounds [(L)Ni(CO)<sub>3</sub>] (TEP, cm<sup>-1</sup>). Copied from a publication by Kelly III *et al.* (2008).<sup>94</sup>

Before stable carbenes were discovered, the most common method to compare the steric bulk of a phosphine ligand was to use the cone angle.<sup>98</sup>

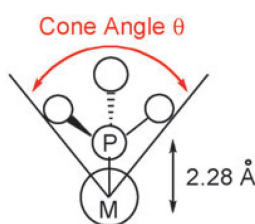


Figure 2.2 Definition of the cone angle for phosphines, taken from a publication by Clavier and Nolan (2010).<sup>98</sup>

This was defined for a metal to phosphine bond length of 2.28 Å, with the outermost atoms of the phosphine substituents acting as the perimeter of the cone. While this system proved very effective for simple phosphines, as science progressed to more complicated ligands such as biarylphosphines, bidentate ligands and N-heterocyclic carbenes, this steric parameter has proven difficult to interpret and sometimes meaningless.<sup>98</sup> In the phosphine ligand, the phosphorus atom is the central component to which the substituents are bound, resulting in the expected cone shape however this is not the case for the carbene ligand. Here, two cone angles could be considered as a result of the planar imidazolium (or 4,5-dihydroimidazolium) centre forcing the substituents to be in a certain orientation in reference to the metal.

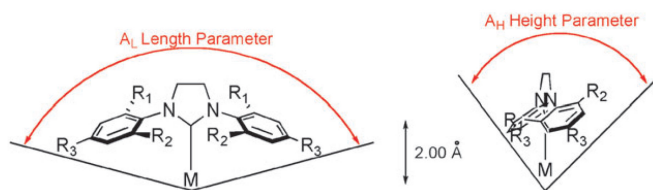


Figure 2.3 Definition of the cone angle for carbenes, taken from a publication by Clavier and Nolan (2010).<sup>98</sup>

Therefore a new method to define the steric bulk of N-heterocyclic carbenes was proposed by Huang *et al* (1999)<sup>99</sup> based on crystallographic data. These are defined with a metal to carbene length of 2 Å, considered to be the average metal-carbene bond length. This again proved to be too simple a model and so a new steric parameter, the per cent buried volume ( $\%V_{\text{bur}}$ ), was proposed by Hillier *et al.*<sup>100</sup> in 2003.

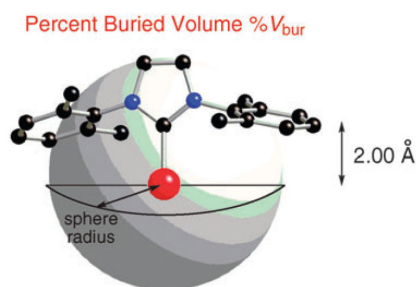


Figure 2.4 Definition of per cent buried volume, taken from a publication by Clavier and Nolan (2010).<sup>98</sup>

Their proposal defined the per cent of buried volume ( $\%V_{\text{bur}}$ ) as the per cent of the total volume of a sphere occupied by a ligand, giving an idea of the size of the ligand in reference to the co-ordination sphere. The sphere has a defined radius and has the metal centre at the core and is calculated using crystallographic data. This also allows for the comparison of the steric bulk of carbenes to that of phosphines.

Data collected from Cavallo *et al.* (2005)<sup>101</sup> and Diez-Gonzalez and Nolan (2007)<sup>102</sup> suggests that there is no significant difference in  $\%V_{\text{bur}}$  between phosphines and carbenes. Using a radius of 3 Å and metal to ligand length of 2 Å, the  $\%V_{\text{bur}}$  of carbenes varies from 23 % for ICy/ITol to 37 % for IAd/I<sup>t</sup>Bu, where for phosphines, it varies from 22 % for PMe<sub>3</sub> to 48 % for PMes<sub>3</sub>.<sup>98</sup> Thus, the change from phosphine to carbene could significantly increase the electronic donation experienced by the metal centre, however changes in the steric bulk can still be controlled by the other substituents used

on the ligands. This has been discussed in relation to the carbenes I have experimentally explored in section 2.3.2.1, pg 124.

#### 2.1.4 Literature-based SABRE results in which carbene-based catalysts are used

Within the literature, work has also been published on the extension of SABRE catalysts including a carbene analogue of the initially used phosphine catalysts. To date, the only carbene containing SABRE catalyst to be published is **IMes(a)**, which utilised the IMes (1,3-bis(2,4,6-trimethylphenyl)imidazol-2-ylidene) ligand. **IMes(a)** has been reported in two communications, the first by Cowley *et al.* (2011)<sup>66</sup> to polarise pyridine and the second by Lloyd *et al.* (2012)<sup>67</sup> to polarise quinoline.

The 2011 paper by Cowley *et al.*<sup>66</sup> reported polarisation transfer to pyridine (0.062 mmol in 0.6 ml methanol) using **IMes(a)** (5 mol %) shaken at Earth's magnetic field at 298 K, where the system exhibited an enhancement of 266 fold enhancement for the *ortho* position of pyridine. This is a significant improvement compared to the PCy<sub>3</sub> analogue published in Atkinson *et al.* (2009)<sup>61</sup>, where an average enhancement of 5 fold was observed under the same conditions. This implies the increase in electronic donation has affected the exchange rate constants observed in such a way that polarisation transfer to pyridine is increased.

## 2.2 Experimental considerations

Throughout this thesis, there are a number of experimental considerations which must be taken into account when discussing the research into SABRE. These are outlined below.

### 2.2.1 Terminology

#### 2.2.1.1 SABRE using an NMR tube – the shake method (method 1)

The shake method (method 1) utilises a 5 mm NMR tube fitted with a J Young valve (called a Young's Tap NMR tube from here on). The following details are standard and so, unless otherwise stated, are the conditions used for the shake method. The catalyst was dissolved in 0.6 ml of deuterated solvent, the substrate added and the sample degassed on a high vacuum line via three 'cool-pump-thaw' cycles. The standard

reagent concentration of catalyst and substrate (ratio of 1:20) was 5 mM catalyst and 100 mM substrate. In an NMR sample, this equates to 0.0031 mmol of catalyst and 0.062 mmol of substrate in 0.6 ml of deuterated solvent. To activate the catalyst for SABRE, the headspace of the Young's Tap NMR tube was charged with 3 bar hydrogen and shaken. The time of activation depends on the catalyst and substrate of interest. To interrogate the active sample using the SABRE technique, the headspace of the Young's Tap NMR tube was charged with 3 bar *parahydrogen* and shaken for 8 s at a field of 0.5 G. It was then introduced to the NMR magnet and interrogated by the desired NMR method. For a repeat experiment, the headspace was evacuated, and replaced with 3 bar of fresh *parahydrogen* to ensure each experiment begins with the same concentration of *parahydrogen*. After activation, these conditions result in a ratio of 1 to 8.5 catalyst to hydrogen (see Experimental). A  $^1\text{H}$  NMR spectrum was collected with a  $90^\circ$  pulse as standard.

### 2.2.1.2 SABRE using a flow probe – the flow method (method 2)

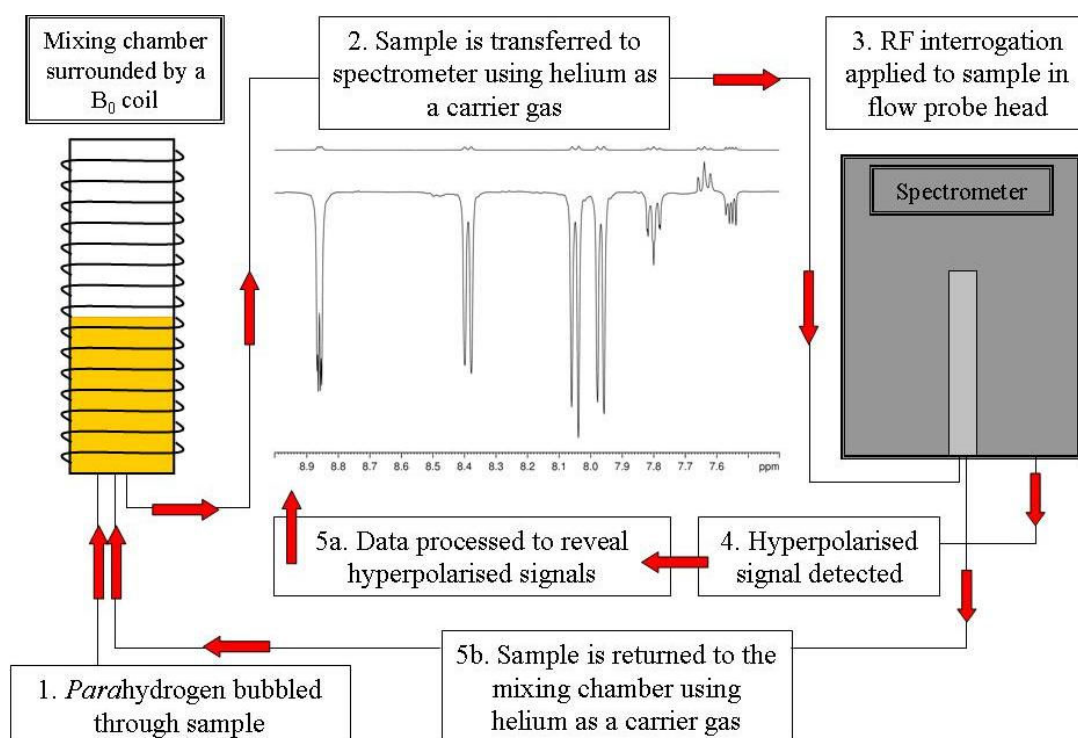


Figure 2.5 Schematic of the polarisor used in method 2. Adapted from a publication by Cowley *et al.* (2011).<sup>66</sup>

The flow method was developed to allow a solution containing the catalyst and substrate to be polarised using *parahydrogen* within a polarisation chamber outside the



main NMR magnet.<sup>66</sup> The following details for the preparation of samples to be studied in the automated polarisor (method 2) are standard and so, unless otherwise stated, are the conditions used for the method 2. The standard reagent concentrations of catalyst and substrate (ratio of 1:20) are 5 mM and 100 mM respectively. Samples for method 2 require 3 ml of deuterated solvent and therefore this equates to 0.0155 mmol of catalyst and 0.31 mmol of substrate. This sample was then injected into the mixing chamber of the polarisor. *Parahydrogen* was then introduced into this solution via six inlet tubes at a pressure of 3 bar for 6 s (unless otherwise stated). The resulting solution was then transferred into a Bruker Avance III series 400 MHz spectrometer that was equipped with a flow probe, where the flow cell volume was 200  $\mu$ l, by a flow of helium gas. Unless otherwise stated, a single scan of the nucleus of interest was then recorded. A  $^1\text{H}$  or  $^{13}\text{C}$  NMR spectrum was collected with a  $90^\circ$  pulse as standard. Once interrogated, the solution was returned to the mixing chamber after which the process can be repeated as required.

The polarisor has been developed during the progression of this thesis and consequently three systems have been utilised: the MKI, MKII and MKIII. I am very grateful to Bruker for allowing me to use the various polarisors, and allowing me to contribute data to help in their development.

The MKI polariser was the first polarisor to be used, in conjunction with a TXO flow probe. This system was automated to the extent that it can be controlled by the pulse sequence however sample loading and wash cycle are manually operated. The chamber was fixed to the legs of the spectrometer giving the option to move the chamber through the stray field of the main NMR magnet allowing limited control over the field experienced by the sample during the addition of *parahydrogen*. This is because the field is not consistent over the length of the mixing chamber, as it is controlled by the stray field.



Figure 2.6 Photo of MKI polarisor.

The MKII polarisor improved on the MKI as it contains a coil surrounding the mixing chamber such that a magnetic field can be generated in the  $z$  direction. This coil was designed to produce a static direct current field in the range of  $-150$  G to  $+150$  G, capable of increments of  $1$  G. This system is automated to the extent that it can be controlled by the pulse sequence however sample loading and wash cycles of the system are still manually operated.

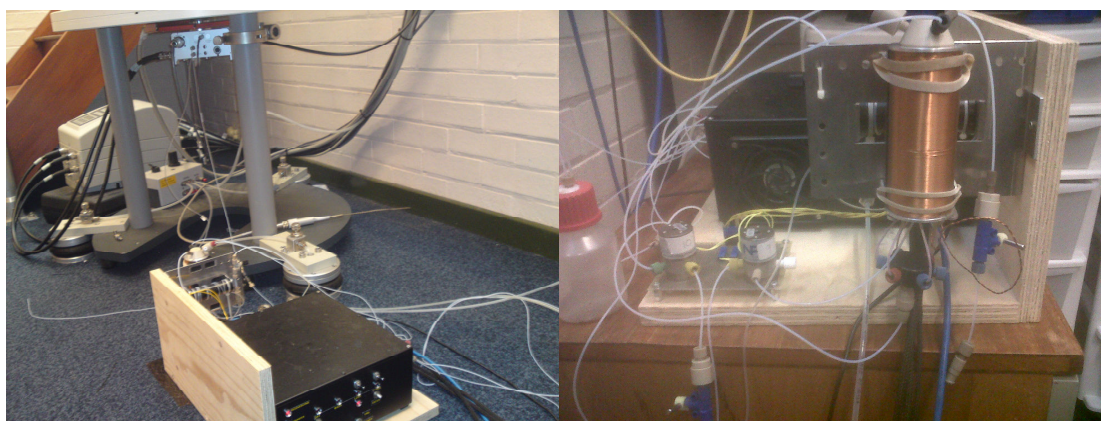


Figure 2.7 Photos of MKII polarisor.

The MKIII polarisor refines the MKII design further however, now a TXI flow probe was utilised. This also contains a coil around the polarisation chamber which is capable of producing a static direct current field in the range of  $-150$  G to  $+150$  G in the  $z$ -direction however it is capable of increments of  $0.01$  G. It also possesses different valves giving more control over pressures within the system and additional functionality such that it is fully integrated with TopSpin, the processing package used on Bruker spectrometers, allowing all commands to be completed through the TopSpin interface.

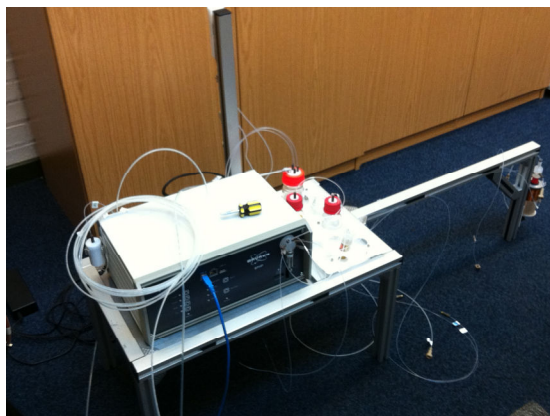


Figure 2.8 Photo of MKIII polarisor.

### 2.2.1.3 Comparison of method 1 to method 2

Table 2.2 outlines the advantages and disadvantages of both method 1 and method 2.

	Method 1 – Shake	Method 2 – Flow
Instrumentation	Young's TAP NMR tube	Mixing chamber and modified flow probe
Average consumables	2 mg catalyst + 7 mg substrate + 0.6 ml solvent	10 mg catalyst + 35 mg substrate + 3 ml solvent
Reproducibility	10 % error	5 % error
NMR methods	Single scan only (includes single scan 2D methods)	Can incorporate standard 2D methods and phase cycles
Field control	Crude (using stray field of spectrometer)	-150 - +150G increments of 1 (MKII) or 0.01 (MKIII)
Temperature control	Crude (water bath)	Not currently possible
Speed of repeat experiments	~ 3 min	~ 30 s

Table 2.2 Comparison of the two methods, method 1 and method 2, which can be used in the application of SABRE in NMR.

Each method holds its own advantages and disadvantages. Method 1 uses much less substrate and catalyst, and also allows a quick route to check the applicability of SABRE to a new substrate or catalyst (Chapter 6) and can be completed with a standard NMR probe. It is also possible to complete temperature studies with method 1 (Chapters 3 and 4), which is currently not possible with method 2 as it is not possible to gain temperature control with the polarisor. Method 1 does suffer from some drawbacks however. The regeneration period between each hyperpolarised experiment is relatively

long (~ 3 mins) and it is very difficult and time consuming to complete 1- or 2D spectra which require more than 1 transients.

Method 2 holds the major advantages that it is automated, can accurately control the field of polarisation (Chapter 3), and can be applied to methods which require more than one scan (phase cycles and 2D spectra, Chapter 5). Its main drawback, however, is that the samples require a 5x larger volume and therefore is comparatively expensive due to deuterated methanol consumption, and consumes catalyst much quicker.

Both method 1 and method 2 should be considered when interrogating a new substrate or catalyst as optimisation of polarisation transfer using temperature control can only be completed using method 1, but optimisation using polarisation transfer field (PTF) can only be completed using method 2.

#### 2.2.1.4 Considerations when discussing the effect of the magnetic field of polarisation

The standard unit of magnetic field is tesla (T) however throughout this thesis the unit of magnetic field used is gauss (G), where 1 T is equal to 10,000 G. This is because only low polarisation transfer fields are used in the range 0 G to 150 G. In tesla, this is equal to 0 T to 0.015 T.

Whenever a polarisation transfer field (PTF) is quoted, this refers to the magnetic field present during the addition of *parahydrogen* to the sample, the polarisation transfer step. In method 1, the field is applied during the time the sample is shaken in the presence of *parahydrogen*. This is typically completed at two fields, Earth's magnetic field (0.5 G) and a higher field measured to be around 65 G which is achieved by shaking in the stray field of the spectrometer. In reality, this means the higher field utilised in method 1 is highly variable as the shake process causes the sample to cross over a range of field values.

In method 2, the field is applied during the bubbling of *parahydrogen* through the solution. For the MK I polarisor, the field is again applied using the stray field of the magnet however, the chamber is now stationary so the magnetic field range experienced by the sample is much less than that of method 1. For the MK II and MK III polarisors, the magnetic field is induced by a current introduced to the coil surrounding the sample. The magnetic field experienced by the sample can therefore be controlled by the amount

of current in the coil; this corresponds to the value input by the user. The coil controls the field experienced in the vertical ( $z$ ) direction and has additional turnings at each end of the coil to ensure homogeneity over the length of the coil. As the chamber is not stored at 0 G, but as close to Earth's magnetic field as possible considering the required proximity to the spectrometer, the stated value is offset slightly. The chamber is used in the same position during all experiments and so this field offset is constant. The standard method employed to understand the effect of changing the field of polarisation is to take a sample of standard concentrations, and interrogate it starting at -150 G and increasing the field by 10 G until an experiment at +10 G has been completed, unless otherwise stated. The field dependence is not studied to +150 G to save time but a spectrum at +10 G is collected to prove it is the same as -10 G, and therefore the dependence is symmetrical around 0 G. For each field, six  $^1\text{H}$  NMR spectra are taken to ensure reproducibility.

#### 2.2.1.5 Effect of changing the sign of magnetic field of polarisation on resultant $^1\text{H}$ NMR spectra

Another important factor to consider is the effect of changing the sign of the magnetic field of polarisation. A series of experiments were completed using method 2 to understand the effect of moving through the zero point.

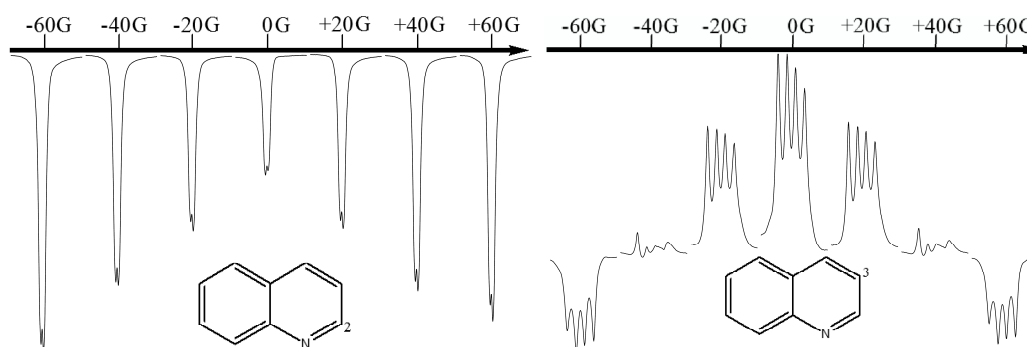


Figure 2.9 Observed  $^1\text{H}$  NMR signal of selected quinoline resonances, where quinoline is polarised with **IMes(c)**. This data is presented with the field of addition of *parahydrogen* taking place at -60 G to +60 G in increments of +20 G.

These data presented in Figure 2.9 imply the sign and magnitude of the resultant signal after polarisation by SABRE is dependent only upon the magnitude of the applied magnetic field, and not upon the sign of the applied magnetic field. The symmetry of

the spectra allow us to infer that the stated zero is quite close to true zero because if its offset was significant, the difference between -20 G and +20 G would be noticeable.

#### 2.2.1.6 Calculation of enhancements

There are a number of ways in which the extent of polarisation has been calculated. The most simple of these is to compare signal to noise ratios, most common in the case where a thermal spectrum cannot be collected such as for low intensity nuclei like  $^{13}\text{C}$  or  $^{15}\text{N}$ . A second method is to consider a direct signal enhancement. This is achieved by comparing the integral of a signal corresponding to thermal distribution and the signal corresponding to the hyperpolarised distribution. This is the method used throughout this thesis. For calculation of the  $^1\text{H}$  NMR signal enhancement, the following equation was used (Equation 2.1).

$$E = \frac{S_{pol}}{S_{unpol}}$$

Equation 2.1 Equation used to calculate the  $^1\text{H}$  NMR signal enhancement.

Equation 2.1 is true where:  $E$  = enhancement,  $S_{pol}$  = integral of the area under the signal of polarised sample and  $S_{unpol}$  = integral of the area under the signal of unpolarised (thermally polarised reference) sample.

Owing to the nature of *parahydrogen* derived hyperpolarisation, a sample interrogated by NMR in the presence of *parahydrogen* may result in both enhanced adsorption signals and enhanced emission signals (see Chapter 1). Consequently, the integral for an enhanced emission peak is negative. This sign has been carried through in the equation to the resulting calculated enhancement. This means that where a negative enhancement is quoted, the peak was in emission.

The level of hyperpolarisation can also be considered through quoting the percentage of nuclei that have been observed. On a superficial level, this is equal to the observed signal enhancement (calculated as in Equation 2.1) multiplied by the thermal polarisation which is based on the Boltzmann distribution and the magnetic field strength of the spectrometer. The thermal polarisation in a 400 MHz spectrometer (9.4 T) is equal to 0.003 %. It is much easier to appreciate the effects of SABRE through

comparison of signal enhancement as the numbers are more accessible and therefore this is the method used throughout this thesis.

### 2.2.1.7 Catalyst forms

Throughout this thesis, a number of different catalyst precursor systems have been utilised to form the active species  $[\text{Ir}(\text{carbene})(\text{H})_2(\text{sub})_3]^+$ . This has been necessary for certain substrates which are not able to form the salt of the catalyst prior to activation by hydrogenation (Chapter 4). The precursor systems have been labelled as **Carbene(a)**, **Carbene(b)** and **Carbene(c)**, shown in Figure 2.10. In general, **Carbene(a)** implies the catalyst was used directly with no further modifications. **Carbene(b)** implies the catalyst was used as its  $\text{PF}_6$  salt. **Carbene(c)** implies the catalyst was used with the addition of a stoichiometric amount of acetonitrile to promote activation.

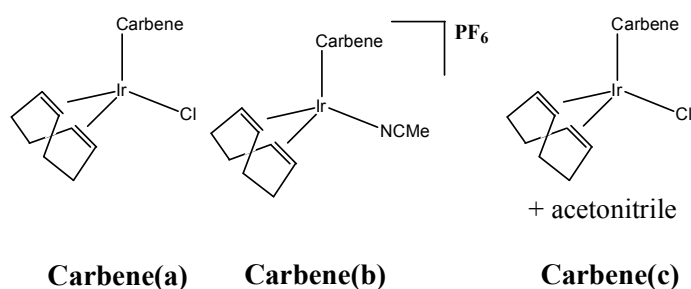


Figure 2.10 Structures of the generic catalyst precursor systems used throughout this thesis namely **Carbene(a)**, **Carbene(b)** and **Carbene(c)**.

Upon addition of hydrogen and substrate (usually a nitrogen heterocycle in a 20 fold excess), these systems form the active catalysts shown in Figure 2.11. In the case of **Carbene(b)** and **Carbene(c)**, it is both the substrate of interest and acetonitrile which can bind to receive polarisation through SABRE.

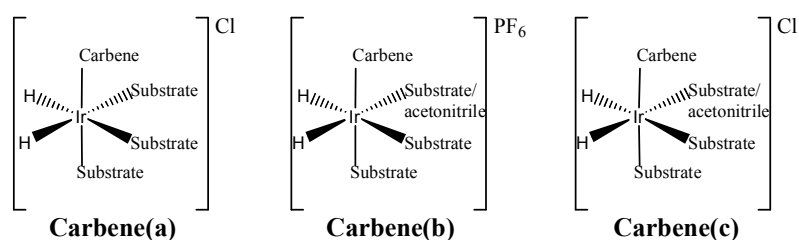


Figure 2.11 Structures of each catalyst in its active form after the addition of hydrogen and substrate in a 20 fold excess.

These catalytic systems were used in conjunction with the carbenes outlined in Figure 2.12. IMes (1,3-bis(2,4,6-trimethylphenyl)imidazol-2-ylidene) was the first carbene investigated by the group, and investigations into this carbene began before the research into this thesis. As a part of this research project, investigations with the IMes based catalyst, and new catalysts based on SIMes (1,3-bis(2,4,6-trimethylphenyl)-4,5-dihydroimidazol-2-ylidene) and ICy (1,3-bis(cyclohexyl)imidazol-2-ylidene), were performed. These are discussed further in Chapter 2.2.5 (pg 122).

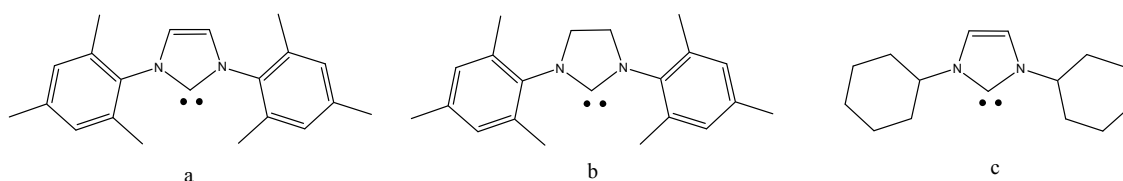


Figure 2.12 Structures of carbenes used within this thesis, namely a) IMes, b) SIMes and c) ICy.

The structures in Figure 2.10 and Figure 2.12 are combined to describe the catalytic precursor system used in each experiment. For instance, if an experiment was completed using an NMR tube with  $[\text{Ir}(\text{SIMes})(\text{COD})(\text{NCMe})]\text{PF}_6$  it would be stated as ‘completed using method 1 with **SIMes(b)**’. If an experiment was completed using the flow system with  $[\text{Ir}(\text{ICy})(\text{COD})\text{Cl}]$  in the presence of a stoichiometric volume of acetonitrile, it would be stated as ‘completed using method 2 with **ICy(c)**’. Each catalyst in the precursor and active forms are characterised in (see Experimental) and **IMes(a)**, **SIMes(a)** and **ICy(a)** are discussed further in Section 2.2.5, pg 122.

## 2.2.2 Effect of method 1 on the resultant $^1\text{H}$ NMR spectra obtained without incorporation of enriched *parahydrogen*

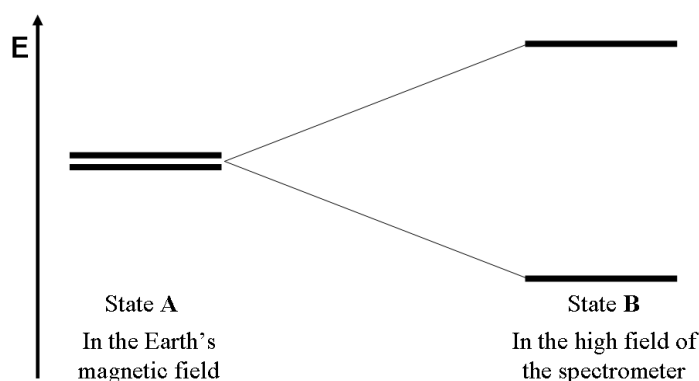


Figure 2.13 Relative energy difference of magnetic states in an NMR sample at Earth's magnetic field and the high field of an NMR spectrometer.



Normally, it takes five times the  $T_1$  of the nuclei involved for equilibration of the magnetic states to be achieved after a large change in magnetic field, such as that observed during a shake experiment in method 1. Considering Figure 2.13, the sample is shaken at State A, then rapidly transported to State B and interrogated immediately. The sample is often interrogated quicker than the time required for equilibration of the magnetic states so as to observe maximum polarisation possible before the polarised magnetic states relax to thermally polarised levels, resulting in potentially less intense signals. To add to this complication, during method 1, the sample is also shaken for 8 s prior to being transferred into the spectrometer and therefore sample turbulence may also be present during interrogation, potentially affecting the quality of the resultant spectra. It is therefore important to understand the effect of the process of method 1 on a standard thermal sample on  $^1\text{H}$  NMR spectra before interpreting results derived from *parahydrogen* experiments. Four samples of **IMes(a)** with pyridine were investigated using method 1, where *parahydrogen* was replaced with normal hydrogen. As normal hydrogen is composed of 25 % *parahydrogen* (Chapter 1), two additional samples were also interrogated using method 1 where the headspace was filled with air.<sup>103</sup>

	Gas in headspace of the NMR tube	Observed $^1\text{H}$ NMR signal reduction		
		<i>Ortho</i>	<i>Meta</i>	<i>Para</i>
Sample 1	Normal $\text{H}_2$	0.14	0.25	0.08
Sample 2		0.23	0.31	0.19
Sample 3		0.18	0.22	0.14
Sample 4		0.22	0.22	0.16
Sample 5	Air	0.38	0.37	0.35
Sample 6		0.33	0.32	0.31

Table 2.3 Effect of method 1 on a sample shaken with normal hydrogen or air.

The values in Table 2.3 are calculated in the same way as the enhancements where the integral of the signal from the spectrum collected after method 1 is divided by the same signal in the thermally polarised spectrum. Each sample was investigated with *parahydrogen* after these experiments were completed to ensure the catalyst was active. This ensures that these control samples are as close as possible to those investigated during polarisation experiments. The resultant signals from this experiment were calculated to be an average of 20 % that of the normal thermal trace (ranging from 0.08 to 0.31). This suggests that any experimentally observed enhancement values of

between 0 and +1 cannot confirm or disprove polarisation transfer, as the value could result from the interrogation taking place before the 5 times  $T_1$  wait for equilibrium in the higher field to be reached. Throughout these experiments, no emission peaks were observed, suggesting any negative enhancement value must be derived from transfer from *parahydrogen*.

### 2.2.3 Reproducibility of NMR spectra when SABRE is implemented

#### 2.2.3.1 Reproducibility of method 1

Three samples were prepared from a stock solution of **IMes(a)** and pyridine in methanol to produce samples with exactly the same concentration, across the three NMR tubes. Each sample was interrogated after an 8 s shake at 2 G under an atmosphere of 3 bar *parahydrogen*, and the experiment repeated 3 times.

	<i>Ortho</i>	<i>Meta</i>	<i>Para</i>
Sample 1	14.58	179.85	197.13
	10.15	169.33	189.19
	10.10	154.62	203.53
Sample 2	11.88	183.87	225.31
	2.49	172.95	230.02
	19.27	185.18	219.86
Sample 3	1.40	160.76	201.19
	8.90	176.06	219.22
	16.90	162.07	194.79

Table 2.4 Results from reproducibility experiment for method 1 with **IMes(a)** and pyridine, presented as absolute values.

The *ortho* signal in all three samples showed antiphase character and consequently, a significantly lower enhancement than expected, and varying results. The results based on enhancement in the *ortho* signal have therefore not been included in the calculation of errors. The errors quoted here have been calculated in reference to the average of the values in question. The results within sample 1 are reproducible to  $\pm 8\%$  for the *meta* position and  $\pm 5\%$  for the *para* position, within sample 2 to  $\pm 5\%$  for both *meta* and *para* positions, and within sample 3 to  $\pm 6\%$  for the *meta* position and  $\pm 7\%$  for the *para* position.

There are two potential reasons for the variance of enhancement values observed within a single sample. The first is that the sample is shaken by hand and therefore the shake time cannot be precisely 8 s for every experiment. The second reason is the sample is shaken close to the spectrometer so it can be interrogated as quickly as possible, however this could result in unwanted variations field.

Across the three samples, enhancement to the *meta* and *para* positions is reproducible to  $\pm 10\%$ . The variation across the three samples is potentially due to slightly different Young's Tap NMR tube volumes, and therefore different *parahydrogen* excesses. The idea of hydrogen excess in the sample is discussed further in the Experimental.

### 2.2.3.2 Reproducibility of method 2

A series of thirty  $^1\text{H}$  NMR spectra were collected of quinoline hyperpolarised with **IMes(c)** using method 2 at a PTF of -50 G, the results of which are shown in Figure 2.14.

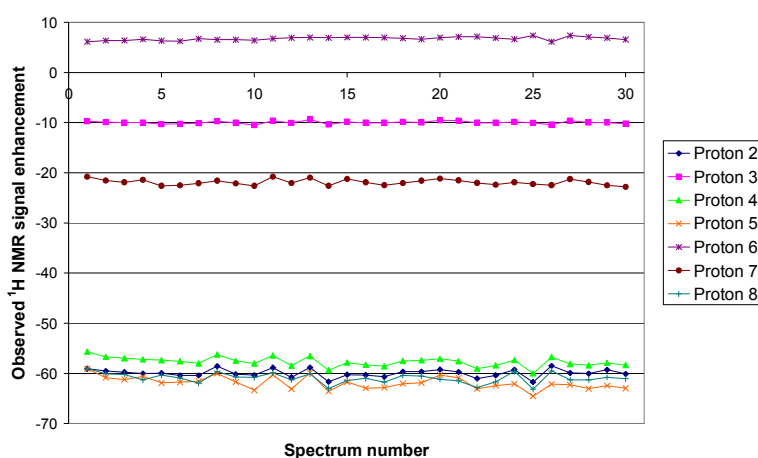


Figure 2.14 Graphical representation of the observed  $^1\text{H}$  signal enhancement in thirty NMR spectra of quinoline hyperpolarised with **IMes(c)** using method 2.

The spectra were found to be reproducible to within 5 % based on the observed signal enhancements for all positions but position 6 which was found to be reproducible to within 10 %. This large variation is due to the phase of the signal corresponding to the 6 position present at the PTF used for this experiment (see Chapters 1 and 4).

### 2.2.4 Mechanism of activation of SABRE catalysts

Over the course of the research, it was noticed that not all catalytic systems activate in the same way. For instance, quinoline does not exhibit polarisation transfer with **IMes(a)**, but the addition of acetonitrile to the solution (to produce **IMes(c)**) or a change of catalyst to **IMes(b)** allows significant polarisation transfer to quinoline. In a paper published by Cowley *et al.*,<sup>66</sup> initial studies into the mechanism of activation were described. NMR and mass spectroscopy were utilised to find an intermediate in the mechanism of activation.

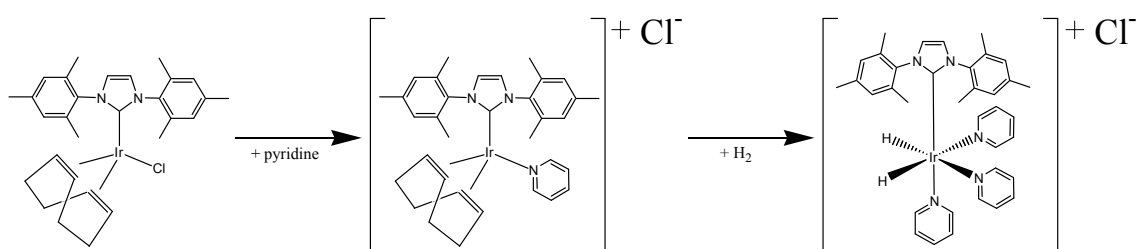


Figure 2.15 Mechanism of the activation of  $[\text{Ir}(\text{IMes})(\text{COD})\text{Cl}]$  proposed by Cowley *et al.*<sup>66</sup>

It was decided to test if the same intermediate was observed for  $[\text{Ir}(\text{SIMes})(\text{COD})\text{Cl}]$ .  $[\text{Ir}(\text{SIMes})(\text{COD})\text{Cl}]$  was dissolved in methanol with a 2 fold excess of pyridine, and a yellow solid was isolated from the solution through evaporation of methanol. This was redissolved in chloroform for interrogation by NMR spectroscopy.

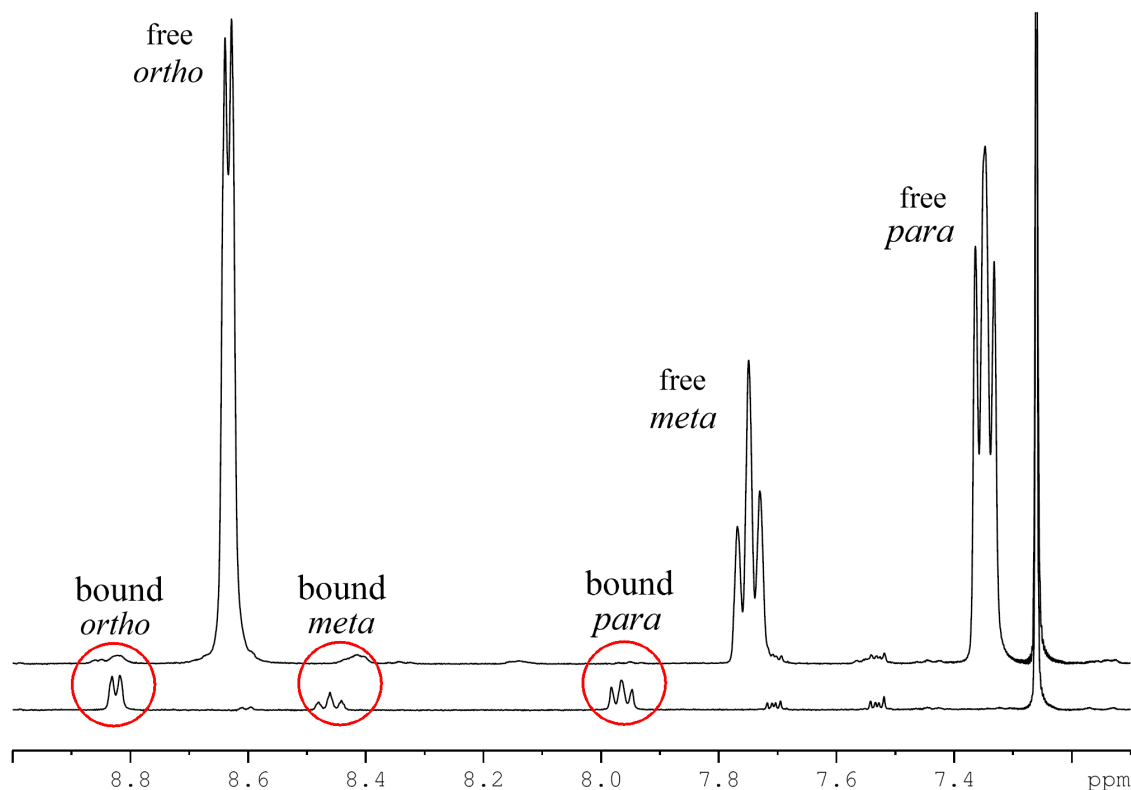


Figure 2.16 Bottom:  $^1\text{H}$  NMR spectrum of  $[\text{Ir}(\text{SIMes})(\text{COD})(\text{py})]\text{Cl}$  in  $\text{CDCl}_3$  and top: the same sample with added pyridine.

Figure 2.16 shows that when the product isolated from the reaction of  $[\text{Ir}(\text{SIMes})(\text{COD})\text{Cl}]$  with pyridine is interrogated by  $^1\text{H}$  NMR, there are clear signals due to the bound pyridine. To prove these are not due to residual pyridine, an excess of pyridine was added which revealed the free pyridine signals. The signals for free and bound pyridine are in distinctly different positions supporting the idea that  $[\text{Ir}(\text{SIMes})(\text{COD})(\text{py})]\text{Cl}$  has been formed. This is further supported by a crystal structure of  $[\text{Ir}(\text{SIMes})(\text{COD})(2\text{-methylpyridine})]\text{PF}_6$ , discussed in section 2.3.2.2, pg 126. It can also be observed that after the addition of excess pyridine to the solution, the signals corresponding to bound pyridine become broader, suggesting that they are exchanging with the excess free pyridine in solution.

These experiments may go some way to help explain why some substrates do not polarise with the **IMes(a)** but do with **IMes(b)**. If the substrate is either not basic enough to displace the chloride ion, or it's too bulky to form a  $[\text{Ir}(\text{IMes})(\text{COD})(\text{sub})]\text{Cl}$  complex, activation of the catalyst might not occur. An example of this is in Chapter 4.

### 2.2.5 Mechanism of reversible exchange of active species

The mechanisms of pyridine and hydride ligand loss from **IMes(a)** were discussed in a paper by Cowley *et al.*<sup>66</sup> through investigations using density functional theory (DFT). Initial investigations were completed by measuring the thermodynamic data corresponding to the loss of both ligands, with results presented in Table 2.5.

	Loss of hydride ligands	Loss of pyridine ligands
Rate constant / s <sup>-1</sup> (300 K)	9	11.7 (per mol py)
$\Delta H^\ddagger$ / kJ mol <sup>-1</sup>	79 ± 1	93 ± 3
$\Delta S^\ddagger$ / J K <sup>-1</sup> mol <sup>-1</sup>	41 ± 3	97 ± 9
$\Delta G_{300}^\ddagger$ / kJ mol <sup>-1</sup>	66 ± 0.3	64 ± 2

Table 2.5 Thermodynamic data collected and published by Cowley *et al.*<sup>66</sup> for the loss of pyridine and hydride ligands from **IMes(a)**.

A density functional theory (DFT) study of the process predicted that the loss of pyridine occurs through a dissociative mechanism. The theory was corroborated experimentally with the knowledge that the measured  $\Delta S^\ddagger$  value was positive for the process, and increasing the concentration of pyridine had little effect on the measured rate constant for the loss of pyridine.

The mechanism was found to be much less simple for hydride ligand loss. Experimentally, it was observed that the rate constant of hydride ligand loss decreased upon increasing pyridine concentration, implying the rate determining step for the process occurs after pyridine dissociation. The rate constant also increased with increasing hydrogen pressure and therefore addition of H<sub>2</sub> to the complex must also be involved in the mechanism of hydride ligand loss. These data confirm however that the mechanism cannot be dissociative like that observed for pyridine loss. Three potential mechanisms of hydride loss were therefore considered by DFT, as outlined in Figure 2.17.

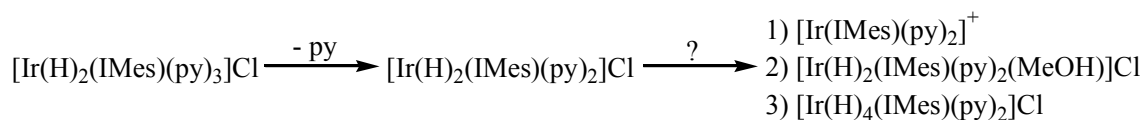


Figure 2.17 Potential intermediates in the route of hydride ligand loss from **IMes(a)** investigated by DFT published in a paper published by Cowley *et al.*<sup>66</sup>

DFT predicted that the formation of intermediate 1 in Figure 2.17 would be stable however its formation would be thermodynamically unfavourable requiring  $117 \text{ kJ mol}^{-1}$  of free energy, and is inconsistent with the experimentally measured kinetic data. DFT also predicted that the binding of methanol, such as for intermediate 2 in Figure 2.17, would be easy requiring  $13 \text{ kJ mol}^{-1}$  of free energy however the subsequent elimination of hydrogen would require a further  $83 \text{ kJ mol}^{-1}$  of free energy. This makes the formation of intermediates 1 and 2 unlikely routes for the loss of hydride ligands.

This leaves the possibility of intermediate 3 as the viable route for hydrogen elimination. According to DFT calculations, the formation of this intermediate is favourable, liberating  $11 \text{ kJ mol}^{-1}$  of free energy via a barrier of  $27 \text{ kJ mol}^{-1}$ . It also predicted however that the complex solely takes the form  $[\text{Ir}(\text{H})_2(\eta^2\text{-H}_2)(\text{IMes})(\text{py})_2]^+$ . In this complex, the second hydrogen molecule is bound as dihydrogen which relaxes much faster than the hydride ligands, and requires a total of  $44 \text{ kJ mol}^{-1}$  free energy to form from  $[\text{Ir}(\text{H})_2(\text{IMes})(\text{py})_3]\text{Cl}$ . If this is the route to hydrogen elimination, intermediate 3 must be short lived so as to avoid the conversion of *parahydrogen* to *orthohydrogen*.

### 2.3 Effect of changing the carbene ligand on polarisation transfer efficiency

The first carbene-based SABRE catalyst the group prepared was **IMes(a)** and this was shown to be much more effective than the previously tested phosphine catalysts.<sup>61,66</sup> It was therefore decided to investigate if the catalyst could be further optimised by modification of this carbene. In changing the carbene, it is possible to change the flexibility, electronic properties and steric properties of the carbene and therefore, the resultant catalyst.

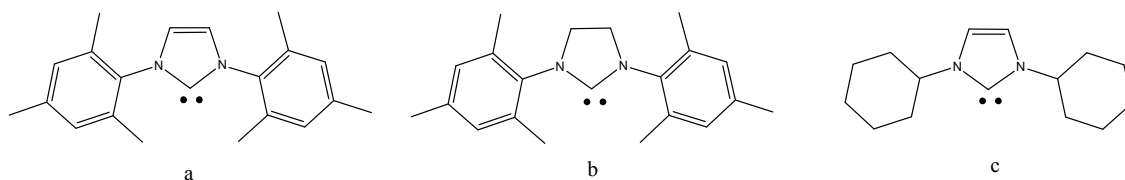


Figure 2.18 Structures of carbene ligands used within this thesis, namely a) IMes, b) SIMes and c) ICy

**IMes(a)** is prepared using the carbene, IMes (1,3-bis(2,4,6-trimethylphenyl)imidazol-2-ylidene, Figure 2.18a), and so a natural progression from this is to look at SIMes (1,3-bis(2,4,6-trimethylphenyl)-4,5-dihydroimidazol-2-ylidene, Figure 2.18b). The R groups

on the imidazolium centre have remained as mesitylene groups, however the imidazolium centre itself is now saturated across the double bond. SIMes is found to exhibit a very similar electron donating ability (TEP of SIMes =  $2051.5 \text{ cm}^{-1}$ )<sup>94</sup> to IMes (TEP =  $2050.7 \text{ cm}^{-1}$ )<sup>94</sup> however the slightly longer single bond in the imidazolium centre of SIMes introduces a little more flexibility and consequently, slightly different steric properties. A further carbene, ICy (1,3-bis(cyclohexyl)imidazol-2-ylidene, Figure 2.18) was also investigated. In this case, the R groups bound to the two nitrogens of the imidazolium centre are cyclohexyl groups.

### 2.3.1 Synthesis

All three catalyst precursors, **IMes(a)**, **SIMes(a)** and **ICy(a)**, were prepared by the same method. The hydrochloride salt of each carbene was deprotonated with potassium *tert*-butoxide and reacted with  $[\text{Ir}(\text{COD})\text{Cl}]_2$  in THF. This synthesis is based on similar results published by S. Wolf *et. al.*<sup>104</sup> After purification by silica gel column chromatography with an eluent of 19:1 DCM : acetone, a crystalline yellow solid was isolated, corresponding to  $[\text{Ir}(\text{carbene})(\text{COD})\text{Cl}]$ . Further details are given in the Experimental.

### 2.3.2 Comparison of structural properties

A comparison of the structural properties of the carbenes (and of those within the catalyst precursors and active forms) will allow an understanding of how changing certain properties of the carbenes may improve polarisation transfer for certain substrates.

#### 2.3.2.1 Comparison of TEP, cone angle and buried volume of $\text{PCy}_3$ , IMes, SIMes and ICy

In this section, the electronic and steric properties of the carbenes used in this thesis (IMes, SIMes and ICy) have been compared to each other and to  $\text{PCy}_3$ , the most commonly used phosphine in SABRE to date.<sup>58,61</sup> A number of methods can be used to investigate the structural properties of phosphines and carbenes. These include the TEP, the  $\nu_{\text{co}}$  for iridium, the percent of buried volume ( $\%V_{\text{bur}}$ ), and repulsiveness, as described in section 2.1.3, pg 104.



All the complexes used in this thesis have an iridium centre, not nickel, and therefore a similar parameter for iridium complexes is also considered. The values used in Table 2.6 are the  $\nu_{\text{Co(Ir)}}^{\text{av}}$  ( $\text{cm}^{-1}$ ) for the Ir analogue  $[(\text{NHC})\text{Ir}(\text{CO})_2\text{Cl}]$ ,<sup>94</sup> corresponding to the average of the two CO stretches observed when  $[(\text{NHC})\text{Ir}(\text{CO})_2\text{Cl}]$  is interrogated using infra-red spectroscopy.

The percent of buried volume ( $\%V_{\text{bur}}$ ) values presented in Table 2.6 are from Clavier and Nolan<sup>98</sup> where it is based on  $[(\text{NHC})\text{IrCl}(\text{COD})]$  with a sphere radius of 3.5 Å and M to ligand bond length of 2 Å.

In a paper published by D. G. Gusev (2009),<sup>105</sup> a descriptor correlating to the ease of loss of a CO ligand from a  $\text{Ni}(\text{CO})_3(\text{NHC})$ -type complex is introduced. This is termed the ‘repulsiveness’ parameter,  $\mathbf{r}$  and is calculated from the  $\Delta\text{H}$  and TEP for any carbene. The higher  $\mathbf{r}$  is, the more ‘repulsive’ that carbene is. The parameter  $\mathbf{r}$  is therefore a measure of direct repulsive interactions between the carbene and carbonyl ligands of  $[\text{Ni}(\text{CO})_3(\text{NHC})]$ .

Ligand	TEP ( $\text{cm}^{-1}$ ) <sup>94,105</sup>	$\nu_{\text{Co(Ir)}}^{\text{av}}$ ( $\text{cm}^{-1}$ ) <sup>94</sup>	$\%V_{\text{bur}}$ <sup>98</sup>	$\mathbf{r}$ <sup>105</sup>
PCy <sub>3</sub>	2056.4	2028	37.1	
IMes	2050.7	2023.1	33.0	1.5
SIMes	2051.5	2024.6	34.5	1.9
ICy	2049.6	2023.0	27.3	1.6

Table 2.6 Comparison of the structural properties of the carbene ligands investigated in this thesis, IMes, SIMes and ICy. Values for PCy<sub>3</sub> have also been included.

Considering the TEP values, the strongest electron donor is ICy, followed by IMes, followed by SIMes which is the weakest carbene electron donor. The TEP range of the three carbenes however is quite small, with the difference between the strongest and weakest donors being 1.9  $\text{cm}^{-1}$ . Although the absolute differences between the TEP values of the three investigated carbenes is small, the group of carbenes are clearly higher than the most commonly used phosphines (see Table 2.1), with the strongest phosphine in the table, PCy<sub>3</sub>, exhibiting a TEP value of 2056.4  $\text{cm}^{-1}$ .<sup>94</sup> The difference between the TEPs for the PCy<sub>3</sub> ligand and least electron donating carbene, the SIMes ligand, is 4.9  $\text{cm}^{-1}$ , 2.5 times larger than the range of the carbenes. This trend is continued when looking at the  $\nu_{\text{Co}}$  values for the iridium complex  $[(\text{NHC})\text{IrCl}(\text{COD})]$ , where the strongest donor is ICy and weakest is SIMes. Again, a small range is

observed ( $1.6 \text{ cm}^{-1}$ ), which is just under half the range observed within the carbenes ( $3.4 \text{ cm}^{-1}$ ).

A slightly different trend is observed when considering the repulsiveness factor, described by Gusev (2009).<sup>105</sup> IMes is the least repulsive, followed by ICy, then SIMes which is the most repulsive of the three carbenes. This means SIMes loses CO most easily from the  $[\text{Ni}(\text{CO})_3(\text{L})]$  complex when compared to ICy and IMes.

Analysis of the buried volume shows SIMes is the most sterically hindering carbene, followed by IMes then ICy as the smallest carbene. As a comparator, the  $\%V_{\text{bur}}$  of the phosphine ( $\text{PCy}_3$ ) used in Adams *et al.* (2009)<sup>58</sup> and Atkinson *et al.* (2009)<sup>61</sup> is 37.1% when calculated with a M-P length of  $2 \text{ \AA}$ , the standard metal to carbene length used for the other ligands considered.<sup>98</sup> This reduces to 31.8 % when calculated with a M-P length of  $2.8 \text{ \AA}$ , the standard metal to phosphine length.<sup>98</sup> This implies the investigated carbenes have less steric bulk than the most commonly used phosphine in SABRE, but also that the carbenes are more electron rich.

### 2.3.2.2 Comparison of **IMes(a)**, **SIMes(a)** and **ICy(a)**

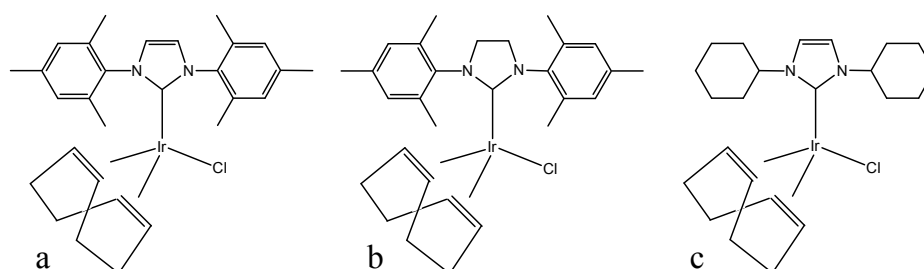


Figure 2.19 Structures of a) **IMes(a)**, b) **SIMes(a)** and c) **ICy(a)**.

The active species of SABRE catalysts cannot be isolated and therefore the properties of the isolatable precursor systems are considered first. The structures of **IMes(a)**, **SIMes(a)** and **ICy(a)** shown in Figure 2.19, are most easily considered when looking at the X-ray crystal structures. A crystal of **SIMes(a)** was grown for X-ray diffraction analysis. The structure of this complex has been reported by Kelly *et al.* (2008)<sup>94</sup> with cell lattice parameters; a, b and c unit cell lengths of  $15.4063(12) \text{ \AA}$ ,  $11.8278(10) \text{ \AA}$  and  $15.0331(12) \text{ \AA}$  respectively with  $\alpha$ ,  $\beta$  and  $\gamma$  unit cell angles of  $90^\circ$ ,  $107.0260(10)^\circ$  and  $90^\circ$  respectively and unit cell volume of  $2619.3(4) \text{ \AA}^3$ . The **SIMes(a)** crystal grown as part of this research were analysed to reveal cell lattice parameters; a, b and c unit cell

length of 15.3964(22) Å, 11.8206(13) Å and 15.0337(16) Å with  $\alpha$ ,  $\beta$  and  $\gamma$  unit cell angles of 89.995(14)°, 107.000(13)° and 90.099(13)° and unit cell volume of 2616.34(65) Å<sup>3</sup>. The unit cell data collected matched very closely to that published and so a full diffraction study was not completed.

The crystal structures shown in Figure 2.20 were obtained from Kelly *et al.*<sup>94</sup> along with the corresponding bond length data and bond angle data.

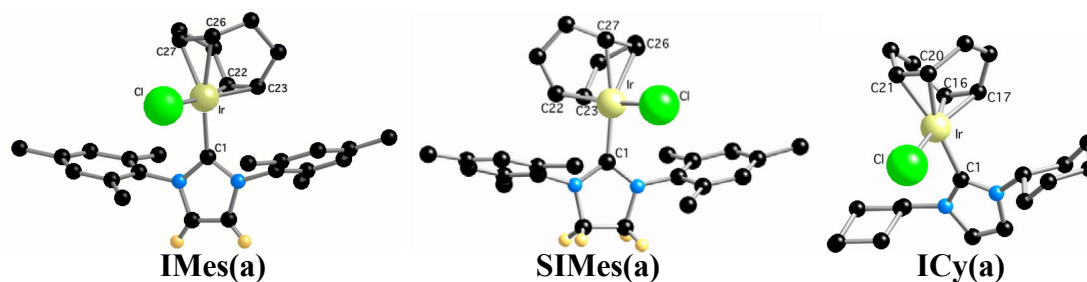


Figure 2.20 The crystal structures of **IMes(a)**, **SIMes(a)** and **ICy(a)** copied from a publication by Kelly *et al.*<sup>94</sup>

Catalyst	Cl-Ir-C <sup>NHC</sup>	C <sup>NHC</sup> -Ir-C <sup>cis-cod</sup> (av)	C <sup>NHC</sup> -Ir-C <sup>trans-cod</sup> (av)
<b>IMes(a)</b>	89.82(14)°	94.45(3)°	161.6(3)°
<b>SIMes(a)</b>	91.87(9)°	93.5851(19)°	161.585(22)°
<b>ICy(a)</b>	88.5(3)°	91.7(7)°	162.9(8)°

Table 2.7 Selected angles for [(NHC)Ir(COD)Cl] from a publication by Kelly *et al.*<sup>94</sup> where *cis* and *trans* are relative to the carbene.

The angles shown in Table 2.7 imply each structure adopts a distorted square planar arrangement, with both Cl-Ir-C<sup>NHC</sup> and C<sup>NHC</sup>-Ir-C<sup>cis-cod</sup>(av) angles being close to 90°, but the C<sup>NHC</sup>-Ir-C<sup>trans-cod</sup>(av) angles are quite distorted from the archetypal 180°. This distortion is a result of the bidentate COD ligand.

Catalyst	Ir-C <sup>NHC</sup>	Ir-Cl	Ir-C <sup>cis-cod</sup> (av)	Ir-C <sup>trans-cod</sup> (av)
<b>IMes(a)</b>	2.055(5) Å	2.3527(14) Å	2.118(7) Å	2.1845(8) Å
<b>SIMes(a)</b>	2.041(3) Å	2.3550(9) Å	2.121(4) Å	2.181(6) Å
<b>ICy(a)</b>	2.090(13) Å	2.357(3) Å	2.1015(18) Å	2.169(21) Å

Table 2.8 Selected bond lengths for [(NHC)Ir(COD)Cl] in Å, from a publication by Kelly *et al.*<sup>94</sup> where *cis* and *trans* are relative to the carbene.

Considering the Ir-C<sup>NHC</sup> bond, this is approximately equal in **IMes(a)** and **SIMes(a)** suggesting the bond strength is approximately the same, however the same bond in **ICy(a)** is slightly longer suggesting a weaker bond. These bond lengths broadly

correlate to the  $\%V_{\text{bur}}$  presented in Table 2.6, where a shorter bond length corresponds to a larger  $\%V_{\text{bur}}$ . The opposite trend is observed with both Ir-COD bond lengths, where those in the **ICy(a)** are slightly shorter and therefore stronger than those in **IMes(a)** and **SIMes(a)**.

In these distorted square planer complexes, the chloride ion is always positioned *trans* to one of the COD bonds as a result of the bidentate nature of the COD ligand. This means the Ir-Cl bond length remains broadly the same across the three carbene complexes.

$^1\text{H}$  and  $^{13}\text{C}$  NMR data was collected for each catalyst precursor, and selected data are presented in Table 2.9.

Catalyst precursor	COD protons (ppm)		Imidazolium protons (ppm)	Carbene carbon (ppm)
	CH	CH <sub>2</sub>		
<b>IMes(a)</b>	3.99, 3.08	1.68, 1.30	7.22	179.3
<b>SIMes(a)</b>	3.94, 3.21	1.63, 1.31	3.95	206.0
<b>ICy(a)</b>	4.46, 3.04	Under multiplet	7.16	176.5

Table 2.9 Selected NMR data for the catalytic precursors **IMes(a)**, **SIMes(a)** and **ICy(a)** in methanol.

The data presented in Table 2.9 indicates the significant changes observed in the NMR data corresponding to each catalyst. The most significant difference between each catalytic precursor is the signal corresponding to the carbene carbon resonance. As expected, the strongest electron donor, **ICy**, has the lowest  $^{13}\text{C}$  carbene resonance of the three systems, and **SIMes**, the weakest electron donor has the highest  $^{13}\text{C}$  carbon resonance. Another significant difference is observed in the  $^1\text{H}$  signals corresponding to the imidazolium protons. **SIMes(a)** contains a saturated backbone and therefore the signals corresponding to these four protons are observed at around 4 ppm as opposed to the two analogous protons in **IMes(a)** and **ICy(a)** which are observed at around 7 ppm. These differences indicate there are significant differences between the three catalyst precursors.

A crystal of  $[\text{Ir}(\text{SIMes})(\text{COD})(2\text{-methylpyridine})]\text{PF}_6$  was also grown for X-ray diffraction analysis, shown in Figure 2.21.

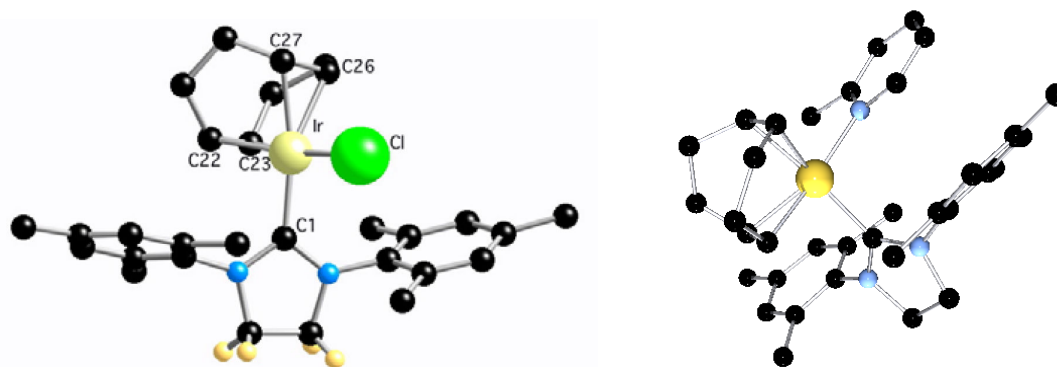


Figure 2.21 Crystal structures of **SIMes(a)** ( $[\text{Ir}(\text{SIMes})(\text{COD})\text{Cl}]$ ) taken from a publication by Kelly *et al.*<sup>94</sup> and  $[\text{Ir}(\text{SIMes})(\text{COD})(2\text{-methylpyridine})]\text{PF}_6$  collected as part of this thesis. The  $\text{PF}_6$  counter ion for the latter has been omitted for clarity. Presented with C in black, N in blue, Ir in yellow, H in peach and Cl in green.

This crystal structure supports the information derived in section 2.2.4, pg 120 about the mechanism of activation for the catalysts. A comparison of the crystal structure of  $[\text{Ir}(\text{SIMes})(\text{COD})(2\text{-methylpyridine})]\text{PF}_6$  with that of  $[\text{Ir}(\text{SIMes})(\text{COD})\text{Cl}]$  (**SIMes(a)**) was completed.

Catalyst	X-Ir-C <sup>NHC</sup>	C <sup>NHC</sup> -Ir-C <sup>cis-cod</sup> (av)	C <sup>NHC</sup> -Ir-C <sup>trans-cod</sup> (av)
$[\text{Ir}(\text{SIMes})(\text{COD})\text{Cl}]$	91.87(9) <sup>o</sup> (X=Cl)	93.5851(19) <sup>o</sup>	161.585(22) <sup>o</sup>
$[\text{Ir}(\text{SIMes})(\text{COD})(2\text{-methylpyridine})]\text{PF}_6$	97.55(11) <sup>o</sup> (X=N)	91.36(12) <sup>o</sup>	160.4(12) <sup>o</sup>

Table 2.10 Selected angles for  $[\text{Ir}(\text{SIMes})(\text{COD})\text{Cl}]$  (**SIMes(a)**) from a publication by Kelly *et al.*<sup>94</sup> and  $[\text{Ir}(\text{SIMes})(\text{COD})(2\text{-methylpyridine})]\text{PF}_6$  collected as part of this thesis, where *cis* and *trans* are relative to the carbene.

$[\text{Ir}(\text{SIMes})(\text{COD})(2\text{-methylpyridine})]\text{PF}_6$  also adopts a distorted square planar arrangement however, now the distortion is much greater than that observed in **SIMes(a)**. The N-Ir-C<sup>NHC</sup> angle is distorted by over 7<sup>o</sup> compared to 2<sup>o</sup> distortion for the analogous Cl-Ir-C<sup>NHC</sup> angle of **SIMes(a)**. The C<sup>NHC</sup>-Ir-C<sup>trans-cod</sup>(av) angle is also slightly more distorted.

Catalyst	Ir-C <sup>NHC</sup>	Ir-X (Å)	Ir-C <sup>cis-cod</sup> (av)	Ir-C <sup>trans-cod</sup> (av)
[Ir(SIMes)(COD)Cl]	2.041(3) Å	2.3550(9) (X=Cl)	2.121(4) Å	2.181(6) Å
[Ir(SIMes)(COD)(2-methylpyridine)]PF <sub>6</sub>	2.078(3) Å	2.116(3) (X=N)	2.138(3) Å	2.165(3) Å

Table 2.11 Selected bond lengths for [Ir(SIMes)(COD)Cl] (**SIMes(a)**) from a publication by Kelly *et al.*<sup>94</sup> and [Ir(SIMes)(COD)(2-methylpyridine)]PF<sub>6</sub><sup>6</sup> collected as part of this thesis, where *cis* and *trans* are relative to the carbene.

In contrast, the Ir-C<sup>NHC</sup>, Ir-C<sup>cis-cod</sup>(av) and Ir-C<sup>trans-cod</sup>(av) bond lengths are broadly similar for the two complexes, however the Ir-N bond in [Ir(SIMes)(COD)(2-methylpyridine)]PF<sub>6</sub> is much shorter than the analogous Ir-Cl bond in **SIMes(a)**. This could provide a reason for the more severe distortion from the square planar arrangement exhibited by [Ir(SIMes)(COD)(2-methylpyridine)]PF<sub>6</sub>, as the chlorine atom has been replaced with a much bulkier substituent with a shorter bond to iridium. The Ir-N bond has also been measured in [Ir(SIMes)(COD)(py)]PF<sub>6</sub> by Lee *et al.*<sup>74</sup> to be 2.107 Å, shorter than the analogous bond length observed for [Ir(SIMes)(COD)(2-methylpyridine)]PF<sub>6</sub>. Pyridine has a pK<sub>a</sub> of 5.2 and 2-methylpyridine has a pK<sub>a</sub> of 5.97.<sup>106,107</sup> It would therefore be expected for 2-methylpyridine to exhibit a shorter bond length however due to the steric hinderence of the *ortho* substituent, the pyridine-iridium bond length is shorter and therefore stronger.

This section has shown that small changes in the carbene ligand used to produce precursors to active SABRE catalysts can have a significant effect on the steric and electronic properties of that complex.

### 2.3.2.3 Comparison of the active hydrogenation products of **IMes(a)**, **SIMes(a)** and **ICy(a)**

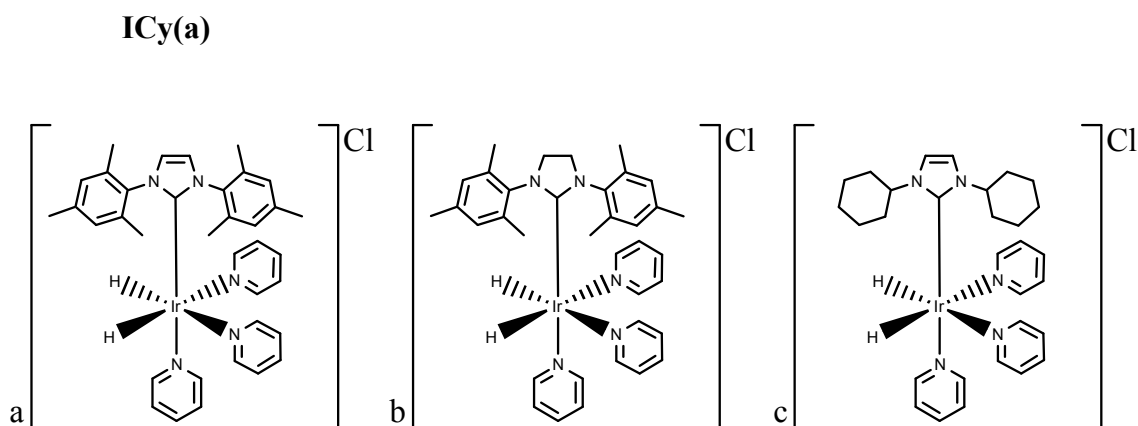


Figure 2.22 Structures of the active hydrogenation products of **IMes(a)**, **SIMes(a)** and **ICy(a)**.

As polarisation does not transfer into the substrate through the catalytic precursor, but through the hydrogenation product, it is prudent to also investigate the properties of these compounds.

An important observation to make at this point is the time required for a catalyst to hydrogenate from the precursor to the fully active form. In the case of **IMes(a)** and **SIMes(a)**, full activation of the catalyst occurs within 5 minutes of addition of hydrogen and a short shake to incorporate the hydrogen gas into the solution is all that is required. However in the case of **ICy(a)**, this time is increased to around 18 hours.

In 2011, Cowley *et al.*<sup>66</sup> published a crystal structure of the active form of the carbene-based SABRE catalyst,  $[\text{Ir}(\text{H})_2(\text{IMes})(\text{py})_3]^+$ , with the ORTEP plot shown in Figure 2.23.

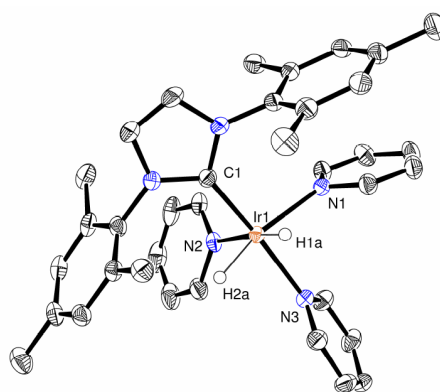


Figure 2.23 X-ray crystal structure of  $[\text{Ir}(\text{H})_2(\text{IMes})(\text{py})_3]^+$ . Structure taken from a publication by Cowley *et al.* 2011.<sup>66</sup>

Catalyst precursor	Hydride ligands (ppm)	Bound pyridine (ppm)				Imidazolium protons (ppm)	Carbene carbon (ppm)
		Position to hydrides (eq.)	<i>ortho</i>	<i>meta</i>	<i>para</i>		
<b>IMes(a)</b>	-22.52	<i>cis</i> (1)	8.09	7.00	7.69	7.18	180.9*
		<i>trans</i> (2)	8.34	7.14	7.79		
<b>SIMes(a)</b>	-22.69	<i>cis</i> (1)	7.97	6.97	7.66	3.9	208.6
		<i>trans</i> (2)	8.32	7.12	7.76		
<b>ICy(a)</b>	-22.49	<i>cis</i> (1)	8.31	7.27	7.94	7.22	197.6
		<i>trans</i> (2)	8.75	7.47	8.00		

Table 2.12 Selected NMR data for the active catalysts in methanol, where 'eq' indicates the number of equivalents observed. The carbene value \* for **IMes(a)** is quoted for  $[\text{Ir}(\text{IMes})(\text{py})_2(\text{H})_2\text{Cl}]$  in DCM.

The first important observation to be made from Table 2.12 is that each catalyst takes the same form when activated. This is evident by the fact that the pyridine ligands bound *cis* and *trans* to the hydride ligands are in the same proportion in each case. The different chemical environments observed in the precursor systems are also observed in the active catalysts. The chemical shifts of the hydride ligand resonances are also dependent on the electron donation properties of the carbene. As the carbene donates more electrons to the metal centre, it in turns shares this between the other ligands, including the hydride ligands. The differences between the catalytic systems also extend to produce different bound signals for the pyridine protons. It is predicted that these differences will have a significant effect on the extent of polarisation transfer observed with each catalyst.

### 2.3.3 Comparison of ligand exchange rate constants and activation parameters of **IMes(a)**, **SIMes(a)** and **ICy(a)**

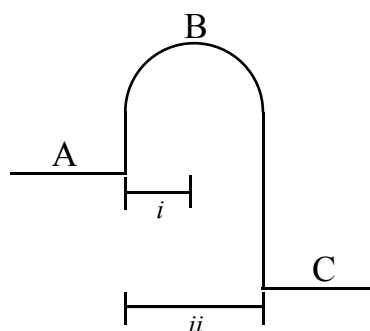


Figure 2.24 The reaction co-ordinate for the dissociative reaction for loss of ligand.

A series of 1D EXSY experiments were completed to enable the calculation of the pyridine and hydride ligand exchange rate constants in the active forms of **IMes(a)**, **SIMes(a)** and **ICy(a)** as a function of temperature. The associated rate constants of ligand exchange were determined by application of the Dynafit<sup>108</sup> programme. These data are expected to provide us with a better understanding of the effect the carbene ligand has on catalyst activity.

In this case, the measured rate constant corresponds to the transformation from bound ligand (hydride/substrate) to free ligand, A to C in Figure 2.24. When calculating  $\Delta H^\ddagger$ ,  $\Delta S^\ddagger$  and  $\Delta G^\ddagger$ , the rate constant data used should refer to the rate constant of reaching the transition state (B) which is twice the measured rate constant. This is because once the



molecule has reached point B, it is possible for it to fully disassociate to form C, or re-associate to form A. Consequently, the Eyring plots for activation parameters of both hydride ligand and pyridine loss are calculated using a graph of  $\ln(2x_{\text{measured rate/temperature}})$  vs  $1/\text{temperature}$ .<sup>109</sup> In all cases, the raw rate constants are measured as per mole of iridium catalyst, and not per mole of hydride ligand or pyridine.

The measured rate constants for loss of pyridine and hydride ligands can be very informative however the thermodynamic parameters for the loss of pyridine ligands are much more reliable than those for the loss of hydride ligands. This is because the mechanism for the loss of pyridine ligands is independent of hydride ligand loss however the mechanism for hydride ligand loss is partly dependent on the loss of pyridine ligands. This was discussed in section 2.2.5.

### 2.3.3.1 Thermodynamic activation parameters observed for the loss of pyridine *trans* to the hydride ligands from hydrogenated **IMes(a)**, **SIMes(a)** and **ICy(a)**

	<b>PCy<sub>3</sub></b>	<b>IMes(a)</b> <sup>66</sup>	<b>SIMes(a)</b>	<b>ICy(a)</b>
$\nu_{\text{Co(Ir)}}^{\text{av}} (\text{cm}^{-1})$ <sup>94</sup>	2028.0	2023.1	2024.6	2023.0
$\%V_{\text{bur}}$ <sup>98</sup>	37.1	33.0	34.5	27.3
Raw Rate constant / s <sup>-1</sup> (300 K)	3.6 <sup>66</sup>	23.4	44.8*	1.1
$\Delta H^{\ddagger} / \text{kJ mol}^{-1}$	97.4 ( $\pm 9$ ) <sup>61</sup>	93 ( $\pm 3$ )	75.6 ( $\pm 0.4$ )	94.3 ( $\pm 1.1$ )
$\Delta S^{\ddagger} / \text{J K}^{-1} \text{mol}^{-1}$	84 ( $\pm 31$ ) <sup>61</sup>	97 ( $\pm 9$ )	44.6 ( $\pm 1.5$ )	77.6 ( $\pm 3.7$ )
$\Delta G_{300}^{\ddagger} / \text{kJ mol}^{-1}$	72.2*	64 ( $\pm 2$ )	62.3 ( $\pm 0.05$ )	71.1 ( $\pm 0.04$ )

Table 2.13 Activation parameters for the loss of pyridine when **IMes(a)**, **SIMes(a)** and **ICy(a)** precursors are used. Data for **IMes(a)** was quoted in a publication by Cowley *et al.* (2011).<sup>66</sup> \* denotes value was calculated either by extrapolation in the case of **SIMes(a)** or using published data in the case of **PCy<sub>3</sub>**.

Full exchange rate constant data can be found in the Appendix, sections 9.1.5 and 9.1.6. For **IMes(a)**, the raw rate constant for pyridine loss quoted in the publication by Cowley *et al.* (2011)<sup>66</sup> has been doubled as the rate constant is quoted per mole of pyridine, where the data here is quoted as per mole of iridium catalyst. For **SIMes(a)**, the raw rate constant has been calculated from the Eyring plot for that system as the rate constant is too fast to measure by NMR methods. Looking at the enthalpies for the activation of loss of pyridine, it is possible to see that the value for **IMes(a)**, **ICy(a)** and **PCy<sub>3</sub>** are similar to each other. **SIMes(a)** has a significantly lower enthalpy, and therefore requires less energy than for either **IMes(a)**, **ICy(a)** and **PCy<sub>3</sub>**. These values appear to

show a weak correlation to the  $\nu_{\text{Co(Ir)}}^{\text{av}}$ . In all cases, the loss of pyridine is entropically favourable. The greatest increase in entropy is of activation of loss of pyridine is found for **IMes(a)**, then **ICy(a)** and **PCy<sub>3</sub>**, then **SIMes(a)**. The Gibbs free energy at 300 K is also positive in all cases, suggesting pyridine loss is not spontaneous. Within the carbenes, the Gibbs free energy values quoted are consistent with the observed rate constants for loss of pyridine and  $\%V_{\text{bur}}$ , where **ICy(a)** shows the slowest rate constant of loss and highest Gibbs free energy. The phosphine, **PCy<sub>3</sub>**, shows a slow rate constant of exchange and also one of the highest Gibbs free energies. These data do not appear to correlate to the electron donation as the  $\nu_{\text{Co(Ir)}}^{\text{av}}$  for **IMes(a)** and **ICy(a)** are near identical, however the related Gibbs free energies are significantly different.

### 2.3.3.2 Thermodynamic activation parameters observed for the loss of hydride ligands from hydrogenated **IMes(a)**, **SIMes(a)** and **ICy(a)** in the presence of pyridine

	<b>PCy<sub>3</sub></b>	<b>IMes(a)</b> <sup>66</sup>	<b>SIMes(a)</b>	<b>ICy(a)</b>
$\nu_{\text{Co(Ir)}}^{\text{av}}$ (cm <sup>-1</sup> ) <sup>94</sup>	2028.0	2023.1	2024.6	2023.0
$\%V_{\text{bur}}$ <sup>98</sup>	37.1	33.0	34.5	27.3
Raw Rate constant / s <sup>-1</sup> (300 K)		9	36.18*	0.213
$\Delta H^\ddagger$ / kJ mol <sup>-1</sup>		79 (± 1)	74.9 (± 0.2)	88.7 (± 0.6)
$\Delta S^\ddagger$ / J K <sup>-1</sup> mol <sup>-1</sup>		41 (± 3)	40.3 (± 0.7)	43.4 (± 2.0)
$\Delta G_{300}^\ddagger$ / kJ mol <sup>-1</sup>		66.4 (± 0.3)	62.8 (± 0.02)	75.7 (± 0.02)

Table 2.14 Activation parameters for the loss of hydride ligands when **IMes(a)**, **SIMes(a)** and **ICy(a)** precursors are used. Data for **IMes(a)** was quoted in a publication by Cowley *et al.* (2011).<sup>66</sup> \* denotes the value was calculated by extrapolation.

Full exchange rate constant data can be found in the Appendix, sections 9.1.5 and 9.1.6. For **SIMes(a)**, the raw rate constant at 300 K has been calculated from the Eyring plot for that system as the rate constant is too fast to measure by NMR methods. Looking at the enthalpies of activation of loss of hydrogen, it is possible to see that the values for **IMes(a)** and **SIMes(a)** are similar. It can also be observed that **ICy(a)** has a significantly higher enthalpy, meaning the loss of hydrogen requires significantly more energy than for either **IMes(a)** or **SIMes(a)**. These data appear to show a weak correlation to the  $\nu_{\text{Co(Ir)}}^{\text{av}}$ . In all cases, the loss of hydrogen is entropically favourable as this increases the disorder in the system. The greatest increase in entropy is observed for the loss of hydrogen from **SIMes(a)** with **ICy(a)** following, then **IMes(a)** however the

values cannot be considered statistically different from each other. The Gibbs free energy at 300 K is also positive in all cases, suggesting activation of the loss of hydrogen is not spontaneous for any of the catalysts. The largest barrier is observed for **ICy(a)** and this is reflected in the small observed rate constant for loss of hydrogen. The Gibbs free energy values appear to show a correlation to the % $V_{\text{bur}}$  values. These data do not appear to correlate to the electron donation as the  $\nu_{\text{co(Ir)}}^{\text{av}}$ , as **IMes(a)** and **ICy(a)** are near identical, however the related Gibbs free energies are significantly different.

#### 2.3.4 Comparison of polarisation transfer efficiency into pyridine of **IMes(a)**, **SIMes(a)** and **ICy(a)**

Now that the structural and electronic differences between the three catalytic precursors have been compared and contrasted, it is prudent to investigate the effect these differences have on the ability of each catalyst to transfer hyperpolarised states from *parahydrogen*-derived hydride ligands to the substrate. In the case of **ICy(a)**, polarisation transfer is only considered after a minimum activation time of 18 hours. For **IMes(a)** and **SIMes(a)**, polarisation transfer is considered after a minimum activation time of 5 minutes.

It is known that changing the ligand from a phosphine to a carbene had the effect of significantly increase the extent of polarisation transfer to pyridine using SABRE. The phosphine in question, PCy<sub>3</sub> has a higher TEP value than the investigated carbenes, and also has more steric bulk. It might therefore be possible to predict that reducing the steric bulk and increasing the electron donation will increase polarisation transfer to pyridine through SABRE. Polarisation transfer to pyridine using **IMes(a)**, **SIMes(a)** and **ICy(a)** was initially compared using method 1.

Catalyst precursor		<b>IMes(a)</b>	<b>SIMes(a)</b>	<b>ICy(a)</b>
Electronic and steric properties	$\nu_{\text{co(Tr)}}^{\text{av}}$ ( $\text{cm}^{-1}$ ) <sup>94</sup>	2023.1	2024.6	2023.0
	$\%V_{\text{bur}}$ <sup>98</sup>	33.0	34.5	27.3
Rate constant of ligand loss ( $\text{s}^{-1}$ ) (300 K)	Hydride ligand	9	36.2	0.2
	Pyridine	23.4	44.8	1.1
Obs. <sup>1</sup> H NMR pyridine signal enhancement	<i>Ortho</i>	-160	-107	-37
	<i>Meta</i>	68	46	24
	<i>Para</i>	-142	-68	-34

Table 2.15 Typical observed <sup>1</sup>H NMR signal enhancement to pyridine when **IMes(a)**, **SIMes(a)** and **ICy(a)** are used as precursors in method 1 hyperpolarised at 2 G.

Based on results observed for the polarisation of pyridine with the PCy<sub>3</sub> phosphine based catalyst<sup>61</sup> and **IMes(a)**,<sup>66</sup> it had been predicted that a decrease in steric bulk and increase in electronic donation of the carbene ligand may increase observed polarisation transfer to pyridine. This has been proven to be wrong. **IMes(a)** has exhibited the greatest <sup>1</sup>H NMR signal enhancements in the spectrum of pyridine, although **ICy(a)** has a greater electron donation and the lowest steric bulk.

It can be observed from the data in Table 2.15 that the maximum enhancement to pyridine is observed when **IMes(a)** is used, then **SIMes(a)** then **ICy(a)**. **ICy(a)** shows a significantly slower pyridine and hydride ligand exchange rate constant at 300 K than both **IMes(a)** and **SIMes(a)** and this may be the reason for the lower amount of polarisation transfer observed. **IMes(a)** shows the most significant polarisation transfer however, it exhibits the middle rate constant for pyridine and hydride ligand exchange at 300 K. This suggests an optimum exchange rate constant for both pyridine and hydride ligands exist to promote maximum polarisation transfer. This could further suggest that an optimum contact time is required i.e. the time both hydride ligands and pyridine are bound to the iridium centre at the same time.

The trends in the observed <sup>1</sup>H NMR signal enhancement can also be compared according to the TEP,  $\nu_{\text{co(Tr)}}^{\text{av}}$ ,  $\%V_{\text{bur}}$  and repulsivness factor **r**. The trend for the two descriptors of electron donation, TEP and  $\nu_{\text{co(Tr)}}^{\text{av}}$ , are the same with the carbene ICy showing the strongest donation, followed by IMes, then SIMes. Considering the trend in observed rate constants of loss of pyridine and hydride ligands, the slowest rate constant of loss of ligands is observed in the strongest electron donor of the carbenes investigated, **ICy(a)**, which in turn shows the least observed polarisation transfer to

pyridine. Also, the fastest rate constant of loss of ligands is observed in the weakest electron donor of the carbenes investigated, **SIMes(a)**, however, it does not show the greatest observed polarisation transfer. The middle rate constants of loss of ligands observed in **IMes(a)** corresponds to the middle electron donation, resulting in the highest polarisation transfer into pyridine. This trend is also extended into the % $V_{bur}$  with ICy exhibiting the least steric bulk, followed by IMes, with SIMes exhibiting the highest steric bulk. Considering the repulsiveness factor, **r**, a trend with polarisation transfer cannot be derived.

Looking at all factors considered here, no single factor can be named that has a sole impact on the level of polarisation transfer into pyridine. There is no factor that can be infinitely increased or decreased to observe maximum polarisation transfer into a pyridine, and consequently, a balance must be achieved. It is assumed this will be true for all substrates considered.

The theory predicts that the extent of polarisation transfer is dependent on the chemical shift difference and J-coupling network of the system (see Introduction). Changing the electron donation properties of the carbene has the effect to change the chemical shifts and couplings of the pyridine and hydride ligands and this, combined with the changing contact times as a result of different exchange rates, could be the reason for different levels of polarisation transfer into pyridine. Further investigations into the theory of polarisation transfer by SABRE are required to investigate this further.

## 2.4 Summary

Within this chapter, the fundamental properties of some SABRE catalysts have been discussed, comparing the structural and electronic properties and understanding how these have an effect on the catalysts ability to complete polarisation transfer. More specifically, the chapter looks at three carbene-based catalysts, **IMes(a)**, **SIMes(a)** and **ICy(a)** and compares them to the analogous phosphine-based catalyst which uses a  $PCy_3$  ligand in place of the carbene. The most significant difference between the phosphine and carbenes is the electron donation properties of that ligand, with the carbenes exhibiting significantly larger electron donation properties. The carbenes also exhibit significantly shorter metal to ligand (M-C) bonds when compared to the same bond of the phosphine ligand (M-P). It might be assumed that the shorter metal to

ligand bond would result in a higher steric bulk of the ligand, however due to the orientation of the carbene based ligands to that of the phosphine based ligands, the buried volumes of the two do not vary significantly from each other.

This analysis was also extended to include the active complex. Some of the most significant information here can be obtained through comparing the rate constants of ligand loss and the associated thermodynamic parameters. The observed rate constants of loss of pyridine and hydride ligands do not appear to correlate to the electron donation or buried volume properties when all four catalysts are considered.

Correlations can however be derived when considering the carbene catalysts alone. For both pyridine and hydride ligand loss, increasing the electron donation of the carbene had the result to increase the enthalpy of ligand loss. It can also be stated that the more sterically encumbered a carbene is, the lower the Gibbs free energy required for ligand loss. In the case of loss of hydride ligands, the entropy term also decreases as the carbene becomes larger. It is observed that all ligand loss processes investigated are entropically favourable due to the increase in disorder of the system.

These data were then used to compare the polarisation transfer efficiency of the considered polarisation transfer catalysts. Of the three carbene based catalysts, **IMes(a)** has the middle value for Gibbs free energy and rate constants of hydride and pyridine ligand loss, electronic donation and buried volumes. It has therefore been postulated that an optimum contact time is required to facilitate maximum polarisation transfer into pyridine and assumed therefore that will be true for all substrates.

The data presented in this chapter indicate that the hyperpolarisation properties of a potential SABRE catalyst cannot be predicted. The efficiency of a new catalyst must be decided by measurement, and can be optimised by changing the magnetic field and temperature of the polarisation step, discussed in the following chapter.

### 3 Chapter 3 - Investigation of SABRE effect

#### 3.1 Introduction

In order to gain the most from the newest hyperpolarisation technique SABRE, it is important to understand how to optimise the method such that the maximum signal enhancement can be observed. There are a number of variables that can be altered to affect the extent of polarisation transfer into a substrate which includes the catalyst used (discussed in Chapter 2), the magnetic field in which the hyperpolarisation step takes place, the temperature at which the hyperpolarisation step takes place, and the concentration of the catalyst or substrate. From an applicability point of view, it is also important to understand the effect of varying the solvent used, as not all substrates are soluble in methanol. This chapter details the experiments completed to investigate these effects.

#### 3.2 Effect of magnetic field during the polarisation transfer step on polarisation transfer efficiency

The effect of changing the magnetic field in which the hyperpolarised states are prepared is well known for *parahydrogen* induced polarisation (PHIP)<sup>43,45,46</sup> formally known as PASADENA and ALTADENA (further discussed in Chapter 1). There are a number of publications where this situation has been found relevant to the SABRE technique.<sup>61,65,66</sup>

The predicted theory behind the polarisation transfer mechanism of SABRE has been previously described in Chapter 1.<sup>59</sup> This shows how the extent of polarisation transfer is dependent on the fine balance between scalar coupling and chemical shift effects. It is the chemical shifts dependence on the magnetic field that induces this behaviour.

The first experimental paper in which the idea of changing the magnetic field of polarisation was published in 2009 by Atkinson *et al.*<sup>61</sup> Here, a sample of  $[\text{Ir}(\text{PCy}_3)(\text{H})_2(\text{py})_3]\text{BF}_4$  with a 24 fold excess of pyridine was prepared in  $d_4$ -methanol and interrogated using method 1 where the polarisation transfer step occurs at two magnetic fields, the Earth's magnetic field (0.5 G) and a higher field during which the

sample was shaken across the range 5 G to 100 G. The results from this experiment are outlined in Table 3.1.

Magnetic field of polarisation	Observed $^1\text{H}$ NMR signal enhancement		
	<i>Ortho</i>	<i>Meta</i>	<i>Para</i>
0.5 G	-72	110	-47
5 G – 100 G	-0.3	1.6	-0.2

Table 3.1 Results reported in a publication by Atkinson *et al.* (2009)<sup>61</sup> upon changing the field of polarisation on a sample of pyridine polarised by SABRE using  $[\text{Ir}(\text{PCy}_3)(\text{H})_2(\text{py})_3]\text{BF}_4$ .

It can be observed that changing the field of polarisation has had a great effect on the level of polarisation transfer observed to pyridine. Preparing the states by shaking the sample in the range of fields varying from 5 G to 100 G had the effect to significantly reduce the observed  $^1\text{H}$  NMR signal enhancement. These experiments outlined a non-rigorous idea of the magnetic field dependence of polarisation transfer using SABRE.

The effect was also investigated in a publication by Cowley *et al.* (2011)<sup>66</sup> using the carbene-based SABRE catalyst **IMes(a)**. For this purpose, a flow system (method 2) was employed, giving a great advantage over the shake method employed published in Atkinson *et al.* (2009),<sup>61</sup> as it was possible to investigate the enhancement observed when the sample is polarised at discrete fields.

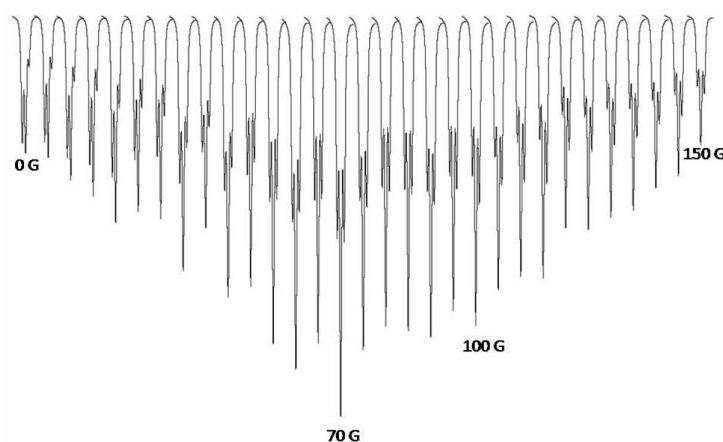


Figure 3.1 Intensity of the  $^1\text{H}$  NMR signal enhancement of the *para* proton resonance of pyridine when polarised using **IMes(a)** at the indicated fields from 0 G to 150 G, in increments of 5 G. Image taken from the supplementary information of the publication by Cowley *et al.* (2011).<sup>66</sup>

It is possible to observe in Figure 3.1 that a maximum level of polarisation was transferred to pyridine at 70 G. This is significantly different to the results observed



with  $[\text{Ir}(\text{PCy}_3)(\text{H})_2(\text{py})_3]\text{BF}_4$  and pyridine, where polarisation transfer into pyridine decreased upon increase in magnetic field of polarisation. There are two possible reasons for this difference. The main reason for this observed difference is the use of a different catalyst in each case however this difference could also be due to the different methods of interrogation used to investigate the dependence. In the publication by Atkinson *et al.* (2009),<sup>61</sup> the higher field is investigated by shaking the NMR tube across a range of field values, and in the publication by Cowley *et al.* (2011),<sup>66</sup> an automatised polarisor is used to allow investigation at discrete magnetic fields.

The magnetic field dependence of SABRE was also considered in a publication by Dücker *et al.* (2012)<sup>65</sup> in a study which investigated polarisation transfer to a number of pyrazoles (Figure 3.2) by the catalyst  $[\text{Ir}(\text{COD})(\text{PCy}_3)(\text{py})]^+$ , activated in the presence of hydrogen and substrate to form  $[\text{Ir}(\text{PCy}_3)(\text{sub})_3(\text{H})_2]^+$ . The choice of catalyst therefore means 1 equivalent of pyridine is present in all samples.

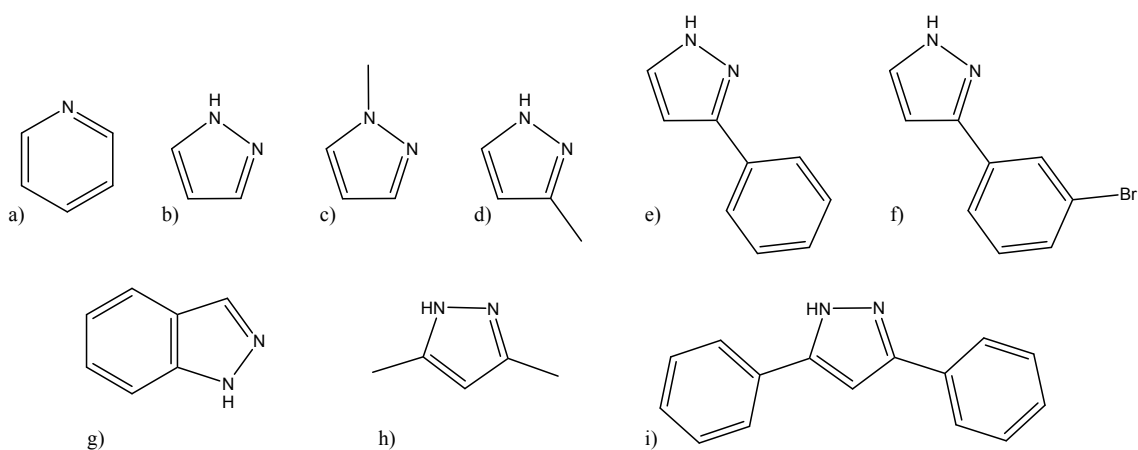


Figure 3.2 Structures of pyridine and the pyrazole-based substrates investigated in the publication by Dücker *et al.* (2012)<sup>65</sup> labelled as a) pyridine, b) pyrazole, c) 1-methylpyrazole, d) 3-methylpyrazole, e) 3-phenylpyrazole, f) 3-(3-bromophenyl)pyrazole, g) indazole, h) 3,5-dimethylpyrazole and i) 3,5-diphenylpyrazole.

The field dependence results published in Dücker *et al.*<sup>65</sup> differ from those previously reported, as the measurements were made on a 300 MHz rather than 400 MHz spectrometer. These results were collected by the shake method (method 1) in the stray field of the spectrometer, resulting in errors from inhomogeneous field effects.

When Dücker *et al.*<sup>65</sup> examined polarisation transfer to pyridine, they found the maximum  $^1\text{H}$  NMR signal enhancement was observed at 130 G. This value is different

to that previously reported by Cowley *et al.* (2011)<sup>66</sup> of 70 G. This is a result of the different catalysts used in each case. Atkinson *et al.* (2009)<sup>61</sup> reported on polarisation transfer to pyridine with the same catalyst as used by Dücker *et al.*,<sup>65</sup> however only two magnetic fields were investigated, 0.5 G and a range of 5 G to 100 G, and they observed a decrease in polarisation transfer efficiency with increase in magnetic field.

When Dücker *et al.*<sup>65</sup> investigated pyrazole itself, a maximum enhancement of ~150 fold was found at 140 G. Although the absolute enhancement is much less than that observed for pyridine, the profile of an enhancement vs field graph is similar for the two substrates. This trend was continued with the other substrates including 1-methylpyrazole, 3-methylpyrazole and 3-phenylpyrazole (in which no polarisation was noted into the phenyl ring). Preliminary investigations into 3-(3-bromophenyl)pyrazole exhibited near identical results to 3-phenylpyridine and therefore a full magnetic field dependence profile was not completed. For the remaining substrates, very low or no polarisation was observed, and therefore studies on the dependence with magnetic field were not completed.

### 3.2.1 Effect of magnetic field during the polarisation transfer step on polarisation transfer efficiency into pyridine

In Chapter 2, method 1 was used to explore the polarisation transfer efficiency of **IMes(a)**, **SIMes(a)** and **ICy(a)** to pyridine. To optimise the enhancement values obtained, the <sup>1</sup>H NMR signal enhancement was monitored as a function of polarisation transfer field (PTF) for each catalyst. Changing the PTF during a shake in method 1 is inaccurate and difficult to reproduce as it involves the sample being shaken in the stray field of the spectrometer magnet. A more rigorous study was therefore completed using method 2 detailed in Chapter 2 and Experimental. It should be noted that samples using **ICy(a)** were activated in an ampoule prior to being injected into the mixing chamber of the polarisor (see Experimental). This is completed by sealing the sample in an ampoule under an atmosphere of H<sub>2</sub>, shaking and storing at room temperature overnight. This is because **ICy(a)** has comparatively long activation times which cannot be accommodated by the mixing chamber.

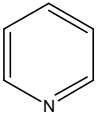
Substrate	Catalyst	Polarisation field of max. pol. transfer / G	Observed $^1\text{H}$ NMR signal enhancement		
			<i>Ortho</i>	<i>Meta</i>	<i>Para</i>
	<b>IMes(a)</b>	-70	-322	-241	-535
	<b>SIMes(a)</b>	-90	-83	-63	-103
	<b>ICy(a)</b>	-60	-8	-5	-9

Table 3.2  $^1\text{H}$  NMR signal enhancement of pyridine observed for **IMes(a)**, **SIMes(a)** and **ICy(a)** using method 2, quoted at the magnetic field which resulted in the maximum observed  $^1\text{H}$  NMR signal enhancement.

The field value for the maximum observed  $^1\text{H}$  NMR signal enhancement for each catalyst considered is presented in Table 3.2. It can be seen that they differ only slightly from each other. It is assumed this difference must be as a result of each catalyst producing slightly different J-Couplings between the hydride ligands and bound pyridine ligands however this coupling is not observable in  $^1\text{H}$  NMR spectra.

### 3.2.2 Effect of magnetic field during the polarisation transfer step on polarisation transfer efficiency into deuterated pyridines

A series of experiments were completed to further understand the polarisation transfer process employed in SABRE by using the two deuterated pyridines, 3,4,5- $d_3$ -pyridine and 2,6- $d_2$ -pyridine, with structures shown in Figure 3.3. These experiments were completed using **SIMes(a)**.

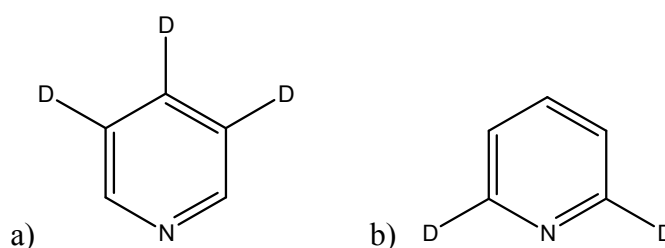


Figure 3.3 Structures of a) 3,4,5- $d_3$ -pyridine and b) 2,6- $d_2$ -pyridine.

The first deuterated pyridine to be investigated by method 2 using **SIMes(a)** was 3,4,5- $d_3$ -pyridine. The initial intention of investigating this substrate was to focus polarisation transfer into one site, thereby causing a build-up in that position and consequently a higher enhancement. The production of a hyperpolarised single signal also has a great advantage in MRI experiments as it prevents ghosting.

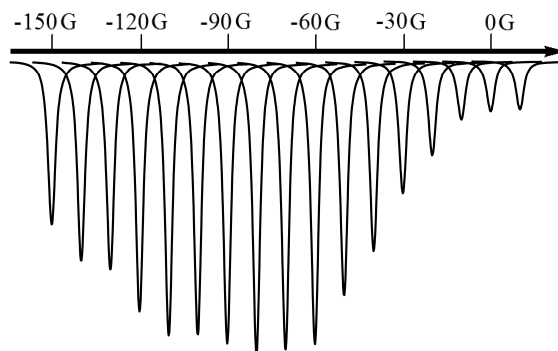


Figure 3.4 Relative  $^1\text{H}$  NMR signal strength of the *ortho* proton resonance of 3,4,5- $d_3$ -pyridine polarised by **SIMes(a)**. These data are presented as a function of the magnetic field of polarisation which varies from -150 G to +10 G in increments of +10 G.

The maximum level of polarisation transfer in 3,4,5- $d_3$ -pyridine using **SIMes(a)** was achieved at a magnetic field of polarisation of -80 G. The corresponding enhancement was -177 fold for the *ortho* proton resonance of 3,4,5- $d_3$ -pyridine. This means that the level of polarisation transfer to the *ortho* proton resonance increases by nearly 2 fold, through deuteration of the 3, 4 and 5 proton resonances, relative to  $h_5$ -pyridine, as predicted. No signals were observed for the 3, 4 or 5 proton resonances.

2,6- $d_2$ -pyridine (Figure 3.3b) was then investigated. The deuteration of both *ortho* sites was predicted to block polarisation transfer into the substrate if transfer involved J coupling between the hydride ligands and the *ortho* protons. It was therefore predicted that polarisation transfer into the 3, 4 and 5 protons would not occur.

The results from the experiments showed the polarisation transfer efficiency into the *para* proton increased when the polarisation transfer step was completed towards 0 G magnetic field (Figure 3.5).

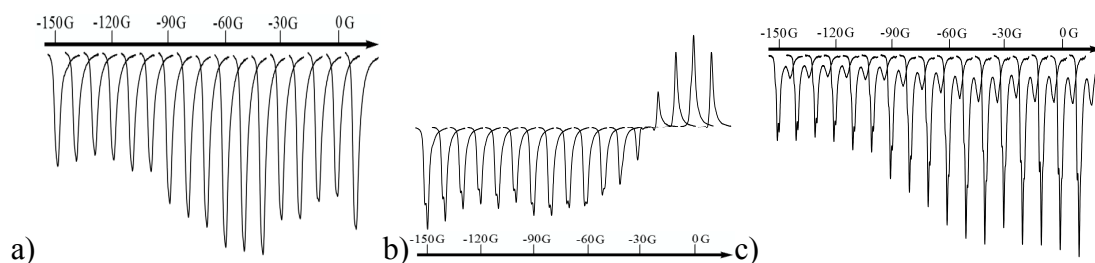


Figure 3.5 Relative  $^1\text{H}$  NMR signal strength of the a) *ortho*, b) *meta* and c) *para* proton resonance of 2,6- $d_2$ -pyridine polarised with **SIMes(a)**. These data are presented as a function of the magnetic field of polarisation which varies from -150 G to +10 G in increments of +10 G.

The data was collected for a second time however the magnetic field of polarisation was then decreased from 10 G to -150 G. Now, a different trend was observed (Figure 3.6).

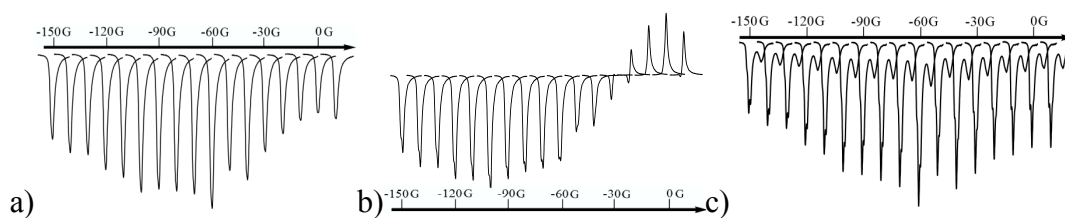


Figure 3.6 Observed  $^1\text{H}$  NMR signal of a) *ortho*, b) *meta* and c) *para* proton resonance of 2,6- $d_2$ -pyridine polarised with **SIMes(a)**. This data is presented with the field of addition of *parahydrogen* taking place at -150 G to +10 G in increments of +10 G, but collected from +10 G to -150 G.

The *para* position of 2,6- $d_2$ -pyridine now exhibits a maximum polarisation level at -60 G. The reason for this change proved to be due to deuteration of the *ortho* sites. This was revealed by comparison of thermal  $^1\text{H}$  NMR spectra taken before and after these measurements as shown in Figure 3.7.

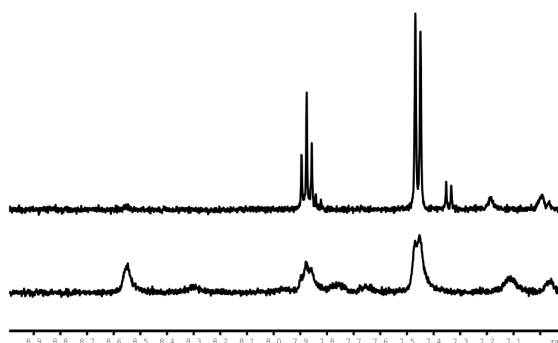


Figure 3.7 Thermal  $^1\text{H}$  NMR spectra of 2,6- $d_2$ -pyridine recorded before (top) and after (bottom) the investigation using **SIMes(a)** with method 2.

It is clear that the 2,6- $d_2$ -pyridine is changed dramatically. Further investigations revealed  $^1\text{H}/^2\text{H}$  exchange is too rapid in the presence of **SIMes(a)** to be able to probe the effect of deutrating the *ortho* positions of pyridine. This is a known reaction of this type of catalyst, discussed in Chapters 1 and 2.<sup>77,78</sup>

### 3.3 Effect of temperature during the polarisation transfer step on polarisation transfer efficiency

The concept that changing the temperature during the polarisation transfer step can result in a change in the polarisation transfer efficiency of a system was first reported

experimentally in a publication by Atkinson *et al.* (2009),<sup>61</sup> where polarisation transfer to pyridine was investigated at 25 °C (298 K) and 80 °C (353 K) with  $[\text{Ir}(\text{COD})(\text{PCy}_3)(\text{py})_3(\text{H})_2]\text{BF}_4$ . They showed that at 0.5 G, the level of polarisation transfer to all three sites of pyridine decreased by increasing the temperature to 80 °C.

This effect was also investigated in a publication by Cowley *et al.* (2011)<sup>66</sup> for both  $[\text{Ir}(\text{COD})(\text{PCy}_3)(\text{py})_3(\text{H})_2]\text{BF}_4$  and **IMes(a)** catalysts with the polarisation transfer step taking place at 25 °C (298 K) and 45 °C (318 K). Now, an increase in polarisation transfer efficiency was observed to pyridine with  $[\text{Ir}(\text{COD})(\text{PCy}_3)(\text{py})_3(\text{H})_2]\text{BF}_4$  with increase in temperature, but a decrease for **IMes(a)**.

In each report, the polarisation transfer to pyridine was only investigated at two temperatures. It is therefore important to investigate the effect more precisely, looking at a larger number of temperatures, both above and below room temperature.

It is assumed that the reason why catalysts exhibit different polarisation transfer properties using SABRE is due to each catalyst having a different rate constant of hydride ligands and substrate loss. Consequently, the effect of changing the temperature at which the polarisation step occurs will be significant. Theory<sup>59</sup> suggests the extent of polarisation transfer is dependent on the lifetime of the complex  $[\text{Ir}(\text{carbene})(\text{py})_3(\text{H})_2]^+$  (see Chapter 1). This time is known as the contact time.<sup>59</sup> It can therefore be assumed that changing the temperature at which the polarisation transfer step occurs will affect the extent of polarisation transfer through changing the contact time. Generally, an increase in temperature will make exchange rates faster and decreasing the temperature will slow the exchange rates (see Appendix).

Temperature		Hydride ligand loss ( $\text{s}^{-1}$ )			Pyridine loss ( $\text{s}^{-1}$ )		
°C	K	<b>IMes(a)</b>	<b>SIMes(a)</b>	<b>ICy(a)</b>	<b>IMes(a)</b>	<b>SIMes(a)</b>	<b>ICy(a)</b>
0	273	0.3	2	0.006	0.5	2	0.03
20	293	4	17	0.09	9	21	0.5
30	303	12	49	0.3	31	62	2
40	313	33	131	1	105	166	7
50	323	85	330	3	330	420	21

Table 3.3 Predicted rate constants of hydride and pyridine ligand loss calculated from thermodynamic data in Chapter 2 for **IMes(a)**, **SIMes(a)** and **ICy(a)** at the indicated temperatures.

It can be predicted that **IMes(a)** exhibits exchange rate constants closest to the optimum (Table 3.3) as it exhibits the highest level of polarisation transfer at 300 K of the three catalysts. The effect of changing the temperature of addition of *parahydrogen* to a SABRE catalyst was investigated using method 1. To complete these experiments the sample must first be put under a *parahydrogen* atmosphere but not shaken. It is then stored at the desired temperature for three minutes with as little disturbance as possible. The NMR tube is then quickly wiped dry, shaken for 8 s and interrogated by NMR. The temperature dependence of polarisation transfer via SABRE to pyridine with **IMes(a)**, **SIMes(a)** and **ICy(a)** was investigated.

### 3.3.1 Effect of changing the temperature of polarisation transfer efficiency into pyridine using **IMes(a)**

**IMes(a)** was the first catalyst to be investigated with respect to a temperature dependence.

<b>IMes(a)</b> and pyridine		Temperature / °C				
		0	20	30	40	50
Rate of loss (s <sup>-1</sup> )	Hydride ligands	0.3	4	12	33	85
	Pyridine	0.5	9	31	105	330
Pyridine resonance	<i>Ortho</i>	-64	-78	-69	-96	-85
	<i>Meta</i>	98	96	101	51	61
	<i>Para</i>	-120	-126	-119	-79	-90

Table 3.4 <sup>1</sup>H NMR signal enhancement to the *ortho*, *meta* and *para* proton resonances of pyridine in the presence of **IMes(a)** in methanol when the polarisation transfer step occurs at the indicated temperatures with the predicted rate constants of hydride and pyridine ligand exchange calculated from thermodynamic data in Chapter 2.

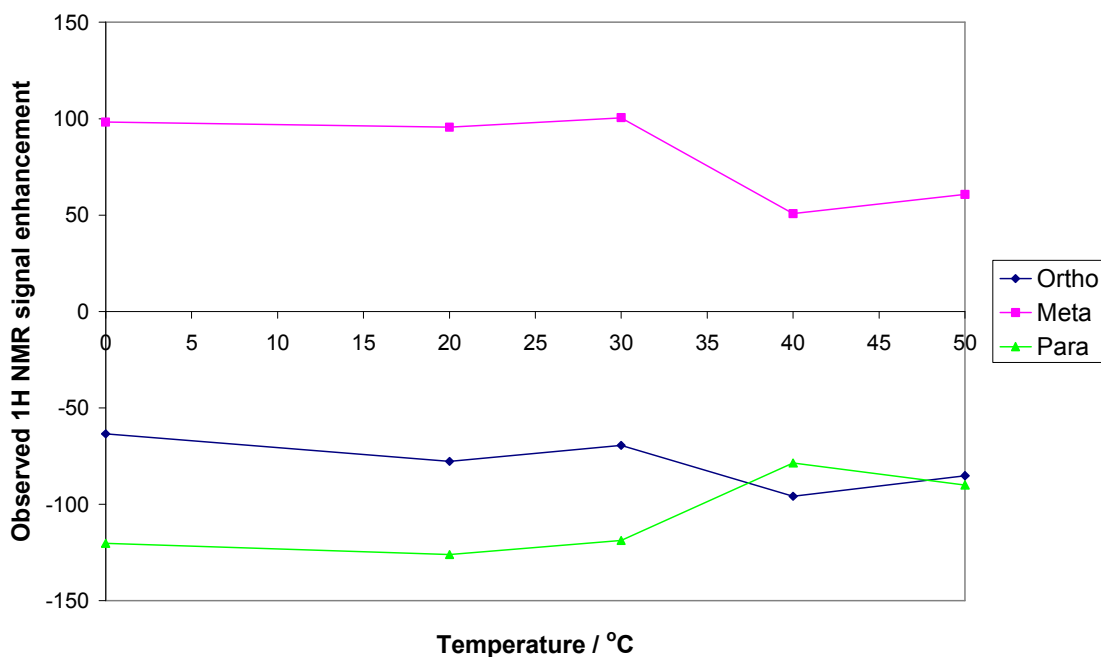


Figure 3.8 Relative  $^1\text{H}$  NMR signal enhancement to pyridine resonances obtained with **IMes(a)** as a function of temperature.

Analysis of these data, presented in Table 3.4 and Figure 3.8, shows that a linear dependence is not present. In addition, it varies for each resonance; cooling from room temperature to 0 °C appeared to have little real effect, however increasing the temperature has a clear effect. Firstly, the *ortho* resonance exhibits a small, but significant increase in the polarisation transfer level observed when the temperature is increased to 30 °C. Increasing the temperature further to 40 °C and 50 °C results in a further drop in the polarisation transfer level. Very similar effects are observed for the *meta* and *para* resonances. This experiment has shown that for the **IMes(a)** and pyridine system, the optimal temperature of the five temperatures investigated is room temperature.

### 3.3.2 Effect of changing the temperature of polarisation transfer efficiency into pyridine using **SIMes(a)**

The temperature dependence of **SIMes(a)** with pyridine was investigated. Both pyridine and hydride exchange rate constants for **SIMes(a)** are known to be faster than the exchange rate constants for **IMes(a)** (Table 3.3). Consequently, it is predicted increasing the temperature of polarisation, and therefore increasing the exchange rates



further, will decrease polarisation transfer to pyridine, and vice versa. The results from this experiment are outlined in Table 3.5 and Figure 3.9.

SIMes(a) and pyridine		Temperature / °C				
		0	20	30	40	50
Rate of loss (s <sup>-1</sup> )	Hydride ligands	2	17	49	131	330
	Pyridine	2	21	62	166	420
Pyridine resonance	<i>Ortho</i>	-126	-121	-83	-61	-43
	<i>Meta</i>	86	76	40	27	17
	<i>Para</i>	-98	-95	-64	-43	-32

Table 3.5 Observed <sup>1</sup>H NMR signal enhancement to the *ortho*, *meta* and *para* proton resonances of pyridine in the presence of SIMes(a) in methanol when the polarisation transfer step occurs at various temperatures with the predicted rate constants of hydride and pyridine ligand exchange calculated from thermodynamic data in Chapter 2.

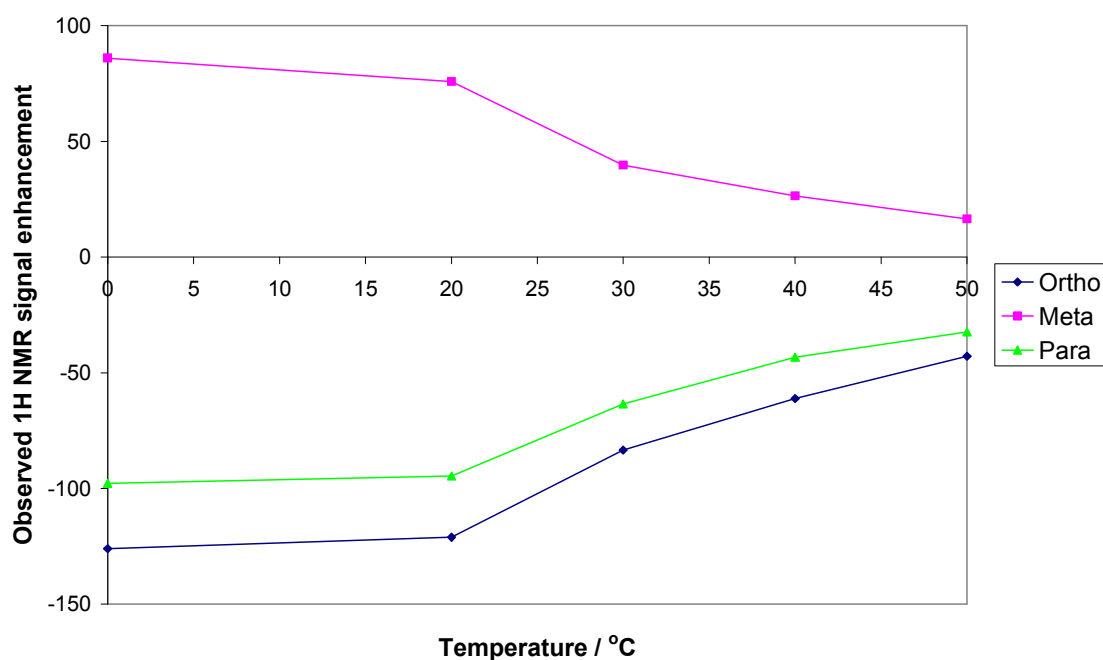


Figure 3.9 Relative <sup>1</sup>H NMR signal enhancement to pyridine resonances obtained with SIMes(a) as a function of temperature.

As predicted, increasing the temperature above room temperature reduces the level of polarisation transfer. In contrast, a small increase in the level of polarisation transfer is observed when reducing the temperature to 0 °C.

### 3.3.3 Effect of changing the temperature of polarisation transfer efficiency into pyridine using **ICy(a)**

It is known that the exchange rate constants for both pyridine and hydrides are much slower for **ICy(a)** than for **SIMes(a)** and **IMes(a)** (Table 3.3) and therefore, it is predicted that increasing temperature, and therefore increasing the exchange rates, will increase polarisation transfer into pyridine. The temperature dependence of polarisation of pyridine for **ICy(a)** is presented in Table 3.6.

<b>ICy(a)</b> and pyridine		Temperature / °C				
		0	20	30	40	50
Rate of loss (s <sup>-1</sup> )	Hydride ligands	0.006	0.09	0.3	1	3
	Pyridine	0.03	0.5	2	7	21
Pyridine resonance	<i>Ortho</i>	-3	-6	-9	-11	-13
	<i>Meta</i>	2	6	8	9	10
	<i>Para</i>	-3	-6	-10	-11	-14

Table 3.6 Observed <sup>1</sup>H NMR signal enhancement to the *ortho*, *meta* and *para* proton resonances of pyridine in the presence of **ICy(a)** in methanol when the polarisation transfer step occurs at various temperatures with the predicted rate constants of hydride and pyridine ligand exchange calculated from thermodynamic data in Chapter 2.

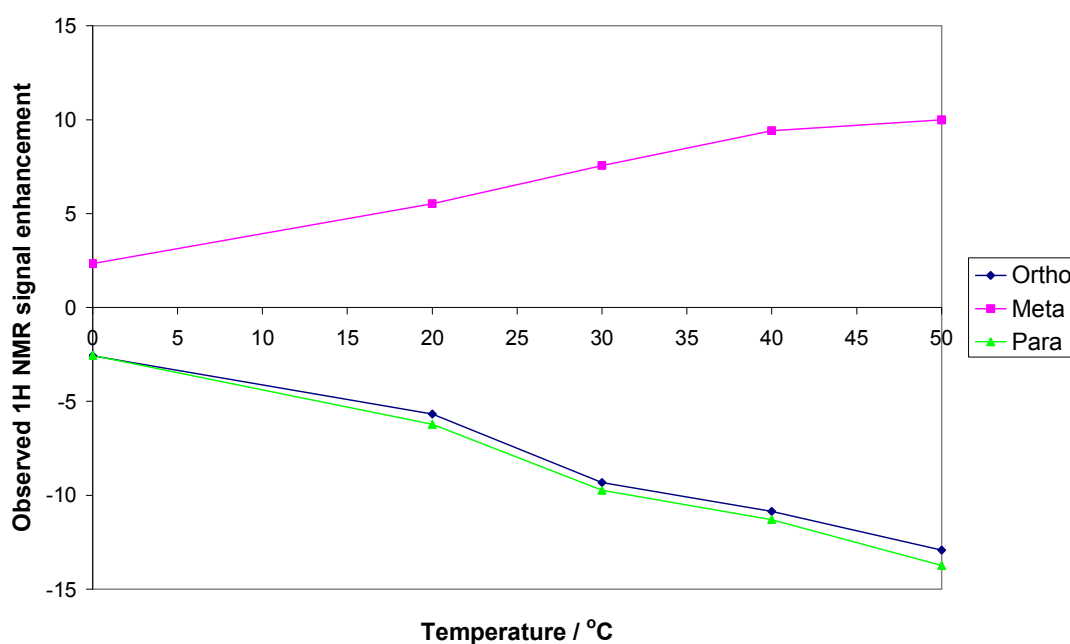


Figure 3.10 Relative <sup>1</sup>H NMR signal enhancement to pyridine resonances obtained with **ICy(a)** as a function of temperature.

Polarisation of pyridine with **ICy(a)** shows a clear dependence on the temperature of polarisation (Figure 3.10), where an increase in temperature leads to an increase in observed polarisation transfer, as predicted. This is predicted to be a result of the slow rate constants of loss of pyridine and hydride ligands from **ICy(a)**.

### 3.3.4 Comparison of the effect of temperature on the polarisation transfer efficiency into pyridine using **IMes(a)**, **SIMes(a)** and **ICy(a)**

The temperature dependence of the above three catalysts, **IMes(a)**, **SIMes(a)** and **ICy(a)** were compared.

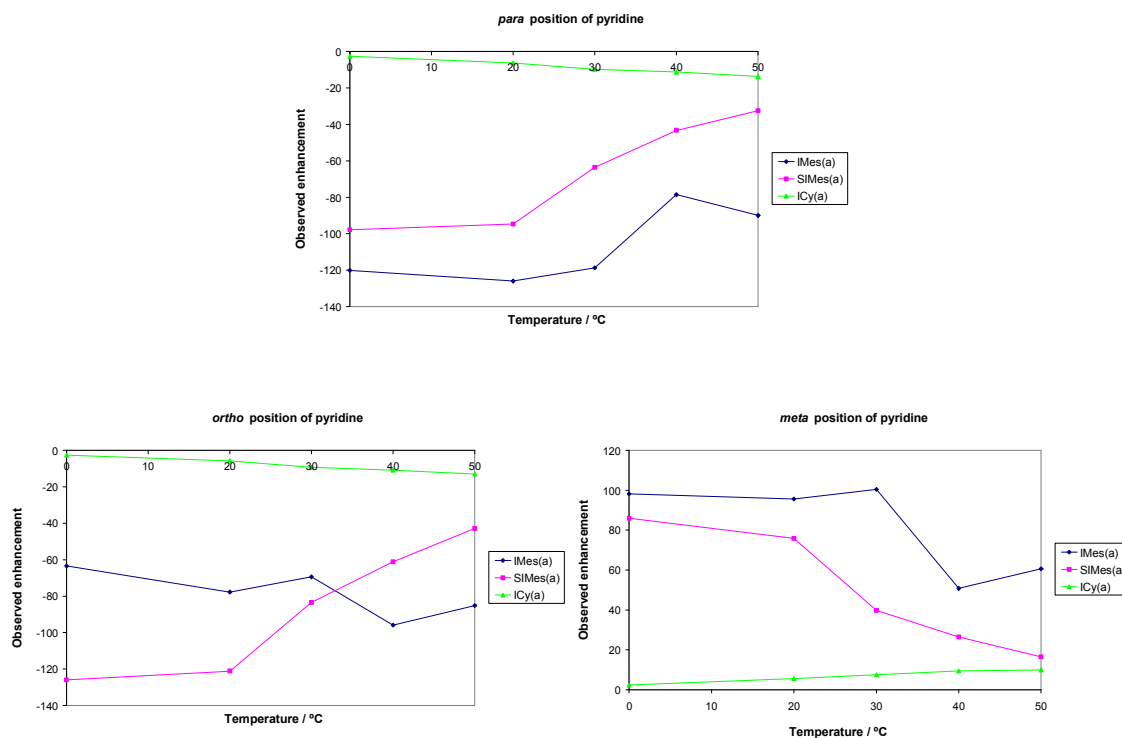


Figure 3.11 Relative <sup>1</sup>H NMR polarisation transfer to the *ortho*, *meta* and *para* resonances of pyridine when **IMes(a)**, **SIMes(a)**, and **ICy(a)** are used as the polarisation transfer catalyst in methanol as a function of temperature of *parahydrogen* addition.

As expected, **IMes(a)** shows the largest signal enhancement of the three catalysts for the *meta* and *para* resonances of pyridine, but not the *ortho* resonance (Figure 3.11). This could be due to a small amount of antiphase nature (see Chapter 1) that is observed on the *ortho* position for the duration of this experiment. For **IMes(a)**, the temperature that gives the maximum polarisation transfer is a little complicated as a maximum is

observed at a different temperature for each position. For **SIMes(a)**, the maximum signal enhancement is observed at 0 °C.

Calculations were completed to understand if some of the above results could be explained through the change in solubility of hydrogen gas in methanol at varying temperatures. Although the headspace of a typical NMR tube used in method 1 has an 8 fold excess of hydrogen gas, when this is extended to consider the number of moles of hydrogen dissolved in solution, the catalyst becomes ~310 fold in excess (see Experimental, section 8.3.2). It is therefore the act of vigorous shaking which allows exchange, and therefore polarisation transfer is minimally dependent on hydrogen solubility, as a change in temperature has a very small effect on the catalyst excess.

These experiments have shown that changing the temperature of polarisation has a significant effect on the extent of transfer experienced to the substrate, and the effect is different for each catalyst. Changing the temperature of polarisation can also be considered as a simple method to increase polarisation transfer into a new substrate when conducting initial investigations in a Young's Tap NMR tube.

Numerous methods to derive a correlation between exchange rates and the extent of polarisation transfer to pyridine have been attempted, including the fastest exchange rate constant, the product of the exchange rates and consideration of the contact time of the complex, however none of these have been successful.

### **3.4 Effect of concentration during the polarisation transfer step on polarisation transfer efficiency**

There are two publications<sup>61,66</sup> which describe a concentration dependence of SABRE. The first is for a phosphine<sup>61</sup> system and the second for a carbene<sup>66</sup> system. In the phosphine study published by Atkinson *et al.*,<sup>61</sup> the concentration of pyridine was kept constant at 103 mM (5 µL in 0.6 ml solvent) and the amount of [Ir(COD)(PCy<sub>3</sub>)(py)]BF<sub>4</sub> added was varied. This corresponded to a catalyst loading from 0.1 mol % to 20 mol %, loadings beyond this point could not be investigated as the solution became saturated with catalyst. Each sample was then heated to 318 K, shaken for 5 s and interrogated by NMR. The results of this experiment are shown pictorially in Figure 3.12.

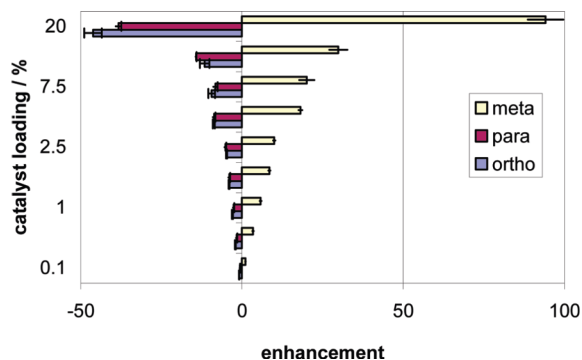


Figure 3.12 Reproduced pictorial description of the results of the catalyst loading study completed in a publication by Atkinson *et al.* (2009).<sup>61</sup>

The maximum  $^1\text{H}$  NMR signal enhancement of 94 fold was observed where the catalyst loading was 20 mol % at 318 K at 2 G. This sample was then diluted to halve the concentration of both catalyst and pyridine, but keeping the same catalyst loading. This lowered the observed  $^1\text{H}$  NMR signal enhancement to 66 fold. The effect is therefore not linear.

The effect of catalyst loading with **IMes(a)** and pyridine has also been reported in the publication by Cowley *et al.*<sup>66</sup> For an **IMes(a)** and pyridine system, the catalyst loading was varied from 0.1 mol % to 10 mol %. Higher loadings could not be investigated due to saturation of the solution. The results of this experiment are shown pictorially in Figure 3.13.

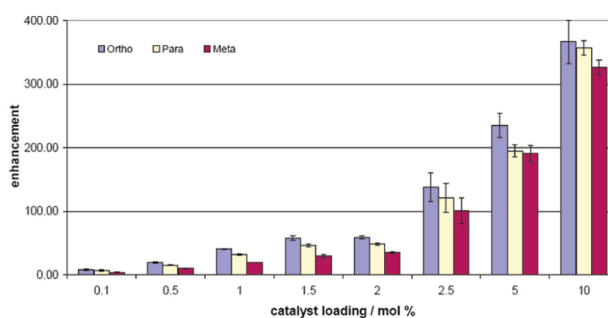


Figure 3.13 Reproduced pictorial description of the results of the catalyst loading study in a publication by Cowley *et al.* (2011).<sup>66</sup>

These data indicate a similar result to that presented for  $[\text{Ir}(\text{COD})(\text{PCy}_3)(\text{py})]\text{BF}_4$ : the higher the catalyst loading, the higher the observed enhancement. In the case of **IMes(a)**, the maximum  $^1\text{H}$  NMR signal enhancement of 360 fold on the *ortho* proton

was observed at 10 mol % catalyst loading. These results are significantly better than those for the phosphine catalyst however the dependence is still not linear.

It can be assumed that the aim of the two catalyst loading experiments reported was to understand the conditions required to gain a maximum signal enhancement for pyridine. From a pharmaceutical point of view, there are a number of reasons it would be advantageous to understand how low concentrations of substrate could be optimally examined. The most simple of these reasons is to limit the amount of substrate used. In some cases, particularly in research in a pharmaceutical company, only very small amounts of substrate are produced for characterisation. This may be too little for interrogation by conventional NMR spectroscopy. Furthermore, the polarisation of low concentration substrates may allow the detection of potentially genotoxic impurities.

The first experiments completed to target this problem concerned changing the concentration of catalyst and substrate together, such that their ratio remained the same. The idea was then extended to investigate polarisation transfer efficiency when the substrate is present in low concentration, but the catalyst concentration remains the same. This process allows us to better understand how polarisation transfer efficiency into a potentially unknown, very low concentration of substrate could be achieved.

#### 3.4.1 Effect of concentration when ratio of pyridine to catalyst remains constant on polarisation transfer efficiency

These investigations were initially completed using method 1. Concentrations of 100 mM pyridine (0.062 mmol, 5  $\mu$ l) with 5 mM **IMes(a)** catalyst (0.0031 mmol, 1.99 mg) in 0.6 ml of deuterated methanol were initially used. A series of samples, both more and less concentrated than the standard sample were then investigated, outlined in Table 3.7. In order to investigate samples at the lower concentrations, a standard concentration solution was diluted with deuterated methanol to produce samples at 10 %, 1 % and 0.1 % of the standard concentration.

	Conc. Rel. to standard	<b>IMes(a)</b>		Pyridine	
		[ <b>IMes(a)</b> ] (mM)	Mass (mg)	[pyridine] (mM)	Volume ( $\mu$ l)
Sample 1	500 %	25	10	500	25
Sample 2	300 %	15	6	300	15
Sample 3	100 %	5	2	100	5
Sample 4	10 %	0.5	0.2	10	0.5
Sample 5	1 %	0.05	0.02	1	0.05
Sample 6	0.1 %	0.005	0.002	0.1	0.005

Table 3.7 The amounts of **IMes(a)** and pyridine used in the concentration experiments. Each sample contained 0.6 ml  $d_4$ -methanol.

For samples 5 and 6, it was not possible to observe any pyridine signals in a thermal single scan. For calculation of enhancements in sample 5, the integral of the thermally derived signals has been estimated. The thermally polarised signal is proportional to the concentration of pyridine and therefore a graph of integral vs pyridine concentration was drawn to calculate the integral at the lower concentration (see Experimental). Enhancements of hyperpolarised signals have not been calculated for sample 6 as the signal strength is barely past the noise level in the spectra. In sample 5 (1% standard concentration), pyridine could be observed after interrogation by SABRE, with the largest of the signals having a signal-to-noise ratio of  $\sim 35$ , thereby giving a small but significant signal. By comparison, sample 4 (10 % standard concentration) yielded hyperpolarised signals with a signal-to-noise ratio of  $\sim 1650$ . The calculated enhancements for samples 1 to 5 and signal-to-noise ratios of samples 1 to 6 are presented in Table 3.8.

Sample	Conc. Rel. to standard	Day	<i>Ortho</i> proton		<i>Meta</i> proton		<i>Para</i> proton	
			Enhan.	S/N	Enhan.	S/N	Enhan.	S/N
1	500 %	1	-17	12172	36	16699	-37	14622
		2	-85	15087	61	12768	-75	8791
		3	-95	10898	66	14607	-77	11188
2	300 %	1	-108	31383	81	13739	-84	11055
		2	-176	23164	90	12211	-132	11047
		3	-151	9310	68	7443	-105	6629
3	100 %	1	-184	19296	137	10025	-163	6895
		2	-357	8192	114	8595	-225	8962
		3	-272	3271	69	6006	-152	5888
4	10 %	1	-351	4180	179	1672	-277	1312
		2	-308	1732	151	1281	-229	1149
		3	-324	1601	111	1076	-244	1048
5	1 %	1	-65*	90	43*	77	-54*	33
		2	-32*	35	22*	21	-43*	19
		3	-12*	11	-8*	8	-15*	7
6	0.1 %	1	-	2	-	2	-	2
		2	-	-	-	-	-	-
		3	-	-	-	-	-	-

Table 3.8 Showing the  $^1\text{H}$  NMR signal enhancement levels, and signal to noise ratios, of free pyridine proton resonances observed with indicated concentrations of **IMes(a)** and pyridine (Table 3.7) across three days. Columns labelled ‘Enhan’ contain the observed  $^1\text{H}$  NMR signal enhancement, and columns labelled ‘S/N’ contain the signal to noise ratio. \*Enhancements for the 1 % sample are calculated based on a predicted thermally polarised signal integral (see Experimental).

It should be noted that for samples 1-4, the thermally polarised spectrum used to calculate the enhancement values is recollected each day to take into account the potential deuteration of the substrate. These data show that hyperpolarisation is still achieved at very low sample concentrations. Even the 1 % sample exhibits significant polarisation, thereby enabling the detection of  $\sim 0.05 \mu\text{l}$  of pyridine ( $\sim 0.049 \text{ mg}$ ) in a single scan (Figure 3.14). It should be noted here the enhancement values in Table 3.8 for the 1 % sample are predicted and do not take into account the effect of poor signal to noise ratios for samples of this concentration. They also do not take potential deuteration of the sample over the three days into account due to the method by which the thermally polarised integral is calculated (see Experimental). Polarisation transfer was also observed in sample 6 (0.1 % standard concentration), enabling the detection of



~0.005  $\mu\text{l}$  pyridine however the signal to noise ratio for these signals was too low to reliably detect them. This might be improved by the completion of a number of averaged scans however method 2 must be used to achieve this.

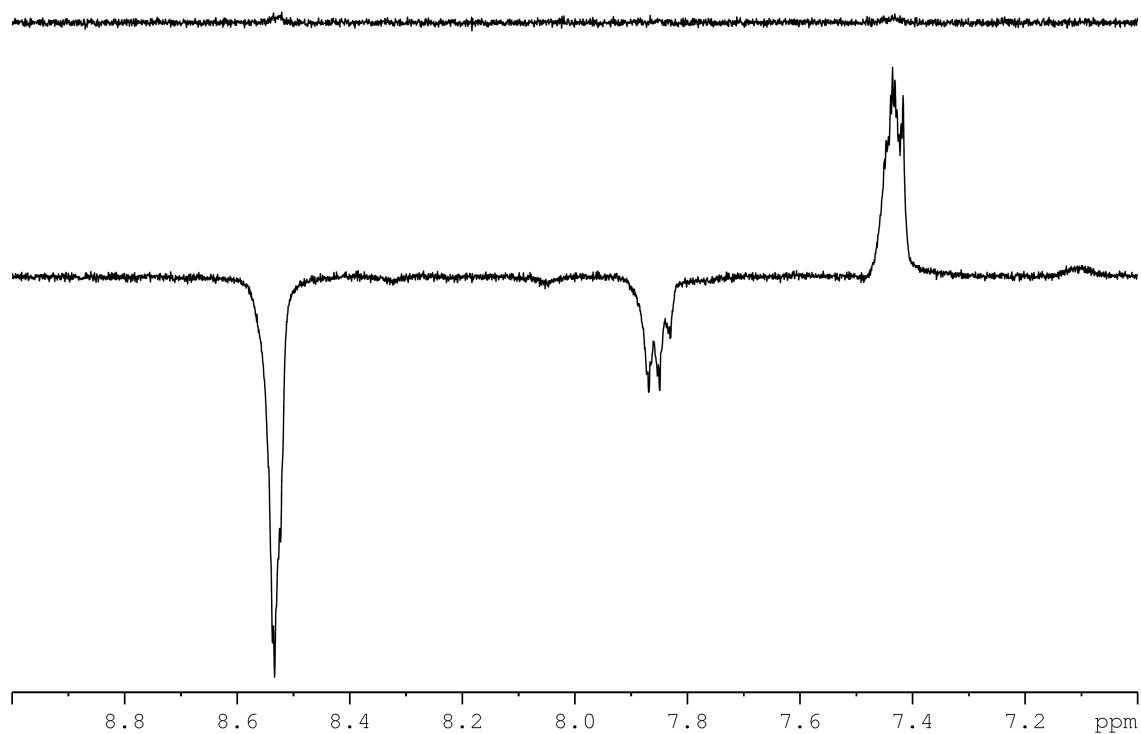


Figure 3.14 Thermal  $^1\text{H}$  NMR spectrum of pyridine (top) and a typical hyperpolarised spectrum (bottom) polarised with **IMes(a)** using method 1 at 2 G. The catalyst and substrate are at 1% of the standard concentration (0.02 mg **IMes(a)** and 0.05  $\mu\text{l}$  pyridine).

The calculated enhancements of samples 1-4 have been represented in graphical form in Figure 3.15.

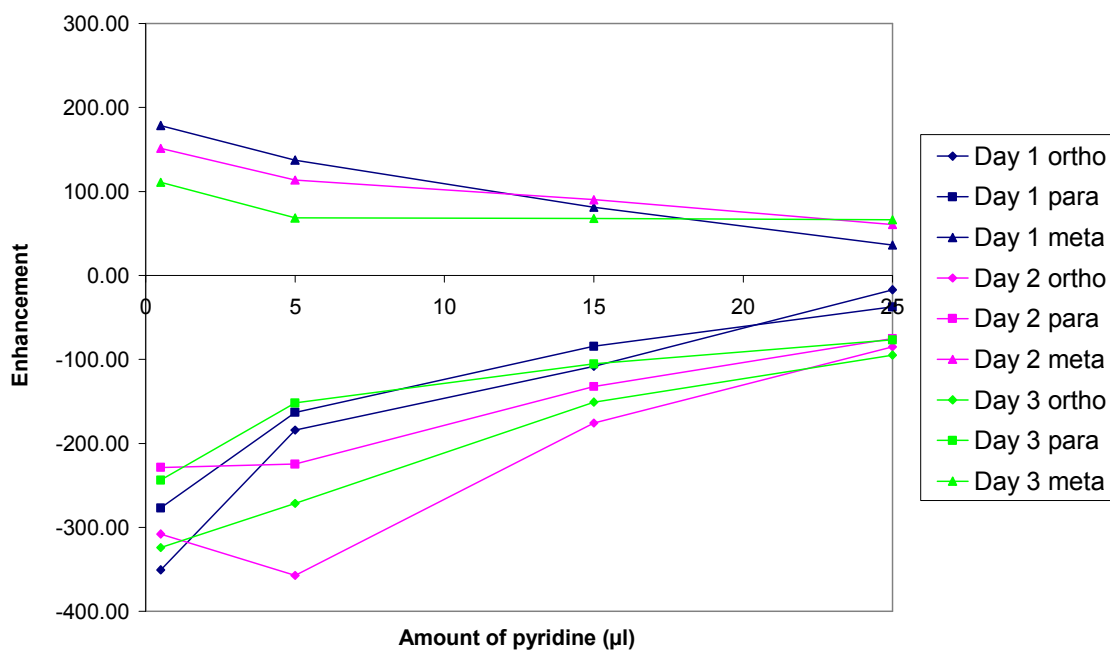


Figure 3.15 Graphical representation of the enhancement observed over three days of a concentration study where the ratio of **IMes(a)** to pyridine is kept constant (Table 3.8).

The higher concentration samples show greater signal enhancement on the second day when compared to the first. This suggests that increasing the concentration of catalyst results in a longer activation time. The highest concentration sample (sample 1) led to the highest signal-to-noise ratios owing to the higher amount of starting materials. However, the signal enhancement level is the lowest of the four samples. As the concentration of *parahydrogen* is constant in all samples, there is less *parahydrogen* per catalytic centre the higher the concentration of catalyst which could lead to the drop in observed enhancement. Generally speaking, the enhancement is greatest for sample 4 (10 % standard concentration). This could be as a result of the increased relative concentration of *parahydrogen*. Based on the calculations set out in the Experimental, there are 8.5 molecules of hydrogen for every molecule of catalyst at standard concentrations and conditions for method 1. When the concentration of catalyst is lowered to 10 % of standard concentrations, there are 76.5 molecules of *parahydrogen* per molecule of catalyst.

This type of catalyst is a known HD exchange catalyst,<sup>77,78</sup> a reaction discussed in Chapters 1 and 2. Completing the experiment over three days also allowed an investigation into the level of pyridine deuteration achieved with **IMes(a)**. This has been based on thermal single scan <sup>1</sup>H NMR spectra.

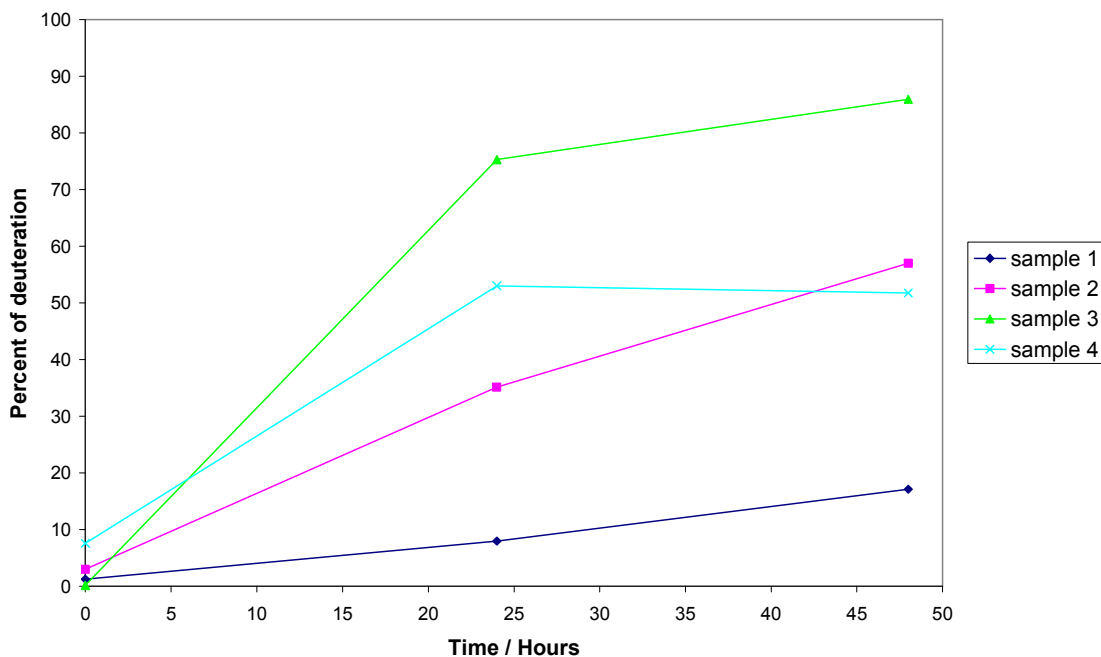


Figure 3.16 Deuteration level of the *ortho* position of pyridine when reacted with **IMes(a)** in  $d_4$ -methanol over a period of 48 hours. For sample numbers, refer to Table 3.7.

The results depicted Figure 3.16 indicate the level of deuteration is significant over a time period of 24 hours. It is therefore pertinent to complete all required experiments as quickly as possible after activation.

This experiment was repeated using method 2, as this could provide a greater net enhancement due to the ability to optimise the polarisation transfer through changing the magnetic field of polarisation. For a flow probe experiment, concentrations of 100 mM pyridine (0.31 mmol, 24  $\mu$ l) and 5 mM **IMes(a)** catalyst (0.0155 mmol, 9.92 mg) in 3 ml of deuterated methanol were initially used. In order to investigate the lower concentration samples, a standard concentration solution was diluted with deuterated methanol to produce samples at 10 %, 1 % and 0.1 % of the standard concentration. The results after analysis are presented in Table 3.9.

[IMes(a)] (mM)	[pyridine] (mM)	Conc. Rel. to standard	Observed <sup>1</sup> H NMR signal enhancement		
			<i>Ortho</i>	<i>Meta</i>	<i>Para</i>
5	100	100 %	-322	-241	-535
0.5	10	10 %	-178	-124	-162
0.05	1	1 %	-65	-15	-7.2
0.005	0.1	0.1 %	-	-	-

Table 3.9 Table showing the extent polarisation transfer achieved in a single scan at the indicated concentrations of IMes(a) and pyridine using method 2, polarised in a magnetic field of 75 G.

The results found are comparable with those found in method 1. As the polarisor is set to a magnetic field of 75 G, a larger net signal enhancement is expected. However, there is a longer time between the addition of *parahydrogen* and the measurement so the hyperpolarised states have had a greater time to decay. It should be noted that the sample at 0.1 % standard concentration resulted in the observation of small peaks however the peaks observed were too small to be reliably assigned.

These data show it is possible to detect a small amount of pyridine in these experiments where the catalyst loading remains constant. When investigating low concentration impurities, the absolute concentration of that impurity will be unknown and therefore adding the correct amount of catalyst will not be possible. A different approach is therefore required.

#### 3.4.2 Effect of concentration when concentration of catalyst remains constant on polarisation transfer efficiency

In the case where an impurity is under investigation, for instance a potentially harmful reactant which has not been removed effectively, the concentration of that impurity will be unknown, and therefore a specified amount of catalyst will be added. This is likely to be in great excess of the impurity of interest. It is known that if IMes(a) is activated with a lower than 1:3 catalyst to substrate ratio, the catalyst becomes unstable and is no longer able to transfer polarisation. To overcome this, a stoichiometric amount of acetonitrile (3 equivalents compared to 1 equivalent of catalyst) is added to act as a stabiliser. The acetonitrile is present in all samples to keep the conditions consistent across the varying pyridine concentrations. This concept was first investigated using method 1 and the results of this study are presented in Table 3.10.

Sample	[pyridine] mM	Ratio of cat. to py	<i>Ortho</i> proton		<i>Meta</i> proton		<i>Para</i> proton	
			Enhan.	S/N	Enhan.	S/N	Enhan.	S/N
1	1000	1 : 200	-7	13771	5	6586	-6	4088
2	500	1 : 100	-16	15335	10	6752	-14	4670
3	100	1 : 20	-83	14250	60	7009	-83	5343
4	10	1 : 2	-273	6271	190	3709	-301	2818
5	1	1 : 0.2	-21	13	81	10	-209*	407*
6	0.1	1 : 0.02	-	54 <sup>+</sup>	-	80 <sup>+</sup>	-	33 <sup>+</sup>

Table 3.10 Table detailing the signal enhancement levels and signal to noise ratios of free pyridine resonances observed with indicated concentrations of pyridine, a standard concentration of **IMes(b)** and a stoichiometric volume of acetonitrile. Columns labelled 'Enhan' contain the observed <sup>1</sup>H NMR signal enhancement, and columns labelled 'S/N' contain the signal to noise ratio. \*donates the bound pyridine signal was not base-line resolved from the free pyridine signal and therefore the value is a combination of both signals. <sup>+</sup>denotes the value refers to the bound pyridine signal alone, not the free signal.

It was not possible to calculate the enhancements for sample 6 as no free pyridine signals were observed in the thermal single scan proton spectrum used for comparison. It should be noted that as a result of the high relative concentration of catalyst to pyridine, in some cases the pyridine remains bound and therefore the signals for the bound resonances are more significant than those of the free pyridine. This is particularly evident in sample 6 where no signals corresponding to free pyridine are observed, however, those corresponding to bound pyridine are observed. In sample 5, the bound signals show greater enhancement and signal to noise ratios than the free signals. Samples 1 to 4 show similar enhancement values for both free and bound pyridine as expected. Here, the free pyridine signals are the most significant in the spectrum.

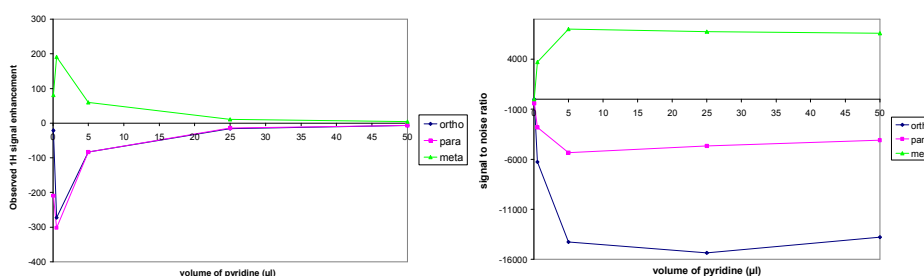


Figure 3.17 Graphical representation of the effect of pyridine concentration on the resultant signal enhancement (left) and signal to noise ratios (right) of free pyridine signals when pyridine is hyperpolarised with a standard concentration of **IMes(b)** in the presence of a stoichiometric amount of acetonitrile.

In Section 3.4.1 (pg 154), it was observed that a slight drop off in enhancement is observed when the concentration of both pyridine and **IMes(a)** was increased past the standard concentration. This was put down to the low relative concentration of *parahydrogen* in the sample compared to the concentration of pyridine. In Table 3.10 and Figure 3.17, a similar drop off in signal enhancement is observed as pyridine concentration is increased however it is much more significant now the relative concentration of catalyst has not been increased by the same proportion. A possible reason for this is the lower concentration of active sites for polarisation transfer due to the lower concentration of catalyst. It can be observed that a drop in concentration from 100 % standard concentration to 10 % concentration results in a significant increase in the level of observed polarisation transfer. This area was therefore investigated more closely to understand if a higher maximum can be obtained. The results are presented in Table 3.11.

Sample	[pyridine] (mM)	Pyridine conc. rel. to standard	Observed <sup>1</sup> H NMR signal enhancement		
			<i>Ortho</i>	<i>Meta</i>	<i>Para</i>
1	100	100 %	-70	62	-78
2	80	80 %	-115	102	-134
3	60	60 %	-111	137	-169
4	40	40 %	-257	193	-265
5	20	20 %	-384	273	-378

Table 3.11 Table detailing the signal enhancement levels and signal to noise ratios of free pyridine resonances observed with indicated concentrations of pyridine, a standard concentration of **IMes(a)** and a stoichiometric volume of acetonitrile.

Table 3.11 is represented graphically below in Figure 3.18.

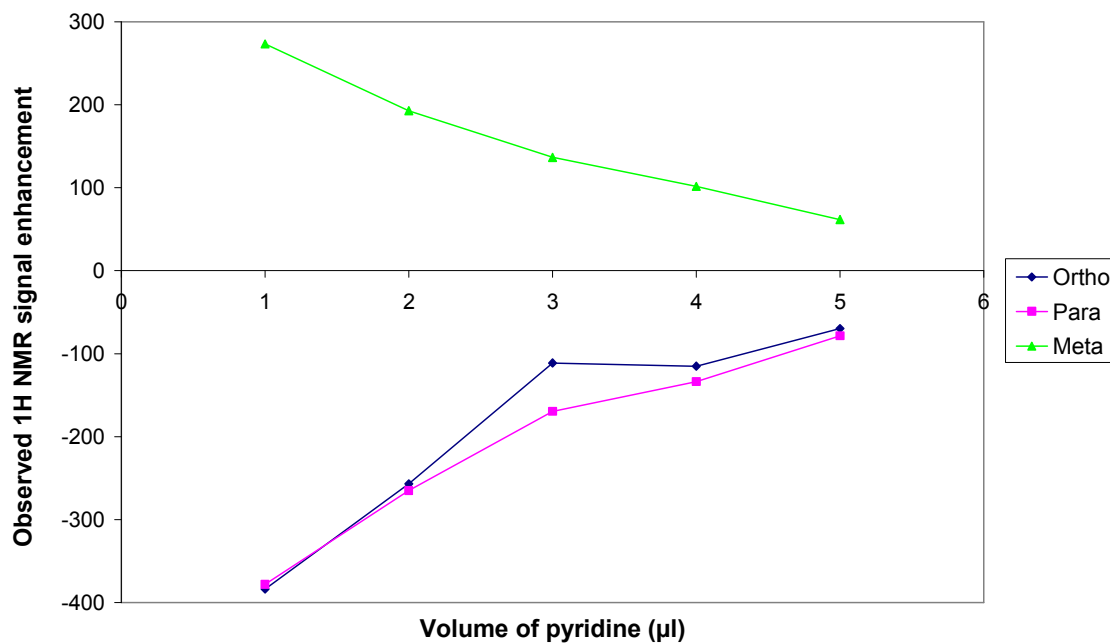


Figure 3.18 The graphical representation of Table 3.11 investigating the effect of pyridine concentration on the resultant signal enhancement of free pyridine signals when hyperpolarised with a standard concentration of **IMes(a)** in the presence of a stoichiometric amount of acetonitrile.

It is possible to observe the polarisation transfer into pyridine increases as the amount of pyridine reduces. With the exception of the enhancement observed on the *ortho* position with an addition of 3 µL pyridine, all points show a near linear correlation, indicating that addition of 1 µL pyridine gives the concentration resulting in the maximum enhancement.

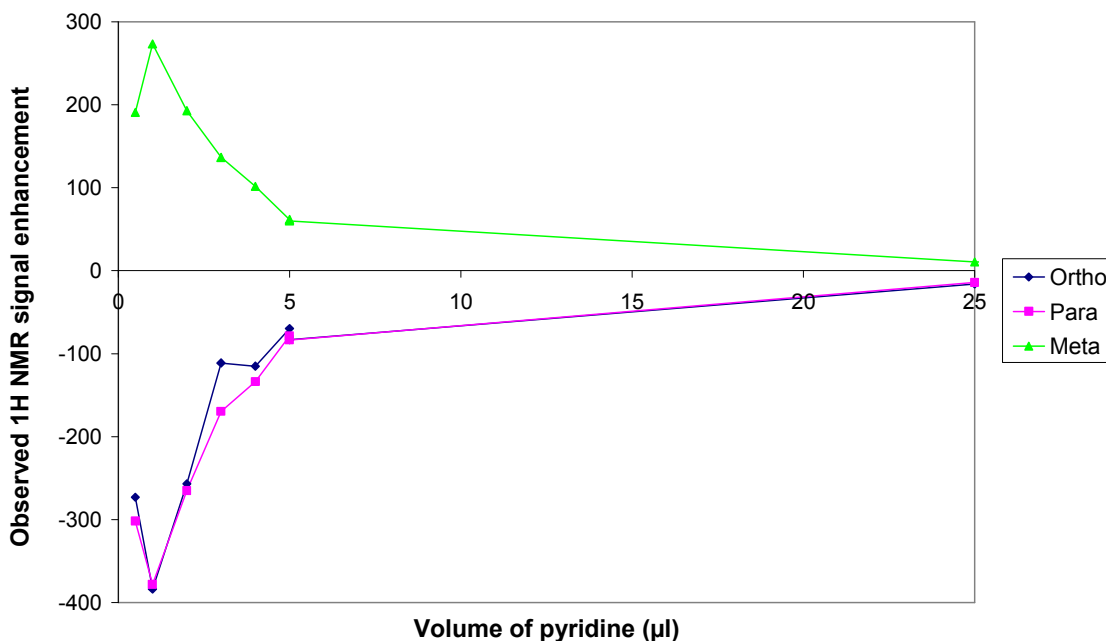


Figure 3.19 The graphical representation of Table 3.10 and Table 3.11 investigating the effect of pyridine concentration on the resultant signal enhancement of free pyridine signals when hyperpolarised with a standard concentration of **IMes(a)** in the presence of a stoichiometric amount of acetonitrile.

Combination of the two sets of data presented in Table 3.10 and Table 3.11 results in a clear maximum being observed, when 1  $\mu\text{L}$  of pyridine is added.

In general it has been seen that lowering the concentration of pyridine, or pyridine and catalyst, increases the level of polarisation transfer into pyridine. A possible reason for this is the increased relative concentration of *parahydrogen* (see Experimental, section 8.3.1). Another factor that can affect the extent of polarisation transfer is the number of available catalytic sites within a sample, and so if the concentration of the substrate is significantly higher than that of the catalyst, low enhancements are observed.

Conversely, if the catalyst is in a significantly higher concentration compared to the substrate, it is difficult to observe enhancements on the free signals of that substrate, however, significant enhancements can be observed on the bound resonances. This is an important observation as the substrate is also in lower concentration than that of the stabilising additive acetonitrile (0.062  $\mu\text{mol}$  pyridine compared to 9.3  $\mu\text{mol}$  acetonitrile), and it is still possible to observe the desired substrate.



### 3.5 Effect of solvent on polarisation transfer efficiency

All of the work described so far has been completed in a methanol solution. Although methanol is suitable for most of the substrates investigated in this thesis, this may not always be the case. Indeed in industry, the most common NMR solvents are chloroform and DMSO. Polarisation transfer to pyridine through SABRE using **IMes(a)** was therefore investigated in six solvents: methanol, ethanol, DCM, chloroform, DMSO and acetone.

Initial experiments revealed that the catalyst activation time was not the same in all solvents. In solvents such as chloroform, activation of the catalyst took much longer. For this reason, each sample was activated for the time outlined in Table 3.12.

Solvent	Time for activation after hydrogen addition
Methanol	Mins at room temperature
Ethanol	Mins at room temperature
DCM	Mins at room temperature
Chloroform	Overnight at 25 °C
DMSO	Overnight at 25 °C
Acetone	Mins at room temperature

Table 3.12 Time required to fully activate **IMes(a)** in the indicated solvents where pyridine is the substrate.

As DMSO and chloroform take a long time to activate fully, these were put under a hydrogen atmosphere, shaken and stored at 25 °C overnight. For those which activate quickly (methanol, ethanol, DCM and acetone), the addition of hydrogen and initial shake were completed ~10 mins before interrogation by SABRE. These were not activated at the same time as the DMSO and chloroform samples to minimise proton – deuterium exchange to the *ortho* position of pyridine as much as possible. Polarisation transfer was then investigated at three temperatures: room temperature, 40 °C and 0 °C. This enables us to monitor the effect of increasing and decreasing the ligand exchange rates in each case. To achieve this, the head space of the NMR tube was filled with *parahydrogen* but not shaken. The sample was then stored at the desired temperature for 3 min, after which the NMR tube was quickly wiped dry, and the sample shaken for 8 s before interrogation by NMR. The results of these experiments are outlined in Table 3.13.

Solvent	Pyridine proton resonance	Temperature / °C		
		0	20	40
Methanol	<i>Ortho</i>	-63.5	-77.7	-95.9
	<i>Meta</i>	98.3	95.6	50.8
	<i>Para</i>	-120.2	-126.0	-78.5
Ethanol	<i>Ortho</i>	-100.3	-135.5	-93.2
	<i>Meta</i>	86.0	116.9	72.1
	<i>Para</i>	-90.5	-111.1	-72.3
DCM	<i>Ortho</i>	-64.4	-39.2	-28.0
	<i>Meta</i>	-24.1	-16.9	-12.4
	<i>Para</i>	-65.9	-38.7	-30.6
Chloroform	<i>Ortho</i>	-40.8	-40.3	-19.2
	<i>Meta</i>	-3.0	-4.2	-2.9
	<i>Para</i>	-43.5	-41.3	-20.6
DMSO	<i>Ortho</i>	n/a	-12.1	-26.0
	<i>Meta</i>	n/a	7.6	15.8
	<i>Para</i>	n/a	-14.4	-33.1
Acetone	<i>Ortho</i>	-24.6	-14.5	-9.7
	<i>Meta</i>	-10.8	-7.4	-5.2
	<i>Para</i>	-24.8	-14.0	-9.7

Table 3.13 Polarisation transfer to pyridine using **IMes(a)** under the indicated conditions. The notation 'n/a' denotes the experiments could not be completed due to the temperature being significantly below melting point of DMSO.

Results could not be collected for DMSO at 0 °C as its melting point is 18 °C.

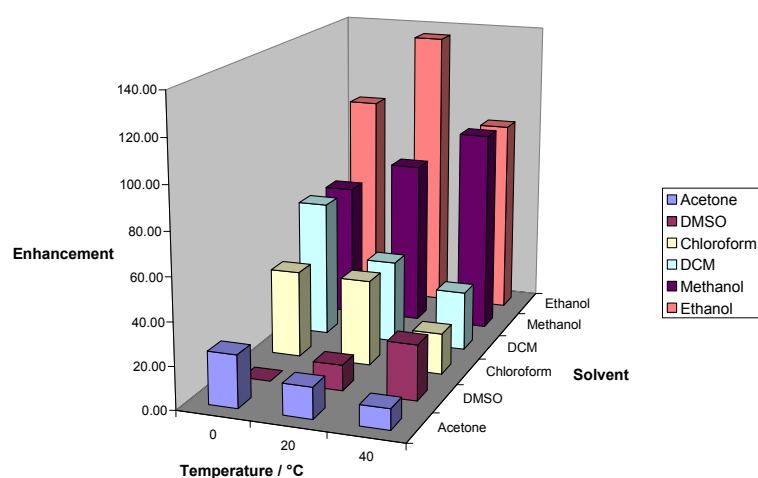


Figure 3.20 A 3D graphical interpretation in magnitude (*ortho* only) of Table 3.13, indicating the polarisation transfer to pyridine with **IMes(a)** under the indicated conditions.

It can be observed that the greatest signal enhancement can be obtained when using ethanol as a solvent. The experiment has also shown that significant polarisation transfer occurs in non-polar solvents such as DCM and chloroform. Chloroform shows an average enhancement of 40 fold and DCM can get as high as 60 fold when the temperature of addition of *parahydrogen* is lowered to 0 °C. The different solvent systems exhibit different polarities and create different binding modes, and therefore have an effect on the observed exchange rates and consequently the level of polarisation transfer observed.

Although interrogation of a sample in ethanol gives the greatest enhancement of the solvent investigated, methanol will be used for the majority of the work in this thesis. This is because methanol still gives significant polarisation transfer however holds the added benefit of being a much cheaper solvent.

### 3.6 Summary

This chapter reports on investigations into a number of variables as potential routes in order to optimise the extent of polarisation transfer into a specific substrate. These include the magnetic field (PTF), temperature, concentration and solvent present during the polarisation transfer step, and how they vary for each of the three previously discussed catalysts. It was found that each variable had a significant effect on the level of polarisation transfer observed within a system, and results also varied with the catalytic system. Taking the effect of changing the PTF on polarisation transfer into pyridine, the observed <sup>1</sup>H NMR signal enhancement for the *para* position increased from 38 fold at a PTF of 0 G to -103 fold at a PTF of -90 G for **SIMes(a)** and from 4 fold at a PTF of 0 G to -9 fold at a PTF of -60 G for **ICy(a)**, where each is quoted for the maximum PTF for the stated catalyst. The studies presented in this chapter demonstrate that the PTF yielding the maximum signal intensity is different for each catalyst. These differ from -90 G to -60 G when considering polarisation transfer into pyridine. It will later be shown that this also differs for different substrates (Chapters 4, 6 and Experimental). It has been postulated that the extent of polarisation transfer is based on a fine balance between the difference in chemical shifts of the nuclei of interest and the J-coupling of the system<sup>59</sup> (Chapter 1) and therefore that the extent of polarisation transfer is dependent on the PTF as this affects the relative chemical shifts of the nuclei. The J-coupling of the system does not change with external field.

The relative chemical shift differences between the key resonances in the catalytic template vary by ca <1 % as evidenced in (Chapter 2) and Table 3.14.

Catalyst	<sup>1</sup> H NMR chemical shifts (ppm)		
	Py trans to hydride	Hydride ligands	Difference
<b>IMes(a)</b>	8.34	-22.53	30.87
<b>SIMes(a)</b>	8.32	-22.69	31.01
<b>ICy(a)</b>	8.75	-22.49	31.24

Table 3.14 The key chemical shifts and chemical shift differences observed for three SABRE catalysts, relevant to the mechanism of polarisation transfer. ‘Py trans to hydride’ refers to the *ortho* proton only.

The change in chemical shift difference is small between the three catalysts while the difference in the extent of polarisation transfer between the three systems is great, varying from ~10 fold for **ICy(a)** to ~500 fold for **IMes(a)**. It is therefore likely that the contact time of the active species is a key variable in the efficiency of polarisation transfer. This has been illustrated through determination of the rate constants of the systems considered and is supported by the fact that increasing the temperature of the **ICy(a)** system (with relatively slow exchange rate constants) but decreasing the temperature of the **SIMes(a)** system (with relatively fast exchange rate constants) has the effect to increase the extent of polarisation transfer. This finding suggests the theory related to polarisation transfer needs to be revised to explore the effect of changing contact time.

In the future, it would be preferable to experimentally investigate the effect of changing both temperature and field of polarisation concurrently. This is not currently possible as our current mixing chamber does not have a temperature control function although this is desirable.

The effect of concentration was investigated for the **IMes(a)** SABRE catalyst only. It was found that decreasing the concentration to one tenth of the standard concentrations had the result of dramatically increasing the extent of polarisation transfer observed into pyridine. This is explained by the relative excess of *parahydrogen* gas available to the sample. With the catalyst at a standard concentration, an excess of 8.5 fold hydrogen gas is present but this is increased to an excess of 77 when the catalyst concentration is reduced to one tenth of the standard concentration. Using the SABRE method, in a 0.6 ml sample, 0.05  $\mu$ L (1 mM) of pyridine can be detected in a single scan producing S/N

ratios of 90, 77 and 33 for the *ortho*, *meta* and *para* resonances of pyridine. This is approximately 0.05 mg of substrate, between 10 and 20 times less than that used for  $^1\text{H}$  spectra in standard practice for NMR spectroscopy. These investigations also revealed an additional complication in the form of deuteration of the *ortho* position of pyridine after an extended period of time.

The solvent has also been shown to play a major role in the efficiency of the SABRE catalyst. The relative chemical shifts of any nuclei are related to the solvent and therefore the chemical shift differences of the active complex are different depending on the solvent used. The solvent also has an effect on the exchange rates experienced by the complex due to differing polarities, an effect which is particularly important in charged systems such as those investigated here. During these experiments it was found possible to obtain enhancements in  $^1\text{H}$  NMR spectra when the catalyst and solvent were dissolved in methanol, ethanol, DCM, chloroform, DMSO and acetone. Of these six, maximum signal enhancements were observed in ethanol, with methanol running a close second. This indicates that SABRE can be completed in other solvents should they be required.

It has been assumed that the solvent is benign in our systems however it is known that acetonitrile, acetone and DMSO can bind to the catalysts. It is also evident in the hydride region of the resultant NMR spectra collected for each solvent, that a combination of active species may be present. An idea for future work within this project would be to characterise these active complexes, and measure the related exchange rate constants.

To conclude, it has been observed that a number of variables can be changed which affect the extent of polarisation transfer into a substrate molecule and these must be considered when optimising the SABRE effect for a new substrate.

## 4 Chapter 4 - Optimisation of quinoline

### 4.1 Introduction

Up to this point, pyridine and mono-substituted pyridine analogues are the only molecules that have been considered as substrates for hyperpolarisation by SABRE. Pyridine itself has acted as a good model substrate however it is most commonly found in larger structures with a number of substitutions. It was therefore thought prudent to investigate a larger system. Quinoline was chosen for this task as it contains a pyridine moiety fused to a benzene ring. This gives an aromatic substrate which contains 7 protons, all of which are magnetically different from each other. The quinoline moiety is also found in many current and potential drug molecules, such as in the treatment for malaria, arrhythmia, and some bacterial infections and potentially in the treatment of Alzheimer's and as targeted cancer therapies. These are discussed in greater detail in the following paragraphs.

#### 4.1.1 Quinoline analogues as drugs

##### 4.1.1.1 Quinine and quinidine

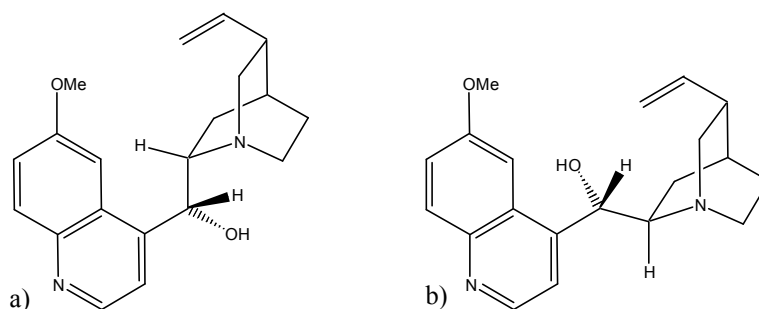


Figure 4.1 Structures of a) quinine and b) quinidine. Copied from Raheem *et al.* (2003).<sup>110</sup>

Quinine and quinidine (Figure 4.1a and Figure 4.1b respectively) are cinchona alkaloids, found in the bark of the cinchona tree.<sup>111</sup> They are diastereoisomers of each other and consequently, despite being composed of the same parts, each holds significantly different pharmaceutical properties.

Quinine is one of the oldest anti-malarial drugs originally administered through the consumption of ground bark from the cinchona tree, and the drug is still used to treat the virus today.<sup>111,112</sup> When the synthetic drug, chloroquine (Section 4.1.1.2) was invented, quinine was used less frequently however resistance to chloroquine soon became apparent, and the use of quinine increased again. As a readily available compound, it is commonly used to treat malaria in resource limited settings as it can be difficult to maintain a steady supply of the alternative, artemisinin-based combination therapy in these areas. Despite concerns about potential complications such as interactions with antiretroviral drugs for HIV treatment or antituberculosis drugs, quinine holds a critical role as a malarial treatment due to its safety during pregnancy.<sup>111</sup>

Quinine and quinidine are also used for the alleviation of muscle cramps in the UK.<sup>113</sup> In the literature review completed by Corbani *et al.* (2008),<sup>113</sup> a series of trials are compared to reveal both quinine and quinidine reduce the frequency of cramps, but not intensity or duration, with few side effects.

Quinidine is used mainly as an antiarrhythmic drug.<sup>114,115</sup> It has been proved effective in treatment of many arrhythmias, such as atrial fibrillation,<sup>116</sup> idiopathic ventricular fibrillation, Brugada Syndrome<sup>117</sup> and Short QT syndrome.<sup>115</sup>

Atrial and ventricular fibrillation is a condition where the muscles in the atria or ventricles are uncoordinated, and consequently, do not contract properly. In 1997, a study was completed by Innes *et al.* (1997)<sup>116</sup> to compare two combination therapies for the treatment of paroxysmal atrial fibrillation (self-terminating, recurrent episodes) in emergency departments. Quinidine was a part of the combination drugs in both groups, which compared the efficacy of vermapamil and quinidine compared to digoxin and quinidine. As a treatment course, the vermapamil or digoxin was administered first and is used to control the ventricular rate. This is then followed by the admission of quinidine, which is used to convert the arrhythmia to a normal sinus rhythm. The study found that the sequential combination of vermapamil followed by quinidine was more effective and quicker in converting to normal sinus rhythm, suggesting vermapamil is more effective at controlling ventricular heart rate.

Idiopathic ventricular fibrillation is a form of ventricular fibrillation which presents with no obvious heart disease.<sup>118</sup> In 1999, a study completed by Belhassen *et al.*<sup>118</sup> was conducted to investigate the effect of quinidine on patients suffering with idiopathic

ventricular fibrillation. The study was based on 27 patients who presented with a normal ECG but suffered with spontaneous ventricular fibrillation or tachycardia which can also be induced in an electrophysiology (EP) study. Of these 27 patients, 25 were given oral quinidine which had the effect to prevent induction of ventricular fibrillation in 96 % of patients. Three of these patients developed an intolerance to quinidine however a transfer onto disopyramide proved successful.

In 2005, Haghjoo *et al.*<sup>117</sup> presented a patient who had been administered quinidine as a treatment for Brugada Syndrome, a subtype of idiopathic ventricular fibrillation resulting in ventricular tachycardia and fibrillation which may have genetic causes.<sup>118</sup> The patient had suffered cardiac arrest twice in 3 months, but showed no evidence of structural heart disease and presented a normal resting ECG, but with typical Brugada changes in provoked ECG. Consequently, an implantable cardioverter-defibrillator (ICD) was implanted, designed to correct sudden ventricular arrhythmias. 10 days after implantation, the ICD appropriately and successfully discharged 9 times in 2 days to terminate ventricular fibrillation. Oral quinidine was therefore administered to have the effect of normalising any previously observed ECG abnormalities, and the patient remained free of symptoms and ICD discharges for the 19 month follow up period.

Short QT syndrome is a genetic disorder which can cause atrial fibrillation and ventricular fibrillation and consequently, an increased risk of sudden cardiac death.<sup>115</sup> Admission of quinidine to patients with Short QT syndrome caused a lengthening of the QT interval, normalising sinus rhythm.

#### 4.1.1.2 Chloroquine and hydroxychloroquine

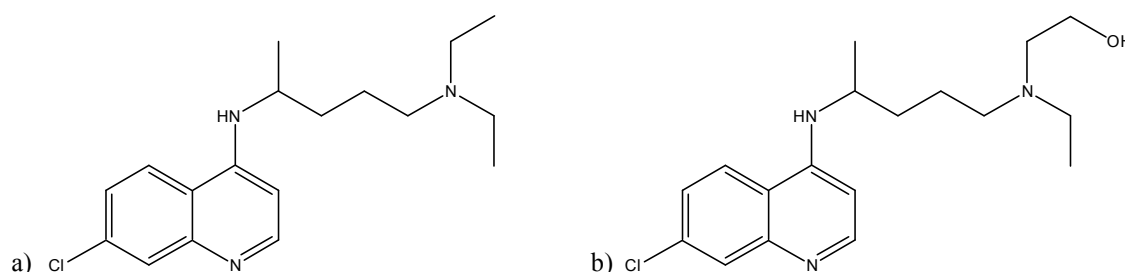


Figure 4.2 Structure of a) chloroquine and b) hydroxychloroquine.

Chloroquine (Figure 4.2a) was first synthesised by Hans Andersag in July 1934.<sup>119</sup> The drug was patented in 1939, and underwent clinical trials, and was used as a first line



antimalarial drug from 1945 for 20 years.<sup>119</sup> At this point, chloroquine-resistant strains of malaria became prevalent, and consequently chloroquine was used much less frequently.<sup>112,120</sup> In 1955, hydroxychloroquine (Figure 4.2b) was introduced as a less toxic version of chloroquine which still holds the same pharmacological advantages.<sup>121</sup> Hydroxychloroquine has also been used to treat malaria.<sup>121-123</sup>

Chloroquine (among other drugs) was administered to soldiers in the Second World War as a preventative measure against malaria. During this time, the soldiers noticed improvements in rashes and inflammatory arthritis, leading to investigations into other potential uses of chloroquine and hydroxychloroquine, such as antimicrobial,<sup>124</sup> metabolic,<sup>125</sup> cardiovascular, antithrombotic<sup>126</sup> and antineoplastic effects.<sup>121</sup>

As an antibacterial agent, hydroxychloroquine is most recognised as part of a combination treatment with doxycycline for chronic Q-fever endocarditis caused by *Coxiella burnetii* bacteria.<sup>121</sup> Chronic Q fever endocarditis is fatal in 25 % to 60 % of patients and the recommended treatment in 1999 of tetracycline and quinolone can be taken from three years to a lifetime due to the high occurrence of relapses.<sup>127</sup> In 1999, Raoult *et al.*<sup>127</sup> completed a study investigating the effectiveness of two combination therapies, doxycycline with quinolone compared to doxycycline with hydroxychloroquine. Of the 14 patients treated with doxycycline and quinolone, 1 patient died, 1 patient was still being treated, 7 relapsed and 5 were cured with a mean duration of treatment to cure being 55 months. Of the 21 patients treated with doxycycline and hydroxychloroquine, 1 patient died, 3 were still being treated, and 17 were cured with a mean duration of treatment to cure being 31 months. No patient who was treated for 18 months or longer relapsed, while only 2 who were treated for 12 months relapsed. This study shows treatment of Q fever endocarditis with doxycycline and hydroxychloroquine shortens the treatment period and reduces the number of relapses compared to the previous treatment of doxycycline with quinolone.<sup>127</sup>

Currently, there are no known cures for the human corona virus, the cause of approximately one third of common colds. In 2003, a resistant strain of the virus was discovered, which was found to be the cause of severe acute respiratory syndrome (SARS). Chloroquine has recently shown the potential to inhibit the replication and spread of the virus in vitro.<sup>128,129</sup> In 2004, a study was completed by Keyaerts *et al.*<sup>128</sup> to

investigate the effect of chloroquine on a cell line infected with SARS-CoV. Results showed that the  $IC_{50}$  of the complex for the virus was 8.8  $\mu$ M. This is around 1,000 fold below the human plasma level reached when chloroquine is administered for treatment of acute malaria, and in the same range as when chloroquine is used in the treatment of rheumatoid arthritis. In 2005, a second study was completed by Vincent *et al.*<sup>129</sup> investigating the effects of chloroquine on the SARS-CoV virus. The results found in this study agreed with those found by Keyaerts *et al.*<sup>128</sup> (discussed above), but were also extended to investigate the preventative ability of chloroquine against SARS-CoV. A cell line was treated with chloroquine for 24 hrs prior to infection to find the drug was able to inhibit SARS-CoV virus. Chloroquine could therefore potentially be used as a prophylactic drug during a breakout or for travellers, or as a treatment in established infections.

In 1987, a study was completed by Smith *et al.*<sup>125</sup> to investigate if this side effect could be used to treat non-insulin-dependent diabetes mellitus. A control group, and group of diabetic patients completed an overnight fast, then drank 200 ml water with 75 g sugar dissolved in it. The levels of glucose and insulin were monitored for three hours. Chloroquine was then administered for two and a half days and the test repeated on the day of the last dose. Chloroquine had little effect on the control group, however, glucose tolerance was significantly improved in the diabetes mellitus group. Today, this treatment has been largely superseded by other drugs.

Hydroxychloroquine has also been shown to help prevent thrombosis in patients with anti-phospholipid antibodies,<sup>130</sup> but also those who also have lupus.<sup>126</sup> It has also been shown to reduce thromboembolic events in patients undergoing total hip replacements.<sup>131</sup>

Chloroquine has been shown to have antineoplastic effects. This was first observed when the drug was administered as a preventative measure against malaria in Tanzania, and a reduced incidence of Burkitts Lymphoma was observed.<sup>121,132</sup> Chloroquine has also been shown to have antineoplastic effects *in vitro* against human lung cancer.<sup>133</sup> In 2008, a study completed by Hu *et al.*<sup>134</sup> aimed to investigate the effect of adding chloroquine to a regime of Akt inhibitors, *in vitro*. The group investigated three breast cancer cell lines and found that chloroquine alone had a very small effect on the growth inhibition factor of these cells, but also low cytotoxicity on normal cells. A different

story was true when considering the addition of chloroquine to 11 different Akt inhibitors. When comparing the Akt as a monotherapy to the Akt plus 20  $\mu\text{M}$  chloroquine, the ratio of the  $\text{GI}_{50}$  of normal cells to cancer cells was increased from an average of 2.47 to 16.65 across the 11 Akt inhibitors. This shows the potential for chloroquine to sensitize cancer cells to Akt inhibitor therapy.

Antineoplastic effects have also been observed with hydroxchloroquine. It has been shown to have antineoplastic effects *in vitro* in solid tumours of breast cancer<sup>135</sup> and induce apoptosis in malignant cells of chronic lymphocytic leukemia.<sup>136</sup>

#### 4.1.1.3 8-hydroxyquinoline analogues

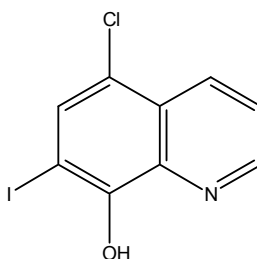


Figure 4.3 Structure of Clioquinol.

The 8-hydroxyquinolines possess a number of therapeutic properties. The best known 8-hydroxyquinoline analogue is Clioquinol (Figure 4.3). Clioquinol was originally used in as an antiparasitic agent however potential neurotoxicity led to the drug being withdrawn in the 1970s as an oral medication but it is still available as a topical treatment.<sup>137</sup> More recently, clioquinol has received attention as a potential treatment for Alzheimers disease.<sup>137,138</sup>

Clioquinol may have a positive effect on the progression of Alzheimers disease because it can bind copper in the brain.<sup>139</sup> It is able to therefore remove copper from the protein aggregates in the brain, potentially reversing the aggregation.<sup>137,140</sup> When the drug underwent pilot phase II clinical trials, it was found that those who were more severely affected by Alzheimers Disease showed the most significant benefit, through the condition worsening minimally.<sup>141</sup>

In 2005, Ding *et al.*<sup>142</sup> published a study to investigate the potential anticancer activity of clioquinol against human cancer cells *in vitro* and *in vivo* in mice. For the *in vitro* studies, a number of cell lines were investigated to cover a range to tissue origins. These

were human B-cell lymphoma lines and breast, ovarian, cervical, bladder and pancreatic cancer cells. Treatment of these cells with clioquinol proved to be cytotoxic to the cancer cells with a maximum  $IC_{50}$  of  $40 \mu\text{mol/L}$ , where reduced cell viability was observed after 72 hours. Clioquinol was also shown to inhibit growth of a human ovarian cancer line grafted to mice without clinical observations of toxicity or weight loss.

The gluconjugates of 8-hydroxyquinolines have recently been synthesised as potential anti-cancer pro-drugs.<sup>143</sup> It was proposed by Oliveri *et al.*<sup>143</sup> that the glucoconjugation strategy may have the effect of creating a selective pro-drug as a result of elevated glycolysis in tumour cells creating increased uptake into tumour cells over normal cells, as well as increasing the drugs solubility in aqueous media.

Substituted quinolines have been shown to be act as a wide range of biologically active drugs. From a pharmaceutical view, this implies a need for a method of rapid characterisation of this type of molecule and the side products and reagents potentially present in the production of these drugs. Quinoline is therefore a good substrate for investigations into hyperpolarisation by SABRE.

#### 4.1.2 Characterisation of quinoline in methanol

This chapter is based solely on quinoline and its analogues, and therefore, quinoline has been fully characterised in  $d_4$ -methanol. The assignments used throughout the chapter are outlined in Figure 4.4 and Table 4.1. Details of collection are outlined in the Experimental, section 8.7.2.1.

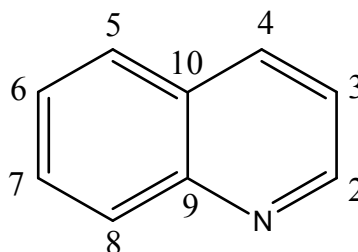


Figure 4.4 Structure of quinoline with positions labelled.

Position	<sup>1</sup> H shift	J <sub>HH</sub>	<sup>13</sup> C shift	J <sub>CH</sub>
2	8.82	dd, 4.3, 1.7	150.0	dq, 178, 4
3	7.52	dd, 8.4, 0.8	121.3	dd, 165, 8
4	8.34	dd, 8.5, 0.8	137.2	dt, 163, 6
5	7.92	dd, 8.2, 1.3	128.0	d(t), 161, (4.9)
6	7.60	d(m), 7.0	126.8	dd, 162, 9
7	7.76	d(m), 7.0	129.9	dd, 161, 9
8	8.02	dd, 8.3, 4.4	127.8	dd, 161, 7
9	/	/	147.5	
10	/	/	128.7	

Table 4.1 The observed <sup>1</sup>H and <sup>13</sup>C NMR shifts of quinoline in *d*<sub>4</sub>-methanol.

## 4.2 Initial studies into polarisation transfer efficiency into quinoline

Quinoline has a significantly different structure to that of pyridine, and therefore may also exhibit different trends with respect to changing catalyst, temperature of polarisation, magnetic field of polarisation or solvent. These concepts will therefore be discussed in reference to quinoline in this section.

### 4.2.1 Effect of changing catalyst on polarisation transfer efficiency into quinoline

Polarisation transfer into quinoline was investigated using **IMes(a)**, **SIMes(a)** and **ICy(a)**, initially using method 1. In the case of **IMes(a)** and **SIMes(a)**, no evidence of polarisation transfer is observed in the standard <sup>1</sup>H NMR spectra, however a small amount of transfer is observed in the <sup>1</sup>H OPSYdq spectra, implying a weak polarisation transfer is present. After activation, neither **IMes(a)** or **SIMes(a)** show evidence of decomposition and both show a single signal around -23 ppm in the <sup>1</sup>H NMR spectrum suggesting the expected complex, [Ir(carbene)(H)<sub>2</sub>(sub)<sub>3</sub>]<sup>+</sup> was formed. For **ICy(a)**, polarisation transfer is observed in the <sup>1</sup>H NMR spectra, leading to a small enhancement in some sites as indicated in Table 4.2.

Catalyst	Observed <sup>1</sup> H NMR signal enhancement						
	2	3	4	5	6	7	8
<b>ICy(a)</b>	-0.2	0.8	-0.2	-0.5	1.5	0.6	-0.8

Table 4.2 <sup>1</sup>H NMR signal enhancement for quinoline when polarised using method 1 with **ICy(a)** at room temperature and a PTF of 2 G.

Considering all three catalysts, the results exhibit a significantly different trend to that observed for pyridine polarised by the same catalysts where all three catalysts promote polarisation transfer to pyridine with **IMes(a)** being most efficient. Quinoline is a much bulkier substrate than pyridine and exhibits a different  $pK_a$  (4.85 for quinoline<sup>144</sup> and 5.2 for pyridine<sup>144,145</sup>) which may have a significant effect on the activation step. To alleviate this concern, the chloride ion can be displaced to form a catalyst similar in structure to Crabtree's catalyst<sup>68</sup> and the first published SABRE catalyst.<sup>58</sup> This can be achieved in two ways in which the IMes carbene is used as an example however the principles apply to all carbenes discussed. Firstly, a reaction of  $[\text{Ir}(\text{COD})(\text{IMes})\text{Cl}]$  with silver hexafluorophosphate in the presence of acetonitrile yields the catalyst  $[\text{Ir}(\text{COD})(\text{IMes})(\text{NCMe})]\text{PF}_6$  (**IMes(b)**). Secondly, acetonitrile can be added to the catalyst *in situ* transforming the catalyst from  $[\text{Ir}(\text{COD})(\text{IMes})\text{Cl}]$  to  $[\text{Ir}(\text{COD})(\text{IMes})(\text{NCMe})]\text{Cl}$ . This *in situ* method is termed **IMes(c)**. Further details of this can be found in Chapter 2.

The three catalysts were consequently investigated in the presence of acetonitrile. Polarisation transfer into quinoline via SABRE was therefore investigated with **IMes(c)**, **SIMes(c)** and **ICy(c)** with results shown in Table 4.3.

Catalyst	Observed <sup>1</sup> H NMR signal enhancement						
	2	3	4	5	6	7	8
<b>IMes(c)</b>	-20	30	-24	-31	35	15	-33
<b>SIMes(c)</b>	-4	7	-5	-6	10	4	-8
<b>ICy(c)</b>	-7	9	-8	-11	19	5	-19

Table 4.3 <sup>1</sup>H NMR signal enhancement for quinoline when polarised using method 1 with **IMes(c)**, **SIMes(c)** and **ICy(c)** at room temperature and a PTF of 2 G.

The addition of a stoichiometric volume of acetonitrile to the catalytic precursors has increased the polarisation transfer efficiency of all three catalysts into quinoline. Due to these results, the **Carbene(c)** catalysts were used when considering quinoline for all other experiments. It should be noted here that acetonitrile is not a benign addition and does receive a small level of polarisation transfer, observed as negatively phased peaks. This could be taking polarisation away from quinoline, the desired substrate, and therefore polarisation transfer to quinoline with **IMes(c)** was investigated with deuterated acetonitrile. The results are presented in Table 4.4.

acetonitrile	Observed $^1\text{H}$ NMR signal enhancement						
	2	3	4	5	6	7	8
Protonated	-17	20	-22	-31	37	11	-41
Deuterated	-14	20	-20	-28	31	10	-32

Table 4.4  $^1\text{H}$  NMR signal enhancement for quinoline when polarised using method 1 with **IMes(c)** with protonated and deuterated acetonitrile, at room temperature and a PTF of 2 G.

The replacement of protonated acetonitrile with deuterated acetonitrile did not have the effect to increase the extent of polarisation transfer into quinoline using **IMes(c)**. In fact, the transfer to each position has either remained constant or decreased a little. This could be an effect of changing the coupling network of the active complex. Whenever a **Carbene(c)** catalyst is used, protonated acetonitrile is added as this provides better polarisation transfer to quinoline.

The addition of acetonitrile has also had an effect on the resultant  $^1\text{H}$  NMR spectrum of the active complex, in that the hydride region now shows two hydrides rather than one. This is discussed in the following section.

#### 4.2.2 Characterisation of **IMes(c)** hydrogenated in the presence of quinoline

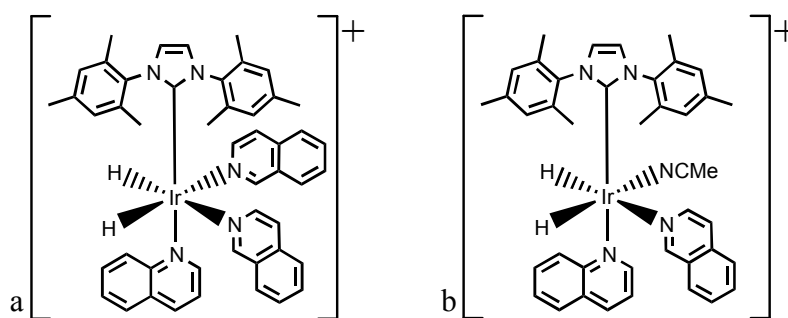


Figure 4.5 Structures of two potential products formed when **IMes(c)** reacts with hydrogen in the presence of quinoline and acetonitrile.

If the structure observed in Figure 4.5a is present when **IMes(c)** is activated with hydrogen in the presence of quinoline, a single hydride resonance might be expected. After activation, the sample was cooled to 243 K to reduce the effects of quinoline and hydride exchange. Figure 4.6 shows the hydride region of the  $^1\text{H}$  NMR spectrum. It is evident that two significantly different signals are observed at -20.4 ppm and -22.5 ppm, each with a splitting of 6.1 Hz.

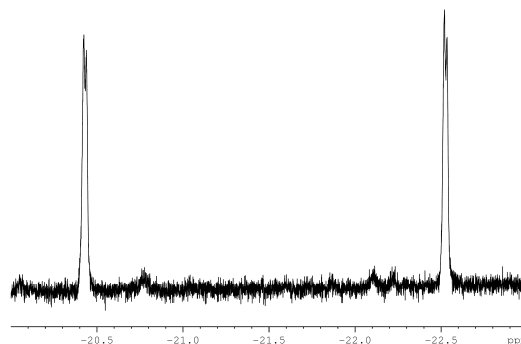


Figure 4.6 The  $^1\text{H}$  NMR signals corresponding to the hydride ligands observed when **IMes(c)** is activated in the presence of quinoline and hydrogen.

These hydrides were confirmed to be coupled to each other by  $^1\text{H}$  NOESY NMR indicating a single complex is present, where each hydride is *trans* to a different ligand. This is consistent with the structure shown in Figure 4.5b.

This hypothesis is further confirmed when comparing the integrals of the bound quinoline resonances. In order to achieve this, a sample with a 1:4 loading, catalyst:quinoline, was prepared for interrogation. Two additional sets of signals corresponding to quinoline bound to the metal are observed labelled 'B' in Figure 4.7. This is consistent with the structure shown in Figure 4.5b.

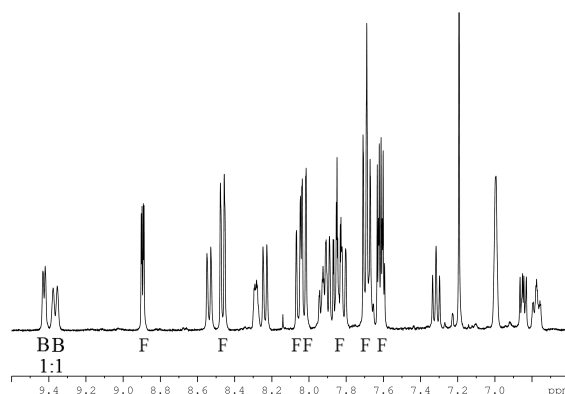


Figure 4.7 The aromatic region of a  $^1\text{H}$  NMR spectrum observed at 243 K when **IMes(c)** is activated in the presence of quinoline and hydrogen, with a ratio of 1:4 catalyst to substrate. 'F' denotes the signals corresponding to free quinoline and 'B' denotes the signals corresponding to proton 2 of quinoline bound to the catalyst.

The two signals at 9.41 ppm and 9.36 ppm are in the ratio 1:1 providing extra evidence for the production of the complex in Figure 4.5b. This is again further confirmed by comparing the integrals of signals corresponding to one bound quinoline resonance and of one hydride ligand resonance. These exhibit a 1:1 ratio. The two signals at 9.41 ppm



and 9.36 ppm therefore correspond to the 2 position of quinoline when bound to the iridium *trans* or *cis* to the hydride ligand (confirmed by  $^1\text{H}$  NOESY NMR), respectively. It was previously discussed that acetonitrile also experiences polarisation transfer and therefore acetonitrile must bind to the complex. It is therefore thought  $[\text{Ir}(\text{IMes})(\text{H})_2(\text{quinoline})_2(\text{NCMe})]^+$  is the active form of the catalyst. Full details of the characterisation of **IMes(c)** in the presence of quinoline can be found in the Experimental.

#### 4.2.3 Rate constants and thermodynamic activation parameters of **IMes(c)** hydrogenated in the presence of quinoline

In order to further understand the extent of polarisation transfer achieved by SABRE, it is important to understand the rate constants for exchange for a given system. In this section, the rate constants for loss of quinoline and hydride ligands from the **IMes(c)** catalyst is compared to the rate constants for loss of pyridine and hydride ligands from the **IMes(a)** catalyst. All data has been collected in the same manner as previously described (see Experimental) and full exchange rate constant data can be found in the Appendix.

##### 4.2.3.1 Thermodynamic activation parameters observed for the loss of hydride ligands from **IMes(c)** hydrogenated in the presence of quinoline

Initial attempts to calculate the data relating to hydride ligand loss were unsuccessful due to the high level of deuterium incorporation experienced into the hydride ligand sites by the sample during the experiment time.<sup>77,78</sup> To overcome this, the rate constants for hydride loss were calculated in a sample dissolved in  $\text{CD}_3\text{OH}$  to eliminate the possibility of HD exchange.

	<b>IMes(c)</b> /quinoline	<b>IMes(a)</b> /pyridine
Raw rate constants / $\text{s}^{-1}$ (300 K)	32	9
$\Delta H^\ddagger$ / $\text{kJ mol}^{-1}$	76.3 ( $\pm$ 0.5)	79 ( $\pm$ 1)
$\Delta S^\ddagger$ / $\text{J K}^{-1} \text{mol}^{-1}$	44.3 ( $\pm$ 1.8)	41 ( $\pm$ 31)
$\Delta G_{300}^\ddagger$ / $\text{kJ mol}^{-1}$	63.0 ( $\pm$ 0.03)	66.4 ( $\pm$ 0.3)

Table 4.5 Activation parameters for the loss of hydrides for the **IMes(c)** and quinoline system compared to the same data for the **IMes(a)** and pyridine system.

Table 4.5 shows that the enthalpy of activation for the loss of hydride ligands of both systems is very similar indicating their similarity. The loss of hydrogen is entropically favourable in both cases as it increases disorder in the system. The  $\Delta G_{300}^\ddagger$  of **IMes(c)**/quinoline is lower than that for **IMes(a)**/pyridine resulting in a higher rate of H<sub>2</sub> loss.

#### 4.2.3.2 Thermodynamic activation parameters observed for the loss of quinoline ligands from hydrogenated **IMes(c)**

	<b>IMes(c)</b> /quinoline	<b>IMes(a)</b> /pyridine
Raw rate constants / s <sup>-1</sup> (300 K)	23.9*	23.4
$\Delta H^\ddagger$ / kJ mol <sup>-1</sup>	69.5 (± 0.6)	93 (± 3)
$\Delta S^\ddagger$ / J K <sup>-1</sup> mol <sup>-1</sup>	19.0 (± 2.2)	97 (± 9)
$\Delta G_{300}^\ddagger$ / kJ mol <sup>-1</sup>	63.8 (± 0.07)	64 (± 2)

Table 4.6 Activation parameters for the loss of substrate for the **IMes(c)** and quinoline system compared to the same data for the **IMes(a)** and pyridine system. \* denotes the value was calculated by extrapolation.

For **IMes(a)**, the raw rate constant for pyridine loss reported in the publication by Cowley *et al.* (2011)<sup>66</sup> has been doubled as the rate constant is quoted per mole of pyridine, where the data here is quoted as per mole of iridium catalyst. The observed rate constant for substrate ligand loss from **IMes(a)**/pyridine and **IMes(c)**/quinoline are near identical at 300 K. This is reflected in the  $\Delta G_{300}^\ddagger$  value, although given the dramatic difference in  $\Delta H^\ddagger$  and  $\Delta S^\ddagger$ , this situation is fortuitous. The reduction in  $\Delta H^\ddagger$  observed by changing systems from **IMes(a)**/pyridine to **IMes(c)**/quinoline may be a result of the change in bond strength, linked to the pK<sub>a</sub> of the two substrates. The entropy difference may be a result of the bulkiness of each system as a relatively large pyridine ligand is replaced by an acetonitrile in **IMes(c)**/quinoline.

As polarisation transfer into pyridine occurs to a much higher extent than into quinoline, the above thermodynamic data suggests that the efficiency of SABRE depends on the lifetime of the complex. The fast exchange of hydrogen in **IMes(c)**/quinoline therefore explains the lower extent of polarisation transfer to quinoline.

### 4.3 Further optimisation of polarisation transfer efficiency into quinoline

It has been shown in previous chapters that polarisation transfer into a certain substrate can be increased through changing certain variables employed during the addition of *parahydrogen* to the sample, shown for pyridine in Chapter 3. These concepts have been utilised to investigate polarisation transfer into quinoline.

#### 4.3.1 Effect of changing temperature during the polarisation transfer step on polarisation transfer efficiency into quinoline

In section 4.2.1 (pg 177), polarisation transfer into quinoline using three different catalysts was investigated. The same three catalysts were investigated at different temperatures to understand if an increase or decrease in temperature leads to a significant increase in the level of polarisation transferred into the substrate. These experiments were completed using method 1 according to the protocol explained in the Experimental. Previous to the temperature studies completed in this section, it is important to point out that the active complexes of **IMes(c)**, **SIMes(c)**, and **ICy(c)** took a similar form, assumed from the observation of two coupled hydrides in the  $^1\text{H}$  NMR spectrum of the active complex.

##### 4.3.1.1 Effect of temperature during the polarisation transfer step on polarisation transfer efficiency into quinoline using **IMes(c)**

Polarisation transfer into quinoline using **IMes(c)** was investigated at five temperatures with results presented in Table 4.7 and Figure 4.8. Considering the rate constant of loss of both quinoline and hydride ligands, it can be predicted that the extent of polarisation transfer into quinoline will decrease when the temperature of polarisation increases, due to the relatively high rate constant of hydrogen loss.

T / °C	Rate constant of ligand loss (s <sup>-1</sup> )		Observed <sup>1</sup> H NMR signal enhancement							
	Hydride	Quinoline	2	3	4	5	6	7	8	
0	1	1	-23	34	-27	-33	44	21	-41	
22	20	15	-20	30	-24	-31	35	15	-33	
30	46	32	-6	10	-8	-9	13	6	-12	
40	125	79	-2	5	-3	-4	6	3	-5	
50	319	187	-1	2	-1	-2	2	1	-2	

Table 4.7 <sup>1</sup>H NMR signal enhancement for quinoline when polarised using **IMes(c)** using method 1 at a PTF of 2 G when the polarisation transfer step occurs at the indicated temperatures with the predicted rate constants of hydride and pyridine ligand exchange calculated from thermodynamic data in Appendix.

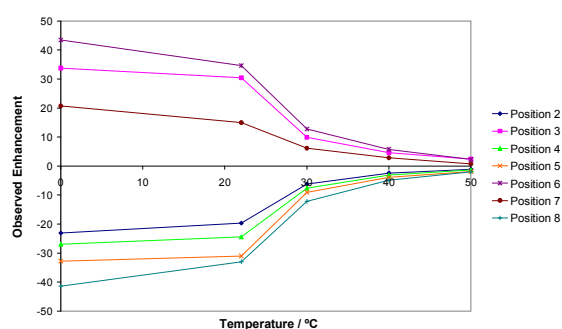


Figure 4.8 Graphical representation of the effect of changing the temperature of the polarisation step on the <sup>1</sup>H NMR signal enhancement of quinoline when polarised with **IMes(c)** at a PTF of 2 G.

Table 4.7 and Figure 4.8 show that temperature of addition of *parahydrogen* has a great effect on the level of polarisation transfer into quinoline using **IMes(c)**. An increase in temperature from room temperature results in a significant reduction in the extent of polarisation transfer into quinoline in all positions. A reduction in the temperature of the polarisation step below room temperature has the effect to increase the observed <sup>1</sup>H NMR polarisation transfer by a small amount in all positions. These data match the prediction based on the rate constant of hydrogen loss. With quinoline as the substrate, the rate constant of loss of hydride ligand is 32 s<sup>-1</sup>, nearly 4 times faster than the rate constant observed when pyridine is the substrate (9 s<sup>-1</sup>). This means the contact time for the complex is relatively short, and this only shortens upon increase in temperature reducing observed polarisation transfer. The increase in enhancement upon dropping the temperature of polarisation to 0 °C is proportionally small and so it is recommended to investigate SABRE at room temperature when considering polarisation transfer to quinoline using **IMes(c)**.

#### 4.3.1.2 Effect of temperature during the polarisation transfer step on polarisation transfer efficiency into quinoline using **SIMes(c)**

Polarisation transfer into quinoline using **SIMes(c)** was investigated at three temperatures, room temperature, 0 °C and 40 °C. To compare the **SIMes(c)**/quinoline system to the **IMes(c)**/quinoline system, the rate of exchange was experimentally determined at one temperature. The quinoline exchange rate constant had to be measured at a cold temperature to ensure the required resonance was base line resolved from all other signals. The exchange rate constant for hydride ligand loss was also completed at a cold temperature due to fast exchange. The results are presented in Table 4.8.

Rate constant of ligand loss / s <sup>-1</sup> (T/K)	<b>IMes(c)</b>	<b>SIMes(c)</b>
Hydride (273)	1.56	2.86
Quinoline (275)	1.74	0.21

Table 4.8 Experimentally measured rate constants of ligand loss from **IMes(c)** and **SIMes(c)** in the presence of quinoline.

At 273 K, the measured exchange rate constant for loss of hydride ligands from **SIMes(c)** in the presence of quinoline is much faster than the same constant for **IMes(c)** under the same conditions, a rate which has already been shown to be too fast for optimal polarisation transfer into quinoline. This therefore suggests that upon cooling the temperature of the polarisation step of a **SIMes(c)**/quinoline sample, the observed signal enhancement will increase due to the slower hydrogen loss exchange. The extent of this increase might be hampered as a result of the lower relative rate of quinoline loss. The results of changing the temperature of the polarisation step on the extent of polarisation transfer into quinoline are shown in Table 4.9 and Figure 4.9.

T / °C	Observed <sup>1</sup> H NMR signal enhancement						
	2	3	4	5	6	7	8
0	-7	14	-10	-13	20	8	-17
22	-4	7	-5	-6	10	4	-8
40	-0.2	1	-0.2	-0.3	1	0.6	-0.4

Table 4.9 <sup>1</sup>H NMR signal enhancement for quinoline when polarised using **SIMes(c)** using method 1 at a PTF of 2 G when the polarisation transfer step occurs at the indicated temperatures.

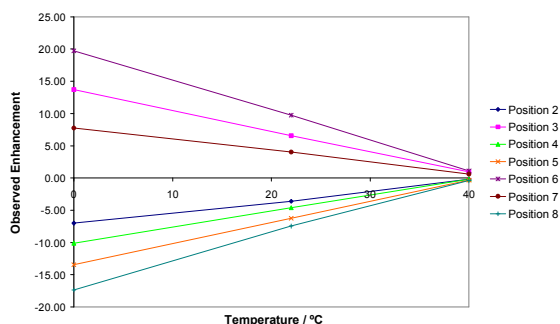


Figure 4.9 Graphical representation of the effect of changing the temperature of the polarisation step on the  $^1\text{H}$  NMR signal enhancement of quinoline when polarised with **SIMes(c)** at a PTF of 2 G.

Table 4.9 and Figure 4.9 show that the effect of temperature on the polarisation transfer to quinoline using **SIMes(c)** is significant. Increasing the temperature of the polarisation step above room temperature had the effect to reduce observed polarisation transfer to all positions to the extent that no enhancement is observed. Decreasing the temperature from room temperature by the same amount had the effect to increase observed polarisation transfer by approximately 2 fold to all positions. The increase in enhancement upon dropping the temperature of polarisation to 0 °C is significant in the case of **SIMes(c)**/quinoline and it is therefore recommended that a temperature of 0 °C is used in this case, however this does not improve on the enhancement levels observed when polarising quinoline using **IMes(c)**. **SIMes(c)** is therefore not recommended as the catalyst to use for SABRE investigations into quinoline.

#### 4.3.1.3 Effect of temperature during the polarisation transfer step on polarisation transfer efficiency into quinoline using **ICy(c)**

Polarisation transfer into quinoline using **ICy(c)** was investigated at three temperatures, 0 °C, room temperature (as stated) and 40 °C. Results are shown in Table 4.10 and Figure 4.10. For this catalyst, a number of hydride and bound quinoline signals were observed in near equal proportions. The calculated exchange rate constants from the  $[\text{Ir}(\text{ICy})(\text{H})_2(\text{Q})_2(\text{NCMe})]^+$  complex would therefore not be representative of the system as a whole.

T / °C	Observed <sup>1</sup> H NMR signal enhancement						
	2	3	4	5	6	7	8
0	-7	9	-8	-11	17	4	-17
20	-7	9	-8	-11	19	5	-19
40	-3	4	-3	-4	7	2	-7

Table 4.10 <sup>1</sup>H NMR signal enhancement for quinoline when polarised using **ICy(c)** using method 1 at a PTF of 2 G when the polarisation transfer step occurs at the indicated temperatures.

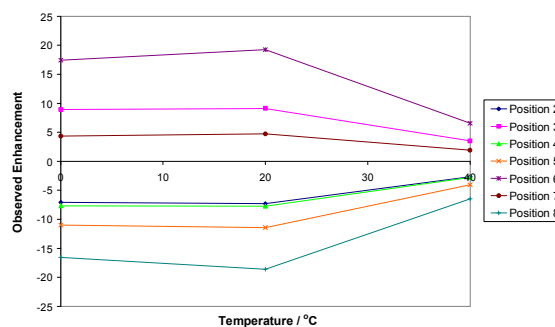


Figure 4.10 Graphical representation of the effect of changing the temperature of the polarisation step on the <sup>1</sup>H NMR signal enhancement of quinoline when polarised with **ICy(c)** at a PTF of 2 G.

Table 4.10 and Figure 4.10 shows that increasing the temperature from room temperature to 40 °C has resulted in a drop in observed polarisation transfer to all positions of quinoline when polarised with **ICy(c)**. The effect of decreasing the temperature to 0 °C does not follow the same trend, showing very similar enhancement levels to those observed at room temperature. This could suggest a maximum polarisation transfer might be observed between 20 °C and 0 °C. If quinoline is to be polarised using the **ICy(c)** catalyst, it would be recommended to polarise at room temperature, however this catalyst does not achieve higher levels of polarisation to quinoline than **IMes(c)**.

#### 4.3.1.4 Comparison of the effect of temperature during the polarisation transfer step on polarisation transfer efficiency into quinoline using **IMes(c)**, **SIMes(c)** and **ICy(c)**

It is important to consider all the three catalysts compared together. To simplify this, polarisation transfer to position 2 of quinoline only is considered, shown in Table 4.11.

T / °C	Observed $^1\text{H}$ NMR signal enhancement on position 2 of quinoline		
	<b>IMes(c)</b>	<b>SIMes(c)</b>	<b>ICy(c)</b>
0	-23	-7	-7
20	-20	-4	-7
40	-2	-0.20	-3

Table 4.11  $^1\text{H}$  NMR signal enhancement for quinoline when polarised using **IMes(c)**, **SIMes(c)** and **ICy(c)** using method 1 at 2 G when the polarisation transfer step occurs at the indicated temperatures .

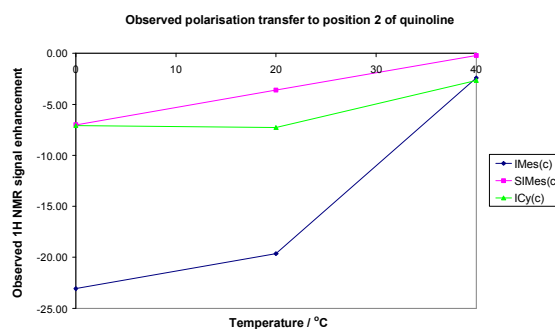


Figure 4.11 Graphical representation of observed  $^1\text{H}$  NMR signal enhancement in the signal for position 2 of quinoline when polarised using **IMes(c)**, **SIMes(c)** and **ICy(c)** using method 1 at a PTF of 2 G and various temperatures.

Figure 4.11 shows that the trend observed by all three catalysts is very similar. Increasing the temperature from room temperature to 40 °C resulted in a decrease in observed polarisation transfer to position 2 of quinoline by all catalysts. Decreasing the temperature from room temperature to 0 °C either has little effect on the polarisation transfer into position 2, or has the effect to increase the transfer observed.

In Chapter 3, the temperature dependence of polarisation transfer to pyridine was discussed for each catalyst. The dependence on temperature of the *para* position of pyridine and 2 position of quinoline are compared in Figure 4.12.



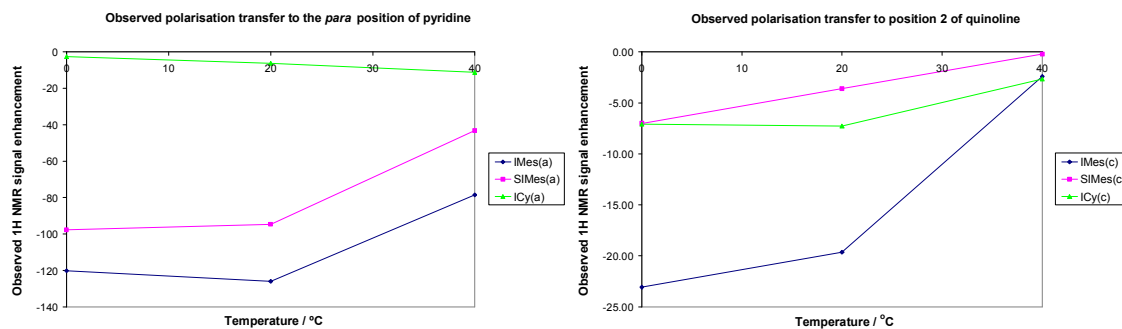


Figure 4.12 Graphical representation of observed  $^1\text{H}$  NMR signal enhancement in the signal for the *para* position of pyridine when polarised using **IMes(a)**, **SIMes(a)** and **ICy(a)** (left) and of observed  $^1\text{H}$  NMR signal enhancement in the signal for the 2 position of quinoline when polarised using **IMes(c)**, **SIMes(c)** and **ICy(c)** (right), both using method 1 at a PTF of 2 G and various temperatures.

The trends observed between the two substrates are similar for all three catalysts. The major difference is that of the SIMes and ICy based catalysts, **SIMes(a)** shows the greater enhancement into pyridine and **ICy(c)** shows the greater enhancement into quinoline, however the IMes based catalyst is still better for both substrates. It would therefore be recommended to use the IMes based catalysts for interrogation of substrates of this type.

#### 4.3.2 Effect of changing magnetic field during the polarisation transfer step on polarisation transfer efficiency into quinoline

It has been shown in Chapter 3 that the magnetic field at which the polarisation step occurs can have a great effect on the resultant observed polarisation transfer. To this point, only single ring systems have been investigated and so the polarisation transfer into the second fused ring of quinoline is of great interest. Quinoline was polarised with **IMes(b)** using method 2.

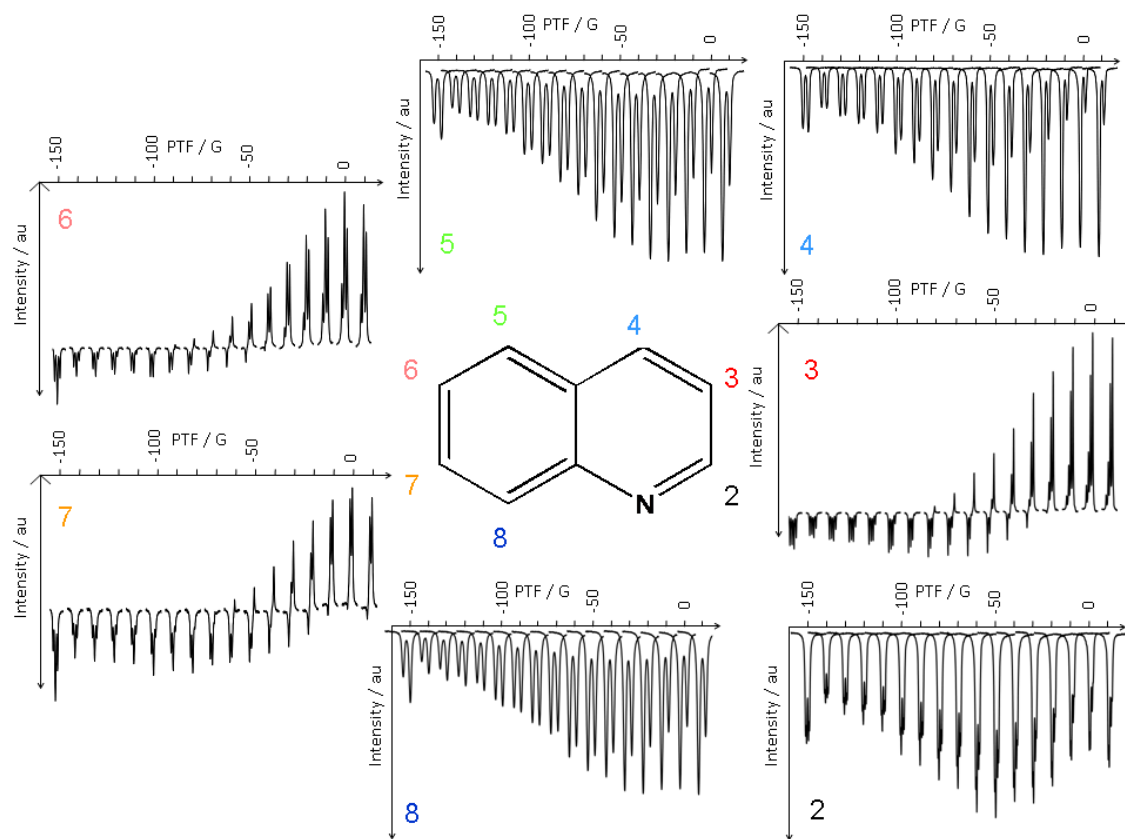


Figure 4.13 Effect of changing the PTF during polarisation of quinoline polarised using method 2 with **IMes(b)**.

Prior to these measurements, the two maximum PTFs for **IMes(a)**/pyridine were found to be 70 G for the standard  $^1\text{H}$  NMR spectra and 0 G for  $^1\text{H}$  OPSYdq NMR spectra.<sup>66</sup> Investigations into **IMes(c)**/quinoline were expected to give a similar result with the  $^1\text{H}$  NMR spectra exhibiting a maximum at a PTF of around 70 G and  $^1\text{H}$  OPSYdq NMR spectra exhibiting a maximum at a PTF of 0 G. The data presented in Figure 4.13 shows that this was a simplified view and care needs to be executed when selecting the PTF. It can be seen that different proton locations show different profiles upon change in magnetic field. Position 2 (*ortho*) shows a maximum at around -50 G and is always of negative phase. In contrast, positions 3, 6 and 7 (*meta*) show a gradual change in phase from negatively phased signals, through some antiphase signals separated by  $J_{\text{HH}}$ , into positively phased signals. The point of inflection appears at -50 G, -60 G and -40 G for positions 3, 6 and 7 respectively. The remaining positions, 4, 5 and 8 (*para*), appear as in-phase emissive doublets, where the intensities of the two components change upon magnetic field. These show a maximum at a magnetic field of 0 G. Owing

to the nature of many of the signals observed, it is easier to consider the enhancements as a graph, shown in Figure 4.14.

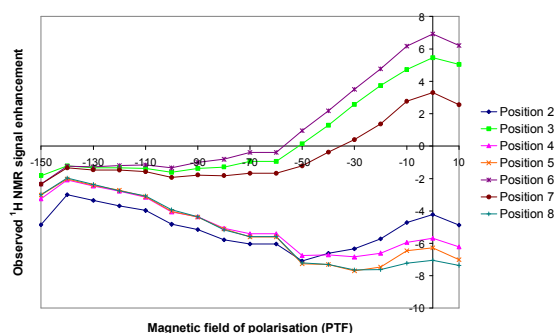


Figure 4.14 Graphical representation of the  $^1\text{H}$  NMR signal enhancement levels of quinoline when polarised with **IMes(b)** at various PTF using method 2.

It can be observed in Figure 4.14 that no single magnetic field results in a maximum observed polarisation transfer to all proton sites in quinoline. For position 2, the proton *ortho* to the binding site in quinoline, the maximum enhancement is observed at a magnetic field -50 G. This shows an enhancement of -7 when completed on the MK II system. If the same experiment is completed using the MK III, an enhancement of -57 is observed.

#### 4.3.3 Effect of changing concentration on polarisation transfer efficiency into quinoline

The effect of lowering the concentration of the samples was completed using method 1, where both lower concentration samples were prepared by dilution of the higher concentration sample with  $d_4$ -methanol.

Conc. rel. to standard	[ <b>IMes(c)</b> ] (mM)	[quinoline] (mM)	Observed $^1\text{H}$ NMR signal enhancement							
			2	3	4	5	6	7	8	
100 %	5	100	-20	30	-24	-31	35	15	-33	
10 %	0.5	10	-23	29	-27	-38	47	14	-44	
1 %	0.05	1	-2	3	-2	-3	4	2	-5	

Table 4.12  $^1\text{H}$  NMR signal enhancement of quinoline when polarised using method 1 with **IMes(c)** at a PTF of 2 G at the indicated concentrations.

Table 4.12 shows that a  $^1\text{H}$  NMR signal enhancement is observed to quinoline at the low concentration of when 1 mM quinoline is present. This is the equivalent of  $0.08\ \mu\text{l}$  of quinoline in a 0.6 ml sample. Significant signal enhancement is also observed when the concentration is reduced to 10 %. However the increase in signal enhancement observed in the **IMes(a)** and pyridine system through the same change in concentration was not observed in the **IMes(c)** and quinoline system.

#### 4.3.4 Effect of changing solvent on polarisation transfer efficiency into quinoline

It has been shown in Chapter 3 that changing the solvent in which the polarisation step takes place can also have a great effect on the extent of polarisation transfer into a substrate. Polarisation transfer into quinoline has therefore been investigated in a range of solvents with results shown in Table 4.13 and Figure 4.15.

Solvent	Observed $^1\text{H}$ NMR signal enhancement						
	2	3	4	5	6	7	8
Methanol	-11.2	20.8	-15.1	-19.1	22.1	12.0	-18.3
Ethanol	-7.8	11.5	-8.1	-9.8	15.1	5.1	-10.6
DCM	0.0	0.4	-0.1	0.0	0.3	-0.1	-0.5
Chloroform	0.7	0.2	1.0	1.4	-0.8	0.5	0.9
DMSO	0.2	0.4	0.4	0.4	0.4	0.4	0.3
Acetone	0.0	0.5	-0.1	0.1	0.5	0.2	0.0

Table 4.13  $^1\text{H}$  NMR signal enhancement when quinoline is polarised with **IMes(c)** at room temperature and a PTF of 2 G in various solvents.

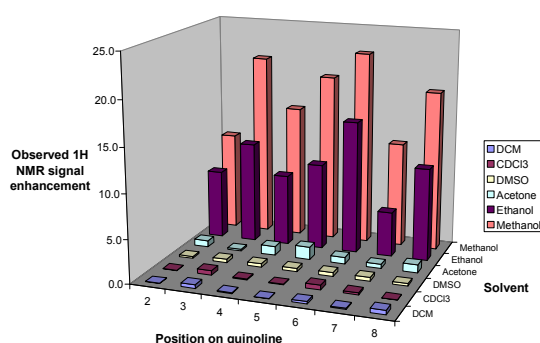


Figure 4.15 A 3D representation of Table 4.13 showing the  $^1\text{H}$  NMR signal enhancement when quinoline is polarised with **IMes(c)** at room temperature and a PTF of 2 G in various solvents.

It is clear to observe in Table 4.13 and Figure 4.15 the highest enhancement is observed in quinoline when methanol is used as a solvent. This differs slightly from the trend

observed when considering polarisation transfer into pyridine (Chapter 3), where ethanol produces the maximum polarisation transfer. Hydride signals are observed around -20 for the **IMes(c)**/quinoline sample in all six solvents suggesting the catalyst was active in all cases. The results gained here were designed to give a preliminary idea into the effect of polarisation transfer into quinoline, and are consequently far from optimised. While methanol exhibits the greatest level of polarisation transfer in this study, if a different solvent were required, it would be possible to optimise polarisation into a substrate.

#### 4.4 Mechanism of polarisation transfer into quinoline using SABRE

During the course of the investigations into polarisation transfer into quinoline, it was observed that similar signal intensities were observed in all positions after application of a 90° pulse. More specifically, there is not a significant difference in the extent of polarisation transfer between the first ring (positions 2, 3 and 4) and the second ring (positions 5, 6, 7 and 8). This is in contrast to the situation observed for the phenylpyridines (discussed in Chapter 6), where the level of polarisation transfer into the second ring is significantly less than the first ring. Current theory on the SABRE effect suggests that the transfer occurs through coupling between the *parahydrogen* derived hydride ligands and the protons of the substrate. The efficiency of this process is dependent on the size of the coupling, and it is likely to promote transfer through the *ortho* proton. In the case of quinoline, this is position 2. The polarisation should then transfer through its scalar coupling network around the substrate. Due to the small coupling constant present between positions 4 and 5 across the ring junction, it is thought polarisation transfer should not be possible between these two positions. The fact that the coupling constant between positions 4 and 5 is very small is strengthened by the thermal COSY of quinoline, presented in Figure 4.16.

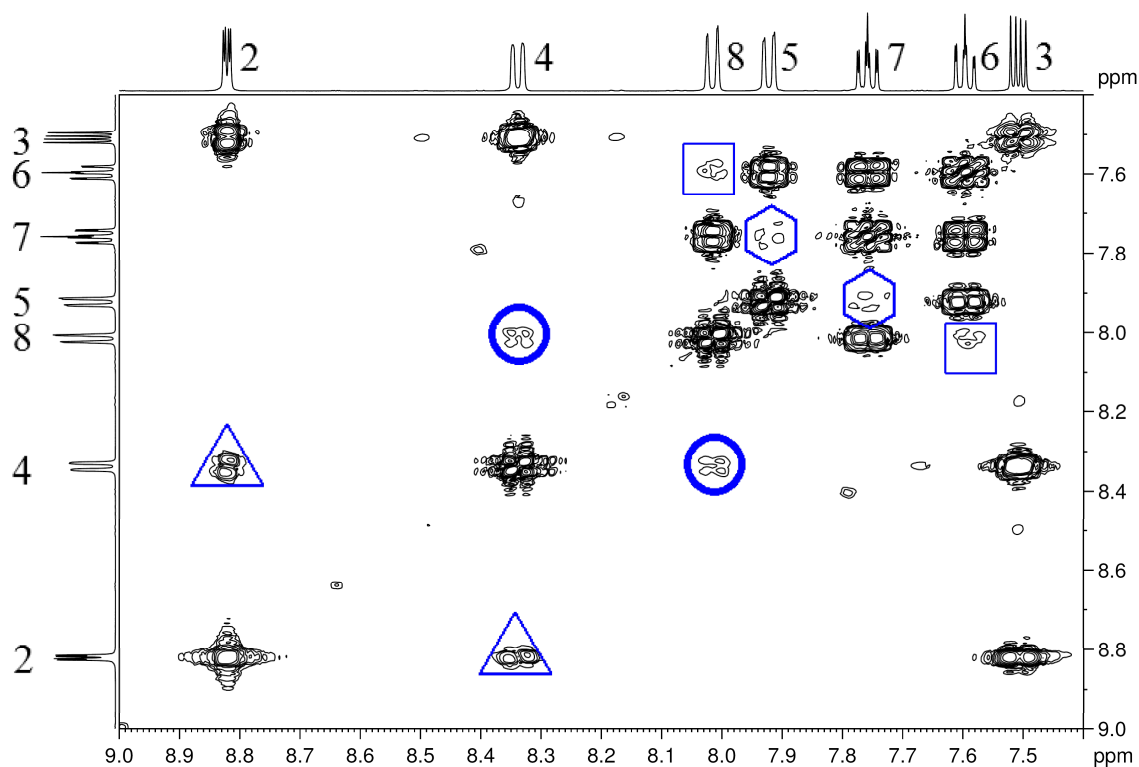


Figure 4.16 Thermally polarised  $^1\text{H}$  NMR COSY of quinoline, with the signal intensity increased such that any weak couplings can be observed.

Figure 4.16 shows that a cross peak signal is not present between positions 4 and 5, even though several two bond correlations are observed, indicated by the triangles (positions 2 and 4), hexagons (positions 5 and 7), and squares (positions 6 and 8). A weak W coupling is also observed between positions 4 and 8, circled. This implies there are two possible modes of polarisation transfer around the quinoline substrate; firstly through the W coupling and secondly through a coupling between the hydride ligands and the proton in the 8 position.

Initial investigations into the mode of polarisation transfer around quinoline began through the investigation of various quinoline analogues, allowing us to block certain potential pathways. The investigation was then extended to include a series of selective  $^1\text{H}$  OPSYdq spectra of the hyperpolarised quinoline, through which it may be possible to understand more about the coupling network.

#### 4.4.1 Polarisation of quinoline derivatives

##### 4.4.1.1 Naphthalene

In the literature, naphthalene has been shown to act as a 2 electron donor<sup>146,147</sup> and also undergoes CH bond activation.<sup>148</sup> This is because of the retention of aromaticity within the structure. This therefore shows this analogue of quinoline is able to bind to metals without the presence of a nitrogen atom, and therefore quinoline might bind through two modes, the nitrogen and an *eta* type bond. This second binding mode might provide a route of polarisation transfer into the second ring. Polarisation transfer into naphthalene was therefore investigated to understand if this route is viable.

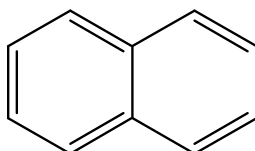


Figure 4.17 Structure of naphthalene.

The extent of polarisation transfer into naphthalene (Figure 4.17) was investigated using method 1 and **IMes(b)**, completed to understand if the quinoline structure was able to accept polarisation transfer through an *eta* type bonding. During this experiment, no signals corresponding to the hydride ligands were observed, and no enhancement or emission peaks were observed. This suggests polarisation transfer was not present through SABRE to naphthalene however this does not exclude the idea this could still be possible for quinoline.

##### 4.4.1.2 Investigation into the effect of changing the position of the nitrogen on polarisation transfer efficiency

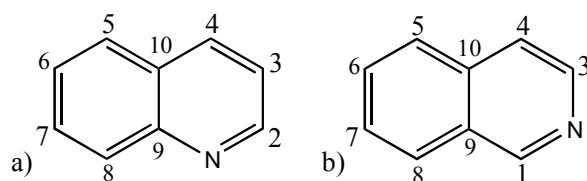


Figure 4.18 Structures of a) quinoline and b) isoquinoline.

These investigations began by introducing the small change of moving the nitrogen from the 1 position in quinoline, to the 2 position in isoquinoline (see Figure 4.18a and b). This was completed to reduce the possibility of polarisation transfer through a coupling between the hydride ligands and 8 position of quinoline and therefore, if this was the only route of polarisation transfer into the second ring, observed enhancements in positions 5, 6, 7 or 8 of isoquinoline will be significantly reduced or not present. The results of this experiment are outlined in Table 4.14.

	Observed <sup>1</sup> H NMR signal enhancement							
	1	2	3	4	5	6	7	8
quinoline	n/a	-25.3	42.8	-35.0	-46.3	53.7	21.8	-47.7
isoquinoline	-44.9	n/a	-58.6	16.4*	-32.8	16.4*	17.0	-20.3

Table 4.14 <sup>1</sup>H NMR signal enhancement when the indicated quinoline analogues are polarised with **IMes(b)** at room temperature and 2 G. \* denotes the signals are not base line resolved in the thermally polarised or hyperpolarised spectrum. Therefore, the quoted signal enhancement correlates to both signals together.

The results of using isoquinoline as a substrate have shown polarisation is able to transfer into the second ring, therefore a coupling between the hydride ligands and the 8 position is not the sole method of transfer into the second ring. It is however noted that the two highest enhancements are observed in the first ring, and transfer into the second ring is reduced in comparison. Investigation using the OPSYdq sequence revealed more intense signals in the first ring (positions 3 and 4) than the second. It was also observed that position 2 showed very little signal.

Isoquinoline has also been investigated using method 2. A maximum enhancement was observed when a PTF of 70 G was employed, resulting in a signal enhancement of 25 fold on position 1.



#### 4.4.1.3 Investigation into the effect of moving a methyl group of methylquinolines on polarisation transfer efficiency

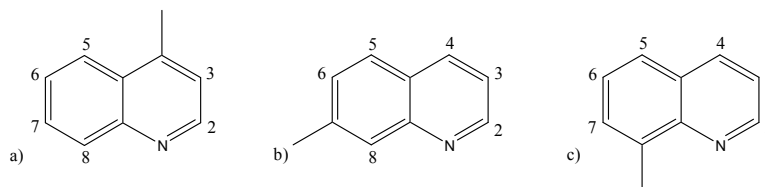


Figure 4.19 Structures of a) 4-methylquinoline, b) 7-methylquinoline and c) 8-methylquinoline.

A series of methylquinolines, namely 4-methylquinoline, 7-methylquinoline and 8-methylquinoline (Figure 4.19) were then investigated. Each methylquinoline has been chosen such that the methyl group acts as a block for polarisation transfer.

In the case of 4-methylquinoline, the placement of the methyl group on the 4 position blocks the possibility of polarisation transfer through the W coupling between positions 4 and 8. Investigation of 7-methylquinoline allows the isolation of positions 5 and 6 from polarisation transfer through position 8. If these positions are hyperpolarised then there must be another mode of polarisation transfer. In the case of 8-methylquinoline, the mode of transfer to position 8 is greatly hindered, allowing information about other transfer modes around the ring system. The results of the study are presented in Table 4.15.

	Observed $^1\text{H}$ NMR signal enhancement							
	2	3	4	5	6	7	8	Methyl
Quinoline	-20	-30	-24	-31	35	15	-33	n/a
4-methyl quinoline	-35	9	n/a	-46	47	19	-39	4
7-methyl quinoline	-20	8*	-14	-14	8*	n/a	-15	5
8-methyl quinoline	0.2	0.2*	0.2	0.3	0.2*	0.3	n/a	0.5

Table 4.15  $^1\text{H}$  NMR signal enhancement when the indicated methylquinolines are polarised with **IMes(b)** at room temperature and 2 G. \* denotes the signals are not base line resolved in the hyperpolarised spectrum. Therefore, the quoted signal enhancement correlates to both signals together.

The first observation to be made from Table 4.15 is that 8-methylquinoline showed no proof of polarisation transfer into the substrate. Analysis of the  $^1\text{H}$  NMR spectrum

revealed 8-methylquinoline does not bind to the **IMes(b)** complex, believed to be due to the steric bulk created by the methyl group on the 8 position. When interrogated using method 1, 4-methylquinoline showed enhancements in all positions. Most interestingly, the three highest enhancement levels in the substrate are observed in the second ring. Although enhancement is observed in the methyl group, this is a relatively small enhancement and consequently, coupling from the 3 position, to the methyl then to the five position is an unlikely transfer route. This supports the idea that polarisation transfer is able to enter the substrate through a coupling between the hydride ligands and proton on the 8 position as well as the 2 position. The OPSYdq sequence was also investigated using method one to reveal very similar signal intensity to all aromatic protons in 4-methylquinoline, with significantly less signal intensity on the signal corresponding to the methyl protons. This would suggest a very weak coupling is present between the methyl protons and aromatic protons, an idea strengthened by the relatively low observed  $^1\text{H}$  NMR signal enhancement. It is also noted that with the exception of proton 3, a greater enhancement is observed in 4-methylquinoline than quinoline. This could be a result of the slightly different exchange rates and coupling network created by changing the substrate from quinoline to 4-methylquinoline.

4-methylquinoline was also investigated using method 2. A maximum polarisation transfer in the  $^1\text{H}$  NMR spectrum was observed with a PTF of -50 G and in the  $^1\text{H}$  OPSYdq NMR spectrum was observed with a PTF of 0 G. The same trend was observed between the signals at all fields, the only difference was the signal intensity.

When interrogating 7-methylquinoline using method 1, polarisation transfer is again observed to all protons in the substrate (see Table 4.15). An important observation is the extent of polarisation transfer observed on the methyl protons, ~5 fold. This has been observed previously however, not to a methyl group on a second ring. Considering the aromatic protons, polarisation transfer appears to be almost equal to both rings. This suggests a route of transfer between the first and second rings must be present which does not involve the 8 position, either from protons 4 to 5 or possibly protons 3 to 5 or 4 to 6. 7-methylquinoline was investigated with the OPSYdq sequence using method one to reveal the signal intensity was greatest for positions 3 and 4, then reduced for the other aromatic signals, and significantly smaller for the methyl signal. This again suggests the methyl group was an unlikely route for polarisation transfer in this substrate. These experiments neither confirm nor disprove potential polarisation transfer

route involving the coupling between the proton on the 8 position of quinoline and the hydride ligands or the W coupling between the 4 and 8 position. They do however prove a second route of polarisation transfer into the second ring is active, evidenced through the enhanced 5 and 6 positions. The extent of polarisation transfer into 7-methylquinoline is less than that observed for quinoline.

While investigations into the methylquinolines have indicated a number of routes must be active to polarisation transfer, they have not confirmed precisely what these are.

#### 4.4.1.4 Phenazine

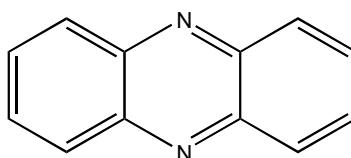


Figure 4.20 Structure of phenazine.

Initial investigations into the polarisation of phenazine, Figure 4.20, started with the **IMes(b)** catalyst. The first shake experiments showed minimal polarisation transfer which yielded no enhancement. The presence of two hydride resonances (-21.00 ppm and -22.27 ppm) suggests the phenazine has bound to the metal centre and a negative peak (Figure 4.21) suggested a weak polarisation transfer must have occurred.

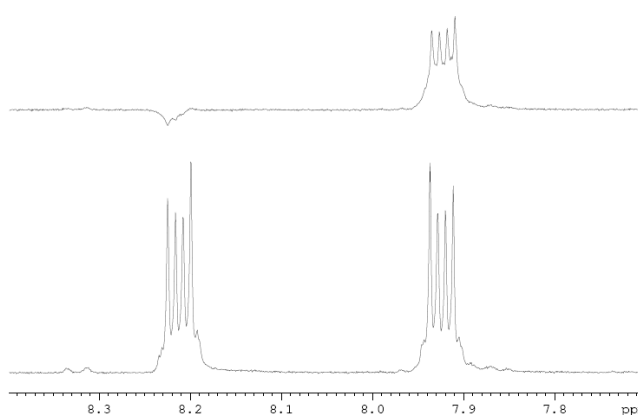


Figure 4.21  $^1\text{H}$  NMR spectrum of phenazine where bottom is thermally polarised and top is hyperpolarised using method 1 with **IMes(b)** in methanol.

It is possible the phenazine group binds too strongly and so pyridine was added to the sample to see if this would boost polarisation transfer to phenazine through changing

the exchange rates. This also gives the opportunity to check the catalyst is active through observing polarisation on pyridine. Results from this showed significant polarisation transfer to pyridine but no transfer was observed to phenazine. The addition of pyridine also resulted in one extra hydride resonance giving three altogether (-21.00 ppm, -22.27 ppm and -22.82 ppm). The sample was investigated again on a second day. In the  $^1\text{H}$  NMR shake experiment, pyridine showed enhancements of over 150 fold, however no polarisation was observed on phenazine. This may be explained by the  $^1\text{H}$  OPSYdq taken. Here, polarisation is observed on signals corresponding to pyridine and the two of the three hydrides which are present without the addition of pyridine (-21.00 ppm and -22.27 ppm). This might suggest significant levels of polarisation cannot transfer to phenazine as it appears to remain on the hydrides in the phenazine based complex.

#### 4.4.2 Investigations in polarisation transfer route into quinoline using the selective OPSYdq sequence

The SABRE method creates  $I_z$  and  $I_zS_z$  type magnetisation (discussed in Chapter 1). Up to this point, experiments using a  $90^\circ$  pulse have mainly considered, where  $I_z$  type magnetisation should be the dominant detected signal, or OPSYdq experiments using hard  $90^\circ$  pulses where  $I_zS_z$  type magnetisation is selected using gradients. If two shaped pulses are used in place of the two hard  $90^\circ$  pulses in the OPSYdq sequence, specific  $I_zS_z$  pairs can be probed. In the following experiments, the two resonances are pulsed selectively and concurrently. For quinoline, the 21 potential pairs are presented in Figure 4.22.

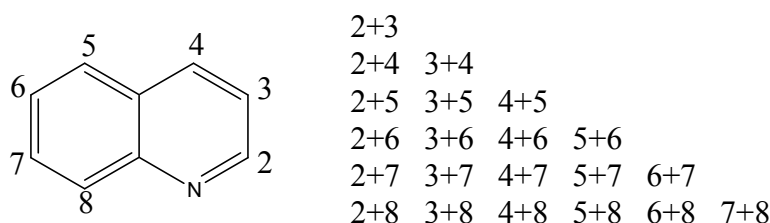


Figure 4.22 Labelled structure of quinoline together with the 21 potential  $I_zS_z$  pairs.

Interrogation of a substrate in this manner allows the interpreter to investigate which proton pairs are active routes for polarisation transfer. To achieve this, every proton pairs mentioned in Figure 4.22 was investigated. It would also be advantageous to

investigate the  $I_zS_z$  pairs involving the bound quinoline and hydride ligands however this is not possible. This is because the bound resonances for quinoline are low in intensity and hindered by the free quinoline resonances but also because the chemical shifts for the signals corresponding to the aromatic region and hydride ligand region are too far apart from each other.

Figure 4.23 illustrates the results obtained when each potential  $I_zS_z$  pair was interrogated for quinoline (100 mM) hyperpolarised using method 2 with **IMes(c)** (5 mM) at a PTF of 0 G. In each series of plots, the vertically aligned rectangular box represents one selected resonance and the square represents the partner selected for that spectrum.

Considering Figure 4.23, a coupling is observed when a signal is present in both the rectangle and square (i.e. for both the resonances selected). The first observation to be made was that the signals corresponding to the first, pyridyl ring are much more intense than those corresponding to the second, phenyl ring.

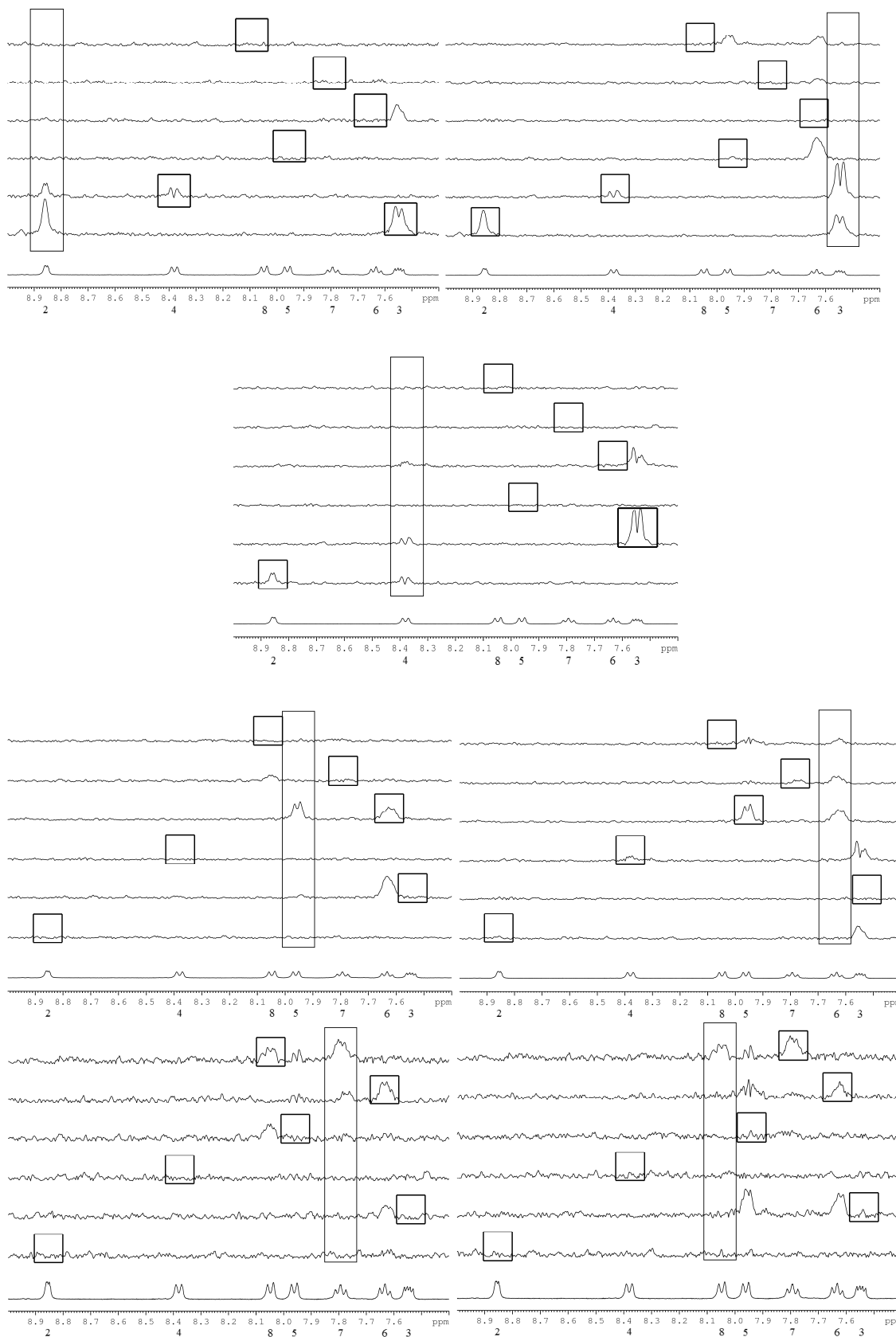


Figure 4.23 A series of selective  $^1\text{H}$  OPSYdq spectra of quinoline polarised with **IMes(c)** using method 2. The bottom spectrum in each set is a thermal  $^1\text{H}$  NMR spectrum to act as a reference. The spectra are grouped by resonance (the rectangle) and the second selected resonance is indicated by a square.

In some cases, signals are observed outside of these two resonances. There are three potential explanations for these unexpected signals. The first explanation is based on experimental error as a result of the required pulses used not being selective enough however the results are not consistent with this concept. For instance, when protons 2 and 6 are selected, a signal is observed for proton 3. If this was a result of the selective pulse on proton 6 being too wide, consequently exciting proton 3 also, a signal would also be observed for proton 2. This is not the case. The second explanation could be the presence of COSY crosspeaks. This explanation is also not consistent with the spectra collected. These could be present in the case where three peaks are observed rather than the expected two, however, in most cases, the additional unexpected peaks are the only observed peak. The third explanation is that while the selective pulses are selective for the signals corresponding to the free quinoline, beneath these signals are others, corresponding to the bound quinoline ligands. Exchange of these bound quinoline ligands into free quinoline during the timescale of the experiment could explain the unexpected signals. The data in Figure 4.23 has also been presented in Table 4.16, compared to observed COSY correlations.

	2		3		4		5		6		7		8	
	O	C	O	C	O	C	O	C	O	C	O	C	O	C
2	na	na	√	√	√	w	X	X	X	X	X	X	X	X
3	√	√	na	na	√	√	X	X	X	X	X	X	X	X
4	√	w	√	√	na	na	X	X	X	X	X	X	X	w
5	X	X	X	X	X	X	na	na	√	√	X	w	X	X
6	X	X	X	X	X	X	√	√	na	na	√	√	X	w
7	X	X	X	X	X	X	X	w	√	√	na	na	√	√
8	X	X	X	X	X	w	X	X	X	w	√	√	na	na

Table 4.16 Correlations observed in free quinoline when interrogated using the selective OPSYdq sequence, where a '√' denotes a correlation was observed, 'w' denotes a weak correlation is observed, 'X' denotes a correlation was not observed, 'O' refers to the selective <sup>1</sup>H OPSYdq NMR experiments and 'C' refers to the <sup>1</sup>H COSY NMR spectrum.

The main piece of information that can be gathered from this experiment is that a correlation was not observed between positions 4 and 5, across the two rings, or between 4 and 8 through the W coupling observed as a long range coupling in the <sup>1</sup>H-<sup>1</sup>H COSY NMR spectrum. This might imply the polarisation transfer is unable to occur

between the two rings. If this is the case, polarisation must transfer into the second ring via a coupling between the hydride ligands and position 8 in quinoline.

#### 4.5 Summary

This chapter focused on developing our understanding of polarisation transfer by extension of the substrate to quinoline. The initial investigations revealed no polarisation transfer when quinoline was polarised in the presence of **IMes(a)** in the absence of an activator. The addition of such an activator such as acetonitrile has led to two new catalytic systems, **IMes(b)** and **IMes(c)**. This results that the active species of catalyst takes the form  $[\text{Ir}(\text{IMes})(\text{H})_2(\text{quinoline})_2(\text{NCMe})]^+$  rather than  $[\text{Ir}(\text{IMes})(\text{H})_2(\text{quinoline})_3]^+$  as is observed in systems without an activator.

Using method 1, the polarisation transfer efficiencies of **IMes(c)**, **SIMes(c)** and **ICy(c)** to quinoline were investigated. This revealed that the **IMes(c)** samples yielded the most significant signal intensities at the three temperatures investigated. This catalyst was therefore investigated using method 2 in order to understand the effect of changing the PTF. Using a 90° pulse on  $^1\text{H}$ , the maximum signal intensity was obtained when a PTF of 50 G is used for the 2 position with **IMes(b)**. Greater enhancements are observed in pyridine however this could be due to pyridine containing 5 protons presenting with three  $^1\text{H}$  NMR resonances and quinoline containing 7 magnetically inequivalent protons. This means the transferred polarisation is spread over more nuclei. There is also the added complication of the acetonitrile added to the quinoline sample. This is able to receive polarisation through the SABRE method and therefore could be absorbing some of the polarisation from the *parahydrogen* derived hydride ligands.

These data therefore call for a need to revise the current theory on SABRE. The template of the **IMes(c)**/quinoline system includes many more spins and two potential ligands for magnetisation transfer (quinoline and acetonitrile), making it structurally different to the **IMes(a)**/pyridine system. There are also significant chemical differences between the two substrates.

Comparing the thermodynamic data for the **IMes(c)**/quinoline and **IMes(a)**/pyridine systems, the rate constants for the loss of substrate ligand are very similar, as are the Gibbs free energies, despite significantly different enthalpy and entropy values. This could be because quinoline is a bulkier ligand with a lower  $\text{p}K_{\text{a}}$  than pyridine and



therefore a weaker Ir-N bond resulting in a lower enthalpy and entropy. The most significant difference is observed in the rate constants for the loss of hydride ligands, where the rate constant is much larger for the **IMes(c)**/quinoline system. This may also explain the lower signal enhancements observed to quinoline when compared to pyridine and is consistent with the effect of temperature on the extent of polarisation transfer.

**IMes(c)** was also taken through to investigate the effect of changing the solvent using method 1 including solvents such as methanol, ethanol, DCM, chloroform, DMSO and acetone. The trend observed for quinoline was significantly different to that observed for pyridine. Like pyridine, **IMes(c)** transfers significant polarisation into quinoline in both methanol and ethanol however the other four solvents yielded only weak polarisation transfer with only one position in one solvent yielding an enhancement.

During the course of these experiments, it was observed that the level of polarisation transfer to  $^1\text{H}$  using a  $90^\circ$  pulse is near equal to all positions in quinoline. This is unexpected due to the very small coupling constants between protons in each ring in the substrate. This idea was investigated through polarisation of various quinoline analogues using method 1, and a series of selective  $^1\text{H}$  OPSYdq NMR spectra using method 2. These experiments proved to be inconclusive.

This chapter has further indicated that optimisation of a polarisation system must be optimised for each catalyst and substrate system.

## 5 Chapter 5 – Implementing SABRE with advanced NMR methods

### 5.1 Introduction

Up to this point in this thesis, only single scan 1D  $^1\text{H}$  NMR spectroscopy has been considered. While these spectra can yield significant information about a substrate, such as the chemical environments of protons in the system and spin-spin coupling constants, there is still a significant amount of information that could be obtained using NMR spectroscopy. A great deal of information can be gained from advanced 1D  $^1\text{H}$  sequences such as the 1D  $^1\text{H}$  NOESY, but consideration of other nuclei such as  $^{13}\text{C}$  is vital in the characterisation of small molecules. Investigations into 2D sequences such as the homonuclear  $^1\text{H}$ - $^1\text{H}$  COSY and heteronuclear  $^1\text{H}$ - $^{13}\text{C}$  HSQC, HMBC and HMQC are also very important as they allow the observation of correlations between nuclei within a molecule indicating even quaternary carbons. However, the successful use of these sequences often requires high concentration samples and long acquisition times. The application of SABRE to these sequences therefore has the potential to significantly reduce sample loading and time required for characterisations.

The model substrate quinoline is used to achieve this goal and the subsequent results are described within this chapter. Quinoline was selected because unlike pyridine, it represents a more complex system, containing two rings and most importantly for the investigations into heteronuclear sequences, two quaternary carbons.

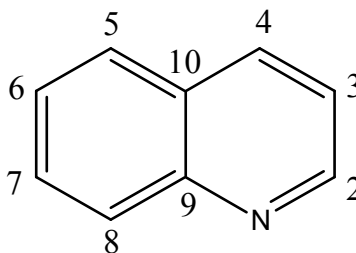


Figure 5.1 Labelled structure of quinoline.

A more detailed characterisation of quinoline can be found in Chapter 4 or Experimental. Much of the work in this chapter contributed towards a Journal of American Chemical Society publication in 2012, presented in the Appendix.<sup>67</sup> Owing to the need for signal averaging and phase cycling, the majority of this chapter has been completed using method 2. This also allows the possibility to reliably change the PTF.

## 5.2 Development of method 2 applied to 1D NMR sequences

This section looks into the application of SABRE to 1D NMR sequences for both  $^1\text{H}$ , looking at the NOESY, and  $^{13}\text{C}$ , including  $^1\text{H}$  coupled,  $^1\text{H}$  decoupled and INEPT sequences.

### 5.2.1 Method 2 applied to 1D $^1\text{H}$ NMR sequences

In order to compare the results gained through investigations into hyperpolarisation by SABRE, a thermally polarised  $^1\text{H}$  NMR spectrum of quinoline is shown in Figure 5.2.

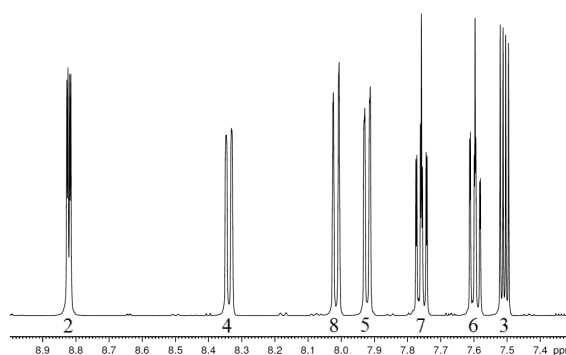


Figure 5.2 Thermally polarised  $^1\text{H}$  NMR spectrum of quinoline.

#### 5.2.1.1 Investigations into the effect of changing exposure time to *parahydrogen* on resultant $^1\text{H}$ NMR spectra

The effect of changing the exposure time to *parahydrogen* was investigated using a standard  $^1\text{H}$  NMR sequence with a  $90^\circ$  pulse using method 2. The results are shown in Figure 5.3.

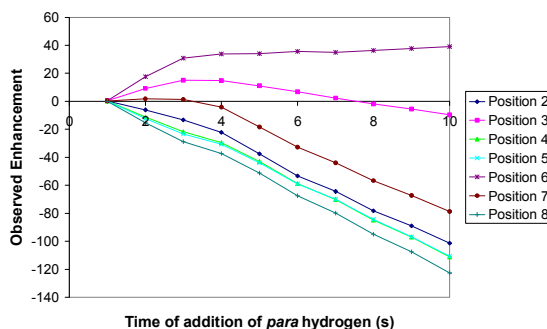


Figure 5.3 Effect of changing the time of addition of *para*hydrogen on the  $^1\text{H}$  enhancement observed to the indicated positions of quinoline (10 mM) when polarised with **IMes(c)** (0.5 mM) using method 2.

Figure 5.3 shows that the longer the time that *para*hydrogen is added to the sample, the greater the extent of observed polarisation transfer. It should also be noted that the relative phase of the signal of positions 3 and 7 changes depending on the bubbling time. Significantly better signal strengths are observed when a bubbling time of 10 s is employed, however it was also observed this resulted in significant ‘blow-off’ of solvent such that only two 2D spectra can be collected before further addition of  $d_4$ -methanol is required. As a compromise, a bubbling time of 6 s is used for the following experiments as this gives sufficient signal without causing too much solvent to be evaporated during the course of the experiment.

#### 5.2.1.2 Method 2 applied to $^1\text{H}$ OPSY NMR sequence

A more full description of the  $^1\text{H}$  OPSY NMR sequences can be found in Chapter 1. When an OPSYdq measurement is completed, double quantum coherences are selected. The effect of changing the PTF on the signal intensity of the resulting  $^1\text{H}$  OPSYdq spectra was investigated using method 2, and the results are shown in Figure 5.4.

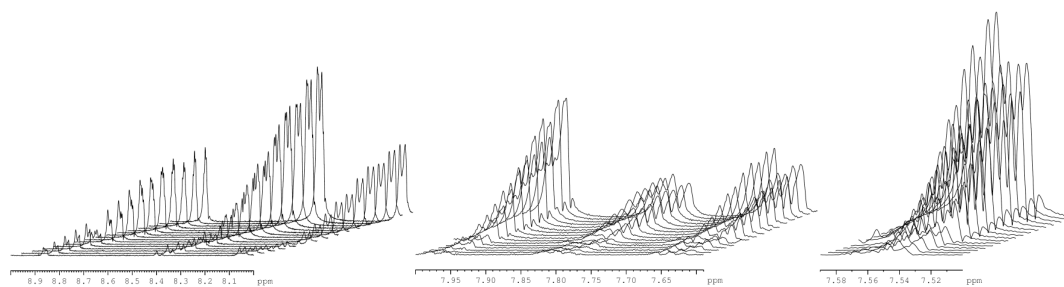


Figure 5.4 Plot of the effect of PTF on the signal intensity in the resultant  $^1\text{H}$  OPSYdq NMR spectrum of quinoline hyperpolarised with **IMes(b)** using method 2 where the PTF is set to -150 G (bottom) to 0 G (top). For clarity, the plot has been split into three sets of equal relative intensity, where the left set shows protons 2, 4 and 8, middle set shows protons 5 7 and 6, and right set shows proton 3.

Figure 5.4 reveals that the maximum signal intensity is observed with a PTF of 0 G. This suggests that the level of  $I_z S_z$  type magnetisation in quinoline produced through SABRE is maximised with a PTF of 0 G. Similar data was also collected for when the related zero quantum and single quantum states are selected through the OPSY sequence, and these also both show maximum signal intensity when a PTF of 0 G is employed. Based on the contrasting data collected in Chapter 4 where the signal intensity of the  $^1\text{H}$  NMR sequence with a  $90^\circ$  pulse is maximised with a PTF of 50 G, the following measurements are recorded with a PTF of 0 G and 50 G.

### 5.2.1.3 Method 2 applied to $^1\text{H}$ NOESY NMR sequence

$^1\text{H}$  NOESY measurements can reveal two important pieces of information. The primary use of the  $^1\text{H}$  NOESY sequence is to ascertain which protons are correlated to each other through nuclear Overhauser interactions. A correlation therefore indicates the two protons concerned are close in space to each other but not necessarily connected through bonds. The second use of the  $^1\text{H}$  NOESY sequence is to investigate exchange of a proton from one environment to another, also called a  $^1\text{H}$  EXSY.

Up to this point, spectra have only been completed using one scan, or by averaging of a number of scans. In order to work, the  $^1\text{H}$  NOESY NMR sequence must complete a phase cycle and therefore successful investigations into using the NOESY sequence would demonstrate a major advance in the application of SABRE. The process of introducing a phase cycle to a sequence during the application of SABRE is complicated by the requirement to repolarise the sample between each measurement. When this is implemented for the NOESY sequence through using a standard loop

within the sequence, failure results due to the incorrect incrementation of the phase cycle. It was also not possible to complete the two required scans in one transit, as the level of polarisation in each scan was significantly different, and therefore many artefacts were present. This can be overcome by the explicit coding of 4 sequential acquisitions within one pulse sequence file as outlined in the Appendix.

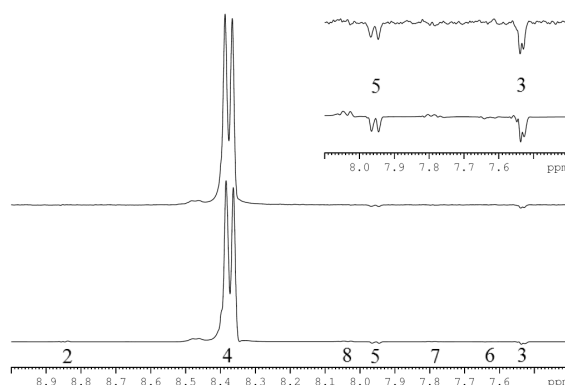


Figure 5.5 Thermally polarised 1D <sup>1</sup>H NOESY spectrum of quinoline (100 mM), top, and hyperpolarised using method 2 with **IMes(c)** (5 mM), bottom, presented on the same scale. Position 4 of quinoline was selected, and the inset traces show the observed nOe correlations to positions 5 and 3.

The hyperpolarised <sup>1</sup>H NOESY spectrum presented in Figure 5.5 was collected with 4 scans using method 2, where quinoline (100 mM) was hyperpolarised using **IMes(c)** (5 mM). In this case, signal corresponding to the 4 position was selected by the selective pulse in the sequence, showing as the large adsorption signal at 8.38 ppm. The <sup>1</sup>H NOESY spectrum then also shows signals corresponding to the 5 and 3 positions of quinoline as emission peaks at 7.95 ppm and 7.53 ppm.

	Position of quinoline			Ratio of S/N	
	4 (8.38 ppm)	5 (7.95 ppm)	3 (7.53 ppm)	4/5	4/3
Thermal, 8 scans	1131	10	19	113	60
SABRE, 4 scans	65036	615	1030	106	63

Table 5.1 Signal to noise ratios relating to the thermally polarised 1D <sup>1</sup>H NOESY spectrum of quinoline (100 mM) and hyperpolarised spectrum achieved using method 2 with **IMes(c)** (5 mM). Position 4 of quinoline was selected, and nOe correlations to positions 5 and 3 were observed.

Table 5.1 shows that the signal to noise ratios for the hyperpolarised <sup>1</sup>H NOESY NMR spectrum are significantly larger than those for the thermally polarised spectrum, 58 times larger on average, despite being completed with half the number of scans. It should also be noted that the ratio between the selected resonance (position 4 on

quinoline) and each NOESY peak (positions 5 and 3 on quinoline) is similar for both the thermally polarised and hyperpolarised spectra.

As the signal to noise ratios of the NOESY signals were in the range of several hundreds, the  $^1\text{H}$  NOESY NMR sequence was investigated at a lower concentration. Using method 2, a hyperpolarised  $^1\text{H}$  NOESY NMR sequence was completed using quinoline (10 mM) hyperpolarised with **IMes(c)** (0.5 mM); 10 % of standard concentrations. The resultant spectrum is presented in Figure 5.6.

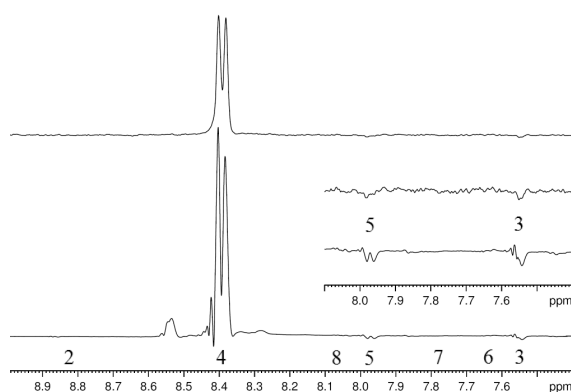


Figure 5.6 Thermally polarised 1D  $^1\text{H}$  NOESY spectrum of quinoline (10 mM), top, and hyperpolarised spectrum achieved using method 2 with **IMes(c)** (0.5 mM), bottom, presented on the same scale. Position 4 of quinoline was selected, and the inset traces show the observed nOe correlations to positions 5 and 3.

While the concentrations of both substrate and catalyst are now 90 % lower than the standard concentration, a very similar spectrum is still observed even though the 3 ml sample now contains only 4  $\mu\text{l}$  of quinoline. This is the equivalent of 0.8  $\mu\text{l}$  of quinoline in a standard 0.6 ml NMR sample. The signal corresponding to the 4 position was again selected.

	Position of quinoline			Ratio of S/N	
	4 (8.39 ppm)	5 (7.97 ppm)	3 (7.54 ppm)	4/5	4/3
Thermal, 128 scans	157	2	3	79	52
SABRE, 4 scans	2642	30	39	88	68

Table 5.2 Signal to noise ratios relating to the thermally polarised 1D  $^1\text{H}$  NOESY spectrum of quinoline (10 mM) and hyperpolarised with **IMes(c)** (0.5 mM). Position 4 of quinoline was selected, and nOe correlations to positions 5 and 3 were observed.

At this concentration of quinoline, it was necessary to complete 128 scans before the NOESY signals in the thermally polarised spectrum were observable. It can be observed

in Table 5.2 that the signal to noise ratios for the hyperpolarised  $^1\text{H}$  NOESY NMR spectrum are larger than those for the thermally polarised spectrum, 15 times larger on average, despite being completed with significantly fewer scans. Like the spectra completed at the higher concentration, the ratio between the selected resonance (position 4 on quinoline) and each NOESY peak (positions 5 and 3 on quinoline) is similar for both the thermally polarised and hyperpolarised spectra, however this similarity is less clear in the lower concentration spectra. It should also be noted that the 4 scan hyperpolarised spectrum was also collected in a much quicker time than the 128 scan thermally polarised spectrum. Both were completed with a mixing time of 1.5 s, and the hyperpolarised spectrum required an additional time to allow for addition of *para*hydrogen to the sample taking a total of 24 s. The total time required to collect the thermally polarised spectrum was 9 min 53 s, where the hyperpolarised spectrum took a total time of 43 s. The application of SABRE has therefore reduced the time required to collect the  $^1\text{H}$  NOESY NMR spectrum of quinoline at a concentration of 10 mM by a little over 9 min.

### 5.2.2 Method 2 applied to 1D $^{13}\text{C}$ and $^{13}\text{C}\{^1\text{H}\}$ NMR sequences

In order to compare the results gained through investigations into hyperpolarisation by SABRE, thermally polarised 1D  $^{13}\text{C}$  and  $^{13}\text{C}\{^1\text{H}\}$  NMR spectra of quinoline are shown in Figure 5.7.



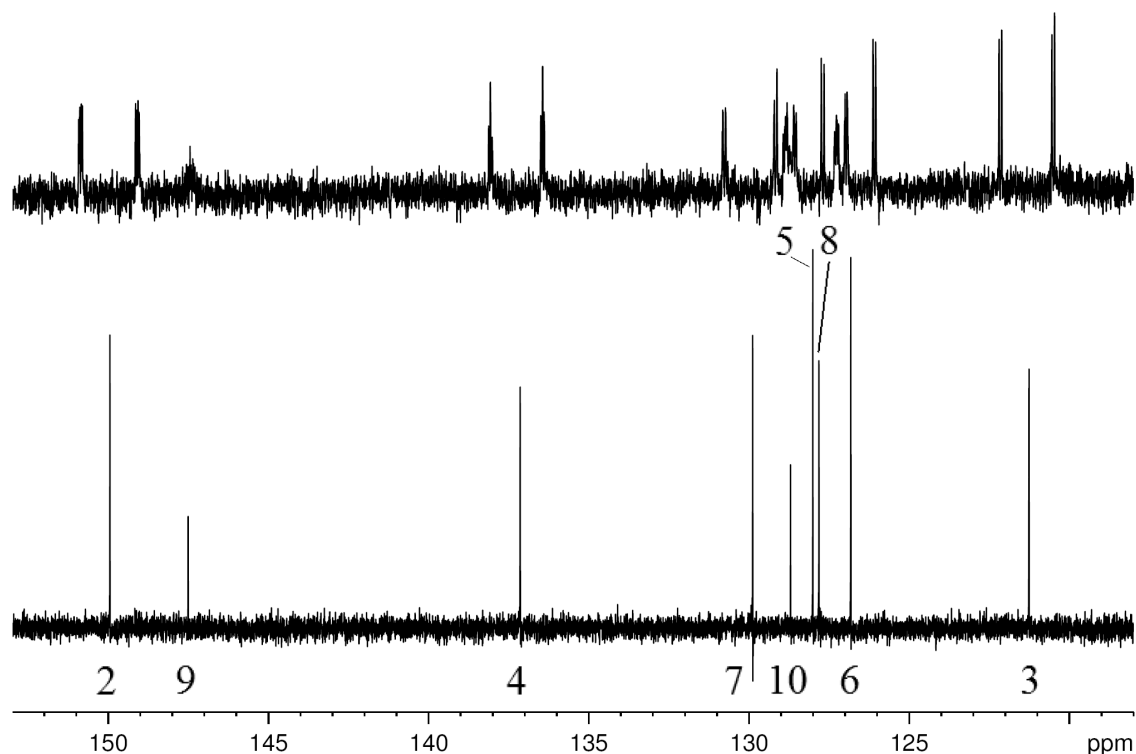


Figure 5.7 Thermally polarised coupled (top, 9216 scans) and decoupled (bottom, 101 scans)  $^{13}\text{C}$  NMR spectra of quinoline.

A  $^{13}\text{C}\{^1\text{H}\}$  NMR spectrum of quinoline is expected to reveal nine resonances. In a  $^{13}\text{C}$  NMR spectrum, each of these resonances is split by the associated  $^1\text{H}$ - $^{13}\text{C}$  couplings. In order to maximise the signal to noise ratios of the carbon signals, decoupling is required. This also has the effect to simplify the resultant spectrum and reduces the number of scans required. This is exemplified in Figure 5.7 in which the presented decoupled  $^{13}\text{C}$  sequence collected with 101 scans exhibits better signal intensity than the coupled  $^{13}\text{C}$  spectra collected in 9216 scans. An alternative is to work at higher concentrations.

It is well established that a range of substrates can receive  $^1\text{H}$  polarisation through the SABRE technique however, polarisation transfer to  $^{13}\text{C}$  has not yet been discussed.

#### 5.2.2.1 Method 2 applied to utilising $^{13}\text{C}$ magnetisation without $^1\text{H}$ decoupling

The resultant hyperpolarised single scan  $^{13}\text{C}$  NMR spectrum is often of poor quality due to the concentration of the sample being too low. An example  $^{13}\text{C}$  NMR spectrum of a 100 mM quinoline sample that has been hyperpolarised using method 2 and **IMes(b)** at a PTF of 10 G is shown in Figure 5.8.

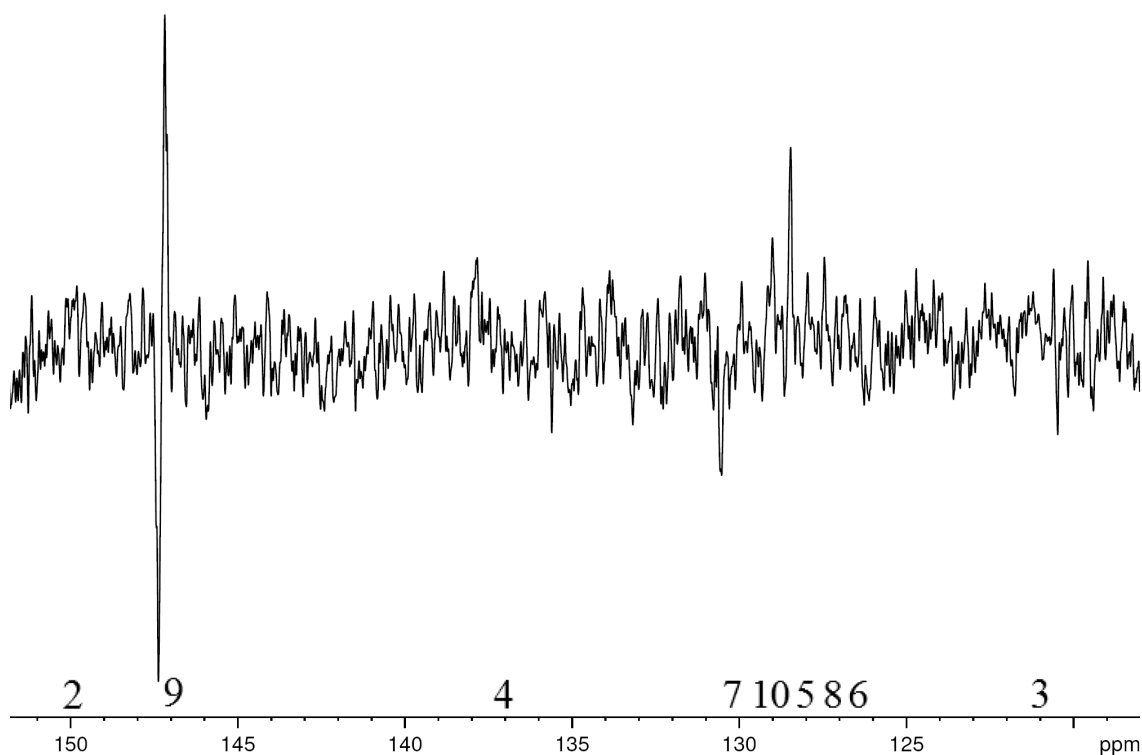


Figure 5.8 Single scan  $^{13}\text{C}$  NMR spectrum of quinoline hyperpolarised with **IMes(b)** at PTF of 10 G using method 2.

Of the nine carbons present in quinoline, signals corresponding to only two of these are clearly observable, both of which exhibit a poor signal to noise ratio. As a result, all investigations into the development and optimisation of 1D  $^{13}\text{C}$  NMR sequences were carried out with a higher concentration of catalyst and substrate with sample concentrations of 15 mM **IMes(b)**/**IMes(c)** and 300 mM quinoline being used, unless otherwise mentioned. Once hyperpolarised using method 2, these higher concentration conditions allow the observation of most  $^{13}\text{C}$  signals in a single scan.

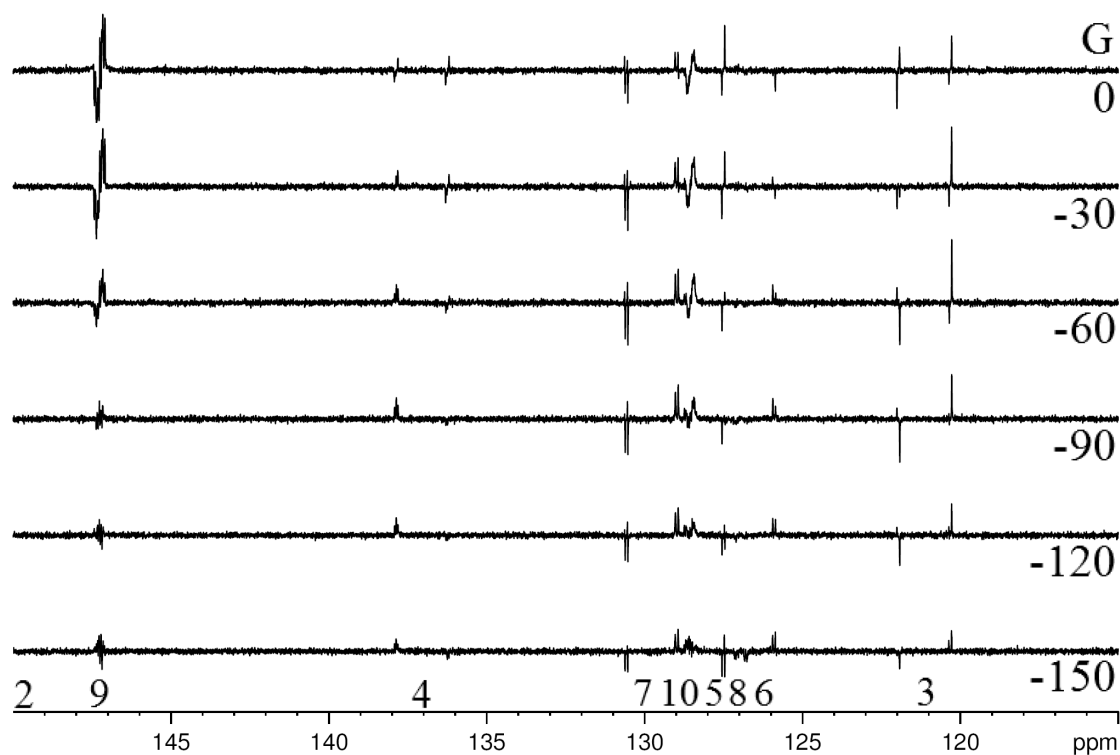


Figure 5.9 A series of single scan  $^{13}\text{C}$  NMR spectra of quinoline hyperpolarised with **IMes(c)** using method 2, where the PTF is increased from -150 G (bottom) to 0 G (top) in increments of 30 G.

Figure 5.9 shows that at when the sample is prepared in a PTF of -150 G, eight of the nine  $^{13}\text{C}$  resonances expected for quinoline are readily detected. The missing resonance corresponds to the carbon centre that is next to the nitrogen in position 2. When the PTF is changed to 0 G, the  $^{13}\text{C}$  spectrum obtained with a  $90^\circ$  read pulse shows that only six of the nine  $^{13}\text{C}$  resonances expected for quinoline are readily detected. The signal to noise ratio for these six signals is however much better than that achieved in the spectrum collected with a PTF of -150 G. These data therefore confirm that as with the  $^1\text{H}$  NMR spectra, the resultant spectra are dependent on the PTF.

The signals for the  $^{13}\text{C}$  centres are split with respect to both one bond and two bond couplings in the coupled spectrum. The application of SABRE has resulted some of these splittings appearing antiphase as a result of the multiple quantum states derived from *parahydrogen*. A very simple schematic of the resultant signals from these multiple quantum states is presented in Figure 5.10. Here, the observed nuclei **I** is considered to be split by two other nuclei, the first, **S**, with a large coupling and the second, **T**, with a small coupling. This situation is analogous to that observed for quinoline in Figure 5.9 where **I** corresponds to a  $^{13}\text{C}$  centre, **S** corresponds to a  $^1\text{H}$  one

bond away implying a large coupling and T corresponds to a  $^1\text{H}$  two bonds away implying a smaller coupling.

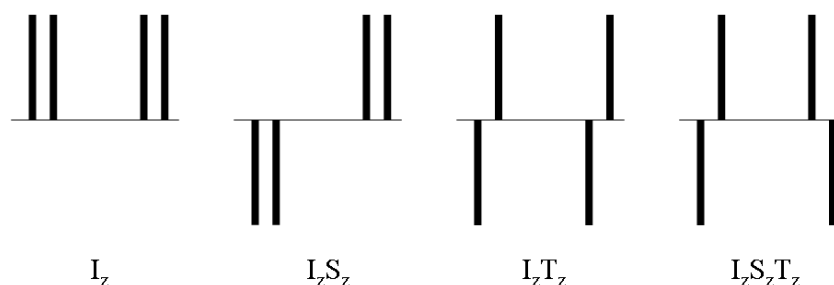


Figure 5.10 Schematic of the effect of multiple quantum states on the resultant signal.

For an  $I_z$  state, the signal is split according to both S and T, into inphase magnetisation. The magnetic state  $I_z S_z$  yields a signal is antiphase with respect to the large coupling to S. The same is true for  $I_z T_z$ , where the signal is antiphase with respect to the small coupling to T. This consequently means that for the magnetic state  $I_z S_z T_z$ , the resultant signal is antiphase with respect to both small and large couplings. The spectra shown in Figure 5.9 reflect the sum of these states in differing proportions. A schematic of selected combinations are presented in Figure 5.11.

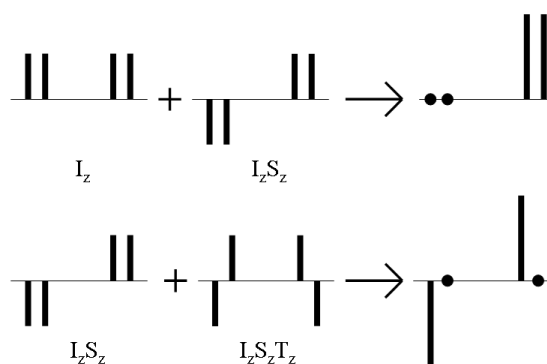


Figure 5.11 Schematic of the effect of selected combinations of multiple quantum states on the resultant signal.

Figure 5.11 represents a simplified schematic of the combination of selected multiple quantum states. They are simplified in the sense that they assume both multiple quantum states are added together in equal proportion which is unlikely to occur in a real system. In Figure 5.9, signals with similar combinations to those observed in Figure 5.10 and Figure 5.11 can be identified. For example, the signal observed for position 9 of quinoline when a PTF of -60 G, -30 G or 0 G was used shows an antiphase nature with respect to the small coupling, corresponding to an  $I_z T_z$  state. The carbon is a

quaternary carbon and therefore shows no large coupling. This state is also observed for the signal corresponding to position 4 of quinoline when a PTF of 0 G is used however in this case, splittings corresponding to both small and large couplings are observed, antiphase with respect to the small coupling. Representative signals with the  $I_zT_z$  state are shown in Figure 5.12.

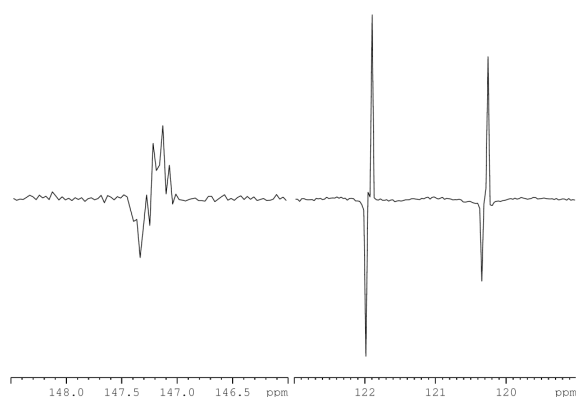


Figure 5.12  $^{13}\text{C}$  signals which present with the  $I_zT_z$  state. Left is a quaternary carbon signal and right is a CH carbon signal.

It can also be observed in Figure 5.9 that as the PTF is decreased through to -150 G, the profile of the signal corresponding to position 4 changes from presenting with  $I_zT_z$  nature to presenting as a combination of  $I_z$  and  $I_zT_z$  nature. A similar change in the appearance of the signal corresponding to position 3 of quinoline is also observed upon changing the PTF. At a PTF of 0 G, the signal presents with  $I_zT_z$  nature to a mixture of  $I_zS_z$  with either  $I_zT_z$  or  $I_zS_zT_z$  states at a PTF of -150 G.

It is consequently possible to observe that a spectrum collected through the use of SABRE can contain a number of different nuclear magnetic states, and these states can present as antiphase to more than one coupling, and to different couplings when using different PTFs. This is an important observation when considering decoupling the hyperpolarised  $^{13}\text{C}$  spectrum.

#### 5.2.2.2 Method 2 applied to utilising $^{13}\text{C}$ magnetisation with $^1\text{H}$ decoupling

As discussed in the previous section, when  $^{13}\text{C}$  is polarised using the SABRE technique, the resulting signals can be antiphase. This means standard decoupling is not possible as the antiphase signals cancel out and consequently become unobservable, as shown in Figure 5.13.

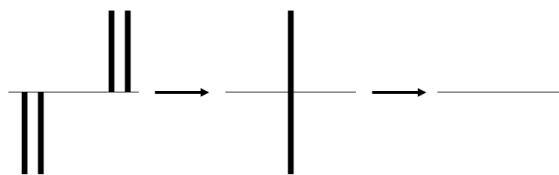


Figure 5.13 Schematic depicting the effect of decoupling on antiphase signals.

This effect is also observed in *parahydrogen* induced polarisation and means decoupling is not possible without further manipulation of the magnetic states present. This was first explored by the addition of a delay period between the  $90^\circ$  pulse and data acquisition as shown in Figure 5.14.

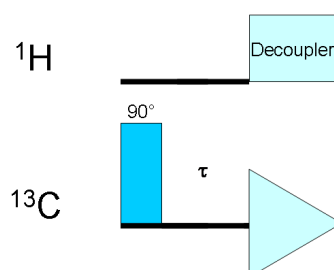


Figure 5.14 Schematic of the refocused  $^{13}\text{C}\{^1\text{H}\}$  NMR sequence termed the  $^{13}\text{C}\{^1\text{H}\}$ \_JR NMR sequence.  $\tau$  denotes a delay corresponding to a  $^1\text{H}$ - $^{13}\text{C}$  coupling constant.

The delay between the pulse and acquisition allows any antiphase signal to refocus into in-phase signals, which can consequently be decoupled during acquisition. This sequence can be optimised depending on the delay used. For the rest of this thesis, the delay is optimised to either a one bond correlation where  $^1J_{\text{HC}}$  is around 165 Hz, or a two bond correlation where  $^2J_{\text{HC}}$  is around 8 Hz, both optimised for position 3. These values were set based on a fully coupled  $^{13}\text{C}$ , the data for which is presented in Chapter 4 or Experimental.

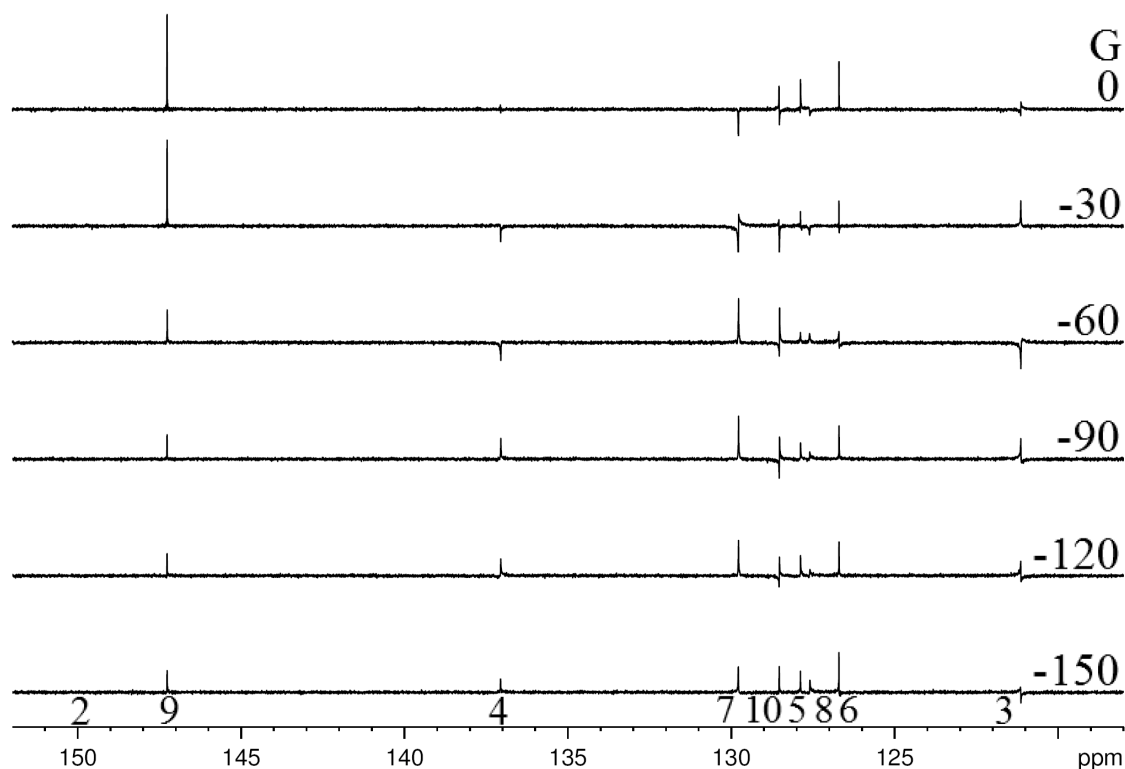


Figure 5.15 A series of single scan  $^{13}\text{C}\{^1\text{H}\}_{\text{JR}}$  NMR spectra optimised for a one bond coupling of quinoline hyperpolarised with **IMes(c)** using method 2 where the PTF is increased from -150 G (bottom) to 0 G (top) in increments of 30 G.

The sequence shown in Figure 5.14 was investigated where the PTF was changed from -150 G to 0 G in increments of 30 G. Figure 5.15 clearly shows that when the sequence is optimised to refocus one bond couplings, eight of the nine expected  $^{13}\text{C}$  signals can be successfully refocused such that they could be decoupled. The signal corresponding to position 2 of quinoline is however unobservable. Based on this dependence on PTF alone, it is possible to see that the best signal intensity is observed for a PTF of 0 G. The data were collected for a sequence that optimised to refocus the smaller two bond couplings. The results of this process are shown in Figure 5.16.

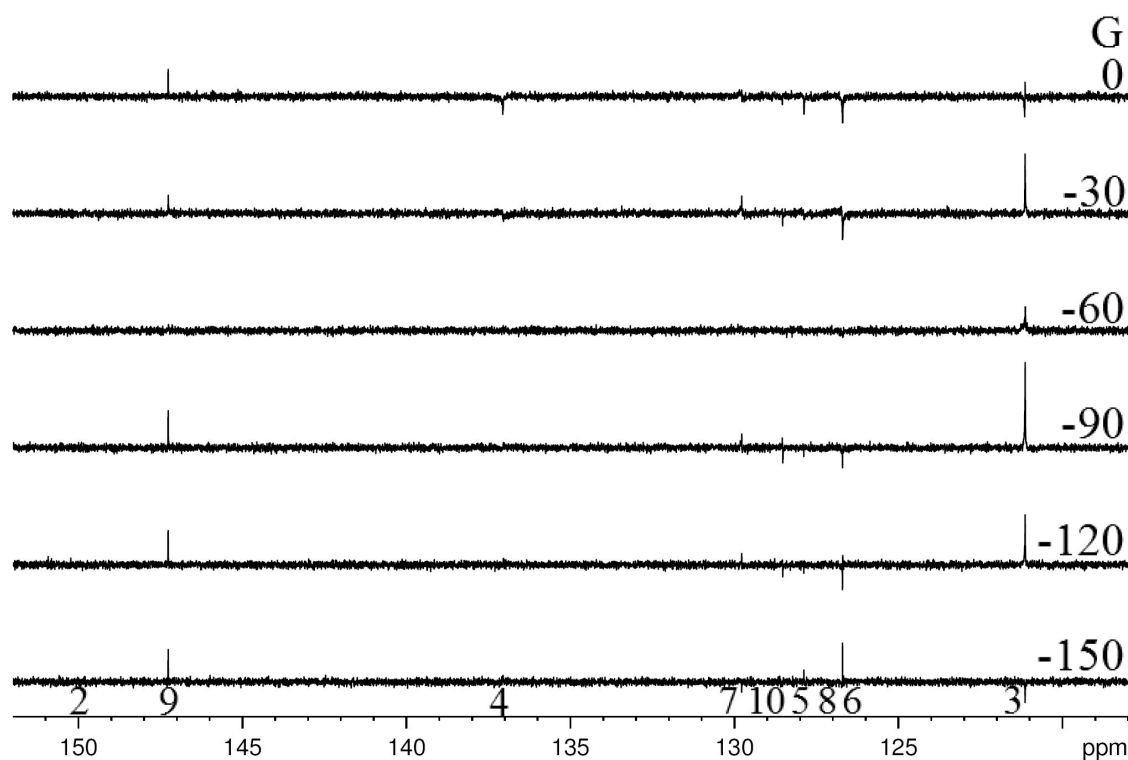


Figure 5.16 A series of single scan  $^{13}\text{C}\{^1\text{H}\}_\text{JR}$  NMR spectra optimised for a two bond coupling of quinoline hyperpolarised with **IMes(c)** using method 2 where the PTF is increased from -150 G (bottom) to 0 G (top) in increments of 30 G.

Figure 5.16 shows that when the  $^{13}\text{C}\{^1\text{H}\}_\text{JR}$  sequence is optimised to refocus a two bond coupling, it is difficult to define a single PTF which yields maximum signal intensity. Compared to the sequences optimised for one bond couplings, fewer signals are now observed, with a maximum of six signals in any one spectrum. The greatest signal intensity is observed when a PTF of -90 G is employed and coincidentally, this is also the PTF which yielded the greatest number of signals. This was therefore chosen for comparison to the spectrum optimised for one bond couplings at a PTF of 0 G shown in Figure 5.17.



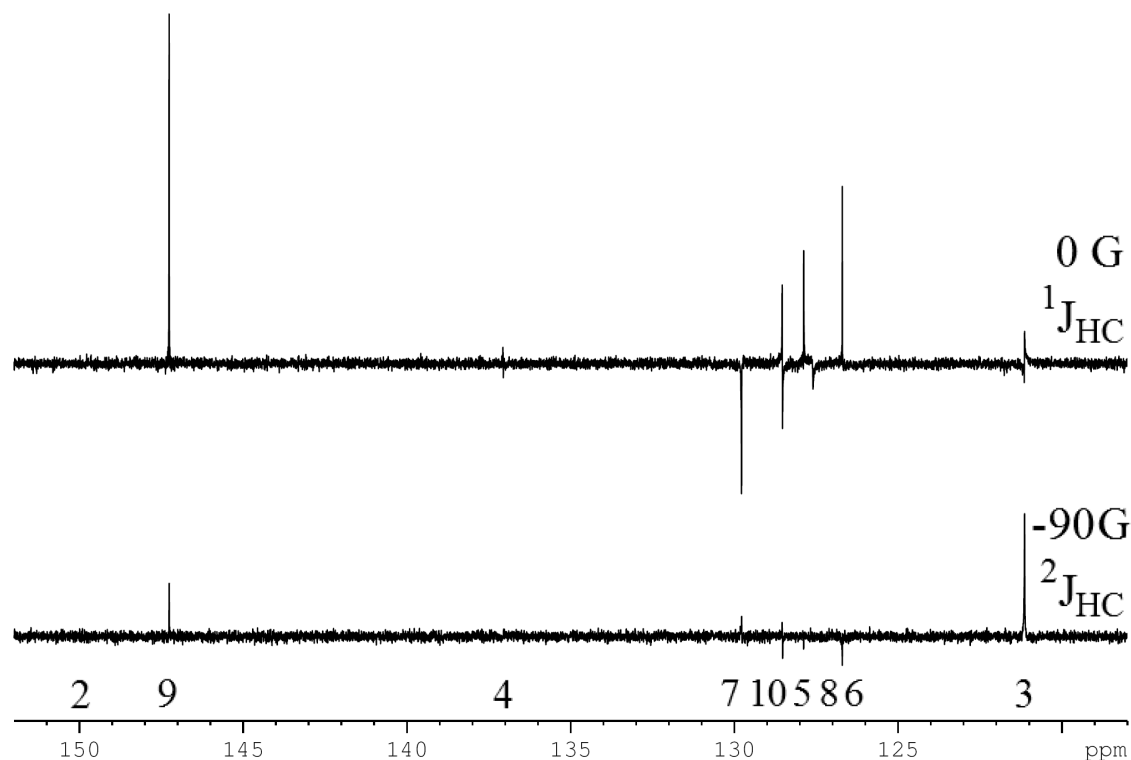


Figure 5.17 Single scan  $^{13}\text{C}\{^1\text{H}\}$ \_JR NMR spectra optimised for a two bond coupling with a PTF of -90 G (bottom) and one bond coupling with a PTF of 0 G (top) of quinoline hyperpolarised using method 2 with **IMes(c)**.

Figure 5.17 shows that when the  $^{13}\text{C}\{^1\text{H}\}$ \_JR sequence is optimised for two bond couplings, only the signal at 121 ppm (C3) has an increased intensity compared to optimisation for one bond couplings. The signal intensity for all the other observed peaks is greater when the sequence is optimised to refocus one bond couplings. It is also possible to observe two more signals when the sequence is optimised for one bond couplings. A possible reason for these observations is that the relaxing hyperpolarised states do not survive the refocusing time. The delay period,  $\tau$  is equal to  $1/2J_{\text{CH}}$ , and therefore if two bond couplings are refocused,  $\tau$  will equal 0.0625 s ( $1/(2 \times 8)$ ). This is a much longer time than the delay used to correspond to one bond couplings, 0.003 s ( $1/(2 \times 165)$ ).

While the signals created using the  $^{13}\text{C}\{^1\text{H}\}$ \_JR sequence have been successfully refocused to the point where they can be decoupled, the decoupled signals are still not in phase with each other. This is because the  $^{13}\text{C}\{^1\text{H}\}$ \_JR sequence allows refocusing with respect to J coupled evolution but not with respect to chemical shift evolution. One method to overcome this is to present the spectrum in magnitude, an example of which

can be seen in Figure 5.37. This can also be rectified through the application of a new sequence termed  $^{13}\text{C}\{^1\text{H}\}_{\text{JCSR}}$ , shown in Figure 5.18.

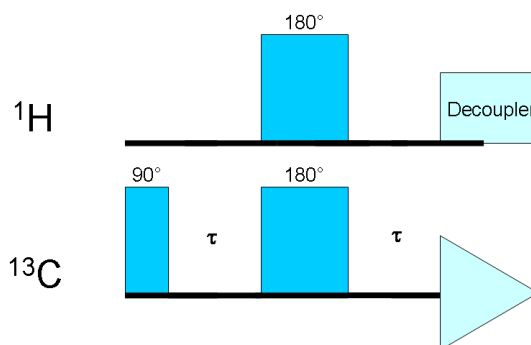


Figure 5.18 Schematic of the refocused  $^{13}\text{C}\{^1\text{H}\}_{\text{JCSR}}$   $^{13}\text{C}$  NMR sequence.  $\tau$  denotes a delay corresponding to a  $^1\text{H}$ - $^{13}\text{C}$  coupling constant.

This refocuses spin evolution due to chemical shift on  $^{13}\text{C}$ , but the  $180^\circ$  pulse on  $^1\text{H}$  allows the state to evolve into an in-phase state. At this point, the  $^1\text{H}$ - $^{13}\text{C}$  couplings can be removed by  $^1\text{H}$ -decoupling and the  $^{13}\text{C}\{^1\text{H}\}$  NMR spectrum recorded.

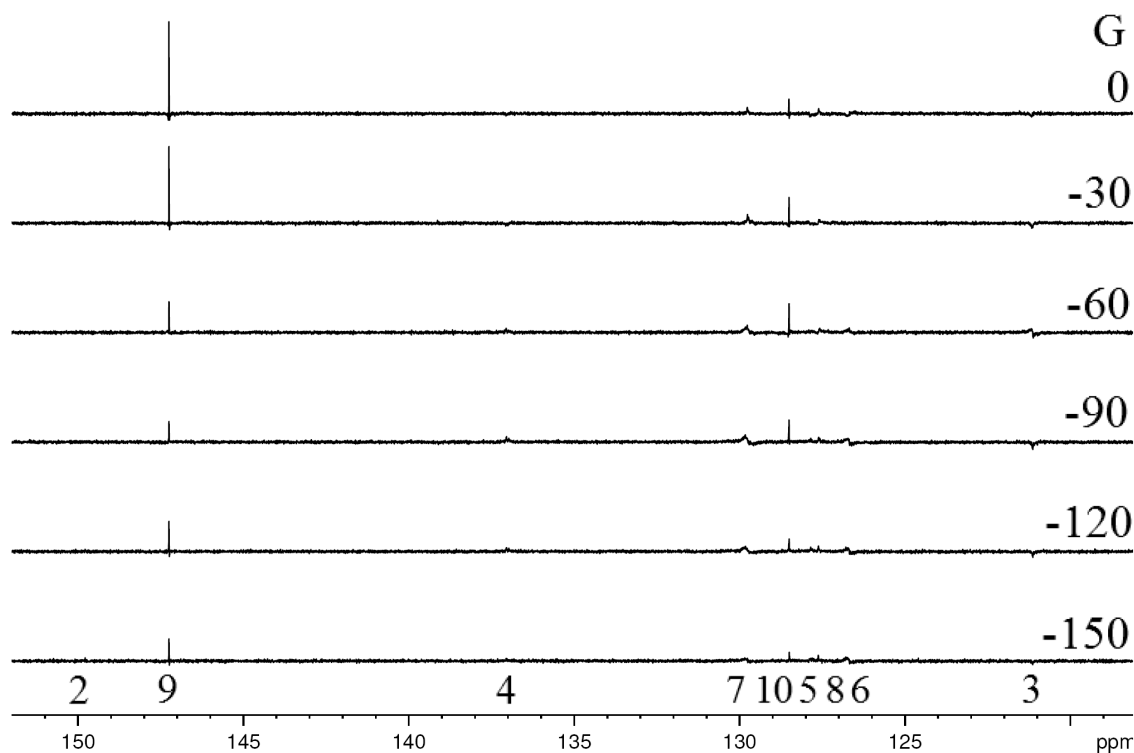


Figure 5.19 A series of single scan  $^{13}\text{C}\{^1\text{H}\}_{\text{JCSR}}$  NMR spectra optimised for a one bond coupling of quinoline hyperpolarised with **IMes(c)** using method 2 where the PTF is increased from -150 G (bottom) to 0 G (top) in increments of 30 G.

Figure 5.19 shows the  $^{13}\text{C}\{^1\text{H}\}$ \_JCSR NMR sequence exhibits most intense signals at a PTF of 0 G and the signals have been decoupled however not all the expected signals are observed. These spectra were repeated when the sequence was optimised for two bond couplings.

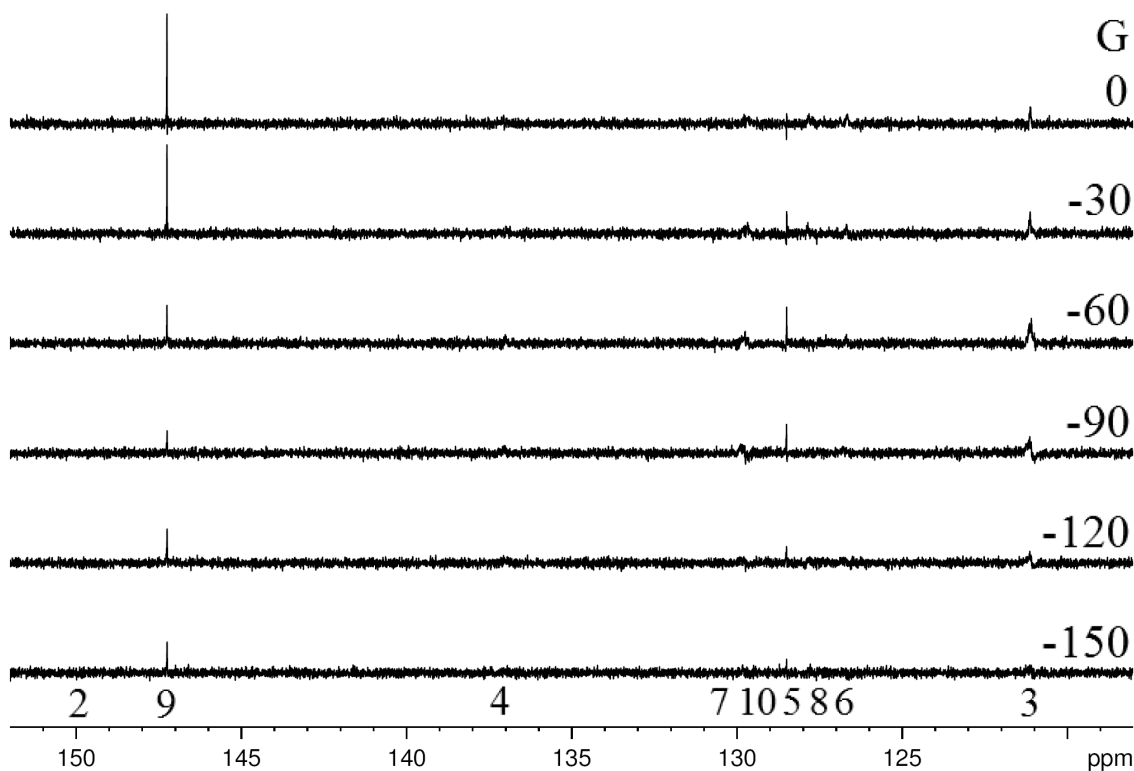


Figure 5.20 A series of single scan  $^{13}\text{C}\{^1\text{H}\}$ \_JCSR NMR spectra optimised for a two bond coupling of quinoline hyperpolarised with **IMes(c)** using method 2 where the PTF is increased from -150 G (bottom) to 0 G (top) in increments of 30 G.

Figure 5.20 again shows maximum signal intensity at a PTF of 0 G, similar to the trend observed when the sequence is optimised for one bond couplings. As this is the case, Figure 5.21 shows the comparison of the spectra resulting from the sequence being optimised for both one and two bond couplings both hyperpolarised at a PTF of 0 G.

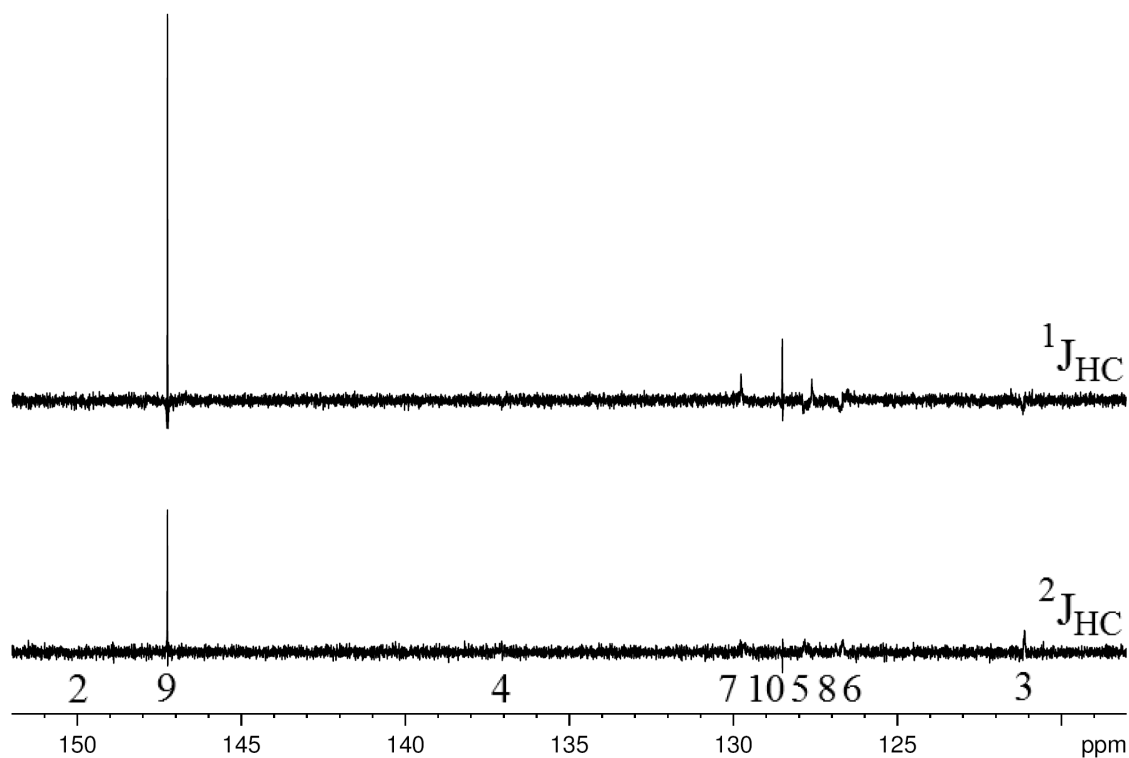


Figure 5.21 Single scan  $^{13}\text{C}\{^1\text{H}\}_\text{JCSR}$  spectra optimised for one bond couplings (top) and two bond couplings (bottom), of quinoline hyperpolarised with **IMes(c)** using method 2 where the PTF is set to 0 G.

Figure 5.21 shows that when the  $^{13}\text{C}\{^1\text{H}\}_\text{JCSR}$  sequence is optimised for two bond couplings, only the signal at 121 ppm (**C3**) has an increased intensity compared to optimisation for one bond couplings, as it is not observable in that spectrum. However, the signal intensity for all the other observed peaks is greater when the sequence is optimised to refocus one bond couplings. The two methods of refocusing a  $^{13}\text{C}$  spectrum in preparation for decoupling are compared to each other in Figure 5.22.

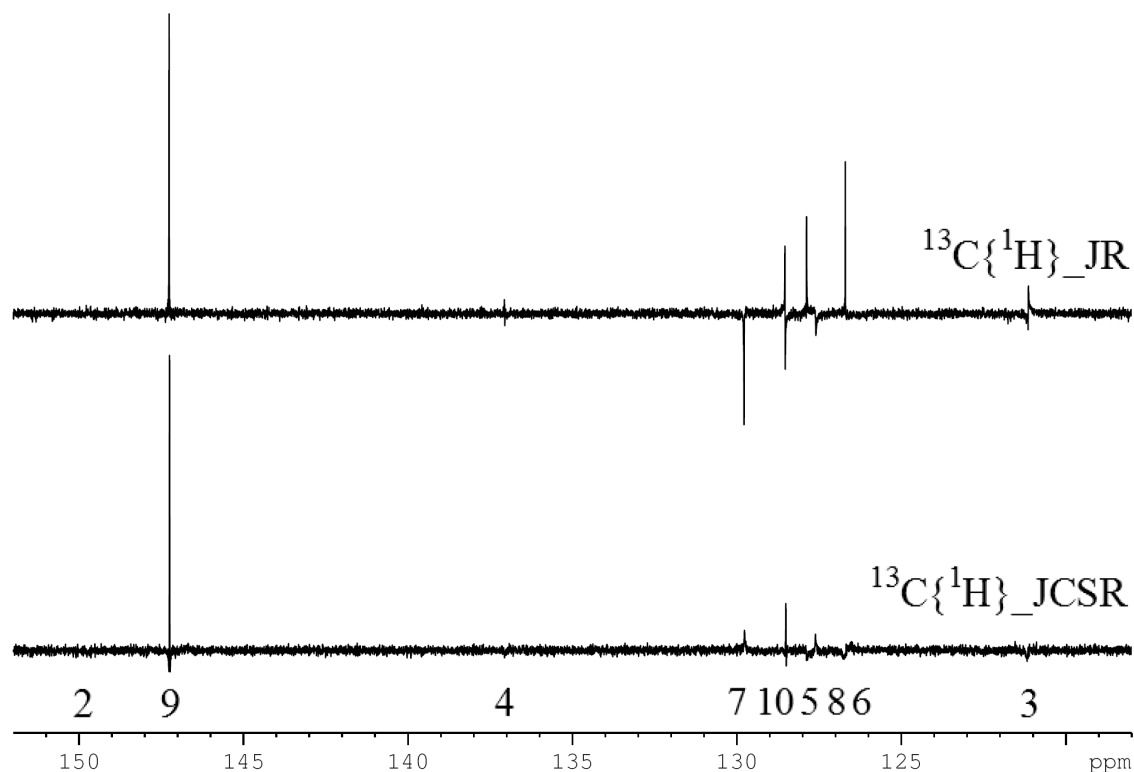


Figure 5.22 Optimised  $^{13}\text{C}\{^1\text{H}\}_{\text{JR}}$  NMR spectrum (top) and optimised  $^{13}\text{C}\{^1\text{H}\}_{\text{JCSR}}$  NMR spectrum.

Figure 5.22 shows the signal corresponding to position 2 of quinoline is of similar intensity for both sequences however the  $^{13}\text{C}\{^1\text{H}\}_{\text{JR}}$  spectrum shows more of the other signals at greater intensity than the  $^{13}\text{C}\{^1\text{H}\}_{\text{JCSR}}$ . Again, it would be recommended these spectra are presented in magnitude mode for ease of assignment.

### 5.2.2.3 Method 2 applied to $^{13}\text{C}$ INEPT NMR sequences

The INEPT sequence (Insensitive Nuclei Enhanced by Polarisation Transfer) is a method by which relatively highly polarised nuclei, most commonly the  $^1\text{H}$ , is used to polarise less sensitive nuclei. It is an integral part of many of the more complicated NMR sequences which are used very successfully to characterise materials, including the heteronuclear 2D sequences discussed later in this chapter (HMQC/HSQC).<sup>8</sup> It was therefore decided to investigate the effect of SABRE on INEPT type procedures in order to fully understand how it might be optimally used, and to apply these observations to later investigations into related 2D heteronuclear experiments.

Due to the previously discussed complications with proton decoupling within  $^{13}\text{C}$  NMR spectroscopy, the hyperpolarised INEPT investigations started with a fully coupled

INEPT sequence. This is termed 'INEPTnd' for the duration of this thesis and the sequence is shown in Figure 5.23.

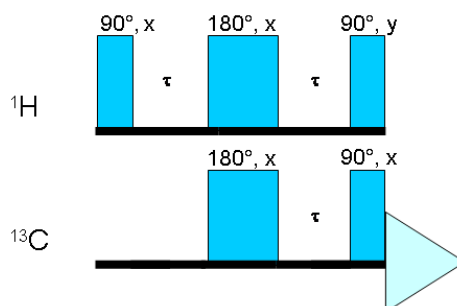


Figure 5.23 Schematic of the standard  $^{13}\text{C}$  INEPTnd sequence.  $\tau$  denotes a delay corresponding to a  $^1\text{H}$ - $^{13}\text{C}$  coupling constant.

Two fully coupled thermally polarised  $^{13}\text{C}$  NMR spectra (Figure 5.24) collected using the standard INEPTnd NMR sequence using the optimal couplings for H3 (165 Hz and 8 Hz) as for the previously investigated  $^{13}\text{C}$  and  $^{13}\text{C}\{^1\text{H}\}$  sequences.

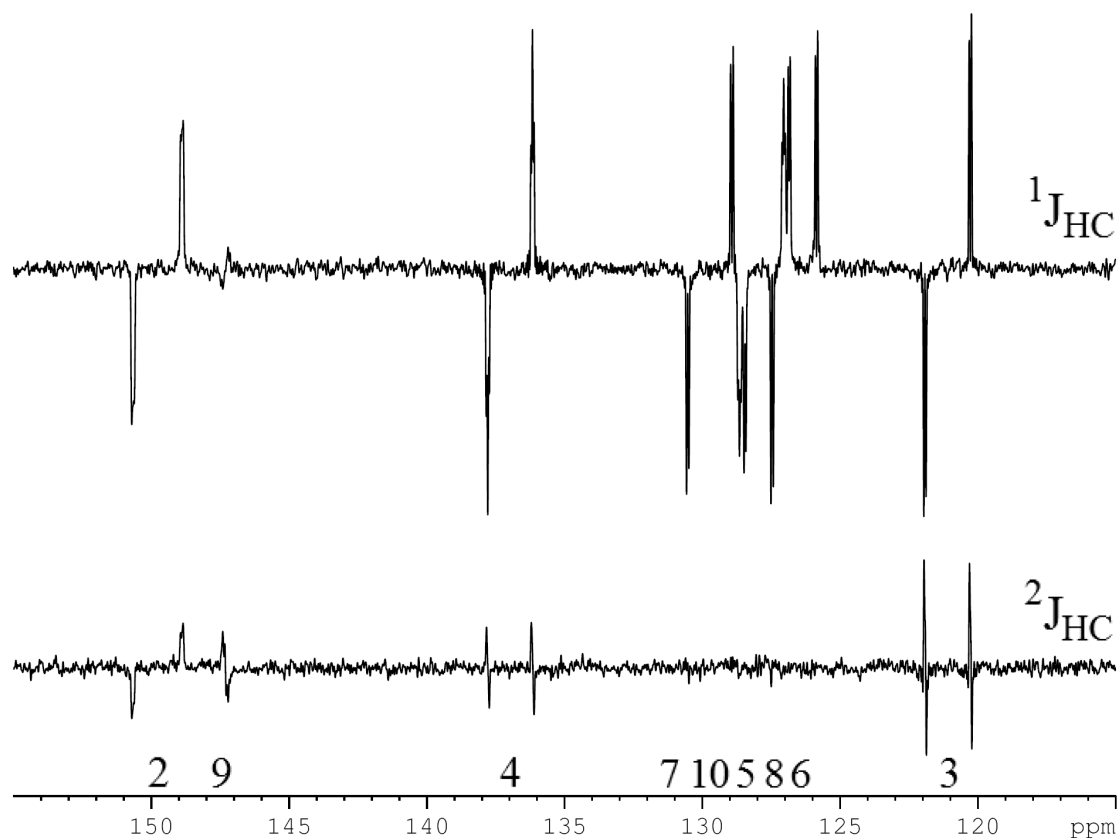


Figure 5.24 Thermally polarised  $^{13}\text{C}$  INEPTnd NMR spectra of quinoline optimised for one bond (top) and two bond (bottom) coupling.

The  $^1\text{H}$ - $^{13}\text{C}$  INEPTnd NMR spectra optimised for one bond couplings were investigated in the range 180 Hz to 150 Hz in increments of 1 Hz, and 161 Hz to 160 Hz in increments of 0.1 Hz. It was observed that little change was observed in the resultant spectra. The  $^1\text{H}$ - $^{13}\text{C}$  INEPTnd NMR spectra optimised for two bond couplings were investigated in the range 20 Hz to 2 Hz in increments of 1 Hz and significant differences were observed in the resultant spectra. In the case of these thermally polarised spectra, the best results were observed when optimised for a 19 Hz coupling.

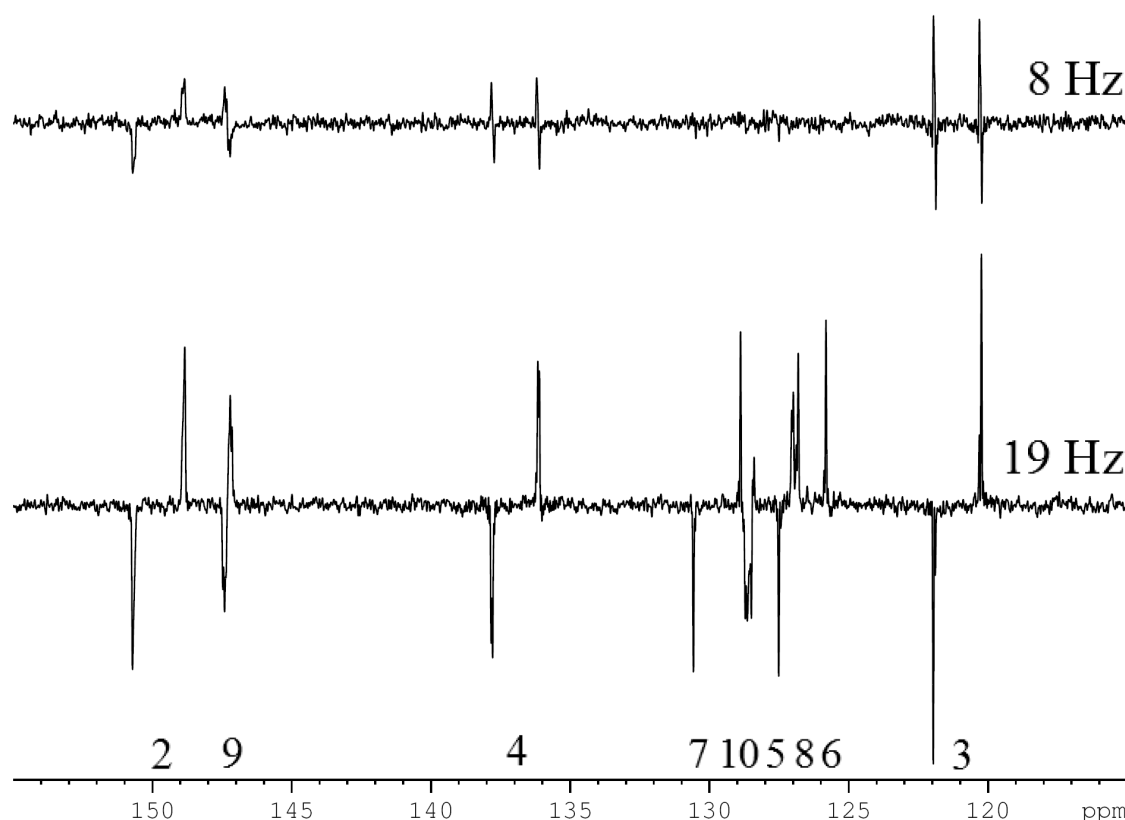


Figure 5.25 Thermally polarised  $^{13}\text{C}$  INEPTnd NMR spectra of quinoline optimised for two bond couplings (8 Hz, top and 19 Hz bottom).

From this thermally polarised data, it is observed that the 19 Hz coupling results in more signals and of greater signal intensity than the spectrum completed at 8 Hz however this value is significantly different from the couplings measured for quinoline using a thermally polarised  $^{13}\text{C}\{^1\text{H}\}$  NMR spectrum (see Chapter 4). Future hyperpolarised investigations will therefore be considered as optimised for the couplings relating to position 3.

The following hyperpolarised experiments were completed using a higher concentration sample of 15 mM **IMes(c)** and 300 mM quinoline, with a single scan, unless otherwise

stated. The effect of the PTF was the first investigated with respect to a hyperpolarised  $^{13}\text{C}$  INEPTnd NMR spectrum. Two PTFs were investigated; 0 G (to maximise  $^1\text{H}$ - $^1\text{H}$   $I_zS_z$ -type magnetisation, section 5.2.1.2, pg 208) and -65 G (to maximise  $^1\text{H}$   $I_z$  magnetisation, Chapter 4), initially optimised for a two bond coupling. The results of this experiment are presented in Figure 5.26.

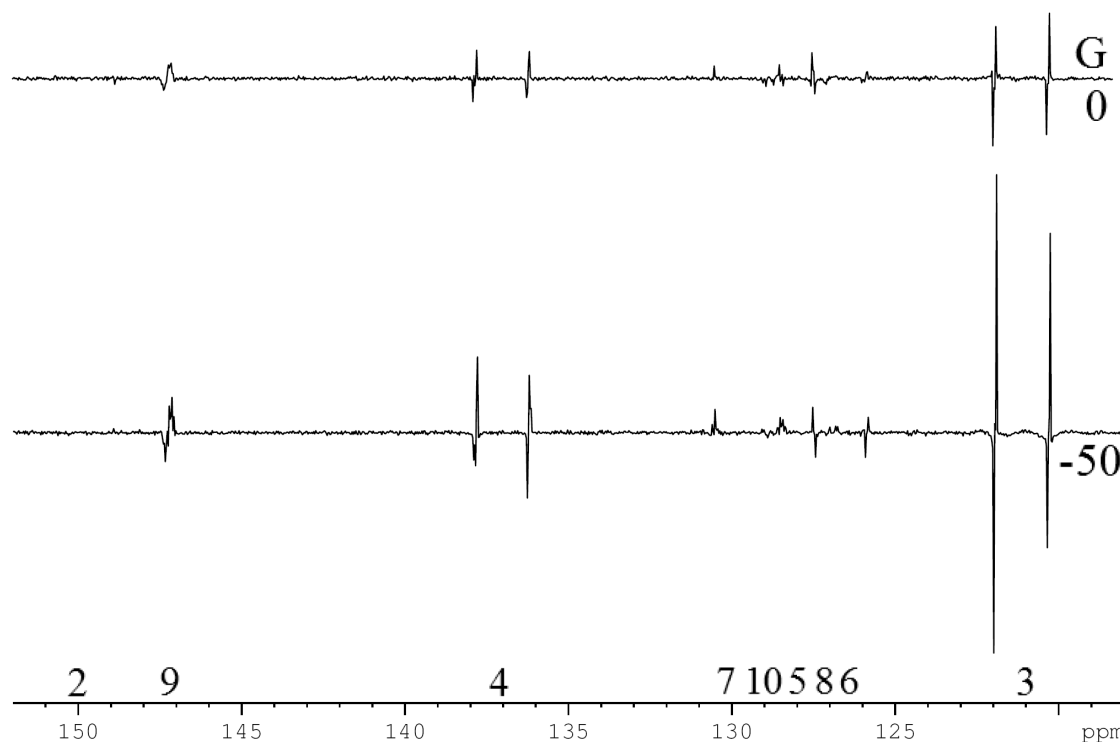


Figure 5.26 Single scan  $^{13}\text{C}$  INEPTnd NMR spectra of quinoline optimised for a two bond coupling, hyperpolarised using method 2 with **IMes(c)** at a PTF of -50 G (bottom) and 0 G (top).

Figure 5.26 shows the signal intensity for the INEPTnd sequence is greatest when a PTF of -50 G is employed. This is expected as the  $^{13}\text{C}$  magnetisation observed is derived from  $^1\text{H}$  polarisation which exhibits a greater polarisation at a PTF of -50 G for the  $I_z$  state.

The first pulse on the  $^1\text{H}$  channel in a standard INEPTnd sequence is a  $90^\circ$  pulse however any  $I_zS_z$  magnetisation will remain unobservable throughout the sequence. In order to detect signal derived from the  $I_zS_z$  magnetisation state, a different pulse is required.<sup>149</sup> This principle was investigated when applying SABRE to the INEPTnd sequence, such that the first pulse in the INEPTnd sequence shown in Figure 5.23 is shortened to a  $45^\circ$  pulse (as described in the Introduction). The resultant spectra yielded similar results however the signal intensity was less than that observed for the spectra



completed with a  $90^\circ$  suggesting the INEPTnd is maximised for the  $I_z$  state. The same trend is observed when the experiments are collected with a PTF of 0 G where  $I_z S_z$  magnetisation is optimised. This further suggests the sequence is optimised when the level of  $I_z$  type magnetisation is optimised.

Until now, the INEPTnd sequence has only been investigated when optimised for a two bond coupling, however it is also important to consider the effect when the sequence is optimised for a one bond coupling. The effect of changing the PTF when the sequence is optimised for one bond couplings is considered first.

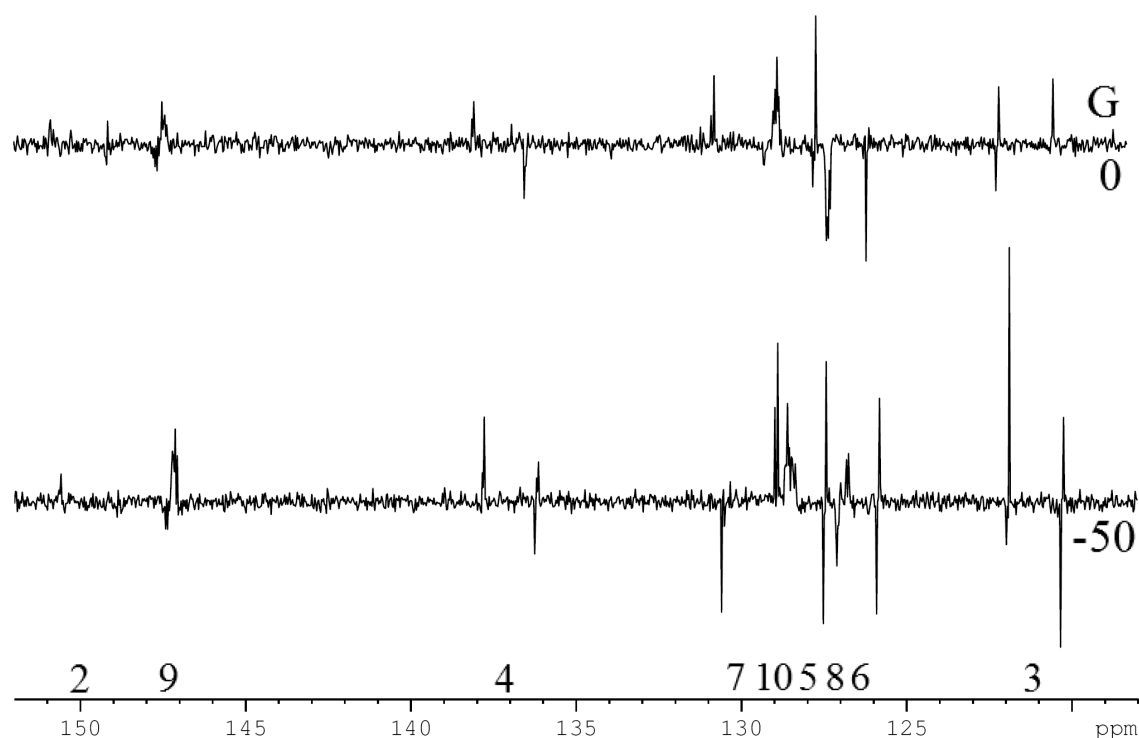


Figure 5.27 Single scan  $^{13}\text{C}$  INEPTnd NMR spectra of quinoline optimised for a one bond coupling, hyperpolarised using method 2 with **IMes(c)** at a PTF of -50 G (bottom) and 0 G (top).

Figure 5.27 shows that when the  $^{13}\text{C}$  INEPTnd sequence is optimised for one bond couplings, greater signal intensity is observed when the PTF is set to -50 G. The sequence optimised for one bond couplings was then investigated with respect to the initial pulse, with  $90^\circ$  and  $45^\circ$  initial pulses investigated as before. The results in this case match those found when the sequence is optimised for two bond couplings, in that the greatest signal to noise is observed when the first pulse is  $90^\circ$ . The sequence optimised for one bond couplings was also investigated at 0 G again showing the same trend that starting the sequence with a  $90^\circ$  pulse gave signals with greater intensity. This

suggests the INEPTnd sequence reveals more intense signals when the sample is hyperpolarised such that the  $I_z$  state on proton is maximised.

In general the  $^{13}\text{C}$  INEPTnd NMR spectra shows greatest signal intensity when the first pulse is  $90^\circ$  and the PTF is set to  $-50$  G. The sequence optimised for one bond couplings is therefore compared to the same sequence optimised for two bond couplings, both under the same conditions. This is shown in Figure 5.28.

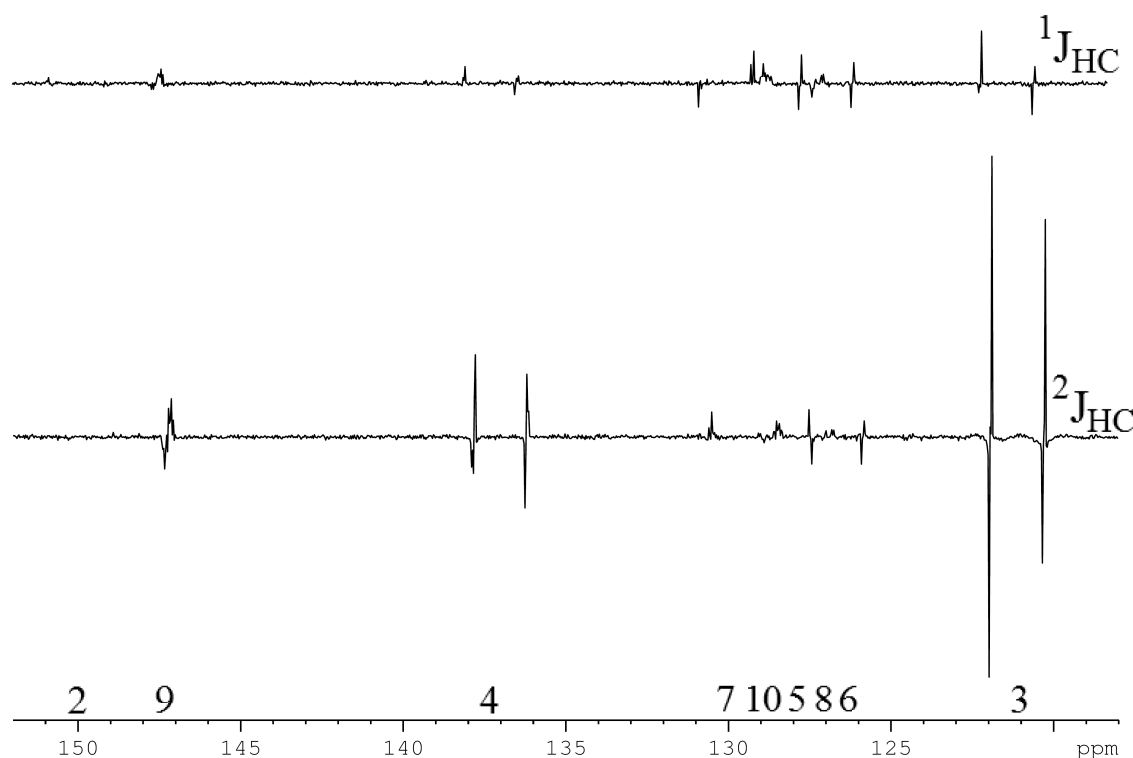


Figure 5.28 Single scan  $^{13}\text{C}$  INEPTnd NMR spectra of quinoline hyperpolarised with **IMes(c)** at a PTF of  $-50$  G where the first pulse is  $90^\circ$  and the sequence is optimised for two bond couplings (bottom) and one bond couplings (top).

It can be seen that the INEPTnd transfer experiment shows much better signal to noise when optimised for two bond couplings. This is unexpected as it would be assumed that the increased delay time required for when optimising for two bond couplings compared to one bond couplings would allow polarisation decay, as is observed in the thermal spectra (Figure 5.24). A possible reason for this is the level of polarised states within the quinoline, for instance, under a one bond coupling sequence, polarisation is received from only one hyperpolarised proton, however in the two bond coupling sequence, polarisation is transferred from two hyperpolarised protons. It is also noting that both

couplings are optimised for position 3, in which the most significant difference is observed.

It can be concluded from the previous experiments that, up to this point, the optimal conditions for the INEPTnd sequence are to optimise for two bond couplings, polarise with a PTF of -50 G and set the first pulse in the sequence to  $90^\circ$ . The spectrum resulting from these conditions is compared to the optimal  $^{13}\text{C}$  NMR spectrum and optimal refocused  $^{13}\text{C}\{^1\text{H}\}$  NMR spectrum in Figure 5.29.

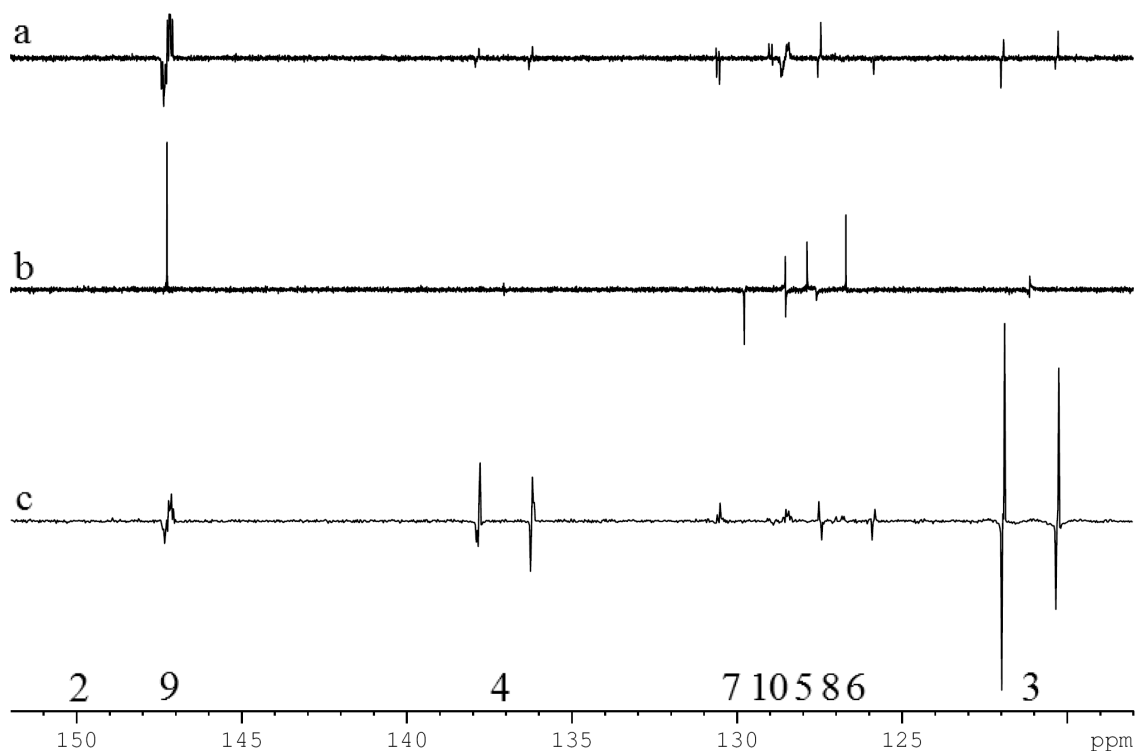


Figure 5.29 Various hyperpolarised coupled and decoupled  $^{13}\text{C}$  NMR spectra of quinoline. a)  $^{13}\text{C}$  NMR spectrum collected at a PTF of 0 G, b) a refocused  $^{13}\text{C}\{^1\text{H}\}$  NMR spectrum collected at a PTF of 0 G and c) a  $^{13}\text{C}$  INEPTnd NMR spectrum optimised for two bond couplings collected at a PTF of -50 G.

An alternative sequence has been published by Haake *et al.*<sup>150</sup> that is designed to maximise polarisation derived from *parahydrogen* in PHIP. This entails changing the phase of the first pulse. The sequence proposed for use with PHIP is presented in Figure 5.30 and is associated with utilising a proton based  $I_z S_z$  starting state.

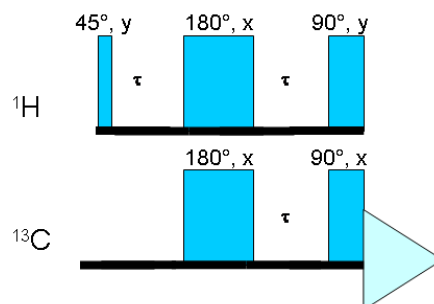


Figure 5.30 Schematic of the  $^{13}\text{C}$  PH\_INEPT NMR sequence, adapted from Haake *et al.*<sup>150</sup> which differs from the INEPTnd sequence in that the first pulse has a  $90^\circ$  phase change and is a  $45^\circ$  pulse. This is adapted for use in this research such that the first pulse can be  $90^\circ$  or  $45^\circ$ , to be termed INEPT\_phase.  $\tau$  denotes a delay corresponding to a  $^1\text{H}$ - $^{13}\text{C}$  coupling constant.

The PH\_INEPT NMR sequence in Figure 5.30 differs from the INEPTnd sequence presented in Figure 5.23 in that the initial pulse is shorter and has a  $90^\circ$  phase change from x to y. The  $45^\circ$  pulse is required in PHIP<sup>149</sup> (see Introduction) but not SABRE and therefore the phase change to the first pulse has been investigated with both  $90^\circ$  and  $45^\circ$  first pulses. The new sequence will be termed INEPT\_phase for the duration of this thesis, described in Figure 5.30. The effect of changing the value of  $\tau$  was the first to be investigated, with results shown in Figure 5.31.

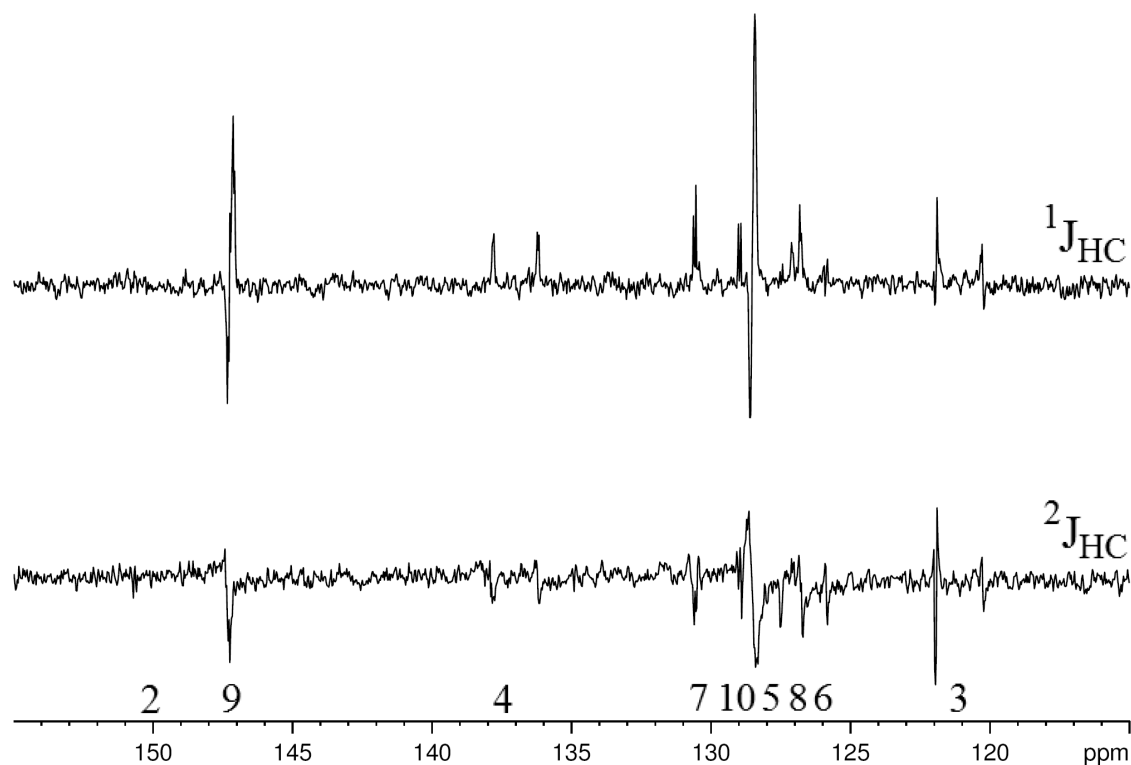


Figure 5.31 Single scan  $^{13}\text{C}$  INEPT\_phase NMR spectra of quinoline hyperpolarised with **IMes(c)** at a PTF -65 G where the first pulse is  $90^\circ$  and the sequence is optimised for two bond couplings (bottom) and one bond couplings (top).

Comparing the spectra in Figure 5.31, it is possible to observe that a better signal to noise is obtained when the sequence is optimised for one bond couplings. This is in contrast to the result found for the INEPTnd sequence. The effect of changing the PTF was then investigated. Results are shown in Figure 5.32.

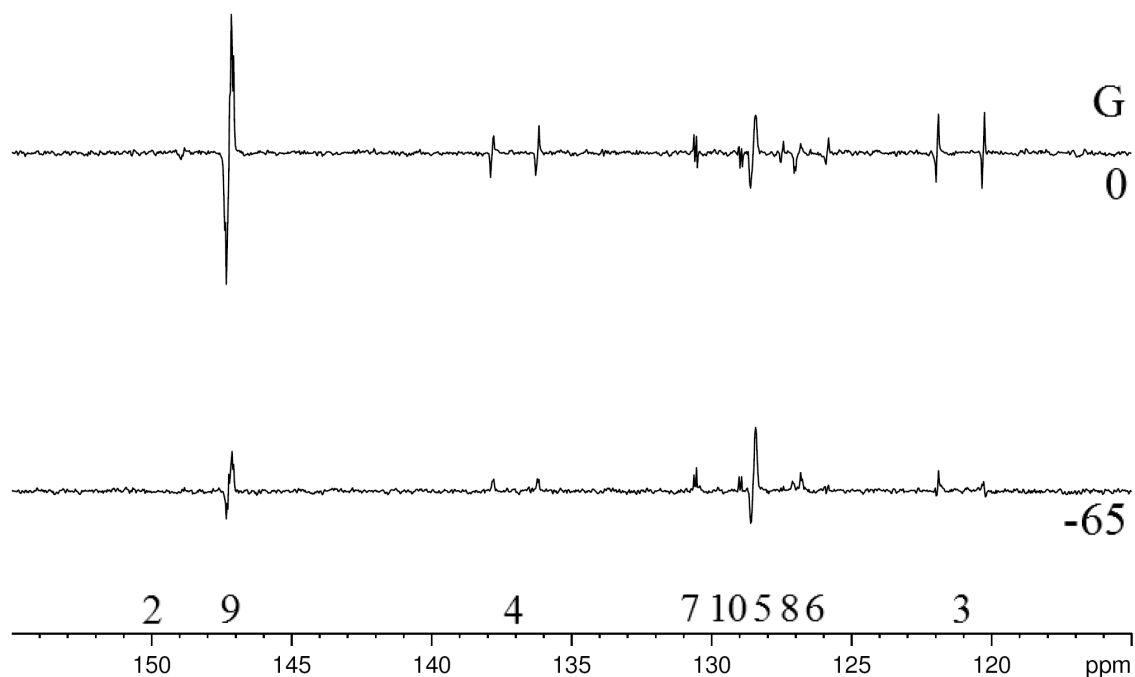


Figure 5.32 Single scan  $^{13}\text{C}$  INEPT<sub>phase</sub> NMR spectra of quinoline optimised for one bond couplings hyperpolarised using method 2 with **IMes(c)**, the first pulse on  $^1\text{H}$  is  $90^\circ$ , and PTF occurs at  $-65$  G (bottom) and  $0$  G (top).

Figure 5.32 shows that more intense signals are observed when PTF is  $0$  G compared to  $-65$  G. This result is expected, as the INEPT<sub>phase</sub> sequence is optimised for PHIP investigations and so consequently, is optimised for double quantum states and these states are maximally transferred at  $0$  G (see section 5.2.1.1, pg 207). The effect of changing the first pulse from  $90^\circ$  to  $45^\circ$  was then investigated, according to the sequence suggested by Haake *et al.*,<sup>150</sup> with results shown in Figure 5.33.

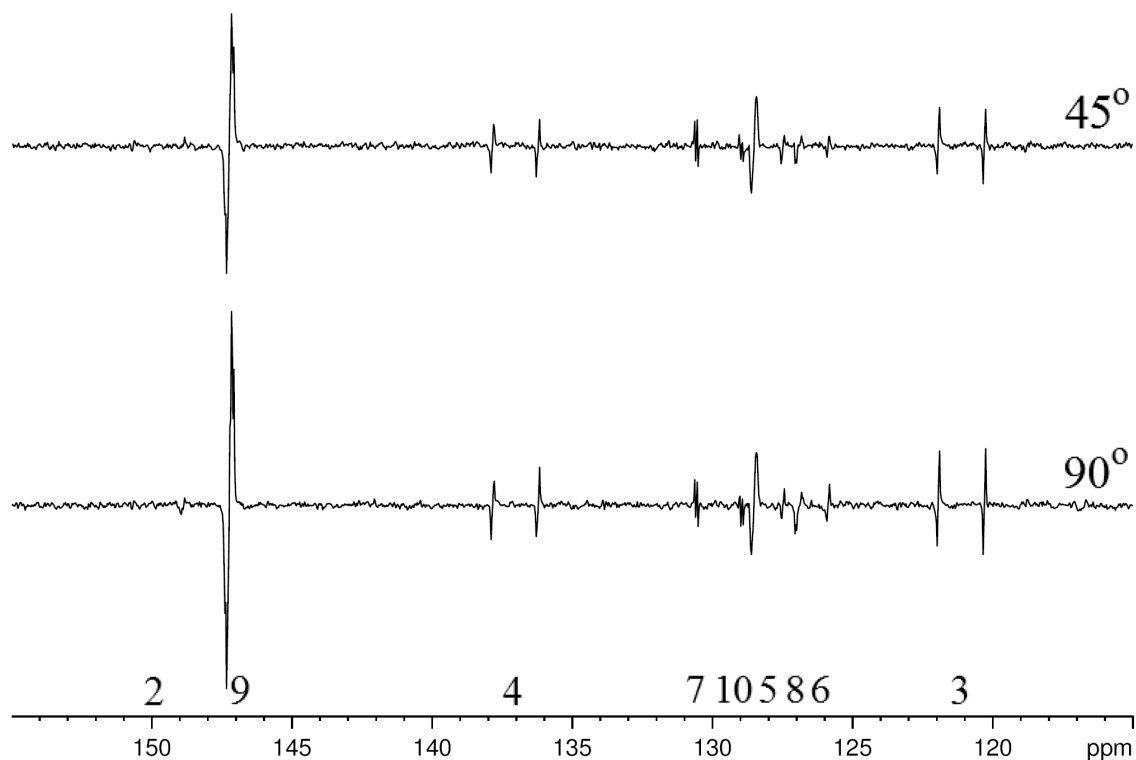


Figure 5.33 Single scan  $^{13}\text{C}$  INEPT\_phase NMR spectra of quinoline optimised for a one bond coupling, hyperpolarised using method 2 with **IMes(c)** at a PTF of -65 G and the first pulse on  $^1\text{H}$  is  $90^\circ$  (bottom) and  $45^\circ$  (top).

Figure 5.33 shows that more intense carbon signals are observed for the  $^{13}\text{C}$  INEPT\_phase NMR spectrum when the first pulse is  $90^\circ$  and the PTF is set to 0 G. This dependence was also investigated with a PTF of -65 G and also showed better signal to noise when the first pulse was set to  $90^\circ$ . This is unexpected as the INEPT\_phase sequence is optimised for double quantum states which should also be optimised with a  $45^\circ$  pulse. The proceeding experiments have shown that the optimal conditions for the INEPT\_phase NMR sequence are to optimise for one bond couplings, use a PTF of 0 G and an initial pulse of  $90^\circ$ .

These results are counter intuitive however they can be explained by the use of product operators. For the INEPT\_phase experiment with a  $45^\circ$  pulse, a spectrum is observed with an  $I_z S_z$  or  $I_z R_z$  starting state, where **I** and **S** correspond to protons and **R** corresponds to  $^{13}\text{C}$ . When the initial pulse is replaced with a  $90^\circ$  pulse, no observable states are retained with an  $I_z$  or  $I_z S_z$  starting state however an  $I_z R_z$  starting state produces observable states on  $^{13}\text{C}$ .<sup>151</sup> This is a double quantum state and so will yield a maximum signal intensity with a PTF at 0 G, however, as a  $^1\text{H}$ - $^{13}\text{C}$  double quantum state, will require a  $90^\circ$  pulse. More information can be found in the Appendix.

The two INEPT sequences investigated to this point have been compared to each other in Figure 5.34, showing the spectrum completed under optimal conditions for each sequence. The INEPTnd NMR sequence is therefore completed optimised for two bond coupling, with a PTF of -65G where the first pulse is  $90^\circ$  (Figure 5.34, bottom), and the INEPT\_phase NMR sequence is completed optimised for one bond couplings, at a PTF of 0 G where the first pulse is  $90^\circ$  (Figure 5.34, top).

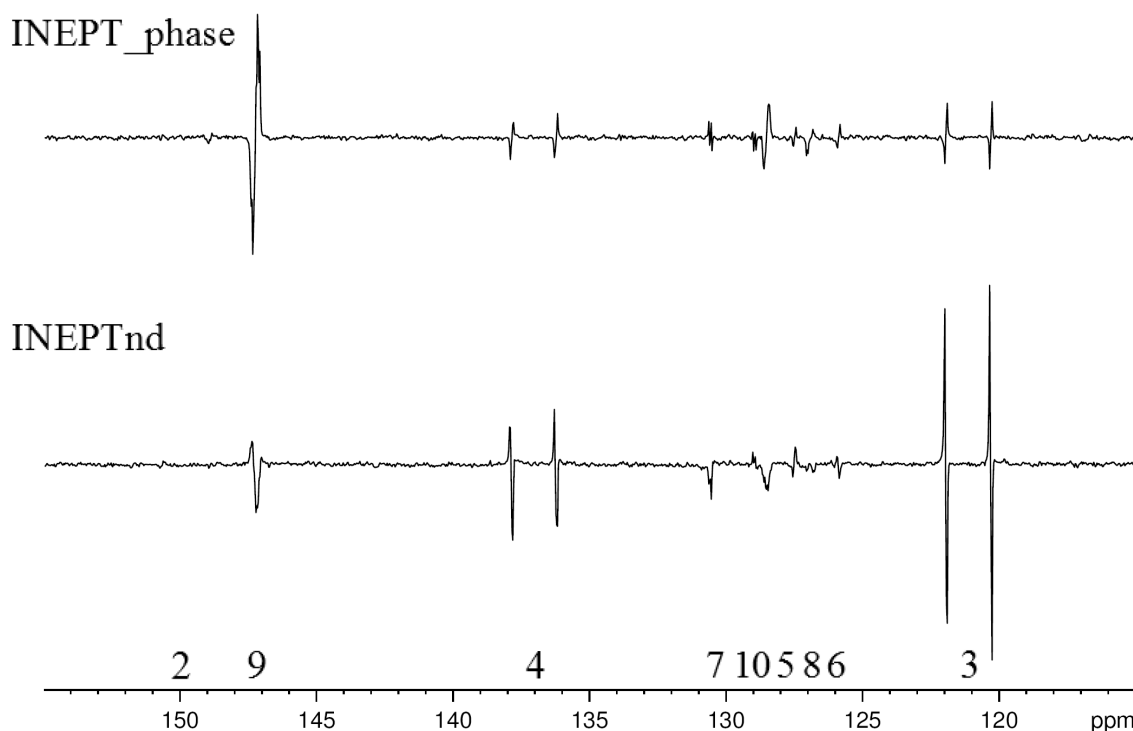


Figure 5.34 Single scan transfer  $^{13}\text{C}$  INEPT NMR spectra of quinoline hyperpolarised with **IMes(c)** showing the optimised INEPTnd (bottom) and optimised INEPT\_phase (top) spectra.

Figure 5.34 shows that neither sequence is preferential over the other. The INEPTnd NMR sequence shows better more intense signals for the **CH** carbons but the INEPT\_phase NMR sequence shows more intense signals for the quaternary carbons. Figure 5.29 indicates the gain observed through using an INEPT sequence over a  $^{13}\text{C}$  sequence and this gain stands for the INEPT\_phase sequence also. It is therefore recommended to complete both sequences as part of a characterisation series in order to obtain maximum information.



#### 5.2.2.4 Method 2 applied to $^1\text{H}$ decoupling of the INEPT sequence

It is also important to consider decoupling the INEPT sequence. As with the  $^{13}\text{C}$  sequences discussed previously, the application of SABRE creates antiphase signals. Consequently, the decoupled INEPT sequence must also include a refocusing section between the INEPT transfer and decoupled acquisition to ensure the signals are in phase and therefore observable. This was completed with the sequence shown in Figure 5.35.

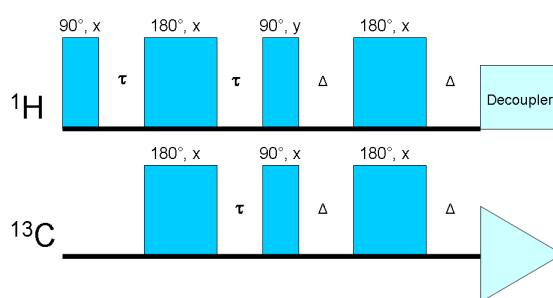


Figure 5.35 Schematic of the  $^{13}\text{C}$  INEPTrd NMR sequence.  $\tau$  and  $\Delta$  denote delays corresponding to a  $^1\text{H}$ - $^{13}\text{C}$  coupling constant.

The INEPTrd sequence is based on the INEPTnd sequence in Figure 5.23 however it includes a refocusing sequence. Both  $\tau$  and  $\Delta$  are delays based on the same coupling constant but manipulated in different ways. The spectra gained as a result of using hyperpolarised INEPTrd sequences often appeared with out of phase signals. Each individual signal could be phased but there is no point at which they all in phase with each other. For this reason, each INEPTrd spectrum is processed with a magnitude calculation. The effect of optimising for one bond or two bond correlations was investigated first.

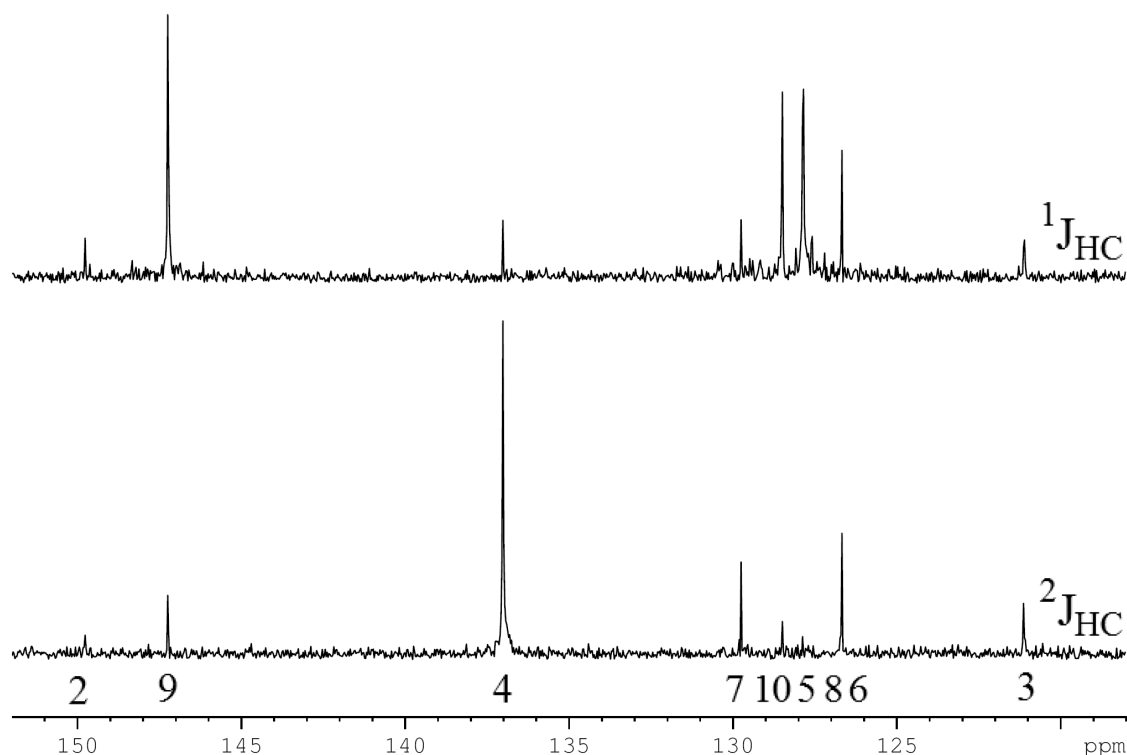


Figure 5.36 Single scan  $^{13}\text{C}\{^1\text{H}\}$  INEPTrd NMR spectra of quinoline hyperpolarised with **IMes(c)** at a PTF of 0 G, optimised for two bond couplings (bottom) and one bond couplings (top). These spectra have been presented in magnitude mode.

The most significant observation to be made from Figure 5.36 is that the INEPT sequence has been successfully proton decoupled under hyperpolarised conditions. It can be observed in Figure 5.36 that the most significant single signal is present when the sequence is optimised for two bond couplings. It should also be noted however that a greater number of signals of close, but lower intensity are observed when the sequence is optimised for one bond couplings. This is therefore considered more successful as a greater number of resonances are identified. The sequence was then investigated when the sample was polarised at a PTF of -50 G and 0 G. This is presented in Figure 5.37.

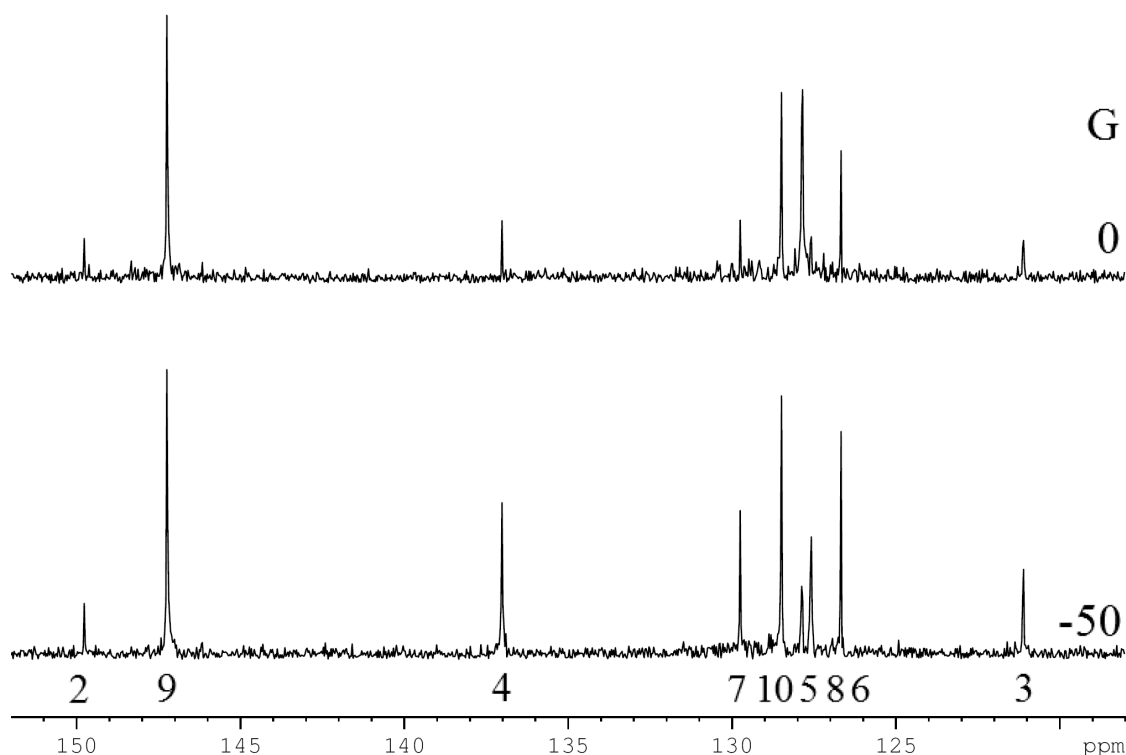


Figure 5.37 Single scan  $^{13}\text{C}\{^1\text{H}\}$  INEPTrd NMR spectra optimised for one bond couplings of quinoline hyperpolarised using method 2 with **IMes(c)** at a PTF of -50 G (bottom) and 0 G (top). These spectra have been presented in magnitude mode.

It is possible to observe in Figure 5.37 that the most significant signals are observed when a PTF of -50 G is used. This is a very significant result as the INEPTrd collected with a PTF of -50 G is the first carbon spectra collected to clearly define all nine resonances associated with quinoline. This was repeated when the sequence was optimised for two bond couplings to give the same trend of maximum signals at a PTF of -50 G.

It was therefore found that the optimal conditions for the INEPTrd sequence are to optimise for one bond couplings and polarise at a PTF of -50 G.

#### 5.2.2.5 Utilisation of polarisation transfer to two different nuclei to increase information gain

Investigations into SABRE have now shown polarisation transfers into  $^{13}\text{C}$  sites as well as  $^1\text{H}$  sites. Therefore, in each hyperpolarised transit between the polarisor and spectrometer, the polarisation that is transferred into the nuclei that are not interrogated is wasted. After optimisation of the  $^{13}\text{C}$  NMR sequences, and most importantly the

INEPT sequences, above, the potential to utilise the polarisation transfer into the whole substrate to gain both coupled and decoupled  $^{13}\text{C}$  spectra in one transit is achievable.

This might be achieved in one of two ways, either an INEPT sequence followed by a  $^{13}\text{C}$  sequence or a  $^{13}\text{C}$  sequence followed by an INEPT sequence. If the INEPT sequence is completed first, polarisation from the  $^1\text{H}$  sites will be transferred to the  $^{13}\text{C}$  sites using RF pulses and then read out. This might result in a higher signal on the first spectra, but removes most of the polarisation from the substrate. It is therefore important to interrogate using polarisation on  $^{13}\text{C}$  first, then use the INEPT sequences to transfer the polarisation still present on  $^1\text{H}$  to repolarise  $^{13}\text{C}$  for the second spectrum. All the spectra in this section have been presented after completion of a magnitude calculation for ease of interpretation.

This was first investigated by completing a  $^{13}\text{C}$  NMR spectrum followed by an INEPTnd sequence in the same transit. The result is shown in Figure 5.38.

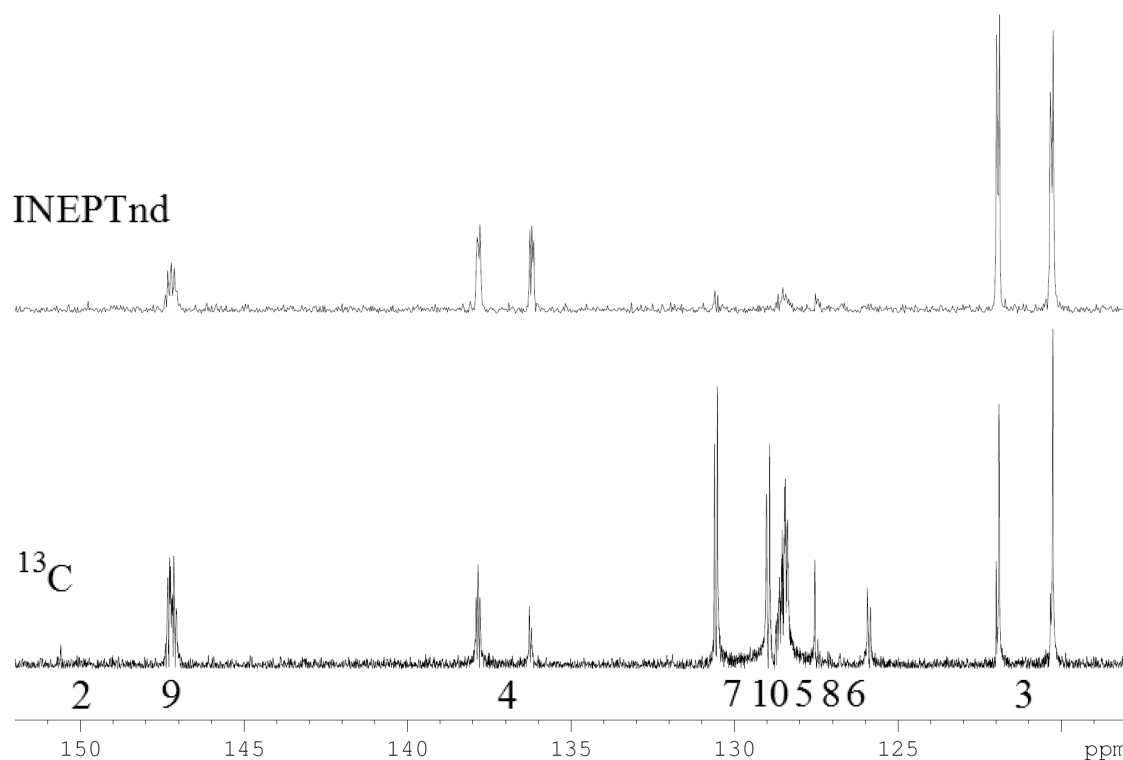


Figure 5.38 Showing a  $^{13}\text{C}$  NMR spectrum of quinoline hyperpolarised at a PTF of -65 G (bottom) and a  $^{13}\text{C}$  INEPTnd NMR spectrum (top) completed immediately after the first sequence. These spectra have been presented in magnitude mode.

Figure 5.38 shows two coupled  $^{13}\text{C}$  NMR spectra have been successfully recorded without requirement of the sample to be repolarised between scans i.e. in a single transit. The ability to do this may hold great advantages as it now may be possible to take a  $^{13}\text{C}$  and  $^{13}\text{C}\{^1\text{H}\}$  spectrum with only one polarisation step. Initially, this was first attempted by completing a  $^{13}\text{C}\{^1\text{H}\}$  first, followed by a coupled INEPT sequence. The result is shown in Figure 5.39.

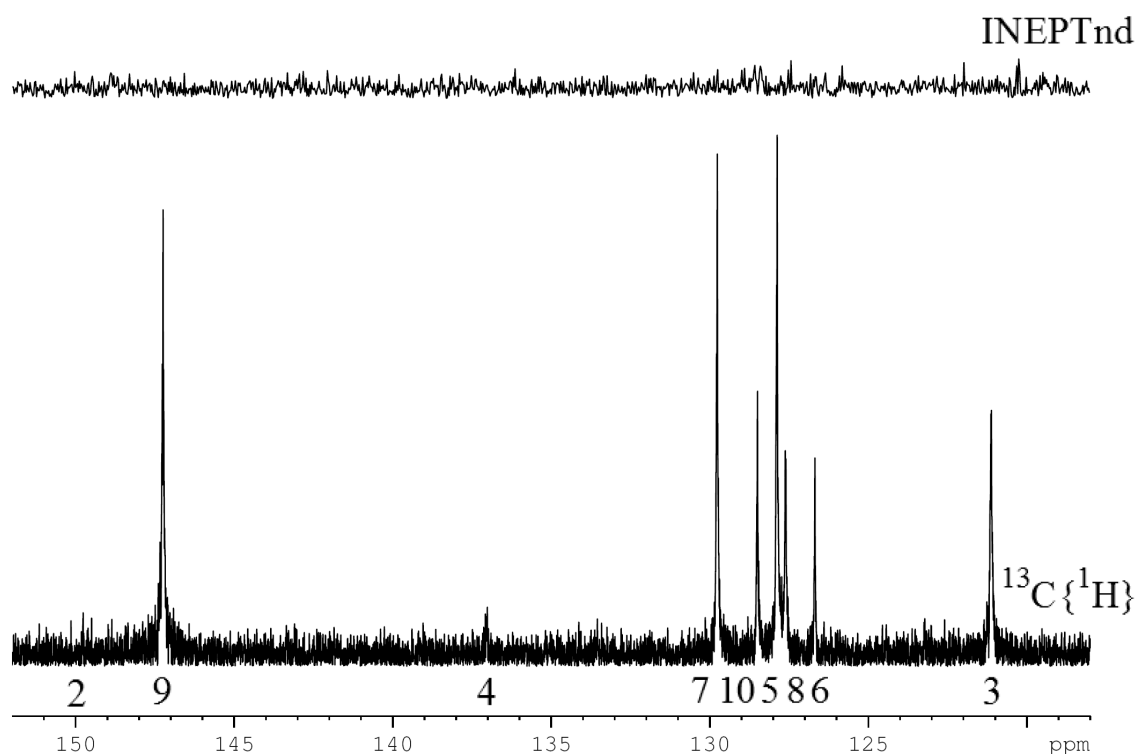


Figure 5.39 Showing a  $^{13}\text{C}\{^1\text{H}\}$  NMR spectrum of quinoline hyperpolarised at a PTF of 0 G (bottom) and a  $^{13}\text{C}$  INEPTnd NMR spectrum (top) completed immediately after the first sequence. These spectra have been presented in magnitude mode.

It can be observed in Figure 5.39 that no  $^{13}\text{C}$  signals are observed in the INEPTnd. This is because during collection of the first  $^{13}\text{C}\{^1\text{H}\}$  NMR spectrum, the polarisation present on  $^1\text{H}$  is quenched due to the decoupling sequence. This experiment has therefore shown it is important to complete a coupled  $^{13}\text{C}$  first, followed by a  $^{13}\text{C}\{^1\text{H}\}$  INEPTrd sequence. The resulting spectra are shown in Figure 5.40.

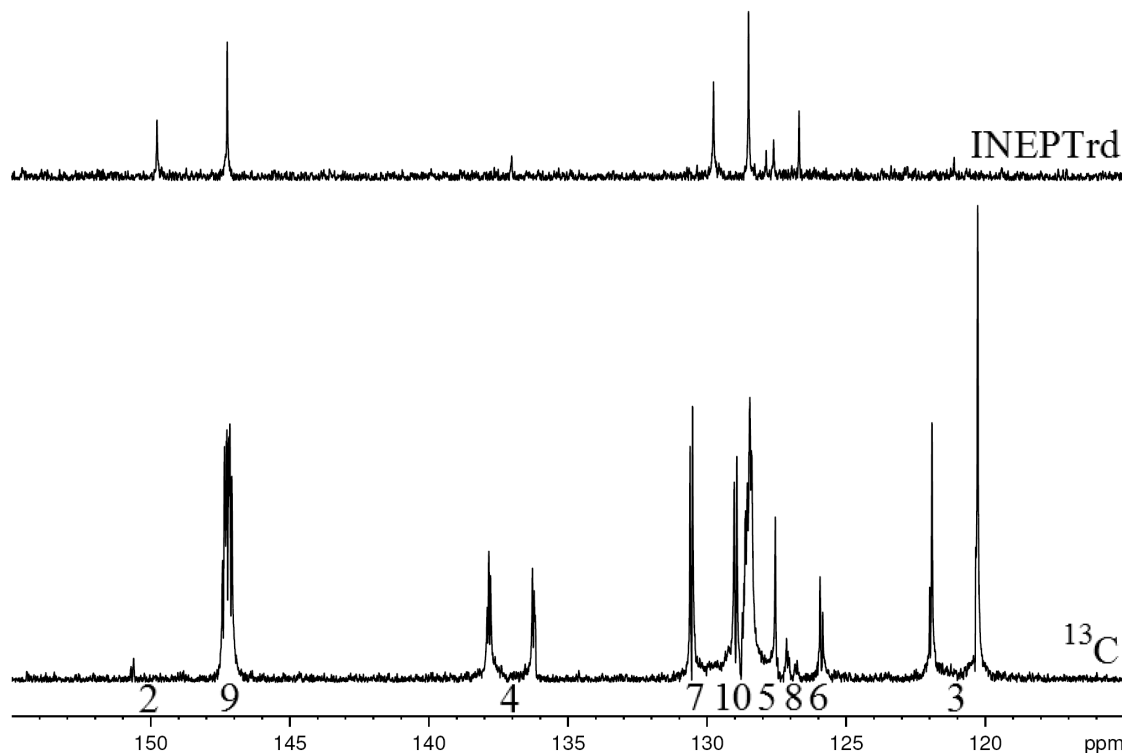


Figure 5.40 Showing: bottom, a  $^{13}\text{C}$  NMR spectrum of quinoline hyperpolarised at a PTF of -50 G and top, a  $^{13}\text{C}\{^1\text{H}\}$  INEPTrd spectrum completed immediately after the first sequence. These spectra have been presented in magnitude mode.

The combination of completing a coupled  $^{13}\text{C}$  NMR spectrum immediately followed by a  $^{13}\text{C}\{^1\text{H}\}$  INEPTrd NMR sequence was investigated at two PTFs. This is because polarisation transfer into  $^1\text{H}$  is optimal when quinoline is hyperpolarised at a PTF of -50 G and  $^{13}\text{C}$  is optimal when the quinoline is hyperpolarised at a PTF of 0 G, however the best result was found at a PTF of -50 G, shown in Figure 5.40. Despite the extra time the  $^1\text{H}$  nuclei have to relax due to acquisition of the  $^{13}\text{C}$  sequence, the nine carbons present on quinoline are observed, although the signal intensity of positions 3, 4 and 5 is weak. The initial acquisition of the  $^{13}\text{C}$  sequence has also yielded all nine carbons signals together with couplings however the signal for position 2 is weak.

These experiments have shown the potential to gain even further information from each hyperpolarisation step than investigated previously. Here, polarisation transfer into both  $^{13}\text{C}$  and  $^1\text{H}$  nuclei on a substrate are utilised to gain both coupled and decoupled  $^{13}\text{C}$  NMR spectra, yielding two different sets of information in one transit from the polarisor.

### 5.2.2.6 Hyperpolarised $^{13}\text{C}$ NMR spectra using standard reagent concentrations

During the optimisation of the sequences used to gain coupled and decoupled  $^{13}\text{C}$  spectra, the sample concentration used was increased to 3 times the standard reagent concentrations. This is impractical for pharmaceutical uses as this concentration equates to approximately 40 mg of the relatively small substrate quinoline, and therefore, for larger substrates this mass will increase greatly. As the INEPTrd was the only sequence to produce all nine of the expected  $^{13}\text{C}$  signals correlating to quinoline, this was used to investigate the ability of SABRE to gain a  $^{13}\text{C}$  spectrum at standard reagent concentrations of quinoline (100 mM) and **IMes(c)** (5 mM). The results are presented in Figure 5.41.

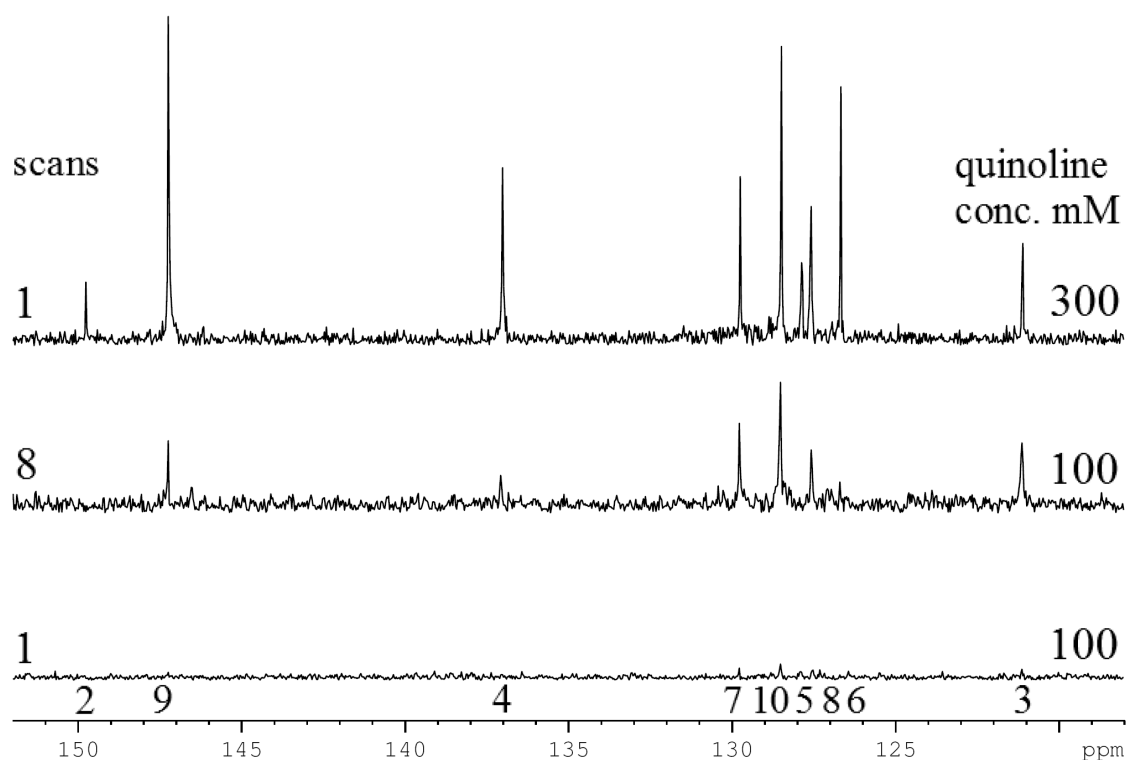


Figure 5.41  $^{13}\text{C}\{^1\text{H}\}$  INEPTrd NMR spectra of quinoline (100 mM) hyperpolarised using method 2 with **IMes(c)** (5 mM) at a PTF of -50 G with 1 scan (bottom), and 8 scans (middle), and  $^{13}\text{C}\{^1\text{H}\}$  INEPTrd NMR spectra of quinoline (300 mM) hyperpolarised using method 2 with **IMes(c)** (15 mM) at a PTF of -50 G with 1 scan (top). These spectra have been presented in magnitude mode, and are scaled relative to each other according to the y-axis.

Figure 5.41 indicates the  $^{13}\text{C}\{^1\text{H}\}$  INEPTrd spectrum does not produce a spectrum with good signal intensity for any of the expected peaks when completed with standard reagent concentrations (100 mM substrate and 5 mM catalyst). The number of scans

was therefore increased to eight with the result that six of the nine expected signals are now observed. To gain a similar level of signal intensity for the  $^{13}\text{C}\{^1\text{H}\}$  NMR spectrum under thermally polarised conditions, 200 scans were required which took  $\sim 7$  minutes to complete, revealing seven of the nine expected carbon resonances of quinoline. Even with 8 scans, the hyperpolarised method requires  $\sim 4$  minutes and therefore is quicker.

### 5.3 Development of method 2 applied to 2D NMR sequences

Investigations into the reproducibility of method two (see Chapter 2) together with the success of the INEPT sequence in conjunction with SABRE have led to the possibility of completing 2D sequences using SABRE. All 2D sequences inherently require more than one scan, as at least one scan per increment in the second dimension is required. It is therefore difficult to complete hyperpolarised 2D sequences using method 1 (without the use of ultrafast methods discussed in section 5.3.2.1, page 248) due to the fast relaxation of the hyperpolarised states, and magnetisation being used up through interrogation. Unless otherwise mentioned, all hyperpolarised 2D spectra were collected using standard reagent concentrations.

#### 5.3.1 Method 2 applied to $^1\text{H}$ - $^1\text{H}$ 2D homonuclear NMR sequences

Investigations into 2D homonuclear sequences extended to proton-proton sequences only. In order to compare the results gained through investigations into hyperpolarisation by SABRE, a thermally polarised  $^1\text{H}$ - $^1\text{H}$  COSY NMR spectrum of quinoline is shown in Figure 5.42.

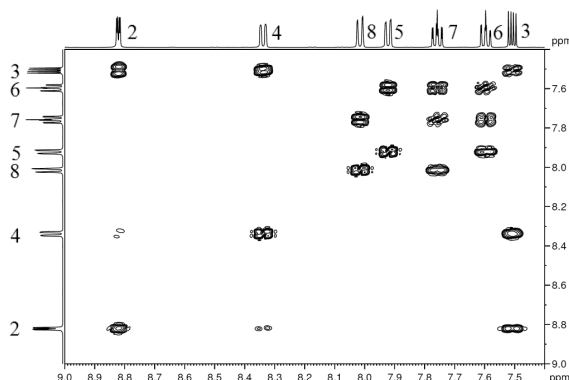


Figure 5.42 Thermally polarised  $^1\text{H}$ - $^1\text{H}$  COSY NMR spectrum of quinoline.



### 5.3.1.1 Method 2 applied to $^1\text{H}$ - $^1\text{H}$ COSY NMR sequence

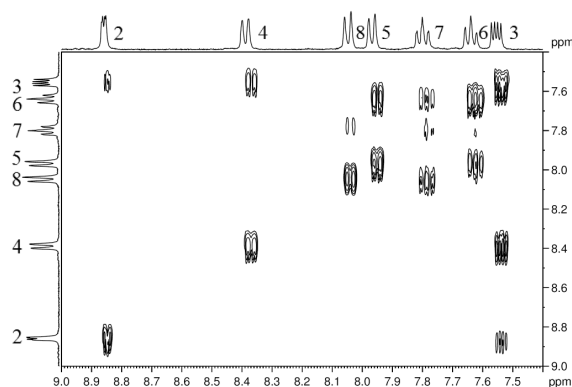


Figure 5.43  $^1\text{H}$ - $^1\text{H}$  COSY NMR spectrum of quinoline hyperpolarised using method 2 with **IMes(c)** at a PTF of 0 G.

Figure 5.43 shows a hyperpolarised  $^1\text{H}$ - $^1\text{H}$  COSY NMR spectrum recorded using method 2 under standard reagent conditions with 64 increments and was collected in 36 min using the MKII polarisor. The successful application of SABRE to the standard COSY sequence resulted in a good spectrum, very similar to that observed in Figure 5.42. All the expected diagonal signals are observed, although the signal for position 7 is of reduced intensity. The expected cross peaks corresponding to single bond correlations are all observed although again two cross peaks relating to the proton in position 7 are of reduced intensity. This sequence was also completed on the MKIII polarisor and which resulted in a very similar spectrum but was completed in the quicker time of 20 min. As the thermally polarised spectrum also presents with cross peaks corresponding to the long range coupling between positions 2 and 4 and can be collected in a significantly shorter time, investigations into the standard COSY NMR spectrum were not continued.

### 5.3.1.2 Method 2 applied to $^1\text{H}$ - $^1\text{H}$ OPSYdq-COSY NMR sequence

The pulse sequence for the  $^1\text{H}$ - $^1\text{H}$  OPSYdq-COSY NMR spectrum was first described in a publication by Aguilar *et al.*<sup>84</sup> in 2007 for use within PHIP and extended to use with SABRE in a publication by Aguilar *et al.*<sup>86</sup> in 2011.

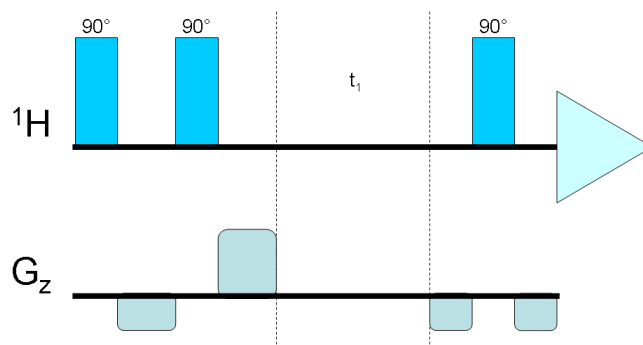


Figure 5.44  $^1\text{H}$ - $^1\text{H}$  OPSY-COSY sequence adapted from that proposed in a publication by Aguilar *et al.*<sup>84</sup> in 2007.

In the case of the  $^1\text{H}$ - $^1\text{H}$  OPSY-COSY sequence, the standard COSY sequence has been adapted in that the initial  $90^\circ$  pulse has been replaced by the OPSY sequence. The most significant advantage of adding an OPSY sequence selecting double quantum states to the beginning of the COSY sequence is that the magnetic states prepared by the OPSYdq sequence lead optimally to those responsible for cross peaks in a COSY sequence. This has the effect that cross peaks are observed before the diagonal, made possible by the use of *parahydrogen*.

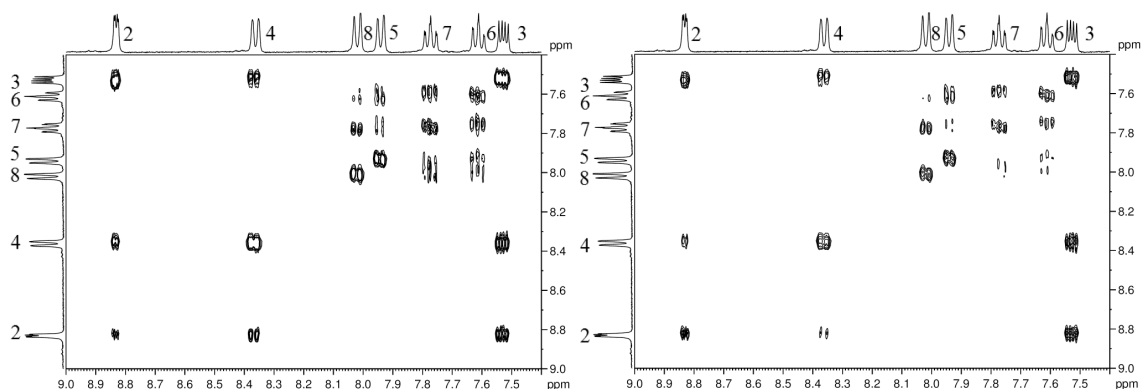


Figure 5.45  $^1\text{H}$ - $^1\text{H}$  OPSYdq-COSY NMR spectra of quinoline (100 mM) hyperpolarised with **IMes(c)** (5 mM) at a PTF of 0 G (left) and -50 G (right).

In Figure 5.45, more intense signals are observed when the PTF is set to 0 G. This is expected as the double quantum states used in a  $^1\text{H}$  OPSYdq spectrum are maximised at a PTF of 0 G (see section 5.2.1.1, pg 207). When collected using method 2 on the MKIII polarisor, the 2D OPSY spectrum takes 20 mins to collect when the solution is bubbled with *parahydrogen* for 6 s before each transient. As the addition of the OPSY sequence to the COSY sequence yields additional information, the sequence was investigated with lower concentrations of quinoline and catalyst. Figure 5.46 shows the

corresponding NMR spectra obtained when of the  $^1\text{H}$ - $^1\text{H}$  OPSYdq-COSY sequence was completed for a sample of 10 mM quinoline and 0.5 mM **IMes(c)**.

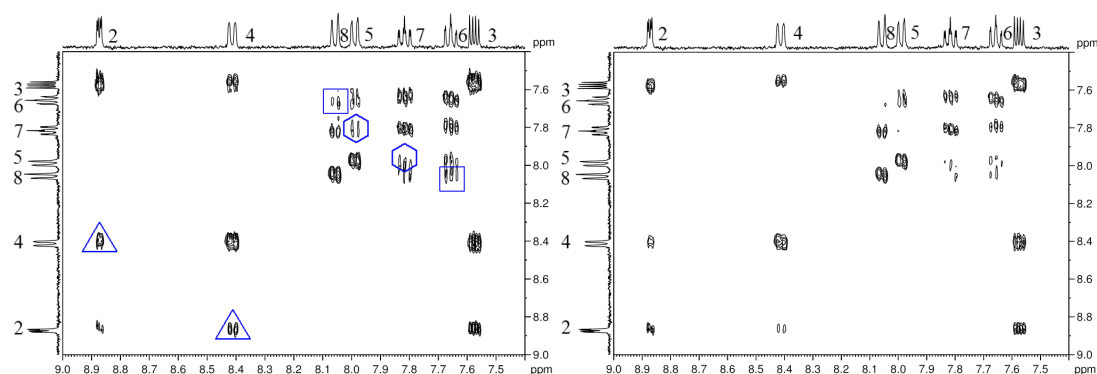


Figure 5.46  $^1\text{H}$ - $^1\text{H}$  OPSYdq-COSY NMR spectra of quinoline (10 mM) hyperpolarised with **IMes(c)** (0.5 mM) at a PTF of 0 G (left) and -50 G (right), with long range correlations labelled between positions 2 and 4 (triangles), positions 5 and 7 (hexagons) and positions 6 and 8 (squares).

Again, in Figure 5.46, the most intense signals are observed when the PTF is set to 0 G, particularly the cross peaks in the second ring of quinoline. These are labelled in Figure 5.46 on the left hand side. The long range correlations between positions 2 and 4 and positions 5 and 7 can be observed on the thermally polarised COSY spectrum of a sample of 10 mM quinoline (see Experimental), however the correlation between positions 6 and 8 are weak. These signals are also much weaker in the thermally polarised COSY spectrum than the hyperpolarised OPSYdq-COSY spectrum. As signal to noise scales with the square of concentration, these plots illustrate the benefit of these methods.

It has been shown that the OPSYCOSY spectrum can be completed in 20 mins on the MKIII polarisor when the *parahydrogen* is added over 6 s per transient. This time of addition of *parahydrogen* can be shortened such that the time required to complete a hyperpolarised OPSYCOSY spectrum can be shortened. Preliminary investigations using the 1D OPSYdq NMR sequence showed the bubbling time could not be shortened to less than 2 s. When this time of addition of *parahydrogen* is applied, the spectrum of 64 increments can be collected in 16 mins.

A thermally polarised 2D COSY NMR spectrum of a 10 mM sample of quinoline can be collected in ~3 minutes. This is significantly quicker than the time required for a hyperpolarised  $^1\text{H}$ - $^1\text{H}$  OPSYCOSY which takes 16 minutes.

### 5.3.2 Method 2 applied to $^1\text{H}$ - $^{13}\text{C}$ 2D heteronuclear NMR sequences

The investigation into the application of SABRE to 2D sequences using method 2 was extended to include heteronuclear sequences such as the HSQC, HMBC and HMQC.

#### 5.3.2.1 Method 2 applied to the $^1\text{H}$ - $^{13}\text{C}$ HSQC NMR sequence

In order to compare the results gained through investigations into hyperpolarisation by SABRE, a thermally polarised  $^1\text{H}$ - $^{13}\text{C}$  HSQC NMR spectrum of quinoline is shown in Figure 5.47.

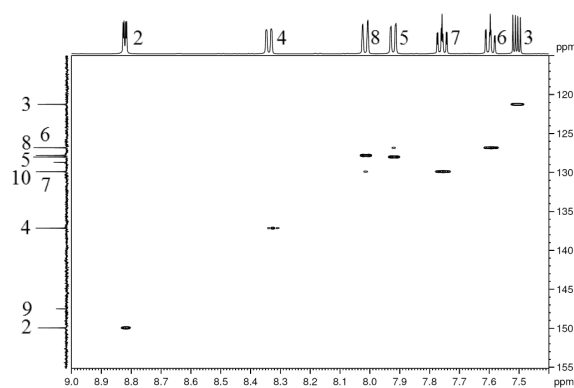


Figure 5.47 Thermally polarised  $^1\text{H}$ - $^{13}\text{C}$  HSQC NMR spectrum of quinoline.

Initially, completion of the  $^1\text{H}$ - $^{13}\text{C}$  HSQC NMR spectrum combined with SABRE led to the observation of no signals corresponding to correlations between the  $^1\text{H}$  and  $^{13}\text{C}$  nuclei. The sequence was then repeated however, the first  $90^\circ$  pulse was changed to a  $45^\circ$  pulse. This process will unlock any  $I_z S_z$  magnetisation present in the substrate, and therefore produce an HSQC spectrum from this. This was initially completed at a PTF of 0 G and 60 G, as shown in Figure 5.48.

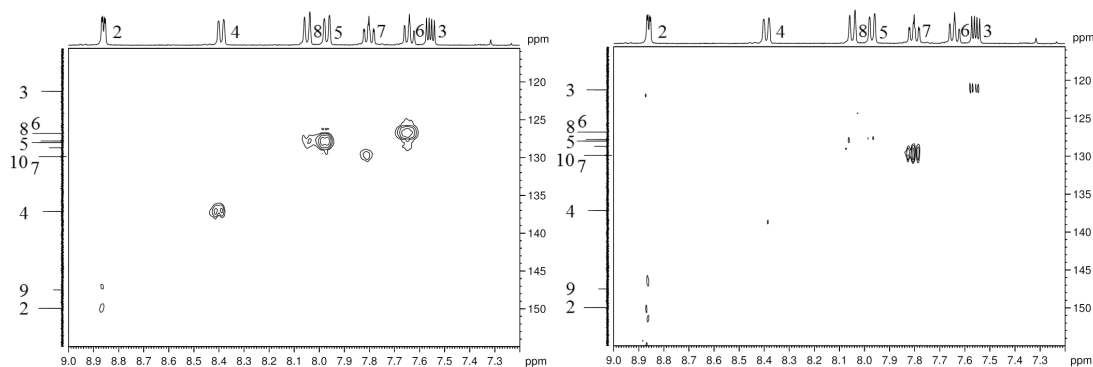


Figure 5.48  $^1\text{H}$ - $^{13}\text{C}$  HSQC NMR spectra of quinoline (100 mM) hyperpolarised using method 2 with **IMes(c)** (5 mM) at a PTF of 0 G (left) and -60 G (right).

Figure 5.48 shows that different  $^1\text{H}$ - $^{13}\text{C}$  correlations within quinoline are observed when the sample is prepared in different fields. At a PTF of 0 G, the sample revealed the  $^1\text{H}$ - $^{13}\text{C}$  correlations corresponding to positions 4, 5, 6 and 7, and weak correlations for positions 2 and 8 also. At a PTF of -60 G, the spectrum revealed intense  $^1\text{H}$ - $^{13}\text{C}$  correlations corresponding to positions 3 and 7, and much less intense correlations for positions 4, 5 and 8. The PTF was therefore changed again to -30 G, in order to observe all correlations.

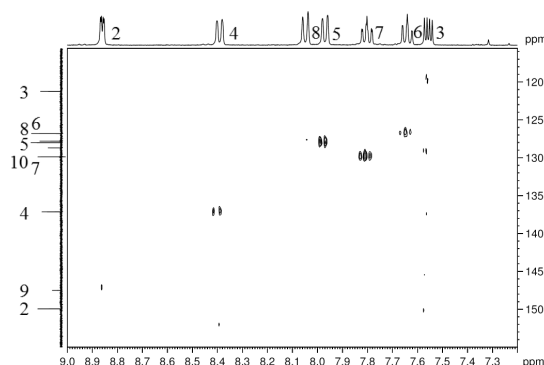


Figure 5.49  $^1\text{H}$ - $^{13}\text{C}$  HSQC NMR spectra of quinoline (100 mM) hyperpolarised with **IMes(c)** (5 mM) at a PTF of -30 G.

Figure 5.49 shows that using a PTF of -30 G does not result in an HSQC spectrum which reveals all seven of the  $^1\text{H}$ - $^{13}\text{C}$  correlations in quinoline. Instead,  $^1\text{H}$ - $^{13}\text{C}$  correlations corresponding to positions 4, 5, 6 and 7 are observed. This therefore means no single PTF is able to produce an HSQC spectrum with all 7  $^1\text{H}$ - $^{13}\text{C}$  correlations present. A second concern has been identified in the hyperpolarised HSQC spectra. A significant proportion of the signal observed in the HSQC NMR spectra has been

encoded incorrectly in the f2 direction and consequently resides in the top and bottom of the spectra, irrespective of the PTF used. This is shown in Figure 5.50.

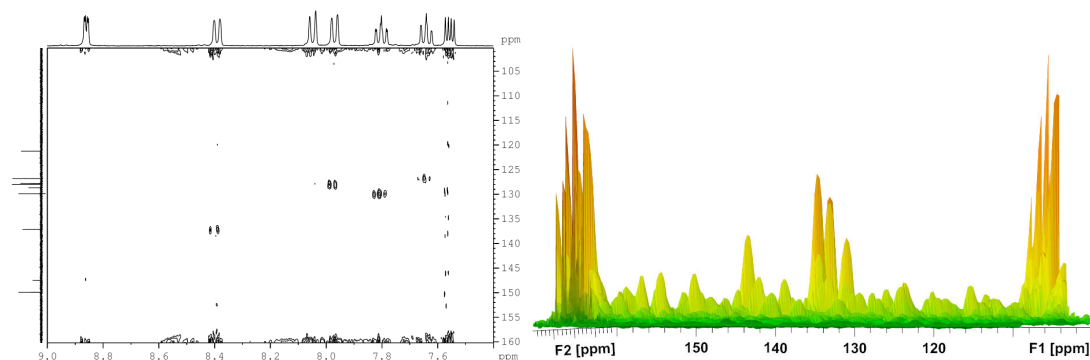


Figure 5.50  $^1\text{H}$ - $^{13}\text{C}$  HSQC NMR spectra of quinoline (100 mM) hyperpolarised using method 2 with **IMes(c)** (5 mM) at a PTF of -30 G, expanded to include the observed noise at the top and bottom of the spectrum (left). The 3D representation is also included on the right.

In Figure 5.50, the two images are from the same spectrum however the right hand image is a 3D representation, looking at the HSQC spectrum from the  $^{13}\text{C}$  axis. This gives the opportunity to directly compare the intensity of the signals corresponding to the expected correlations (see in the centre of the axis) and the signal observed at the top and bottom of the 2D HSQC spectrum (left and right of axis). This 3D representation makes it clear that the noise is much more intense than the expected correlations. It is therefore clear that much of the potential magnetisation is wasted.

### 5.3.2.2 Method 2 applied to the $^1\text{H}$ - $^{13}\text{C}$ HMBC NMR sequence

In order to compare the results gained through investigations into hyperpolarisation by SABRE, a thermally polarised  $^1\text{H}$ - $^{13}\text{C}$  HMBC NMR spectrum of quinoline is shown in Figure 5.51, in which 19 correlations are observed.

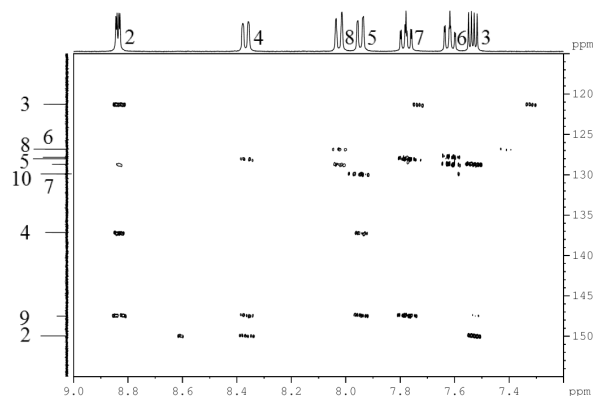


Figure 5.51 Thermally polarised  $^1\text{H}$ - $^{13}\text{C}$  HMBC NMR spectrum of quinoline.

Initially, work into development of the HMBC NMR sequence began on the MKII polarisor and the two required delays were set to correspond to 160 Hz and 8 Hz. The sequence was investigated at two PTFs, with results shown in Figure 5.52.

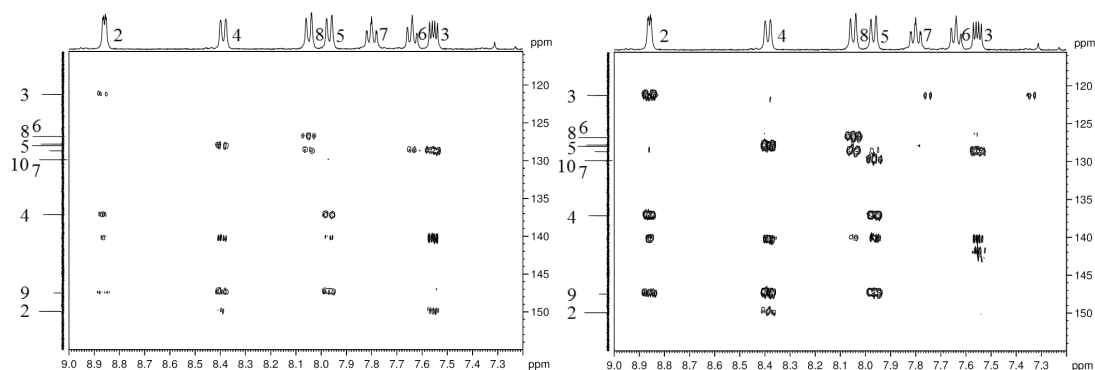


Figure 5.52  $^1\text{H}$ - $^{13}\text{C}$  HMBC NMR spectra of quinoline (100 mM) hyperpolarised with **IMes(c)** (5 mM) utilising the MKII polarisor at a PTF of 0 G (left) and -60 G (right).

Figure 5.52 shows the most intense signals are observed when a PTF of -60 G is used. This is expected as the sequence encodes  $^1\text{H}$  magnetisation according to the proximity to  $^{13}\text{C}$  and therefore, the greater signal intensity is observed when polarisation to  $^1\text{H}$  is optimised. The hyperpolarised HMBC shows thirteen of the nineteen expected correlations at a PTF of 0 G, and fourteen of the nineteen expected correlations at a PTF of -60 G. Different correlations are observed depending on the PTF employed. An important observation here is that many correlations are observed to H2 and C2, a resonance that was difficult to observe in the 1D carbon experiments. At a PTF of 0 G, no correlations to either C7 or H7 are observed and when the PTF is changed to -60 G, there are still no correlations to the H7, although one correlation to C7 is present. It should also be noted that some signal intensity is present on the centre of the fl

dimension (140 ppm), indicating that not all the signal was encoded incorrectly. This artefact appears to increase proportionally to the encoded signals when changing the PTF from 0 G to -60 G. When completed on the MKIII polarisor, each spectrum took 23 min to complete with a bubbling time of 8 s. This is an improvement on the MKII polarisor which requires approximately 30 min to collect the spectrum with a bubbling time of 6 s.

As significant signal intensity is observed when this sequence was used to investigate a 100 mM sample, the sequence was investigated with a sample of 10 % of the standard reagent concentration (10 mM quinoline and 0.5 mM **IMes(c)**). The results of this experiment are shown in Figure 5.53.

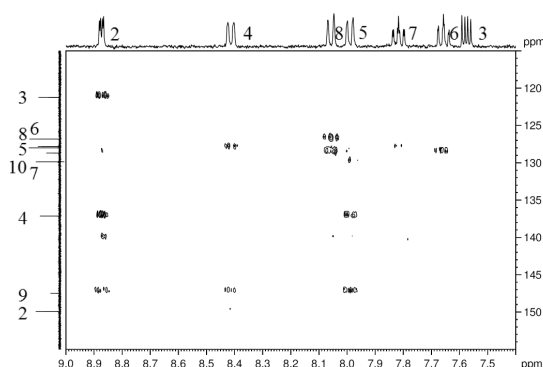


Figure 5.53  $^1\text{H}$ - $^{13}\text{C}$  HMBC NMR spectra of quinoline (10 mM) hyperpolarised with **IMes(c)** (0.5 mM) utilising the MKIII polarisor at a PTF of -50 G.

Figure 5.53 shows significant signal is still present with this lower concentration sample, although thirteen of the nineteen expected correlations are observed, less than for the more concentrated samples. Compared to the standard concentration sample, similar trends are observed in reference to the PTF. It is also possible to observe the artefact on the centre of the f1 axis (140 ppm) is still present but significantly less intense.

It was observed that it was not possible to collect a thermally polarised HMBC of a 10 mM sample of quinoline with the same number of signals at the same intensity in the time it is possible to collect a hyperpolarised spectrum. In fact, the number of scans must be increased to 16 per 128 increments for the same number of correlations to be observed. The result of this is an increase of collection time to around one hour and a half (see Experimental). This means that with respect to  $^1\text{H}$ - $^{13}\text{C}$  HMBC spectra, the



application of SABRE to a low concentration sample can save a significant amount of time.

### 5.3.2.3 Method 2 applied to the $^1\text{H}$ - $^{13}\text{C}$ HMQC NMR sequence

In order to compare the results gained through investigations into hyperpolarisation by SABRE, a thermally polarised  $^1\text{H}$ - $^{13}\text{C}$  HMQC NMR spectrum of quinoline is shown in Figure 5.54.

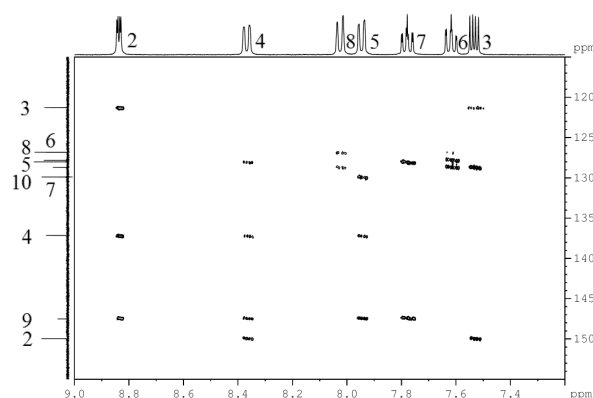


Figure 5.54 Thermally polarised  $^1\text{H}$ - $^{13}\text{C}$  HMQC NMR spectrum of quinoline optimised for two bond couplings.

The thermally HMQC spectrum optimised to investigate two bond couplings is presented in Figure 5.54. This differs slightly from the thermally polarised HMBC spectrum presented in Figure 5.51 in that the decoupling in position 3 is improved and an additional correlation corresponding to the proton in position 4 is observed. There is also one less correlation observed correlating to the proton in position 2, compared to the thermally polarised HMBC spectrum.

Initial work into development of the HMQC NMR sequence began on the MKII polarisor. In the case of the HMQC, it is possible to change a specific delay to optimise the sequence for one bond couplings or two bond couplings. An HMQC sequence was therefore recorded using a delay corresponding to a 160 Hz coupling to optimise for one bond correlations (see Chapter 4 or Experimental) leading to an HSQC-type spectrum, and 8 Hz coupling to optimise for two bond correlations. The HMQC optimised for one bond correlations was investigated first.

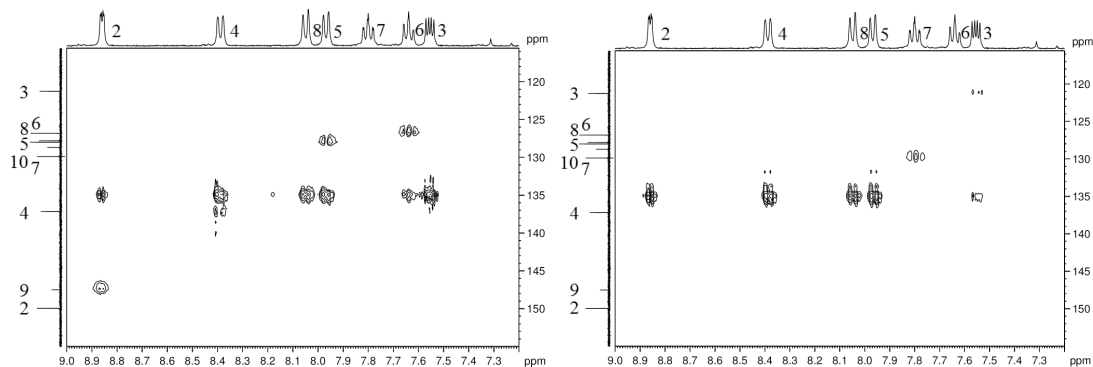


Figure 5.55  $^1\text{H}$ - $^{13}\text{C}$  HMQC NMR spectra of quinoline (100 mM) hyperpolarised using method 2 with **IMes(c)** (5 mM) at a PTF of 0 G (left) and -60 G (right), and optimised for one bond couplings.

The most significant feature of both the HMQC spectra presented in Figure 5.55 is the line of signal that has been encoded incorrectly present on the centre of the f1 direction (135 ppm). When considering the less intense signal outside of this artefact, it is possible to observe HSQC-type correlations (see Figure 5.47). Different correlations are observed depending on the PTF used. The observed correlations are much weaker in intensity than the artefacts.

The HMQC was also investigated when optimised for two bond couplings. The effect of changing the PTF was investigated first with results shown in Figure 5.56.

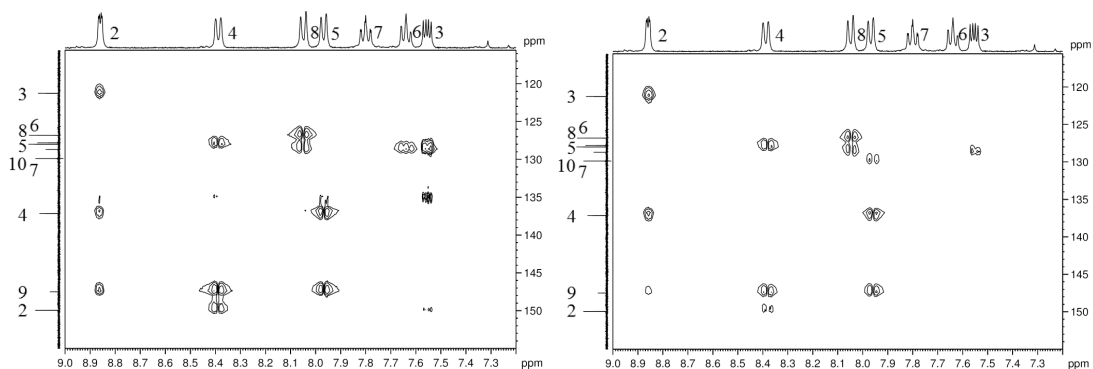


Figure 5.56  $^1\text{H}$ - $^{13}\text{C}$  HMQC NMR spectra of quinoline (100 mM) hyperpolarised using method 2 with **IMes(c)** (5 mM) at a PTF of 0 G (left) and -60 G (right), and optimised for two bond couplings.

Collection of the HMQC was much more successful when optimised for two bond couplings compared to the HMQC optimised for one bond couplings. Figure 5.56 shows the level of artefact is significantly reduced when the sequence is optimised for two bond couplings with less intense artefacts observed in the spectrum collected with a PTF of 0 G and nearly unobservable artefacts in the spectrum collected with a PTF of

-60 G. Just as with the HMBC, the HMQC sequence also presents with many correlations are observed to H2 and C2, a resonance that was difficult to observe in the 1D carbon experiments. Considering the effect of PTF, a greater number of correlations are observed in the HMQC spectrum completed with a PTF of 0 G (thirteen of the nineteen expected correlations compared to twelve observed for a PTF of -60 G). These signals are also of greater intensity than observed when the PTF is set to -60 G.

The HMQC was repeated where the first pulse was shortened to 45° pulse to understand if the incorrectly encoded signal observed on the centre of the f1 dimension was due to unlocked  $I_z S_z$  magnetisation. This was unsuccessful, and the resultant spectrum was not different to that collected with an initial 90° pulse. After development, these experiments were repeated on the MKIII polarisor. Each spectrum took 22 mins to complete with a bubbling time of 8 s, yielding similar results to those observed using the MKII polarisor. Again this is quicker than the MKII polarisor which requires approximately 30 min for collection of the same data.

As significant signal intensity is observed when this sequence was used to investigate a 100 mM sample, the sequence was investigated with a sample of 10 % of the standard reagent concentration (10 mM quinoline and 0.5 mM **IMes(c)**). The results of this experiment are shown in Figure 5.57.

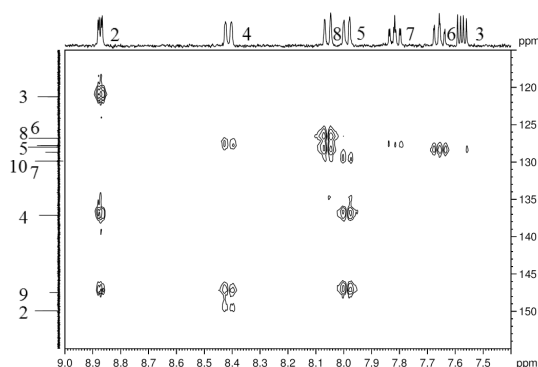


Figure 5.57  $^1\text{H}$ - $^{13}\text{C}$  HMQC NMR spectra of quinoline (10 mM) hyperpolarised with **IMes(c)** (0.5 mM) at a PTF of -50 G and optimised for two bond couplings.

Figure 5.57 shows significant signal is still observed in thirteen of the nineteen expected correlations and the experiments also showed the same trend is observed as with the standard concentration sample with respect to the PTF used.

It was observed that it was not possible to collect a thermally polarised HMQC of a 10 mM sample of quinoline with the same number of signals at the same intensity in 22 minutes, the time it is possible to collect a hyperpolarised spectrum. In fact, to observe the same number of correlations in a thermally polarised spectrum, the number of scans must be increased to 16 per 128 increments which requires around one hour and a half to collect (see Experimental). This means that with respect to  $^1\text{H}$ - $^{13}\text{C}$  HMQC spectra, the application of SABRE to a low concentration sample can save a significant amount of time.

What is clear from these experiments is that hyperpolarisation via SABRE produces significant signal intensity and information pertaining to  $^{13}\text{C}$  nuclei can be extracted from hyperpolarised 2D  $^1\text{H}$ - $^{13}\text{C}$  heteronuclear NMR sequences however, the sample must be repolarised between each scan due to relaxation. This is a major drawback when using method 2 to utilise SABRE as a result of the significantly longer time this requires. It also requires the sample to be five times larger than a standard NMR sample. A method to overcome these issues is to use ultrafast NMR methods. These will be discussed as applied to SABRE in the following section.

#### 5.3.2.4 Investigations into removal of artefacts observed in hyperpolarised 2D NMR spectra

Experimentally, two concepts were employed to reduce the signal intensity or remove the observed artefacts on the centre of the  $f_1$  direction. The first method used was to set the centre of the  $f_1$  direction to outside the area of interest. This was investigated using the HMBC sequence which up to this point was used with a spectral width of 50 ppm centred around 140 ppm in the  $f_1$  direction. To move the artefact from the spectral range, the spectrum was centred around 155 ppm however this led to the need to increase the spectral width to include all correlations. The resultant spectrum is presented in Figure 5.58 (left).

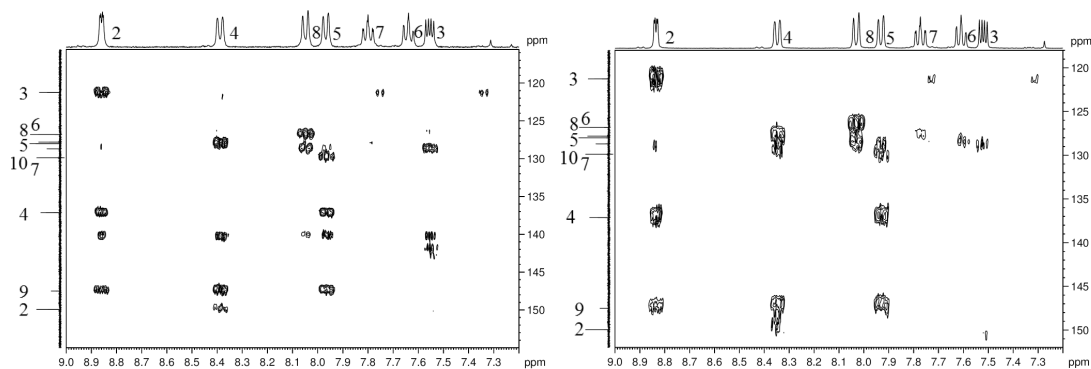


Figure 5.58  $^1\text{H}$ - $^{13}\text{C}$  HMBC NMR spectra of quinoline (100 mM) hyperpolarised using method 2 with **IMes(c)** (5 mM). The spectrum on the left was collected with an f1 spectral width of 50 ppm centred around 140 ppm, and the spectrum on the right was collected with an f1 spectral width of 80 ppm centred around 155 ppm.

Figure 5.58 indicates the resolution in the spectrum presented without artefacts is much poorer than the spectrum presented with artefacts. This is because the spectral width has been increased but the number of increments used has not, resulting in poorer resolution. It should also be noted that the artefacts are observed in the spectrum in Figure 5.58 (right) however the centre of the f1 direction is now at 155 ppm and therefore not presented in the figure. To overcome this loss in resolution, the number of increments was doubled to 128, presented in Figure 5.59.

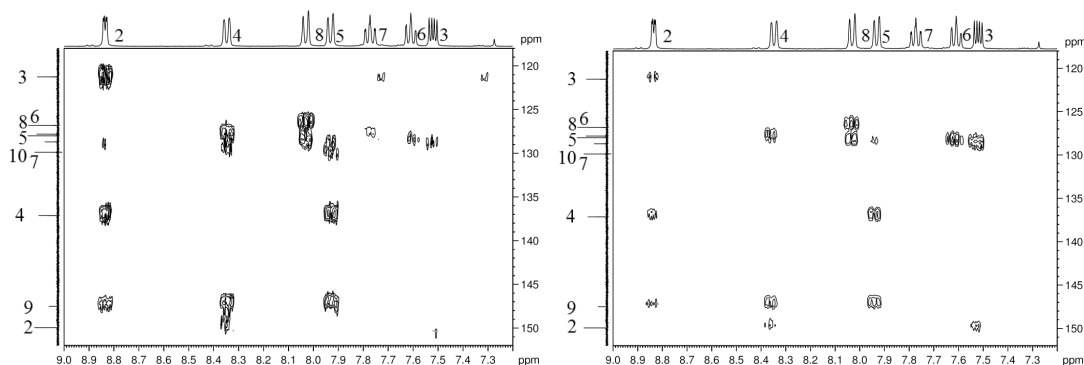


Figure 5.59  $^1\text{H}$ - $^{13}\text{C}$  HMBC NMR spectra of quinoline (100 mM) hyperpolarised using method 2 with **IMes(c)** (5 mM). The spectra were collected with an f1 spectral width of 80 ppm centred around 155 ppm with 64 increments (left) and 128 increments (right).

Figure 5.59 shows that increasing the number of increments has improved the resolution observed in the HMBC spectrum. This has however come at the cost of time and the spectrum took twice as long to collect.

A second method of removing the artefacts observed was also considered. Up until this point, only one scan per increment had been utilised in an attempt to maximise the resolution of a spectrum considering the time required for each hyperpolarisation step. The spectra were therefore collected with two scans per increment, however to keep the collection time the same, the number of increments was reduced to 32. The resultant HMBC and HMQC spectra are presented in Figure 5.60.

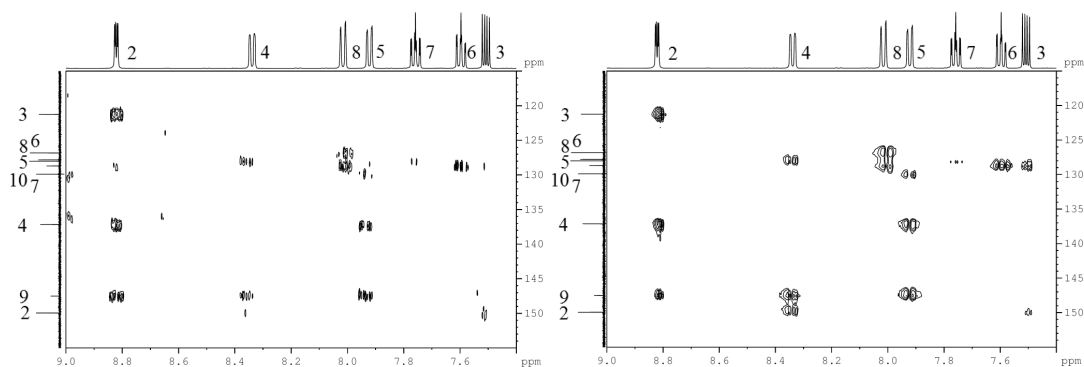


Figure 5.60  $^1\text{H}$ - $^{13}\text{C}$  HMBC NMR spectrum (left) and  $^1\text{H}$ - $^{13}\text{C}$  HMQC NMR spectrum (right) of quinoline hyperpolarised using method 2 with **IMes(c)** at a PTF of -50 G. In each spectrum, 2 scans were used for each of the 32 increments.

In the case of both the HMBC and HMQC spectra presented in Figure 5.60, the artefacts are no longer observable, even with the signal intensity increased greatly (not shown). If the artefacts are still present, they cannot be discerned from noise observed in the spectrum. The HMBC now presents with two additional peaks along the 8.65 ppm line in the f2 direction corresponding with 124 ppm and 136 ppm in the f1 direction, neither of which are expected signals. These could be noise but equally could correspond to a contaminant in the sample or to bound signals of quinoline. It should also be noted that although these spectra were collected in the same time as those which contained artefacts, they only have 32 increments and therefore have lower resolution.

Both the methods discussed have produced presentable spectra where the artefact has either been removed or moved away from the area of interest, however to keep the required resolution, the spectra take a minimum of twice as long. This acts as a significant concern. The reasons behind the presence of the artefact will be discussed later in the Summary for this chapter.

#### 5.4 Development of method 1 applied to 2D NMR sequences

Ultrafast methods applied to NMR spectroscopy were first published by Frydman *et al.*<sup>82</sup> and are an exciting new area in NMR spectroscopy. Investigating a sample by 2D NMR spectroscopy involves collating a number of individual FIDs in such a way that the correlations between protons can be extracted. In the case of ultrafast spectroscopy, these FIDs are collected at the same time through the application of gradients across the NMR tube. The gradients allow the sample to be viewed as a series of discrete levels, each of which produces an FID to gain the correlations. This can be collected in around 1  $\mu$ s.

In a paper published by Mishkovsky and Frydman<sup>152</sup> in 2009, a number of different ultrafast methods are discussed including: real time identification of mixed components subject to a continuous flow separation, monitoring of chemical and biophysical transformations using ultrafast EXSY NMR spectroscopy, TOCSY NMR spectroscopy, HSQC NMR spectroscopy, HMQC NMR spectroscopy, on thermally polarised or hyperpolarised (DNP) samples. These have also been extended to 3D spectra.

In 2012, Queiroz Junior *et al.*<sup>153</sup> published a paper concerning the real-time monitoring of the hydrolysis of 2-(4-nitrophenyl)-1,3-dioxolane acetal using ultrafast HSQC NMR spectroscopy, the reaction of which is shown in Figure 5.61.

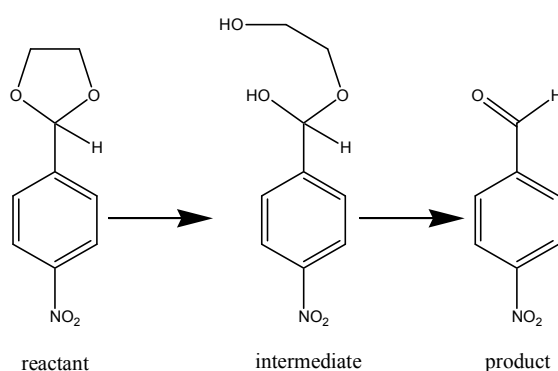


Figure 5.61 Acid-catalysed hydrolysis of 2-(4-nitrophenyl)-1,3-dioxolane acetal (reactant).

The ability to use the ultrafast HSQC NMR sequence allowed the chance to observe the hemiacetal, a notoriously short-lived intermediate.

In 2012, a paper published by Queiroz *et al.*<sup>154</sup> discussed the application of the ultrafast COSY to HPLC-NMR spectroscopy. In this case, a mixture of the natural products

naringin, epicatechin and naringenin were successfully separated by an HPLC system that was coupled to NMR completing continuous ultrafast COSY spectra to monitor elution.

Ultrafast methods have given the opportunity to collect 2D spectra in less than a second. This very short time allows us to apply the hyperpolarisation technique SABRE as each FID for the 2D spectrum is collected at the same time and therefore the fast relaxation of the hyperpolarised states is no longer a factor. The combination of the two techniques was therefore investigated. It was therefore decided to implement the ultrafast methods by Frydman<sup>82</sup> with the SABRE technique using method 1.<sup>83,155,156</sup>

#### 5.4.1 Method 1 applied to $^1\text{H}$ - $^1\text{H}$ 2D homonuclear NMR sequences

The first sample to be investigated contained standard reagent concentrations of quinoline (100 mM) hyperpolarised with **IMes(c)** (5 mM) in 0.6 ml  $d_4$ -methanol completed using method 1. A thermally polarised ufCOSY spectrum was collected and compared to those in which the quinoline had been hyperpolarised at a PTF of 0 G and ~65 G.

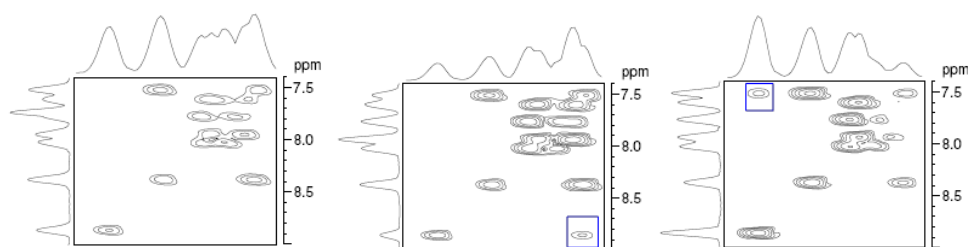


Figure 5.62  $^1\text{H}$ - $^1\text{H}$  ufCOSY NMR spectra of quinoline (100 mM) (L-R) thermally polarised spectra, hyperpolarised using method 1 with **IMes(c)** (5 mM) at a PTF of 0 G and hyperpolarised with **IMes(c)** (5 mM) at a PTF of 65 G, presented with internal projections.

It can be observed in Figure 5.62 (middle and right) that the addition of the SABRE technique to the ufCOSY NMR sequence has resulted in the observation of correlations between positions 2 and 3 (shown in blue squares), which are not observed in the thermally polarised spectrum, Figure 5.62 left. From the presented spectra, it is not clear of the effect that the addition of *parahydrogen* has had on the intensity of the observed signals. This has therefore been considered through the integration of the peaks, where the labelling is outlined in Figure 5.63, and the integration data are presented in Table 5.3.



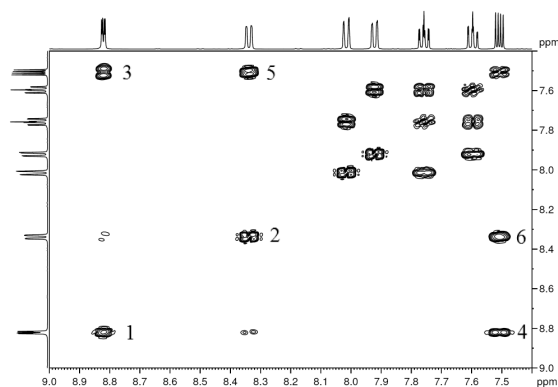


Figure 5.63 A thermally polarised  $^1\text{H}$ - $^1\text{H}$  COSY NMR spectrum including labels corresponding to the peaks integrated.

Signal	Peak	Integrals relative to thermally polarised ufCOSY		
		Thermally polarised	0 G	65 G
1	Diag	1	31	117
2	Diag	1	35	78
3	Cross	1	27	104
4	Cross	1	55	13
5	Cross	1	37	77
6	Cross	1	50	23

Table 5.3 Showing the increased signal intensity of the  $^1\text{H}$ - $^1\text{H}$  ufCOSY NMR spectra of quinoline (100 mM) hyperpolarised with **IMes(c)** (5 mM) at 0 G and hyperpolarised with **IMes(c)** (5 mM) at 65 G, compared to the thermally polarised spectrum.

At a concentration of 100 mM, the ufCOSY spectrum shows nearly all the expected  $^1\text{H}$ - $^1\text{H}$  correlations. The experiment was therefore repeated at the lower concentration of 10 mM quinoline hyperpolarised with 0.5 mM **IMes(c)**. This is 10 % of the standard concentration and correlates to 0.8  $\mu\text{l}$  quinoline hyperpolarised with 0.2 mg **IMes(c)** in 0.6 ml  $d_4$ -methanol, prepared by dilution.

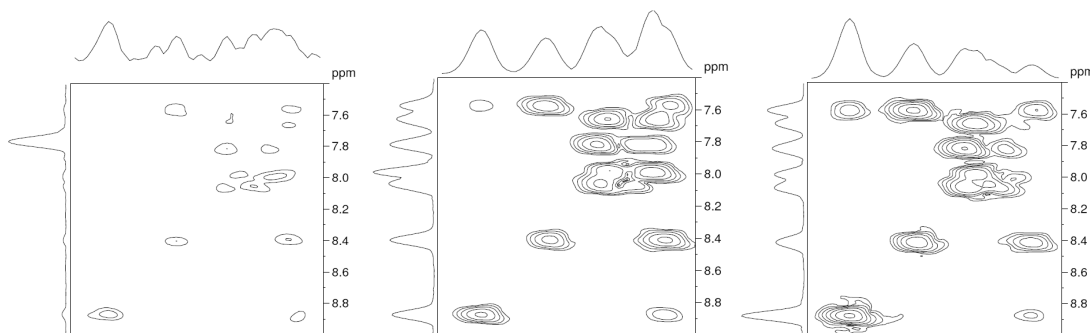


Figure 5.64  $^1\text{H}$ - $^1\text{H}$  ufCOSY NMR spectra of quinoline (10 mM) (L-R) thermally polarised, hyperpolarised using method 1 with **IMes(c)** (0.5 mM) at a PTF of 0 G and hyperpolarised using method 1 with **IMes(c)** (0.5 mM) at a PTF of 65 G, with internal projections.

When completing the ufCOSY NMR sequence on a 10 mM quinoline sample, the signal intensity gain created by hyperpolarisation is clear to see in Figure 5.64. The observed signals are much stronger and the hyperpolarised spectra also show more correlations within the substrate.

The signals are strong in these hyperpolarised spectra, and therefore the solution was diluted again to create a sample of 1 mM quinoline and 0.05 mM **IMes(c)**, correlating to 0.08  $\mu\text{l}$  quinoline and 0.02 mg **IMes(c)**. The sample is now at 1 % of the standard concentrations. The results are shown in Figure 5.65.

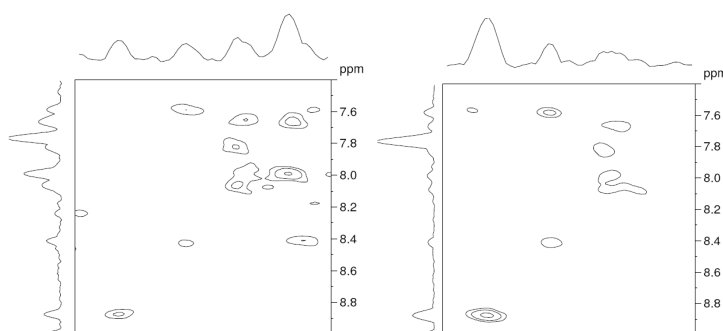


Figure 5.65  $^1\text{H}$ - $^1\text{H}$  ufCOSY NMR spectra of quinoline (1 mM) hyperpolarised with **IMes(c)** (0.05 mM) at 0 G (left) and hyperpolarised with **IMes(c)** (0.05 mM) at a PTF of 65 G (right), presented with internal projections.

For a 1 mM sample of quinoline, the thermally polarised ufCOSY showed no signals corresponding to quinoline, only solvent signals. The addition of *parahydrogen* to the sample resulted in the observation of some  $^1\text{H}$ - $^1\text{H}$  correlations corresponding to quinoline however not all the correlations are observed.

The successful combination of the hyperpolarisation technique SABRE with Frydman's ultrafast COSY sequence has been demonstrated. The maximum signal intensity for both cross peaks and diagonal peaks is produced with a PTF of 65 G. This means that measurements need to be collected at only one PTF, the one at which  $I_z$  magnetisation is a maximum.

## 5.5 Summary

Previous to this chapter, only 1D  $^1\text{H}$  NMR spectra have been discussed. This chapter has extended the concepts gained there to the successful acquisition of more complex hyperpolarised spectra requiring phase cycling, such as the NOESY sequence, polarisation transfer into  $^{13}\text{C}$  and through to 2D sequences.

Considering 1D spectra involving more complex sequences than the  $90^\circ$  pulse acquire sequence have led to the successful acquisition of a  $^1\text{H}$  NOESY NMR spectrum where the sample has a substrate concentration of 10 mM. A significant observation was also made when considering the effect of PTF on the  $^1\text{H}$  OPSYdq spectrum. It was found the maximum signal intensity was observed at 0 G unlike the  $90^\circ$  pulse acquire which gives a maximum signal intensity at 50 G for quinoline. This led to all new sequences after this point being collected at both 0 G and 50 G.

Extensive work has been carried out concerning the acquisition of 1D  $^{13}\text{C}$  NMR spectra. Initially, detection of polarisation from  $^{13}\text{C}$  was considered. It was found that, like  $^1\text{H}$ , polarisation on  $^{13}\text{C}$  nuclei also has a dependence on the PTF used showing maximum signal intensity at 0 G. Owing to the addition of *parahydrogen*, the signals often presented as antiphase in the coupled  $^1\text{C}$  NMR spectrum. This therefore means a refocusing sequence must be completed in order for decoupling to be successful. This was achieved using two methods; refocusing according to J coupling evolution ( $^{13}\text{C}\{^1\text{H}\}_\text{JR}$ ), and refocusing according to J coupling and chemical shift evolution ( $^{13}\text{C}\{^1\text{H}\}_\text{JCSR}$ ). The addition of these refocusing sequences allowed for successful decoupling of the  $^{13}\text{C}$  spectrum however the  $^{13}\text{C}\{^1\text{H}\}_\text{JR}$  sequence allowed the observation of the most signals and yielded the best signal intensity for those signals. This is thought to be due to relaxation of the hyperpolarised states during the second delay period of the  $^{13}\text{C}\{^1\text{H}\}_\text{JCSR}$  sequence.

Hyperpolarised  $^{13}\text{C}$  spectra were also investigated when considering the INEPT transfer sequence. This utilises the polarisation present on  $^1\text{H}$  and uses pulses to transfer this to  $^{13}\text{C}$  for detection. Predictably, this yielded greater signal intensities than those observed when interrogating  $^{13}\text{C}$  magnetisation. These spectra also presented with antiphase peaks and therefore required a refocusing sequence to allow decoupling. This produced the first  $^{13}\text{C}\{^1\text{H}\}$  NMR spectrum collected using SABRE which revealed all nine of the expected signals associated with quinoline.

The successful acquisition of spectra resulting from both  $^{13}\text{C}$  and  $^1\text{H}$  polarisation in the form of the  $^{13}\text{C}$  NMR sequence and  $^{13}\text{C}\{^1\text{H}\}$  INEPT NMR sequence have also allowed for the idea of sequential acquisition. When using method 2 to apply SABRE, the time required to repolarise the sample between acquisitions can be lengthy. Sequential interrogation of polarisation on  $^{13}\text{C}$  nuclei followed by polarisation on  $^1\text{H}$  nuclei in one hyperpolarisation step has allowed the collection of a coupled and decoupled  $^{13}\text{C}$  spectrum in one hyperpolarisation step.

As mentioned in section 5.2.2.3, the thermally polarised INEPTnd sequence exhibited greater signal to noise and a greater number of signals when the sequence was optimised for 19 Hz couplings compared to 8 Hz couplings. It was therefore investigated if the same difference was observed in the hyperpolarised INEPTnd spectra. This work was completed using the MKIII polarisor and therefore required a TXI probe. This therefore meant the number of scans needed to be increased to 8 to obtain a similar signal to noise level as previously reported using TXO probe. The results of this are shown in Figure 5.66.

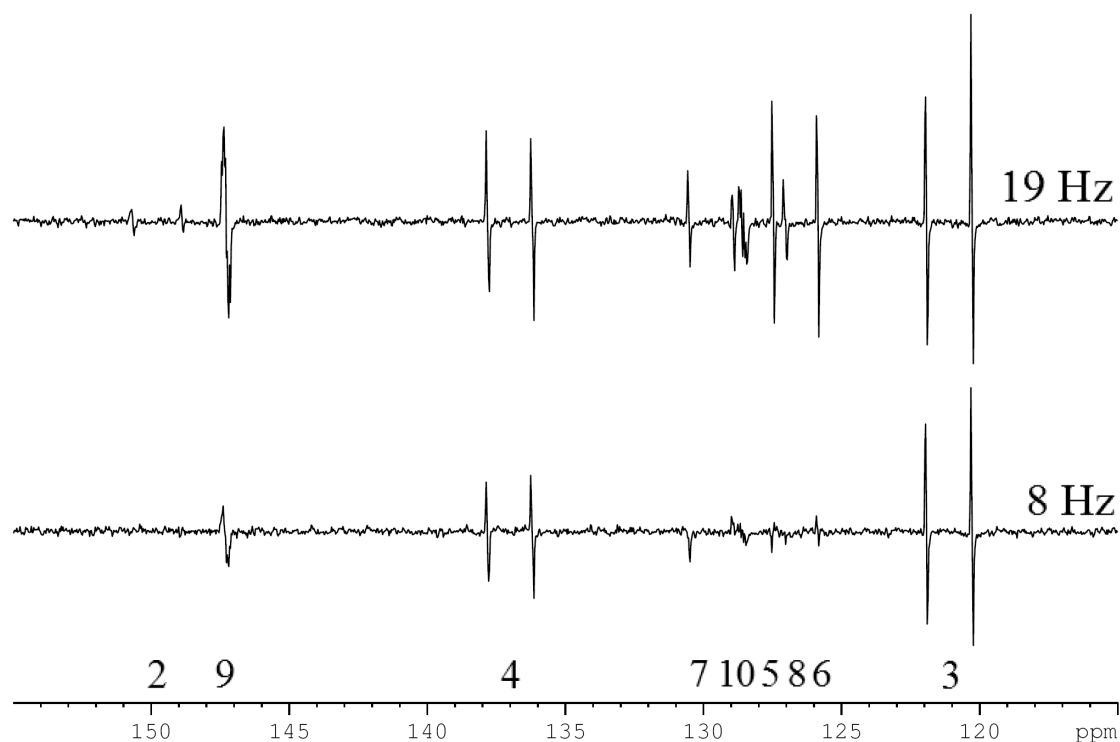


Figure 5.66  $^{13}\text{C}$  INEPTnd NMR spectra of quinoline optimised for two bond couplings (8 Hz, top and 19 Hz bottom) hyperpolarised using **IMes(c)**. Using a TXI probe, each spectrum was collected using an average of 8 scans.

Figure 5.66 indicates changing the sequence to be optimised for 19 Hz couplings had the effect to increase the signal intensity of the observed signals in hyperpolarised  $^{13}\text{C}$  INEPTnd spectra. It is also possible to observe the signal corresponding to **C2**, although the signal is weak.

The polarisor was instrumental in the implementation of SABRE to the classic 2D sequences such as the COSY, HSQC, HMBC and HMQC. The use of *parahydrogen* has also allowed the application of the OPSY COSY, which results in the cross peaks of the COSY spectrum to be more intense than the diagonal. It was also found that development from the MKII polarisor to the MKIII polarisor decreased the amount of time required for a 64 increment 2D spectrum significantly. This was reduced further by reducing the time of addition of *parahydrogen* per increment from 6 s to 2 s, resulting in the collection of a 2D spectrum in 16 min. This is a great improvement on interrogations of low concentration substrates considering  $^1\text{H}$ - $^{13}\text{C}$  spectra such as the HMBC and HMQC.

Considering the 2D  $^1\text{H}$ - $^{13}\text{C}$  NMR spectroscopy, an artefact was observed on the centre of the f2 axis. A possible reason for this is the polarisation within the complex evolves into an observable state after the initial states are encoded in the f1 direction. To understand this better, a hyperpolarised HMQC was completed without decoupling. This was completed to understand the origin of the magnetisation creating the artefact. If the artefact shows splitting, it suggests the artefact is derived from magnetisation on  $^{13}\text{C}$  but if it does not, the artefact is derived from magnetisation on  $^1\text{H}$ . First, the hyperpolarised HMQC is presented with the decoupler on in Figure 5.67.

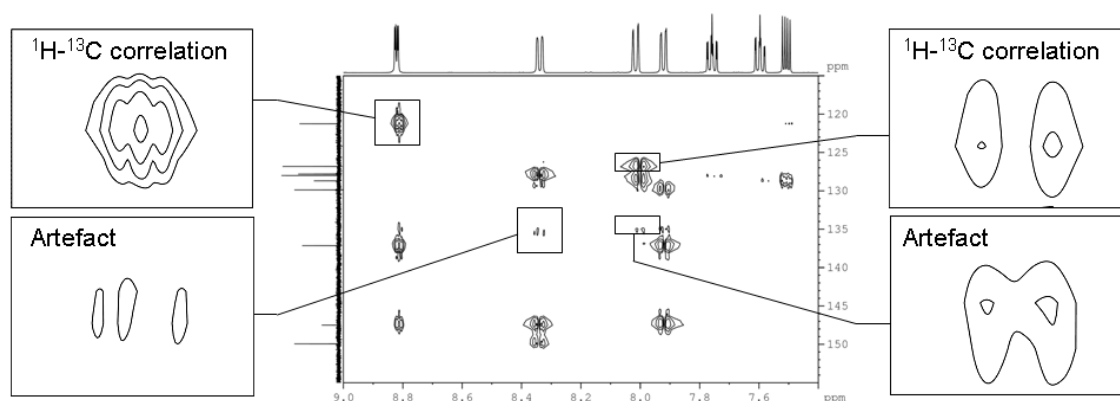


Figure 5.67  $^1\text{H}$ - $^{13}\text{C}$  HMQC NMR spectra of quinoline (100 mM) hyperpolarised with **IMes(c)** (5 mM) at a PTF of -50 G and optimised for two bond couplings with decoupler turned on. Selected signals have been expanded for comparison.

The expansions in Figure 5.67 indicate four signals, two corresponding to the expected  $^1\text{H}$ - $^{13}\text{C}$  correlations and two corresponding to artefacts. The top left signal presents as a singlet, the top right as a doublet and the artefact bottom left presents as a triplet and bottom right presents as a doublet. The spectrum was then repeated with the decoupler off, presented in Figure 5.68.

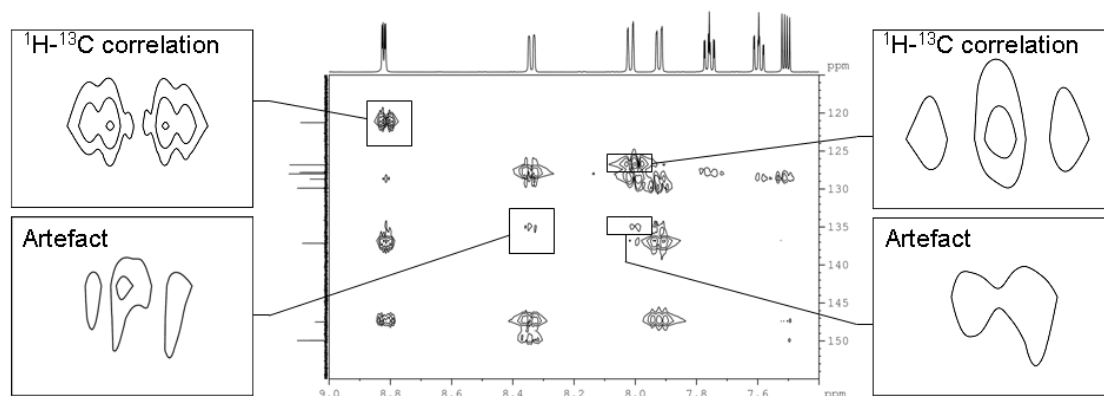


Figure 5.68  $^1\text{H}$ - $^{13}\text{C}$  HMQC NMR spectra of quinoline (100 mM) hyperpolarised with **IMes(c)** (5 mM) at a PTF of -50 G and optimised for two bond couplings with decoupler turned off. Selected signals have been expanded for comparison.

The signals expanded in Figure 5.67 and Figure 5.68 were chosen to exemplify the differences and similarities between the two spectra. In the case of the coupled HMQC, not all the signals experienced additional splittings. The expansions corresponding to expected signals now have different splittings with the singlet on the top left now presenting as a doublet and the doublet on the top right now presents as a triplet. The same cannot be said for the expanded artefacts, whose splittings remain the same. We can therefore infer that the artefact is derived from  $^1\text{H}$  magnetisation that is not  $^{13}\text{C}$  coupled.

Another potential route to overcome the artefact present in the heteronuclear 2D spectra is to apply a gradient across the sample cell such that 2 independent scans can be collected across the height of the cell. This means for each transient, 2 scans can be collected, and consequently two scans per increment can be used for each 2D spectrum without doubling the experiment time. It will be interesting to develop this idea in the future. This may indicate a need to change the way data is collected when using SABRE hyperpolarised NMR spectroscopy. For instance, a 2D spectrum with a large spectral width but poor resolution might be collected to gain a rough idea of the position of correlations, followed by a series of small spectra width spectra with good resolution chosen to observe the required correlations only. The application of SABRE to hyperpolarised 2D  $^1\text{H}$ - $^{15}\text{N}$  spectra is also of great future interest as it would provide the potential to bring  $^{15}\text{N}$  spectroscopy into the routine of a pharmaceutical chemist. Initial investigations into this have been completed by the group however significant challenges were revealed with respect to phase coherence of the spectra.

The SABRE technique has also been successfully applied to the ufCOSY sequence by Frydman using method 1. It has therefore been possible to obtain a hyperpolarised COSY of 10 mM quinoline in less than a second.

This chapter has demonstrated that the SABRE technique can be applied to a number of routine and non-routine NMR sequences, yielding a great deal of information. In the case of low concentration samples, this information can also be gained much quicker than possible with thermally polarised samples. From the work completed in this chapter, it is recommended that the following strategies are implemented when polarisation a substrate using SABRE hyperpolarised NMR spectroscopy. First investigations into a substrate should include a series of  $^1\text{H}$  NMR spectra acquired with  $90^\circ$  pulse and  $^1\text{H}$  OPSYdq NMR spectra collected at a number of PTFs to gain an idea of which field each state is transferred maximally. To complete a  $^{13}\text{C}\{^1\text{H}\}$  spectrum, the INEPTrd sequence should be collected at the PTF yielding maximum  $I_z$  states. Considering acquisition of 2D data, the ultrafast methods are clearly much quicker to acquire once optimised however, the optimisation of the ultrafast sequence to detect a new substrate takes longer than collection by standard sequences using the flow system. Therefore, a 2D OPSYdq NMR spectrum collected at the PTF yielding the maximum signal intensity for the 1D OPSYdq NMR spectrum should be collected for  $^1\text{H}$ - $^1\text{H}$  correlations followed by an HMBC to gain information about  $^1\text{H}$ - $^{13}\text{C}$  correlations as this yielded better resolution than the HMQC.



## 6 Chapter 6 – Applying SABRE

### 6.1 Introduction

Modern day drugs have many different substructures, not just those based on pyridine. It was therefore thought prudent to investigate derivatives of pyridine and other potential substructures. Many important biologically relevant molecules are indole analogues.

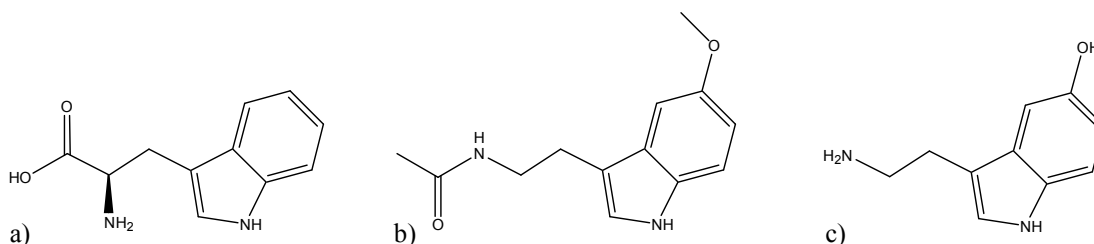


Figure 6.1 Structures of a) tryptophan, b) melatonin and c) serotonin.

Analogues of the bicyclic heterocycle indole, consisting of a benzene ring fused to a pyrrole ring, are found within important molecules such as tryptophan (one of the 20 standard amino acids in humans and a key precursor to neurotransmitters), melatonin (an important antioxidant) and serotonin (5-hydroxytryptamine, 5HT, Figure 6.1). Serotonin, an important neurotransmitter, and its analogues are very important molecules within the body regulating appetite,<sup>157</sup> emesis,<sup>158</sup> digestive track movements<sup>159</sup> and many neurological disorders<sup>160</sup> such as depression,<sup>157</sup> anxiety,<sup>157</sup> obsessive compulsive disorder,<sup>160</sup> autism,<sup>160</sup> schizophrenia<sup>160</sup> and sudden infant death syndrome.<sup>160</sup> Drugs with an indole substructure have shown cytotoxic (Cediranib<sup>161</sup>), anti-inflammatory,<sup>162</sup> antiviral,<sup>162</sup> antimicrobial,<sup>162</sup> and antidepressant<sup>158</sup> properties.

The thiazole analogues are also very important. A natural thiazole analogue is vitamin B<sub>1</sub> (Figure 6.2), an important vitamin in human biology, playing a pivotal role in the metabolism of carbohydrates, fats and proteins, and the production of adenosine triphosphate.

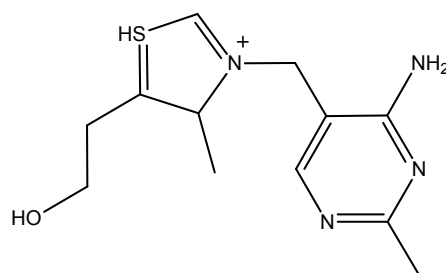


Figure 6.2 Structure of Thiamine, Vitamin B<sub>1</sub>.

Many commercial drug molecules are also thiazole analogues, such as Ritonavir<sup>163</sup> (used in combination with other drugs as a antiretroviral), Abafungin (an antifungal drug) and Tiazofurin (an antineoplastic drug).<sup>164,165</sup> In recent research they have been found to be biologically active in many areas including exhibiting anti-inflammatory,<sup>165</sup> analgesic,<sup>166</sup> antifungal,<sup>167</sup> antibiotic, antimicrobial activity<sup>168</sup> and antitumour<sup>164</sup> activities. The substructure has even shown promise in the fight against breast cancer.<sup>169-171</sup>

In 1999, Pandeya *et al.*<sup>167</sup> published a paper investigating a series of thiazole containing compounds derived from isatin for their antibacterial, antifungal and anti-HIV activities.

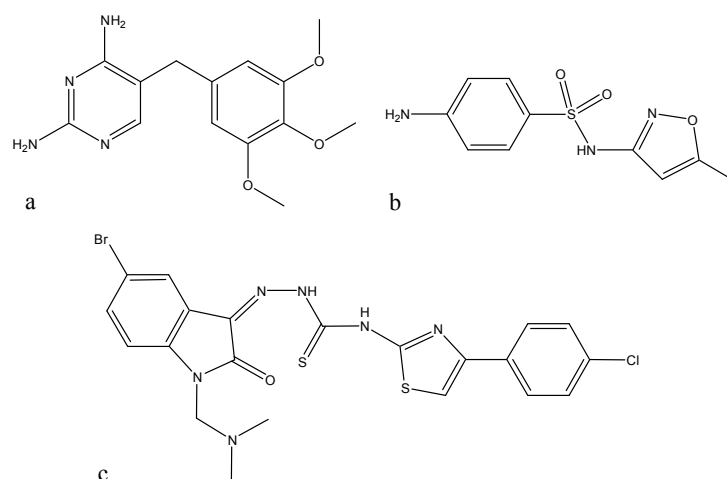


Figure 6.3 Structures of a) trimethoprim b) sulphamethoxazole and c) 1-[*N,N*-dimethylaminomethyl]-5-bromoisatin-3-{1'-[4''-(*p*-chlorophenyl) thiazole-2''-yl] thio semicarbazone}.<sup>167</sup>

A series of 12 compounds were tested against 28 pathogenic bacteria and the minimum inhibitory concentration (MIC) compared to that of trimethoprim (Figure 6.3a) and sulphamethoxazole (Figure 6.3b). Of these 12, newly synthesised compounds, 1-[*N,N*-dimethylaminomethyl]-5-bromoisatin-3-{1'-[4''-(*p*-chlorophenyl) thiazole-2''-yl] thio semicarbazone} (Figure 6.3c) proved to show the most favourable antibacterial activity,

showing increased activity against 27 of the 28 bacteria compared to sulphamethoxazole and against 18 of the 28 bacteria compared to trimethoprim.

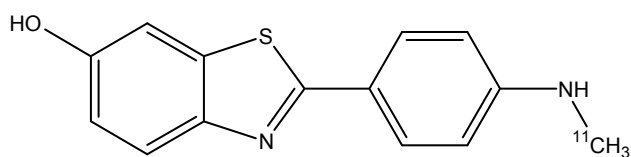


Figure 6.4 Structure of Pittsburgh B.

Another important thiazole analogue is found in the form of benzothiazole in complexes such as Pittsburgh B, a fluorescent dye which can emit positrons in the body as a result of the presence of  $^{11}\text{C}$ . It can therefore be used in positron emission tomography (PET). It is able to produce scans of beta-amyloid plaques in neuronal tissues, giving the ability to complete investigational studies of Alzheimer's disease, such as a more quantitative premortum tool to understand the effectiveness of potential new drugs.

Within this chapter, a series of commercial drugs were investigated. These include albendazole, mebendazole, anastrozole, bicalutamide, esomeprazole and gefitinib, provided by AstraZeneca, shown in Figure 6.5.

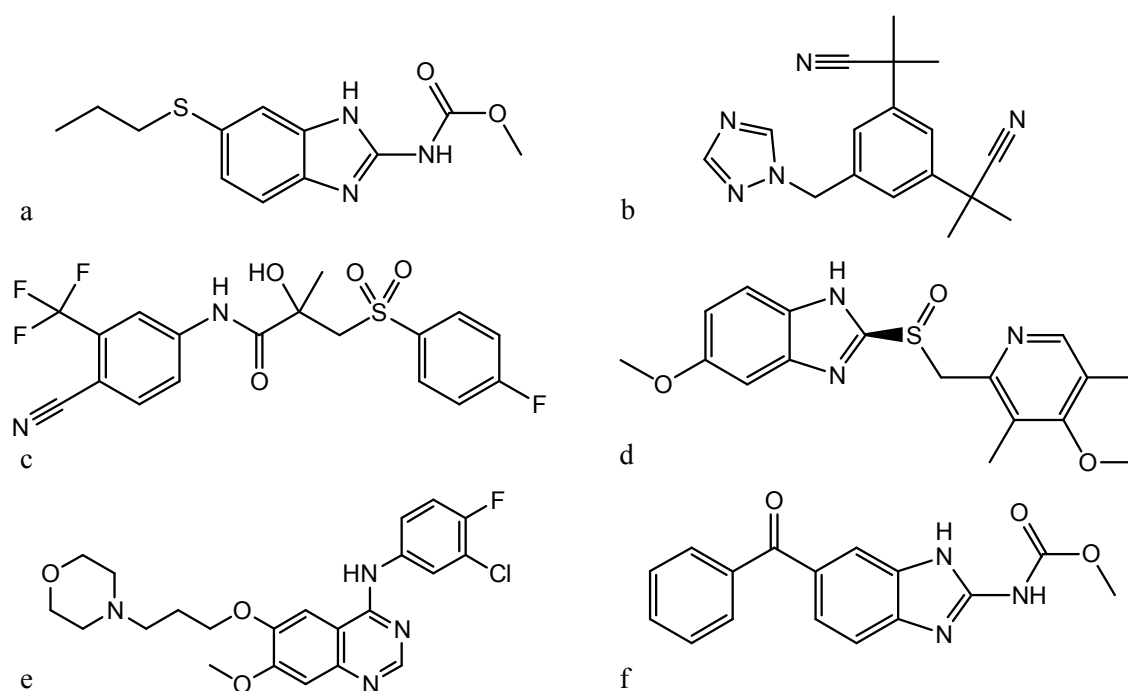


Figure 6.5 Structures of a) albendazole, b) anastrozole, c) bicalutamide, d) esomeprazole, e) gefitinib and f) mebendazole.

Albendazole has been shown as an effective treatment against a number of worm infestations in a range of mammals.<sup>172,173</sup> An infestation of worms in children can result in chronic debilitating effects from severe abdominal pain and anemia to stunted growth and impaired cognitive development.<sup>174</sup> For this reason, the charity Children Without Worms<sup>174</sup> use Albendazole donated by GlaxoSmithKline (GSK) as a method to treat school age children, improving their quality of life. It has also been used in humans to treat solitary cysticercus granuloma, such that seizures are reduced, less calcification is observed and in some cases, the lesion disappears.<sup>175</sup> Albendazole is a benzimidazole analogue which contains the nitrogen available for binding to the metal centre.

Mebendazole, like Albendazole, has been shown effective against parasitic worms,<sup>173</sup> and is also used by Children Without Worms,<sup>174,176</sup> where mebendazole is donated by Johnson & Johnson. Mebendazole has also been shown effective in keeping a carcinoma stable.<sup>177</sup> A patient with adrenocortical carcinoma who had experienced failure of or intolerance to conventional treatments was prescribed mebendazole as a single agent. In the 19 months this treatment was taken, the metastases initially regressed and then remained stable from that point, with minimal side effects and good quality of life. This has shown the possibility for Mebendazole to control this form of carcinoma over an extended period of time. Mebendazole is a benzimidazole analogue which contains the nitrogen available for binding to the metal centre.

Tamoxifen has been one of the main treatments for breast cancer for many years by blocking the production of oestrogen however, some of the side effects restrict its use. Anastrozole, which works by the same route as tamoxifen, is a drug developed by AstraZeneca which has shown great promise over the use of tamoxifen as an adjuvant therapy.<sup>178-181</sup> A five year study<sup>179</sup> of 9,366 post-menopausal women with localised breast cancer was completed comparing anastrozole to tamoxifen. The most significant results of this were to show anastrozole gave prolonged disease-free survival and reduced distant metastases compared to Tamoxifen. Anastrozole also exhibited fewer serious side effects than Tamoxifen such as significantly fewer occurrences of vascular events (deep vein thrombosis, for example), gynaecological problems and cataracts, however increased occurrences of fractures and arthralgia. The study suggested anastrozole should be the preferred initial treatment for postmenopausal women with localised hormone-receptor-positive breast cancer. This was strengthened in a second study<sup>178</sup> in which patients were switched to anastrozole after two years of tamoxifen

treatment, to reduce the side effects experienced by tamoxifen treatment over the course of 5 years. This reported a 40 % decrease in the risk of an event (defined as local or distant metastases, or contralateral breast cancer) in the group transferred to anastrozole compared to those who stayed on tamoxifen. Anastrozole is a triazole analogue with carbonitrile functional groups, both of which contain nitrogen available for binding to the metal centre.

Bicalutamide is a drug developed by AstraZeneca which is effective against prostate cancer.<sup>182,183</sup> As a monotherapy, it has been reported to preserve bone mineral density, muscle strength and provide significant health-related quality of life benefits for men suffering with prostate cancer and osteoporosis,<sup>182</sup> providing an alternative to castration. Bicalutamide has also been used in combination therapies to increase the effectiveness of both drugs involved compared to either when used as a monotherapy.<sup>184,185</sup> A phase II study of sorafenib in combination with bicalutamide<sup>184</sup> showed increased effectiveness in stabilising the disease however, the same level of side effects were observed. This has been used in combination with carbidopa against castration resistant prostate tumours, with promising results *in vitro* and *in vivo* (in mice).<sup>185</sup> Bicalutamide contains a carbonitrile functional group which contains nitrogen available for binding to the metal centre.

Esomeprazole is a proton pump inhibitor (PPI) developed by AstraZeneca which is used in the treatment of acid reflux and related diseases.<sup>186</sup> A randomised controlled trial<sup>187,188</sup> of 554 patients with well-established gastroesophageal reflux disease who responded well to PPIs were split into two groups. The first underwent optimised esomeprazole treatment (266 patients) and the second were recommended for laparoscopic antireflux surgery (LARS, 288 patients, 248 of whom went through with the surgery). During this study, it was found that both methods of treatment achieve and maintain remission for the five year period the trial was conducted. The two methods were not significantly different from each other and consequently, should patients wish to avoid the risks and side effects of surgery, esomeprazole is a viable option.

Esomeprazole is also used in acid production control in the treatment of chronic gastritis and gastric ulcers caused by the bacteria, *Helicobacter pylori*,<sup>189,190</sup> in combination with suitable antibiotics. Esomeprazole is a benzimidazole analogue which contains nitrogen available for binding to the metal centre.

Gefitinib is a drug developed by AstraZeneca which has been FDA approved for treatment of locally advanced or metastatic non-small-cell lung cancer since May 2003.<sup>191,192</sup> Clinical trials are also underway to investigate its effectiveness against other cancers such as certain breast cancers<sup>181</sup> and head and neck<sup>192</sup> cancers. Gefitinib is a quinazoline analogue which contains nitrogen available for binding to the metal centre.

It is clear to see from the previous few paragraphs there are many commercially available drugs which are nitrogen-containing aromatic analogues (see Figure 6.5). This gives them the potential to bind to SABRE catalysts. This gives SABRE the potential to investigate the effectiveness and mechanism of drugs within cells or within the body. It is important to first understand the extent of this potential and consequently investigations will concentrate on the smaller moieties to ensure first polarisation transfer is possible and the extent of observed increase in signal intensity. It is also clear to see these drugs also include a number of potentially interfering or hindering additional functional groups.

The intention of this chapter is therefore to develop an understanding of the limitations of SABRE, but not to optimise it for each of the substrates described here. To become applicable as a general method, it is important to understand the tolerances and limitations of SABRE with respect to various functional groups, including bulkier groups such as the benzoyl moiety. This need introduces a number of further complications such as the effect of basicity of the substrate, steric bulk and whether the substrate can activate the catalyst.

A number of investigations were completed to achieve this. Firstly, the tolerance of SABRE to different functional groups is described by reference to a series of 4-substituted pyridines. A study on steric effect then follows, investigating the effect of polarisation transfer to various groups outside of the pyridine ring, such as methyl, phenyl and benzoyl groups. This is followed by the investigation of polarisation transfer to new binding groups such as those found in indole and thiazole, and of polarisation transfer to a selection of commercially available drugs. Potential real life complications are then investigated, looking into the situation where more than one substrate is present or the elimination of impurities that may be found in a reaction mixture.

Another potential of SABRE is to investigate the metabolism of some molecules within the body. This is observed in DNP by reference to pyruvate, the potential to differentiate between normal and cancerous cells in animal and human cancer cells.<sup>37,38,193,194</sup> The potential for SABRE to complete a similar metabolism is investigated by reference to the spontaneous reaction of 4-carboxaldehydepiperidine with methanol.

## 6.2 Investigations into polarisation transfer efficiency to pyridine analogues

Initial investigations into the general applicability of SABRE began with pyridine analogues. Within this section, the effect of changing the basicity of the pyridine analogue, the effect of changing the spacer between the pyridine ring and second phenyl ring.

### 6.2.1 The effect of basicity on the level of observed polarisation transfer in a series of *para*-substituted pyridines

The basicity (considered through the  $pK_a$ ) of the substrate is an important factor when considering polarisation transfer; both binding strength (whether the substrate can displace the halide bound to the iridium centre, forming the catalytic salt, see Chapter 2) and exchange rates are dependent on it. To investigate the effect of the  $pK_a$ , it is necessary to eliminate both steric and activation effects, and consequently a series of *para*-substituted pyridines were selected. This series of substituted pyridines also provides a range of functional groups with which to investigate the tolerance of SABRE. These are shown in Figure 6.6.

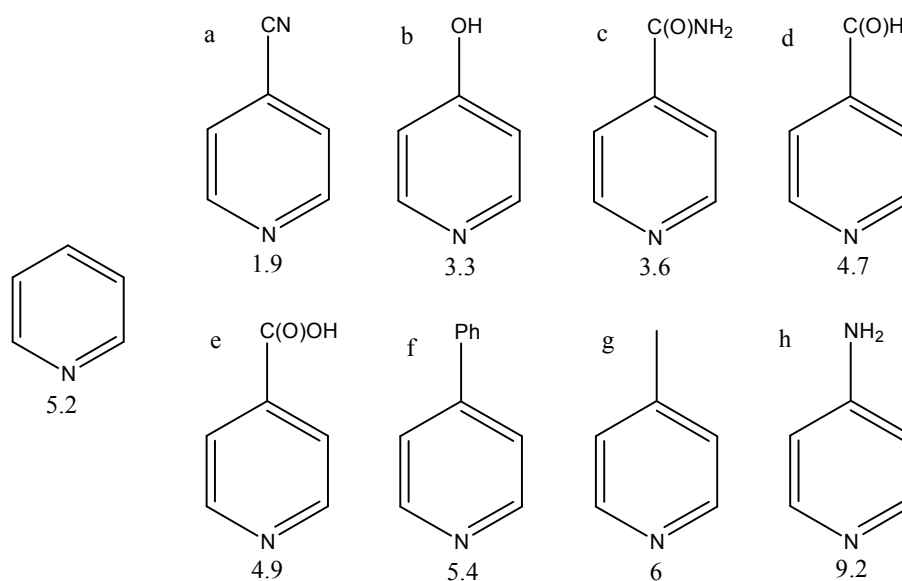


Figure 6.6 List of the 4-substituted pyridines investigated, namely: (a) 4-cyanopyridine, (b) 4-hydroxypyridine, (c) 4-carboxamidepyridine, (d) 4-carboxaldehydepyridine, (e) isonicotinic acid, (f) 4-phenylpyridine, (g) 4-methylpyridine and (h) 4-aminopyridine. Each substrate is presented with the pK<sub>a</sub> of the nitrogen position. <sup>106,145,195-202</sup>

In order to complete this study, the substrates were polarised using method 1 and **IMes(a)**. Polarisation transfer to pyridines (a) – (h) (Figure 6.6) was investigated for <sup>1</sup>H NMR at a PTF of 2 G and 65 G and <sup>1</sup>H OPSYdq NMR at a PTF of 2 G. This was completed at these magnetic fields because in the standard <sup>1</sup>H NMR spectrum, maximum transfer to pyridine is observed at a PTF of 75 G and maximum transfer for the <sup>1</sup>H OPSYdq is observed at a PTF of 2 G. The observed enhancements to the *ortho* and *meta* <sup>1</sup>H resonances of these substrates are presented in Table 6.1. The data collected for standard <sup>1</sup>H spectra is presented as the average of three points. The data collected for <sup>1</sup>H OPSYdq spectra are a single point only, as the aim of this sequence is to prove transfer of double quantum states derived from *parahydrogen*. This average approach is applied to all data in this chapter unless otherwise stated.

Pyridines (d) and (e) proved unsuitable for comparison because (d) showed a reaction with methanol (further investigated in chapter 6.5.1, pg 305) and (e) exhibited low solubility in methanol. Although polarisation transfer is observed to both substrates, neither is at standard concentration and so cannot be compared to the other substrates due to the known concentration dependence of SABRE (see Chapters 3 and 4).

Polarisation transfer to the phenyl and methyl groups of pyridines (f) and (g) (Figure 6.6) will be discussed later in this chapter (Section 6.2.2, pg 280). It is also important to



note the exchangeable protons in groups such as the amine or hydroxyl group can become deuterated due to the experiment being carried out in  $d_4$ -methanol.

<i>Para</i> substituent	$pK_a$	Observed $^1\text{H}$ NMR signal enhancement					
		$^1\text{H}$ at 2 G		$^1\text{H}$ at 65 G		$^1\text{H}$ OPSYdq at 2 G	
		<i>Ortho</i>	<i>Meta</i>	<i>Ortho</i>	<i>Meta</i>	<i>Ortho</i>	<i>Meta</i>
-carbonitrile	1.9 <sup>195</sup>	-37	18	-69	1	13	15
-hydroxy	3.3 <sup>106,196,198</sup>	-49	44	-60	26	8	10
-carboxamide	3.6 <sup>199</sup>	-69	59	-86	42	6	5
-phenyl	5.3 <sup>200</sup>	-91	4	-116	7	7	1
-methyl	6 <sup>145</sup>	-35	25	97	-60	23	22
-amino	9.2 <sup>197,199,201</sup>	68	112	127	46	19	20

Table 6.1  $^1\text{H}$  polarisation observed with a PTF of 2 G and 65 G, and  $^1\text{H}$  OPSYdq polarisation observed with a PTF of 2G for the *ortho* and *meta* position of a series of 4-substituted pyridines.

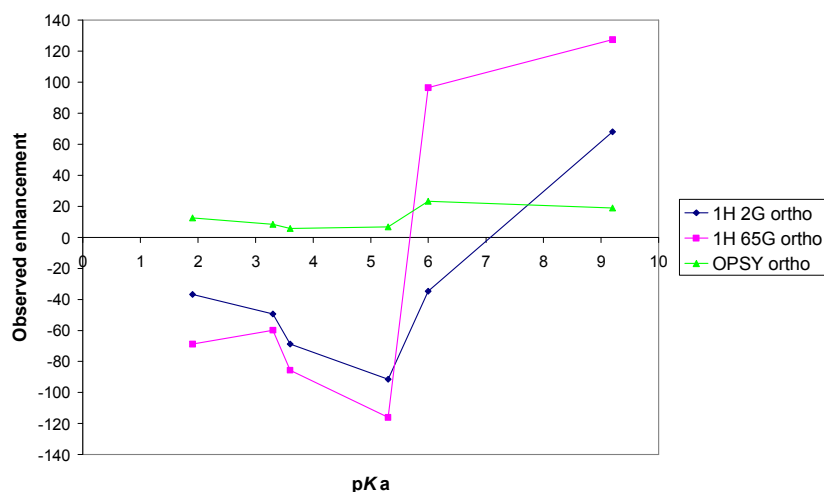


Figure 6.7 Showing the observed polarisation to the *ortho* position of a series of four substituted pyridines compared to the  $pK_a$  of the N-position of those substrates.

In Figure 6.7, it is possible to observe increasing polarisation transfer to the *ortho* position of the pyridine analogues upon increasing  $pK_a$ , however after 5.3, a phase change of the observed signals is experienced, affecting calculated enhancement. The  $^1\text{H}$  OPSYdq is processed in magnitude mode and therefore a phase change cannot be observed. The extent of polarisation transfer observed by the  $^1\text{H}$  OPSYdq NMR spectra does not appear to follow a trend.

These data are presented in a different way in Table 6.2, through the addition of the magnitudes of observed signal enhancement to *ortho* and *meta* positions of the 4-substituted pyridines.

<i>Para</i> substituent	$pK_a$	Sum of the $^1\text{H}$ NMR signal enhancement observed on <i>ortho</i> and <i>meta</i> positions		
		$^1\text{H}$ at 2 G	$^1\text{H}$ at 65 G	$^1\text{H}$ OPSYdq at 2 G
-carbonitrile	1.9 <sup>195</sup>	55	70	28
-hydroxy	3.3 <sup>106,196,198</sup>	93	86	18
-carboxamide	3.6 <sup>199</sup>	128	128	11
-phenyl	5.3 <sup>200</sup>	95	-123	8
-methyl	6 <sup>145</sup>	60	157	45
-amino	9.2 <sup>197,199,201</sup>	180	173	39

Table 6.2 The sum of the observed  $^1\text{H}$  polarisation with a PTF of 2 G and 65 G, and  $^1\text{H}$  OPSYdq polarisation with a PTF of 2G for the *ortho* and *meta* position of a series of 4-substituted pyridines.

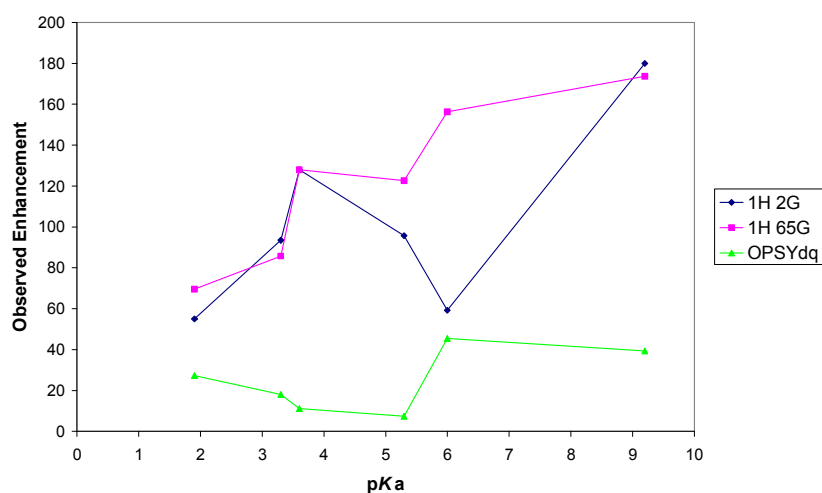


Figure 6.8 Showing the sum of the modulus of polarisation transfer to both *ortho* and *meta* positions of a series of four substituted pyridines compared to the  $pK_a$  of the N-position of those substrates.

Looking at Figure 6.8, no simple correlation, linear or curved, can be observed. In some cases, polarisation transfer to the substrate from *parahydrogen* can result in  $I_zS_z$ -type states leading to antiphase signals, particularly with a PTF of 2 G, which greatly effects the calculated enhancement. It might also be due to the additional interactions created by the different R groups in *para*-position. For instance, any group containing a nitrogen or oxygen may be able to bind to the metal centre, creating a kinetic motif

which is not solely dependent on the  $pK_a$  of the nitrogen centre. While it is unlikely polarisation can be transferred when binding occurs through the substituent, this could greatly affect the contact time when binding through the N position. To investigate this idea, the hydride region of a thermal  $^1\text{H}$  NMR spectrum of each sample was analysed (Figure 6.9).

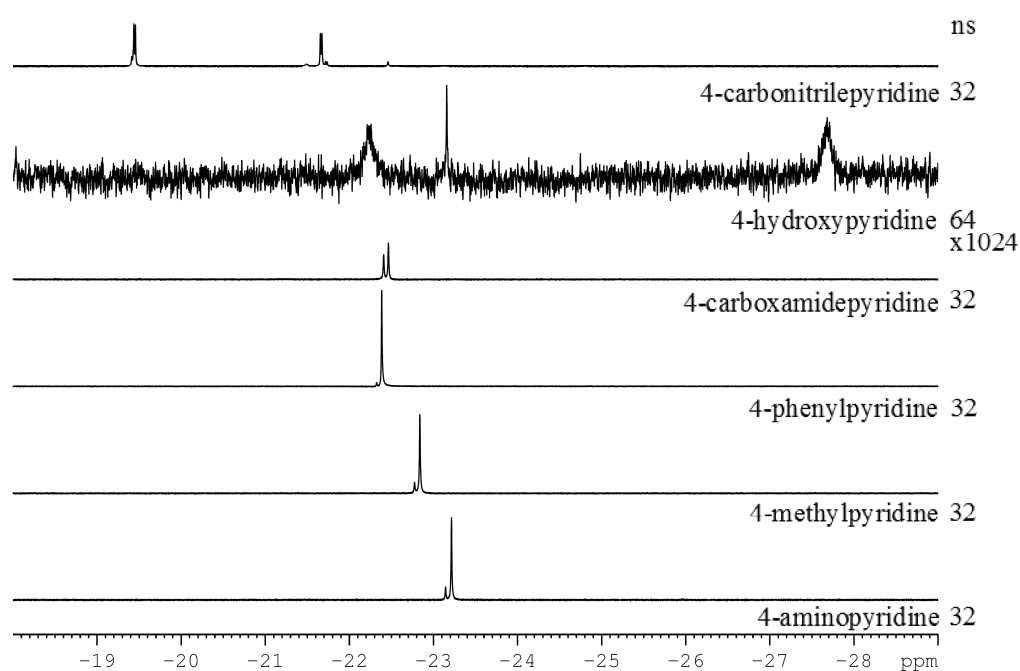


Figure 6.9 Hydride region of thermal  $^1\text{H}$  NMR spectra of the named substrates polarised using method 1 and **IMes(a)**.

Evidence for the expected singlet hydride corresponding to  $[\text{Ir}(\text{IMes})(\text{H})_2(\text{sub})_3]\text{Cl}$  is observed in all 6 spectra, together with a limited level of deuteration. A smaller peak can also be observed next to these corresponding to the HD analogue. In the cases of 4-hydroxypyridine and 4-carbonitrilepyridine, additional hydrides are observable suggesting the nitrogen in the pyridine ring is not the only binding atom in the substrate.

To investigate this, polarisation transfer to phenol and benzonitrile (Figure 6.10) was investigated using method 1 and **IMes(a)**.

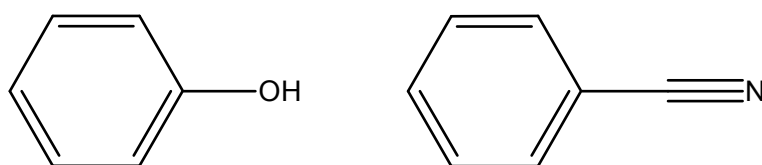


Figure 6.10 Structures of phenol and benzonitrile.

These substrates have analogous structures to 4-hydroxypyridine and 4-carbonitrilepyridine however the nitrogen in the ring is replaced with a carbon to form a phenyl derivative rather than a pyridine derivative. Hydrogenation of **IMes(a)** in the presence of these substrates will show if they are able to activate the catalyst and form a stable complex, and therefore binding through the OH or CN functional groups.

In the case of phenol, polarisation transfer was not observed in the standard  $^1\text{H}$  spectra however, signals were observed in the  $^1\text{H}$  OPSYdq spectra suggesting weak polarisation transfer must have occurred. A number of hydrides are also observed. Together, this information proves the hydroxyl group is able to activate and stabilise **IMes(a)** and shows a small level of polarisation transfer is possible through this route.

In the case of benzonitrile, polarisation transfer was observed in the standard  $^1\text{H}$  spectra (in the form of an emission peak) and  $^1\text{H}$  OPSYdq NMR spectra however this did not lead to an enhancement value. A single hydride resonance was observed at -21.15 ppm. This proves the nitrile group is also able to activate and stabilise **IMes(a)** and the polarisation transfer is possible through this route.

While it was not possible to ascertain a simple correlation, this experiment has shown that a significant polarisation transfer can be gained with both weak and strong interactions between the ligand and metal. It has also shown that the SABRE technique is tolerant to many different functional groups such as hydroxyl, carbonitrile, amino, amide and phenyl groups.

#### 6.2.2 Effect of substitution on the level of polarisation transfer to the binding pyridine ring and substituents

In this section, the aim is to explore how steric interactions play a role in the ability of SABRE to operate. The challenge in achieving this goal is that it has already been shown that basicity plays a role in the modulation of the polarisation level. The two effects are therefore clearly linked. The three simple substituted 2-, 3- and 4-methylpyridines will be examined first.

## 6.2.2.1 Polarisation transfer efficiency trends observed within the methylpyridines

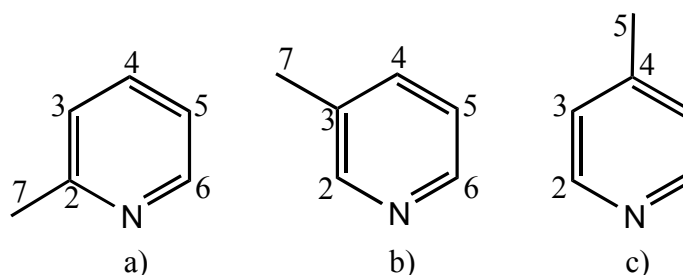


Figure 6.11 Labelled structures of a) 2-methylpyridine, b) 3-methylpyridine and c) 4-methylpyridine.

Using method 1, **IMes(a)** and **SIMes(a)** employed at a PTF of 2 G were used to examine 2-, 3- and 4-methylpyridine. The results obtained with **IMes(a)** are discussed first (Table 6.3).

	$pK_a$		<i>ortho</i>		<i>meta</i>		<i>para</i>	methyl
2-methyl pyridine	5.97 <sup>106,107</sup>	Position	-	6	3	5	4	7
		Enhancement	-	-4	0.5	1	-4	0.2
3-methyl pyridine	5.68 <sup>106,107</sup>	Position	2	6	-	5	4	7
		Enhancement	-66	-82	-	61	-181	-8
4-methyl pyridine	6.02 <sup>106,107</sup>	Position	2	-	3	-	-	5
		Enhancement	151	-	-37	-	-	12

Table 6.3 Observed <sup>1</sup>H enhancements of 2-, 3- and 4-methylpyridine when polarised with **IMes(a)**.

In the case of 4-methylpyridine, the *ortho* and *meta* positions show some  $I_zS_z$ -type character. The greatest signal enhancement to the methyl group is observed in 4-methylpyridine. It can also be observed that very little polarisation transfer is observed into any position of 2-methylpyridine.

4- and 3- methylpyridine were investigated using **SIMes(a)** in deuterated methanol and reacted in the expected way. For 2-methylpyridine, no activity was observed and **SIMes(b)** was used. This resulted in the observation of polarisation transfer. Results for all three methylpyridines are outlined in Table 6.4.

	$pK_a$		<i>ortho</i>		<i>meta</i>		<i>para</i>	methyl
2-methyl pyridine	5.97 <sup>106,107</sup>	Position	-	6	3	5	4	7
		Enhancement	-	-1	0.8	1.2	-0.9	0.6
3-methyl pyridine	5.68 <sup>106,107</sup>	Position	2	6	-	5	4	7
		Enhancement	-17	-14	-	11	-9	2
4-methyl pyridine	6.02 <sup>106,107</sup>	Position	2	-	3	-	-	5
		Enhancement	-83	-	8	-	-	8

Table 6.4 Observed <sup>1</sup>H enhancements of 3- and 4-methylpyridine when polarised with **SIMes(a)** and 2-methylpyridine when polarised with **SIMes(b)**.

Within the methyl pyridines, a clear trend can be observed. The least hindered substrate, 4-methylpyridine ( $pK_a = 6.02^{106,107}$ ), shows greatest enhancement on all positions, then 3-methylpyridine ( $pK_a = 5.68^{106,107}$ ) and the most hindered substrate, 2-methylpyridine ( $pK_a = 5.97^{106,107}$ ) shows the least enhancement. The presence of emission peaks in the 2-methylpyridine spectrum indicates polarisation has transferred to the substrate. In all the methylpyridine cases, less polarisation transfer is observed with the SIMes based catalysts compared to **IMes(a)**.

#### 6.2.2.2 Polarisation transfer efficiency trends observed within the phenylpyridines

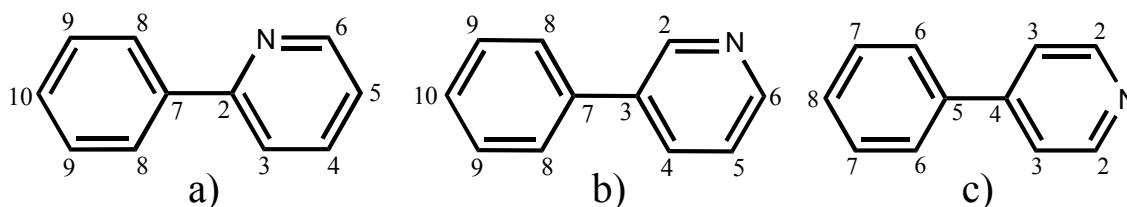


Figure 6.12 Labelled structures of a) 2-phenylpyridine, b) 3-phenylpyridine and c) 4-phenylpyridine.

Polarisation transfer into the phenylpyridines was investigated in order to investigate transfer to a bulkier substrate and transfer into a second aromatic ring. This differs from quinoline in that in the phenyl pyridines, the two aromatic rings are separated by a single C-C bond. 4-phenylpyridine has a  $pK_a$  of 5.55, 3-phenylpyridine has a  $pK_a$  of 4.8 and 2-phenylpyridine has a  $pK_a$  of 4.48. All three phenylpyridines were investigated using method 1 and **IMes(a)**. No polarisation transfer was observed to 2-phenylpyridine using **IMes(a)** or **IMes(b)**. The polarisation transfer observed with 3- and 4-phenylpyridine is outlined in Table 6.5.

	$pK_a$		Ring 1 (pyridine)				Ring 2 (phenyl)	
3-phenyl pyridine	$4.8^{107}$	Position	2	4	5+9	6	8	10
		Enhancement	-67.4	-44.7	22.3	-77.1	3.6	3.4
4-phenyl pyridine	$5.55^{107}$	Position	2	-	3	-	6	7+8
		Enhancement	-50.8	-	27.9	-	4.3	2.9

Table 6.5 Comparison of the enhancement observed for 3-phenylpyridine and 4-phenylpyridine.

In Table 6.5, the enhancement for positions 5 and 9 of 3-phenylpyridine, and 7 and 8 of 4-phenylpyridine have been calculated as one value. This is because the resonances are not base line resolved in the spectra and cannot be separated for integration. In the first ring, it can be observed that the highest polarisation is observed in the ‘ortho’ positions (2 and 6) of 3-phenylpyridine, showing greater enhancement than the ‘ortho’ position (2) of 4-phenylpyridine. The next highest is then the ‘para’ position of 3-phenylpyridine. The lowest enhancements in the first ring are observed in the ‘meta’ positions, however unlike the ‘ortho’ positions, it is now 4-phenylpyridine (position 3) showing the greatest enhancement compared to 3-phenylpyridine (position 5). This trend is continued into the second ring where the ‘ortho’ position of 4-phenylpyridine (6) shows greater enhancement than that of 3-phenylpyridine (8), however this enhancement is significantly lower than those observed in the first ring. The trend switches again when looking at the ‘meta’ and ‘para’ positions of the second ring, with 3-phenylpyridine exhibiting greater enhancement. Generally speaking, greater polarisation transfer is observed within 3-phenyl pyridine. The  $^1\text{H}$  OPSYdq spectra show greater polarisation transfer into the first ring than the second for both 3- and 4-phenylpyridine.

An investigation followed to find a method to increase the polarisation transferred into the second ring. This work was completed with 3-phenylpyridine using method 2 **IMes(a)**. The polarisation transfer was investigated with a PTF of 60 G where the length of time *parahydrogen* is added to the sample (bubbling time) is altered. The results are represented graphically in Figure 6.13.

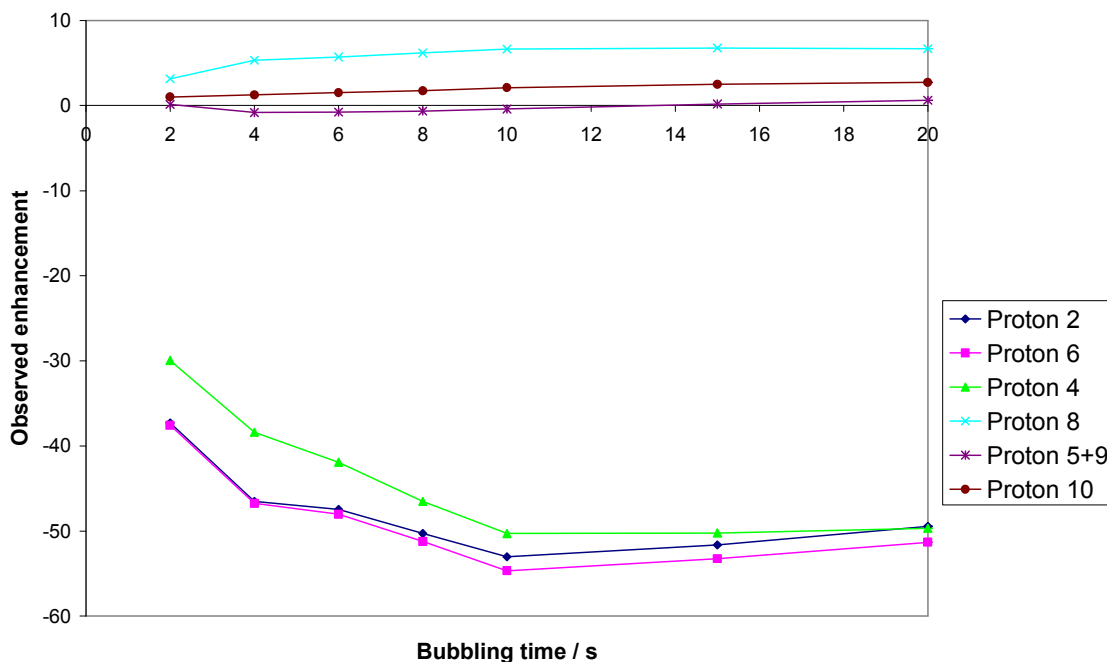


Figure 6.13 Graphical representation of the effect of changing bubbling time on the polarisation transfer to 3-phenylpyridine.

The bubbling time of *parahydrogen* was increased from 2 seconds to 20 seconds. An increase in polarisation transfer to 3-phenylpyridine can be observed up to a bubbling time of 10 s, however after this time, the polarisation transfer either decreases or stabilises for different protons. This did not have the effect of significantly increasing polarisation transfer into the second ring.

### 6.2.2.3 Polarisation of 3-benzoylpyridine and 4-(4-chlorobenzoyl)pyridine

3-benzoylpyridine and 4-(4-chlorobenzoyl)pyridine (Figure 6.14) were interrogated to extend the investigation of polarisation transfer into a second aromatic ring. In the case of these two substrates, the second ring is separated from the first by a carbonyl group.

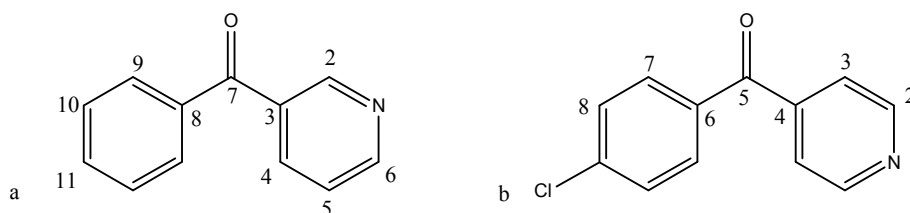


Figure 6.14 Structure of 3-benzoylpyridine and 4-(4-chlorobenzoyl)pyridine.



3-benzoylpyridine was hyperpolarised by method 1 and **IMes(a)**. Results are outlined in Table 6.6.

3-benzoylpyridine	Observed <sup>1</sup> H NMR signal enhancement					
	2	4	5 + 10	6	9	11
Polarised at 2 G	-52.2	34.0	14.7	-53.2	1.6	2.6
Polarised at ~65 G	-53.8	-39.0	2.4	-46.6	1.9	0.7

Table 6.6 Observed <sup>1</sup>H NMR polarisation transfer to 3-benzoylpyridine polarised with **IMes(a)** at a PTF of 2 G and 65 G.

In Table 6.6, the enhancement for positions 5 and 10 of 3-benzoylpyridine have been calculated as one value. This is because the resonances are not base line resolved in the spectra and cannot be separated for integration. It is possible to see polarisation transfer was achieved in this system, including into the second ring. Changing the PTF to ~65 G did not increase polarisation transferred into the second ring.

4-(4-chlorobenzoyl)pyridine was hyperpolarised using method 1 and **IMes(a)**.

4-(4-chlorobenzoyl)pyridine	Observed <sup>1</sup> H NMR signal enhancement			
	2	3	7	8
Polarised at 2 G	-64.7	46.3	-0.8	2.4
Polarised at ~65 G	-46.8	0.4	0.9	0.7

Table 6.7 Observed <sup>1</sup>H NMR polarisation transfer to 4-(4-chlorobenzoyl)pyridine polarised with **IMes(a)** with a PTF of 2 G and 65 G.

It is possible to see polarisation transfer was achieved in this system, including a small amount into the second ring. Changing the PTF to ~65 G did not increase polarisation transfer into the substrate. The polarisation transfer observed into H(3) with a PTF of ~65 G was comparable to that for H(2) at the same PTF, but the signal exhibited significant antiphase ( $I_z S_z$ -type) behaviour and consequently, has a low calculated enhancement.

Investigations into the two substrates, 3-benzoylpyridine and 4-(4-chlorobenzoyl)pyridine have shown polarisation can transfer across a fairly large spacer with no protons between the pyridine and phenyl rings.

### 6.3 Polarisation of substrates without a pyridine subunit

In the previous chapters, pyridine (and substituted pyridines) and quinoline (and substituted quinolines) are the only substrates that have been considered. In this section, polarisation transfer to the indole subunit, the thiazole subunit and to commercially available drugs is investigated.

#### 6.3.1 Investigation into the polarisation of indole

Indole analogues are important biologically (see Section 6.1), and so an investigation into whether it would be possible to hyperpolarise indole was undertaken. It also gives us the opportunity to investigate polarisation to a 5-membered N-heterocyclic ring, and if polarisation is possible where an NH is present. Two substrates were investigated; indole and 1-methylindole (Figure 6.15).

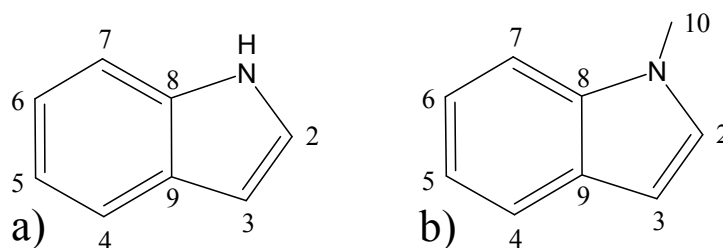


Figure 6.15. Structures of a) indole and b) 1-methylindole.

Both substrates were initially investigated using method 1 and **IMes(a)** however, in both cases, no polarisation was observed in either the  $^1\text{H}$  NMR spectrum or  $^1\text{H}$  OPSYdq NMR spectrum.

The investigation was then extended to include **IMes(c)**. With this new catalyst, polarisation transfer is now observed in the form of emission peaks in the  $^1\text{H}$  and significant peaks in the  $^1\text{H}$  OPSYdq for indole, however an enhancement is not observed (Table 6.8). No transfer is observed in the case of 1-methylindole.

Indole	2	3	4	5	6	7
Enhancement	-0.03	0.15	-0.52	0.49	0.69	-0.51

Table 6.8. Observed  $^1\text{H}$  polarisation transfer to indole in the presence of **IMes(c)**.

It was thought the low level of polarisation transfer observed could be due to the proton/methyl group present on the nitrogen atom, which limits the substrate from

binding. Potassium tert-butoxide was added to the indole and **IMes(c)** sample to attempt to deprotonate the proton on the nitrogen in indole and consequently make binding to the metal through the nitrogen more accessible, however no evidence for polarisation transfer was observed. During this experiment, it was found catalyst did not decompose upon addition of the base. This was confirmed by adding the base to a standard pyridine and **IMes(a)** sample, in which the catalyst did not decompose, however the addition resulted in greatly reducing the expected polarisation transfer into pyridine in this system.

### 6.3.2 Investigation into the polarisation of thiazole

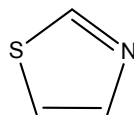


Figure 6.16 Structure of thiazole.

The structure of thiazole is shown in Figure 6.16. Investigations of this structure will show the effect of reducing the binding ring from 6-membered to 5-membered while maintaining the binding motif in the ring. Unlike indole, there is an additional sulfur atom within the ring, and consequently, the nitrogen does not have a proton bound to it, hindering its ability to bind to the metal catalyst. It is known that iridium can accept both hard and soft donors<sup>203</sup> and therefore investigations into thiazole will also give the opportunity to determine if the iridium centre in  $[\text{Ir}(\text{IMes})(\text{H})_2(\text{sub})_3]^+$  prefers hard (N) or soft (S) donors.

#### 6.3.2.1 Investigation into the polarisation of 2-aminothiazole

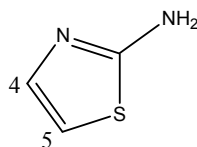


Figure 6.17 Structure of 2-aminothiazole.

2-aminothiazole (Figure 6.17) was the first thiazole analogue to be investigated using method 1 and **IMes(a)**. Polarisation transfer is observed to the two  $^1\text{H}$  resonances, proton 4 and proton 5, in 2-amino thiazole which exhibited an average enhancement of

-19 and -41 fold respectively. SABRE is therefore tolerant to the amino functional group and the presence of a sulphur atom in the ring. When polarisation transfer to  $^{13}\text{C}$  is examined, one  $^{13}\text{C}$  resonance is observed which appears with a S/N ratio of 5.46. This corresponds to the quaternary carbon which is bound to the amino group at 170.31 ppm. The quaternary carbon is more prominent than the other carbons in the system due to a long  $T_1$ . This data set revealed a second important piece of information; an amount of polarisation is also transferred to the OH proton of methanol (enhancement of -0.51). A typical  $^1\text{H}$  NMR spectrum is presented in Figure 6.18.

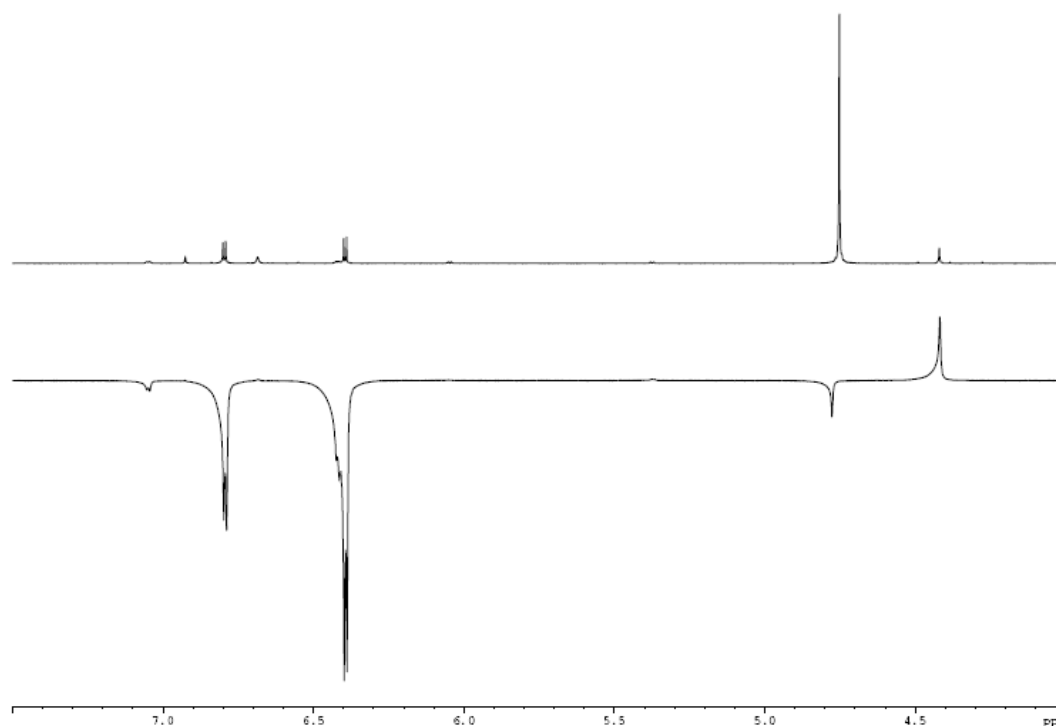


Figure 6.18 Thermal  $^1\text{H}$  NMR spectrum of 2-aminothiazole (top) with a typical hyperpolarised spectrum of 2-aminothiazole (bottom) polarised with method 1 and **IMes(a)**.

In the hydride region of the corresponding  $^1\text{H}$  NMR spectrum, the dominant signal appears at -23.0 ppm. This suggests the complex of the form  $[\text{Ir}(\text{IMes})(\text{H})_2(\text{sub})_3]\text{Cl}$  is present, where each bound 2-amino thiazole is bound through the nitrogen. Two further pairs of hydrides observed in the hyperpolarised  $^1\text{H}$  OPSYdq NMR spectrum, indicating the presence of two complexes with inequivalent hydrides, with relative intensities of ~5% (-21.58 ppm and -22.38 ppm,  $J_{\text{H-H}} = 6.15$  Hz) and ~2% (-21.70 ppm and -22.59 ppm,  $J_{\text{H-H}} = 6.83$  Hz) compared to the dominant singlet hydride.

2-aminothiazole has a significantly different structure compared to pyridine as it is based around a 5-membered ring, where pyridine is a 6-membered ring. While pyridine shows a maximum observed  $^1\text{H}$  NMR enhancement with a PTF of  $-70\text{ G}$ ,<sup>66</sup> it was thought 2-aminothiazole may exhibit a different trend owing to the different coupling network through the 5-membered ring. Therefore, 2-aminothiazole was tested next using method 2 and **IMes(a)**, varying the PTF in the range  $-150\text{ G}$  to  $+10\text{ G}$  in increments of  $10\text{ G}$ . Results are shown in Figure 6.19.

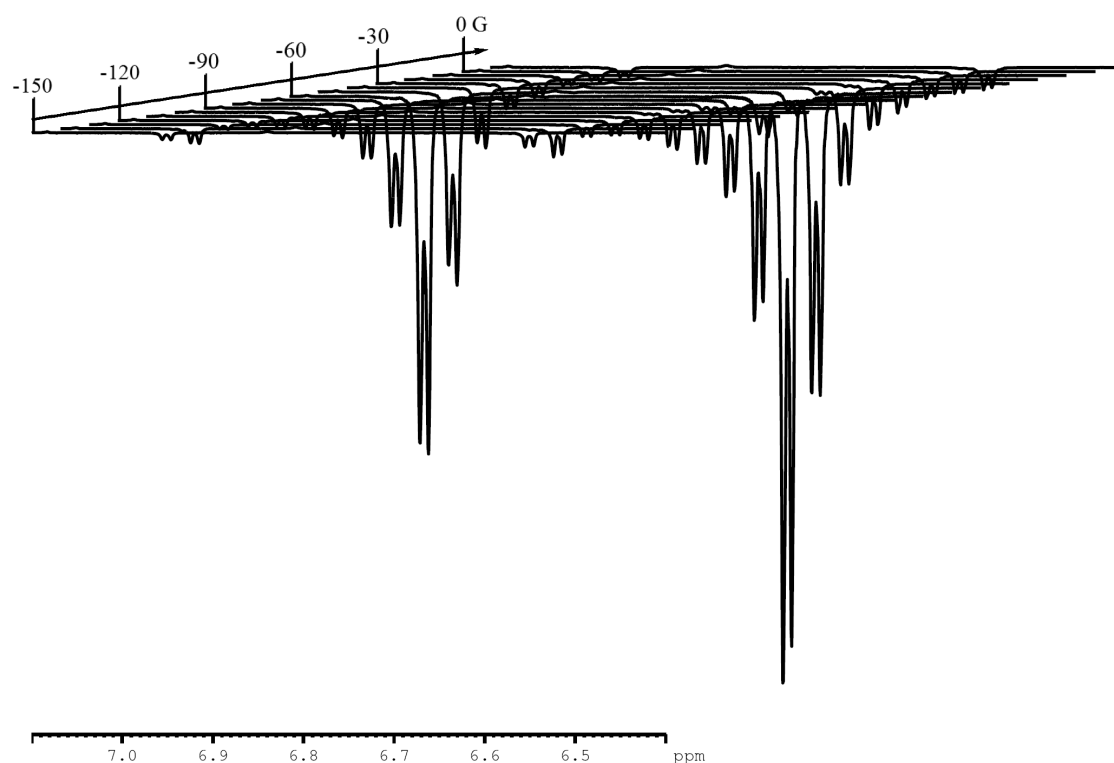


Figure 6.19 Observed  $^1\text{H}$  NMR signal enhancement of 2-aminothiazole hyperpolarised at a PTF of  $-150\text{ G}$  to  $+10\text{ G}$  in increments of  $10\text{ G}$  using method 2 and **IMes(a)**.

It is possible to observe the maximum enhancement for both proton environments in 2-aminothiazole polarised with **IMes(a)** is obtained with a PTF of  $-60\text{ G}$ . This is slightly offset when compared to the magnetic field dependence of pyridine.

These experiments prove that a thiazole analogue is able to bind to the iridium catalyst and can accept polarisation from *parahydrogen* via the metal template. It also shows this polarisation transfer is subject to a field of polarisation dependence which is similar to that of pyridine.

### 6.3.2.2 Investigation into the polarisation of 2-amino-4-methyl thiazole, 2-amino-4-phenyl thiazole and 2-amino-4-(4-chlorophenyl) thiazole

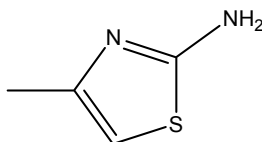


Figure 6.20 Structure of 2-amino-4-methyl thiazole.

Transfer of polarisation to 2-aminothiazole could occur when the substrate is bound to the iridium centre by either nitrogen or sulphur atoms. The addition of substituents on the 4 position of 2-aminothiazole will give an insight into the binding preferences of **IMes(a)**. This was first investigated by polarisation of 2-amino-4-methyl thiazole (Figure 6.20) using method 1 and **IMes(a)**. Weak polarisation transfer was observed in the thiazole proton only, and not methyl group of 2-amino-4-methylthiazole, shown in Table 6.9. However, weak double quantum polarisation transfer was observed to both thiazole and methyl proton signals. Using **IMes(c)** increases the observed enhancement on the thiazole proton by 6 fold.

	Observed $^1\text{H}$ NMR signal enhancement	
	Thiazole ( $\sim 6.1$ ppm)	Methyl ( $\sim 2.1$ ppm)
2-amino-4-methyl thiazole	-0.43	0.64
2-amino-4-methyl thiazole + NCMe	-2.60	0.12

Table 6.9 Observed  $^1\text{H}$  NMR signal enhancement for 2-amino-4-methyl thiazole.

As polarisation transfer is observable on both methyl and thiazole protons, the methyl group may provide a method of polarisation transfer to the thiazole proton.

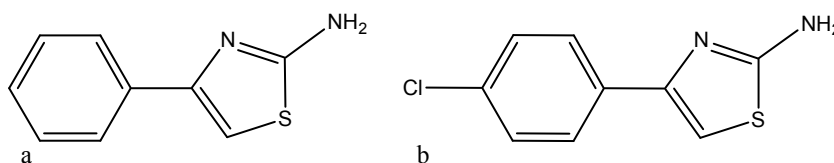


Figure 6.21 Structures of (a) 2-amino-4-phenyl thiazole and (b) 2-amino-4-(4-chlorophenyl) thiazole.

In the cases of 2-amino-4-phenyl thiazole (Figure 6.21a) and 2-amino-4-(4-chlorophenyl) thiazole (Figure 6.21), no enhancement was observed with a  $90^\circ$  pulse, regardless of whether **IMes(a)** or **IMes(c)** was employed. The use of the  $^1\text{H}$  OPSYdq

NMR sequence yielded weak polarisation transfer into the phenyl ring of both substrates. A series of experiments were designed to prove these signals are truly signals derived from double quantum states, and not thermal breakthrough. This was completed with 2-amino-4-(4-chlorophenyl) thiazole as it showed slightly greater signal in the  $^1\text{H}$  OPSYdq spectrum compared to 2-amino-4-phenyl thiazole.

First, a  $^1\text{H}$  OPSYdq sequence was completed without the presence of *parahydrogen*, where no peaks were observed. Second, the crusher gradients of the  $^1\text{H}$  OPSYdq were increased from 60 % to 80 % during a hyperpolarised experiment, increasing the selectivity of the filter. The signals on the phenyl ring were still observable, suggesting they derived from double quantum states, not thermal breakthrough. A third test is to investigate the field dependence of this transfer. 2-amino-4-(4-chlorophenyl)thiazole was consequently interrogated using method 2 and **IMes(c)**, varying the PTF in the range -140 G to 0 G with increments of 20 G, shown in Figure 6.22.

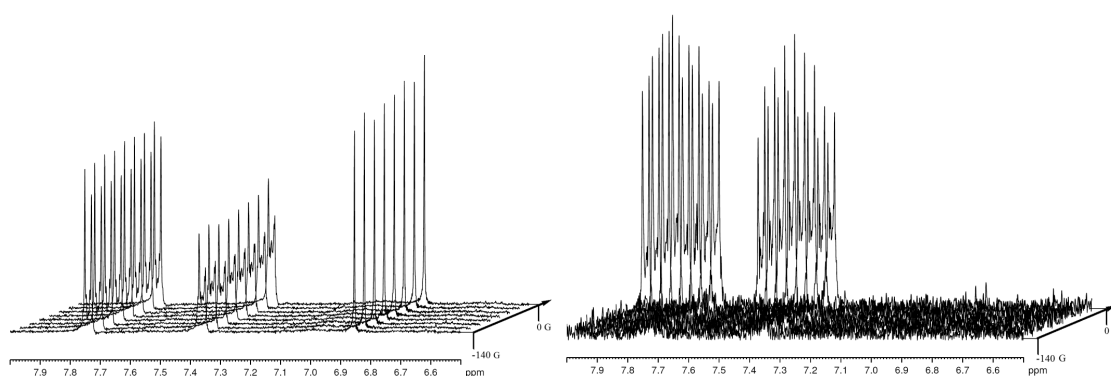


Figure 6.22 Observed NMR signal enhancement of 2-amino-4-(4-chlorophenyl)thiazole polarised with **IMes(c)**. This data is presented with a PTF of -140 G (bottom) to 0 G in increments of 20 G. The left shows the effect on  $^1\text{H}$  NMR spectra and the right shows the effect on the  $^1\text{H}$  OPSYdq NMR spectra.

It appears that a small dependence is observed in the  $^1\text{H}$  NMR spectra (Figure 6.22, left) but this has not led to an enhancement of the signal, with the largest peak having an absolute integral of only 75 % of the same signal in the thermal trace. As this could result from turbulence within the signal reducing the lock (see Chapter 2), and no antiphase ( $I_zS_z$ -type) or emission (negative phase) peaks are observed, it is not possible to prove if this 25 % drop in signal intensity is due to polarisation transfer. A different dependence is observed in the  $^1\text{H}$  OPSYdq NMR spectra (Figure 6.22, right) however, with significant signal observed in the signals corresponding to the phenyl ring, and none observed in the shift that would correspond to the proton in the thiazole ring. Not

only that, but the  $^1\text{H}$  OPSYdq NMR spectra appear to show a field dependence with a maximum observed with a PTF of -80 G. The experiment was repeated with a PTF in the range -100 G to -60 G in increments of 5 G to double check these results. The same trends were observed for both  $^1\text{H}$  NMR spectra and the  $^1\text{H}$  OPSYdq NMR spectra. This suggests the signals must derive from double quantum states and are not due to selectivity issues with the OPSY sequence, as thermal breakthrough would not exhibit a dependence on magnetic field of polarisation. This suggests that polarisation does transfer from *parahydrogen* to the 4-substituted 2-aminothiazoles via SABRE however, the interaction is weak. This consequently suggests transfer to this range of substrates may be optimised by the use of a different SABRE catalyst.

### 6.3.2.3 Investigation into the polarisation of benzothiazole

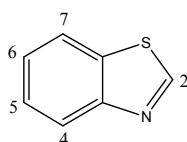


Figure 6.23 Structure of benzothiazole.

Initially, the polarisation transfer to benzothiazole was investigated using method 1 and **IMes(a)**. This resulted in the observation of significant polarisation transfer to most positions however the observed enhancement on position 2 is significantly less than the other positions (Table 6.10). Benzothiazole was also investigated using **IMes(c)**, as it was thought this might alter the system enough to encourage a more equal spread of polarisation transfer around the system. In most positions, this had the effect to significantly increase the polarisation transfer observed, particularly to position 2.

Benzothiazole	Observed $^1\text{H}$ NMR signal enhancement				
	2	4	5	6	7
<b>IMes(a)</b>	9.6	79.9	46.8	63.8	72.0
<b>IMes(c)</b>	95.9	114.1	49.5	105.6	103.0

Table 6.10 Observed  $^1\text{H}$  NMR signal enhancement for benzothiazole using method 1 and **IMes(a)** and **IMes(c)**.

Polarisation transfer to this substrate has proved to be strong and consequently further investigations have been completed. First, the effect of changing the PTF was investigated using method 2 and **IMes(c)**.



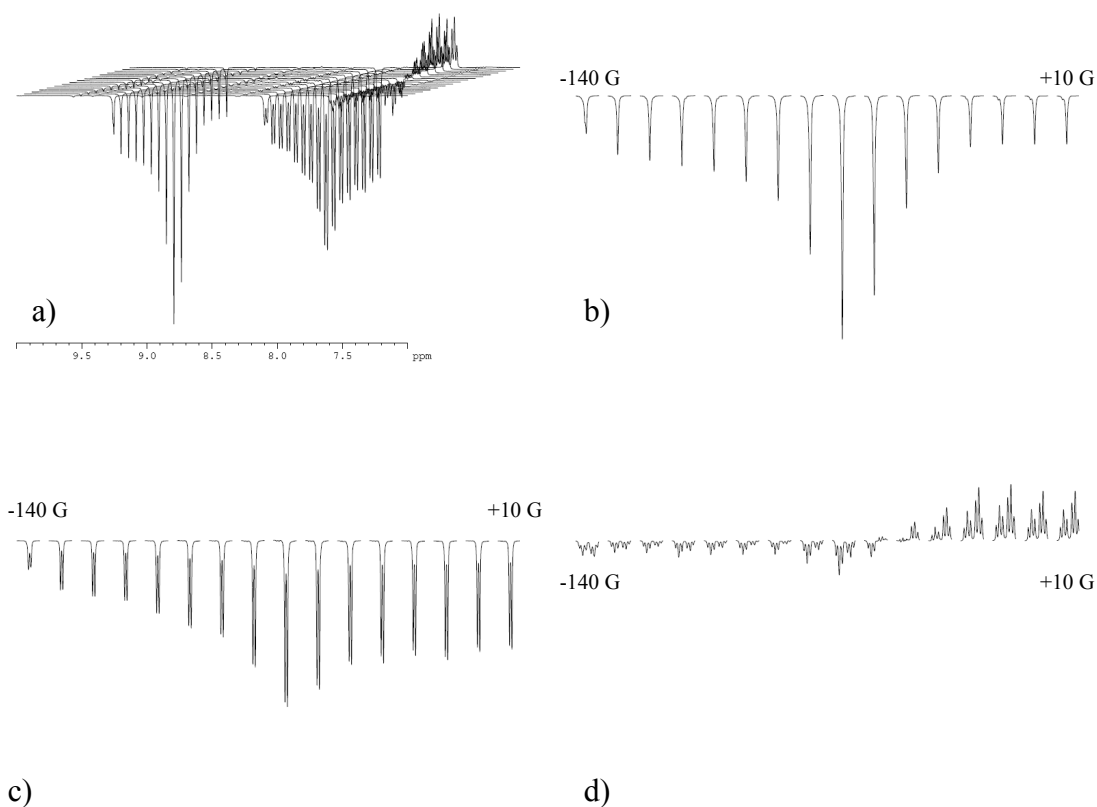


Figure 6.24 Effect of changing field of hydrogen addition on polarisation transfer to benzothiazole using method 2 and **IMes(c)**. a) shows all  $^1\text{H}$  resonances, b) shows signals corresponding to the proton 2, c) to protons 4 and 7 and d) to protons 5 and 6.

This experiment revealed the maximum polarisation transfer is experienced at with a PTF of -60 G (Figure 6.24) for benzothiazole. This is the same as 2-aminothiazole and quinoline (Section 6.3.2.1, pg 287, and Chapter 4 respectively). Significant polarisation transfer was also observed into all positions of benzolthiazole.

PTF	Observed $^1\text{H}$ NMR signal enhancement				
	2	4	5	6	7
0 G	-13	-30	16	25	-31
-60 G	-84	-62	-23	-12	-61

Table 6.11 Observed polarisation transfer to benzothiazole using **IMes(c)** and method 2 with a PTF of 0 G and -60 G.

As transfer was so significant, polarisation transfer to  $^{13}\text{C}$  was also investigated. At standard concentration, it was possible to obtain a completed  $^{13}\text{C}$  spectra after 8 scans, hyperpolarised with a PTF of -60 G.

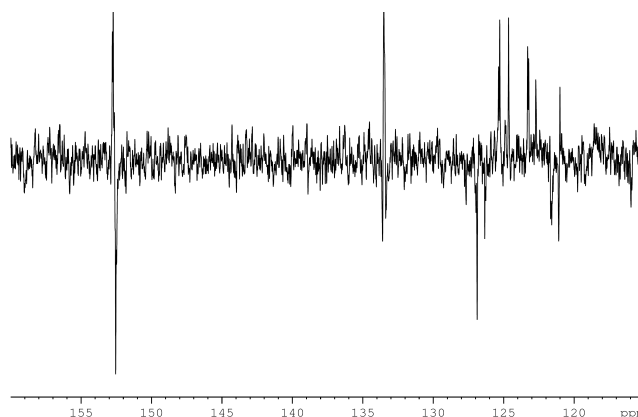


Figure 6.25  $^{13}\text{C}$  spectra of benzothiazole after 8 scans hyperpolarised with a PTF of -60 G.

Investigations into these thiazole analogues have shown polarisation transfer is achievable to a five membered ring which contains a binding nitrogen and sulfur. Investigations suggest  $[\text{Ir}(\text{IMes})(\text{H})_2(\text{sub})_3]^+$  prefers hard donor ligands, as polarisation transfer to the 5 position should be much more prominent in the 4-substituted-2-aminothiazoles if binding through the sulfur was dominant. It is observed, however, that unlike pyridine analogues, weak polarisation is observed with the presence of a substituent adjacent to the binding nitrogen. It is thought the reduced steric hindrance of the 5-membered thiazole compared to the 6-membered pyridine have allowed this transfer.

### 6.3.3 Polarisation of commercial drugs

A series of commercial drug molecules, discussed in the introduction of this chapter, were also investigated. This was completed to gain an idea of the real life potential of the application of SABRE to the pharmaceutical industry.

The polarisation of albendazole, anastrozole, bicalutamide, esomeprazole, gefitinib and mebendazole (shown in Figure 6.5) was investigated using method 1 and **IMes(a)**. Albendazole and mebendazole were found to be insoluble in methanol, and a screen of other solvents revealed they were also insoluble in ethanol, water, acetone, dimethylsulphoxide (DMSO), chloroform and dichloromethane (DCM) at standard concentration. They were consequently not investigated any further. Gefitinib was found to have limited solubility in methanol and so at standard concentration, not all the substrate was in solution. This substrate was therefore investigated in chloroform in which solubility was much better, although an increase in temperature to 40 °C was

required for all the substrate to dissolve. Use of the SABRE technique on this sample resulted in the observation of a small level of polarisation transfer into the substrate however this did not result in enhancement of the signals within the  $^1\text{H}$  NMR spectrum. Esomeprazole exhibited no polarisation transfer when interrogated with a standard  $^1\text{H}$  NMR sequence, however utilisation of the  $^1\text{H}$  OPSYdq sequence revealed a small level of polarisation transfer into the substrate. Esomeprazole was therefore investigated using **IMes(c)** which resulted in an increase in polarisation transfer observed within the  $^1\text{H}$  OPSYdq sequence but no evidence of polarisation transfer was observed within the standard  $^1\text{H}$  sequence.

Neither of the final two commercial drugs investigated, bicalutamide and anastrozole, showed evidence of polarisation transfer. In the case of anastrozole, significant antiphase hydrides were observed in the standard hyperpolarised  $^1\text{H}$  NMR spectrum which also show large signals within the  $^1\text{H}$  OPSYdq spectrum. This suggests the metal catalyst creates a very stable complex when bound to anastrozole.

This work has indicated some potential future complications. Many of these drugs showed solubility issues but also, many drugs have more than one binding site, which may cause stable complexes or dimers.

## **6.4 Effect of polarisation transfer efficiency in complex mixtures**

### 6.4.1 Effect of polarisation transfer efficiency to competing substrates

One of the long term goals for this technique is to use it for the identification of small amounts of contaminant such as potentially genotoxic impurities in a pharmaceutical mixture. It is therefore important to understand the behaviour of the system when more than one substrate is present.

	Catalyst	Substrate 1	Substrate 2	Overall sub. Conc.
	Conc. (mM)	Conc. (mM)	Conc. (mM)	
1	5	100		100
2	5		100	100
3	5	100	100	200
4	5	50		50
5	5		50	50
6	5	50	50	100

Table 6.12 Outlining the concentrations of catalyst and substrate for each sample in 0.6 ml *d*<sub>4</sub>-methanol for a standard competition study between two substrates.

This was designed such that the two substrates are tested as the sole substrate at standard concentration and then investigated in competition with each other. The various combinations on concentrations were completed to create groups of where either the concentration of each substrate was kept constant, or the ratio of catalyst concentration to overall substrate concentration was kept constant.

During these experiments, the two substrates had to be chosen carefully. Most importantly, the spectra of each substrate within the competition study had to be fully base line resolved from each other meaning the observed polarisation can be easily assigned to the correct substrate. The catalyst required for particular substrates must also be considered, for instance, to investigate sterics with a larger substrate such as quinoline, **IMes(a)** would not be suitable and **IMes(b)** or **IMes(c)** would be required. All competition studies were completed using method 1.

#### 6.4.1.1 Competition between pyridine and 2-aminothiazole

The first competition study to be investigated was between pyridine and 2-aminothiazole (Figure 6.26). This is because the proton spectra of both substrates are baseline resolved from each other and both polarise when the catalyst **IMes(a)** is used.

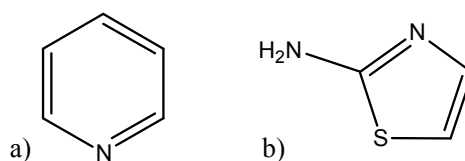


Figure 6.26 Structures of a) pyridine and b) 2-aminothiazole.

The samples were prepared according to Table 6.12.

No.	Pyridine (mM)	Thiazole (mM)	Overall sub. conc. (mM)	Observed <sup>1</sup> H NMR signal enhancement				
				<i>Ortho</i>	<i>Meta</i>	<i>Para</i>	T4	T5
1		100	100				-10.6	-14.5
2	100		100	-69.8	86.5	-121.8		
3	100	100	200	-50.0	41.2	-57.1	-2.5	-3.9
4		50	50				-10.2	-15.7
5	50		50	-198.2	174.6	-199.6		
6	50	50	100	-114.4	85.0	-119.2	-5.9	-10.4

Table 6.13 Observed <sup>1</sup>H NMR signal enhancement for the competition study between pyridine (*ortho*, *meta* and *para*) and 2-aminothiazole (T4 and T5) using **IMes(a)**.

It can be seen that adding a second substrate has a great effect on the polarisation transfer to both substrates (Table 6.13). Comparing samples 1, 2 and 3, it is possible to see that the combination of the two substrates reduces the polarisation transfer to both substrates, although the enhancement observed 2-aminothiazole is reduced by a greater per cent than for pyridine. This trend is continued for samples 4, 5 and 6, where enhancement is less for both substrates after combination of the two substrates.

When comparing the samples where the overall substrate concentration is the same for all three samples, a different trend is observed. The polarisation transferred to 2-aminothiazole (samples 1 and 6) drops after combination of the two substrates, but the polarisation transferred to pyridine (samples 2 and 6) appears to increase. It is also possible to draw a conclusion on the comparison of samples 1 with 4, 2 with 5, and 3 with 6. This gives the general trend that reducing the concentration increases polarisation transfer.

While it is clear from this experiment that both substrates polarise when in the presence of each other, it is difficult to understand which substrate is preferred, if one is preferred at all. This could be explained by looking at the polarisation transfer to each substrate individually. When these substrates are tested without a competitor, the observed polarisation transfer is greatly different between pyridine and 2-aminothiazole (comparing samples 1 and 2 and samples 4 and 5, Table 6.13). To overcome this hurdle, the experiment was repeated with two substrates that exhibit similar levels of polarisation transfer to each other before competition.

## 6.4.1.2 Competition between 2-aminothiazole and quinoline

Looking through all the substrates tested up until this time, 2-aminothiazole and quinoline (Figure 6.27) show the most similar levels of polarisation transfer (an average enhancement factor of around 30 for both, see section 6.3.2.1, pg 287, for 2-aminothiazole and Chapter 4 for quinoline). The signals for each substrate are base line resolved from each other however **IMes(c)** is required to polarise quinoline. Consequently, to keep consistency, **IMes(c)** was used for all six samples.

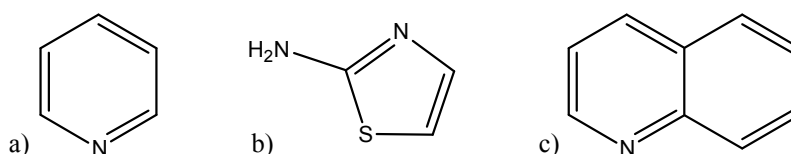


Figure 6.27 Structures of a) pyridine, b) 2-aminothiazole and c) quinoline.

No.	Thia (mM)	Quin (mM)	Overall sub. conc. (mM)	Observed <sup>1</sup> H NMR signal enhancement								
				T4	T5	Q2	Q3	Q4	Q5	Q6	Q7	Q8
1	100		100	-1	-2	-	-	-	-	-	-	-
2		100	100	-	-	-26	44	-32	-49	66	14	-56
3	100	100	200	-0.2	-0.3	-1	-2	-1	1	-2	1	1

Table 6.14 Results from the competition study between 2-aminothiazole (Thia, T4 and T5) and quinoline (Quin, Q2, Q3, Q4, Q5, Q6 and Q7).

The use of **IMes(c)** to polarise 2-aminothiazole appears to promote a side reaction, which is not understood. As 2-aminothiazole polarises with **IMes(a)** giving an average enhancement of 30 fold, the observed side reaction must be a result of the additional acetonitrile resulting in a significant reduction in polarisation transfer. Due to this complication leading to a drop in observed polarisation transfer, the second half of the experiment was not completed.

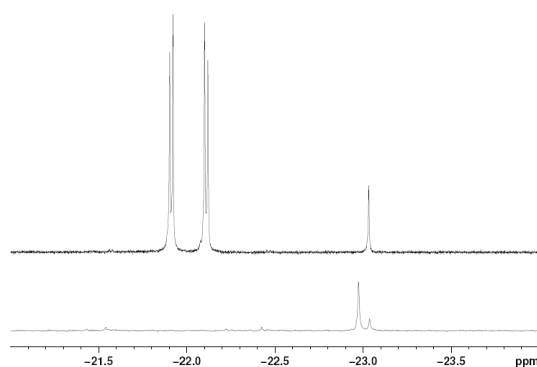


Figure 6.28 The hydride region of the reaction of hydrogen with 2-aminothiazole with **IMes(a)** (bottom) or **IMes(c)** (top).

The hydride region (Figure 6.28) shows a different profile to that expected. This may suggest that a significant amount of acetonitrile is binding to the catalyst, perhaps pushing the 2-aminothiazole into the *trans* position, therefore hindering polarisation transfer to that substrate. If this was the case, the polarisation would be expected to transfer into the acetonitrile however, while some polarisation is observed, a large amount appears to remain on the ‘new’ hydrides (Figure 6.29).

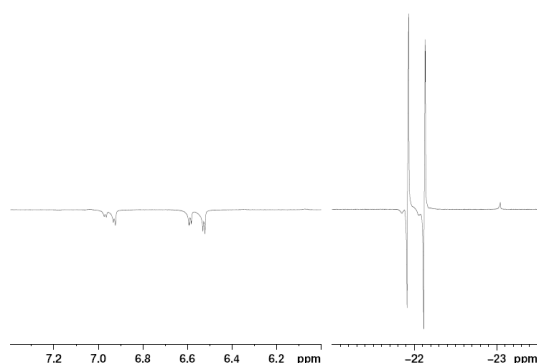


Figure 6.29 The  $^1\text{H}$  NMR spectrum of 2-aminothiazole hyperpolarised with **IMes(c)** using method 1, with 2-aminothiazole and hydride regions depicted.

When quinoline is also added to the system so the two substrates are in competition, as for sample 3 (Table 6.14), polarisation transfer is not observed in quinoline either. It can be observed that the hydride region for 2-aminothiazole in the presence of **IMes(c)** looks the same with or without the presence of quinoline (Figure 6.30). This suggests that the complex created by the addition of acetonitrile is too strong to allow the binding of quinoline.

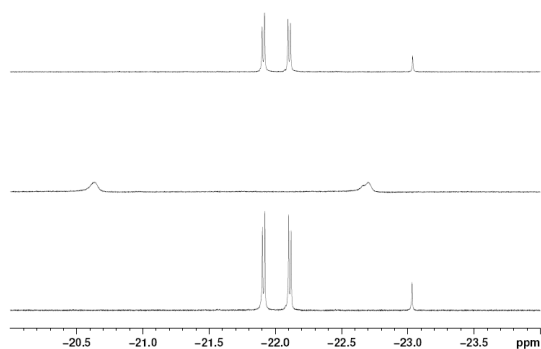


Figure 6.30 The hydride region observed for the following, bottom to top; sample 1 (2-aminothiazole and **IMes(c)**), sample 2 (quinoline and **IMes(c)**) and sample 3 (quinoline, 2-aminothiazole and **IMes(c)**) from Table 6.14.

To understand the reason behind this, a new experiment was completed. Here, 2-aminothiazole was polarised with **IMes(a)** to result in the expected level of polarisation transfer to this substrate. Acetonitrile was then added to the sample and it was then interrogated again. This resulted in a significant reduction in polarisation transfer to 2-aminothiazole, suggesting the addition of acetonitrile to this substrate is problematic.

This competition study between 2-aminothiazole and quinoline has shown that adverse reactions can occur through combination of some substrates resulting in significant reduction in observed polarisation transfer.

#### 6.4.1.3 Competition between 4-methylpyridine and 4-phenylpyridine

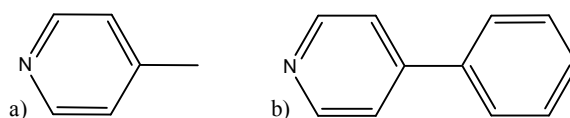


Figure 6.31 Structures of a) 4-methylpyridine and b) 4-phenylpyridine.

Due to the complications of mixing 2-aminothiazole with acetonitrile (see section 6.4.1.2, pg 298), it became necessary to investigate substrates where **IMes(b)** or **IMes(c)** are not required. This has the added advantage of removing further complications through addition of a third viable substrate. A much simpler comparison was made between 4-methylpyridine and 4-phenylpyridine. Both are base line resolved from each other and polarise with **IMes(a)**. The observed polarisation transfer is also similar for the pyridine ring in both cases.



	Substrate conc. (mM)			Observed <sup>1</sup> H NMR signal enhancement						
	Substituent		Total	4-methylpyridine			4-phenylpyridine			
	Me	Ph		<i>ortho</i>	<i>meta</i>	methyl	<i>o</i> -py	<i>m</i> -py	<i>o</i> -ph	<i>m+p</i> -ph
1	100	-	100	-25	31	14	-	-	-	-
2	-	100	100	-	-	-	-38	20	0	1
3	100	100	200	-19	4	2	-22	11	0	1
4	50	-	50	-60	55	18	-	-	-	-
5	-	50	50	-	-	-	-105	54	-6	4
6	50	50	100	-87	24	6	-86	49	0	3

Table 6.15 Results from the competition study between 4-methylpyridine (*ortho*, *meta* and methyl) and 4-phenylpyridine (*o*-py and *m*-py of the pyridyl ring, and *o*-ph and *m+p*-ph of the phenyl ring).

This experiment has led to some interesting results. Comparing samples 1, 2 and 3 (Table 6.15), it is possible to see that combination of both substrates has reduced the observed polarisation on each substrate despite experiencing similar polarisation levels without a competitor. Comparing samples 4, 5 and 6, a similar result can be observed, with a drop in polarisation in most signals for both substrates when they are in competition with each other. This observation excludes the *ortho* position of 4-methylpyridine, however in this instance, the drop in calculated enhancement arises from the antiphase nature of the signal when 4-methylpyridine is polarised without a competitor. Antiphase ( $I_zS_z$ -type) signals are observed for 4-methylpyridine at both investigated concentrations but it is not present when 4-methylpyridine is polarised in competition with 4-phenylpyridine.

In contrast to the first competition study between pyridine and 2-aminothiazole (see section 6.4.1.1, pg 296), a different trend is observed when comparing samples 1, 2 and 6 (Table 6.15), keeping the concentration of overall substrate constant. All positions of 4-phenylpyridine have increased in observed polarisation transfer. While the *ortho* position of 4-methylpyridine has also greatly increased in observed polarisation transfer, this could be due to a low calculated enhancement for sample 1 (due to the antiphase presentation of the signal). The observed enhancement of the other two signals within 4-methylpyridine dropped. This might suggest that in this situation, it is preferential to transfer polarisation to 4-phenylpyridine. This is an unexpected result as 4-phenylpyridine is the larger substrate and consequently, sterics would suggest 4-methylpyridine would bind preferentially. As greater polarisation is observed on 4-phenylpyridine, it is thought an interaction exists between the phenyl ring and

mesitylene rings on the 'IMes' group. It is also possible that by chance, the addition of these two substrates together had led to a more optimal exchange rate for 4-phenylpyridine.

It can also be observed by comparing samples 1 with 4, 2 with 5 and 3 with 6 (Table 6.15) that lowering the concentration of substrate by 2 fold has again significantly increased the observed polarisation transfer in all cases investigated in this study.

#### 6.4.2 Utilisation of the $^1\text{H}$ OPSYdq NMR sequence

As outlined in the introduction, the overall aim of this project is to develop the SABRE technique such that it can be utilised for characterisation in a pharmaceutical setting or for the detection of small amounts of genotoxic impurities. In such cases, the samples used may be a part of a complex mixture and so the ability to separate out a single set of resonances may prove useful. The OPSY sequence has the ability to probe nuclear spins which are scalar coupled to *parahydrogen*-derived nuclei or have at some point been scalar coupled to them at a metal centre and subsequently dissociated from that metal complex. This therefore means only those resonances which are polarised by *parahydrogen* are detectable.

To begin an investigation into this, a sample of **IMes(a)** and pyridine in methanol was prepared with a series of other substrates whose chemical shifts are in a similar vicinity to the shifts of pyridine, but will not become hyperpolarised. In this case, toluene, 1-methylindole, 2-amino-4-(4-chlorophenyl) thiazole and 8-methylquinoline were added. Under normal thermal conditions, this leaves a complicated spectrum (Figure 6.32, bottom).

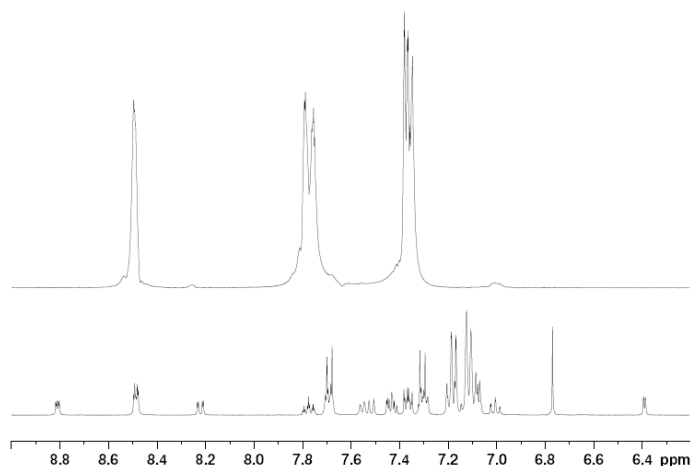


Figure 6.32 The  $^1\text{H}$  NMR spectra of a mixture of compounds with (bottom) the thermal  $^1\text{H}$  NMR spectrum and (top) the  $^1\text{H}$  OPSYdq NMR spectrum hyperpolarised with **IMes(a)** by method 1.

It can be seen in Figure 6.32 that the OPSYdq sequence has filtered out the peaks of the interferents showing clearly the position of the pyridine signals. In this particular case, the pyridine signals can be picked out by a simple hyperpolarised  $^1\text{H}$  NMR spectrum as the substrate and interferents are of approximately the same concentration. However, if the compound to be hyperpolarised is a contaminant in very low concentration, such as a genotoxic impurity, this method may enable its observation.

This experiment also included the removal of solvent peaks, such that hyperpolarised experiments could be completed in protonated solvents. An experiment was completed where the catalyst and pyridine were dissolved in 90 % protonated methanol and 10 % deuterated methanol (required to gain a lock on the spectrometer).

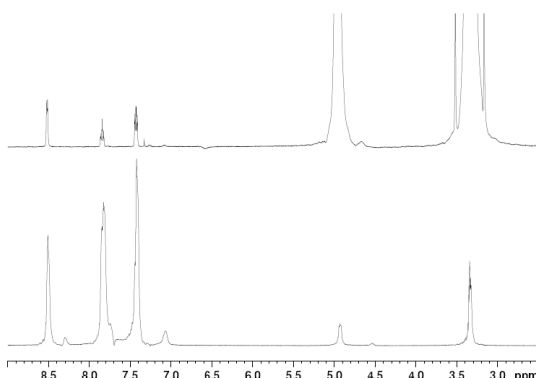


Figure 6.33  $^1\text{H}$  NMR spectra of pyridine completed in 90 % protonated methanol. Top, thermal  $^1\text{H}$  NMR spectrum and, bottom,  $^1\text{H}$  OPSYdq NMR spectrum.

Comparing single scan thermal  $^1\text{H}$  NMR spectrum and single scan hyperpolarised  $^1\text{H}$  OPSYdq NMR spectrum, the effect has been to increase the intensity of the pyridine signals by between 5 and 18 times, and reduce the intensity of the methanol signals by 111 times (calculated by integration). This has provided a method of significantly reducing solvent signals without a solvent suppression sequence, and has been achieved by using only one scan.

### 6.5 Reaction of 4-carboxaldehydepiperidine with methanol

During a literature search, a study by Plater *et al.*<sup>204</sup> was found which reported a spontaneous reaction of an aldehyde with methanol (Figure 6.36). The group were aiming to crystallise the quinoline analogue with a bound aldehyde (Figure 6.34a) in methanol, but the crystal structure returned to show the solvent methanol had spontaneously reacted with the compound to produce the quinoline analogue with a bound hemiacetal (Figure 6.34b).

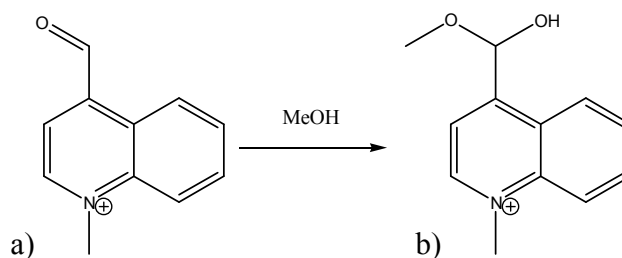


Figure 6.34 Spontaneous reaction reported in a publication by Plater *et al.*<sup>204</sup>

It was also observed that a reaction of this type could be furthered by the addition of a strong acid. During a literature search to understand the spontaneous reaction described above, it was observed that the addition of a suitable acid, such as triflic acid (TfOH,  $pK_a = -15$ ),<sup>205</sup> sulphuric acid ( $pK_a = -9$ ),<sup>206</sup> hydrochloric acid ( $pK_a = -7$ ),<sup>207</sup> or *p*-toluene sulphonic acid ( $pK_a = -2.8$ ),<sup>208</sup> can force a further reaction with a second equivalent of alcohol to a new acetal product.

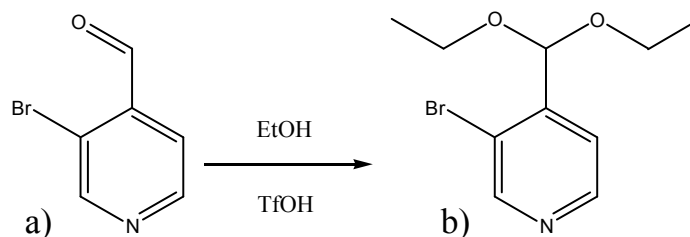


Figure 6.35 Reaction reported in a publication by de la Fuente and Dominguez.<sup>205</sup>

In the 2009 paper<sup>205</sup>, a method to produce azepine rings by reductive cyclisation used the step outlined in Figure 6.35 as a protection step. The production of an acetal was also employed by Chavarot *et al.* (1997)<sup>209</sup> in the synthesis of an adenine-pyridinaldoxime-acridine conjugate. Here, the reaction is not acid catalysed but proceeds by reaction with trimethylsilyl chloride (TMSCl) and methanol.

It was therefore decided to investigate the potential for SABRE to investigate these reactions with reference to 4-carboxaldehydepipridine.

#### 6.5.1 The spontaneous reaction of 4-carboxaldehydepipridine with methanol

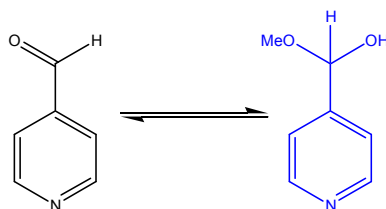


Figure 6.36 Spontaneous reaction of 4-carboxaldehydepipridine in the presence of methanol.

The reaction of 4-carboxaldehydepipridine with methanol was investigated, shown in Figure 6.36. First, the expected chemical shifts associated with 4-carboxaldehydepipridine were recorded (Figure 6.37).

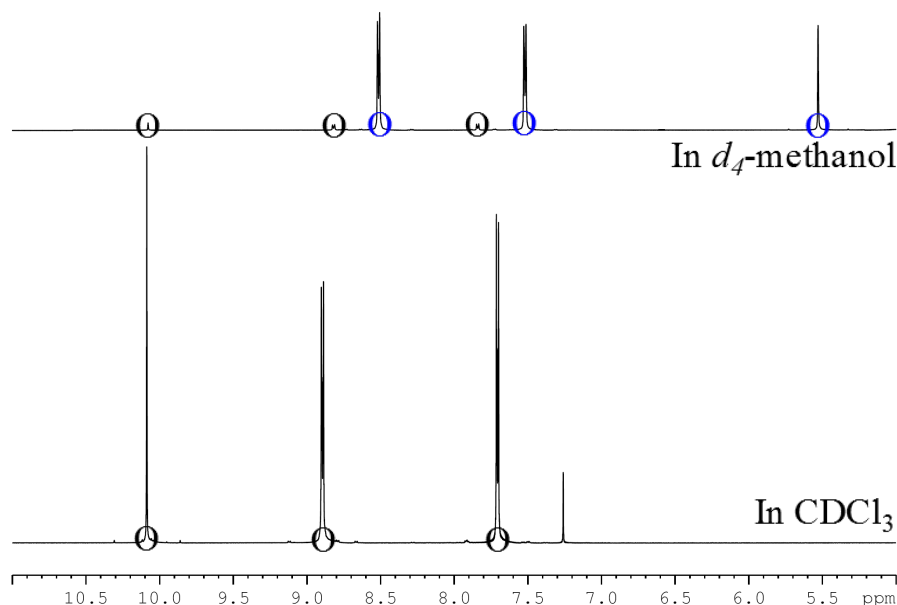


Figure 6.37 Thermal  $^1\text{H}$  NMR spectra of 4-carboxaldehydepiperidine in  $d_4$ -methanol and  $\text{CDCl}_3$ , where black circles correspond to 4-carboxaldehydepiperidine, and blue circles correspond to the hemiacetal product.

When 4-carboxaldehydepiperidine is dissolved in chloroform, three resonances are observed, corresponding to the three proton environments in the substrate. If the solvent is changed to methanol, it is clear to see the signals corresponding to 4-carboxaldehydepiperidine are not dominant (circled in black). Instead, three signals corresponding to a new product are present. These have similar multiplicity and 2:2:1 intensity however, they correspond to the hemiacetal product (circled in blue). The signals corresponding to the hemiacetal product are 18 times more intense than those for 4-carboxaldehydepiperidine based on the integral of the aldehyde/hemiacetal proton. This is because methanol is in a large excess as it is the solvent.

To understand this reaction further, a sample of 4-carboxaldehydepiperidine dissolved in chloroform- $d_1$  was prepared, and protonated methanol added to the solution. When the reaction is completed in  $d_4$ -methanol, the protons associated with the methoxy group and hydroxyl group are NMR invisible due to deuteration. Establishing the same equilibrium as observed previously, but reacting with protonated methanol allows the observation of all protons on the hemiacetal product, rather than just the pyridyl and hemiacetal protons. Completing the reaction in chloroform- $d_1$  means all observed hemiacetal product has been produced with protonated methanol.

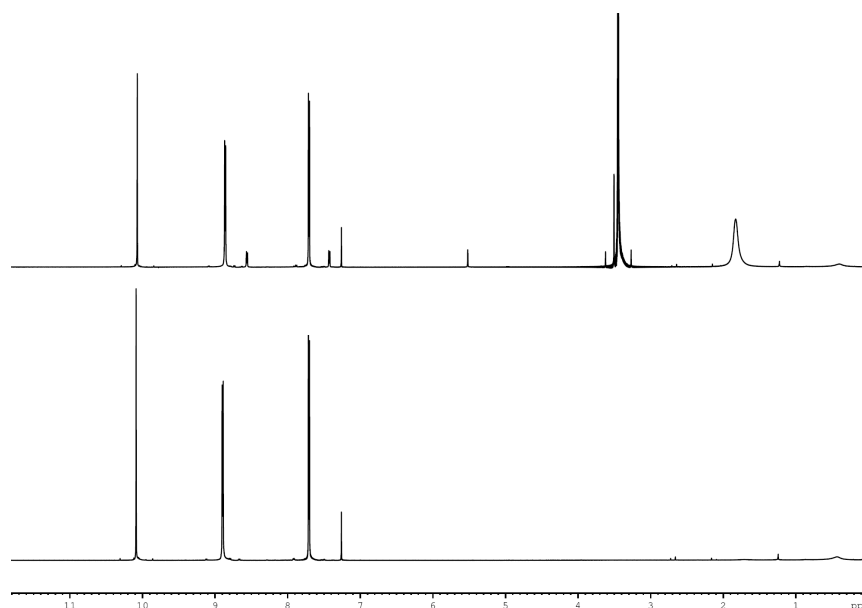


Figure 6.38  $^1\text{H}$  NMR spectra in chloroform of bottom, 4-carboxaldehyde-pyridine and top, 4-carboxaldehyde-pyridine and protonated methanol.

It is possible to observe that upon addition of protonated methanol to 4-carboxaldehyde-pyridine in chloroform- $d_1$ , the hemiacetal product is formed but now the signals corresponding to the hemiacetal product are 9 times smaller than those for 4-carboxaldehyde-pyridine. The proportion of the product can be increased by increasing the amount of protonated methanol. This has also allowed the opportunity to observe the signal corresponding to the previously unobservable methoxy group of the hemiacetal product. It is therefore possible to characterise both 4-carboxaldehyde-pyridine and the hemiacetal product (see Experimental).

An investigation was then completed to understand if the reaction was reversible through the use of  $^1\text{H}$  EXSY NMR spectra (Figure 6.39). To complete these experiments, protonated methanol was added until the proportion of 4-carboxaldehyde-pyridine to hemiacetal product was approximately 1:1. This was completed to ensure all potential nOe correlations are observed, and are not missed due to low concentration of one of the investigated products.

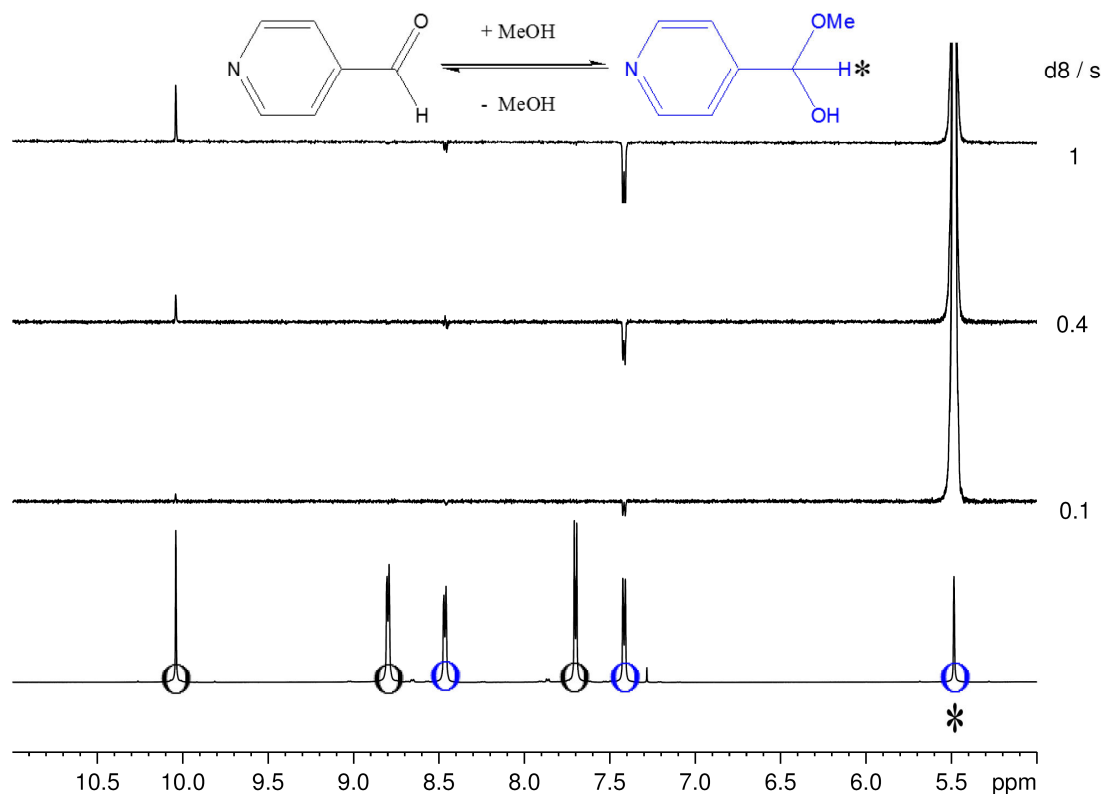


Figure 6.39 Thermal  $^1\text{H}$  NMR spectrum (bottom) of 4-carboxaldehydepyridine dissolved in chloroform- $d_1$  with an addition of methanol and  $^1\text{H}$  EXSY spectra of the same sample with various mixing times (d8) where the 4-(CH(OMe)(OH))py of the hemiacetal is excited (top three). The \* symbol denotes the excited resonance.

The  $^1\text{H}$  EXSY experiments allowed us to confirm a reversible exchange was taking place. In Figure 6.39, after excitation of the hemiacetal proton, 4-(CH(OMe)(OH))py, nOe interactions (inverted signals) are observed to the pyridyl ring of the hemiacetal, but also exchange interactions to the CH(O) of 4-carboxaldehydepyridine. This is supported by the fact that the intensity of the exchange peak increases as the mixing time is increased. To confirm it is an exchange process, EXSY experiments are also completed where the CH(O) of 4-carboxaldehydepyridine is excited, shown in Figure 6.40.



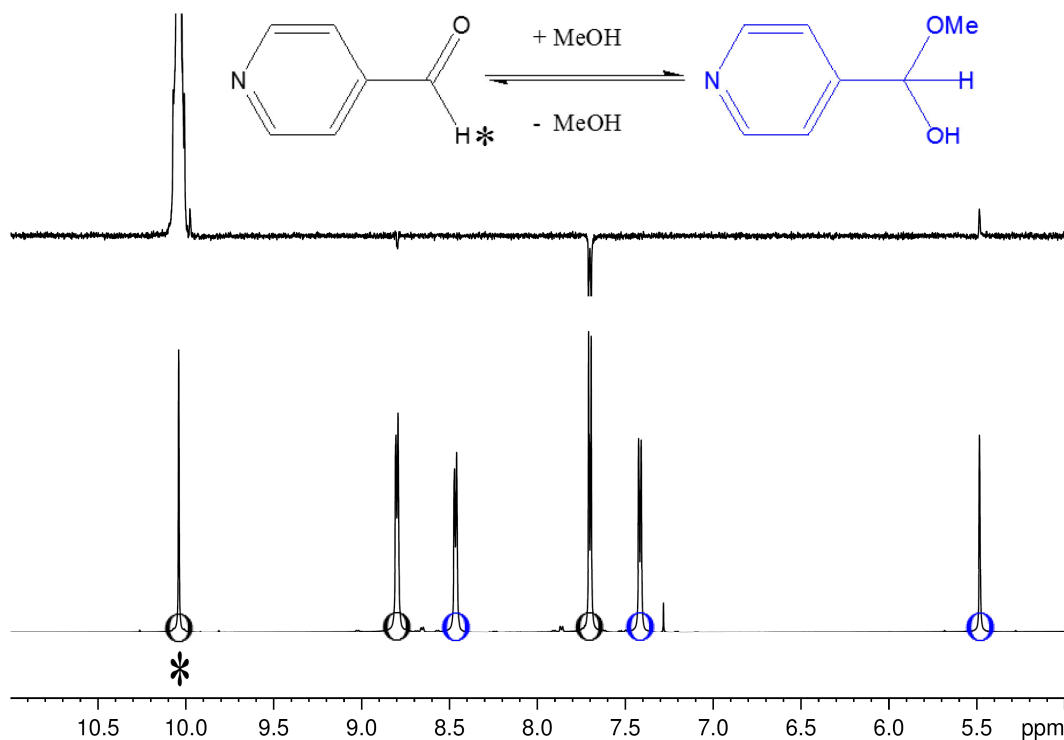


Figure 6.40 Thermal  $^1\text{H}$  NMR spectrum (bottom) of 4-carboxaldehydepyridine dissolved in chloroform- $d_1$  with an addition of methanol and  $^1\text{H}$  NOESY spectrum of the same sample where the 4-( $\text{CH}(\text{O})$ )py of 4-carboxaldehydepyridine is excited (top). The \* symbol denotes the excited resonance.

NOe excitation of the  $\text{CH}(\text{O})$  proton of 4-carboxaldehydepyridine (Figure 6.40) yields NOe interactions into the pyridyl protons of 4-carboxaldehydepyridine and also exchange into the hemiacetal. An exchange is observed in both directions, this confirms the reaction is reversible.

A variable temperature study was completed in which the percentage of each compound involved in the reversible reaction was monitored as a function of temperature (Table 6.16).

T / K	Aldehyde (% , black)	Hemiacetal (% , blue)
298	74	26
308	83	17
318	87	13
308	84	16
298	80	20

Table 6.16 Percentage of each compound involved in the reversible reaction of 4-carboxyaldehydepyridine with methanol as a function of temperature. The calculations are based on the integrals of the  $\text{CH}(\text{O})$  of 4-carboxyaldehydepyridine and  $\text{CH}(\text{OMe})(\text{OH})$  of the corresponding hemiacetal.

It was observed that an increase in temperature led to an increase in 4-carboxaldehydepuridine. This is expected as entropy drives the reaction towards 4-carboxaldehydepuridine (two molecules compared to one), and consequently, an increase in temperature leads to an increase of 4-carboxaldehydepuridine.

4-carboxaldehydepuridine was also shown to react in a similarly spontaneous manner with ethanol, Figure 6.41.

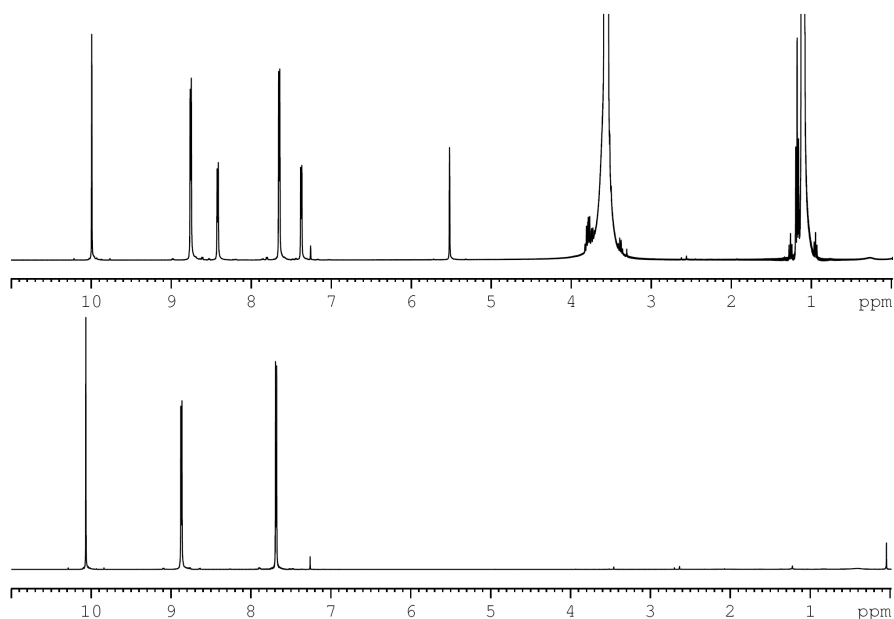


Figure 6.41  $^1\text{H}$  NMR spectra in chloroform of bottom, 4-carboxaldehydepuridine and top, 4-carboxaldehydepuridine and protonated ethanol.

### 6.5.2 Monitoring the spontaneous reaction of 4-carboxaldehydepuridine with methanol using SABRE

Polarisation transfer to both 4-carboxaldehydepuridine and the hemiacetal product were initially investigated in  $d_4$ -methanol.

	Observed $^1\text{H}$ NMR signal enhancement			
	<i>ortho</i>	<i>meta</i>	C(O)H	C(OCH <sub>3</sub> )(OH)H
Aldehyde	-200	35	-94	-
Hemiacetal	-179	118	-	16

Table 6.17 Observed  $^1\text{H}$  polarisation transfer to 4-carboxaldehydepuridine (aldehyde) and the hemiacetal product (hemiacetal) found in a sample of 4-carboxaldehydepuridine dissolved in  $d_4$ -methanol in the presence of **IMes(a)**.

Due to the large excess of methanol, the hemiacetal product is dominant over 4-carboxaldehydepiperidine, and consequently the concentrations of each substrate are different to each other. It can however be observed that significant polarisation transfer is present in both substrates. When  $d_4$ -methanol is used as a solvent, the additional resonances corresponding to the  $-OH$  and  $-OMe$  groups are deuterated because they originate from the deuterated solvent. They are therefore not observable by  $^1H$  NMR spectroscopy. The experiment was therefore repeated in  $d_1$ -chloroform where 4-carboxaldehydepiperidine is reacted with protio-methanol.

Solvent	Observed $^1H$ NMR signal enhancement						
	4-carboxaldehydepiperidine			Hemiacetal product			
	<i>ortho</i>	<i>meta</i>	C(O)H	<i>ortho</i>	<i>meta</i>	C(OCH <sub>3</sub> )(OH)H	-OCH <sub>3</sub>
Chloroform	-198	-127	-106	-	-	-	-
Chloroform and methanol	-176	-10	-47	-41	2	-0.3	1.8

Table 6.18 Observed  $^1H$  polarisation transfer to 4-carboxaldehydepiperidine (aldehyde) and the hemiacetal product (hemiacetal) found in a sample of 4-carboxaldehydepiperidine dissolved in  $d_1$ -chloroform in the presence of **IMes(a)**, with and without the presence of protonated methanol.

It was important to first investigate polarisation transfer to 4-carboxaldehydepiperidine in chloroform without the presence of methanol. This proves that direct polarisation transfer is possible to 4-carboxaldehydepiperidine, and the previously observed enhancement is not a result of transfer to the hemiacetal product, which then converts into the aldehyde. In  $d_1$ -chloroform (see Table 6.18), it is possible to observe that the polarisation transfer to the *ortho* and C(O)H protons of 4-carboxaldehydepiperidine exhibit similar levels of enhancement to those found in methanol (see Table 6.17), however the enhancement observed to the *meta* position is much higher in chloroform than methanol. The addition of 0.02 ml protonated methanol to the sample resulted in the spontaneous production of the hemiacetal in the ratio 1:0.4 4-carboxaldehydepiperidine to hemiacetal. It is possible to observe polarisation transfer to the hemiacetal in  $d_1$ -chloroform also, although the observed enhancement is less than that observed in methanol. It is however now possible to observe transfer to the  $-OMe$  group.

These experiments have shown that it is possible to polarise 4-carboxaldehyde pyridine, and its hemiacetal produced upon reaction with methanol, however the reaction is very fast and therefore cannot be monitored using SABRE.

### 6.5.3 The acid catalysed reaction of 4-carboxaldehyde pyridine with methanol

In the introduction to this section, 4-carboxaldehyde pyridine has also been shown to react with a second equivalent of methanol upon the addition of an acid. Initially, this acid catalysed reaction of 4-carboxaldehyde pyridine with methanol was investigated by using mass spectroscopy. Four samples of 4-carboxaldehyde pyridine dissolved in methanol were prepared. 1 drop of concentrated sulphuric acid was added to two of these, then one neutral and one acidified sample was moved to an oven at 50 °C, while the other two were stored at room temperature. After three days stored at the stated temperature, the samples were analysed by mass spectroscopy (Figure 6.42, Figure 6.43, Figure 6.44 and Figure 6.45).

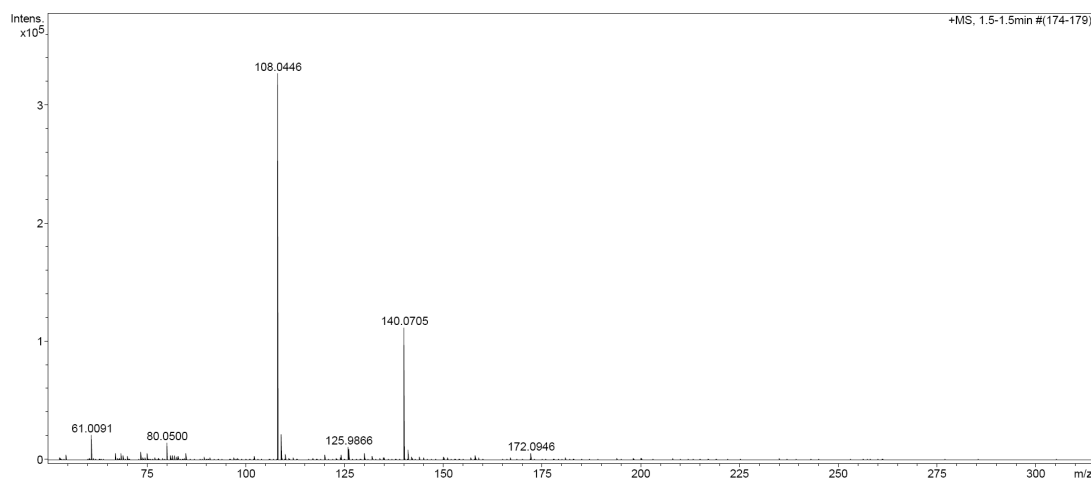


Figure 6.42 ESI mass spectrum of 4-carboxaldehyde pyridine in methanol stored at room temperature without the presence of acid.

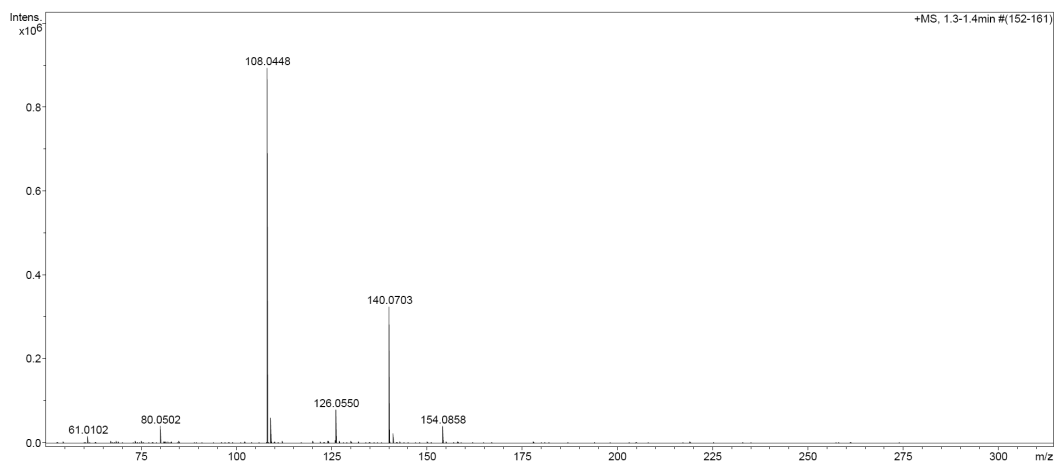


Figure 6.43 ESI mass spectrum of 4-carboxaldehyde-pyridine in methanol stored at room temperature in the presence of acid.

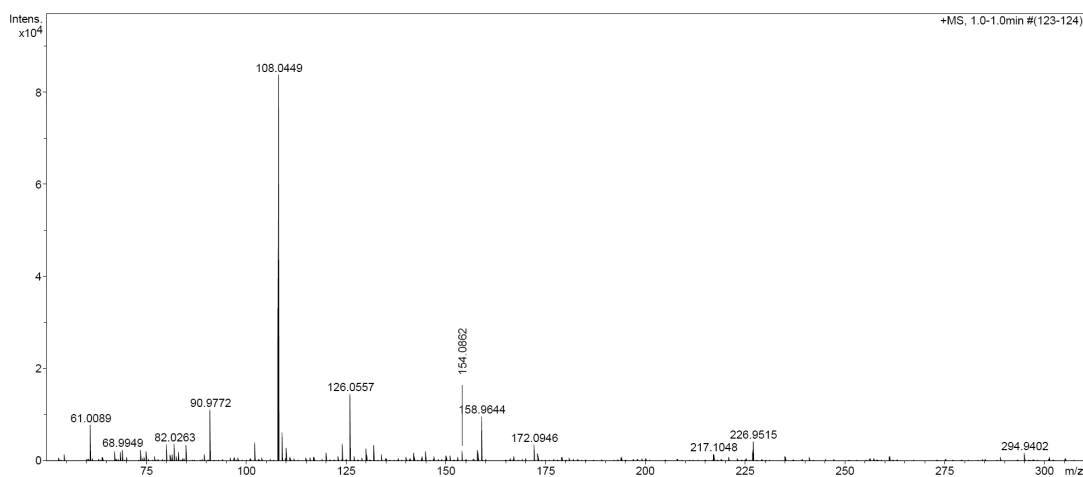


Figure 6.44 ESI mass spectrum of 4-carboxaldehyde-pyridine in methanol stored at 50 °C, without the presence of acid.

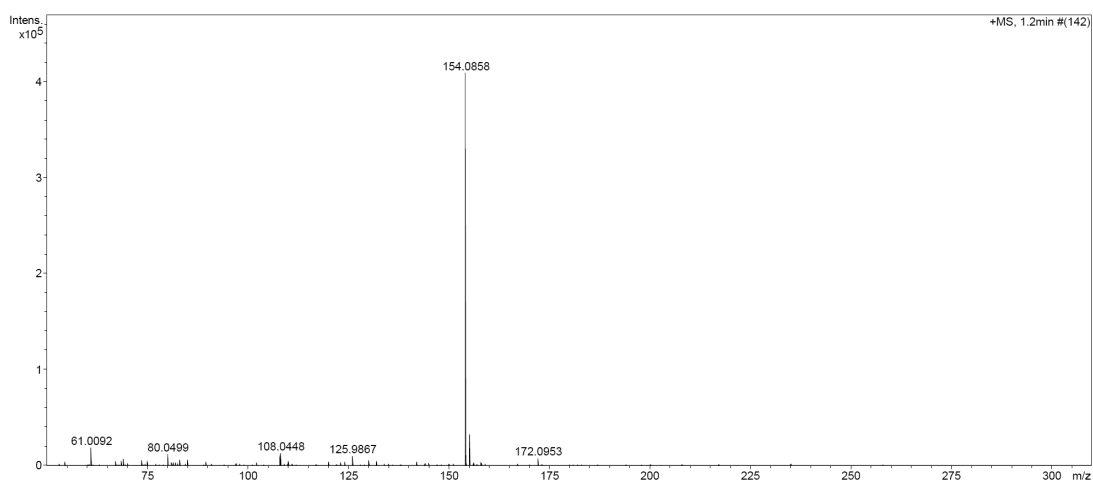


Figure 6.45 ESI mass spectrum of 4-carboxaldehyde-pyridine in methanol stored at 50 °C in the presence of acid.

The significant structures observed in this experiment are detailed in Figure 6.46 and significant results of the experiment are outlined in Table 6.19. Four peaks of significance were observed. The most important of these show a mass-to-charge ratio of 108, 140 and 154 corresponding to 4-carboxaldehyde pyridine (1, 107 g/mol), the hemiacetal product (2, 139 g/mol) and dimethoxyacetal product (3, 154 g/mol) respectively. The mass spectroscopy was completed in a solvent of water and acetonitrile, and this led to an additional product with a mass to charge ratio of 126. This corresponds to a dihydroxyl product (4, 125 g/mol) produced by the same reversible reaction as observed with methanol, but with the solvent water molecules.

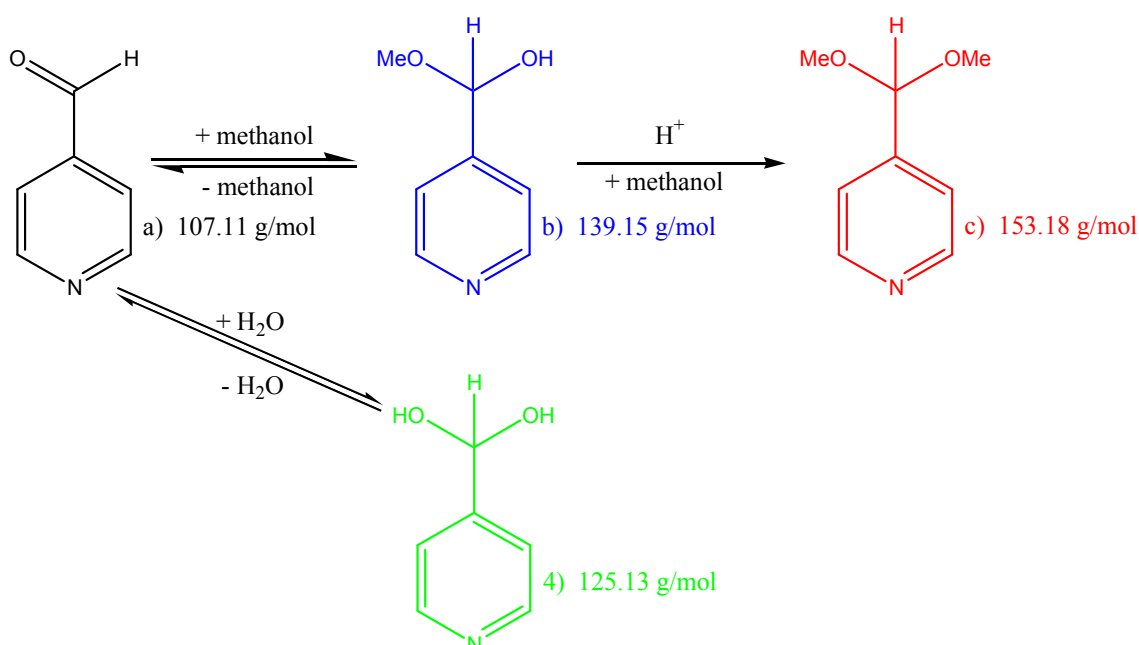


Figure 6.46 Reaction products of 4-carboxaldehyde pyridine observed in mass spectroscopy.

In reference to Figure 6.46		Stored at room temperature	Stored at 50 °C
No added acid	1 (107.1 g/mol)	$3.3 \times 10^5$	$0.8 \times 10^5$
	2 (139.2 g/mol)	$1.1 \times 10^5$	
	3 (153.2 g/mol)		$0.05 \times 10^5$
	Ratio 1 : 2 : 3	10 : 3.3 : 0	10 : 0 : 0.6
With acid	1 (107.1 g/mol)	$9.5 \times 10^5$	$0.1 \times 10^5$
	2 (139.2 g/mol)	$3.5 \times 10^5$	
	3 (153.2 g/mol)	$0.4 \times 10^5$	$4.1 \times 10^5$
	Ratio 1 : 2 : 3	10 : 3.7 : 0.4	10 : 0 : 410

Table 6.19 Collated data from mass spectroscopy study of the reaction products of 4-carboxaldehyde pyridine with methanol. The stated ratios are based on the response factors from the mass spectroscopy.

The room temperature sample with no acid showed the two expected products with no presence of the third. In the sample at room temperature with acid, all three products are observed, although the dimethoxyacetal product (3 in Figure 6.46). This suggests the addition of sulphuric acid catalyses the reaction to produce a dimethoxyacetal product (3). It was previously shown that increasing the temperature pushes the equilibrium from the hemiacetal (2) to 4-carboxaldehyde-pyridine (1), which is further proved in the 50 °C experiments. At this temperature no hemiacetal (2) is present in the mass spectra, suggesting that the dynamic equilibrium which is formed between hemiacetal (2), 4-carboxaldehyde-pyridine (1) and the dimethoxyacetal (3) is not favourable towards the formation of hemiacetal (2). When no acid is present, there is a very small amount of the dimethoxyacetal (3) observed, however the addition of acid at 50 °C has a great effect. The dimethoxyacetal product (3) is now in excess. This has shown that 4-carboxaldehyde-pyridine does undergo a reaction similar to that reported by de la Fuente and Domiguez<sup>205</sup> upon addition of sulphuric acid at 50 °C. It was therefore thought it might be possible to follow the reaction through SABRE.

#### 6.5.4 Monitoring the acid catalysed reaction of 4-carboxaldehyde-pyridine with methanol using SABRE

A sample of 4-carboxaldehyde-pyridine and **IMes(a)** in methanol-*d*<sub>4</sub> was prepared and activated by the addition of hydrogen. Initial experiments with *para*-hydrogen yielded the expected polarisation transfer to 4-carboxaldehyde-pyridine and the hemiacetal product. As the mass spectroscopy suggested an increase in temperature produces a small amount of dimethoxyacetal product (3, Figure 6.46), the sample was stored at 50 °C for 3 days to see if it could be observed. However, this was not successful as the dimethoxyacetal product could not be observed in standard NMR, SABRE or mass spectroscopy. A small amount of concentrated sulphuric acid was added to the sample. This yielded the dimethoxyacetal product (3), as expected however it was not possible to follow this using the SABRE technique as the sulphuric acid caused the catalyst to severely degrade, rendering it unable to act as a polarisation transfer catalyst. This meant a weaker acid may be required, such as nicotinic acid. The carboxylic acid group of nicotinic acid has a  $pK_a$  of 2<sup>106</sup> (and the nitrogen in the pyridyl ring has a  $pK_a$  of 4.82<sup>106</sup>), where sulphuric acid has a  $pK_a$  of -9,<sup>210</sup> and therefore nicotinic acid is much weaker.

In a solution of 4-carboxaldehyde-pyridine and nicotinic acid in methanol, nicotinic acid is not acidic enough to promote the full reaction to the dimethoxyacetal (product 3) however nicotinic acid is able to bind to the SABRE catalysts. It was thought the proximity of both the hemiacetal product and nicotinic acid when bound to the catalyst might be enough to promote the reaction. A sample of **IMes(a)**, nicotinic acid and 4-carboxaldehyde-pyridine in methanol was prepared for interrogation by  $^1\text{H}$  NMR using method 1. The sample was activated and interrogated with the SABRE technique to show polarisation transfer to both substrates however no dimethoxyacetal product was observed. The solution was given time to react ( $\sim 2$  days) and interrogated again, however there was no evidence of the dimethoxyacetal by either NMR or MS.

An acid with a  $\text{p}K_{\text{a}}$  between that of nicotinic acid and sulphuric acid was required. *P*-toluene sulphonic acid was therefore investigated, which has a  $\text{p}K_{\text{a}}$  of -2.8.<sup>211</sup> A sample of 4-carboxaldehyde-pyridine with stoichiometric amount of *p*-toluene sulphonic acid in the presence of **IMes(a)** was prepared and interrogated by SABRE. Before the control experiments for this sample were completed, the reaction to the dimethoxyacetal had already gone to near completion. This sample was interrogated using method 1, however only very weak polarisation transfer is observed using the  $^1\text{H}$  OPSYdq sequence. This is not observable in the  $^1\text{H}$  spectra, however roughly equal signal intensity is observed in both the dimethoxyacetal product and *p*-toluene sulphonic acid in the  $^1\text{H}$  OPSYdq spectrum. The sample was stored at 50 °C overnight to see if the weak polarisation transfer was a result of there not being enough active catalyst present in the sample. Weak polarisation transfer was observed in both the  $^1\text{H}$  and  $^1\text{H}$  OPSYdq spectra, however this did not lead to an enhancement in the  $^1\text{H}$  spectra. The transfer to the dimethoxyacetal was much more significant than that to the acid in the OPSYdq spectrum. This suggests heating the sample did have the effect to increase polarisation transfer to the dimethoxyacetal product however this had not led to an enhancement. A small amount of acetonitrile was added to the sample to promote the polarisation transfer to the product. Significant polarisation transfer was observed to acetonitrile however this again did not have the effect to increase polarisation transfer to the dimethoxyacetal product.

A potential reason for this unexpectedly low level of polarisation transfer could be a result of the high concentration of the acid, which has been shown to exhibit polarisation transfer and consequently must be binding to the catalyst. The catalyst may



therefore be binding irreversibly to the catalyst, or in a chelating manor, both of which could hinder the potential for the dimethoxyacetal to bind to the catalyst. The experiment was repeated with 90 % less *p*-toluene sulphonic acid. Two samples of 4-carboxaldehydepiperidine in the presence of *p*-toluene sulphonic acid were prepared in methanol and chloroform. A small amount of protonated methanol was also added to the chloroform to produce the hemiacetal product. These samples were interrogated after an hour at room temperature to show no evidence of the dimethoxyacetal product by NMR. The samples were consequently left at room temperature for three days and interrogated again to show no evidence of the dimethoxyacetal product by  $^1\text{H}$  NMR or MS. **IMes(a)** was added to make a standard concentration sample for interrogation by method 1. The sample was hydrogenated and interrogated however, the dimethoxyacetal product was still not observed. Again, the samples were left at room temperature overnight however no evidence for the desired product was observed by NMR or MS.

In summary, 4-carboxaldehydepiperidine has been shown to undergo a spontaneous and acid catalysed reaction with alcohols. The spontaneous reaction with methanol has been monitored using SABRE, however so far, it has not been possible to monitor the acid catalysed reaction using SABRE.

## 6.6 Summary

In this chapter, significant polarisation transfer has been observed into a number of pyridine analogues and other related substrates. Initially investigations were completed to understand the functional group tolerance of SABRE. As a part of this investigation, it was found SABRE was tolerant to hydroxyl, carbonitrile, amino, amide, phenyl, aldehyde, carboxylic acid and chlorine groups, and the presence of sulphur in the ring. This also gave the opportunity to investigate the effect of changing the  $\text{p}K_{\text{a}}$  on the extent of polarisation transfer. As an extension of this investigation, the effect of increasing the steric bulk of the pyridine analogues was also considered, starting from small substituents such as a proton or a methyl group through to bulkier substituents such as a phenyl ring or a benzoyl group. In all cases, a small amount of polarisation transfer is observed into the substituted group. Polarisation transfer was investigated to substrates outside of those based on pyridine, such as indole and thiazole. A series of commercially available drugs, provided by AstraZeneca, have also been investigated.

Another important consideration for the SABRE technique is the idea of competition within a sample, which could be either to observe a single substrate in a complex spectrum, or to understand the effect of polarising two substrates in one sample. The OPSYdq sequence has given the opportunity to successfully filter out and consequently only observe the substrate affected by polarisation transfer from *parahydrogen*. This means experiments can be carried out in protonated solvents, and signals deriving from reaction mixture impurities can be removed. Polarisation transfer to substrates competing for polarisation transfer was also investigated. However, a number of limitations must be considered. Certain combinations of substrates can have adverse effects (such as with 2-aminothiazole and acetonitrile, section 6.4.1.2, pg 298), and not all substrates have the potential to exhibit significant polarisation transfer under the conditions investigated here (such as for indole, section 6.3.1, pg 286).

Some of the most significant results from this chapter are those relating to the reaction of 4-carboxaldehydepiperidine with methanol. A literature search revealed this type of compound could undergo a spontaneous reaction with methanol to create a hemiacetal product, or an acid catalysed reaction with methanol to create a dimethoxyacetal product. Investigations have shown the spontaneous reaction can be observed using SABRE however it is too fast to monitor the transformation. It has also not yet been possible to hyperpolarise the acetal product produced through the addition of a strong acid or to monitor the reaction using SABRE. This is because the required acid degrades the SABRE catalyst.

## 7 Chapter 7 – Conclusions and future work

### 7.1 Conclusions

This thesis has demonstrated recent developments into the application of SABRE within high resolution NMR spectroscopy to characterisation of small molecules. Three catalytic systems were investigated, including **IMes(a)**, **SIMes(a)** and **ICy(a)** and compared to the previously published PCy<sub>3</sub> system. This comparison revealed that the TEP is lower for the carbenes indicating they are stronger donors compared to the phosphine and that the buried volumes for the carbenes are smaller in comparison. This is a result of the geometry of the ligands. Analysis of the rate constants and associated thermodynamic properties for the loss of pyridine and hydride ligands revealed the expected correlations to electron donation and steric bulk in that increasing electron donation increases the enthalpy value and increasing the steric bulk decreases the Gibbs free energy. Despite this, no single property can be infinitely increased or decreased to produce an ever increasing level of polarisation transfer into pyridine. The most significant factor affecting the efficiency of the polarisation transfer catalyst is the contact time, determined by the rate constants for both ligands. Again, there is no clear correlation between the observed rate constants of ligand loss with either the TEP or buried volume of the associated carbene/phosphine. A potential reason for this can be found in the structure of the carbene/phosphine itself. A methyl group in the mesitylene arms of IMes and SIMes are able to produce a CH-activation product, a competing process for the exchange of pyridine and hydride ligands loss, which may increase the observed rate constants. Together, these data suggest the hyperpolarisation efficiency of a potential SABRE catalyst cannot be predicted. The efficiency of a new catalyst must be decided by measurement, and can be optimised by changing the magnetic field and temperature of the polarisation step, and concentration of the sample.

The effect of changing the temperature and magnetic field of the polarisation transfer step has been investigated for all three catalysts investigated. Changing the temperature of the polarisation step effects the extent of transfer observed into a substrate through changing the rate of exchange and therefore the contact time of the active complex. This has been illustrated through determination of the rate constants of the systems considered and is supported by the fact that increasing the temperature of the **ICy(a)**

system (with relatively slow exchange rate constants) but decreasing the temperature of the **SIMes(a)** system (with relatively fast exchange rate constants) has the effect to increase the extent of polarisation transfer into pyridine. Changing the magnetic field of polarisation affects the extent of polarisation transfer through a different process. It has been postulated that the extent of polarisation transfer is based on a fine balance between the difference in chemical shifts of the nuclei of interest and the J-coupling of the system<sup>59</sup> and therefore that the extent of polarisation transfer is dependent on the PTF as this affects the relative chemical shifts of the nuclei. The J-coupling of the system does not change with external field. The observed <sup>1</sup>H NMR signal enhancement for the *para* position increased from 38 fold at a PTF of 0 G to -103 fold at a PTF of -90 G for **SIMes(a)** and from 4 fold at a PTF of 0 G to -9 fold at a PTF of -60 G for **ICy(a)**, where each is quoted for the maximum PTF for the stated catalyst. This demonstrates that the PTF which yields the greatest extent of observed polarisation transfer changes for a single substrate depending on which catalyst is used. The thesis also demonstrates that a specific catalyst will exhibit a different PTF for maximum transfer depending on which substrate is investigated.

The effects of changing the concentration and solvent on the extent of polarisation transfer has been investigated for **IMes(a)** only. It was found that maximum signal enhancements were observed when the concentration of the catalyst and substrate were dropped to 10 % of that used as standard. A possible explanation for this is the significantly increased proportion of *parahydrogen* available to the sample. Using the SABRE method, in a 0.6 ml sample, 0.05  $\mu$ L (1 mM) of pyridine can be detected in a single scan producing S/N ratios of 90, 77 and 33 for the *ortho*, *meta* and *para* resonances of pyridine. This is approximately 0.05 mg of substrate, between 10 and 20 times less than that used for <sup>1</sup>H spectra in standard practice for NMR spectroscopy. Similar results were observed for the polarisation transfer to quinoline using **IMes(c)**.

The role of the solvent also has a significant effect on the extent of polarisation transfer into pyridine and quinoline. In this case, two mechanisms affect the extent of transfer. The relative chemical shifts of any nuclei are related to the solvent and therefore the chemical shift differences of the active complex are different depending on the solvent used. The solvent also has an effect on the exchange rates experienced by the complex due to differing polarities, an effect which is particularly important in charged systems such as those investigated here. The polarisation transfer into pyridine and quinoline

was investigated where methanol, ethanol, DCM, chloroform, DMSO and acetone were the solvents used. For pyridine, maximum signal enhancements were observed in ethanol, with methanol running a close second. For quinoline, significant enhancement is only observed in methanol and ethanol, and not the other solvents.

During investigations of polarisation transfer into quinoline, a new catalytic complex in the form  $[\text{Ir}(\text{carbene})(\text{H})_2(\text{quinoline})_2(\text{NCMe})]^+$  was developed, as it was found the complex in the form  $[\text{Ir}(\text{carbene})(\text{H})_2(\text{quinoline})_3]^+$  did not yield significant polarisation transfer into quinoline. It was found **IMes(c)** yielded the greatest signal enhancement of the three catalysts investigated. Using a  $90^\circ$  pulse on  $^1\text{H}$ , the maximum signal intensity was obtained when a PTF of 50 G is used for the 2 position with **IMes(b)**.

Comparing the thermodynamic data for the **IMes(c)**/quinoline and **IMes(a)**/pyridine systems, the rate constants for the loss of substrate ligand are very similar, as are the Gibbs free energies, despite significantly different enthalpy and entropy values. This could be because quinoline is a bulkier ligand with a lower  $\text{p}K_a$  than pyridine and therefore a weaker Ir-N bond resulting in a lower enthalpy and entropy. The most significant difference is observed in the rate constants for the loss of hydride ligands, where the rate constant is much larger for the **IMes(c)**/quinoline system. This may also explain the lower signal enhancements observed to quinoline when compared to pyridine and is consistent with the effect of temperature on the extent of polarisation transfer.

This thesis has also investigated the application of SABRE to standard NMR pulse sequences. Due to many sequences requiring phase cycling or in the case of 2D spectra, many increments, a new, automated flow system is required.

Considering 1D spectra involving more complex sequences than the  $90^\circ$  pulse acquire sequence have led to the successful acquisition of a  $^1\text{H}$  NOESY NMR spectrum where the sample has a substrate concentration of 10 mM. A significant observation was also made when considering the effect of PTF on the  $^1\text{H}$  OPSYdq spectrum. It was found the maximum signal intensity was observed at 0 G, unlike the  $90^\circ$  pulse acquire which gives a maximum signal intensity at 50 G for quinoline. This led to all new sequences after this point being collected at both 0 G and 50 G.

Extensive work has been carried out concerning the acquisition of 1D  $^{13}\text{C}$  NMR spectra. Initially, detection of polarisation from  $^{13}\text{C}$  was considered. It was found that, like  $^1\text{H}$ , polarisation on  $^{13}\text{C}$  nuclei also has a dependence on the PTF used showing maximum signal intensity at 0 G. Owing to the addition of *parahydrogen*, the signals often presented as antiphase in the coupled  $^{13}\text{C}$  NMR spectrum. This therefore means a refocusing sequence must be completed in order for decoupling to be successful. This was achieved using two methods; refocusing according to J coupling evolution ( $^{13}\text{C}\{^1\text{H}\}_{\text{JR}}$ ), and refocusing according to J coupling and chemical shift evolution ( $^{13}\text{C}\{^1\text{H}\}_{\text{JCSR}}$ ). The addition of these refocusing sequences allowed for successful decoupling of the  $^{13}\text{C}$  spectrum however the  $^{13}\text{C}\{^1\text{H}\}_{\text{JR}}$  sequence allowed the observation of the most signals and yielded the best signal intensity for those signals. This is thought to be due to relaxation of the hyperpolarised states during the second delay period of the  $^{13}\text{C}\{^1\text{H}\}_{\text{JCSR}}$  sequence.

Hyperpolarised  $^{13}\text{C}$  spectra were also investigated when considering the INEPT transfer sequence. This utilises the polarisation present on  $^1\text{H}$  and uses pulses to transfer this to  $^{13}\text{C}$  for detection. Predictably, this yielded greater signal intensities than those observed when interrogating  $^{13}\text{C}$  magnetisation. These spectra also presented with antiphase peaks and therefore required a refocusing sequence to allow decoupling. This produced the first  $^{13}\text{C}\{^1\text{H}\}$  NMR spectrum collected using SABRE which revealed all nine of the expected signals associated with quinoline.

The successful acquisition of spectra resulting from both  $^{13}\text{C}$  and  $^1\text{H}$  polarisation in the form of the  $^{13}\text{C}$  NMR sequence and  $^{13}\text{C}\{^1\text{H}\}$  INEPT NMR sequence have also allowed for the idea of sequential acquisition. When using method 2 to apply SABRE, the time required to repolarise the sample between acquisitions can be lengthy. Sequential interrogation of polarisation on  $^{13}\text{C}$  nuclei followed by polarisation on  $^1\text{H}$  nuclei in one hyperpolarisation step has allowed the collection of a coupled and decoupled  $^{13}\text{C}$  spectrum in one hyperpolarisation step.

The polarisor was instrumental in the implementation of SABRE to the classic 2D sequences such as the COSY, HSQC, HMBC and HMQC. The use of *parahydrogen* has also allowed the application of the OPSYCOSY, which results in the crosspeaks of the COSY spectrum to be more intense than the diagonal. It was also found that development from the MKII polarisor to the MKIII polarisor decreased the amount of

time required for a 64 increment 2D spectrum significantly. This was reduced further by reducing the time of addition of *parahydrogen* per increment from 6 s to 2 s, resulting in the collection of a 2D spectrum in 16 min. This is a great improvement on interrogations of low concentration substrates considering  $^1\text{H}$ - $^{13}\text{C}$  spectra such as the HMBC and HMQC. The SABRE technique has also been successfully applied to the *uf*COSY sequence by Frydman using method 1. It has therefore been possible to obtain a hyperpolarised COSY of 10 mM quinoline in less than a second. In the case of low concentration samples, information gathered from 2D spectra can also be gained much quicker than possible with thermally polarised samples.

This applications based investigation was extended to include understanding the functional group tolerance of SABRE, increasing steric bulk of pyridine analogues, competition effects, and potential for transfer into commercially available drugs provided by AstraZeneca.

SABRE was found to be tolerant to hydroxyl, carbonitrile, amino, amide, phenyl, aldehyde, carboxylic acid and chlorine groups, and the presence of sulphur in the ring. Investigations were also carried out into substrates which do not contain a pyridyl ring such as indole and thiazole analogues. The effect of increasing the steric bulk of the pyridine analogues was also considered, starting from small substituents such as a proton or a methyl group through to bulkier substituents such as a phenyl ring or a benzoyl group. In all cases, a small amount of polarisation transfer is observed into the substituted group.

Another important consideration for the SABRE technique is the idea of competition within a sample, which could be either to observe a single substrate in a complex spectrum, or to understand the effect of polarising two substrates in one sample. The OPSYdq sequence has given the opportunity to successfully filter out and consequently only observe the substrate affected by polarisation transfer from *parahydrogen*. This means experiments can be carried out in protonated solvents, and signals deriving from reaction mixture impurities can be removed. Polarisation transfer to substrates competing for polarisation transfer was also investigated.

Investigation also extended to the reaction of 4-carboxaldehydepiperidine with methanol. A literature search revealed this type of compound could undergo a spontaneous reaction with methanol to create a hemiacetal product, or an acid catalysed reaction with

methanol to create a dimethoxyacetal product. Investigations have shown the spontaneous reaction can be followed using SABRE however this has not yet been possible with the acid catalysed reaction due to the effect of the acid on the SABRE catalyst.

While this thesis has aimed to demonstrate the applicability of SABRE to high resolution NMR, it has also demonstrated some limitations. The extent of polarisation transfer is dependent on the lifetime of the active complex and the chemical shift differences and J-coupling network and as such each catalyst and substrate system exhibits different dependencies on the investigated variables. This therefore means the optimisation of polarisation transfer is difficult to predict and therefore potentially a lengthy process for a new catalyst or substrate. It has also been observed that the addition of certain substrates can cause adverse effects. For instance, it has been shown that SABRE is tolerant to acetonitrile and is in fact required to observe polarisation transfer into quinoline, however if it is added to a sample of 2-aminothiazole, the hyperpolarised states no longer transfer into 2-aminothiazole. Instead, they remain on the hydride ligands, resulting in significantly enhanced hydride signals. It should also be noted that not all substrates investigated have exhibited signal enhancement, however these have not been optimised considering all the potential variables and other SABRE catalysts which have not yet been discovered.

## 7.2 Future work

A number of areas for investigation in future work have been suggested below.

1. During the course of these studies, a new catalyst type was observed in the form  $[\text{Ir}(\text{ICy})_2(\text{COD})]\text{Cl}$  (Figure 7.1b) which hydrogenates to form  $[\text{Ir}(\text{H})_2(\text{ICy})_2(\text{py})_2]\text{Cl}$ .



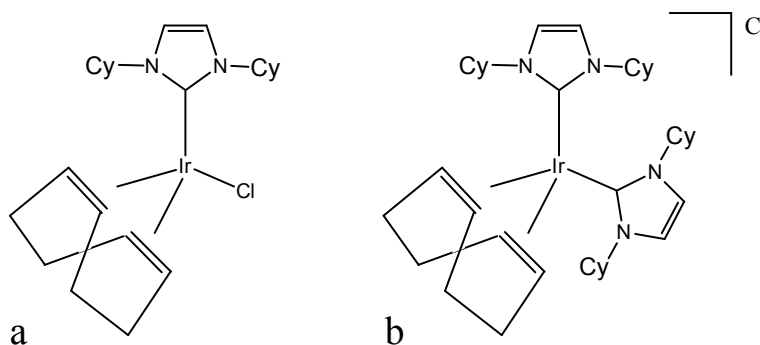


Figure 7.1 Structures of **ICy(a)** and **ICy<sub>2</sub>(a)**.

The polarisation transfer efficiency of this catalyst was compared to that of **ICy(a)** in reference to pyridine, 3-methylpyridine, 4-methylpyridine, quinoline and 2-aminothiazole.  $[\text{Ir}(\text{H})_2(\text{ICy})_2(\text{py})_2]\text{Cl}$  was found to exhibit a greater signal enhancement than **ICy(a)** in all the five previously mentioned substrates. This therefore demonstrates a new catalyst group which warrants further investigation.

- From a technological development point of view, a new polarisor which has the ability to heat or cool the sample concurrently with changing the magnetic field of the polarisation step. This will allow a complete optimisation for each catalyst/substrate system.
- During the investigations into the effect of changing solvent on the extent of polarisation transfer, it was observed that  $[\text{Ir}(\text{H})_2(\text{carbene})(\text{py})_3]^+$  was not the only species present in all solvents. It has been assumed that the solvent is benign in our systems however it is known that acetonitrile, acetone and DMSO can bind to the catalysts. It is also evident in the hydride region of the resultant NMR spectra collected for each solvent, that a combination of active species may be present. An idea for future work within this project would be to characterise these active complexes, and compare them through measured rate constants for loss of substrates.
- Further investigations into the routes of polarisation transfer into quinoline are also required. This includes a revision of the theory to include the larger spin system and presence of acetonitrile ligand.

5. 2D experiments completed using the SABRE technique with the automated flow system are collected using one scan per increment. This significantly saves time of collection for each 2D spectrum however it also results in an artefact on the centre of the f1 direction. A potential route to overcome this artefact without doubling collection time required is to apply a gradient across the sample cell such that 2 independent scans can be collected across the height of the cell. This means for each transient, 2 scans can be collected, and consequently two scans per increment can be used for each 2D spectrum without doubling the experiment time. It will be interesting to develop this idea in the future.
6. The application of SABRE to hyperpolarised 2D  $^1\text{H}$ - $^{15}\text{N}$  spectra is also of great future interest as it would provide the potential to bring  $^{15}\text{N}$  spectroscopy into the routine of a pharmaceutical chemist.

## 8 Chapter 8 – Experimental

### 8.1 Instrumentation and chemical sources

#### 8.1.1 NMR spectrometers

Characterisations of complexes and substrates by NMR spectroscopy have been completed using a number of Bruker spectrometers. These include an Avance III 400 MHz, Avance III 500 MHz, Avance II 600 MHz and Avance II 700 MHz, where the  $^1\text{H}$  frequency is measured at 400.13 MHz, 500.23 MHz, 600.12 MHz and 700.13 MHz and  $^{13}\text{C}$  frequency is measured at 100.62 MHz, 125.80 MHz, 150.90 MHz and 176.07 MHz. The aforementioned spectrometers have also been used in the calculation of thermodynamic parameters. When completing hyperpolarised experiments with SABRE, the aforementioned 400 MHz spectrometer was used. Data acquisition and processing is carried out using the Bruker program TopSpin. During the course of this PhD, versions 2.1 and 3.1 have been used.

During the course of these experiments, six NMR solvents are used:  $d_4$ -methanol is referenced to residual  $\text{CHD}_2\text{OD}$ ,  $d_1$ -chloroform is referenced to residual  $\text{CHCl}_3$ ,  $d_6$ -ethanol is referenced to residual  $\text{CHD}_2\text{CD}_2\text{OD}$ ,  $d_2$ -dichloromethane (DCM) is referenced to residual  $\text{CDHCl}_2$ ,  $d_6$ -dimethylsulphoxide (DMSO) is referenced to residual  $(\text{OS})\text{CD}_3\text{CD}_2\text{H}$  and  $d_6$ -acetone is referenced to residual  $(\text{OC})\text{CD}_3\text{CD}_2\text{H}$ .

#### 8.1.2 Preparation of *parahydrogen*

*Parahydrogen* was prepared by cooling hydrogen gas over  $\text{Fe}_2\text{O}_3$ . The first *parahydrogen* rig was made in house and the exact catalyst and temperature used in this system to prepare *parahydrogen* has changed over the course of this work. It used a hydrogen cylinder as a source of normal hydrogen. Towards the end of the work, a rig was also provided by Bruker, which used a hydrogen generator as the source of normal hydrogen. These changes result in the exact percentage of hydrogen in the *para* state being constant for each individual experiment, but inconsistent across the three years.

### 8.1.3 Source of solvents and chemicals

General solvents for synthetic chemistry were dried using an Innovative Technology anhydrous solvent engineering system or were distilled from an appropriate drying agent under N<sub>2</sub> as necessary. Deuterated solvents were obtained from Sigma-Aldrich and used as supplied. High purity gases were obtained from BOC and used as received.

## 8.2 Standard methods

### 8.2.1 Hyperpolarisation method 1 – shake method

Samples investigated using hyperpolarisation method 1 were completed using a 5 mm NMR tube fitted with a J Young valve (called a Young's Tap NMR tube from here on in) containing a solution of catalyst (5 mM,  $3.1 \times 10^{-6}$  mol), substrate (100 mM,  $6.2 \times 10^{-5}$  mol) and solvent (0.6 ml), unless otherwise stated. These are standard reagent conditions. The sample was degassed prior to activation by hydrogen gas at a pressure of 3 bar.

For each experiment, the headspace of the Young's NMR tube was evacuated, and replenished with 3 bar *parahydrogen*. The sample was then shaken for 8 s in the desired magnetic field (using the fringe field of the magnet) before being rapidly transported into the magnet for interrogation by NMR spectroscopy. A <sup>1</sup>H NMR spectrum was collected with a 90° pulse as standard.

### 8.2.2 Hyperpolarisation method 2 – flow method

Samples investigated using hyperpolarisation method 2 were completed using a polarisation chamber charged with a solution of catalyst (5 mM,  $1.55 \times 10^{-5}$  mol), substrate (100 mM,  $3.1 \times 10^{-4}$  mol) and deuterated solvent (3 ml), unless otherwise stated. These are standard reagent conditions. *Parahydrogen* was introduced to the solution via six inlet tubes at a pressure of 3 bar for 6 s (unless otherwise stated). This solution was then transferred into the Bruker Avance III series 400 MHz spectrometer equipped with a flow probe head (flow cell volume = 200 µl) for interrogation by NMR using helium as a flow gas. Unless otherwise stated, a single transient was recorded for the nucleus of interest. A <sup>1</sup>H NMR spectrum was collected with a 90° pulse as standard.

Once interrogated, the solution was returned to the polarising chamber with a helium flow gas and the process repeated as required.

It was standard to activate a sample for interrogation by method 2 in the polarisor itself however this was not always possible. In the case of the **ICy(a)** catalyst for instance, the sample must be pre-activated in an ampoule as it takes too long to activate in the polarisor. To achieve this, the sample was prepared as required, then degassed in an ampoule. This was then put under an atmosphere of 3 bar hydrogen gas, shaken and stored at room temperature until the catalyst was active. When ready, the sample was injected as quickly as possible into the mixing chamber of the polarisor, trying to minimise exposure to air as much as possible. The system was then ready for interrogation by NMR.

During the progression of this thesis, the technology for the polarisation chamber was in development and so consequently, three polarisation chambers have been used. For the first polarisation chamber (MK I), the applied magnetic field was controlled by the position of the polarisation chamber within the fringe field of the magnet and used a TXO flow probe. For the second (MK II) and third (MK III, Bruker) polarisation chamber, the magnetic field was controlled by a coil that surrounds the reaction chamber such that a magnetic field can be generated in the *z* direction, to produce static DC fields in the range of  $-150$  to  $150 \times 10^{-4}$  T. The MK II was connected to a TXO flow probe and the MK III connected to a TXI flow probe.

### 8.2.3 Calculation of $^1\text{H}$ NMR enhancement factors

For calculation of the enhancement of  $^1\text{H}$  NMR signals the following formula was used:

$$E = \frac{S_{\text{pol}}}{S_{\text{unpol}}}$$

Equation 8.1 Equation used to calculate the  $^1\text{H}$  NMR signal enhancement.

Equation 8.1 is true where:  $E$  = enhancement,  $S_{\text{pol}}$  = signal of polarised sample measured by integral and  $S_{\text{unpol}}$  = signal of unpolarised (thermally polarised) reference sample measured by integral.

Experimentally, reference spectra were acquired after the sample had spent 5-10 minutes at high magnetic field to ensure it was fully equilibrated to the Boltzmann distribution of spins, before any *parahydrogen* was added to the sample. The reference and polarised spectra were collected using identical acquisition parameters, particularly the receiver gain. The raw integrals of the relevant resonances in the polarised and thermal spectra were used to determine the enhancement level using Equation 8.1.

Owing to the nature of *parahydrogen* derived hyperpolarisation, a sample interrogated by NMR in the presence of *parahydrogen* may result in both enhanced adsorption signals and enhanced emission signals. Consequently, the integral for an enhanced emission peak is negative. This sign has been carried through in the equation to the resulting calculated enhancement. This means that where a negative enhancement is quoted, the peak was in emission. In the case of an antiphase signal, the integral of whole peak is taken and therefore contains a mixture of both absorption and emission character. The quoted enhancement is therefore lower as a result of cancellation of the antiphase signal.

In some sections, the enhancement relating to the OPSYdq sequence (see Chapter 1) has been quoted. As an OPSY without presence of *parahydrogen* results in no signal, the enhancement of these hyperpolarised spectra are based on a standard thermal  $^1\text{H}$  NMR spectra of the same receiver gain (16 for the OPSYdq sequence).

#### 8.2.4 Considerations when discussing the effect of the magnetic field of polarisation on polarisation transfer efficiency

Whenever a magnetic field in Gauss is quoted, this refers to the magnetic field present during the addition of *parahydrogen* to the sample, the polarisation transfer step. In method 1, the field is applied during the time the sample is shaken in the presence of *parahydrogen*. This is typically completed at two fields, Earth's magnetic field (0.5 G) and a higher field measured to be around 65 G which is achieved by shaking in the stray field of the spectrometer. In reality, this means the higher field utilised in method 1 is highly variable as the shake process causes the sample to cross over a range of field values.

In method 2, the field is applied during the bubbling of *parahydrogen* through the solution. For the MK I polarisor, the field is again applied using the stray field of the magnet however, the chamber is now stationary so the magnetic field range experienced by the sample is much less than that of method 1. For the MK II and MK III polarisors, the magnetic field is induced by a current introduced to the coil surrounding the sample. The magnetic field experienced by the sample can therefore be controlled by the amount of current in the coil; this corresponds to the value input by the user. The coil controls the field experienced in the vertical ( $z$ ) direction and has additional turnings at each end of the coil to ensure homogeneity over the length of the coil. As the chamber is not stored at 0 G, but as close to Earth's magnetic field as possible considering the required proximity to the spectrometer, the stated value is modulated slightly. The chamber is used in the same position during all experiments and so this modulation is constant. The standard method employed to understand the effect of changing the field of polarisation is to take a sample of standard concentrations, and interrogate it starting at -150 G and increasing the field by 10 G until an experiment at +10 G has been completed, unless otherwise stated. For each field, six  $^1\text{H}$  NMR spectra are taken to ensure reproducibility.

## 8.2.5 Effect of changing PTF on the polarisation transfer efficiency into various substrates

### 8.2.5.1 Effect of changing PTF on polarisation transfer efficiency into pyridine with

#### SIMes(a)

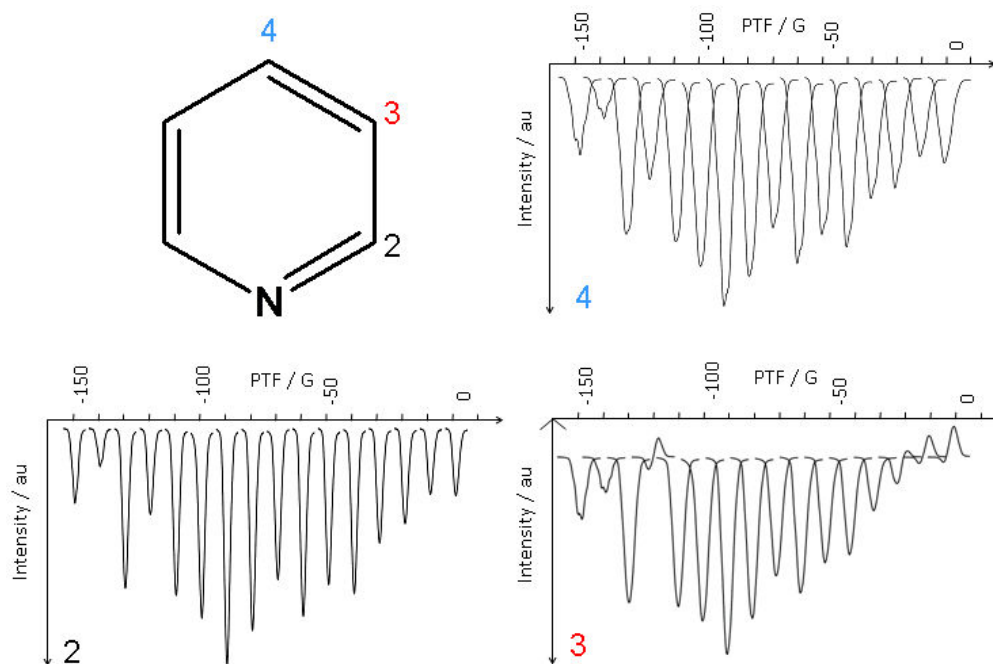


Figure 8.1 Effect of changing PTF on polarisation transfer efficiency into pyridine using **SIMes(a)**.

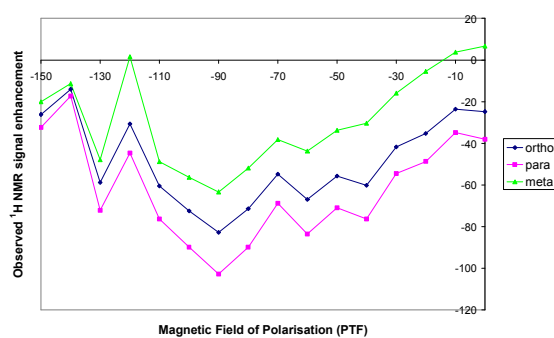


Figure 8.2 Graphical representation of the effect of changing PTF on polarisation transfer efficiency into pyridine using **SIMes(a)**.



### 8.2.5.2 Effect of changing PTF on polarisation transfer efficiency into pyridine using ICy(a)

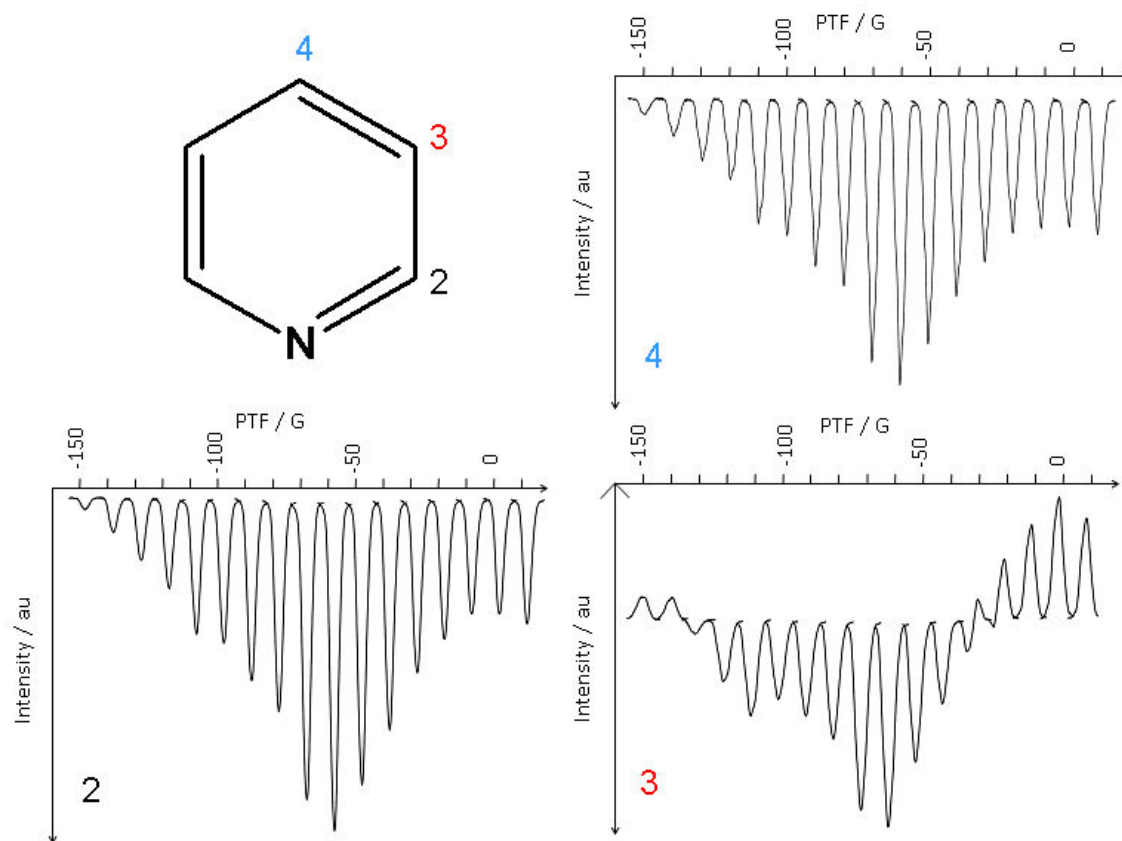


Figure 8.3 Effect of changing PTF on polarisation transfer efficiency into pyridine using ICy(a).

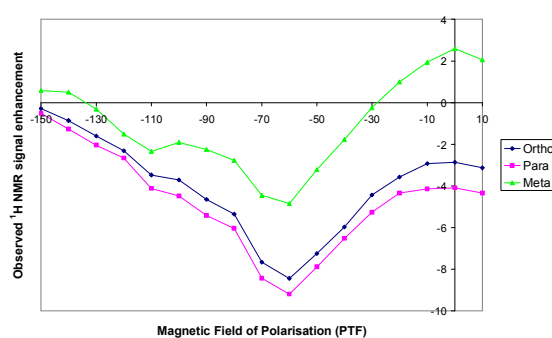


Figure 8.4 Graphical representation of the effect of changing PTF on polarisation transfer efficiency into pyridine using ICy(a).

### 8.2.5.3 Effect of changing PTF on polarisation transfer efficiency into pyridine using $\text{ICy}_2(\mathbf{a})$

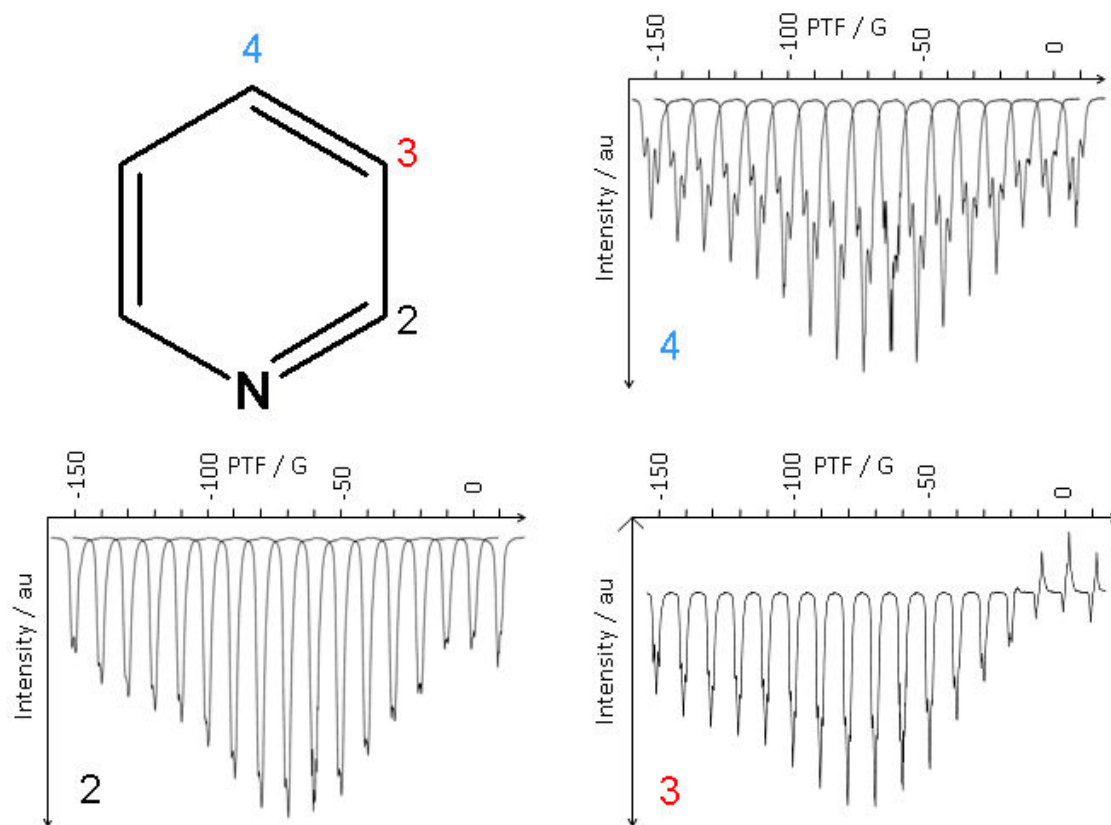


Figure 8.5 Effect of changing PTF on polarisation transfer efficiency into pyridine using  $\text{ICy}_2(\mathbf{a})$ .

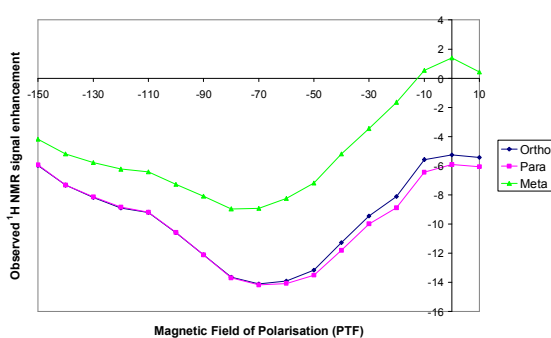


Figure 8.6 Graphical representation of the effect of changing PTF on polarisation transfer efficiency into pyridine using  $\text{ICy}_2(\mathbf{a})$ .

#### 8.2.5.4 Effect of changing PTF on polarisation transfer efficiency into 3,4,5-d<sub>3</sub>-pyridine using **SIMes(a)**

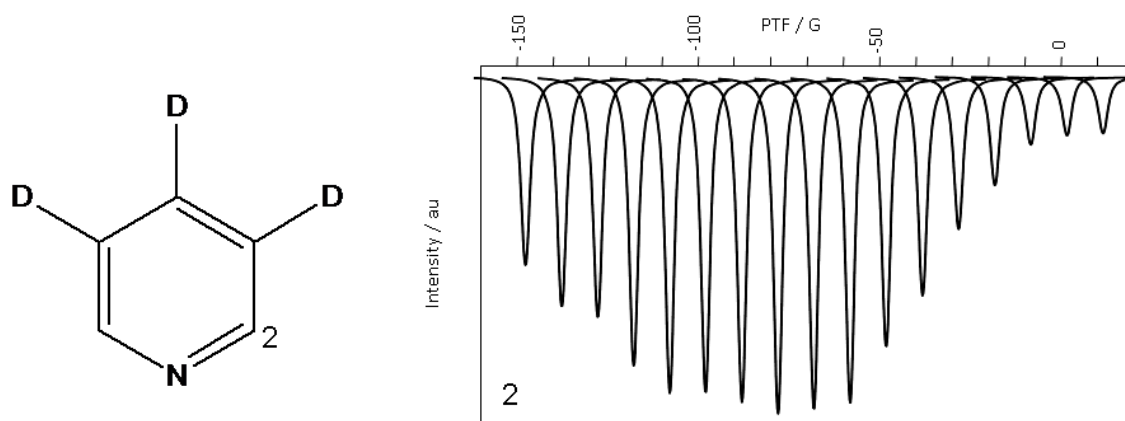


Figure 8.7 Effect of changing PTF on polarisation transfer efficiency into 3,4,5-d<sub>3</sub>-pyridine using **SIMes(a)**.

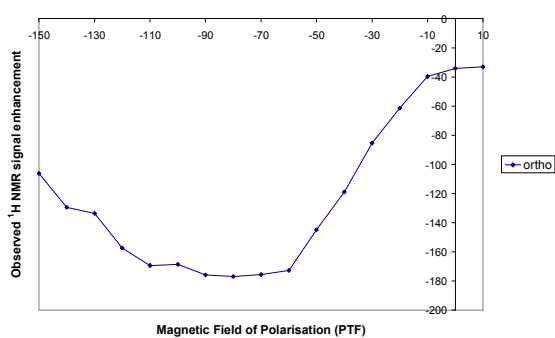
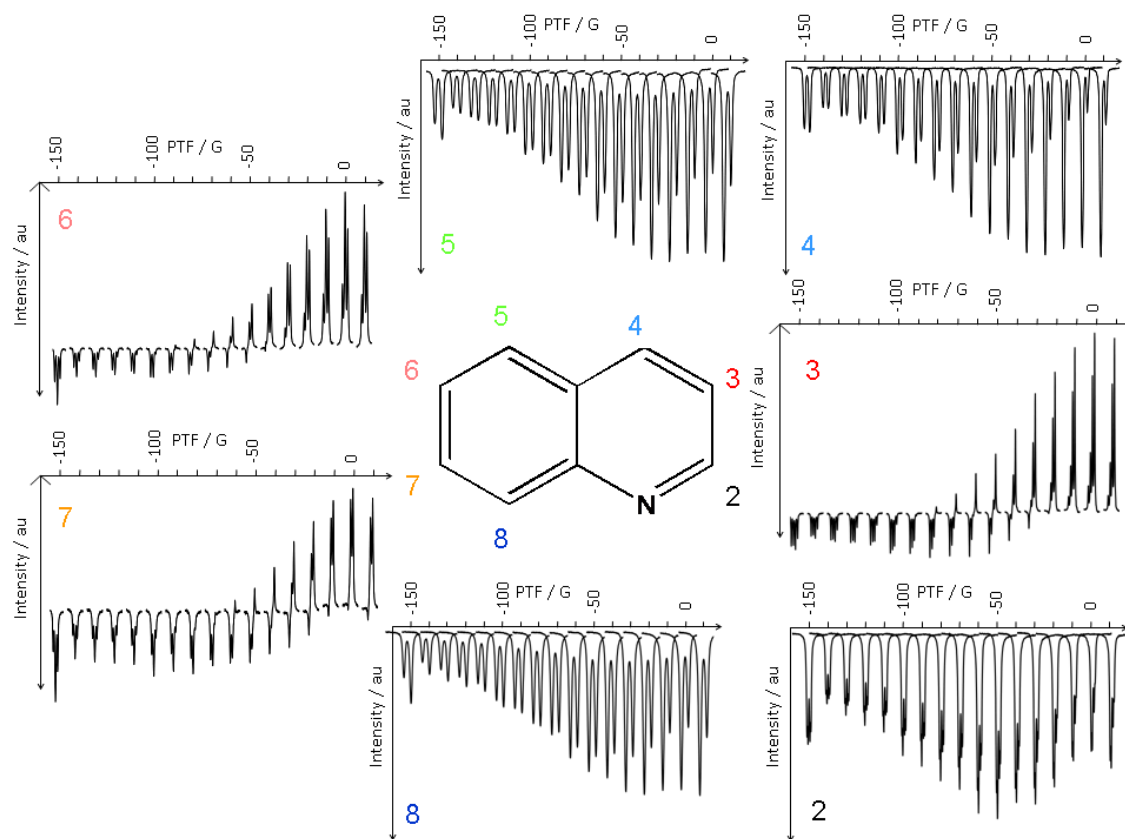
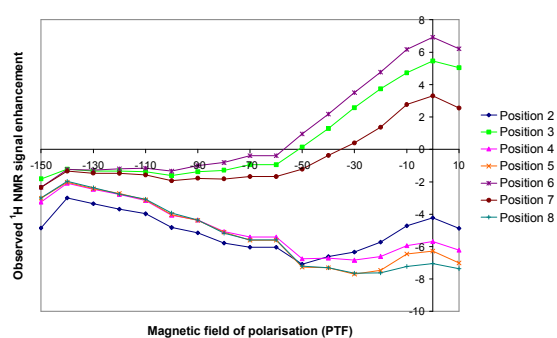


Figure 8.8 Graphical representation of the effect of changing PTF on polarisation transfer efficiency into 3,4,5-d<sub>3</sub>-pyridine using **SIMes(a)**.

## 8.2.5.5 Effect of changing PTF on polarisation transfer efficiency into quinoline using

**IMes(b)**Figure 8.9 Effect of changing PTF on polarisation transfer efficiency into quinoline using **IMes(b)**.Figure 8.10 Graphical representation of the effect of changing PTF on polarisation transfer efficiency into quinoline using **IMes(b)**.

### 8.2.5.6 Effect of changing PTF on polarisation transfer efficiency into 4-methylpyridine using **SIMes(a)**

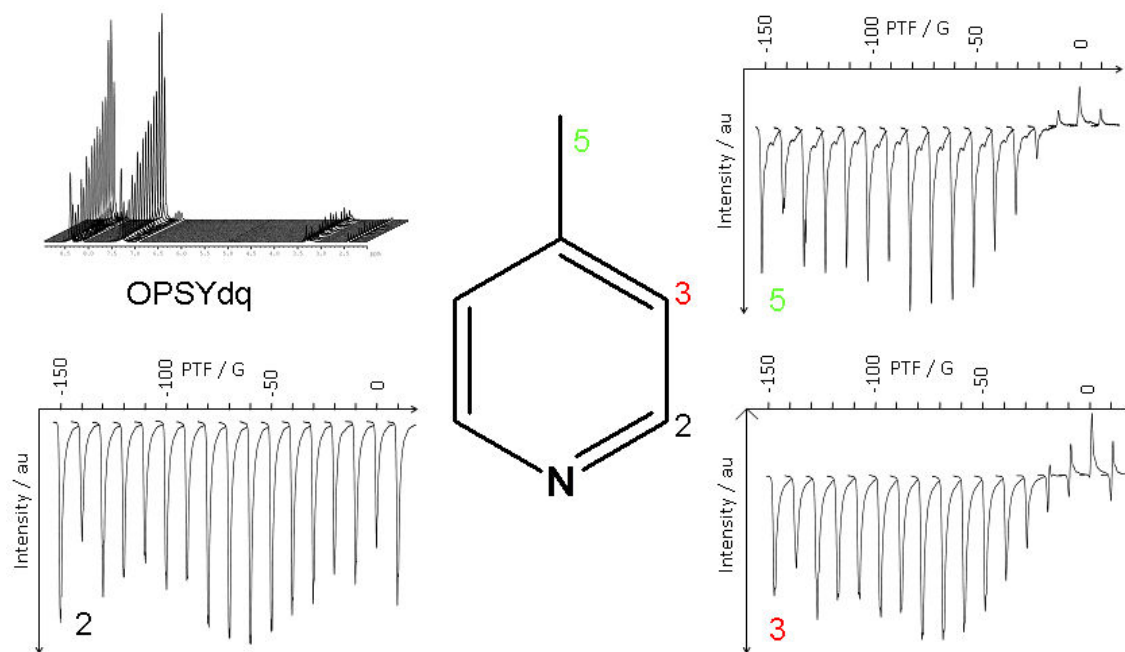


Figure 8.11 Effect of changing PTF on polarisation transfer efficiency into 4-methylpyridine using **SIMes(a)**.

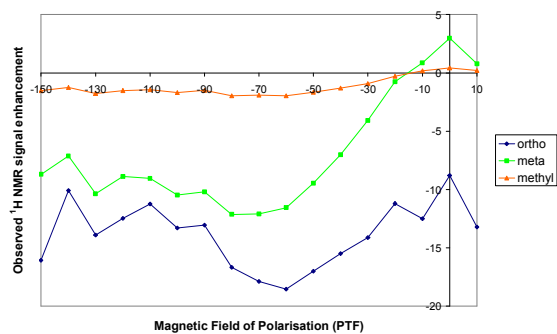


Figure 8.12 Graphical representation of the field profile of **SIMes(a)** with 4-methylpyridine.

### 8.2.5.7 Effect of changing PTF on polarisation transfer efficiency into 3-methylpyridine using SIMes(a)

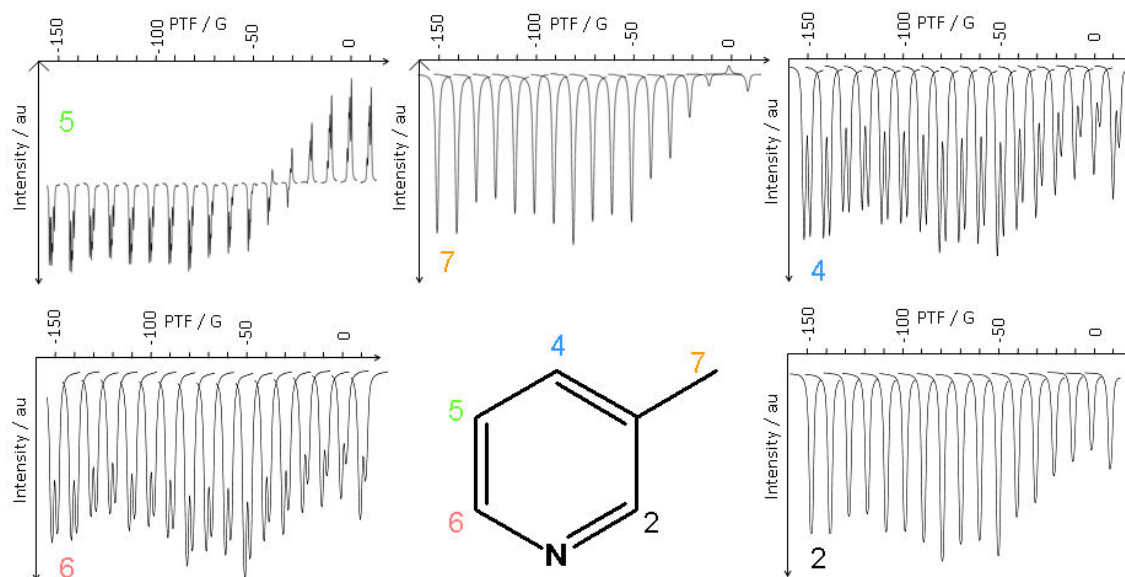


Figure 8.13 Effect of changing PTF on polarisation transfer efficiency into 3-methylpyridine using SIMes(a).

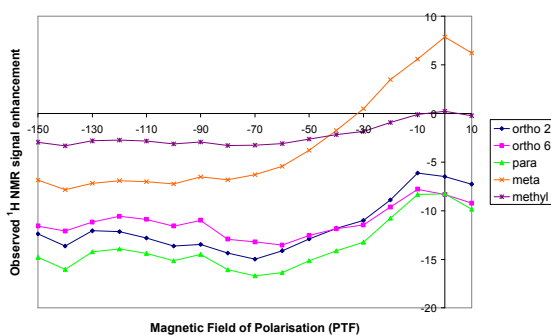


Figure 8.14 Graphical representation of the effect of changing PTF on polarisation transfer efficiency into 3-methylpyridine using SIMes(a).

### 8.2.5.8 Effect of changing PTF on polarisation transfer efficiency into 2-aminothiazole using **IMes(a)**

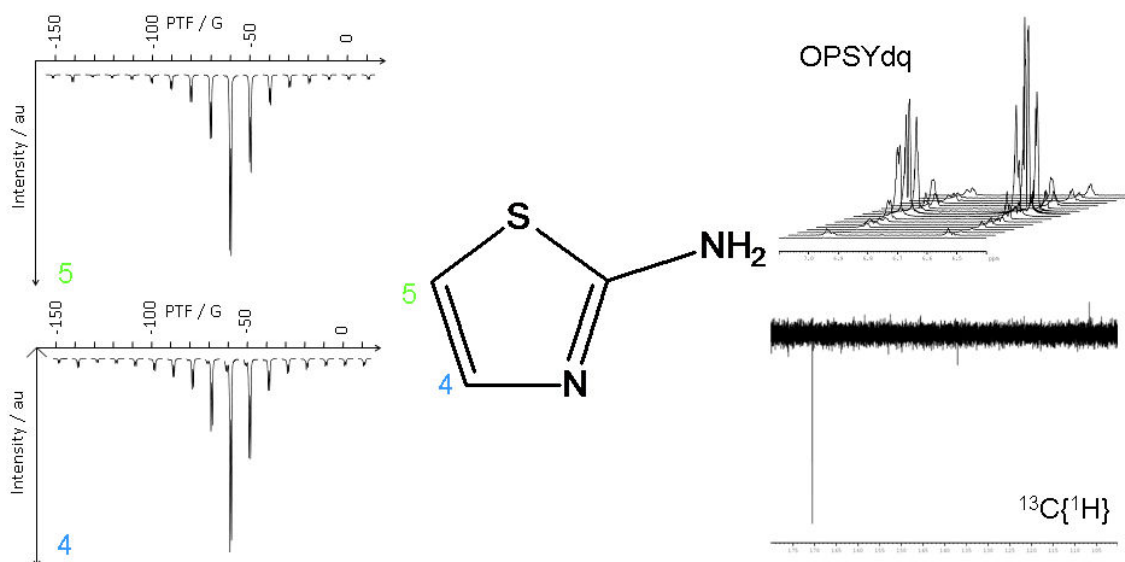


Figure 8.15 Effect of changing PTF on polarisation transfer efficiency into 2-aminothiazole using **IMes(a)**.

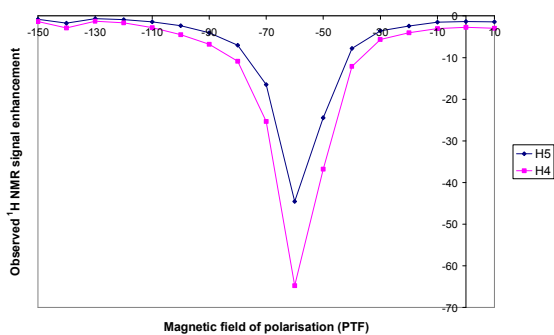


Figure 8.16 Graphical representation of the effect of changing PTF on polarisation transfer efficiency into 2-aminothiazole using **IMes(a)**.

### 8.2.5.9 Effect of changing PTF on polarisation transfer efficiency into 3-phenylpyridine using **IMes(a)**

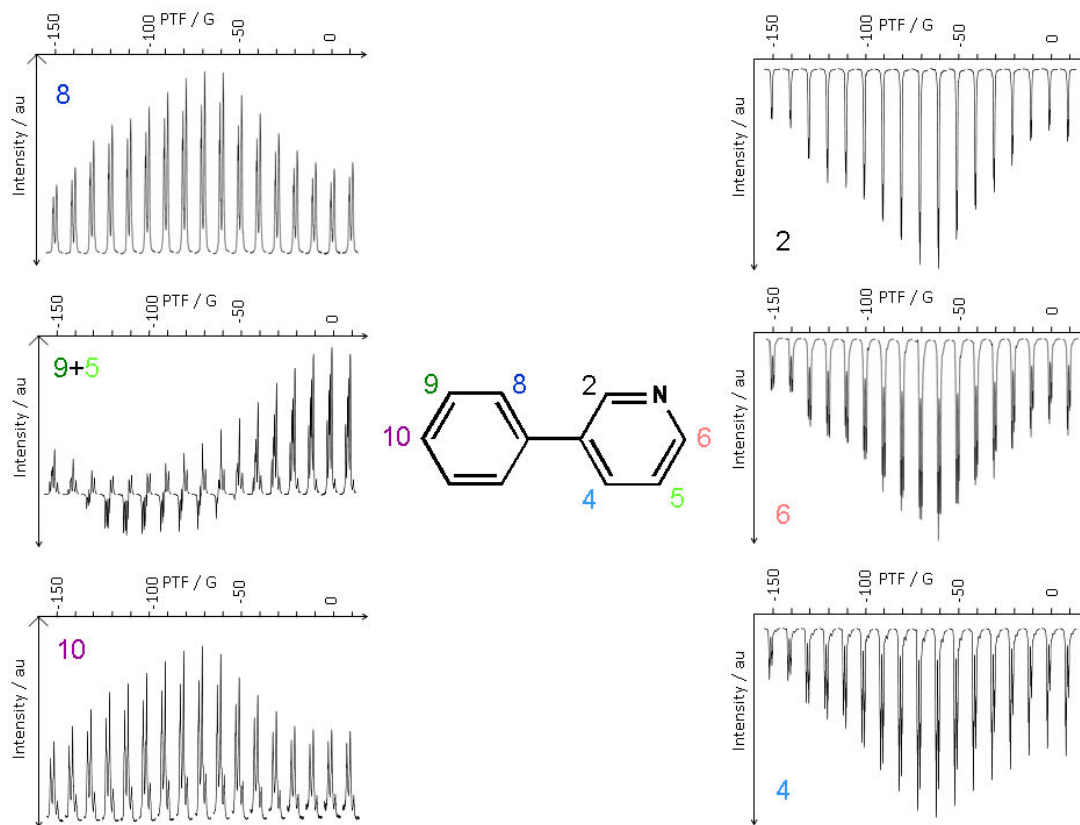


Figure 8.17 Effect of changing PTF on polarisation transfer efficiency into 3-phenylpyridine using **IMes(a)**.

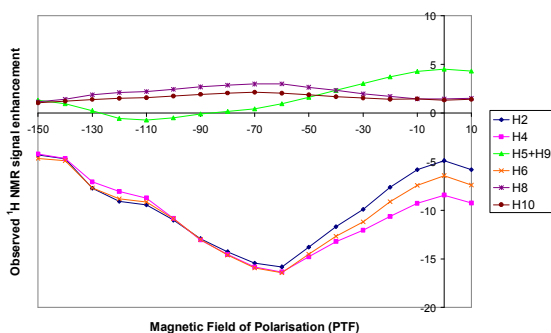


Figure 8.18 Graphical representation of the effect of changing PTF on polarisation transfer efficiency into 3-phenylpyridine using **IMes(a)**.

The enhancements corresponding to the signals of protons 5 and 9 are not representative of the enhancement for each individual signal. The values are low as a result of the combination of positive and negative signals.



### 8.2.5.10 Effect of changing PTF on polarisation transfer efficiency into 4-phenylpyridine using **IMes(a)**

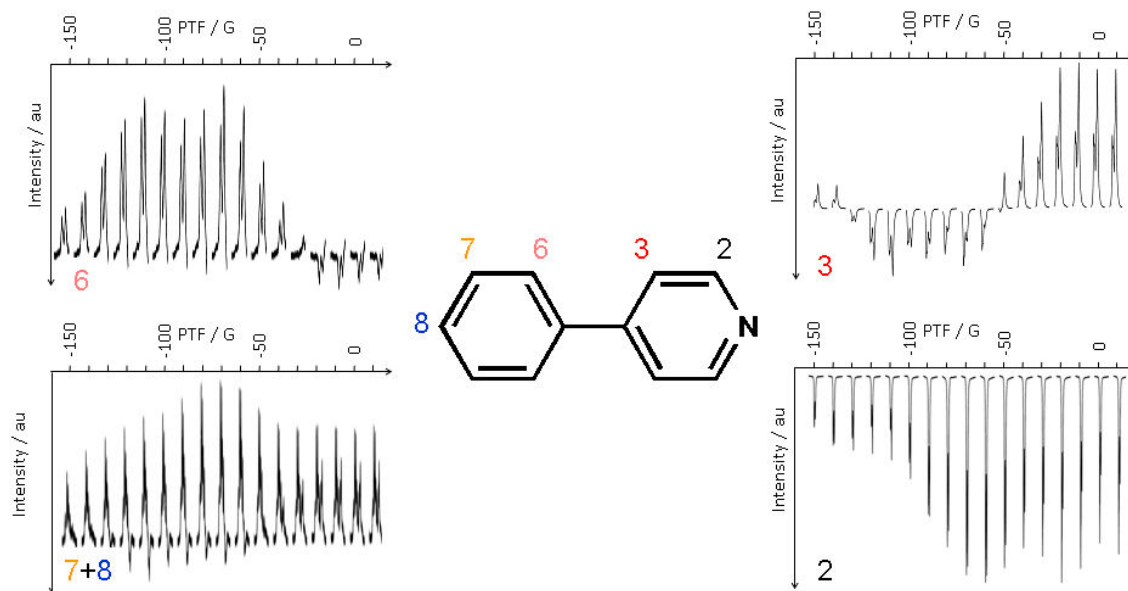


Figure 8.19 Effect of changing PTF on polarisation transfer efficiency into 4-phenylpyridine using **IMes(a)**.

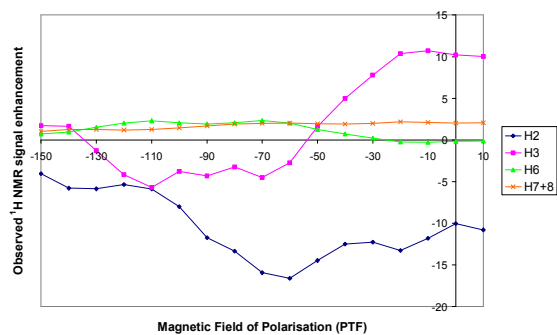


Figure 8.20 Graphical representation of the effect of changing PTF on polarisation transfer efficiency into 4-phenylpyridine using **IMes(a)**.

### 8.2.6 Calculation of rate constants for ligand loss and thermodynamic activation parameters

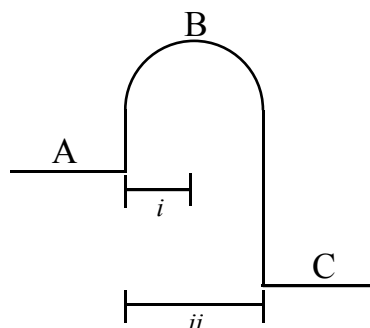


Figure 8.21 The reaction co-ordinate for the dissociative reaction for loss of ligand.

A series of 1D EXSY experiments were completed to enable the calculation of the pyridine and hydride ligand exchange rates in the active forms of **IMes(a)**, **SIMes(a)** and **ICy(a)** as a function of temperature. The associated rates of ligand exchange were determined by application of the Dynafit<sup>108</sup> programme. These data are expected to provide us with a better understanding of the effect the carbene ligand has on catalyst activity.

In this case, the measured rate corresponds to the transformation from bound ligand (hydride/substrate) to free ligand, A to C in Figure 8.21, and is quoted per mole of iridium complex. When calculating  $\Delta H^\ddagger$ ,  $\Delta S^\ddagger$  and  $\Delta G^\ddagger$ , the rate data used should refer to the rate of reaching the transition state (B) which is twice the measured rate. This is because once the molecule has reached point B, it is possible for it to fully disassociate to form C, or re-associate to form A. Consequently, the Eyring plots for activation parameters of both hydride ligand and pyridine loss are calculated using a graph of  $\ln(2 \times \text{measured rate}/\text{temperature})$  vs  $1/\text{temperature}$ .<sup>109</sup> In all cases, the raw rates are measured as per mole of iridium catalyst, and not per mole of hydride ligand or pyridine.

### 8.2.7 Procedure for investigating the effect of changing temperature of polarisation on polarisation transfer efficiency

The effect of changing the temperature of addition of *para*hydrogen to a SABRE catalyst was investigated using method 1. To complete these experiments the sample

must first be put under a *parahydrogen* atmosphere but not shaken. It is then stored at the desired temperature for three minutes with as little disturbance as possible. The NMR tube is then quickly wiped dry, shaken for 8 s and interrogated by NMR spectroscopy. Although a small amount of loss of *parahydrogen* will be experienced, if it is refreshed after the wait at the stated temperature, the sample will equilibrate towards room temperature. Refreshing the head space before getting the sample to the desired temperature minimises the loss (or gain) in temperature during the shake. It is also difficult to evacuate the sample ready for fresh *parahydrogen* when the sample is at an elevated temperature due to the solvent being volatile. Evacuation also has the effect to cool the sample. The volatility of the solvent also means the effect of increasing the temperature above 50 °C is not practical.

### 8.3 Additional experiments

#### 8.3.1 Relative excess of hydrogen gas present in an NMR sample interrogated using method 1

In order to fully understand the effects of changing the concentration of catalyst and substrate in a sample to be interrogated by method 1, it is important to understand how many moles of gas are present in the sample. To calculate this, a standard Youngs tap NMR tube was weighed when empty (29.6343 g). It was then filled with water and 0.6 ml water was removed to allow for the space taken up by the sample. The NMR tube was weighed again (31.5361 g) and the two masses subtracted from each other (1.9018 g). As water has a density of 1 g/ml, this suggests the headspace in a typical NMR tube is ~1.9 ml. This value was then used in the ideal gas law to calculate the number of moles of hydrogen present in the headspace when 3 bar of pressure is applied at room temperature (293 K).

$PV = nRT$ , where  $P = 3 \text{ bar} = 300,000 \text{ Pa}$ ,  $V = 1.9 \text{ ml} = 1.9 \times 10^{-6} \text{ m}^3$ ,  $n = x \text{ moles}$ ,  $R = 8.314 \text{ JK}^{-1}\text{mol}^{-1}$  and  $T = 293 \text{ K}$ . When rearranged this means the headspace contains  $2.34 \times 10^{-5} \text{ mol}$  which is equal to 0.0234 mmol. This is the number of moles of hydrogen present in a sample prior to activation. After activation, it is important to recognise that there will be an additional number of moles of hydrogen in the sample corresponding to those bound to the metal catalyst as hydride ligands. These must also be taken into account. These calculations have been presented for standard concentration samples.

In a standard 0.6 ml 100 mM sample, there is 0.0031 mmol of catalyst. Before activation, the catalyst and hydrogen are therefore present in the ratio 0.0031 : 0.0234 which indicates that there is a 7.5 fold excess of hydrogen. After activation, each mole of catalyst has two hydrides and therefore a mole of hydrogen. Taking this into account, the catalyst and hydrogen in the sample are in the ratio 0.0031 : (0.0234 + 0.0031) which is equal to 0.0031 : 0.0265, giving an 8.5 fold excess of hydrogen in the sample. These results, together with those corresponding to other concentrations used in this thesis are presented in Table 8.1.

Percent of std conc.	[Cat.] mM	Cat. mmol	Excess of hydrogen in NMR tube	
			Before activation	After activation
1000	50	0.031	0.75	1.75
500	25	0.0155	1.51	2.5
100	5	0.0031	7.55	8.5
10	0.5	0.00031	75.5	76.5
1	0.05	0.000031	755	756

Table 8.1 The excess of hydrogen present in sample interrogated by method 1 at various levels of catalyst loading.

### 8.3.2 Calculations relating to the solubility of hydrogen gas in methanol

#### 8.3.2.1 Calculations based on equations reported in Solubility of Gases in Liquids<sup>212</sup>

The book, Solubility of Gases in Liquids, proposes that Equation 8.2 can be used to calculate the mole fraction of hydrogen dissolved in methanol at various temperatures, with a pressure of 1.013 bar.

$$\ln(x_g) = -7.3644 - (408.38/T)$$

Equation 8.2 Mole fraction of hydrogen,  $x_g$ , dissolved in methanol at 1.013 bar pressure of gas, where T = temperature in K, taken from Solubility of Gases in Liquids.<sup>212</sup>

The mole fraction of hydrogen in methanol has been calculated according to Equation 8.2 at the temperatures used in method 1, and presented in Table 8.2. Assuming hydrogen is an ideal gas, the second column shows the calculated values multiplied by 3 to take into account the increase in pressure present in method 1 experiments.

T / K	Mole fraction of hydrogen in methanol, $x_g$		Dissolved hydrogen (mmol)
	1.013 bar	3 bar	
273	0.000142	0.000426	0.0000100
293	0.000157	0.000472	0.0000110
303	0.000165	0.000494	0.0000116
313	0.000172	0.000515	0.0000121
323	0.000179	0.000537	0.0000126

Table 8.2 Amount of dissolved hydrogen (mmol) in a standard method 1 sample at various temperatures, predicted as by Equation 8.2.

Table 8.2 indicates that the number of moles of dissolved  $H_2$  is very low, and the catalyst is predicted to be in excess by 310 fold in solution, despite the excess of hydrogen present in the headspace. In order for **IMes(a)** to fully convert into active catalyst,  $H_2$  must dissolve during the reaction, a process which does not happen rapidly. This is revealed by the fact that if a sample of **IMes(a)** is left to activate overnight with no disturbance at all, only the top  $\sim 6^{\text{th}}$  of the sample is colourless and therefore active. The remaining  $\sim 5/6$ ths of the sample exhibits no colour change and remains as **IMes(a)**. A paper published by Iggo *et al.*<sup>213</sup> in 1998 reports similar examples of slow hydrogen dissolution into  $CDCl_3$  and design a high pressure flow cell to overcome this hurdle. Our SABRE samples are therefore vigorously shaken to force hydrogen gas into solution with the result that the whole sample becomes colourless and therefore active within 5 minutes, proven by NMR.

### 8.3.2.2 Calculations based on equations reported by Liu *et al.*<sup>214</sup>

The previous calculations were based on an equation which was produced for a standard pressure (1.013 bar). In the case that  $H_2$  is not an ideal gas, a different method was therefore sought to include the effect of pressure. This was based on that in a paper published by Liu *et al.*<sup>214</sup> in which hydrogen solubility is measured over a range of temperatures (23.1 °C to 140.3 °C) and pressures (5 bar to 16 bar). These data were combined to produce Equation 8.3a which can be used to calculate a value for Henry's law constant at a specified temperature and pressure. This is then used in Equation 8.3b to calculate the mole fraction of  $x_{H_2}$  in methanol.

$$\text{a) } \ln H = 122.3 - 4815.6/T - 17.5 \ln T + 1.4 \times 10^{-7} P$$

$$\text{b) } H = P_{\text{H}_2}/x_{\text{H}_2}$$

Equation 8.3 a) To calculate Henry's Law constant for hydrogen dissolved in methanol, where  $H$  = Henry's Law constant (MPa),  $T$  = temperature in K and  $P$  = pressure in Pa, taken from Liu *et al.*<sup>214</sup> b) Henry's Law correct at a specified temperature, where  $x_{\text{H}_2}$  is the mole fraction of hydrogen dissolved in methanol.

Table 8.3 presents the mole fraction of hydrogen in methanol in each temperature calculated according to Equation 8.3a+b.

T/K	H	$x_{\text{H}_2}$	Dissolved hydrogen (mmol)
273	689.99	0.000435	0.0000102
293	667.46	0.000449	0.0000105
303	638.17	0.000470	0.0000110
313	600.73	0.000499	0.0000117
323	557.86	0.000538	0.0000126

Table 8.3 The amount of dissolved hydrogen (mmol) in method 1 samples at various temperatures as predicted by Equation 8.3a+b.

These data matched those presented in Table 8.2 very closely. They have revealed therefore that  $\text{H}_2$  dissolution is a major factor when considering activation and polarisation transfer of method 1 samples. This explains the need for vigorous shaking before interrogation by NMR. The reliance of the method on the shake itself explains the poor reproducibility of the method as it is very difficult to shake a sample with exactly the same force for exactly the same time, every time the method is implemented.

### 8.3.3 Calculation of estimated integrals of thermally polarised spectra for low concentration samples

When investigating the effect of concentration on the extent of polarisation transfer, it was not possible to observe thermally polarised signals for pyridine in the low concentration samples in a single scan. To obtain an idea of enhancements with these samples, the integral of the thermally polarised signals are estimated based on extrapolation of the integrals of the higher pyridine concentration samples (Table 8.4). This was only required for sample 5 of the investigation where the ratio of catalyst and

substrate were kept constant as in all other cases, the hyperpolarised signals were also too small.

	Absolute integral of thermally polarised spectrum			
	500	300	100	10
Conc. Py (mM)	500	300	100	10
Volume of py ( $\mu\text{L}$ )	25	15	5	0.5
<i>ortho</i> proton	1533121	835784	276097	28628
<i>meta</i> proton	1535088	832981	276110	28921
<i>para</i> proton	776220	430658	138223	15485

Table 8.4 The absolute integrals of the three positions of pyridine observed in a single scan  $^1\text{H}$  NMR spectrum at the indicated volumes.

The data in Table 8.4 is presented graphically in Figure 8.22. The equations are derived in Excel through the trendline function and the intercept has been set to zero.

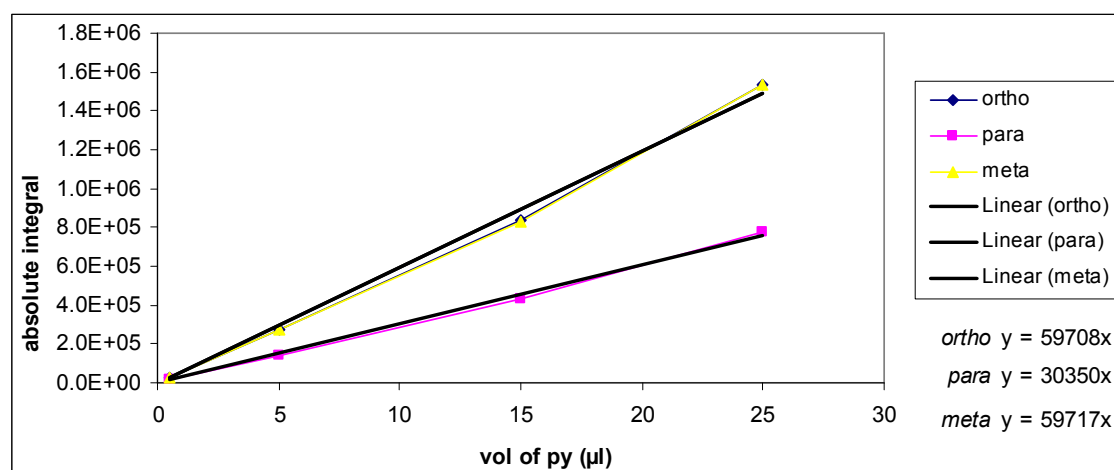


Figure 8.22 Graphical representation of the absolute integrals of the three positions of pyridine observed in a single scan  $^1\text{H}$  NMR spectrum at the indicated volumes. The equations of the trend lines are included.

The equation for the trend line of each position is used to estimate the integral of the signal observed in a single  $^1\text{H}$  NMR spectrum of a pyridine sample at lower concentrations. The integrals of the thermally polarised signals used for calculations of enhancements are therefore presented in Table 8.5.

	Absolute integral of thermally polarised spectrum				
Conc. Py (mM)	500	300	100	10	1
Volume of py ( $\mu\text{L}$ )	25	15	5	0.5	0.05
<i>ortho</i> proton	1533121	835784	276097	28628	2985.4
<i>meta</i> proton	1535088	832981	276110	28921	1517.5
<i>para</i> proton	776220	430658	138223	15485	2985.85

Table 8.5 The absolute integrals of the three positions of pyridine observed in a single scan  $^1\text{H}$  NMR spectrum at the indicated volumes. The integrals for the 1 mM (0.05  $\mu\text{L}$ ) sample have been calculated according to Figure 8.22.

For the 1 mM sample, the enhancements for each of the three days were based on the calculations for day 1. This is so that deuteration of the higher concentration samples does not affect the predicted integral. This however means the enhancement calculation does not take into account any deuteration that occurred to the 1 mM sample across the three days.

#### 8.3.4 Thermally polarised spectra of quinoline using standard concentrations for comparison

The 2D techniques described in Chapter 5 must be compared to thermally polarised spectra. To achieve this, a series of spectra have been collected using a standard concentration of quinoline in a sample without any catalyst present. The spectra have therefore been collected using a 100 mM, 10 mM and 1 mM sample of quinoline. The spectra have been completed in two ways. Firstly, with the same parameters as are used in the hyperpolarised spectrum. These are presented in Table 8.6. Secondly, in the case this does not yield a spectrum with the majority of the expected correlations, the number of increments and/or scans per increment were increased to produce the expected spectrum.

Sequence	sw (ppm)	centre (ppm)	rg	ns	td	aq (s)
$^1\text{H}$ - $^1\text{H}$ COSY	3, 3	8.25, 8.25	64	1	64	0.85
$^1\text{H}$ - $^{13}\text{C}$ HSQC	3, 50	8.25, 140	2050	1	64	0.85
$^1\text{H}$ - $^{13}\text{C}$ HMBC	3, 50	8.25, 140	2050	1	64	0.85
$^1\text{H}$ - $^{13}\text{C}$ HMQC	1.6, 40	8.2, 135	2050	1	64	0.8

Table 8.6 Parameters used for selected 2D sequences with the flow system, where 'sw' is the spectral width, 'centre' is the centre of the spectral width, 'rg' is the receiver gain, 'ns' is the number of scans, 'td' is the number of increments and 'aq' is the acquisition time of each scan.



For the 100 mM quinoline sample, the spectra collected with the standard parameters used in the flow experiments were sufficient to gain good quality spectra in which most correlations were observed. To observe all correlations in the  $^1\text{H}$ - $^{13}\text{C}$  HMBC and  $^1\text{H}$ - $^{13}\text{C}$  HMQC NMR spectra, the number of scans was increased to 4 per 128 increments increasing the time of collection to 21 min and 27 sec and 20 min and 30 sec respectively.

For the 10 mM quinoline sample, only the spectra collected with standard parameters used in the flow experiments for the  $^1\text{H}$ - $^1\text{H}$  COSY and  $^1\text{H}$ - $^{13}\text{C}$  HSQC NMR sequences contained all the expected correlations. For the  $^1\text{H}$ - $^{13}\text{C}$  HMBC and  $^1\text{H}$ - $^{13}\text{C}$  HMQC NMR spectra, the number of scans had to be increased to 16 per 128 increments for all expected correlations to be observed. This increased the collection time for each spectra to increase to 1 hr 23 min 47 sec for the  $^1\text{H}$ - $^{13}\text{C}$  HMBC NMR spectrum and 1 hr 24 min 9 sec for the  $^1\text{H}$ - $^{13}\text{C}$  HMQC NMR spectrum.

For the 1 mM quinoline sample, only the spectra collected with standard parameters used in the flow experiments for the  $^1\text{H}$ - $^1\text{H}$  COSY NMR sequence contained all the expected correlations, although the signals were weak. For the remaining 3 heteronuclear sequences the number of scans was increased to 64 per 128 increments, making the collection an average to 5 hours and a half. Even after this time, none of the expected correlations were observed.

## 8.4 Reactions

All experimental procedures were performed under an atmosphere of either dinitrogen or argon, using standard Schlenk line techniques or an MBraun Unilab glovebox, unless otherwise stated. All NMR samples were made up in standard 5 mm NMR tubes of those equipped with a Young's tap where required.

### 8.4.1 $[\text{Ir}(\text{COD})\text{Cl}]_2$ <sup>215</sup>

$\text{IrCl}_3 \cdot 3\text{H}_2\text{O}$  (2.0012 g,  $352.69 \text{ g mol}^{-1}$ , 5.67 mmol) was suspended in water and 2-propanol (17 : 34 ml) in a 2-necked round bottomed flask and degassed with  $\text{N}_2$  for 20 min. COD (6 ml, 5.292 g,  $108 \text{ g mol}^{-1}$ , 0.0489 mol) was added under  $\text{N}_2$  and the mixture was heated at reflux at  $100 \text{ }^\circ\text{C}$  for a minimum of 24 hours. The dark solution turned from brown to yellow with a red precipitate. After this time, the mixture was

allowed to cool and the red precipitate was then filtered off and washed in a minimum amount of cold methanol. This was further dried on the high vacuum line. A red solid was collected (1.1647 g, 671.34 g mol<sup>-1</sup>, 1.73 mmol, 61 %). If the mixture had an oily appearance after the initial cooling, it was refluxed for a further 24 hours, then allowed to cool again and filtered as described before.

#### 8.4.2 [Ir( $\mu$ -MeO)(COD)]<sub>2</sub><sup>216</sup>

All the solvents used were dried and degassed before the experiment took place. The experiment was carried out under N<sub>2</sub> throughout.

KOH (0.1709 g, 56.1 g mol<sup>-1</sup>, 3 mmol) and [Ir(COD)Cl]<sub>2</sub> (1.0183 g, 671.34 g mol<sup>-1</sup>, 1.5 mmol) were weighed out into separate Schlenk tubes and both were evacuated. Methanol (120 ml) was evacuated and degassed. This was then transferred onto the solids by cannula (34 ml to KOH and 68 ml to the dimer). Once the KOH had dissolved, the solution was transferred to the iridium solution by cannula. This was then stirred at room temperature for a minimum of 30 min, until the mixture had turned a golden yellow.

Degassed water was then added by cannula and a yellow solid precipitated out. This was filtered out over a sinter glass (grade 3) immediately and dried on the high vac line. The yellow solid is the product (0.7621 g, 662.44 g mol<sup>-1</sup>, 1.15 mmol, 77 %). The solid must be filtered and dried as soon as possible as the solid can degrade in solution.

#### 8.4.3 [Ir(IMes)(COD)Cl]<sup>104</sup> (**IMes(a)**)

*Bis*-1,3-(2,4,6-trimethylphenyl) imidazole hydrochloride (IMes.HCl, 0.923 g, 2.72 mmol) and potassium tert-butoxide (0.336 g, 3 mmol) were added to a Schlenk flask. Dry THF (20 ml) was added to the flask and the reaction mixture was stirred for 30 min. [IrCl(COD)]<sub>2</sub> (0.915 g, 1.36 mmol) was dissolved in a minimum volume of dry THF and added to the first schlenk by cannula transfer and stirred for 1 hour. The solvent was then removed under vacuum and the resulting solid purified by column chromatography with an eluent of DCM:Acetone (19:1) resulting in a yellow/orange powder (1.12 g, 64 %).

#### 8.4.4 [Ir(IMes)(COD)NCMe]PF<sub>6</sub><sup>80</sup> (**IMes(b)**)

A solution of [IrCl(COD)(IMes)] (0.102 g, 0.160 mmol) in dry acetone (5 ml) was treated with AgPF<sub>6</sub> (46.5 mg, 0.184 mol) and stirred for 30 min at room temperature in the dark. This was then filtered through Celite under N<sub>2</sub>. Acetonitrile (1 ml) was then added to the solution and stirred under N<sub>2</sub> for 30 min at room temperature. The solvent was removed under vacuum to give an orange solid (0.0977 g, 78 %).

#### 8.4.5 [Ir(SIMes)(COD)Cl]<sup>104</sup> (**SIMes(a)**)

Under N<sub>2</sub>, a Schlenk tube was charged with [Ir(μ-OMe)(COD)]<sub>2</sub> (0.1416 g, 662.44 g mol<sup>-1</sup>, 0.21 mmol) and *bis*-1,3-(2,4,6-trimethylphenyl) imidazoline hydrochloride (SIMes.HCl, 0.139 g, 342.71 g mol<sup>-1</sup>, 0.40 mmol). Dry acetone (dried on a still over CaCO<sub>3</sub>, 15 ml) was added to the Schlenk tube by cannula. The bright yellow solution was stirred at room temperature for 30 mins, after which time it had turned a golden yellow colour. The solvent was removed in *vacuo* to give a golden yellow solid. The solid product was purified by flash column chromatography on silica in 19:1 DCM:acetone. (0.1989 g, 642.28 g mol<sup>-1</sup>, 77 %).

#### 8.4.6 [Ir(SIMes)(COD)NCMe]PF<sub>6</sub><sup>80</sup> (**SIMes(b)**)

A solution of [Ir(SIMes)Cl(COD)] (0.1302 g, 642.04 g mol<sup>-1</sup>, 0.2 mmol) in acetone (3 ml) was treated with silver hexafluorophosphate (50 mg, 252.83 g mol<sup>-1</sup>, 0.198 mmol) and stirred for 30 min at room temperature in the dark. This was filtered through celite (under a N<sub>2</sub> atmosphere) and acetonitrile (1 ml) added. This was stirred for 30 min at room temperature. The solvent was evaporated under vacuum. The resulting orange solid was isolated (0.0534, 796.89 g mol<sup>-1</sup>, 0.067 mmol, 33 %).

#### 8.4.7 *Bis*-1,3-cyclohexyl imidazole hydrochloride (ICy.HCl)<sup>217</sup>

A nitrogen atmosphere is required wherever possible. Cyclohexylamine (4.3 ml, 4.96 g, 99.17 g mol<sup>-1</sup>, 50 mmol) was added to toluene (50 ml) in a 250 ml round bottomed flask. Under N<sub>2</sub> and with intense stirring, paraformaldehyde (1.5 g, 50 mmol) was added. This was stirred intensely for 30 min at room temperature and then cooled to 0 °C. A further portion of cyclohexylamine (4.3 ml, 4.96 g, 99.17 g mol<sup>-1</sup> 50 mmol) was added and the solution stirred at 0 °C for a further 10 min.

3.3 M HCl (15 ml, 50 mmol) was added drop-wise and the solution allowed to warm up to room temperature. 40 % aqueous glyoxal (72.5 ml, 50 mmol) was added slowly and stirred at 50 °C for 12 hours. It was then allowed to cool. Diethyl ether (50 ml) was added followed by saturated sodium carbonate solution (25 ml). The layers were then separated.

The aqueous layer was washed with diethyl ether (3 x 50 ml) and the volatiles were removed under vacuum. This was then extracted with dichloromethane (75 ml), dried with magnesium sulphate, filtered and solvent removed under vacuum. A light brown solid (1.3451 g, 268.5 g mol<sup>-1</sup>, 5 mmol, 10 %) was produced which was stored under N<sub>2</sub>.

#### 8.4.8 [Ir(ICy)(COD)Cl]<sup>104</sup> (**ICy(a)**)

*Bis*-1,3-cyclohexyl imidazole hydrochloride (ICy.HCl, 381 mg, 1.4 mmol) and potassium tert-butoxide (160 mg, 1.4 mmol) were added to a Schlenk flask. Dry THF (20 ml) was added to the flask under an inert atmosphere and the reaction mixture was stirred for 30 min. [IrCl(COD)]<sub>2</sub> (240 mg, 0.36 mmol) was dissolved in a minimum volume of dry THF and added to the first schlenk by cannula transfer and stirred for 1 hour. The solvent was then removed under vacuum and the resulting solid purified by column chromatography with an eluent of DCM:Acetone (19:1) resulting in a yellow/orange powder (46 mg, 12 %).

#### 8.4.9 [Ir(ICy)<sub>2</sub>(COD)]Cl<sup>104</sup> (**ICy<sub>2</sub>(a)**)

*Bis*-1,3-cyclohexyl imidazole hydrochloride (ICy.HCl, 381 mg, 1.4 mmol) and potassium tert-butoxide (160 mg, 1.4 mmol) were added to a Schlenk flask. . Dry THF (20 ml) was added to the flask and the reaction mixture was stirred for 30 min. [IrCl(COD)]<sub>2</sub> (240 mg, 0.36 mmol) was dissolved in a minimum volume of dry THF and added to the first schlenk by cannula transfer and stirred for 1 hour. This produced a red solid which was filtered off in air (47 mg, 9 %).

## 8.5 Characterisation of catalyst precursors and active polarisation transfer catalysts

A series of typical  $^1\text{H}$  and appropriate 2D data is presented in section 8.5.5 for the characterisation of  $[\text{Ir}(\text{IMes})(\text{quinoline})_2(\text{H})_2(\text{NCMe})]\text{Cl}$  as a representative example of the procedures used.

### 8.5.1 $[\text{Ir}(\text{COD})\text{Cl}]_2$

NMR matches previously reported data and the solid was the expected colour.

### 8.5.2 $[\text{Ir}(\mu\text{-MeO})(\text{COD})]_2$

NMR matches previously reported data and the solid was the expected colour.

### 8.5.3 $[\text{Ir}(\text{IMes})(\text{COD})\text{Cl}]$ (**IMes(a)**)

$^1\text{H}$  NMR (MeOD, 400 MHz, 300 K): 7.22 (s, 2H, N-CH-CH-N), 7.04 (s, broad, 4H, CH<sup>mes</sup>), 3.99 (m, 2H, CH<sup>COD</sup>), 3.08 (m, 2H, CH<sup>COD</sup>), 2.36 (s, 6H, CH<sub>3</sub><sup>mes</sup>), 2.29 (s, 6H, CH<sub>3</sub><sup>mes</sup>), 2.18 (s, 6H, CH<sub>3</sub><sup>mes</sup>), 1.68 (m, 4H, CH<sub>2</sub><sup>COD</sup>), 1.30 (m, 4H, CH<sub>2</sub><sup>COD</sup>).  $^{13}\text{C}\{^1\text{H}\}$  NMR (MeOD, 300 K): 179.3 (N-C-N), 138.5 (qC<sup>ar</sup>), 136.8 (qC<sup>ar</sup>), 136.2 (N-qC<sup>ar</sup>), 134.5 (qC<sup>ar</sup>), 129.2 (CH<sup>ar</sup>), 127.9 (CH<sup>ar</sup>), 123.8 (N-CH-CH-N), 81.4 (CH<sup>cod</sup>), 51.8 (CH<sup>cod</sup>), 32.7 (CH<sub>2</sub><sup>cod</sup>), 28.3 (CH<sub>2</sub><sup>cod</sup>), 19.8 (CH<sub>3</sub><sup>mes</sup>), 18.7 (CH<sub>3</sub><sup>mes</sup>), 17.2 (CH<sub>3</sub><sup>mes</sup>).

These results are similar to those in the literature<sup>94</sup> which were completed in chloroform.

### 8.5.4 $[\text{Ir}(\text{IMes})(\text{py})_3(\text{H})_2]\text{Cl}$

$^1\text{H}$  NMR (MeOD, 500 MHz, 243 K): 8.58 (d,  $J = 4.37$  Hz, 38H, *o*H, free py), 8.34 (d,  $J = 4.98$  Hz, 4H, *o*H, py trans to hydride), 8.09 (d,  $J = 5.43$  Hz, 2H, *o*H, py cis to hydride), 7.93 (tt,  $J = 7.67, 1.74$  Hz, 18H, *p*H, free py), 7.79 (tt,  $J = 7.53, 1.46$  Hz, 2H, *p*H, py trans to hydride), 7.69 (t,  $J = 7.67$  Hz, 1H, *p*H, py cis to hydride), 7.51 (m, 40H, *m*H, free py), 7.18 (s, 2H, N-CH-CH-N), 7.14 (m, 4H, *m*H, py trans to hydride), 6.99 (m, 2H, *m*H, py cis to hydride), 6.67 (s, 4H, CH<sup>mes</sup>), 2.20 (s, 6H, *p*CH<sub>3</sub><sup>mes</sup>), 2.06 (s, 12H, *o*CH<sub>3</sub><sup>mes</sup>), -22.52 (s, 2H, hydrides).

$^{13}\text{C}\{^1\text{H}\}$  NMR (MeOD, 243 K): Q (N-C-N), 167.5 (N-qCH<sup>ar</sup>), 155.3 (*o*C, py cis to hydride), 154.3 (*o*C, py trans to hydride), 148.6 (*o*C, free py), 138.2 (qC<sup>ar</sup>), 137.4 (*p*C, free py), 136.3 (*p*C, py cis to hydride), 135.8 (*p*C, py trans to hydride), 135.1 (qC<sup>ar</sup>), 128.4 (CH<sup>ar</sup>), 125.3 (*m*C, py cis to hydride), 125.2 (*m*C, py trans to hydride), 124.4 (*m*C, free py), 122.4 (N-CH-CH-N), 19.7 (*p*CH<sub>3</sub><sup>mes</sup>), 17.7 ( $\sigma$ CH<sub>3</sub><sup>mes</sup>).

#### 8.5.5 [Ir(IMes)(quinoline)<sub>2</sub>(H)<sub>2</sub>(NCMe)]Cl

It has not been possible to connect the pyridine ring to the phenyl ring in either bound quinoline ligands. The signals corresponding to these protons and carbons are therefore referred to as H-ph and C-ph respectively. ‘nbr’ means the signal is not base line resolved and therefore a reliable integral cannot be collected and it may have not been possible to ascertain correlations to this signal. A labelled chemical structure of quinoline is included in labels of quinoline, see section 8.7.2.1.

$^1\text{H}$  NMR (MeOD, 400 MHz, 250 K): 9.41 (d,  $J = 4.83$  Hz, 1H, H2 trans to hydride), 9.36 (d,  $J = 9.09$  Hz, 1H, H2 cis to hydride), 8.51 (d,  $J = 7.95$  Hz, 1H, H4 trans to hydride), 8.29 (m, 1H, H-ph), 8.19 (d,  $J = 7.95$  Hz, 1H, H-ph), 7.91 (t,  $J = 7.95$  Hz, 1H, H3 cis to hydride), 7.84 (t,  $J = 7.95$  Hz, nbr), 7.77 (m, nbr, H5-ph), 7.67 (nbr, H8-ph), 7.60 (m, 1H, H3 trans to hydride), 7.28 (t,  $J = 7.38$  Hz, 1H, H6-ph), 7.14 (s, 2H, N-CH-CH-N), 6.96 (s, 2H, CH<sup>mes</sup>), 6.83 (m, 1H, H-ph), 6.74 (t,  $J = 7.95$  Hz, 1H, H7-ph), 6.38 (s, 2H, CH<sup>mes</sup>), 2.38 (s, 6H, CH<sub>3</sub><sup>mes</sup>), 2.10 (s, 6H, CH<sub>3</sub><sup>mes</sup>), 2.07 (s, 3H, bound NCCH<sub>3</sub>), 1.71 (t,  $J = 3.00$  Hz, 6H, CH<sub>3</sub><sup>mes</sup>), -20.45 (d,  $J = 6.55$  Hz, 1H, hydride), -22.54 (d,  $J = 6.19$  Hz, 1H, hydride).

$^{13}\text{C}\{^1\text{H}\}$  NMR (MeOD, 250 K): 156.0 (C2 trans to hydride), 154.6 (C-ph), 149.1 (qC9), 147.2 (qC9), 138.4 (C4 trans to hydride), 138.1 (qC<sup>ar</sup>), 137.7 (C-ph), 137.3 (N-qCH<sup>ar</sup>), 135.6 (qC<sup>ar</sup>), 135.3 (qC<sup>ar</sup>), 129.7 (C3 cis to hydride), 129.3 (C7-ph), 128.8 (qC10), 128.4 (CH<sup>mes</sup>), 128.3 (CH<sup>mes</sup>), 126.6 (C6-ph), 122.4 (N-CH-CH-N), 122.1 (qC10), 121.8 (C-ph), 117.8 (NCCH<sub>3</sub>), 19.8 (CH<sub>3</sub><sup>mes</sup>), 17.6 (CH<sub>3</sub><sup>mes</sup>), 17.0 (CH<sub>3</sub><sup>mes</sup>), 1.93 (NCCH<sub>3</sub>).

Below are representative 1D and 2D spectra that are typically used in the characterisation of chemical structures.

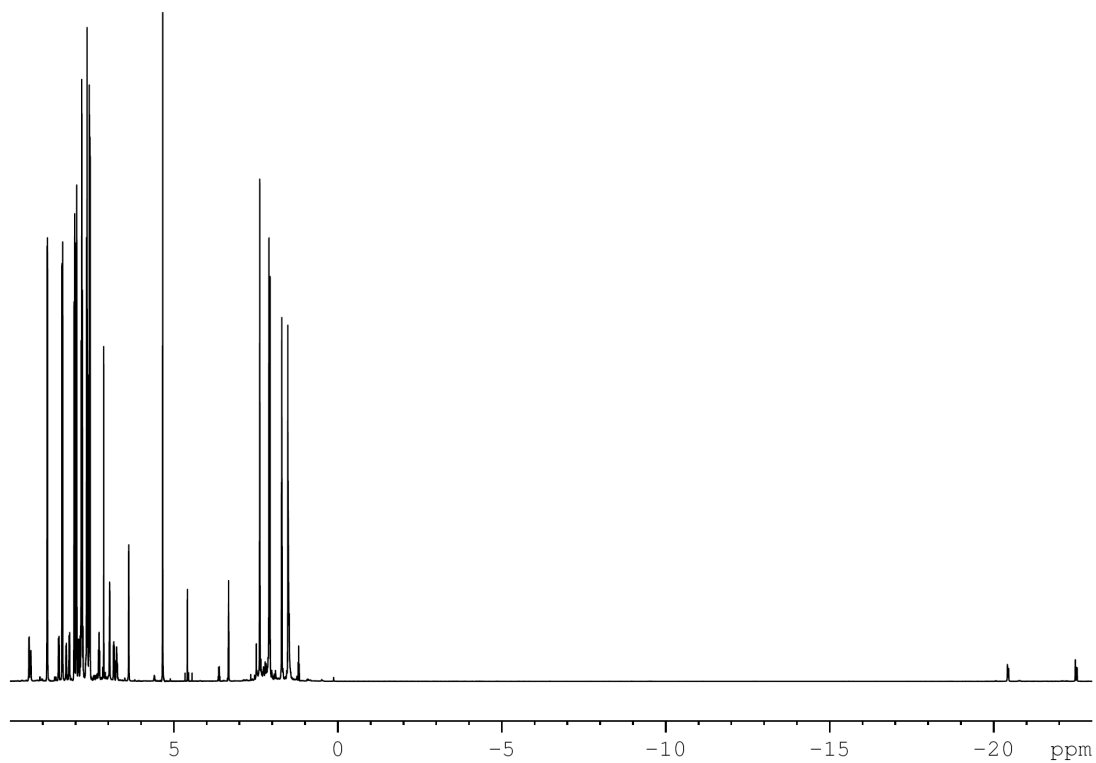


Figure 8.23  $^1\text{H}$  NMR spectrum of  $[\text{Ir}(\text{IMes})(\text{H})_2(\text{quinoline})_2(\text{NCMe})]\text{Cl}$ .

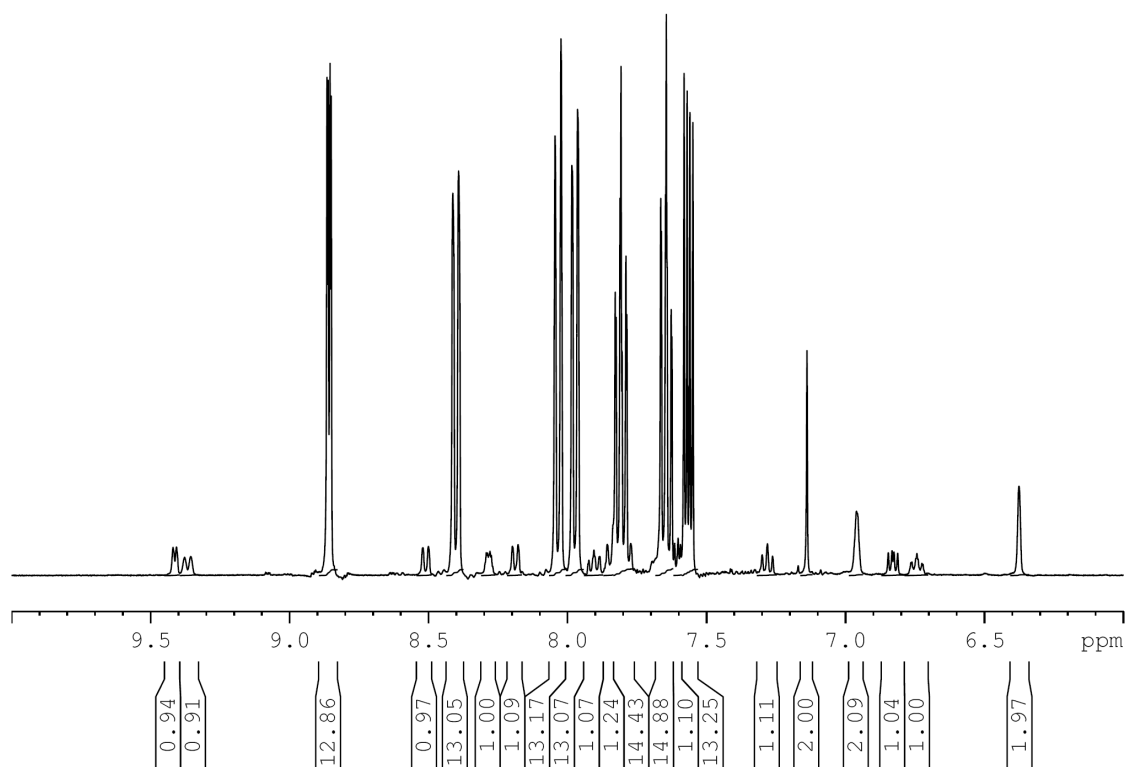


Figure 8.24  $^1\text{H}$  NMR spectrum of  $[\text{Ir}(\text{IMes})(\text{H})_2(\text{quinoline})_2(\text{NCMe})]\text{Cl}$  expanded to show the complicated aromatic region, including the relative integrals of the signals.

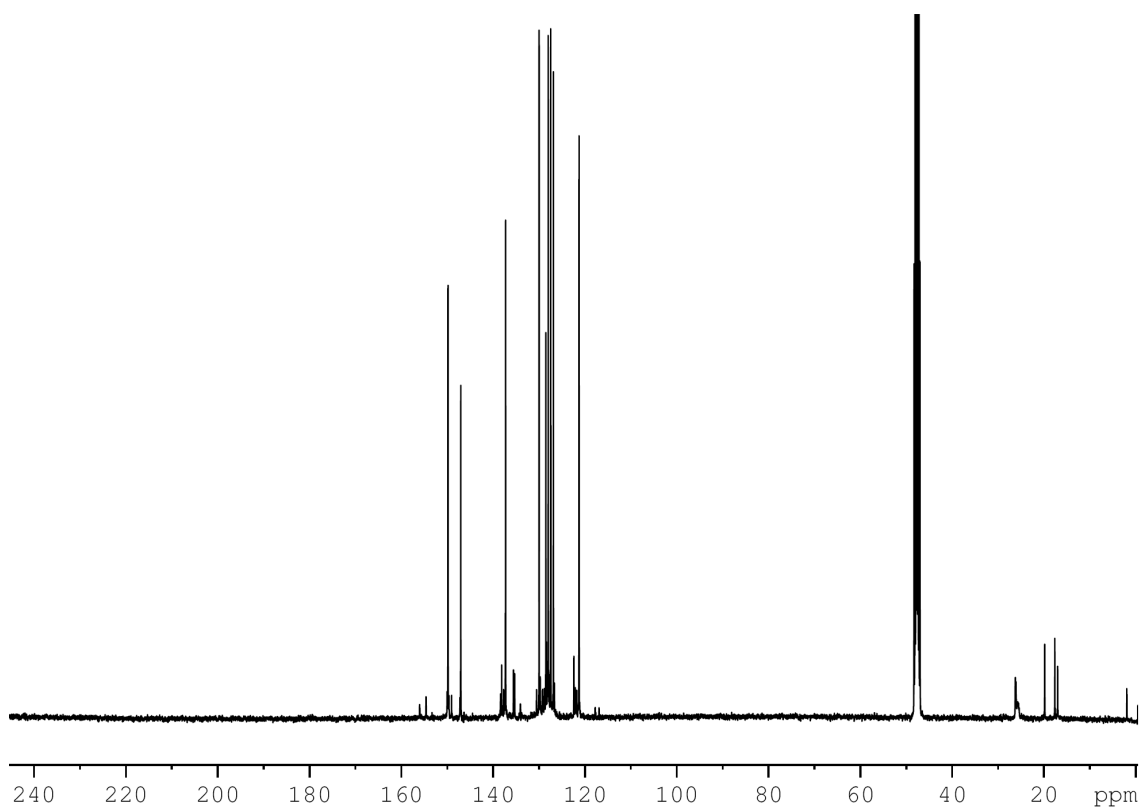


Figure 8.25  $^{13}\text{C}\{^1\text{H}\}$  NMR spectrum of  $[\text{Ir}(\text{IMes})(\text{H})_2(\text{quinoline})_2(\text{NCMe})]\text{Cl}$ .

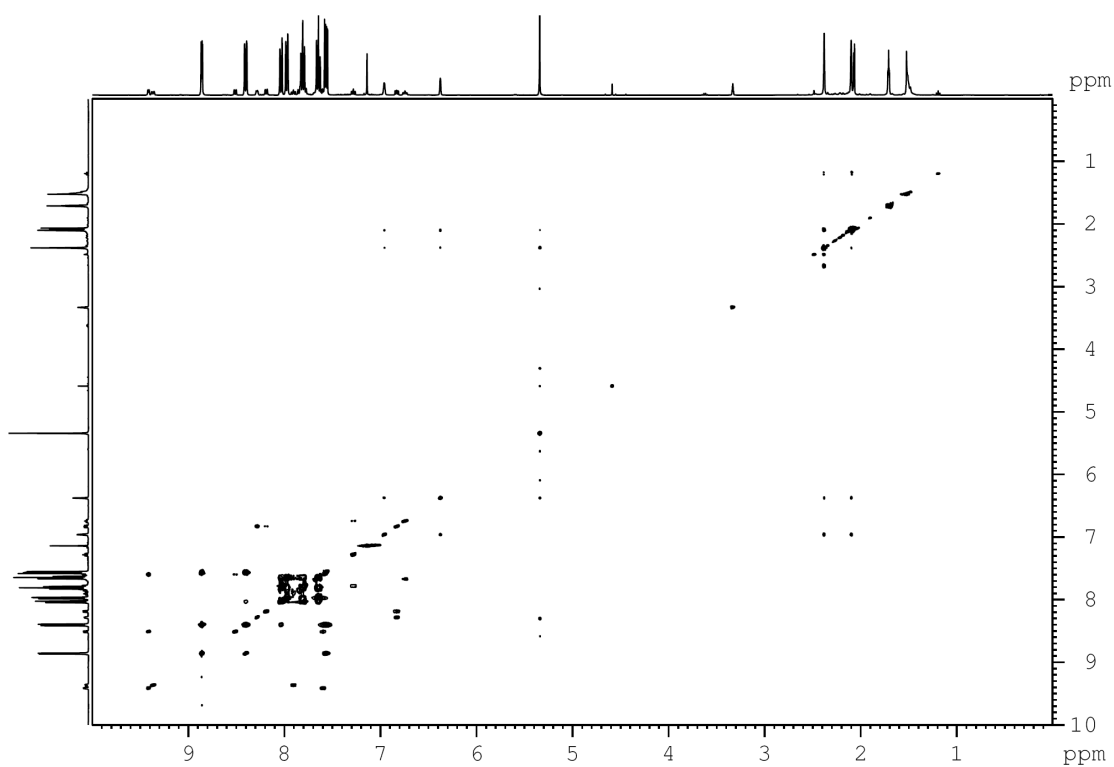


Figure 8.26  $^1\text{H}-^1\text{H}$  COSY NMR spectrum of  $[\text{Ir}(\text{IMes})(\text{H})_2(\text{quinoline})_2(\text{NCMe})]\text{Cl}$ .



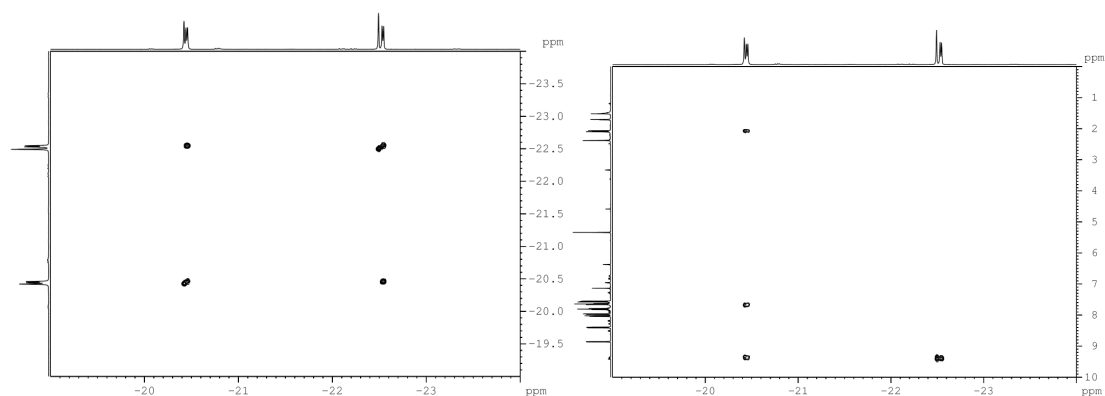


Figure 8.27  $^1\text{H}$ - $^1\text{H}$  COSY NMR spectrum of  $[\text{Ir}(\text{IMes})(\text{H})_2(\text{quinoline})_2(\text{NCMe})]\text{Cl}$  expanded to investigate the correlations corresponding to the hydride ligands. Left shows the correlations of the hydride ligands to each other, and right shows the correlations of the hydride ligands to the others protons in the complex.

In Figure 8.27 left, it is possible to observe not only the two doublets corresponding to the hydride ligands but also a singlet to the left of each. These singlets correspond to the two possible HD exchange products.

$^1\text{H}$ - $^{13}\text{C}$  HMQC NMR spectra are also collected, optimised for one, two and three bond couplings. Figure 8.28 represents such a spectrum.

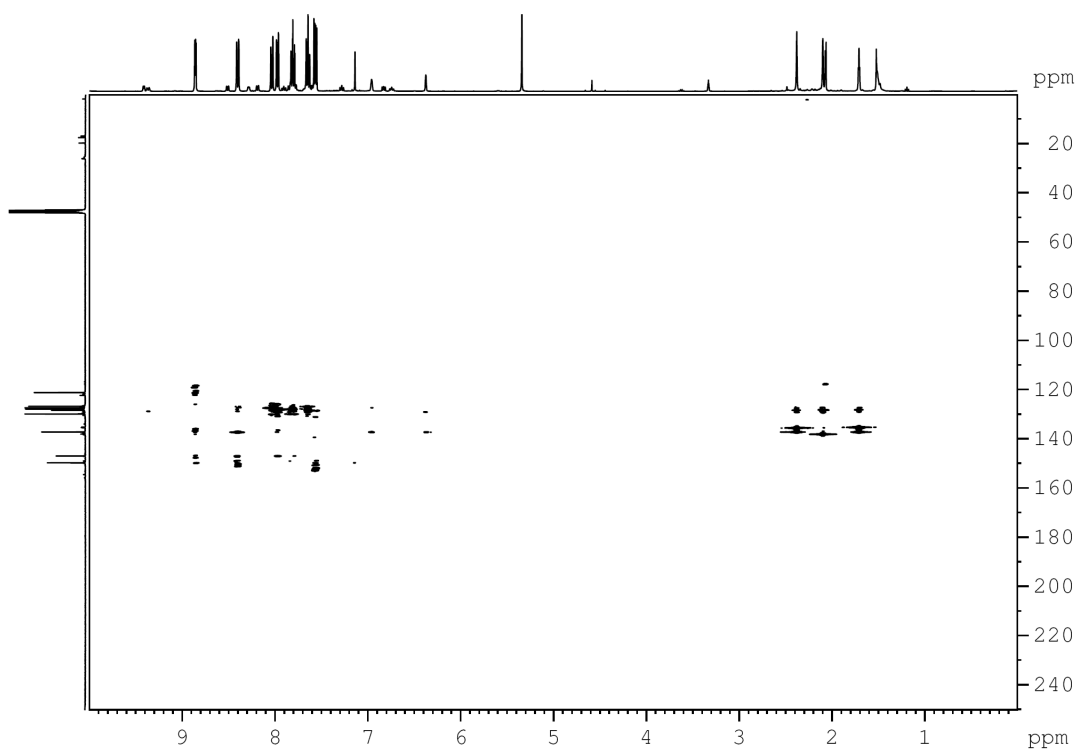


Figure 8.28  $^1\text{H}$ - $^{13}\text{C}$  HMQC NMR spectrum  $[\text{Ir}(\text{IMes})(\text{H})_2(\text{quinoline})_2(\text{NCMe})]\text{Cl}$  optimised for 2 bond couplings.

The signal intensity of the above spectra can be altered to observe different correlations.

#### 8.5.6 [Ir(IMes)(COD)(NCMe)]PF<sub>6</sub> (**IMes(b)**)

<sup>1</sup>H NMR (CDCl<sub>3</sub>, 500 MHz, 298 K): 7.125 (s, 2H, N-CH-CH-N), 7.09 (s, broad, 4H, CH<sup>mes</sup>), 4.021 (m, 2H, CH<sup>COD</sup>), 3.466 (m, 2H, CH<sup>COD</sup>), 2.415 (s, 6H, CH<sub>3</sub><sup>mes</sup>), 2.188 (s, 12H, CH<sub>3</sub><sup>mes</sup>), 1.857 (m, 2H, CH<sub>2</sub><sup>COD</sup>), 1.732 (m, 2H, CH<sub>2</sub><sup>COD</sup>), 1.573 (m, 4H, CH<sub>2</sub><sup>COD</sup>).  
<sup>13</sup>C{<sup>1</sup>H} NMR (CDCl<sub>3</sub>, 298 K): 213.8 (N-C-N), 173.3 (N-qC<sup>ar</sup>), 162.6 (CH<sup>cod</sup>), 145.9 (CH<sup>cod</sup>), 140.0 (qC<sup>ar</sup>), 135.0 (qC<sup>ar</sup>), 129.36 (CH<sup>ar</sup>), 124.96 (q-NCCH<sub>3</sub>), 124.27 (CH<sup>ar</sup>), 29.0 (CH<sub>2</sub><sup>cod</sup>), 32.88 (CH<sub>2</sub><sup>cod</sup>), 32.75 (CH<sub>2</sub><sup>cod</sup>), 21.06 (CH<sub>3</sub><sup>mes</sup>), 18.35 (CH<sub>3</sub><sup>mes</sup>).

#### 8.5.7 [Ir(SIMes)(COD)Cl] (**SIMes(a)**)

<sup>1</sup>H NMR (MeOD, 400 MHz, 295 K): 6.99 (s, 2H, CH<sup>mes</sup>), 6.97 (s, 2H, CH<sup>mes</sup>), 3.95 (m, 4H, N-CH<sub>2</sub>-CH<sub>2</sub>-N), 3.94 (m, 2H, CH<sup>COD</sup>), 3.21 (m, 2H, CH<sup>COD</sup>), 2.51 (s, 6H, CH<sub>3</sub><sup>mes</sup>), 2.38 (s, 6H, CH<sub>3</sub><sup>mes</sup>), 2.33 (s, 6H, CH<sub>3</sub><sup>mes</sup>), 1.63 (m, 4H, CH<sub>2</sub><sup>COD</sup>), 1.31 (m, 4H, CH<sub>2</sub><sup>COD</sup>).  
<sup>13</sup>C{<sup>1</sup>H} NMR (MeOD, 295 K): 206 (N-C-N), 137.6 (qC<sup>ar</sup>), 137.5 (qC<sup>ar</sup>), 136.3 (qC<sup>ar</sup>), 135.4 (qC<sup>ar</sup>), 129.2 (CH<sup>ar</sup>), 128.2 (CH<sup>ar</sup>), 82.4 (CH<sup>cod</sup>), 51.7 (CH<sup>cod</sup>), 51.5 (N-CH<sub>2</sub>-CH<sub>2</sub>-N), 32.9 (CH<sub>2</sub><sup>cod</sup>), 28.15 (CH<sub>2</sub><sup>cod</sup>), 19.8 (CH<sub>3</sub><sup>mes</sup>), 18.8 (CH<sub>3</sub><sup>mes</sup>), 17.4 (CH<sub>3</sub><sup>mes</sup>).

MS (ESI) *m/z* (%): 648 (M+ -Cl + acetonitrile), 607 (M+ -Cl).

These results are similar to those in the literature<sup>94,218</sup> which were completed in chloroform.

#### 8.5.8 [Ir(SIMes)(py)<sub>3</sub>(H)<sub>2</sub>]Cl

<sup>1</sup>H NMR (MeOD, 600 MHz): 8.57 (d, J = 4.31 Hz, 21H, *o*H, free py), 8.32 (broad, 4H, *o*H, py trans to hydride), 7.97 (d, J = 4.39 Hz, 2H, *o*H, py cis to hydride), 7.88 (tt, J = 7.66, 1.39 Hz, 8H, *p*H, free py), 7.76 (broad, 2H, *p*H, py trans to hydride), 7.66 (tt, J = 7.56, 1.64 Hz, 1H, *p*H, py cis to hydride), 7.46 (broad, 20H, *m*H, free py), 7.12 (broad, 4H, *m*H, py trans to hydride), 6.97 (t, J = 6.72 Hz, 2H, *m*H, py cis to hydride), 6.63 (s, 4H, CH<sup>Ar, mes</sup>), 4.58 (s, 4H, free H<sub>2</sub>), 3.90 (s, 4H, N-CH<sub>2</sub>-CH<sub>2</sub>-N), 2.27 (s, 12H, *o*CH<sub>3</sub><sup>mes</sup>), 2.16 (s, 6H, *p*CH<sub>3</sub><sup>mes</sup>), -22.69 (s, 2H, hydrides).

$^{13}\text{C}\{^1\text{H}\}$  NMR (MeOD): 208.6 (N-C-N), 179.7 (N-qCH<sup>ar</sup>), 154.8 (oC, py trans to hydride), 154.0 (oC, py cis to hydride), 148.6 (oC, free py), 138.4 (pC, py trans to hydride), 137.1 (pC, free py), 136.4 (qC<sup>ar</sup>), 135.9 (pC, py cis to hydride), 128.7 (CH<sup>ar</sup>), 128.4 (qC<sup>ar</sup>), 125.1 (mC, py cis to hydride), 124.9 (mC, py trans to hydride), 124.4 (mC, free py), 50.4 (N-CH<sub>2</sub>-CH<sub>2</sub>-N), 19.4 (pCH<sub>3</sub><sup>mes</sup>), 17.4 (oCH<sub>3</sub><sup>mes</sup>).

#### 8.5.9 Bis-1,3-cyclohexyl imidazole hydrochloride (ICy.HCl)

$^1\text{H}$  NMR (CDCl<sub>3</sub>, 500 MHz, 298 K): 10.97 (s, 1H, N-CH-N), 7.31 (s, 2H, N-CH-CH-N), 4.59 (tt, J = 12.0, 3.8 Hz, 2H, CH<sup>cy</sup>), 2.24 (d, J = 11.5 Hz, 4H, CH<sub>2</sub><sup>cy</sup>), 1.93 (dm, J = 13.9 Hz, 4H, CH<sub>2</sub><sup>cy</sup>), 1.76 (m, 4H, CH<sub>2</sub><sup>cy</sup>), 1.52 (qt, J = 13.2, 3.2 Hz, 4H, CH<sub>2</sub><sup>cy</sup>), 1.28 (qt, J = 13.1, 3.7 Hz, 4H, CH<sub>2</sub><sup>cy</sup>).  $^{13}\text{C}\{^1\text{H}\}$  NMR (CDCl<sub>3</sub>, 298 K): 136.6 (N-CH-N), 119.1 (N-CH-CH-N), 59.7 (CH<sup>cy</sup>), 33.53 (CH<sub>2</sub><sup>cy</sup>), 24.8 (CH<sub>2</sub><sup>cy</sup>), 24.6 (CH<sub>2</sub><sup>cy</sup>).

MS (ESI) *m/z* (%): 234 (ICy -Cl), 233 (ICy -Cl -H)

#### 8.5.10 [Ir(ICy)(COD)Cl] (ICy(a))

$^1\text{H}$  NMR (MeOD, 400 MHz, 300 K): 7.16 (s, 2H, N-CH-CH-N), 5.13 (m, 2H, CH<sup>Cy</sup>), 4.46 (m, 2H, CH<sup>COD</sup>), 3.04 (m, 2H, CH<sup>COD</sup>), 2.3 – 1.0 (m, 28H, CH<sub>2</sub><sup>Cy</sup> and CH<sub>2</sub><sup>COD</sup>).  $^{13}\text{C}\{^1\text{H}\}$  NMR (MeOD, 300 K): 176.5 (N-C-N), 117.5 (N-CH-CH-N), 82.6 (CH<sup>cod</sup>), 59.9 (CH<sup>Cy</sup>), 51.3 (CH<sup>cod</sup>), 33.7, 33.6, 33.3, 29.2, 25.8, 25.5, 24.9 (CH<sub>2</sub><sup>Cy</sup> and CH<sub>2</sub><sup>COD</sup>).

MS (ESI) *m/z* (%): 531.2 (M - Cl - H), 574.3 (M - Cl +acetonitrile).

These results are similar to those in the literature<sup>94,95</sup> which were completed in DCM.

#### 8.5.11 [Ir(ICy)(py)<sub>3</sub>(H)<sub>2</sub>]Cl

$^1\text{H}$  NMR (MeOD, 400 MHz, 280 K): 8.75 (d, J = 4.82 Hz, 4H, oH, py trans to hydride), 8.54 (dt, J = 4.36, 1.52 Hz, 13H, oH, free py), 8.31 (d, J = 5.04 Hz, 2H, oH, py cis to hydride), 8.00 (tt, J = 7.69, 1.54 Hz, 2H, pH, py trans to hydride), 7.94 (tt, J = 7.69, 1.54 Hz, 1H, pH, py cis to hydride), 7.88 (tt, J = 7.69, 1.68 Hz, 4.5H, pH, free py), 7.47 (under free py signal, correlation observed in COSY, mH, py trans to hydride), 7.46 (m, 16H, mH, free py), 7.27 (m, 2H, mH, py cis to hydride), 7.22 (s, 4H, N-CH-CH-N), 4.30 (m, 2H, CH<sup>Cy</sup>), 2.25-0.6 (m, 20H, CH<sub>2</sub><sup>Cy</sup>), -22.49 (s, 2H, hydrides).

$^{13}\text{C}\{^1\text{H}\}$  NMR (MeOD, 280 K): 197.6 (N-C-N), 156.4 (*o*C, py cis to hydride), 154.7 (*o*C, py trans to hydride), 148.7 (*o*C, free py), 137.39 (*p*C, py trans to hydride), 137.2 (*p*C, free py), 136.8 (*p*C, py cis to hydride), 126.3 (*m*C, py trans to hydride), 125.9 (*m*C, py cis to hydride), 124.3 (*m*C, free py), 117.7 (N-CH-CH-N), 59.2 ( $\text{CH}^{\text{Cy}}$ ), 33.0 ( $\text{CH}_2^{\text{Cy}}$ ), 25.6 ( $\text{CH}_2^{\text{Cy}}$ ), 24.8 ( $\text{CH}_2^{\text{Cy}}$ ).

8.5.12  $[\text{Ir}(\text{ICy})_2(\text{COD})]\text{Cl}$  (**ICy<sub>2</sub>(a)**, 800.58 g mol<sup>-1</sup>)

$^1\text{H}$  NMR (MeOD, 400 MHz, 300 K): 7.45 (s, 4H, N-CH-CH-N), 5.50 (s, 4H,  $\text{CH}^{\text{Cy}}$ ), 4.01 (m, 4H,  $\text{CH}^{\text{COD}}$ ), 2.5 - 0.8 (m, 28H,  $\text{CH}_2^{\text{Cy}}$  and  $\text{CH}_2^{\text{COD}}$ ).  $^{13}\text{C}\{^1\text{H}\}$  NMR (MeOD, 300 K): 174.7 (N-C-N), 119.1 (N-CH-CH-N), 74.1 ( $\text{CH}^{\text{cod}}$ ), 59.6 ( $\text{CH}^{\text{Cy}}$ ), 35.3, 33.2, 31.8, 25.3, 25.1, 24.5 ( $\text{CH}_2^{\text{Cy}}$  and  $\text{CH}_2^{\text{COD}}$ ).

MS (ESI) *m/z* (%): 765.4 (M<sup>+</sup> -Cl).

These results are similar to those in the literature<sup>95</sup> which were completed in DCM.

## 8.6 Acetal and hemiacetal products of 4-carboxaldehydepiperidine and methanol

4-carboxaldehydepiperidine (Figure 8.29a) undergoes a spontaneous reaction with methanol to produce a hemiacetal product (Figure 8.29b), and upon addition of a suitable acid, reacts with a further equivalent of methanol to produce an acetal product (Figure 8.29c).

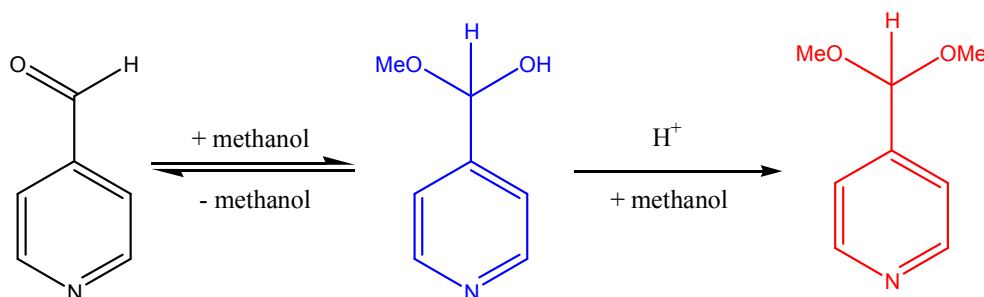


Figure 8.29 The spontaneous and acid catalysed reactions of 4-carboxaldehydepiperidine (a) with methanol producing a hemiacetal (b) and an acetal (c).

The substrates presented in Figure 8.29 are characterised in the following sections.

Mass spectrometry data for these products are presented in Chapter 6.

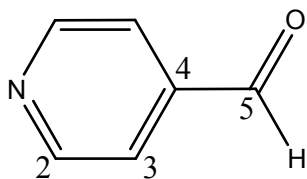
8.6.1  $^1\text{H}$  and  $^{13}\text{C}$  NMR data for 4-carboxaldehyde pyridine

Figure 8.30 Labelled structure of 4-carboxaldehyde pyridine.

$^1\text{H}$  NMR ( $d_1$ -chloroform, 400 MHz, 298 K): 10.11 (s, 1H, **H5**), 8.95 (d,  $J = 4.5$  Hz, 2H, **H2**), 7.73 (d,  $J = 4.47$  Hz, 2H, **H3**).  $^{13}\text{C}\{^1\text{H}\}$  NMR ( $d_1$ -chloroform, 298 K): 191.6 (**C5**), 151.1 (**C2**), 141.5 (q, **C4**), 122.2 (**C3**).

$^1\text{H}$  NMR ( $d_4$ -methanol, 400 MHz): 10.09 (s, 1H, **H5**), 8.82 (d,  $J=4.46$  Hz, 2H, **H2**), 7.84 (d,  $J=4.42$  Hz, 2H, **H3**).

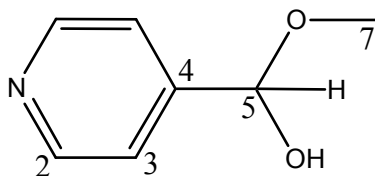
8.6.2  $^1\text{H}$  and  $^{13}\text{C}$  NMR data for the hemiacetal product,  $\text{NC}_5\text{H}_4\text{-}p\text{-CH(OMe)(OH)}$ 

Figure 8.31 Labelled structure of the hemiacetal product resulting from the spontaneous reaction of 4-carboxaldehyde pyridine with methanol.

$^1\text{H}$  NMR ( $d_1$ -chloroform, 400 MHz, 280 K): 8.49 (d,  $J = 5.86$  Hz, 2H, **H2**), 7.45 (d,  $J = 5.71$  Hz, 2H, **H3**), 5.51 (s, 1H, **H5**), 3.49 (s, **H7**).  $^{13}\text{C}\{^1\text{H}\}$  NMR ( $d_1$ -chloroform, 280 K): 150.3 (**C5**), 149.1 (**C2**), 121.5 (**C3**), 96.0 (q**C4**), 54.5 (**C7**).

The signal for **H7** of the  $\text{CH}_3$  isotopomer of this product is observed at 3.49 ppm and is nearly coincident with the signal for free methanol and its integral is therefore an overestimate of the number of protons present in that environment. The signal corresponding to **C7** is however clearly observed in the  $^{13}\text{C}\{^1\text{H}\}$  NMR spectrum at 54.5 ppm.

$^1\text{H}$  NMR ( $d_4$ -methanol, 400 MHz): 8.51 (d,  $J = 4.68$  Hz, 2H, **H2**), 7.52 (d,  $J = 4.47$  Hz, 2H, **H3**), 5.53 (s, 1H, **H5**). When this reaction was completed with deuterated methanol,

and therefore the methyl groups are deuterated, the signal corresponding to the methyl groups is not observed.

### 8.6.3 $^1\text{H}$ and $^{13}\text{C}$ NMR data for the acetal product, $\text{NC}_5\text{H}_4\text{-}p\text{-CH(OMe)}_2$

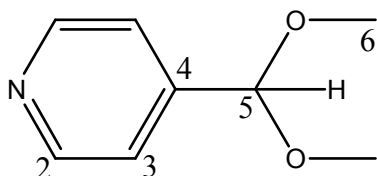


Figure 8.32 Labelled structure of the acetal product resulting from the acid catalysed reaction of 4-carboxaldehydepipridine with methanol.

$^1\text{H}$  NMR ( $d_4$ -methanol, 400 MHz): 8.87 (m, 2H, **H2**), 8.18 (m, 2H, **H3**), 5.75 (s, 1H, **H5**). When this reaction was completed with deuterated methanol, and therefore the methyl groups are deuterated, the  $^1\text{H}$  signal corresponding to the methyl groups (**H6**) is not observed.

## 8.7 $^1\text{H}$ and $^{13}\text{C}$ NMR data for substrates in methanol

The following  $^1\text{H}$  and  $^{13}\text{C}$  NMR data are completed at 298 K unless otherwise stated.

### 8.7.1 Substituted pyridines

#### 8.7.1.1 3-phenylpyridine

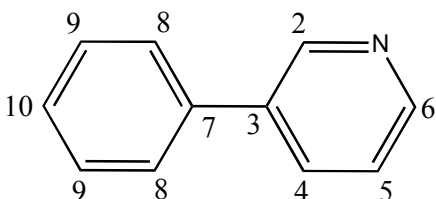


Figure 8.33 Labelled structure of 3-phenylpyridine.

$^1\text{H}$  NMR ( $d_4$ -methanol, 500 MHz): 8.77 (dd,  $J = 0.75, 2.31$  Hz, 1H, **H2**), 8.49 (dd,  $J = 1.56, 4.89$  Hz, 1H, **H6**), 8.06 (ddd,  $J = 1.61, 2.63, 7.95$  Hz, 1H, **H4**), 7.63 (m, 2H, **H8**), 7.49 (m, 1H, **H5**), 7.47 (m, 2H, **H9**), 7.40 (m,  $J = 7.40$ , 1H, **H10**).  $^{13}\text{C}\{^1\text{H}\}$  NMR ( $d_4$ -methanol): 147.5 (**C6**), 147.1 (**C2**), 137.5 (qC), 137.4 (qC), 135.3 (**C4**), 129.0 (**C9**), 128.2 (**C10**), 126.9 (**C8**), 124.2 (**C5**).

## 8.7.1.2 4-phenylpyridine

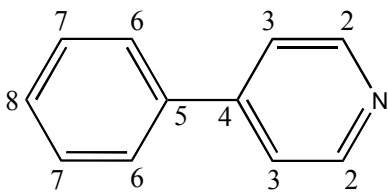


Figure 8.34 Labelled structure of 4-phenylpyridine.

$^1\text{H}$  NMR ( $d_4$ -methanol, 500 MHz): 8.56 (dd,  $J = 1.7, 4.59$  Hz, 2H, **H2**), 7.74 (m, 2H, **H6**), 7.69 (dd,  $J = 1.63, 4.66$  Hz, 2H, **H3**), 7.50 (m, 2H, **H7**), 7.45 (m, 2H, **H8**).  $^{13}\text{C}\{^1\text{H}\}$  NMR ( $d_4$ -methanol): 149.5 (qC), 149.3 (C2), 137.6 (qC), 129.3 (C8), 129.1 (C7), 126.8 (C6), 121.9 (C3).

## 8.7.1.3 3-benzoylpyridine

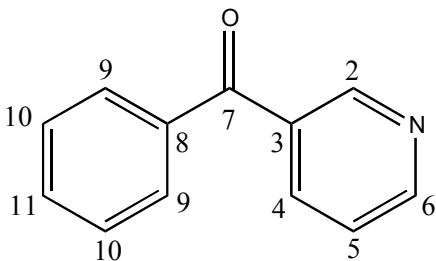


Figure 8.35 Labelled structure of 3-benzoylpyridine.

$^1\text{H}$  NMR ( $d_4$ -methanol, 500 MHz): 8.87 (dd,  $J = 0.83, 2.19$  Hz, 1H, **H2**), 8.75 (dd,  $J = 1.62, 4.93$  Hz, 1H, **H6**), 8.17 (ddd,  $J = 1.73, 2.19, 7.95$  Hz, 1H, **H4**), 7.79 (m, 2H, **H9**), 7.67 (m,  $J = 1.28$ , 1H, **H11**), 7.58 (ddd,  $J = 0.91, 4.94, 7.90$ , 1H, **H5**), 7.54 (m, 2H, **H10**).  $^{13}\text{C}\{^1\text{H}\}$  NMR ( $d_4$ -methanol): 194.8 (q, C=O, C7), 152.2 (C6), 149.9 (C2), 137.8 (C4), 136.7 (qC8), 133.8 (qC3), 133.2 (C11), 129.8 (C9), 128.6 (C10), 123.9 (C5).

## 8.7.1.4 4-(4-chlorobenzoyl)pyridine

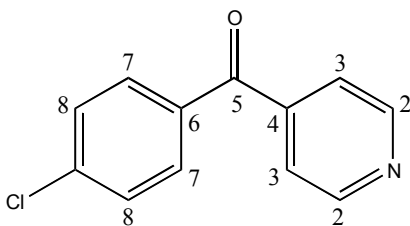


Figure 8.36 Labelled structure of 4-(4-chlorobenzoyl)pyridine.

$^1\text{H}$  NMR ( $d_4$ -methanol, 500 MHz): 8.76 (dd,  $J = 1.66, 4.39$  Hz, 2H, **H2**), 7.81 (m,  $J = 9.03$  Hz, 2H, **H7**), 7.66 (dd,  $J = 1.66, 4.43$  Hz, 2H, **H3**), 7.57 (m,  $J = 9.09$  Hz, 2H, **H8**).  
 $^{13}\text{C}\{^1\text{H}\}$  NMR ( $d_4$ -methanol): 193.82 (q, C=O, **C5**), 149.81 (**C2**), 145.05 (q**C4**), 139.9 (**C9**), 134.4 (q**C6**), 131.5 (**C7**), 128.9 (**C8**), 123.1 (**C3**).

## 8.7.2 Quinoline and substituted quinolines

### 8.7.2.1 Quinoline

The spectra used in the characterisation of quinoline are shown in Chapter 5.

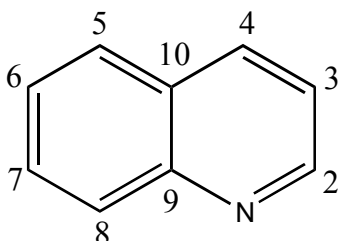


Figure 8.37 Labelled structure of quinoline.

$^1\text{H}$  NMR ( $d_4$ -methanol, 500 MHz): 8.82 (dd,  $J = 1.71, 4.31$  Hz, 1H, **H2**), 8.34 (dd,  $J = 0.82, 8.41$  Hz, 1H, **H4**), 8.02 (dd,  $J = 0.82, 8.47$  Hz, 1H, **H8**), 7.92 (dd,  $J = 1.3, 8.2$  Hz, 1H, **H5**), 7.76 ((m)d,  $J = 1.44, 6.90$  Hz, 1H, **H7**), 7.60 ((m)d,  $J = 1.09, 6.97$  Hz, 1H, **H6**), 7.52 (dd,  $J = 4.37, 8.34$  Hz, 1H, **H3**).

$^{13}\text{C}\{^1\text{H}\}$  NMR ( $d_4$ -methanol): 149.9 (dq,  $J = 4, 178$  Hz, **C2**), 147.5 (q**C9**), 137.1 (dt,  $J = 5.5, 163$  Hz, **C4**), 129.9 (dd,  $J = 9.2, 161$  Hz, **C7**), 128.7 (q**C10**), 128.0 (d,  $J = 161$  Hz, **C5**), 127.8 (dd,  $J = 7, 161$  Hz, **C8**), 126.8 (dd,  $J = 8.5, 162$  Hz, **C6**), 121.3 (dd,  $J = 8.4, 165$  Hz, **C3**).

### 8.7.2.2 Isoquinoline

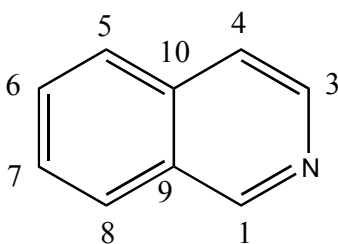


Figure 8.38 Labelled structure of isoquinoline.



$^1\text{H}$  NMR ( $d_4$ -methanol, 500 MHz): 9.17 (s, 1H, **H1**), 8.38 (d,  $J = 5.75$  Hz, 1H, **H3**), 8.04 (d,  $J = 8.17$  Hz, 1H, **H8**), 7.88 (d,  $J = 8.57$  Hz, 1H, **H5**), 7.76 (d,  $J = 5.85$  Hz, 1H, **H4**), 7.74 (m,  $J = 1.21$  Hz, 1H, **H6**), 7.64 (m,  $J = 1.11$  Hz, 1H, **H7**).  $^{13}\text{C}\{^1\text{H}\}$  NMR ( $d_4$ -methanol): 151.9 (**C1**), 141.5 (**C3**), 136.2 (q**C10**), 131.0 (**C6**), 128.9 (q**C9**), 127.7 (**C7**), 127.7 (**C8**), 126.4 (**C5**), 121.1 (**C4**).

### 8.7.2.3 4-methylquinoline

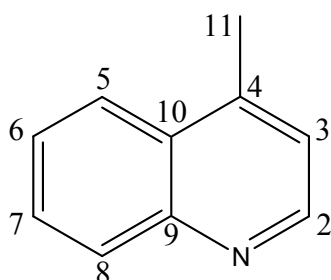


Figure 8.39 Labelled structure of 4-methylquinoline.

$^1\text{H}$  NMR ( $d_4$ -methanol, 500 MHz): 8.66 (d,  $J = 4.51$  Hz, 1H, **H2**), 8.10 (d,  $J = 8.43$  Hz, 1H, **H5**), 8.00 (d,  $J = 8.43$  Hz, 1H, **H8**), 7.74 (m, 1H, **H7**), 7.62 (m, 1H, **H6**), 7.36 (d,  $J = 4.43$  Hz, 1H, **H3**), 2.73 (s, 3H, **H11**).  $^{13}\text{C}\{^1\text{H}\}$  NMR ( $d_4$ -methanol): 149.6 (**C2**), 147.1 (q**C9**), 146.1 (q**C4**), 129.6 (**C7**), 128.4 (q**C10**), 128.3 (**C8**), 126.6 (**C6**), 124.1 (**C5**), 121.9 (**C3**), 17.4 (**C11**).

### 8.7.2.4 7-methylquinoline

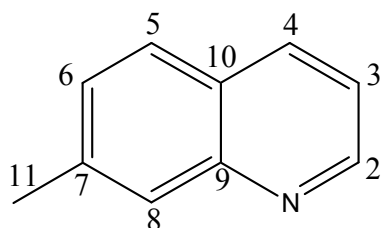


Figure 8.40 Labelled structure of 7-methylquinoline.

$^1\text{H}$  NMR ( $d_4$ -methanol, 500 MHz): 8.76 (dd,  $J=4.3, 1.75$  Hz, 1H, **H2**), 8.28 (d,  $J=8.33$ , 1H, **H4**), 7.81 (m, 1H, **H5**), 7.79 (m, 1H, **H8**), 7.45 (m, 1H, **H6**), 7.44 (m, 1H, **H3**), 2.55 (s, 3H, **H11**).  $^{13}\text{C}\{^1\text{H}\}$  NMR ( $d_4$ -methanol): 149.8 (**C2**), 147.7 (q**C9**), 140.7 (q**C**), 136.8 (**C4**), 129.0 (**C6**), 127.7 (**C5**), 126.8 (q**C**), 126.6 (**C8**), 120.5 (**C3**), 20.7 (**C11**).

## 8.7.2.5 8-methylquinoline

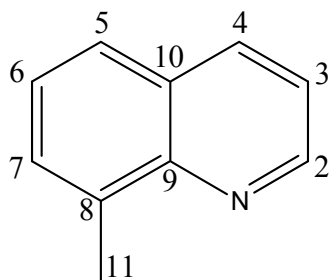


Figure 8.41 Labelled structure of 8-methylquinoline.

$^1\text{H}$  NMR ( $d_4$ -methanol, 400 MHz): 8.85 (dd,  $J = 4.21, 1.72$  Hz, 1H, **H2**), 8.29 (d,  $J = 8.28$ , 1H, **H4**), 7.75 (d,  $J = 8.21$  Hz, **H5**), 7.60 (d,  $J = 7.1$  Hz, 1H, **H7**), 7.50 (m, 1H, **H3**), 7.47 (m, 1H, **H6**), 2.75 (s, 3H, **H11**).  $^{13}\text{C}\{^1\text{H}\}$  NMR ( $d_4$ -methanol): 148.8 (**C2**), 146.6 (q**C9**), 136.9 (**C4**), 136.0 (q**C8**), 129.8 (**C7**), 128.6 (q, **C10**), 126.2 (**C6**), 126.0 (**C5**), 120.7 (**C3**), 17.0 (**C11**).

## 8.7.3 Other substrates

## 8.7.3.1 Indole

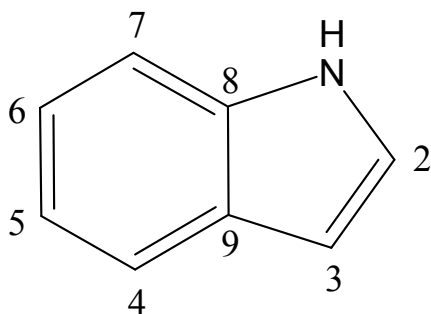


Figure 8.42 Labelled structure of indole.

$^1\text{H}$  NMR ( $d_4$ -methanol, 400 MHz): 10.39 (broad s, **H1**), 7.54 (d,  $J = 7.9$  Hz, 1H, **H7**), 7.38 (d,  $J = 8.23$  Hz, 1H, **H4**), 7.22 (d,  $J = 3.21$  Hz, 1H, **H2**), 7.09 (t,  $J = 7.6$  Hz, 1H, **H5**), 6.99 (t,  $J = 7.5$  Hz, 1H, **H6**), 6.43 (dd,  $J = 3.1, 0.8$  Hz, 1H, **H3**).  $^{13}\text{C}\{^1\text{H}\}$  NMR ( $d_4$ -methanol): 136.2 (q**C**), 128.0 (q**C**), 124.0 (**C2**), 120.7 (**C5**), 119.7 (**C7**), 118.5 (**C6**), 110.7 (**C4**), 100.8 (**C3**).

## 8.7.3.2 2-amino-4-(4-chlorophenyl)thiazole

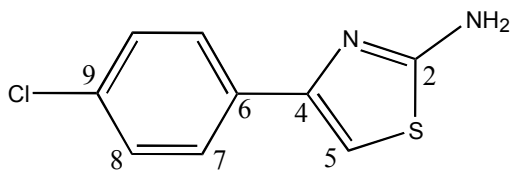


Figure 8.43 Labelled structure of 2-amino-4-(4-chlorophenyl)thiazole.

$^1\text{H}$  NMR ( $d_4$ -methanol, 500 MHz): 7.72 (d,  $J = 8.69$  Hz, 2H, **H7**), 7.34 (d,  $J = 8.69$  Hz, 2H, **H8**), 6.83 (s, 1H, **H5**).  $^{13}\text{C}\{^1\text{H}\}$  NMR ( $d_4$ -methanol): 170.1 (q), 149.3 (q), 133.7 (q), 132.9 (q), 128.3, 127.2, 102.2.

## 8.7.3.3 Benzothiazole

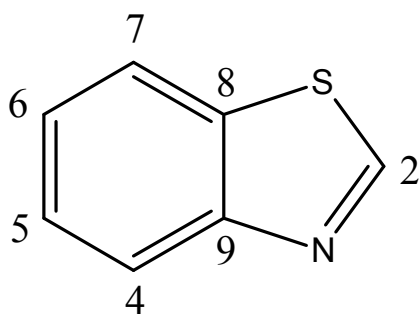


Figure 8.44 Labelled structure of benzothiazole.

$^1\text{H}$  NMR ( $d_4$ -methanol, 400 MHz): 9.25 (s, 1H, **H2**), 8.10 (m, 1H, **H7**), 8.08 (m, 1H, **H4**), 7.58 (t,  $J = 7.44$  Hz, 1H, **H5**), 7.51 (t,  $J = 7.35$  Hz, 1H, **H6**).  $^{13}\text{C}\{^1\text{H}\}$  NMR ( $d_4$ -methanol): 155.6 (C2), 152.6 (qC), 133.4 (qC), 126.1 (C5), 125.5 (C6), 122.4 (C4), 121.9 (C7).

## 9 Chapter 9 - Appendices

### 9.1 Complete data collected for the calculation of thermodynamic activation parameters

This section contains all rate data collected in the calculation of thermodynamic parameters, to calculations to predict rates at the temperatures involved in the temperature dependence investigations.

#### 9.1.1 Collection of NMR data for the calculation of exchange rates

A series of  $^1\text{H}$  EXSY NMR spectra were collected where the bound ligand is selectively excited and after a short mixing time, a NMR spectrum recorded. The mixing time allows for exchange and therefore the relative integrals of the bound and free ligand can be used to monitor the exchange process. The resultant absolute integrals of the bound and free ligands are turned into a percentage of each other and then plotted as a function of mixing time as demonstrated in Figure 9.1.

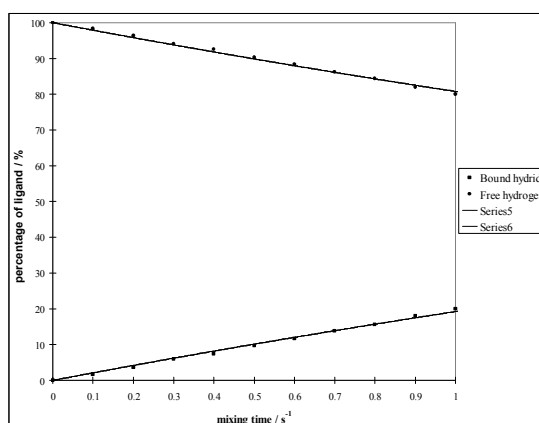


Figure 9.1 A plot of the percentage of bound ligands and free substrate derived from  $^1\text{H}$  EXSY NMR spectra against the mixing time implemented. This data was collected at 300 K and monitored the loss of hydride ligands from **ICy(a)** to free hydrogen.

This data was then entered into Dynafit<sup>108</sup> according to the details described below in section 9.1.2. The result is to gain a series of experimentally derived rate constants at a series of temperatures which can then be used to calculate thermodynamic parameters of activation as described in section 9.1.2.3.

### 9.1.2 Information pertaining to Dynafit<sup>108</sup>

The nonlinear regression module uses the Levenberg-Marquardt algorithm.<sup>219</sup> The time-course of (bio)chemical reactions is computed by the numerical integration of simultaneous first-order ordinary differential equations, using the Livermore Solver of ODE Systems (LSODE).<sup>220</sup> The composition of complex mixtures at equilibrium (e.g., in the concentration jump experiment where a complex mixture is incubated prior to the addition of a reagent) is computed by solving simultaneous nonlinear algebraic equations, namely, the mass balance equations for the component species, by using the multidimensional Newton-Raphson method.<sup>221</sup>

#### 9.1.2.1 Data file used for the model of the determination for the rate of loss of hydride ligands from **Carbene(a)**

Below is an example of the data file imported into Dynafit to complete calculations of rate of loss of hydride ligands from **Carbene(a)**.

[task]

data = progress

task = fit

model = hydrogen exchange

[mechanism]

IrH2 --> Ir + H2 : k1

H2 + Ir --> IrH2 : k2

[constants]

;initial estimates

k1 = 0.11132 ??, k2 = 0.004261 ??

[concentrations]

```

IrH2 = 100

H2 = 0

[responses]

[progress]

directory ./lsl275-h2/295 k/data

extension txt

file IrH2 | response IrH2 = 1

file H2 | response H2 = 1

[output]

directory ./lsl275-h2/295 K/output/fit

[end]

```

Dynafit uses the following equations in the calculation (Equation 9.1).

REACTION MECHANISM	$\text{IrH}_2 \rightleftharpoons \text{Ir} + \text{H}_2 : k_1 \quad k_2$
DIFERENTIAL EQUATIONS	$\frac{d[\text{IrH}_2]}{dt} = -k_1[\text{IrH}_2] + k_2[\text{Ir}][\text{H}_2]$
	$\frac{d[\text{Ir}]}{dt} = +k_1[\text{IrH}_2] - k_2[\text{Ir}][\text{H}_2]$
	$\frac{d[\text{H}_2]}{dt} = +k_1[\text{IrH}_2] - k_2[\text{Ir}][\text{H}_2]$

Equation 9.1 Reaction mechanism and differential equations used by Dynafit together with user data to calculate the rate of loss of hydride ligands from a catalyst.

#### 9.1.2.2 Data file used for the model of the determination for the rate of loss of substrate from **Carbene(a)**

Below is an example of the data file imported into Dynafit to complete calculations of rate of loss of substrate ligands from **Carbene(a)**. In all following calculations, the substrate ligand always refers to that bound *trans* to the hydride ligands.

[task]

data = progress

task = fit

model = pyridine exchange

[mechanism]

$\text{Irpy} \rightarrow \text{Ir} + \text{py} : k_1$

$\text{py} + \text{Ir} \rightarrow \text{Irpy} : k_2$

[constants]

;initial estimates

k1 = 0.801 ??, k2 = 0.7 ??

[concentrations]

Irpy = 100

py = 0

[responses]

[progress]

directory ./lsl275-py/295 k/data

extension txt

file Irpy | response Irpy = 1

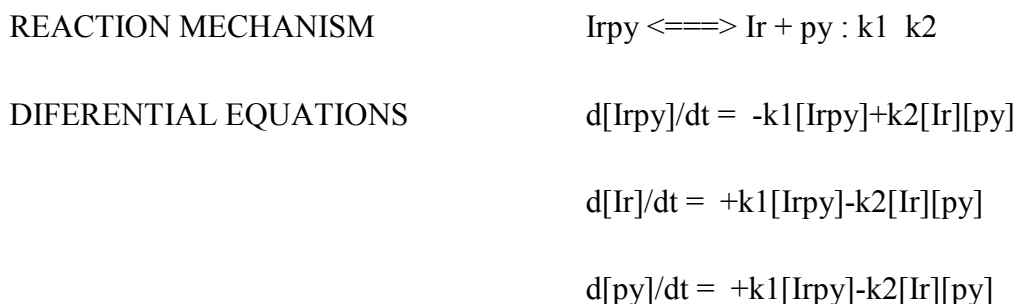
file py | response py = 1

[output]

directory ./lsl275-py/295 K/output/fit

[end]

Dynafit uses the following equations in the calculation (Equation 9.2).



Equation 9.2 Reaction mechanism and differential equations used by Dynafit together with user data to calculate the rate of loss of substrate ligands from a catalyst, with pyridine used as an example.

### 9.1.2.3 Data file used for the model of the determination for the rate of loss of hydride ligands from **IMes(c)** and **SIMes(c)**

Below is an example of the data file imported into Dynafit to complete calculations of rate of loss of hydride ligands from **IMes(c)** and **SIMes(c)** when activated in the presence of quinoline. This complex results in two hydride resonances, one corresponding to the hydride ligands trans to quinoline, and one corresponding to the hydride ligand trans to acetonitrile. The data was therefore measured by exciting just one resonance however this lead to the complication that the rate of interconversion of the two hydride ligands also had to be taken into account. This was completed using the following file.

[task]

data = progress

task = fit

model = hydrogen exchange

[mechanism]

$\text{IrH}_2 \rightarrow \text{Ir} + \text{H}_2 : k_1$

$\text{H}_2 + \text{Ir} \rightarrow \text{IrH}_2 : k_2$

$\text{IrH}_2 \rightarrow \text{Ir}_2\text{H} : k_3$



Ir2H --> IrH2 : k4

[constants]

k1 = 0.72328 ??, k2 = 0.004261 ??, k3 = 0.2 ??, k4 = 0.3 ??

[concentrations]

IrH2 = 100

H2 = 0

Ir2H = 0

[responses]

[progress]

directory ./lsl258-h2/268 k/data

extension txt

file IrH2 | response IrH2 = 1

file H2 | response H2 = 1

file Ir2H | response Ir2H = 1

[output]

directory ./lsl258-h2/268 K/output/fit

[end]

Dynafit uses the following equations in the calculation (Equation 9.3).

REACTION MECHANISM                            IrH2 <====> Ir + H2 : k1 k2

IrH2 <====> Ir2H : k3 k4

DIFERENTIAL EQUATIONS

$$d[\text{IrH}_2]/dt = -k_1[\text{IrH}_2] + k_2[\text{Ir}][\text{H}_2] - k_3[\text{IrH}_2] + k_4[\text{Ir}_2\text{H}]$$

$$d[\text{Ir}]/dt = +k_1[\text{IrH}_2] - k_2[\text{Ir}][\text{H}_2]$$

$$d[\text{H}_2]/dt = +k_1[\text{IrH}_2] - k_2[\text{Ir}][\text{H}_2]$$

$$d[\text{Ir}_2\text{H}]/dt = +k_3[\text{IrH}_2] - k_4[\text{Ir}_2\text{H}]$$

Equation 9.3 Reaction mechanism and differential equations used by Dynafit together with user data to calculate the rate of loss of hydride ligands from **IMes(c)** activated in the presence of quinoline.

### 9.1.3 Calculation of thermodynamic activation parameters

The thermodynamic parameters of activation for each catalytic system were calculated through using the Eyring method. This involves plotting a graph of  $(1/T)$  vs  $\ln(2k/T)$  where  $T$  is temperature in Kelvin and  $k$  is the experimentally measured rate constants in  $\text{s}^{-1}$ . This produces a straight line, the gradient and intercept of which can be used to derive the  $\Delta H^\ddagger$  and  $\Delta S^\ddagger$  according to Equation 9.4.

$$y = mx + c$$

$$\ln(k/T) = (-\Delta H^\ddagger/RT) + \ln(k_b/h) + (\Delta S^\ddagger/R)$$

Equation 9.4 Eyring equation.

### 9.1.4 Treatment of errors

The errors quoted by Dynafit are calculated to be correct to a 95 % confidence level. The standard errors have not been used as it has been published that they underestimate the error,<sup>222</sup> and therefore the ‘exact interval’ lower and upper limits have been presented.

When considering the calculation of thermodynamic activation parameters of loss of pyridine or hydride ligands, the errors are presented as standard errors correct to a 95 % confidence level.

9.1.5 Collected rate constants and thermodynamic activation parameters for a sample of **SIMes(a)** hydrogenated in the presence of pyridine

T / K	Observed rate constant from DynaFit / s <sup>-1</sup>	
	Loss of hydride ligands	Loss of pyridine ligands
261	0.360 (0.345 – 0.377)	0.429 (0.423 – 0.436)
263	0.460 (0.446 – 0.476)	0.541 (0.535 – 0.549)
268	0.889 (0.874 – 0.907)	1.067 (1.060 – 1.077)
272	1.444 (1.422 – 1.472)	1.843 (1.825 – 1.861)
276	2.423 (2.403 – 2.443)	3.126 (3.086 – 3.167)
280	4.016 (3.959 – 4.077)	4.864 (4.823 – 4.907)
284	6.309 (6.256 – 6.385)	7.447 (7.198 – 7.893)

Table 9.1 Rate constants (quoted to 3 d.p.) for the loss of pyridine and hydride ligands from **SIMes(a)** in the presence of pyridine at the indicated temperatures, with corresponding lower and upper limits to a 95 % confidence level.

The data in Table 9.1 was used to produce the Eyring plots shown in Figure 9.2.

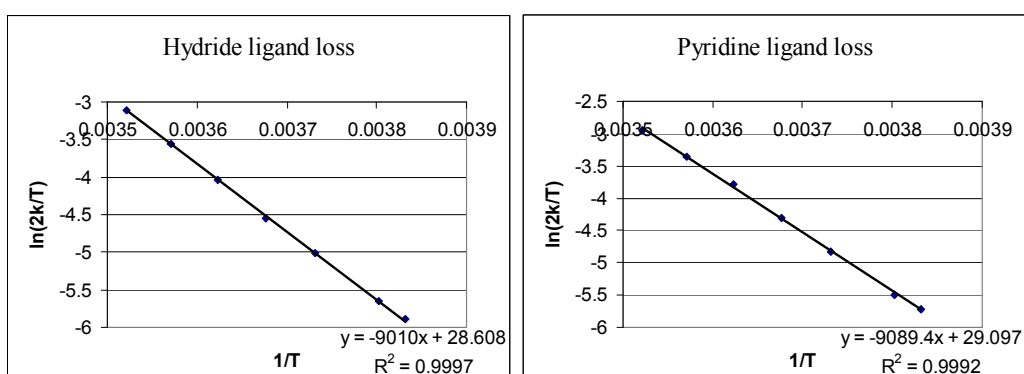


Figure 9.2 The Eyring plots derived for the loss of hydride ligands and pyridine ligands from **SIMes(a)** in the presence of pyridine with associated equations, produced from the data presented in Table 9.1.

Figure 9.2 displays the equations which can be used to calculate the thermodynamic parameters presented in Table 9.2.

Thermodynamic parameters	For ligand loss	
	Hydride	Pyridine
$\Delta H^\ddagger$ (kJ mol <sup>-1</sup> )	74.9 ± 0.2 (0.3 %)	75.6 ± 0.4 (0.5 %)
$\Delta S^\ddagger$ (J K <sup>-1</sup> mol <sup>-1</sup> )	40.3 ± 0.7 (1.7 %)	44.6 ± 1.5 (3.4 %)
$\Delta G_{300}^\ddagger$ (kJ mol <sup>-1</sup> )	62.8 ± 0.02 (0.03 %)	62.3 ± 0.05 (0.08 %)

Table 9.2 The thermodynamic parameters of activation for the loss of hydride ligands and pyridine ligands from **SIMes(a)** in the presence of pyridine.

The data presented in the above section has also been used to predict the rate of loss of pyridine and hydride ligands from **SIMes(a)** at the temperatures investigated by method 1 and 300 K for comparison purposes. The results are presented in Table 9.3.

Temperature		Predicted rate of loss of ligand from <b>SIMes(a)</b>	
°C	K	Hydride ligand	Pyridine ligand
0	273	1.68	2.05
20	293	17.19	21.37
30	303	49.04	61.53
40	313	130.99	165.74
50	323	329.56	420.29
27	300	36.06	45.13

Table 9.3 Predicted rates loss of pyridine and hydride ligands from **SIMes(a)** at the specified temperatures.

9.1.6 Collected rate constants and thermodynamic activation parameters for a sample of **ICy(a)** hydrogenated in the presence of pyridine

T / K	Observed rate constant from DynaFit / s <sup>-1</sup>	
	Loss of hydride ligands	Loss of pyridine ligands
285	N/C	0.204 (0.189 – 0.225)
290.1	N/C	0.308 (0.302 – 0.318)
295	0.112 (0.107 – 0.117)	0.769 (0.728 – 0.813)
300	0.213 (0.209 – 0.218)	1.129 (1.062 – 1.202)
305	0.371 (0.362 – 0.382)	2.175 (1.964 – 2.421)
310	0.632 (0.619 – 0.646)	5.069 (4.549 – 5.681)
315	1.141 (1.121 – 1.170)	8.489 (7.601 – 9.520)
320	1.980 (1.908 – 2.109)	16.34 (12.79 – 21.45)
325	3.665 (3.544 – 3.979)	N/C

Table 9.4 Rate constants (quoted to 3 d.p.) for the loss of pyridine and hydride ligands from **ICy(a)** in the presence of pyridine at the indicated temperatures, with corresponding lower and upper limits to a 95 % confidence level.

The data in Table 9.4 was used to produce the Eyring plots shown in Figure 9.3.

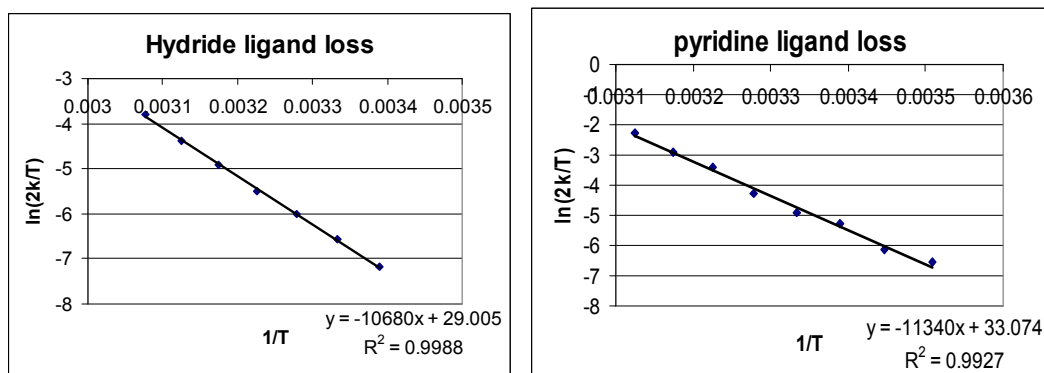


Figure 9.3 The Eyring plots derived for the loss of hydride ligands and pyridine ligands from **ICy(a)** in the presence of pyridine with associated equations, produced from the data presented in Table 9.4.

Figure 9.3 displays the equations which can be used to calculate the thermodynamic parameters presented in Table 9.5.

Thermodynamic parameters	For ligand loss	
	Hydride	Pyridine
$\Delta H^\ddagger$ (kJ mol <sup>-1</sup> )	88.7 ± 0.6 (0.7 %)	94.3 ± 1.1 (1.2 %)
$\Delta S^\ddagger$ (J K <sup>-1</sup> mol <sup>-1</sup> )	43.4 ± 2.0 (4.7 %)	77.6 ± 3.7 (4.8 %)
$\Delta G_{300}^\ddagger$ (kJ mol <sup>-1</sup> )	75.7 ± 0.02 (0.02 %)	71.1 ± 0.04 (0.06 %)

Table 9.5 The thermodynamic parameters of activation for the loss of hydride ligands and pyridine ligands from **ICy(a)** in the presence of pyridine.

The data presented in the above section has also been used to predict the rate of loss of pyridine and hydride ligands from **ICy(a)** at the temperatures investigated by method 1 and 300 K for comparison purposes. The results are presented in Table 9.6.

Temperature		Predicted rate of loss of ligand from <b>ICy(a)</b>	
°C	K	Hydride ligand	Pyridine ligand
0	273	0.0055	0.028
20	293	0.085	0.53
30	303	0.29	1.95
40	313	0.94	6.67
50	323	2.79	21.1
27	300	0.21	1.33

Table 9.6 Predicted rates loss of pyridine and hydride ligands from **ICy(a)** at the specified temperatures.

#### 9.1.7 Collected rate constants and thermodynamic activation parameters for a sample of **IMes(c)** hydrogenated in the presence of quinoline

Rate of loss of hydride ligands		Rate of loss of quinoline ligands	
T / K	Observed rate constant / s <sup>-1</sup>	T/ K	Observed rate constant / s <sup>-1</sup>
268	0.723 (0.674 – 0.778)	255	0.152 (0.145 – 0.161)
273	1.560 (1.496 – 1.632)	260	0.276 (0.264 – 0.294)
278	2.841 (2.733 – 2.965)	265	0.539 (0.523 – 0.557)
283	5.188 (5.000 – 5.415)	270	0.981 (0.957 – 1.010)
288	8.691 (8.442 – 9.013)	275	1.744 (1.683 – 1.824)
293	15.254 (14.694 – 15.840)		
298	25.533 (24.307 – 26.864)		
300	35.591 (34.057 – 37.898)		

Table 9.7 Rate constants (quoted to 3 d.p.) for the loss of quinoline and hydride ligands from **IMes(c)** in the presence of quinoline at the indicated temperatures, with corresponding lower and upper limits to a 95 % confidence level.

The data in Table 9.7 was used to produce the Eyring plots shown in Figure 9.4.

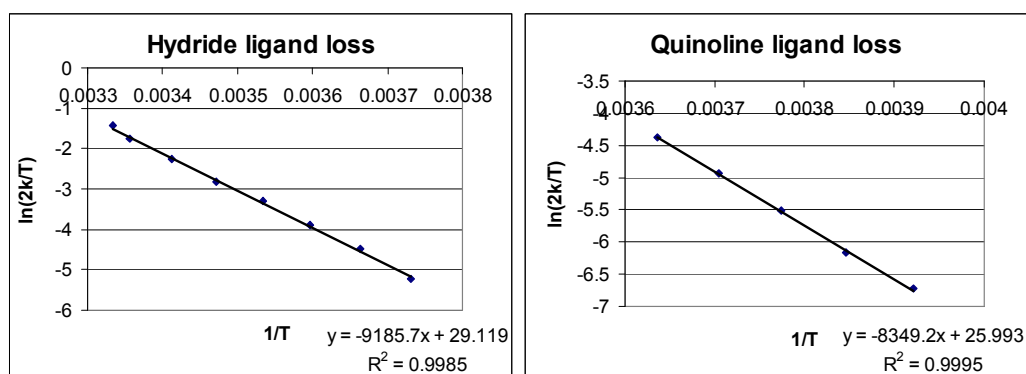


Figure 9.4 The Eyring plots derived for the loss of hydride ligands and quinoline ligands from **IMes(c)** in the presence of quinoline with associated equations, produced from the data presented in Table 9.7.

Figure 9.4 displays the equations which can be used to calculate the thermodynamic parameters presented in Table 9.8.

Thermodynamic parameters	For ligand loss	
	Hydride	Quinoline
$\Delta H^\ddagger$ (kJ mol <sup>-1</sup> )	76.3 ± 0.5 (0.7 %)	69.5 ± 0.6 (0.9 %)
$\Delta S^\ddagger$ (J K <sup>-1</sup> mol <sup>-1</sup> )	44.3 ± 1.8 (4 %)	19.0 ± 2.2 (11.7 %)
$\Delta G_{300}^\ddagger$ (kJ mol <sup>-1</sup> )	63.0 ± 0.03 (0.05 %)	63.8 ± 0.07 (0.1 %)

Table 9.8 The thermodynamic parameters of activation for the loss of hydride ligands and quinoline ligands from **IMes(c)** in the presence of quinoline.

The data presented in the above section has also been used to predict the rate of loss of quinoline and hydride ligands from **IMes(c)** at the temperatures investigated by method 1 and 300 K for comparison purposes. The results are presented in Table 9.9.

Temperature		Predicted rate of loss of ligand from <b>IMes(c)</b>	
°C	K	Hydride ligand	Quinoline ligand
0	273	1.47	1.39
20	293	19.59	14.65
30	303	45.78	31.77
40	313	124.56	79.15
50	323	318.88	186.53
27	300	33.47	23.88

Table 9.9 Predicted rates loss of quinoline and hydride ligands from **IMes(c)** at the specified temperatures.

9.1.8 Collected rate constant data for a sample of **SIMes(c)** hydrogenated in the presence of quinoline

Rate of loss of hydride ligands		Rate of loss of quinoline ligands	
T / K	Observed rate constant / s <sup>-1</sup>	T/ K	Observed rate constant / s <sup>-1</sup>
273	2.86 (2.786 – 2.962)	275	0.214 (0.200 – 0.229)

Table 9.10 Rate constants (quoted to 3 d.p.) for the loss of quinoline and hydride ligands from **SIMes(c)** in the presence of quinoline at the indicated temperatures, with corresponding lower and upper limits to a 95 % confidence level.

## 9.2 Product operators of INEPT NMR experiments prior to FID acquisition

These final product operators are the result of the stated were calculated by Richard Green as part of a review publication of *parahydrogen* derived hyperpolarisation.<sup>151</sup> Various stating states have been considered for each sequence. In each case, **I** and **S** are *parahydrogen* and **R** is a heteronucleus such as <sup>13</sup>C. Only the states which can be observed are included together with information about which nuclei they are observed on.

### 9.2.1 Product operators of the INEPTnd NMR sequence

#### 9.2.1.1 Starting with I<sub>z</sub>

Observable on **I**

$$I_y \cos[2\pi\tau(J_{12})] \cos[2\pi\tau(J_{13})]$$

Observable on **S**

$$I_z S_x 2 \cos[2\pi\tau(J_{13})] \sin[2\pi\tau(J_{12})]$$

Observable on **R**

$$-I_z R_y 2 \cos[2\pi\tau(J_{12})] \sin[2\pi\tau(J_{13})]$$

Plus non-observable states



9.2.1.2 Starting with  $I_z S_z$ 

No observables on **I**, **S** or **R**.

9.2.1.3 Starting with  $I_z R_z$ 

No observables on **I**, **S** or **R**.

9.2.1.4 Starting with  $I_x S_x$ 

No observables on **I**, **S** or **R**.

9.2.2 Product operators of the INEPT<sub>phase</sub> NMR sequence with a 45° initial pulse9.2.2.1 Starting with  $I_z$ 

Observable on **I**

$$I_x(1/\sqrt{2})$$

No other states are observable

9.2.2.2 Starting with  $I_z S_z$ 

Observable on **I**

$$-I_y 1/4 \cos[2\pi\tau(J13)] \sin[2\pi\tau(J12)] + I_x S_z 1/2 \cos[2\pi\tau(J12)] \cos[2\pi\tau(J23)]$$

Observable on **S**

$$-I_z S_x 1/2 \cos[2\pi\tau(J12)] \cos[2\pi\tau(J13)] - S_y 1/4 \cos[2\pi\tau(J23)] \sin[2\pi\tau(J12)]$$

Observable on **R**

$$I_z R_y 1/2 \sin[2\pi\tau(J12)] \sin[2\pi\tau(J13)] + S_z R_y 1/2 \cos[2\pi\tau(J12)] \sin[2\pi\tau(J23)]$$

Plus non-observable states

9.2.2.3 Starting with  $I_zR_z$ Observable on **I**

$$-I_y(1/\sqrt{2})\cos[2\pi\tau(J12)]\sin[2\pi\tau(J13)]$$

Observable on **S**

$$-I_zS_x(1/\sqrt{2})\sin[2\pi\tau(J12)]\sin[2\pi\tau(J13)]$$

Observable on **R**

$$-I_zR_y(1/\sqrt{2})\cos[2\pi\tau(J12)]\cos[2\pi\tau(J13)]$$

Plus non-observable states

## 9.2.3 Product operators of the INEPT\_phase NMR sequence with a 90° initial pulse

9.2.3.1 Starting with  $I_z$ No observables on **I**, **S** or **R**.9.2.3.2 Starting with  $I_zS_z$ No observables on **I**, **S** or **R**.9.2.3.3 Starting with  $I_zR_z$ Observable on **I**

$$-I_y(1/2)\cos[2\pi\tau(J12)]\sin[2\pi\tau(J13)]$$

Observable on **S**

$$-I_zS_x\sin[2\pi\tau(J12)]\sin[2\pi\tau(J13)]$$

Observable on **R**

$$-I_zR_y\cos[2\pi\tau(J12)]\cos[2\pi\tau(J13)]$$

Plus non-observable states

### 9.3 Adapted pulse sequences used within this thesis

During the development of standard sequences for use with the method 2, a series of new sequences had to be written to incorporate the commands associated with the polarisor. These are prefixed with 'ph\_'.

#### 9.3.1 Standard 90° pulse acquire sequence – ph\_zg

This sequence completes a single 90° pulse followed by acquisition. It has been used for both <sup>1</sup>H and <sup>13</sup>C acquisitions.

```

;ph_zg
;zg for use with parahydrogen polariser

#include <Avance.incl>
#include <Polariser.incl>

1 ze
2 lu
  subr POLARISE( d20, d21, d24 ) ;wait for sample and polarise;
transfer when done
3 d1
  p0 ph1
  go=3 ph31
  30m wr #0
  TOPOL                ;transfer sample to polariser
  lo to 2 times l0
  POLPOS                ;wait for sample in polariser
exit

ph1=0 2 2 0 1 3 3 1
ph31=0 2 2 0 1 3 3 1

;d1 : relaxation delay; set to very short for hyperpolarisation
experiments
;ns : number of scans: set to = 1 for hyperpolarisation
experiments
;d20: bubble time for polarisation
;d21: stop bubbling, wait before transferring the sample
;d24: settling after transfer
;l0 : accumulate L0 scans; re-polarising between scans

```

### 9.3.2 $^1\text{H}$ OPSYdq NMR pulse sequence – ph\_OPYdq

This sequence filters the double quantum magnetic states using gradients and transforms them into observable magnetisation. It can be altered to achieve zero quantum or single quantum filtration by changing the proportions of the gradients used.

```
;;start

;ph_OPYdq
;OPSY with double quantum filter modified for use with the
parahydrogen polariser

#include <Avance.incl>
#include <Grad.incl>
#include <Polariser.incl>

1 ze
2 d1
   subr POLARISE( d20, d21, d24 )
3 30m
   d1
   p1 ph1           ; pH MODIFIED
   50u UNBLKGRAD
   p16:gp1*-1
   d16
   20u BLKGRAD
   p1 ph2           ; pH MODIFIED
   50u UNBLKGRAD
   p16:gp1
   d16
   p16:gp1
   d16
   20u BLKGRAD
   go=3 ph31
   30m wr #0
   TOPOL ;transfer sample to polariser
   20u ze
   lo to 2 times l0
   ;POLPOS ;wait for sample in poariser
exit

ph1=1 1 1 1 0 0 0 0
ph2=0 0 0 0 1 1 1 1
ph31=0 0 0 0 1 1 1 1

;d1 : relaxation delay; set to very short for hyperpolarisation
experiments
;d20: bubble time for polarisation
;d21: stop bubbling, wait before transferring the sample
;d24: settling after transfer
```

```
;l0 : accumulate L0 scans
;p11 : f1 channel - power level for pulse (default)
;p1 : f1 channel - 90 degree high power pulse
;p2 : f1 channel - 180 degree high power pulse
;p16: homospoil/gradient pulse
;d16: delay for homospoil/gradient recovery
;NS: 1 * n, total number of scans: NS * TD0
;use gradient ratio:      gpz1= from 80 to 100 %
;p16= 1-3 ms
; increase gpz1 and/or p16 to improve the signal suppression.
;use gradient files:
;gpnam1: SINE.100

;Ralph Adams 12MAY2009

;;stop
```

### 9.3.3 Selective OPSYdq sequence – OPSYdq\_2shaped90\_mkIII

This sequence applies an OPSYdq filter to two selected resonances. It is designed to give an idea of the coupling relationship between the two resonances.

```

;;start
;OPSYdq_2shaped90_mkIII
;OPSY with double quantum filter modified for use with the
parahydrogen polariser
#include <Avance.incl>
#include <Grad.incl>
#include <Polariser3.incl>
1 ze
2 d1
      subr POLARISE( d20, d21, d24 )
3 30m p11:f1 p12:f2
  d1
  (center
  (p12:sp1 ph1):f1
  (p12:sp2 ph1):f2
  )
  50u UNBLKGRAD
  p16:gp1*-1
  d16 p11:f1 p12:f2
  20u BLKGRAD
  (center
  (p12:sp3 ph2):f1
  (p12:sp4 ph2):f2
  )
  50u UNBLKGRAD
  p16:gp1
  d16
  p16:gp1
  d16
  20u BLKGRAD
  go=3 ph31
  30m wr #0
  TOPOL ;transfer sample to polariser
  20u ze
  lo to 2 times l0
  POLPOS ;wait for sample in poariser
exit
ph1=1 1 1 1 0 0 0 0
ph2=0 0 0 0 1 1 1 1
ph3=1 1 1 1 0 0 0 0
ph31=0 0 0 0 1 1 1 1
;d1 : relaxation delay; set to very short for hyperpolarisation
experiments
;d20: bubble time for polarisation
;d21: stop bubbling, wait before transferring the sample
;d24: settling after transfer
;l0 : accumulate L0 scans
;p16: homospoil/gradient pulse

```

```
;d16: delay for homospoil/gradient recovery
;NS: 1 * n, total number of scans: NS * TD0
;use gradient ratio:      gpz1= from 80 to 100 %
;p16= 1-3 ms
; increase gpz1 and/or p16 to improve the signal suppression.
;use gradient files:
;gpnam1: SINE.100
;phcor 1 : phasedifference between power levels sp1 and p11
;choose p11 according to desired selectivity
;the flip-angle is determined by the amplitude
;set O1 on resonance on the multiplet to be excited or use
spoffs
;;stop
```

### 9.3.4 1D <sup>1</sup>H NOESY NMR pulse sequence – ph\_selnogp

This is the standard 1D <sup>1</sup>H NOESY NMR pulse sequence from Bruker adapted for use with the polarisor.

```

;selnogp
;avance-version (07/06/20)
;1D NOESY using selective refocussing with a shaped pulse
;dipolar coupling may be due to noe or chemical exchange.
;
;H. Kessler, H. Oschkinat, C. Griesinger & W. Bermel,
; J. Magn. Reson. 70, 106 (1986)
;J. Stonehouse, P. Adell, J. Keeler & A.J. Shaka,
; J. Am. Chem. Soc 116, 6037 (1994)
;K. Stott, J. Stonehouse, J. Keeler, T.L. Hwang & A.J. Shaka,
; J. Am. Chem. Soc 117, 4199-4200 (1995)
;
;$CLASS=HighRes
;$DIM=1D
;$TYPE=
;$SUBTYPE=
;$COMMENT=

#include <Avance.incl>
#include <Grad.incl>
#include <Polariser.incl>

"p2=p1*2"

"d19=d8*0.5-p16-d16"

"acqt0=-p1*2/3.1416-4u"

1 ze
2 30m
  subr POLARISE( d20, d21, d24 ) ;wait for sample and polarise;
transfer when done
3 30m
  20u p11:f1
  d1
  50u UNBLKGRAD
  (p1 ph1):f1
  3u
  p16:gp1
  d16 p10:f1
  p12:sp2:f1 ph2:r
  3u
  p16:gp1
  d16 p11:f1

```



```

(p1 ph3):f1
d19
p16:gp2
d16
3u
(p2 ph4):f1
3u
p16:gp2*-1
d16
d19
(p1 ph5):f1
4u BLKGRAD
go=3 ph31
TOPOL ;transfer sample to polariser
30m mc #0 to 2 F0(zd)
exit

ph1=0 2
ph2=0 0 1 1 2 2 3 3
ph3=0
ph4=0
ph5=0
ph31=0 2 2 0

;p10 : 120dB
;p11 : f1 channel - power level for pulse (default)
;sp2: f1 channel - shaped pulse
;p1 : f1 channel - 90 degree high power pulse
;p2 : f1 channel - 180 degree high power pulse
;p12: f1 channel - 180 degree shaped pulse
;p16: homospoil/gradient pulse [1
msec]
;d1 : relaxation delay; 1-5 * T1
;d8 : mixing time
;d16: delay for homospoil/gradient recovery
;d19: d8*0.5 - p16 - d16
;d20: bubble time for polarisation
;d21: stop bubbling, wait before transferring the sample
;d24: settling after transfer
;NS: 2 * n, total number of scans: NS * TD0
;DS: 4

;phcor 2 : phasedifference between power levels sp1 and p11

;choose p12 according to desired selectivity
;the flip-angle is determined by the amplitude
;set O1 on resonance on the multiplet to be excited or use
spoffs

;use gradient ratio: gp 1 : gp 2
; 15 : 40

```

```
;for z-only gradients:  
;gpz1: 15%  
;gpz2: 40%
```

```
;use gradient files:  
;gpnam1: SINE.100  
;gpnam2: SINE.100
```

```
;$Id: selnogp,v 1.15.6.1 2007/07/04 13:41:19 ber Exp $
```

### 9.3.5 1D <sup>1</sup>H NOESY NMR pulse sequence – ph\_selnogp\_noloopdummy

This 1D <sup>1</sup>H NOESY NMR pulse sequence has been adapted from the sequence by Bruker to force the phase cycle to be implemented.

```

;ph_selnogp_noloopdummy
;avance-version (07/06/20)
;1D NOESY using selective refocussing with a shaped pulse
;dipolar coupling may be due to noe or chemical exchange.
;
;H. Kessler, H. Oschkinat, C. Griesinger & W. Bermel,
; J. Magn. Reson. 70, 106 (1986)
;J. Stonehouse, P. Adell, J. Keeler & A.J. Shaka,
; J. Am. Chem. Soc 116, 6037 (1994)
;K. Stott, J. Stonehouse, J. Keeler, T.L. Hwang & A.J. Shaka,
; J. Am. Chem. Soc 117, 4199-4200 (1995)
;
;$CLASS=HighRes
;$DIM=1D
;$TYPE=
;$SUBTYPE=
;$COMMENT=

#include <Avance.incl>
#include <Grad.incl>
#include <Polariser3.incl>

"p2=p1*2"

"d19=d8*0.5-p16-d16"

"acqt0=-p1*2/3.1416-4u"

1 ze
2 30m
  subr POLARISE( d20, d21, d24 ) ;wait for sample and polarise;
transfer when done
3 30m
  20u p11:f1
  d1
  50u UNBLKGRAD
  (p1 ph1):f1
  3u
  p16:gp1
  d16 p10:f1
  p12:sp2:f1 ph2:r
  3u
  p16:gp1

```

```

d16 pl1:f1
(p1 ph3):f1
d19
p16:gp2
d16
3u
(p2 ph4):f1
3u
p16:gp2*-1
d16
d19
(p1 ph5):f1
4u BLKGRAD
go=3 ph31
4 TOPOL                ;transfer sample to polariser
5 30m
  subr POLARISE( d20, d21, d24 ) ;wait for sample and polarise;
transfer when done
6 30m
  20u pl1:f1
  d1
  50u UNBLKGRAD
  (p1 ph1):f1
  3u
  p16:gp1
  d16 pl0:f1
  p12:sp2:f1 ph2:r
  3u
  p16:gp1
  d16 pl1:f1
  (p1 ph3):f1
  d19
  p16:gp2
  d16
  3u
  (p2 ph4):f1
  3u
  p16:gp2*-1
  d16
  d19
  (p1 ph5):f1
  4u BLKGRAD
  go=3 ph31
7 30m ze
8 TOPOL                ;transfer sample to polariser
  30m
  subr POLARISE( d20, d21, d24 ) ;wait for sample and polarise;
transfer when done
9 30m
  20u pl1:f1
  d1
  50u UNBLKGRAD
  (p1 ph1):f1
  3u
  p16:gp1
  d16 pl0:f1

```

```

p12:sp2:f1 ph2:r
3u
p16:gp1
d16 p11:f1
(p1 ph3):f1
d19
p16:gp2
d16
3u
(p2 ph4):f1
3u
p16:gp2*-1
d16
d19
(p1 ph5):f1
4u BLKGRAD
go=3 ph31
10 TOPOL ;transfer sample to polariser
11 30m
subr POLARISE( d20, d21, d24 ) ;wait for sample and polarise;
transfer when done
12 30m
20u p11:f1
d1
50u UNBLKGRAD
(p1 ph1):f1
3u
p16:gp1
d16 p10:f1
p12:sp2:f1 ph2:r
3u
p16:gp1
d16 p11:f1
(p1 ph3):f1
d19
p16:gp2
d16
3u
(p2 ph4):f1
3u
p16:gp2*-1
d16
d19
(p1 ph5):f1
4u BLKGRAD
go=3 ph31
13 TOPOL ;transfer sample to polariser

30m mc #0 to 3 F0(zd)
exit

ph1=0 2
ph2=0 0 1 1 2 2 3 3
ph3=0
ph4=0

```

```

ph5=0
ph31=0 2 2 0

;p10 : 120dB
;p11 : f1 channel - power level for pulse (default)
;sp2: f1 channel - shaped pulse
;p1 : f1 channel - 90 degree high power pulse
;p2 : f1 channel - 180 degree high power pulse
;p12: f1 channel - 180 degree shaped pulse
;p16: homospoil/gradient pulse [1
msec]
;d1 : relaxation delay; 1-5 * T1
;d8 : mixing time
;d16: delay for homospoil/gradient recovery
;d19: d8*0.5 - p16 - d16
;d20: bubble time for polarisation
;d21: stop bubbling, wait before transferring the sample
;d24: settling after transfer
;NS: 2 * n, total number of scans: NS * TD0
;DS: 4

;phcor 2 : phasedifference between power levels sp1 and p11

;choose p12 according to desired selectivity
;the flip-angle is determined by the amplitude
;set O1 on resonance on the multiplet to be excited or use
spoffs

;use gradient ratio:      gp 1 : gp 2
;                          15 :    40

;for z-only gradients:
;gpz1: 15%
;gpz2: 40%

;use gradient files:
;gpnam1: SINE.100
;gpnam2: SINE.100

;$Id: selnogp,v 1.15.6.1 2007/07/04 13:41:19 ber Exp $

```

### 9.3.6 1D refocused $^{13}\text{C}\{^1\text{H}\}$ NMR pulse sequence ( $^{13}\text{C}\{^1\text{H}\}_{\text{JR}}$ ) – ph\_zg\_refocus

This is the standard 1D  $^{13}\text{C}$  NMR pulse sequence from Bruker adapted to include a delay between the pulse and acquisition, and for use with the polarisor.

```

;ph_zg_refocus
;zg for use with parahydrogen polariser

#include <Avance.incl>
#include <Polariser.incl>

"d3=1/(2*cnst2)"

1 ze
2 lu
  subr POLARISE( d20, d21, d24 ) ;wait for sample and polarise;
transfer when done
3 d1 pl12:f2
  p0 ph1
  d3 do:f2
  go=3 ph31 cpd2:f2
  30m wr #0 do:f2
  TOPOL                ;transfer sample to polariser
  lo to 2 times l0
  POLPOS                ;wait for sample in polariser
exit

ph1=0 2 2 0 1 3 3 1
ph31=0 2 2 0 1 3 3 1

;d1 : relaxation delay; set to very short for hyperpolarisation
experiments
;ns : number of scans: set to = 1 for hyperpolarisation
experiments
;d20: bubble time for polarisation
;d21: stop bubbling, wait before transferring the sample
;d24: settling after transfer
;l0 : accumulate L0 scans; re-polarising between scans
;cpd2: decoupling according to sequence defined by cpdprg2
;pcpd2: f2 channel - 90 degree pulse for decoupling sequence

```

### 9.3.7 1D $^{13}\text{C}\{^1\text{H}\}$ NMR pulse sequence refocused for both J coupling and chemical shift evolution ( $^{13}\text{C}\{^1\text{H}\}$ \_JCSR) – ph\_zg\_refocused\_J+CS

This is the standard 1D  $^{13}\text{C}\{^1\text{H}\}$  NMR pulse sequence from Bruker adapted to include a refocusing section allowing both J coupling and chemical shift evolution, and for use with the polarisor.

```

;ph_zg_refocus
;zg for use with parahydrogen polariser

#include <Avance.incl>
#include <Polariser3.incl>

"d3=1/(2*cnst2) "

1 ze
2 lu
  subr POLARISE( d20, d21, d24 ) ;wait for sample and polarise;
transfer when done
3 d1 p112:f2
  p0 ph1
  d3 do:f2
  (center (p4 ph2):f2 (p2 ph3) )
  d3
  go=3 ph31 cpd2:f2
  30m wr #0 do:f2
  TOPOL          ;transfer sample to polariser
  lo to 2 times l0
  POLPOS        ;wait for sample in polariser
exit

ph1=0 2 2 0 1 3 3 1
ph2=0 2
ph3=0 2
ph31=0 2 2 0 1 3 3 1

;p112 : f2 channel - power level for pulse (default)
;p0 : f1 channel - 90 degree high power pulse
;p2 : f1 channel - 180 degree high power pulse
;p3 : f2 channel - 180 degree high power pulse
;d1 : relaxation delay; set to very short for hyperpolarisation
experiments
;ns : number of scans: set to = 1 for hyperpolarisation
experiments
;d20: bubble time for polarisation
;d21: stop bubbling, wait before transferring the sample
;d24: settling after transfer
;l0 : accumulate L0 scans; re-polarising between scans
;cpd2: decoupling according to sequence defined by cpdprg2
;pcpd2: f2 channel - 90 degree pulse for decoupling sequence

```



### 9.3.8 1D $^{13}\text{C}$ INEPT NMR pulse sequence – ph\_ineptnd

This is the standard 1D  $^{13}\text{C}$  INEPTnd NMR pulse sequence from Bruker adapted for use with the polarisor.

```

;ph_ineptnd_mkIII
;avance-version (02/05/31)
;INEPT for non-selective polarization transfer
;no decoupling during acquisition
;modified for use with the polariser mkII by REM and LSL
;$CLASS=HighRes
;$DIM=1D
;$TYPE=
;$SUBTYPE=
;$COMMENT=

#include <Avance.incl>
#include <Polariser3.incl>

"p2=p1*2"
"p4=p3*2"
"d4=1s/(cnst2*4)"

1 ze
2 30m
   subr POLARISE( d20, d21, d24 ) ;wait for sample and polarise;
transfer when done
3 d1
   (p5 ph1):f2
   d4
   (center (p4 ph2):f2 (p2 ph4) )
   d4
   (p3 ph3):f2 (p1 ph5)
   go=3 ph31
   30m mc #0 to 2 F0(zd)
   TOPOL           ;transfer sample to polariser
   lo to 2 times 10
   POLPOS          ;wait for sample in polariser and set to
manuel mode
exit

ph1=0 0 0 0 0 0 0 0 2 2 2 2 2 2 2
ph2=0 2
ph3=1 1 3 3
ph4=0 2
ph5=0 0 0 0 1 1 1 1 2 2 2 2 3 3 3 3
ph31=0 0 2 2 1 1 3 3

;p11 : f1 channel - power level for pulse (default)

```

```
;p12 : f2 channel - power level for pulse (default)
;p1 : f1 channel - 90 degree high power pulse
;p2 : f1 channel - 180 degree high power pulse
;p3 : f2 channel - 90 degree high power pulse
;p4 : f2 channel - 180 degree high power pulse
;p5 : f2 channel - 90 or 45 degree pulse as desired
;d1 : relaxation delay; 1-5 * T1
;d4 : 1/(4J(XH))
;d20: bubble time for polarisation
;d21: stop bubbling, wait before transferring the sample
;d24: settling after transfer
;l0 : accumulate L0 scans; re-polarising between scans
;cnst2: = J(XH)
;NS: 4 * n, total number of scans: NS * TD0
;DS: 16
```

```
;$Id: ineptnd,v 1.9 2005/11/10 12:17:00 ber Exp $
```

### 9.3.9 1D $^{13}\text{C}$ INEPT NMR pulse sequence with phase change – ph\_inept\_phase

This is the standard 1D  $^{13}\text{C}$  INEPTnd NMR pulse sequence from Bruker adapted for PHIP protocols according to Haake *et al.*<sup>150</sup> for use with the polarisor.

```

;ph_ineptrd
;avance-version (02/05/31)
;INEPT for non-selective polarization transfer
;with decoupling during acquisition
;Modified for use with the polariser mkII
;$CLASS=HighRes
;$DIM=1D
;$TYPE=
;$SUBTYPE=
;$COMMENT=

#include <Avance.incl>
#include <Polariser.incl>

"p2=p1*2"
"p4=p3*2"
"d3=1s/(cnst2*cnst11)"
"d4=1s/(cnst2*4)"
"d12=20u"

1 ze
2 30m
  subr POLARISE( d20, d21, d24 ) ;wait for sample and polarise;
  transfer when done
3 30m do:f2
  d1
  d12 p12:f2
  (p5 ph1):f2
  d4
  (center (p4 ph2):f2 (p2 ph4) )
  d4
  (p3 ph3):f2 (p1 ph5)
  d3
  (center (p4 ph2):f2 (p2 ph6) )
  d3 p12:f2
  go=3 ph31 cpd2:f2
  30m do:f2 mc #0 to 2 F0(zd)
  TOPOL ;transfer sample to polariser
  lo to 2 times l0
  POLPOS ;wait for sample in polariser and set to
manuel mode
exit

ph1=1 0 0 0 0 0 0 0 2 2 2 2 2 2 2 2
ph2=0 2

```

```

ph3=1 1 3 3
ph4=0 2
ph5=0 0 0 0 1 1 1 1 2 2 2 2 3 3 3 3
ph6=0 2 0 2 1 3 1 3
ph31=0 0 2 2 1 1 3 3

```

```

;p11 : f1 channel - power level for pulse (default)
;p12 : f2 channel - power level for pulse (default)
;p112: f2 channel - power level for CPD/BB decoupling
;p1 : f1 channel - 90 degree high power pulse
;p2 : f1 channel - 180 degree high power pulse
;p3 : f2 channel - 90 degree high power pulse
;p4 : f2 channel - 180 degree high power pulse
;p5 : f2 channel - 90 or 45 degree high power pulse
;d1 : relaxation delay; 1-5 * T1
;d3 : 1/(6J(XH)) XH, XH2, XH3 positive
;      1/(4J(XH)) XH only
;      1/(3J(XH)) XH, XH3 positive, XH2 negative
;d4 : 1/(4J(XH))
;d12: delay for power switching [20 usec]
;d20: bubble time for polarisation
;d21: stop bubbling, wait before transferring the sample
;d24: settling after transfer
;l0 : accumulate L0 scans; re-polarising between scans
;cnst2: = J(XH)
;cnst11: 6 XH, XH2, XH3 positive
;         4 XH only
;         3 XH, XH3 positive, XH2 negative
;NS: 4 * n, total number of scans: NS * TD0
;DS: 16
;cpd2: decoupling according to sequence defined by cpdprg2
;pcpd2: f2 channel - 90 degree pulse for decoupling sequence

```

```

;$Id: ineptrd,v 1.9 2005/11/10 12:17:00 ber Exp $

```

9.3.10 1D  $^{13}\text{C}\{^1\text{H}\}$  INEPT NMR pulse sequence – ph\_ineptrd

This is the standard 1D  $^{13}\text{C}\{^1\text{H}\}$  INEPTrd NMR pulse sequence from Bruker adapted for use with the polarisor.

```

;ph_ineptrd_mkIII
;avance-version (02/05/31)
;INEPT for non-selective polarization transfer
;with decoupling during acquisition
;Modified for use with the polariser mkII
;$CLASS=HighRes
;$DIM=1D
;$TYPE=
;$SUBTYPE=
;$COMMENT=

#include <Avance.incl>
#include <Polariser3.incl>

"p2=p1*2"
"p4=p3*2"
"d3=1s/(cnst2*cnst11)"
"d4=1s/(cnst2*4)"
"d12=20u"

1 ze
2 30m
  subr POLARISE( d20, d21, d24 ) ;wait for sample and polarise;
  transfer when done
3 30m do:f2
  d1
  d12 p12:f2
  (p5 ph1):f2
  d4
  (center (p4 ph2):f2 (p2 ph4) )
  d4
  (p3 ph3):f2 (p1 ph5)
  d3
  (center (p4 ph2):f2 (p2 ph6) )
  d3 p12:f2
  go=3 ph31 cpd2:f2
  30m do:f2 mc #0 to 2 F0(zd)
  TOPOL ;transfer sample to polariser
  lo to 2 times 10
  POLPOS ;wait for sample in polariser and set to
manuel mode
exit

ph1=0 0 0 0 0 0 0 0 2 2 2 2 2 2 2
ph2=0 2

```

```

ph3=1 1 3 3
ph4=0 2
ph5=0 0 0 0 1 1 1 1 2 2 2 2 3 3 3 3
ph6=0 2 0 2 1 3 1 3
ph31=0 0 2 2 1 1 3 3

;p11 : f1 channel - power level for pulse (default)
;p12 : f2 channel - power level for pulse (default)
;p112: f2 channel - power level for CPD/BB decoupling
;p1 : f1 channel - 90 degree high power pulse
;p2 : f1 channel - 180 degree high power pulse
;p3 : f2 channel - 90 degree high power pulse
;p4 : f2 channel - 180 degree high power pulse
;p5 : f2 channel - 90 or 45 degree high power pulse
;d1 : relaxation delay; 1-5 * T1
;d3 : 1/(6J(XH)) XH, XH2, XH3 positive
;      1/(4J(XH)) XH only
;      1/(3J(XH)) XH, XH3 positive, XH2 negative
;d4 : 1/(4J(XH))
;d12: delay for power switching [20 usec]
;d20: bubble time for polarisation
;d21: stop bubbling, wait before transferring the sample
;d24: settling after transfer
;l0 : accumulate L0 scans; re-polarising between scans
;cnst2: = J(XH)
;cnst11: 6 XH, XH2, XH3 positive
;         4 XH only
;         3 XH, XH3 positive, XH2 negative
;NS: 4 * n, total number of scans: NS * TD0
;DS: 16
;cpd2: decoupling according to sequence defined by cpdprg2
;pcpd2: f2 channel - 90 degree pulse for decoupling sequence

;$Id: ineptrd,v 1.9 2005/11/10 12:17:00 ber Exp $

```

9.3.11 2D  $^1\text{H}$ - $^1\text{H}$  OPSYdq-COSY NMR pulse sequence – ph\_OPYdq\_2D

In this sequence, the first  $90^\circ$  pulse of the COSY sequence is replaced by an OPSYdq sequence such that only double quantum states are filtered for use in the COSY section of the sequence.

```
;;start

;ph_OPYdq_2D
;OPSY with double quantum filter modified for use with the
parahydrogen polariser
;Modified to work like a COSYgpqf but by selecting only two spin
order terms

#include <Avance.incl>
#include <Grad.incl>
#include <Polariser.incl>

"d0=3u"

"d13=4u"
"in0=inf1"

1 ze
2 d1
   subr POLARISE( d20, d21, d24 )
3 30m
   d1
   p1 ph1           ; pH MODIFIED
   50u UNBLKGRAD
   p16:gp1*-1
   d16
   20u BLKGRAD
   p1 ph2           ; pH MODIFIED
   50u UNBLKGRAD
   p16:gp1
   d16
   p16:gp1
   d16
   20u BLKGRAD
   d0
   50u UNBLKGRAD
   p19:gp2
   d16
   p0 ph2
   d13
   p19:gp2
   d16
   4u BLKGRAD
   go=3 ph31
   TOPOL ;transfer sample to polariser
   d1 mc #0 to 2 F1QF(id0)
```

```
POLPOS ;wait for sample in poariser
exit

ph1=0 2
ph2=0 0 2 2
ph3=0 2
ph31=0 2

;d1 : relaxation delay; set to very short for hyperpolarisation
experiments
;d13: short delay [4 usec]
;d20: bubble time for polarisation
;d21: stop bubbling, wait before transferring the sample
;d24: settling after transfer
;l0 : accumulate L0 scans
;p11 : f1 channel - power level for pulse (default)
;p1 : f1 channel - 90 degree high power pulse
;p2 : f1 channel - 180 degree high power pulse
;p16: homospoil/gradient pulse
;p19: gradient pulse for single quantum filter
;d16: delay for homospoil/gradient recovery
;NS: 1 * n, total number of scans: NS * TD0
;in0: 1/(1 * SW) = 2 * DW
;use gradient ratio:      gpz1= 70%    gpz2=10%
;p16= 1-3 ms
;p19= 600 us
; increase gpz1 and/or p16 to improve the signal suppression.
;use gradient files:
;gpnam1: SINE.100
;gpz1 70% refers to the gradient filter used to select double
quantum coherences
;gpz2 10% refers to the single quantum filter (used in the last
90)

;Ralph Adams 12MAY2009

;;stop
```



### 9.3.12 2D NMR pulse sequences

This has been completed through the addition of an 'include' file to correspond to the commands for the polarisor to be used, and three subroutines relating to control of the polarisor. These additions have been made to all the standard 2D sequences used for hyperpolarisation via SABRE using method 2. This has been exemplified through the adaptation of the standard 2D  $^1\text{H}$ - $^1\text{H}$  COSY NMR pulse sequence from Bruker for use with the polarisor.

```

;COSY using gradient pulse
;ph_cosygpqf
;For use with the parahydrogen polariser

#include <Avance.incl>
#include <Grad.incl>
#include <Polariser.incl>

"d13=4u"
"in0=inf1"
"d0=3u"
"d27=50m"

1 ze
2 d1
   subr POLARISE( d20, d21, d24 ) ;wait for sample and polarise;
transfer when done
3 p1 ph1
   d0
   50u UNBLKGRAD
   p16:gp1
   d16
   p0 ph2
   d13
   p16:gp1
   d16
   4u BLKGRAD
   go=3 ph31
   TOPOL ;transfer sample to polariser
   d1 mc #0 to 2 F1QF(id0)
   POLPOS ;wait for sample in polariser
exit

ph1=0 2
ph2=0 0 2 2
ph31=0 2

;d1 : relaxation delay; set to very short for hyperpolarisation
experiments
;d13: short delay [4 usec]

```

```
;d16: delay for gradient recovery  
;d20: bubble time for polarisation  
;d21: stop bubbling, wait before transferring the sample  
;d24: settling after transfer  
;10 : accumulate L0 scans; re-polarising between scans
```

#### 9.4 X-ray crystallography data for [Ir(SIMes)(COD)(2-methylpyridine)]PF<sub>6</sub>

Single crystals of C<sub>37</sub>HN<sub>22</sub>F<sub>11</sub>PIr were grown in methanol in the freezer. A suitable crystal was selected, extracted using oil on a loop and interrogated on an Oxford Diffraction SuperNova diffractometer. The crystal was kept at 110.00(10) K during data collection. Using Olex2,<sup>223</sup> the structure was solved with the XS structure solution program using Direct Methods and refined with the XL<sup>224</sup> refinement package using Least Squares minimisation.

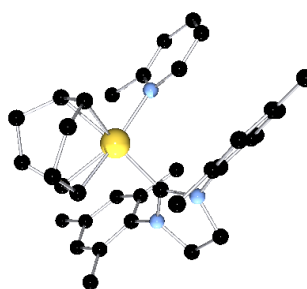


Figure 9.5 X-ray crystallography structure of [Ir(SIMes)(COD)(2-methylpyridine)]PF<sub>6</sub>.

Identification code	sbd1108
Empirical formula	C <sub>37</sub> HN <sub>22</sub> F <sub>11</sub> PIr
Formula weight	1184.76
Temperature/K	110.00(10)
Crystal system	monoclinic
Space group	P2 <sub>1</sub> /c
a/Å	9.7857(4)
b/Å	21.6745(10)
c/Å	16.1768(6)
α/°	90.00
β/°	95.804(4)
γ/°	90.00
Volume/Å <sup>3</sup>	3413.5(2)
Z	4
ρ <sub>calc</sub> /mg/mm <sup>3</sup>	2.305
m/mm <sup>-1</sup>	4.094
F(000)	2268.0

Crystal size/mm <sup>3</sup>	0.1709 × 0.1563 × 0.121
2 $\theta$ range for data collection	5.62 to 64.26°
Index ranges	-6 ≤ h ≤ 13, -30 ≤ k ≤ 24, -23 ≤ l ≤ 24
Reflections collected	20731
Independent reflections	10763[R(int) = 0.0333]
Data/restraints/parameters	10763/0/422
Goodness-of-fit on F <sup>2</sup>	1.035
Final R indexes [I ≥ 2 $\sigma$ (I)]	R <sub>1</sub> = 0.0337, wR <sub>2</sub> = 0.0734
Final R indexes [all data]	R <sub>1</sub> = 0.0468, wR <sub>2</sub> = 0.0809
Largest diff. peak/hole / e Å <sup>-3</sup>	1.78/-1.31

Atom	x	y	z	U(eq)
Ir36	3098.58(11)	5960.80(5)	1899.39(7)	17.99(4)
P41	9057.7(10)	6753.5(5)	5839.0(6)	30.6(2)
F42	8334(3)	6106.7(14)	5577.6(17)	64.2(8)
F43	8825(3)	6964.3(14)	4896.8(14)	60.1(8)
F44	9802(3)	7380.4(11)	6118.8(18)	57.8(7)
F45	10504(2)	6458.0(12)	5687.7(15)	46.9(6)
F4	7613(2)	7051.3(15)	5989.5(17)	65.1(8)
N40	4454(3)	5653.4(13)	2918.4(16)	23.1(5)
F38	9246(3)	6518.5(13)	6781.6(14)	55.4(7)
C24	1549(3)	5778.2(16)	912(2)	23.9(6)
N25	462(3)	6424.2(12)	2628.3(16)	21.9(5)
C0AA	2114(3)	6361.3(16)	776.5(19)	23.9(6)
N8	2199(3)	7041.8(13)	2889.1(16)	21.6(5)
C1AA	4271(3)	7188.3(15)	3838.5(19)	24.1(6)
C10	3568(3)	7287.7(15)	3051.6(19)	22.1(6)
C11	4787(3)	5937.2(14)	1158(2)	21.6(6)
C12	7498(4)	8155.4(18)	3664(3)	35.4(8)
C13	-1344(3)	5790.7(15)	1896(2)	21.0(6)
C14	4123(3)	7654.5(15)	2459.0(19)	22.9(6)
C15	1819(3)	5191.2(17)	461(2)	27.8(7)
C16	-155(3)	6959.8(16)	3025(2)	29.6(7)
C17	-2061(3)	5233.4(15)	1830.4(19)	21.9(6)
C27	-1813(3)	4765.7(15)	2407(2)	24.2(6)

C28	1820(3)	6488.9(15)	2567.6(18)	20.6(6)
C5	4228(3)	5338.4(15)	1145.3(19)	22.1(6)
C3	5550(3)	7468.8(16)	4025(2)	26.1(7)
C35	-840(3)	4863.0(16)	3085(2)	26.4(7)
C32	-315(3)	5861.7(14)	2555(2)	20.5(6)
C4AA	6136(3)	7835.9(16)	3441(2)	27.7(7)
C19	4319(4)	5093.7(17)	3259(2)	30.2(7)
C1	3083(3)	6478.3(17)	113(2)	28.6(7)
C2	-2599(4)	4165.4(17)	2320(3)	35.9(8)
C29	3364(3)	5081.1(16)	390(2)	25.5(7)
C2AA	4600(3)	6392.9(16)	448(2)	25.6(7)
C3AA	1054(3)	7404.7(16)	3180(2)	28.9(7)
C23	5565(3)	6007.1(17)	3189(2)	28.7(7)
C48	-1686(3)	6297.3(15)	1266(2)	25.5(7)
C33	-88(3)	5410.6(15)	3174(2)	23.8(6)
C34	5417(3)	7913.8(15)	2669(2)	25.6(7)
C37	5274(4)	4890(2)	3902(2)	39.4(9)
C30	6529(4)	5825(2)	3819(2)	37.7(9)
C4	3357(4)	7775.4(16)	1619(2)	28.4(7)
C51	3708(4)	6776.3(17)	4473(2)	30.4(7)
C52	6376(4)	5262(2)	4184(2)	43.4(10)
C5AA	3179(4)	4683.0(17)	2913(2)	34.4(8)
C49	890(3)	5514.6(18)	3944(2)	30.6(7)

Table 9.11 Fractional Atomic Coordinates ( $\times 10^4$ ) and Equivalent Isotropic Displacement Parameters ( $\text{\AA}^2 \times 10^3$ ) for sbd1108.  $U_{\text{eq}}$  is defined as 1/3 of the trace of the orthogonalised  $U_{\text{ij}}$  tensor.

Atom	$U_{11}$	$U_{22}$	$U_{33}$	$U_{23}$
Ir36	17.75(6)	16.45(6)	19.75(6)	-2.59(5)
P41	36.7(5)	28.7(5)	25.9(4)	-0.9(4)
F42	83(2)	55.4(18)	51.6(16)	-2.9(14)
F43	73.9(18)	72(2)	33.7(13)	19.5(13)
F44	59.3(16)	24.5(12)	89(2)	-11.5(14)
F45	45.4(13)	39.7(14)	56.5(15)	-6.7(12)
F4	40.0(14)	95(2)	60.9(17)	-3.5(17)
N40	23.5(13)	23.5(14)	22.4(12)	-3.8(11)
F38	81.0(19)	55.3(18)	29.1(12)	2.9(12)
C24	18.2(14)	27.6(17)	25.9(15)	-5.1(14)
N25	21.7(12)	15.2(12)	29.7(13)	-4.2(11)

C0AA	21.9(15)	26.5(17)	22.7(14)	-3.0(13)
N8	20.7(12)	20.5(13)	23.8(12)	-5.0(11)
C1AA	26.2(15)	22.9(16)	23.0(14)	-3.5(13)
C10	22.2(14)	19.8(15)	24.3(14)	-6.2(13)
C11	19.0(14)	21.6(15)	24.5(14)	-3.5(13)
C12	28.6(18)	26.3(18)	50(2)	-6.5(17)
C13	19.2(14)	20.0(14)	24.7(15)	1.1(12)
C14	26.4(15)	18.7(15)	23.8(14)	-5.5(13)
C15	22.9(15)	29.4(18)	31.0(17)	-10.8(15)
C16	26.1(16)	22.4(17)	41.8(19)	-9.9(15)
C17	21.0(14)	20.1(15)	25.1(15)	-2.0(13)
C27	28.3(16)	17.1(15)	28.1(15)	-0.6(13)
C28	23.8(15)	18.5(15)	19.3(13)	-0.2(12)
C5	20.2(14)	22.7(16)	23.8(14)	-4.4(13)
C3	26.4(16)	24.9(17)	26.2(15)	-5.7(14)
C35	29.5(17)	23.5(17)	26.3(15)	3.3(14)
C32	19.5(14)	16.5(14)	26.4(15)	-2.4(12)
C4AA	25.0(16)	19.5(16)	38.4(18)	-7.0(15)
C19	36.1(19)	28.6(18)	27.1(16)	1.4(15)
C1	31.4(17)	31.4(19)	23.5(15)	3.2(14)
C2	48(2)	20.8(17)	40(2)	-0.5(16)
C29	21.5(15)	25.7(17)	29.4(16)	-11.4(14)
C2AA	24.7(15)	23.3(16)	29.5(16)	1.4(14)
C3AA	25.3(16)	23.0(17)	39.0(19)	-9.4(15)
C23	24.4(16)	34(2)	27.2(16)	-9.2(15)
C48	22.6(15)	21.7(16)	32.0(17)	3.5(14)
C33	25.5(15)	21.4(16)	24.8(15)	-0.2(13)
C34	28.5(16)	19.5(15)	29.4(16)	-2.8(14)
C37	51(2)	40(2)	28.2(18)	7.2(17)
C30	30.0(18)	57(3)	25.5(17)	-10.6(18)
C4	37.1(18)	20.6(16)	27.0(16)	-0.7(14)
C51	36.7(18)	30.6(19)	24.2(15)	-3.2(15)
C52	39(2)	63(3)	26.9(18)	-1(2)
C5AA	40(2)	24.6(18)	41(2)	2.1(16)
C49	30.3(17)	35(2)	25.5(16)	1.1(15)

Table 9.12 Anisotropic Displacement Parameters ( $\text{\AA}^2 \times 10^3$ ) for sbd1108. The Anisotropic displacement factor exponent takes the form:  $-2\pi^2[h^2a^*U_{11} + \dots + 2hka \times b \times U_{12}]$ .

Atom	Atom	Length/Å	Atom	Atom	Length/Å
Ir36	N40	2.116(3)	C10	C14	1.397(4)
Ir36	C24	2.125(3)	C11	C5	1.408(4)
Ir36	C0AA	2.151(3)	C11	C2AA	1.512(5)
Ir36	C11	2.138(3)	C12	C4AA	1.514(5)
Ir36	C28	2.078(3)	C13	C17	1.396(4)
Ir36	C5	2.192(3)	C13	C32	1.400(4)
P41	F42	1.608(3)	C13	C48	1.512(4)
P41	F43	1.585(2)	C14	C34	1.396(4)
P41	F44	1.586(3)	C14	C4	1.507(4)
P41	F45	1.595(2)	C15	C29	1.546(4)
P41	F4	1.595(3)	C16	C3AA	1.528(5)
P41	F38	1.601(2)	C17	C27	1.383(4)
N40	C19	1.345(4)	C27	C35	1.394(5)
N40	C23	1.365(4)	C27	C2	1.511(5)
C24	C0AA	1.406(5)	C5	C29	1.520(4)
C24	C15	1.503(5)	C3	C4AA	1.402(5)
N25	C16	1.484(4)	C35	C33	1.396(5)
N25	C28	1.349(4)	C32	C33	1.401(4)
N25	C32	1.435(4)	C4AA	C34	1.379(5)
C0AA	C1	1.523(4)	C19	C37	1.397(5)
N8	C10	1.441(4)	C19	C5AA	1.492(5)
N8	C28	1.343(4)	C1	C2AA	1.539(4)
N8	C3AA	1.484(4)	C23	C30	1.375(5)
C1AA	C10	1.401(4)	C33	C49	1.508(4)
C1AA	C3	1.397(4)	C37	C52	1.386(6)
C1AA	C51	1.506(5)	C30	C52	1.372(6)

Table 9.13 Bond Lengths for sbd1108.

Atom	Atom	Atom	Angle/°	Atom	Atom	Atom	Angle/°
N40	Ir36	C24	150.47(13)	C1AA	C10	N8	118.1(3)
N40	Ir36	C0AA	167.61(11)	C14	C10	N8	120.3(3)
N40	Ir36	C11	88.29(11)	C14	C10	C1AA	121.5(3)
N40	Ir36	C5	85.87(11)	C5	C11	Ir36	73.12(17)
C24	Ir36	C0AA	38.37(13)	C5	C11	C2AA	125.0(3)

C24	Ir36	C11	96.17(12)		C2AA	C11	Ir36	111.7(2)
C24	Ir36	C5	80.16(12)		C17	C13	C32	118.1(3)
C0AA	Ir36	C5	89.23(12)		C17	C13	C48	120.1(3)
C11	Ir36	C0AA	80.89(12)		C32	C13	C48	121.8(3)
C11	Ir36	C5	37.92(11)		C10	C14	C4	121.7(3)
C28	Ir36	N40	97.55(11)		C34	C14	C10	117.9(3)
C28	Ir36	C24	94.12(12)		C34	C14	C4	120.4(3)
C28	Ir36	C0AA	88.57(12)		C24	C15	C29	112.8(3)
C28	Ir36	C11	147.68(12)		N25	C16	C3AA	102.8(2)
C28	Ir36	C5	173.13(12)		C27	C17	C13	122.1(3)
F43	P41	F42	88.96(16)		C17	C27	C35	118.6(3)
F43	P41	F44	92.55(16)		C17	C27	C2	121.0(3)
F43	P41	F45	90.65(14)		C35	C27	C2	120.3(3)
F43	P41	F4	89.26(15)		N25	C28	Ir36	129.0(2)
F43	P41	F38	177.62(17)		N8	C28	Ir36	122.4(2)
F44	P41	F42	178.19(17)		N8	C28	N25	107.4(3)
F44	P41	F45	89.94(14)		C11	C5	Ir36	68.96(17)
F44	P41	F4	89.90(16)		C11	C5	C29	122.3(3)
F44	P41	F38	89.74(16)		C29	C5	Ir36	113.7(2)
F45	P41	F42	89.05(16)		C1AA	C3	C4AA	121.3(3)
F45	P41	F4	179.81(18)		C27	C35	C33	121.4(3)
F45	P41	F38	89.98(14)		C13	C32	N25	119.4(3)
F4	P41	F42	91.11(18)		C13	C32	C33	121.2(3)
F4	P41	F38	90.12(15)		C33	C32	N25	119.3(3)
F38	P41	F42	88.76(15)		C3	C4AA	C12	120.6(3)
C19	N40	Ir36	121.6(2)		C34	C4AA	C12	121.1(3)
C19	N40	C23	118.9(3)		C34	C4AA	C3	118.3(3)
C23	N40	Ir36	119.3(2)		N40	C19	C37	120.2(4)
C0AA	C24	Ir36	71.80(18)		N40	C19	C5AA	119.0(3)
C0AA	C24	C15	126.4(3)		C37	C19	C5AA	120.6(4)
C15	C24	Ir36	112.0(2)		C0AA	C1	C2AA	112.3(3)
C28	N25	C16	113.4(3)		C5	C29	C15	110.7(2)
C28	N25	C32	126.8(3)		C11	C2AA	C1	112.6(3)
C32	N25	C16	117.7(2)		N8	C3AA	C16	102.2(3)
C24	C0AA	Ir36	69.82(19)		N40	C23	C30	122.8(4)
C24	C0AA	C1	122.9(3)		C35	C33	C32	118.4(3)
C1	C0AA	Ir36	113.8(2)		C35	C33	C49	119.7(3)
C10	N8	C3AA	117.6(3)		C32	C33	C49	121.8(3)



C28	N8	C10	128.0(3)		C4AA	C34	C14	122.5(3)
C28	N8	C3AA	114.1(3)		C52	C37	C19	120.1(4)
C10	C1AA	C51	122.0(3)		C52	C30	C23	118.5(4)
C3	C1AA	C10	118.4(3)		C30	C52	C37	119.4(4)
C3	C1AA	C51	119.5(3)					

Table 9.14 Bond angles for sbd1108

Atom	<i>x</i>	<i>y</i>	<i>z</i>	U(eq)
H24	598	5801	1087	29
H0AA	1491	6715	869	29
H11	5702	5969	1492	26
H12A	7341	8555	3921	53
H12B	7958	8219	3160	53
H12C	8078	7899	4056	53
H15A	1326	5207	-104	33
H15B	1449	4839	758	33
H16A	-514	6839	3553	35
H16B	-909	7144	2651	35
H17	-2741	5173	1375	26
H5	4811	5026	1471	27
H3	6033	7410	4559	31
H35	-684	4550	3495	32
H1A	2945	6904	-100	34
H1B	2856	6191	-356	34
H2A	-3115	4108	2802	54
H2B	-1953	3823	2288	54
H2C	-3237	4176	1813	54
H29A	3538	4633	344	31
H29B	3629	5283	-118	31
H2AA	5121	6247	-8	31
H2AB	4985	6797	639	31
H3AA	891	7789	2855	35
H3AB	1236	7509	3777	35
H23	5675	6395	2932	34
H48A	-2072	6115	739	38
H48B	-850	6527	1179	38

H48C	-2360	6578	1472	38
H34	5819	8153	2265	31
H37	5167	4497	4146	47
H30	7285	6084	3998	45
H4A	3512	7434	1243	43
H4B	3687	8160	1391	43
H4C	2372	7811	1675	43
H51A	2836	6945	4620	46
H51B	4366	6754	4970	46
H51C	3556	6362	4239	46
H52	7020	5127	4626	52
H5AA	2424	4934	2650	52
H5AB	2849	4439	3363	52
H5AC	3514	4406	2499	52
H49A	556	5857	4265	46
H49B	1803	5615	3783	46
H49C	946	5139	4283	46

Table 9.15 Hydrogen Atom Coordinates ( $\text{\AA}\times 10^4$ ) and Isotropic Displacement Parameters ( $\text{\AA}^2\times 10^3$ ) for sbd1108.

9.5 Publications<sup>67</sup>

## Utilization of SABRE-Derived Hyperpolarization To Detect Low-Concentration Analytes via 1D and 2D NMR Methods

Lyrelle S. Lloyd,<sup>†</sup> Ralph W. Adams,<sup>†</sup> Michael Bernstein,<sup>‡</sup> Steven Coombes,<sup>§</sup> Simon B. Duckett,<sup>\*,†</sup> Gary G. R. Green,<sup>||</sup> Richard. J. Lewis,<sup>⊥</sup> Ryan E. Mewis,<sup>†</sup> and Christopher J. Sleight<sup>‡</sup>

<sup>†</sup>Department of Chemistry, University of York, Heslington, York YO10 5DD, U.K.

<sup>‡</sup>AstraZeneca R&D Charnwood, Bakewell Road, Loughborough LE11 5RH, U.K.

<sup>§</sup>AstraZeneca R&D Pharmaceutical Development, Silk Road Business Park, Charter Way, Macclesfield, Cheshire SK10 2NA, U.K.

<sup>||</sup>York Neuroimaging Centre, The Biocentre, York Science Park, Innovation Way, Heslington, York YO10 5SN, U.K.

<sup>⊥</sup>AstraZeneca R&D Mölndal, Respiratory & Inflammation Innovative Medicines, Pepparedsleden 1, S-431 83 Mölndal, Sweden

**S** Supporting Information

**ABSTRACT:** The characterization of materials by the inherently insensitive method of NMR spectroscopy plays a vital role in chemistry. Increasingly, hyperpolarization is being used to address the sensitivity limitation. Here, by reference to quinoline, we illustrate that the SABRE hyperpolarization technique, which uses *para*-hydrogen as the source of polarization, enables the rapid completion of a range of NMR measurements. These include the collection of <sup>13</sup>C, <sup>13</sup>C{<sup>1</sup>H}, and NOE data in addition to more complex 2D COSY, ultrafast 2D COSY and 2D HMQC spectra. The observations are made possible by the use of a flow probe and external sample preparation cell to re-hyperpolarize the substrate between transients, allowing repeat measurements to be made within seconds. The potential benefit of the combination of SABRE and 2D NMR methods for rapid characterization of low-concentration analytes is therefore established.

The rate at which structurally informative two-dimensional (2D) NMR spectra, such as correlation spectroscopy (COSY), heteronuclear single-quantum coherence (HSQC), and heteronuclear multiple-quantum correlation (HMQC) spectra, and spatially instructive 1D nuclear Overhauser effect (NOE) spectra can be collected was increased remarkably by the introduction of pulsed field gradients to select desirable coherence transfer pathways. NMR experiments have since been limited by the signal available in a single transient rather than by the necessity to phase-cycle pulses to produce clean, artifact-free results.<sup>1,2</sup> In standard experiments, the signal produced is directly linked to the concentration of the sample, meaning that low-concentration samples require significant signal averaging to generate useful information.<sup>3</sup> Methods have been developed to reduce the associated long scan times substantially, offering significant opportunities for the characterization of materials by NMR spectroscopy.<sup>4–6</sup>

The non-Boltzmann populations produced through the use of hyperpolarization methods can be exploited to generate NMR signals that can be several orders of magnitude larger than those achievable in standard experiments. The formation of nonequilibrium populations of nuclear spin states has been

achieved using techniques as diverse as dynamic nuclear polarization (DNP), optical pumping, and hydrogenative *para*-hydrogen (*p*-H<sub>2</sub>)-induced polarization (PHIP).<sup>7–12</sup> These methods typically deliver a burst of hyperpolarized substrate molecules that must be rapidly monitored. Like PHIP, signal amplification by reversible exchange (SABRE)<sup>13</sup> is able to produce a hyperpolarized substrate in a few seconds. However, unlike PHIP, SABRE does not result in incorporation of *p*-H<sub>2</sub> into the substrate. Instead, it uses a labile complex that possesses two hydride ligands and a weakly bound substrate to facilitate polarization transfer. Polarization is transferred at low magnetic field through the temporary scalar coupling network between what was previously *p*-H<sub>2</sub> and the substrate. Equilibration of the free and bound substrate molecules over a period of a few seconds produces hyperpolarized material in solution. Unlike other hyperpolarization methods, SABRE allows rapid and repeatable production of a hyperpolarized sample without chemical modification of the contained analytes.<sup>14–16</sup>

SABRE was first demonstrated using [Ir(COD)(PCy<sub>3</sub>)(Py)]-[BF<sub>4</sub>] (Crabtree's catalyst; COD = cyclooctadiene, Cy = cyclohexyl),<sup>17</sup> and pyridine (Py). Under these conditions, >100-fold signal enhancements were observed for the <sup>1</sup>H, <sup>13</sup>C, and <sup>15</sup>N NMR signals of free Py. Modification of the polarization transfer catalyst used in SABRE to incorporate a carbene in place of the phosphine produced a >1000-fold <sup>1</sup>H NMR signal enhancement for free Py.<sup>18</sup> This change in ligand gives the polarization transfer catalyst precursor used in this study: [Ir(COD)(IMes)Cl] (**1**) [IMes = 1,3-bis(2,4,6-trimethylphenyl)imidazole-2-ylidene]. It has been postulated that the increase in signal is a consequence of a higher exchange rate that results from the greater electron-donating capability of IMes<sup>19</sup> over PCy<sub>3</sub>.<sup>20</sup> The effect is therefore very simple in concept, but the detailed rationalization of the polarization transfer process is actually highly complex and requires the inclusion of a number of variables.<sup>21</sup>

Herein we illustrate how inorganic chemistry and *p*-H<sub>2</sub> can be combined through SABRE to provide reproducible levels of hyperpolarized material consistently, thereby allowing the rapid

Received: May 25, 2012

Published: July 19, 2012

acquisition of 2D NMR spectra. This approach is shown to address the NMR insensitivity issue and enable “single shot” hyperpolarization methods to be used. An apparatus consisting of an integrated reaction cell and flow probe was employed to achieve this aim. This apparatus was used previously to enable the study of sample hyperpolarization levels and SABRE-created nuclear spin states.<sup>18</sup> Briefly, the apparatus has a polarization chamber that contains the sample solution (located in a predefined but variable magnetic field) and can be purged with *p*-H<sub>2</sub>. For measurement, a series of gas valves shuttle the hyperpolarized sample solution to and from the flow probe, which is connected to the polarization chamber via a transfer line. This aspect of operation is controlled from within the spectrometer software. The polarization transfer catalyst **1** is activated by the addition of hydrogen in the presence of quinoline (20-fold excess) and acetonitrile (1-fold excess). First, acetonitrile displaces the chloride ligand of **1**, thereby activating the newly formed adduct for subsequent hydrogenation of COD. Quinoline then enters the coordination sphere of the metal, forming the active polarization transfer catalyst, [Ir(IMes)(quinoline)<sub>3</sub>(H<sub>2</sub>)Cl]. When such a sample was purged with H<sub>2</sub> gas enriched to 93% *p*-H<sub>2</sub> in a magnetic field of 50 G for 6 s prior to transfer into the flow probe, the <sup>1</sup>H NMR trace shown in Figure 1 was obtained. All seven <sup>1</sup>H

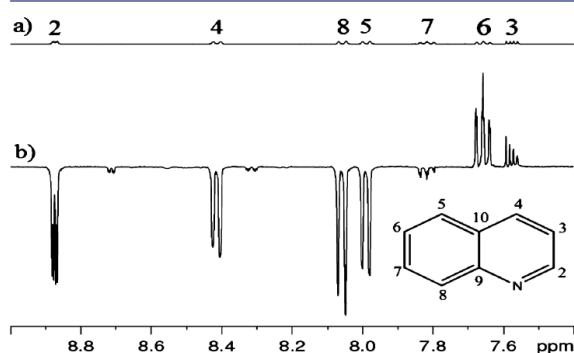


**Figure 1.** <sup>1</sup>H NMR spectra showing (a) the thermally polarized trace of quinoline and (b) the corresponding SABRE-hyperpolarized trace in methanol-*d*<sub>4</sub> achieved with the catalyst [Ir(IMes)(COD)Cl] (**1**) in a 50 G polarization transfer field.

resonances of quinoline were enhanced well beyond their thermally polarized level. The level of enhancement was maximized for the H(2) proton, which showed >60-fold enhancement when 2 μmol of quinoline was detected. This single response resulted in a signal-to-noise (S/N) ratio of 730:1 for the H(2) signal. When the sample detected amount was reduced to the 0.2 μmol level, the corresponding S/N ratio was 15:1. These data therefore serve to illustrate the potential of this method for detection of low-concentration analytes; when nicotinamide was used as the substrate, a 20 nmol sample produced a S/N ratio of 60:1.

When the 2 μmol quinoline sample was purged with *p*-H<sub>2</sub> for the increased time of 20 s, the level of signal enhancement increased by a further factor of 2.6, thereby illustrating how even lower concentrations of this analyte could be examined with SABRE.

Such samples can easily be returned to the polarization chamber and exposed to fresh *p*-H<sub>2</sub> prior to a second NMR measurement. The total time for this process is dominated by

the purge duration. This approach produces hyperpolarized signals with an intensity that is reproducible to within a 5% tolerance when the measurement interval is 30 s and the purge time 6 s. This approach of shuttling the sample between the hyperpolarization chamber and the probe enables signal averaging, a key requirement of many NMR experiments. The completion of a range of multiscan NMR measurements are now shown to benefit from hyperpolarization achieved by SABRE.

A hyperpolarized quinoline sample was probed using the 1D NOE sequence of Stott, Keeler, and Shaka<sup>22</sup> with four polarization transfer steps. Examination of the resulting four-scan-hyperpolarized H(4) resonance, in conjunction with a 1.5 s NOE contact time, led to a cross-peak with an intensity of 0.9% at the H(5) resonance position. In contrast, when thermal polarization was used, the NOE transfer peak achieved a similar S/N value only after a potentially prohibitive 15 000 scans. Consequently, the normal measurement, which takes 20 h to implement at this 2 μmol sample loading, was completed in just 81 s. This multiscan observation establishes the utility of SABRE in examining low-concentration analytes by such 1D methods.

The same flow and replenishment approach was used to record a 2D <sup>1</sup>H OPSY–COSY spectrum for the 2 μmol sample (Figure 2); OPSY denotes the only *para*-hydrogen spectroscop-

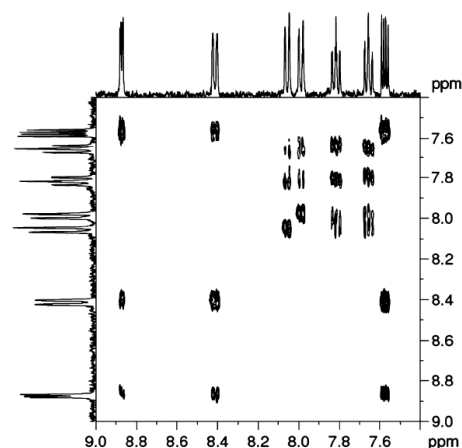


**Figure 2.** <sup>1</sup>H 2D OPSY–COSY NMR spectrum of hyperpolarized quinoline in methanol-*d*<sub>4</sub> achieved using **1** and *p*-H<sub>2</sub> with an applied polarization transfer field of 0 G.<sup>27</sup>

py protocol,<sup>23</sup> which was set for use as a double-quantum filter.<sup>24</sup> In this case, the *p*-H<sub>2</sub> purge time was 2 s and 64 increments were completed using the sample-shuttling process, giving a total experiment time of 16 min. This NMR spectrum could be recorded against a strong proton background because the OPSY filter removed any signals that did not originate from polarization transferred under SABRE. Unusually, cross-peak encoding was optimized at the start of the 2D data cascade for this SABRE-derived polarization, causing the cross-peaks to appear before the diagonal. Hence, far fewer increments were necessary for cross-peak mapping, with the diagonal peaks building up according to  $\sin(\pi J_{HH}t)$ ; normally this term corresponds to the cross-peak buildup.<sup>25</sup> In this experiment, <sup>4</sup>J<sub>HH</sub> couplings within the rings, such as those between protons



H(5) and H(7), were readily visible. For them to be visible in a normal experiment, a very good S/N ratio would be required.

We also note that the increased sensitivity provided by hyperpolarization enables the completion of a 2D COSY measurement using ultrafast methods.<sup>4</sup> In this case, a single purge of  $p\text{-H}_2$  yields sufficient hyperpolarization to allow the complete assignment of the coupling framework within quinoline in the 6  $\mu\text{mol}$  sample in under 1 s.<sup>4,5</sup> A typical trace resulting from polarization transfer at 65 G is shown in Figure 3; a plot obtained at the 0.6  $\mu\text{mol}$  level is reproduced in the Supporting Information.

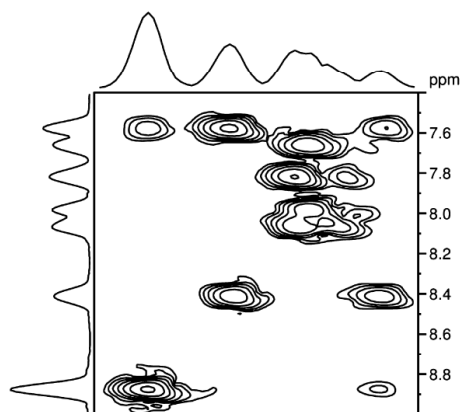


**Figure 3.** Ultrafast  $^1\text{H}$  COSY spectrum of a 6  $\mu\text{mol}$  sample of hyperpolarized quinoline in methanol- $d_4$  collected using a single transient.

The collection of  $^{13}\text{C}$  data is routinely even harder to achieve than a COSY measurement because of the inherent 6400-fold drop in sensitivity associated with the direct detection of a  $^{13}\text{C}$  signal relative to that of  $^1\text{H}$ . Figure 4a shows the resulting single-scan, fully coupled  $^{13}\text{C}$  signal acquired for a 60  $\mu\text{mol}$  sample that was monitored after a  $90^\circ$  read pulse and polarization transfer at 50 G. While all nine of the expected

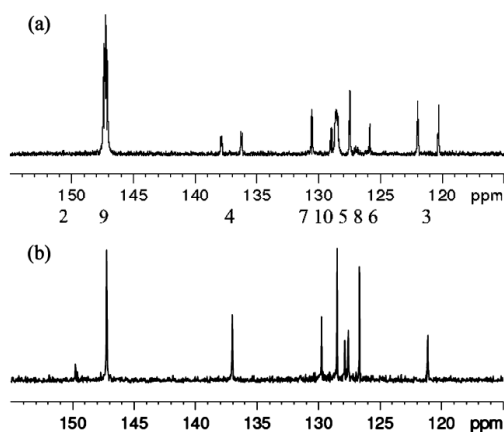


**Figure 4.** (a) Single-scan  $^{13}\text{C}$  NMR spectrum of SABRE-hyperpolarized quinoline presented in magnitude mode after polarization transfer at 0 G with 1 in methanol- $d_4$  acquired using a  $90^\circ$  excitation pulse. (b) Corresponding refocused  $^{13}\text{C}\{^1\text{H}\}$  INEPT NMR spectrum of a similar sample hyperpolarized at 50 G.

signals for quinoline can be identified, the intensity of the signal corresponding to the C(2) position at  $\delta$  150.8 is significantly reduced.

The detected resonances appear with a degree of antiphase character (which can be ascribed to the detection of signals associated with the combinations of the product operators  $2I_{1z}S_x$  and  $4I_{1z}I_{2z}S_x$  at each  $^{13}\text{C}$  location); this effect has been overcome in Figure 4 by presenting these data in magnitude mode. The populations of the magnetic states created with SABRE vary with the magnitude of the magnetic field at which polarization transfer occurs. This affects both  $^1\text{H}$ – $^1\text{H}$  and  $^1\text{H}$ – $^{13}\text{C}$  spin pairs.<sup>18</sup> Consequently, if these  $^{13}\text{C}$ – $^1\text{H}$  terms are to be observed via a  $^1\text{H}$ -decoupled low-sensitivity  $^{13}\text{C}$  response, the antiphase character must be refocused. This was readily achieved by using an insensitive nuclei enhanced by polarization transfer (INEPT) refocusing scheme,<sup>26</sup> which allowed all nine  $^{13}\text{C}$  signals for quinoline to be readily detected and resulted in a S/N ratio of 40:1 for the C(9) resonance of the 60  $\mu\text{mol}$  sample after a single scan (Figure 4B). When a traditional  $^{13}\text{C}\{^1\text{H}\}$  measurement was completed using an equivalent nonhyperpolarized sample, a recycle time of 3.6 s, and a  $30^\circ$  flip angle, an equivalent S/N ratio was obtained after 4096 scans.

Since the SABRE approach simultaneously hyperpolarizes both  $^{13}\text{C}$  and  $^1\text{H}$  nuclei, a new approach to data collection can be envisaged. First, it is possible to use the multiple-receive facility of a modern NMR spectrometer to collect sequential/simultaneous SABRE-hyperpolarized  $^{13}\text{C}$  and  $^1\text{H}$  data. This enables the rapid observation of both types of nuclei after a single hyperpolarization transfer step. A refinement of this approach enables the collection of two hyperpolarized  $^{13}\text{C}$  NMR traces from a single polarization transfer cycle. The first of these corresponds to the measurement of a fully proton-coupled  $^{13}\text{C}$  acquisition, thereby utilizing the hyperpolarized  $^{13}\text{C}$  magnetization. The second acquisition also records  $^{13}\text{C}$  data, but here a refocused and decoupled INEPT transfer protocol is employed to record the  $^{13}\text{C}\{^1\text{H}\}$  NMR spectrum. This second measurement uses unaffected  $^1\text{H}$  hyperpolarization to sensitize the second  $^{13}\text{C}$  NMR spectrum. Figure 4b presents a typical hyperpolarized  $^{13}\text{C}$  INEPT (refocused) trace.

It is also possible to use the flow method to collect a hyperpolarized  $^1\text{H}$ – $^{13}\text{C}$  heteronuclear 2D NMR spectrum. The result of this for a 2  $\mu\text{mol}$  sample loading is shown in Figure 5. This HMBC spectrum of quinoline was collected as a 32-increment data set after polarization transfer at 60 G, with a single scan per increment. The total experiment time was 16 min. Cross-peaks now locate all nine of the  $^{13}\text{C}$  signals and arise primarily through long-range rather than direct coupling pathways. When the polarization transfer step is completed with an applied field of 0 G, the corresponding cross-peaks are derived from short-range couplings.

The results presented here demonstrate that the SABRE technique enables rapid completion of a wide range of structurally informative 1D and 2D NMR experiments on low-concentration analytes. By variation of the strength of the polarization transfer field, it is possible to control the type of magnetization created in the hyperpolarized analyte. If the field strength is set to maximize the formation of correlated longitudinal two-spin order terms, the optimum characteristics for creating cross-peaks in both 2D OPSY–COSY and heteronuclear correlation experiments result. Consequently, both long- and short-range couplings and hence structural connections within molecules can be probed both rapidly and

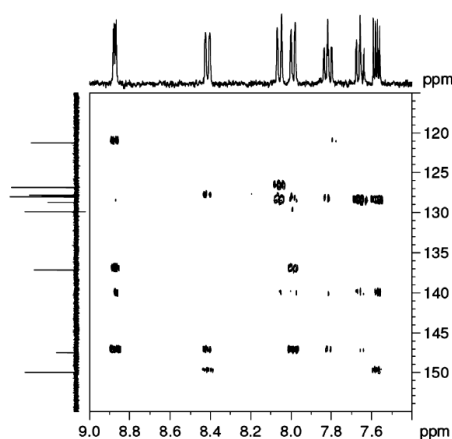


**Figure 5.** 2D  $^1\text{H}$ - $^{13}\text{C}$  HMBC NMR spectrum collected with quinoline that was hyperpolarized at 60 G in methanol- $d_4$  using **1** and  $p\text{-H}_2$ .<sup>27</sup>

at high sensitivity. This means that the user can select the type of magnetization required and hence tailor the measurement to the specific information element that is required. In view of the fact that SABRE has previously been reported to provide an 8600-fold  $^1\text{H}$  signal enhancement for pyridine,<sup>18</sup> its potential to allow rapid NMR analysis of very low concentration species is an exciting future prospect for this method. Research is ongoing to demonstrate that mixtures can be examined using this method and that absolute concentrations can be determined using suitable calibration curves.

## ■ ASSOCIATED CONTENT

### Supporting Information

Details of the samples and NMR procedures. This material is available free of charge via the Internet at <http://pubs.acs.org>.

## ■ AUTHOR INFORMATION

### Corresponding Author

simon.duckett@york.ac.uk

### Notes

The authors declare no competing financial interest.

## ■ ACKNOWLEDGMENTS

We are grateful for financial support from the EPSRC (R.E.M., L.S.L., Grants EP/G009546/1 and EP/H029575/1) and AstraZeneca (studentship for L.S.L.). Bruker BioSpin supported this project by providing equipment. We acknowledge helpful discussions with Dr. J. A. B. Lohman, Dr. D. Kilgour, and colleagues. We are also grateful to Dr. P. Giraudeau for support with the single-shot experiments.

## ■ REFERENCES

- (1) Ernst, R. R. *Angew. Chem., Int. Ed. Engl.* **1992**, *31*, 805.
- (2) Wuthrich, K. *Angew. Chem., Int. Ed.* **2003**, *42*, 3340.
- (3) Barker, P.; Freeman, R. *J. Magn. Reson.* **1985**, *64*, 334.
- (4) Frydman, L.; Scherf, T.; Lupulescu, A. *Proc. Natl. Acad. Sci. U.S.A.* **2002**, *99*, 15858.
- (5) Frydman, L.; Lupulescu, A.; Scherf, T. *J. Am. Chem. Soc.* **2003**, *125*, 9204.
- (6) Tal, A.; Frydman, L. *Prog. Nucl. Magn. Reson. Spectrosc.* **2010**, *57*, 241.
- (7) Bowers, C. R.; Weitekamp, D. P. *J. Am. Chem. Soc.* **1987**, *109*, 5541.

(8) Ardenkjaer-Larsen, J. H.; Fridlund, B.; Gram, A.; Hansson, G.; Hansson, L.; Lerche, M. H.; Servin, R.; Thaning, M.; Golman, K. *Proc. Natl. Acad. Sci. U.S.A.* **2003**, *100*, 10158.

(9) Abragam, A.; Goldman, M. *Rep. Prog. Phys.* **1978**, *41*, 395.

(10) Navon, G.; Song, Y. Q.; Room, T.; Appelt, S.; Taylor, R. E.; Pines, A. *Science* **1996**, *271*, 1848.

(11) Duckett, S. B.; Mewis, R. E. *Acc. Chem. Res.* **2012**, DOI: 10.1021/ar2003094.

(12) Green, R. A.; Adams, R. W.; Duckett, S. B.; Mewis, R. E.; Williamson, D. C.; Green, G. G. R. *Prog. Nucl. Magn. Reson. Spectrosc.* **2012**, DOI: 10.1016/j.pnmrs.2012.03.001.

(13) Duckett, S. B.; Adams, R. W.; Aguilar, J. A.; Atkinson, K. D.; Cowley, M. J.; Elliott, P. I. P.; Green, G. G. R.; Khazal, I. G.; Lopez-Serrano, J.; Williamson, D. C. *Science* **2009**, *323*, 1708.

(14) Duecker, E. B.; Kuhn, L. T.; Muennemann, K.; Griesinger, C. *J. Magn. Reson.* **2012**, *214*, 159.

(15) Gloeggler, S.; Mueller, R.; Colell, J.; Emondts, M.; Dabrowski, M.; Bluemich, B.; Appelt, S. *Phys. Chem. Chem. Phys.* **2011**, *13*, 13759.

(16) Gloeggler, S.; Emondts, M.; Colell, J.; Mueller, R.; Bluemich, B.; Appelt, S. *Analyst* **2011**, *136*, 1566.

(17) Crabtree, R. H.; Felkin, H.; Morris, G. E. *J. Organomet. Chem.* **1977**, *141*, 205.

(18) Cowley, M. J.; Adams, R. W.; Atkinson, K. D.; Cockett, M. C. R.; Duckett, S. B.; Green, G. G. R.; Lohman, J. A. B.; Kerssebaum, R.; Kilgour, D.; Mewis, R. E. *J. Am. Chem. Soc.* **2011**, *133*, 6134.

(19) Gusev, D. G. *Organometallics* **2009**, *28*, 6458.

(20) Atkinson, K. D.; Cowley, M. J.; Elliott, P. I. P.; Duckett, S. B.; Green, G. G. R.; López-Serrano, J.; Whitwood, A. C. *J. Am. Chem. Soc.* **2009**, *131*, 13362.

(21) Adams, R. W.; Duckett, S. B.; Green, R. A.; Williamson, D. C.; Green, G. G. R. *J. Chem. Phys.* **2009**, *131*, No. 194505.

(22) Stott, K.; Keeler, J.; Van, Q. N.; Shaka, A. J. *J. Magn. Reson.* **1997**, *125*, 302.

(23) Aguilar, J. A.; Adams, R. W.; Duckett, S. B.; Green, G. G. R.; Kandiah, R. *J. Magn. Reson.* **2011**, *208*, 49.

(24) Piantini, U.; Sorensen, O. W.; Ernst, R. R. *J. Am. Chem. Soc.* **1982**, *104*, 6800.

(25) Delaglio, F.; Wu, Z. R.; Bax, A. *J. Magn. Reson.* **2001**, *149*, 276.

(26) Morris, G. A.; Freeman, R. *J. Am. Chem. Soc.* **1979**, *101*, 760.

(27) The external projections employed in Figures 2 and 5 were taken from experiments recorded with a high concentration of quinoline and are intended to enable the reader to see how the hyperpolarized cross-peaks shown in the 2D plots map to the expected correlations.

## 10 Abbreviations

$\%V_{\text{bur}}$  : per cent buried volume

Å : angstrom

ALTADENA : Adiabatic Longitudinal Transport After Dissociation Engenders  
Nuclear Alignment

av. : average

BBI : Broadband inverse probe

cat : catalyst

$\text{CDCl}_3$  : deuterated chloroform

CIDNP : Chemically Induced Dynamic Nuclear Polarisation

COD : 1,5-cyclooctadiene

COE : cyclooctene

conc. : concentration

COSY : Correlation Spectroscopy

Cy : cyclohexyl

D : deuterium

DCM : Dichloromethane

DFT : Density Functional Theory

DMSO : Dimethylsulphoxide

DNP : Dynamic Nuclear Polarisation

dq : double quantum

E : enhancement

eq.	: equivalent(s)
ESI	: electrospray ionisation
Et	: ethyl
EXSY	: Exchange spectroscopy
FID	: Free Induction Decay
G	: Gauss
GI <sub>50</sub>	: A quantitative measure of how much of a compound is required to cause a 50 % reduction in proliferation of cancer cells
H	: Proton (and Henry's Law constant in Experimental)
HMBC	: Heteronuclear multiple-bond correlation spectroscopy
HMQC	: Heteronuclear multiple-quantum correlation spectroscopy
HSQC	: Heteronuclear single-quantum correlation spectroscopy
IC <sub>50</sub>	: A quantitative measure of how much of a compound is required to inhibit a given biological process by half
ICy	: Bis-1,3-cyclohexyl imidazole hydrochloride
IMe	: Bis-1,3-methyl imidazole hydrochloride
IMes	: Bis-1,3-(2,4,6-trimethylphenyl) imidazole hydrochloride
INEPT	: Insensitive Nuclei Enhanced by Polarisation Transfer
<sup>i</sup> Pr	: isopropyl
IR	: infrared
K	: Kelvin
L	: ligand



M	: metal
Me	: methyl
MeO	: methoxy ligand
MeOD	: deuterated methanol
MIC	: minimum inhibitory concentration
MKI/II/III	: referring to the first (Mark1), second (Mark 2) and third (mark 3) generation mixing chamber
MRI	: Magnetic Resonance Imaging
MS	: Mass spectroscopy
NCMe	: Acetonitrile
nd	: Not decoupled, in reference to the INEPT pulse sequence
NH-PHIP	: Non-hydrogenative parahydrogen induced polarisation
NHC	: N-heterocyclic carbene
NMR	: Nuclear Magnetic Resonance
NOESY	: nuclear Overhauser effect spectroscopy
obs.	: observed
OPSY	: Only <i>parahydrogen</i> spectroscopy
OPSYdq	: Only <i>parahydrogen</i> spectroscopy optimised for double quantum states
ORTEP	: Oak Ridge Thermal Ellipsoid Plot
PASADENA	: Parahydrogen And Synthesis Allow Dramatically Enhanced Nuclear Alignment
PCy <sub>3</sub>	: tricyclohexyl phosphine

Ph	: Phenyl
<i>p</i> H <sub>2</sub>	: parahydrogen
PHIP	: Parahydrogen induced polarisation
PPh <sub>3</sub>	: triphenyl phosphine
ppm	: parts per million
PTF	: polarisation transfer field
py	: pyridine
q	: quinoline
<b>r</b>	: repulsivity factor
R	: any group
rd	: refocused and decoupled, in reference to the INEPT pulse sequence
rel.	: relative
RF	: radio frequency
S/N	: signal to noise ratio
SABRE	: Signal Amplification By Reversible Exchange
SIMes	: bis-1,3-(2,4,6-trimethylphenyl) imidazoline hydrochloride
Sub	: substrate
T	: tesla
<sup>t</sup> Bu	: tert-butyl
TEP	: Tolman's Electronic Parameter
THF	: tetrahydrofuran
TOCSY	: Total correlation spectroscopy

TXI : Triple Resonance Inverse Probe

TXO : Triple Resonances Obverse Probe

ufCOSY : ultrafast COSY

UV : ultraviolet

## 11 References

- (1) Malet-Martino, M.; Holzgrabe, U. *Journal of Pharmaceutical and Biomedical Analysis* **2011**, *55*, 1.
- (2) Holzgrabe, U. *Progress in Nuclear Magnetic Resonance Spectroscopy* **2010**, *57*, 229.
- (3) Powers, R. *Magnetic Resonance in Chemistry* **2009**, *47*, S2.
- (4) Geppi, M.; Mollica, G.; Borsacchi, S.; Veracini, C. A. *Applied Spectroscopy Reviews* **2008**, *43*, 202.
- (5) Sanchez, S.; Ziarelli, F.; Viel, S.; Delaurent, C.; Caldarelli, S. *Journal of Pharmaceutical and Biomedical Analysis* **2008**, *47*, 683.
- (6) Brettmann, B. K.; Myerson, A. S.; Trout, B. L. *Journal of Pharmaceutical Sciences* **2012**, *101*, 2185.
- (7) Singh, S.; Handa, T.; Narayanam, M.; Sahu, A.; Junwal, M.; Shah, R. P. *Journal of Pharmaceutical and Biomedical Analysis* **2012**, *69*, 148.
- (8) Claridge, T. D. W. *High-Resolution NMR Techniques in Organic Chemistry*; Elsevier, 2008; Vol. 19.
- (9) Arnold, J. T.; Dharmatti, S. S.; Packard, M. E. *The Journal of Chemical Physics* **1951**, *19*, 507.
- (10) Freeman, R. *Khimiya Geterotsiklicheskikh Soedinenii* **1995**, 1157.
- (11) Nelson, F. A.; Weaver, H. E. *Science* **1964**, *146*, 223.
- (12) <http://www.bruker.com/en/products/mr/nmr/probes/cryoprobes.html>  
Accessed on 31/01/2013
- (13) Molinski, T. F. *Natural Product Reports* **2010**, *27*, 321.
- (14) Schlotterbeck, G.; Ross, A.; Hochstrasser, R.; Senn, H.; Kühn, T.; Marek, D.; Schett, O. *Analytical Chemistry* **2002**, *74*, 4464.
- (15) Abragam, A.; Proctor, W. G. *Physical Review* **1958**, *109*, 1441.
- (16) Gadian, D. G.; Panesar, K. S.; Perez Linde, A. J.; Horsewill, A. J.; Kockenberger, W.; Owers-Bradley, J. R. *Physical Chemistry Chemical Physics* **2012**, *14*, 5397.
- (17) Krjukov, E. V.; O'Neill, J. D.; Owers-Bradley, J. R. *Journal of Low Temperature Physics* **2005**, *140*, 397.
- (18) Goodson, B. M. *Journal of Magnetic Resonance* **2002**, *155*, 157.

- (19) Bouchiat, M. A.; Carver, T. R.; Varnum, C. M. *Physical Review Letters* **1960**, *5*, 373.
- (20) Berthault, P.; Huber, G.; Desvaux, H. *Progress in Nuclear Magnetic Resonance Spectroscopy* **2009**, *55*, 35.
- (21) Costella, S.; Kirby, M.; Maksym, G. N.; McCormack, D. G.; Paterson, N. A. M.; Parraga, G. *Respirology* **2012**, *17*, 1237.
- (22) Albert, M. S.; Balamore, D. *Nuclear Instruments and Methods in Physics Research Section A: Accelerators, Spectrometers, Detectors and Associated Equipment* **1998**, *402*, 441.
- (23) Bifone, A.; Song, Y.-Q.; Seydoux, R.; Taylor, R. E.; Goodson, B. M.; Pietrass, T.; Budinger, T. F.; Navon, G.; Pines, A. *Proceedings of the National Academy of Sciences* **1996**, *93*, 12932.
- (24) Swanson, S. D.; Rosen, M. S.; Agranoff, B. W.; Coulter, K. P.; Welsh, R. C.; Chupp, T. E. *Magnetic Resonance in Medicine* **1997**, *38*, 695.
- (25) Navon, G.; Song, Y. Q.; Rõõm, T.; Appelt, S.; Taylor, R. E.; Pines, A. *Science* **1996**, *271*, 1848.
- (26) Bowers, C. R.; Long, H. W.; Pietrass, T.; Gaede, H. C.; Pines, A. *Chemical Physics Letters* **1993**, *205*, 168.
- (27) Lisitza, N.; Muradian, I.; Frederick, E.; Patz, S.; Hatabu, H.; Chekmenev, E. Y. *Journal of Chemical Physics* **2009**, *131*.
- (28) Cherubini, A.; Payne, G. S.; Leach, M. O.; Bifone, A. *Chemical Physics Letters* **2003**, *371*, 640.
- (29) Spence, M. M.; Rubin, S. M.; Dimitrov, I. E.; Ruiz, E. J.; Wemmer, D. E.; Pines, A.; Yao, S. Q.; Tian, F.; Schultz, P. G. *Proceedings of the National Academy of Sciences* **2001**, *98*, 10654.
- (30) Spence, M. M.; Ruiz, E. J.; Rubin, S. M.; Lowery, T. J.; Winssinger, N.; Schultz, P. G.; Wemmer, D. E.; Pines, A. *Journal of the American Chemical Society* **2004**, *126*, 15287.
- (31) Maly, T.; Debelouchina, G. T.; Bajaj, V. S.; Hu, K.-N.; Joo, C.-G.; Mak-Jurkauskas, M. L.; Sirigiri, J. R.; van der Wel, P. C. A.; Herzfeld, J.; Temkin, R. J.; Griffin, R. G. *Journal of Chemical Physics* **2008**, *128*.
- (32) Atsarkin, V. A. *Journal of Physics: Conference Series* **2011**, *324*, 012003.
- (33) Ardenkjær-Larsen, J. H.; Fridlund, B.; Gram, A.; Hansson, G.; Hansson, L.; Lerche, M. H.; Servin, R.; Thaning, M.; Golman, K. *Proceedings of the National Academy of Sciences of the United States of America* **2003**, *100*, 10158.
- (34) Wolber, J.; Ellner, F.; Fridlund, B.; Gram, A.; Johannesson, H.; Hansson, G.; Hansson, L. H.; Lerche, M. H.; Mansson, S.; Servin, R.; Thaning, M.; Golman, K.;

Ardenkjaer-Larsen, J. H. *Nuclear Instruments & Methods in Physics Research Section a-Accelerators Spectrometers Detectors and Associated Equipment* **2004**, 526, 173.

(35) Day, I. J.; Mitchell, J. C.; Snowden, M. J.; Davis, A. L. *Applied Magnetic Resonance* **2008**, 34, 453.

(36) Joo, C.-G.; Hu, K.-N.; Bryant, J. A.; Griffin, R. G. *Journal of the American Chemical Society* **2006**, 128, 9428.

(37) Wilson, D. M.; Keshari, K. R.; Larson, P. E. Z.; Chen, A. P.; Hu, S.; Crieckinge, M. V.; Bok, R.; Nelson, S. J.; Macdonald, J. M.; Vigneron, D. B.; Kurhanewicz, J. *Journal of Magnetic Resonance* **2010**, 205, 141.

(38) Park, I.; Bok, R.; Ozawa, T.; Phillips, J. J.; James, C. D.; Vigneron, D. B.; Ronen, S. M.; Nelson, S. J. *Journal of Magnetic Resonance Imaging* **2011**, 33, 1284.

(39) Duckett, S. B.; Newell, C. L.; Eisenberg, R. *Journal of the American Chemical Society* **1993**, 115, 1156.

(40) Duckett, S. B.; Wood, N. J. *Coordination Chemistry Reviews* **2008**, 252, 2278.

(41) Natterer, J.; Bargon, J. *Progress in Nuclear Magnetic Resonance Spectroscopy* **1997**, 31, 293.

(42) Bowers, C. R.; Weitekamp, D. P. *Physical Review Letters* **1986**, 57, 2645.

(43) Bowers, C. R.; Weitekamp, D. P. *Journal of the American Chemical Society* **1987**, 109, 5541.

(44) Hommeltoft, S. I.; Berry, D. H.; Eisenberg, R. *Journal of the American Chemical Society* **1986**, 108, 5345.

(45) Eisenschmid, T. C.; Kirss, R. U.; Deutsch, P. P.; Hommeltoft, S. I.; Eisenberg, R.; Bargon, J.; Lawler, R. G.; Balch, A. L. *Journal of the American Chemical Society* **1987**, 109, 8089.

(46) Pravica, M. G.; Weitekamp, D. P. *Chemical Physics Letters* **1988**, 145, 255.

(47) Duckett, S. B.; Sleight, C. J. *Progress in Nuclear Magnetic Resonance Spectroscopy* **1999**, 34, 71.

(48) Duckett, S. B.; Mewis, R. E. *Accounts of Chemical Research* **2012**, 45, 1247.

(49) Duckett, S. B.; Blazina, D. *European Journal of Inorganic Chemistry* **2003**, 2901.

(50) Blazina, D.; Duckett, S. B.; Dyson, P. J.; Lohmann, J. A. B. *Chemistry – A European Journal* **2003**, 9, 1046.

- (51) Duckett, S. B.; Newell, C. L.; Eisenberg, R. *Journal of the American Chemical Society* **1994**, *116*, 10548.
- (52) Duckett, S. B.; Newell, C. L.; Eisenberg, R. *Journal of the American Chemical Society* **1997**, *119*, 2068.
- (53) Bhattacharya, P.; Ross, B. D.; Bunger, R. *Experimental Biology and Medicine* **2009**, *234*, 1395.
- (54) Reineri, F.; Viale, A.; Giovenzana, G.; Santelia, D.; Dastru, W.; Gobetto, R.; Aime, S. *Journal of the American Chemical Society* **2008**, *130*, 15047.
- (55) Kadlecsek, S.; Vahdat, V.; Nakayama, T.; Ng, D.; Emami, K.; Rizi, R. *NMR in Biomedicine* **2011**, *24*, 933.
- (56) Wood, N. J.; Brannigan, J. A.; Duckett, S. B.; Heath, S. L.; Wagstaff, J. *Journal of the American Chemical Society* **2007**, *129*, 11012.
- (57) Korchak, S. E.; Ivanov, K. L.; Yurkovskaya, A. V.; Vieth, H. M. *Physical Chemistry Chemical Physics* **2009**, *11*, 11146.
- (58) Adams, R. W.; Aguilar, J. A.; Atkinson, K. D.; Cowley, M. J.; Elliott, P. I. P.; Duckett, S. B.; Green, G. G. R.; Khazal, I. G.; Lopez-Serrano, J.; Williamson, D. C. *Science* **2009**, *323*, 1708.
- (59) Adams, R. W.; Duckett, S. B.; Green, R. A.; Williamson, D. C.; Green, G. G. R. *Journal of Chemical Physics* **2009**, *131*.
- (60) Wolfram Research, Inc.: Champaign, Illinois, USA, 2007.
- (61) Atkinson, K. D.; Cowley, M. J.; Elliott, P. I. P.; Duckett, S. B.; Green, G. G. R.; Lopez-Serrano, J.; Whitwood, A. C. *Journal of the American Chemical Society* **2009**, *131*, 13362.
- (62) Gong, Q.; Gordji-Nejad, A.; Blümich, B.; Appelt, S. *Analytical Chemistry* **2010**, *82*, 7078.
- (63) Theis, T.; Ledbetter, M. P.; Kervern, G.; Blanchard, J. W.; Ganssle, P. J.; Butler, M. C.; Shin, H. D.; Budker, D.; Pines, A. *Journal of the American Chemical Society* **2012**, *134*, 3987.
- (64) Gloggler, S.; Muller, R.; Colell, J.; Emondts, M.; Dabrowski, M.; Blumich, B.; Appelt, S. *Physical Chemistry Chemical Physics* **2011**, *13*, 13759.
- (65) Dücker, E. B.; Kuhn, L. T.; Münnemann, K.; Griesinger, C. *Journal of Magnetic Resonance* **2012**, *214*, 159.
- (66) Cowley, M. J.; Adams, R. W.; Atkinson, K. D.; Cockett, M. C. R.; Duckett, S. B.; Green, G. G. R.; Lohman, J. A. B.; Kerssebaum, R.; Kilgour, D.; Mewis, R. E. *Journal of the American Chemical Society* **2011**, *133*, 6134.

- (67) Lloyd, L. S.; Adams, R. W.; Bernstein, M.; Coombes, S.; Duckett, S. B.; Green, G. G. R.; Lewis, R. J.; Mewis, R. E.; Sleigh, C. J. *Journal of the American Chemical Society* **2012**, *134*, 12904.
- (68) Crabtree, R. H.; Felkin, H.; Morris, G. E. *Journal of Organometallic Chemistry* **1977**, *141*, 205.
- (69) Crabtree, R. *Accounts of Chemical Research* **1979**, *12*, 331.
- (70) Crabtree, R. H.; Davis, M. W. *The Journal of Organic Chemistry* **1986**, *51*, 2655.
- (71) Ellames, G. J.; Gibson, J. S.; Herbert, J. M.; McNeill, A. H. *Tetrahedron* **2001**, *57*, 9487.
- (72) Bartoszewicz, A.; Marcos, R.; Sahoo, S.; Inge, A. K.; Zou, X. D.; Martin-Matute, B. *Chemistry – A European Journal* **2012**, *18*, 14510.
- (73) Vazquez-Serrano, L. D.; Owens, B. T.; Buriak, J. M. *Inorganica Chimica Acta* **2006**, *359*, 2786.
- (74) Lee, H. M.; Jiang, T.; Stevens, E. D.; Nolan, S. P. *Organometallics* **2001**, *20*, 1255.
- (75) Di Giuseppe, A.; Castarlenas, R.; Perez-Torrente, J. J.; Crucianelli, M.; Polo, V.; Sancho, R.; Lahoz, F. J.; Oro, L. A. *Journal of the American Chemical Society* **2012**, *134*, 8171.
- (76) Mercks, L.; Albrecht, M. *Chemical Society Reviews* **2010**, *39*, 1903.
- (77) Brown, J. A.; Irvine, S.; Kennedy, A. R.; Kerr, W. J.; Andersson, S.; Nilsson, G. N. *Chemical Communications* **2008**, 1115.
- (78) Nilsson, G. N.; Kerr, W. J. *Journal of Labelled Compounds & Radiopharmaceuticals* **2010**, *53*, 662.
- (79) Scott, N. M.; Pons, V.; Stevens, E. D.; Heinekey, D. M.; Nolan, S. P. *Angewandte Chemie International Edition* **2005**, *44*, 2512.
- (80) Torres, O.; Martin, M.; Sola, E. *Organometallics* **2009**, 863.
- (81) Tang, C. Y.; Smith, W.; Vidovic, D.; Thompson, A. L.; Chaplin, A. B.; Aldridge, S. *Organometallics* **2009**, *28*, 3059.
- (82) Frydman, L.; Scherf, T.; Lupulescu, A. *Proceedings of the National Academy of Sciences of the United States of America* **2002**, *99*, 15858.
- (83) Frydman, L.; Lupulescu, A.; Scherf, T. *Journal of the American Chemical Society* **2003**, *125*, 9204.
- (84) Aguilar, J. A.; Elliott, P. I. P.; Lopez-Serrano, J.; Adams, R. W.; Duckett, S. B. *Chemical Communications* **2007**, 1183.



- (85) Hore, P. J.; Jones, J. A.; Wimperis, S. *NMR: The Toolkit*, Oxford University Press, 2000.
- (86) Aguilar, J. A.; Adams, R. W.; Duckett, S. B.; Green, G. G. R.; Kandiah, R. *Journal of Magnetic Resonance* **2011**, *208*, 49.
- (87) Canet, D.; Aroulanda, C.; Mutzenhardt, P.; Aime, S.; Gobetto, R.; Reineri, F. *Concepts in Magnetic Resonance Part A* **2006**, *28A*, 321.
- (88) Tayler, M. C. D.; Levitt, M. H. *Physical Chemistry Chemical Physics* **2011**, *13*, 9128.
- (89) Ulrich, C.; Bargon, J. *Magnetic Resonance in Chemistry* **2000**, *38*, 33.
- (90) Evans, D. F. *Journal of the Chemical Society (Resumed)* **1959**, 2003.
- (91) Rosen, E. L.; Varnado, C. D.; Tennyson, A. G.; Khramov, D. M.; Kamplain, J. W.; Sung, D. H.; Cresswell, P. T.; Lynch, V. M.; Bielawski, C. W. *Organometallics* **2009**, *28*, 6695.
- (92) Zinner, S. C.; Rentzsch, C. F.; Herdtweck, E.; Herrmann, W. A.; Kuhn, F. E. *Dalton Transactions* **2009**, 7055.
- (93) Frey, G. D.; Rentzsch, C. F.; von Preysing, D.; Scherg, T.; Mühlhofer, M.; Herdtweck, E.; Herrmann, W. A. *Journal of Organometallic Chemistry* **2006**, *691*, 5725.
- (94) Kelly, R. A.; Clavier, H.; Giudice, S.; Scott, N. M.; Stevens, E. D.; Bordner, J.; Samardjiev, I.; Hoff, C. D.; Cavallo, L.; Nolan, S. P. *Organometallics* **2008**, *27*, 202.
- (95) Prinz, M.; Veiros, L. F.; Calhorda, M. J.; Romão, C. C.; Herdtweck, E.; Kühn, F. E.; Herrmann, W. A. *Journal of Organometallic Chemistry* **2006**, *691*, 4446.
- (96) Leuthäuser, S.; Schwarz, D.; Plenio, H. *Chemistry – A European Journal* **2007**, *13*, 7195.
- (97) Tolman, C. A. *Chemical Reviews* **1977**, *77*, 313.
- (98) Clavier, H.; Nolan, S. P. *Chemical Communications* **2010**, *46*, 841.
- (99) Huang, J.; Schanz, H.-J.; Stevens, E. D.; Nolan, S. P. *Organometallics* **1999**, *18*, 2370.
- (100) Hillier, A. C.; Sommer, W. J.; Yong, B. S.; Petersen, J. L.; Cavallo, L.; Nolan, S. P. *Organometallics* **2003**, *22*, 4322.
- (101) Cavallo, L.; Correa, A.; Costabile, C.; Jacobsen, H. *Journal of Organometallic Chemistry* **2005**, *690*, 5407.
- (102) Díez-González, S.; Nolan, S. P. *Coordination Chemistry Reviews* **2007**, *251*, 874.

- (103) Bargon, J.; Kandels, J.; Woelk, K. *Zeitschrift Fur Physikalische Chemie-International Journal of Research in Physical Chemistry & Chemical Physics* **1993**, *180*, 65.
- (104) Wolf, S.; Plenio, H. *Journal of Organometallic Chemistry* **2009**, *694*, 1487.
- (105) Gusev, D. G. *Organometallics* **2009**, *28*, 6458.
- (106) Casasnovas, R.; Frau, J.; Ortega-Castro, J.; Salva, A.; Donoso, J.; Munoz, F. *Journal of Molecular Structure-Theochem* **2009**, *912*, 5.
- (107) Grandberg, I. I.; Faizova, G. K.; Kost, A. N. *Chemistry of Heterocyclic Compounds* **1967**, *2*, 421.
- (108) Kuzmič, P. *Analytical Biochemistry* **1996**, *237*, 260.
- (109) Green, M. L. H.; Wong, L. L.; Sella, A. *Organometallics* **1992**, *11*, 2660.
- (110) Raheem, I. T.; Goodman, S. N.; Jacobsen, E. N. *Journal of the American Chemical Society* **2003**, *126*, 706.
- (111) Achan, J.; Talisuna, A. O.; Erhart, A.; Yeka, A.; Tibenderana, J. K.; Baliraine, F. N.; Rosenthal, P. J.; D'Alessandro, U. *Malaria Journal* **2011**, *10*.
- (112) Kremsner, P. G.; Krishna, S. *The Lancet* **2004**, *364*, 285.
- (113) Corbani, A.; Manousou, P.; Calvaruso, V.; Xirouchakis, I.; Burroughs, A. K. *Digestive and Liver Disease* **2008**, *40*, 794.
- (114) Yang, F.; Hanon, S.; Lam, P.; Schweitzer, P. *American Journal of Medicine* **2009**, *122*, 317.
- (115) Kaufman, E. S. *Journal of Cardiovascular Electrophysiology* **2007**, *18*, 665.
- (116) Innes, G. D.; Vertesi, L.; Dillon, E. C.; Metcalfe, C. *Annals of Emergency Medicine* **1997**, *29*, 126.
- (117) Haghjoo, M.; Arya, A.; Heidari, A.; Sadr-Ameli, M. A. *Journal of Cardiovascular Electrophysiology* **2005**, *16*, 674.
- (118) Belhassen, B.; Viskin, S.; Fish, R.; Glick, A.; Setbon, I.; Eldar, M. *Journal of Cardiovascular Electrophysiology* **1999**, *10*, 1301.
- (119) Krafts, K.; Hempelmann, E.; Skórska-Stania, A. *Parasitology Research* **2012**, *111*, 1.
- (120) Greenwood, B. M.; Bojang, K.; Whitty, C. J. M.; Targett, G. A. T. *The Lancet* **2005**, *365*, 1487.
- (121) Ben-Zvi, I.; Kivity, S.; Langevitz, P.; Shoenfeld, Y. *Clinical Reviews in Allergy and Immunology* **2012**, *42*, 145.

- (122) Nietocaicedo, M. *American Journal of Tropical Medicine and Hygiene* **1956**, *5*, 681.
- (123) Hoekenga, M. T. *American Journal of Tropical Medicine and Hygiene* **1955**, *4*, 221.
- (124) Rolain, J.-M.; Colson, P.; Raoult, D. *International Journal of Antimicrobial Agents* **2007**, *30*, 297.
- (125) Smith, G. D.; Amos, T. A.; Mahler, R.; Peters, T. J. *British Medical Journal (Clinical Research Edition)* **1987**, *294*, 465.
- (126) Tektonidou, M. G.; Laskari, K.; Panagiotakos, D. B.; Moutsopoulos, H. M. *Arthritis & Rheumatism-Arthritis Care & Research* **2009**, *61*, 29.
- (127) Raoult, D.; Houpikian, P.; Dupont, H. T.; Riss, J. M.; Arditi-Djiane, J.; Brouqui, P. *Archives of Internal Medicine* **1999**, *159*, 167.
- (128) Keyaerts, E.; Vijgen, L.; Maes, P.; Neyts, J.; Ranst, M. V. *Biochemical and Biophysical Research Communications* **2004**, *323*, 264.
- (129) Vincent, M.; Bergeron, E.; Benjannet, S.; Erickson, B.; Rollin, P.; Ksiazek, T.; Seidah, N.; Nichol, S. *Virology Journal* **2005**, *2*, 69.
- (130) Erkan, D.; Yazici, Y.; Peterson, M. G.; Sammaritano, L.; Lockshin, M. D. *Rheumatology* **2002**, *41*, 924.
- (131) Johnson, R.; Gharnley, J. *Clinical Orthopaedics and Related Research* **1979**, *144*, 174.
- (132) Geser, A.; Brubaker, G.; Draper, C. C. *American Journal of Epidemiology* **1989**, *129*, 740.
- (133) Fan, C.; Wang, W.; Zhao, B.; Zhang, S.; Miao, J. *Bioorganic & Medicinal Chemistry* **2006**, *14*, 3218.
- (134) Hu, C.; Solomon, V. R.; Ulibarri, G.; Lee, H. *Bioorganic & Medicinal Chemistry* **2008**, *16*, 7888.
- (135) Zhou, Q.; McCracken, M. A.; Strobl, J. S. *Breast Cancer Research and Treatment* **2002**, *75*, 107.
- (136) Lagneaux, L.; Delforge, A.; Carlier, S.; Massy, M.; Bernier, M.; Bron, D. *British Journal of Haematology* **2001**, *112*, 344.
- (137) Mao, X.; Schimmer, A. D. *Toxicology Letters* **2008**, *182*, 1.
- (138) Budimir, A. *Acta Pharmaceutica* **2011**, *61*, 1.
- (139) Bareggi, S. R.; Cornelli, U. *Cns Neuroscience & Therapeutics* **2012**, *18*, 41.

- (140) Deraeve, C.; Pitie, M.; Mazarguil, H.; Meunier, B. *New Journal of Chemistry* **2007**, *31*, 193.
- (141) Ritchie, C. W.; Bush, A. I.; Mackinnon, A.; Macfarlane, S.; Mastwyk, M.; MacGregor, L.; Kiers, L.; Cherny, R.; Li, Q. X.; Tammer, A.; Carrington, D.; Mavros, C.; Volitakis, I.; Xilinas, M.; Ames, D.; Davis, S.; Beyreuther, K.; Tanzi, R. E.; Masters, C. L. *Archives of Neurology* **2003**, *60*, 1685.
- (142) Ding, W. Q.; Liu, B. L.; Vaught, J. L.; Yamauchi, H.; Lind, S. E. *Cancer Research* **2005**, *65*, 3389.
- (143) Oliveri, V.; Giuffrida, M. L.; Vecchio, G.; Aiello, C.; Viale, M. *Dalton Transactions* **2012**, *41*, 4530.
- (144) Hosmane, R. S.; Liebman, J. F. *Structural Chemistry* **2009**, *20*, 693.
- (145) Gero, A.; Markham, J. J. *Journal of Organic Chemistry* **1951**, *16*, 1835.
- (146) Hubig, S. M.; Lindeman, S. V.; Kochi, J. K. *Coordination Chemistry Reviews* **2000**, *200–202*, 831.
- (147) Tagge, C. D.; Bergman, R. G. *Journal of the American Chemical Society* **1996**, *118*, 6908.
- (148) Chin, R. M.; Dong, L.; Duckett, S. B.; Partridge, M. G.; Jones, W. D.; Perutz, R. N. *Journal of the American Chemical Society* **1993**, *115*, 7685.
- (149) Kuhn, L. T.; Bargon, J. In *In Situ Nmr Methods in Catalysis*; Bargon, J., Kuhn, L. T., Eds.; Springer-Verlag Berlin: Berlin, 2007; Vol. 276, p 25.
- (150) Haake, M.; Natterer, J.; Bargon, J. *Journal of the American Chemical Society* **1996**, *118*, 8688.
- (151) Green, R. A.; Adams, R. W.; Duckett, S. B.; Mewis, R. E.; Williamson, D. C.; Green, G. G. R. *Progress in Nuclear Magnetic Resonance Spectroscopy* **2012**, *67*, 1.
- (152) Mishkovsky, M.; Frydman, L. *Annual Review of Physical Chemistry* **2009**, *60*, 429.
- (153) Queiroz Junior, L. H. K.; Giraudeau, P.; dos Santos, F. A. B.; de Oliveira, K. T.; Ferreira, A. G. *Magnetic Resonance in Chemistry* **2012**, *50*, 496.
- (154) Queiroz Junior, L. H. K.; Queiroz, D. P. K.; Dhooghe, L.; Ferreira, A. G.; Giraudeau, P. *Analyst* **2012**, *137*, 2357.
- (155) Giraudeau, P.; Akoka, S. *Journal of Magnetic Resonance* **2010**, *205*, 171.
- (156) <http://madoc.univ-nantes.fr/course/view.php?id=24710> Accessed on 31/01/2013

- (157) Kochanowska-Karamyan, A. J.; Hamann, M. T. *Chemical Reviews* **2010**, *110*, 4489.
- (158) Cardinali, D. P.; Srinivasan, V.; Brzezinski, A.; Brown, G. M. *Journal of Pineal Research* **2012**, *52*, 365.
- (159) Trinkley, K. E.; Nahata, M. C. *Journal of Clinical Pharmacy and Therapeutics* **2011**, *36*, 275.
- (160) Deneris, E. S.; Wyler, S. C. *Nature Neuroscience* **2012**, *15*, 519.
- (161) Mulders, P.; Hawkins, R.; Nathan, P.; de Jong, I.; Osanto, S.; Porfiri, E.; Protheroe, A.; van Herpen, C. M. L.; Mookerjee, B.; Pike, L.; Jurgensmeier, J. M.; Gore, M. E. *European Journal of Cancer* **2012**, *48*, 527.
- (162) Gul, W.; Hamann, M. T. *Life Sciences* **2005**, *78*, 442.
- (163) Manosuthi, W.; Thongyen, S.; Nilkamhang, S.; Manosuthi, S.; Sungkanuparph, S. *AIDS research and therapy* **2012**, *9*, 8.
- (164) Popsavin, M.; Spaic, S.; Svircev, M.; Kojic, V.; Bogdanovic, G.; Popsavin, V. *Bioorganic & Medicinal Chemistry Letters* **2007**, *17*, 4123.
- (165) Siddiqui, N.; Arshad, M. F.; Ahsan, W.; Alam, M. S. *International Journal of Pharmaceutical Sciences* **2009**, *1*, 136.
- (166) Luo, R.; Liu, G.; Liu, W.; Pei, F.; Zhou, Z.; Li, J.; Shen, B.; Kang, P.; Xie, Q.; Ma, X. *International Orthopaedics* **2011**, *35*, 1409.
- (167) Pandeya, S. N.; Sriram, D.; Nath, G.; DeClercq, E. *European Journal of Pharmaceutical Sciences* **1999**, *9*, 25.
- (168) Du, Q. L.; Wang, H. H.; Xie, J. P. *International Journal of Biological Sciences* **2011**, *7*, 41.
- (169) Kwok, J. M.-M.; Myatt, S. S.; Marson, C. M.; Coombes, R. C.; Constantinidou, D.; Lam, E. W.-F. *Molecular Cancer Therapeutics* **2008**, *7*, 2022.
- (170) Bhat, U. G.; Halasi, M.; Gartel, A. L. *Plos One* **2009**, *4*, e5592.
- (171) Halasi, M.; Zhao, H.; Dahari, H.; Bhat, U. G.; Gonzalez, E. B.; Lyubimov, A. V.; Tonetti, D. A.; Gartel, A. L. *Cell Cycle* **2010**, *9*, 1214.
- (172) Theodorides, V. J.; Gyurik, R. J.; Kingsbury, W. D.; Parish, R. C. *Experientia* **1976**, *32*, 702.
- (173) Steinmann, P.; Utzinger, J.; Du, Z. W.; Jiang, J. Y.; Chen, J. X.; Hattendorf, J.; Zhou, H.; Zhou, X. N. *Plos One* **2011**, *6*, e25003.
- (174) <http://www.childrenwithoutworms.org/> Accessed on 20/06/2012
- (175) Khurana, N.; Garg, R. K.; Verma, R.; Malhotra, H. S.; Singh, M. K.; Shukla, R. *Journal of the Neurological Sciences* **2012**, *316*, 36.

- (176) Chesnaye, N.; Sinuon, M.; Socheat, D.; Koporc, K.; Mathieu, E. *Acta Tropica* **2011**, *118*, 21.
- (177) Dobrosotskaya, I. Y.; Hammer, G. D.; Schteingart, D. E.; Maturen, K. E.; Worden, F. P. *Endocrine practice : official journal of the American College of Endocrinology and the American Association of Clinical Endocrinologists* **2011**, *17*, e59.
- (178) Jakesz, R.; Jonat, W.; Gnant, M.; Mittlboeck, M.; Greil, R.; Tausch, C.; Hilfrich, J.; Kwasny, W.; Menzel, C.; Samonigg, H.; Seifert, M.; Gademann, G.; Kaufmann, M. *The Lancet* **2005**, *366*, 455.
- (179) ATAC Trialists' Group *The Lancet* **2005**, *365*, 60.
- (180) Masuda, N.; Sagara, Y.; Kinoshita, T.; Iwata, H.; Nakamura, S.; Yanagita, Y.; Nishimura, R.; Iwase, H.; Kamigaki, S.; Takei, H.; Noguchi, S. *Lancet Oncology* **2012**, *13*, 345.
- (181) Curigliano, G. *Cancer treatment reviews* **2012**, *38*, 303.
- (182) Wadhwa, V. K.; Weston, R.; Parr, N. J. *Bju International* **2010**, *107*, 1923.
- (183) Lehmusvaara, S.; Erkkila, T.; Urbanucci, A.; Waltering, K.; Seppala, J.; Larjo, A.; Tuominen, V. J.; Isola, J.; Kujala, P.; Lahdesmaki, H.; Kaipia, A.; Tammela, T. L. J.; Visakorpi, T. *Journal of Pathology* **2012**, *227*, 336.
- (184) Beardsley, E. K.; Hotte, S. J.; North, S.; Ellard, S. L.; Winqvist, E.; Kollmannsberger, C.; Mukherjee, S. D.; Chi, K. N. *Investigational new drugs* **2012**, *30*, 1652.
- (185) Thomas, C.; Wafa, L. A.; Lamoureux, F.; Cheng, H.; Fazli, L.; Gleave, M. E.; Rennie, P. S. *Prostate* **2012**, *72*, 875.
- (186) Peng, S.; Xiao, Y. L.; Cui, Y.; Lin, J. K.; Zhang, N.; Hu, P. J.; Chen, M. H. *Journal of Gastroenterology and Hepatology* **2012**, *27*, 893.
- (187) Triadafilopoulos, G. *Evidence-based medicine* **2012**, *17*, 17.
- (188) Galmiche, J. P.; Hatlebakk, J.; Attwood, S.; Ell, C.; Fiocca, R.; Eklund, S.; Langstrom, G.; Lind, T.; Lundell, L.; Collaborators, L. T. *Archives of Surgery* **2011**, *146*, 1093.
- (189) Polat, Z.; Kadayifci, A.; Kantarcioglu, M.; Ozcan, A.; Emer, O.; Uygun, A. *European Journal of Internal Medicine* **2012**, *23*, 165.
- (190) Sanchez-Delgado, J.; Garcia-Iglesias, P.; Castro-Fernandez, M.; Bory, F.; Barenys, M.; Bujanda, L.; Lisozaín, J.; Calvo, M. M.; Torra, S.; Gisbert, J. P.; Calvet, X. *Alimentary Pharmacology & Therapeutics* **2012**, *36*, 190.
- (191) Soria, J.-C.; Mok, T. S.; Cappuzzo, F.; Janne, P. A. *Cancer treatment reviews* **2012**, *38*, 416.

- (192) Kundu, S. K.; Nestor, M. *Tumor Biology* **2012**, *33*, 707.
- (193) von Morze, C.; Larson, P. E. Z.; Hu, S.; Yoshihara, H. A. I.; Bok, R. A.; Goga, A.; Ardenkjaer-Larsen, J. H.; Vigneron, D. B. *Magnetic Resonance Imaging* **2012**, *20*, 305.
- (194) Park, I.; Larson, P. E. Z.; Zierhut, M. L.; Hu, S.; Bok, R.; Ozawa, T.; Kurhanewicz, J.; Vigneron, D. B.; VandenBerg, S. R.; James, C. D.; Nelson, S. J. *Neuro-Oncology* **2010**, *12*, 133.
- (195) Mason, S. F. *Journal of the Chemical Society* **1959**, 1247.
- (196) Albert, A.; Phillips, J. N. *Journal of the Chemical Society* **1956**, 1294.
- (197) Albert, A.; Goldacre, R.; Phillips, J. *Journal of the Chemical Society* **1948**, 2240.
- (198) Watson, G. K.; Houghton, C.; Cain, R. B. *Biochemical Journal* **1974**, *140*, 265.
- (199) Jaffe, H. H.; Doak, G. O. *Journal of the American Chemical Society* **1955**, *77*, 4441.
- (200) Deng, F.; Testa, A. C. *Journal of Photochemistry and Photobiology a-Chemistry* **1998**, *112*, 191.
- (201) Angyal, S. J.; Angyal, C. L. *Journal of the Chemical Society* **1952**, 1461.
- (202) Handloser, C. S.; Chakrabarty, M. R.; Mosher, M. W. *Journal of Chemical Education* **1973**, *50*, 510.
- (203) Housecroft, C. E.; Sharpe, A. G. *Inorganic Chemistry*; 2nd ed.; Pearson Education Limited, 2005.
- (204) Plater, M. J.; Barnes, P.; McDonald, L. K.; Wallace, S.; Archer, N.; Gelbrich, T.; Horton, P. N.; Hursthouse, M. B. *Organic & Biomolecular Chemistry* **2009**, *7*, 1633.
- (205) de la Fuente, M. C.; Domínguez, D. *Tetrahedron* **2009**, *65*, 3653.
- (206) Takechi, H.; Kusano, M.; Yuki Gosei Kogyo Co., Ltd., Japan . 2011, p 9pp.
- (207) Passarella, D.; Belinghieri, F.; Scarpellini, M.; Pratesi, G.; Zunino, F.; Gia, O. M.; Via, L. D.; Santoro, G.; Danieli, B. *Bioorganic & Medicinal Chemistry* **2008**, *16*, 2431.
- (208) Watson, S. E.; Markovich, A. *Heterocycles* **1998**, *48*, 2149.
- (209) Chavarot, M.; Socquet, S.; Kotera, M.; Lhomme, J. *Tetrahedron* **1997**, *53*, 13749.
- (210) Solomons, T. W. G.; Fryhle, C. B. *Organic Chemistry*; 9th ed., 2007.

- (211) Guthrie, J. P. *Canadian Journal of Chemistry* **1978**, *56*, 2342.
- (212) Fogg, P. G. T.; Gerrard, W. *Solubility of Gases in Liquids*
- (213) Iggo, J. A.; Shirley, D.; Tong, N. C. *New Journal of Chemistry* **1998**, *22*, 1043.
- (214) Liu, Q.; Takemura, F.; Yabe, A. *Journal of Chemical & Engineering Data* **1996**, *41*, 1141.
- (215) Herde, J. L.; Lambert, J. C.; Senoff, C. V. *Inorganic Synthesis* **1974**, *15*, 18.
- (216) Uson, R.; Oro, L. A.; Cabeza, J. A. *Inorganic Chemistry* **1985**, *23*, 128.
- (217) Hermann, W. A.; Kocher, C.; Gooben, L. J.; Artus, G. R. J. *Chemistry – A European Journal* **1996**, *2*, 1627.
- (218) Vazquez-Serrano, L. D.; Owens, B. T.; Buriak, J. M. *Chemical Communications* **2002**, 2518.
- (219) Seber, G. A. F.; Wild, C. J. *Nonlinear Regression*; Wiley: New York, 1989.
- (220) Hindmarsh, A. C. *Scientific Computing* Amsterdam, North Holland, 1983.
- (221) Kreyszig, E. *Advanced Engineering Mathematics*; 7th ed.; John Wiley: New York, 1993.
- (222) *Methods in Enzymology - Computer Methods, Part B*, 2009; Vol. 467.
- (223) Dolomanov, O. V.; Bourhis, L. J.; Gildea, R. J.; Howard, J. A. K.; Puschmann, H. *Journal of Applied Crystallography* **2009**, *42*, 339.
- (224) Sheldrick, G. *Acta Crystallographica Section A* **2008**, *64*, 112.